Physics of the Solid State, Vol. 45, No. 3, 2003, pp. 409–413. Translated from Fizika Tverdogo Tela, Vol. 45, No. 3, 2003, pp. 385–389.

METALS AND SUPERCONDUCTORS

Phase Diagram of a Wide Current-Carrying Superconducting Film

A. N. Artemov and Yu. V. Medvedev

Donetsk Physicotechnical Institute, National Academy of Sciences of Ukraine, Donetsk, 83114 Ukraine

e-mail: medvedev@kinetic.ac.donetsk.ua

Received December 14, 2001; in final form, May 18, 2002

Abstract—A model of current heating of a wide superconducting film is suggested assuming nonlinearity of the film conductance. Within this model, the parameters of the film can be characterized by a single dimensionless coefficient of thermal balance which includes both thermal and resistive parameters of the system. The stability of the state of the current-carrying film is analyzed. A phase diagram of the film is constructed in terms of the coefficient of thermal balance and the average current density. The propagation velocity of a stationary nonuniform temperature distribution in the film is calculated as a function of current density at various values of the coefficient of thermal balance. © *2003 MAIK "Nauka/Interperiodica".*

1. INTRODUCTION

A current-carrying type-II superconductor is a rather complex object. Depending on temperature and current density, it can exhibit a superconducting, resistive, or normal state. Its states can also be homogeneous and inhomogeneous, as well as stationary and nonstationary. Experimental and theoretical studies of the states of the superconductor, their stability, and the physical processes responsible for these states are widely discussed in the literature [1]. However, many aspects of the behavior of a superconductor with a current remain unstudied. One of such topical problems is related to current-carrying wide superconductive films.

Thermal or electromagnetic influences on type-II superconductors can stimulate the occurrence of self-maintained nonuniform dissipative regions in them [1–6]. The evolution of these regions manifests itself in the variety of current–voltage (*I–V*) characteristics (see, e.g., [4]) and may result in the transition of the whole sample into resistive and normal states or in the restoring of the dissipative state. Such transitions are accompanied by the propagation of "switching waves" through the sample. The calculation of the velocities of these waves allows one to describe, under particular simplifying assumptions, the development of excitations in superconductors [7–10] in both the presence and absence of a magnetic field. In the latter case, the instability of the superconducting state is related to the nonisothermal dynamics of magnetic vortices penetrating into the sample due to the magnetic field created by the current.

In the general case of nonisothermal dynamics of magnetic flux, analysis of the destruction (restoration) of the superconducting properties of a current-carrying element requires the use of the equation of thermal balance and the model description of the resistivity ρ of a resistive region in order to characterize the power of heat source $\dot{Q}(J, T)$ in the conductor. For composite superconductors and narrow superconductive films, this analysis is commonly simplified by using a one-dimensional heat conduction equation under the assumption of linear surface heat removal [$W(T) = h(T - T_0)$, where h is the coefficient of heat transfer and T_0 is the temperature of the thermostat] and of the resistivity being a step function of temperature [1]. However, in high-temperature superconductors with a layered structure, a topological phase transition can occur, which is inherent in two-dimensional systems. In this case, it is important to take into account the nonlinear dependence of ρ on current density J. Nonlinearity of the function $\rho(J)$ in highly anisotropic layered systems is caused by internal physical processes, namely, by dissociation of fluctuation-induced pairs of the vortex–antivortex type under the action of a current. Nonlinearity determines the condition for the existence and stability of uniform and nonuniform stationary states [11, 12].

A similar mechanism of nonlinearity can be observed in wide superconducting films carrying a current. The resistivity in such systems is caused by the motion of magnetic vortices penetrating through the film edge under the action of the Lorentz force. The flux flow resistivity ρ_f, responsible for the resistive losses, depends on the concentration of vortices n_v in the superconductor: $\rho_f \sim \rho_n \pi \xi^2 n_v$. The concentration of vortices surmounting the edge barrier and entering the sample is a function of the current density flowing in the sample. This dependence is the main cause of the nonlinearity of resistive losses in wide superconducting films.

1063-7834/03/4503-0409$24.00

The authors of [2] considered the kinetics of flux flow in wide films and their I–V characteristics and found that the time-averaged longitudinal electric field E in a resistive region is a nonlinear function of the average current density in the film (in the absence of vortex pinning) and has the form

$$E = \rho_n J f(J, T), \quad (1)$$

$$f(J, T) = (1 - J_c/J)/[1 - J_c/J + A(J, T)], \quad (2)$$

where ρ_n is the resistivity of the film in a normal state, J_c is the average density of the critical current I_c for the onset of dissipation in the film, $A(J, T) = \alpha(J_c/J)[(T_c - T)/T_c]^{3/2}$, α is a dimensionless constant of the order of unity, and T_c is the critical temperature of the superconductor.

The present article is devoted to the study of the evolution of stationary states of a wide superconducting film associated with the process of heat production due to dissipative effects of viscous motion of magnetic flux. We use a model expression for the power of the heat source $\dot{Q}(J, T)$ which generalizes the results obtained in [2].

Within the model proposed, the phase diagram of the film is constructed to show the dependence of the film state on the average current density and on the coefficient of thermal balance, which includes both the thermal characteristics of the substrate and the superconductor parameters determining the heat production power. In addition, nonuniform stationary solutions are found, namely, superconducting–normal and superconducting–resistive phase switching waves (S–N and S–R waves, respectively), similar to those considered in [11]. The propagation velocities of these waves as a function of current density in the film are also found.

2. MODEL

If the vortices that have penetrated into the film move perpendicular to the direction of the current and the thermal length is considerably larger than all characteristic lengths of the sample, then the state of the superconducting film can be studied by using a one-dimensional equation of heat transfer:

$$D_s C_s \frac{\partial T}{\partial t} = D_s k_s \frac{\partial^2 T}{\partial x^2} + d_f \dot{Q}(J, T) - W(T). \quad (3)$$

Here, D_s is the substrate thickness; C_s and k_s are the specific heat and heat conductivity of the substrate, respectively; d_f is the film thickness; and the x axis coincides with the current direction. The rate of heat removal is assumed to be a linear function:

$$W(T) = h(T - T_0), \quad (4)$$

where $h = k_s/D_s$ is the effective coefficient of heat removal.

All calculations of thermal processes will be made by ignoring the heating nonuniformity across the sample width caused by the nonuniformity of current distribution [13]. This means that the current density in Eq. (3) is averaged over the cross section of the film. For a large resistive region, this approximation is quite justified, because the current has enough time to be redistributed and become uniform over the region; the heat production, being a function of the current, also becomes almost constant along the vortex path.

The function $\dot{Q}(J, T)$, describing the heat production, is a local function and depends on the current density and temperature at a given point of the film. We are interested in solutions to Eq. (3) that describe inhomogeneous states. In this case, superconducting, resistive, and normal states can simultaneously exist in the film. The function $\dot{Q}(J, T)$ accounts for these possible states; it is a piecewise continuous function and can be written as $\dot{Q}(J, T) = \rho_n J^2 f(J, T)$, where the function $f(J, T)$ has the form

$$f(J, T) = \begin{cases} 1, & T \geq T_n \\ (1 - J_c/J)/[1 - J_c/J + A(J, T)], & T_n \geq T \geq T_r \\ 0, & T \leq T_r. \end{cases} \quad (5)$$

Our definition of the nonlinear function $f(J, T)$ is somewhat different from Eq. (2) used in [2]. We take into account that the film transforms into the normal state not at the temperature T_c, as assumed in [2], but at T_n, where the average current density J becomes equal to the dispairing current density J_{GL}. For this reason, we redefine the quantity α in $f(J, T)$ and assume it to be not a constant but rather dependent on the current density. This quantity becomes equal to zero at the temperature T_n (which is always lower than T_c) and has the form $\alpha = 1 - J/J_{LG}(T)$. The temperature of the transition of the film to the resistive state T_r is determined by the relation $J = J_c(T_r)$.

The model proposed contains many parameters describing the resistive properties of the superconductor and the thermal characteristics of the substrate. In order to derive universal dependences of the properties of our model on these parameters, we conveniently write the equations in a dimensionless form. For this reason, we introduce the dimensionless variables

$$l = \frac{x}{D_s}, \quad \tau = \frac{k_s}{C_s D_s^2} t,$$

$$\theta = \frac{T}{T_c}, \quad j = \frac{J}{J_c(0)}$$

and the dimensionless coefficient of thermal balance

$$\eta = \frac{k_s}{D_s}\frac{T_c}{d_f \rho_n J_c^2(0)},$$

which depends both on the resistive properties of the film (ρ_n, $J_c(0)$, d_f) and on the conditions of heat removal (k_s, D_s). In this notation, the basic equation of our model takes the form

$$\frac{\partial \theta}{\partial \tau} = \frac{\partial^2 \theta}{\partial l^2} + \dot{q}(j, \theta) - w(\theta), \qquad (6)$$

where $\dot{q}(j, \theta) = \eta^{-1} j^2 f(j, \theta)$ is the dimensionless power of heat production and $w(\theta) = \theta - \theta_0$ is the rate of heat removal. Now, it is clearly seen that the basic parameters of the superconductor and the substrate are combined into a single parameter η which, therefore, determines the behavior of the model. Apart from this coefficient, the model is also characterized by the dimensionless dispairing current $j_{GL} = J_{GL}/J_c(0)$ and the dimensionless temperature of the thermostat $\theta_0 = T_0/T_c$. Such a reduction in the number of essential parameters of the model considerably facilitates the understanding of how the properties of the superconductor and substrate affect the behavior of the whole system.

3. STATIONARY STATES OF A WIDE SUPERCONDUCTING FILM CARRYING A CURRENT

The character of stationary solutions to thermal conduction equation (6) depends on the number and character of its singular points determined by the condition

$$\dot{q}(\theta) - w(\theta) = 0. \qquad (7)$$

Depending on the parameters and the magnitude of the current, there can exist a single or three singular points in our model. In the former case, we have a stable superconducting, resistive, or normal state. The criterion of stability is the inequality $\partial w/\partial\theta > \partial\dot{q}/\partial\theta$. In this case, only homogeneous states can be stable and stationary.

If Eq. (7) has three roots, stable states correspond to the maximum and the minimum root (θ_1, θ_2), whereas the third root θ_3 ($\theta_1 < \theta_3 < \theta_2$) corresponds to an unstable state. In this temperature range, along with the uniform states mentioned above, there can exist a nonuniform stable state, which is called a switching wave between the θ_1 and θ_2 states. The switching wave is a self-similar solution to Eq. (6) and represents a nonuniform temperature distribution. This distribution moves with a constant velocity v which is an eigenvalue of Eq. (6). The features of such solutions are considered in the next section.

In this section, we study the regions of existence of various types of stable stationary states depending on the average current density j and the magnitude of the effective thermal balance coefficient η. In actual experiments, the coefficient η can be altered by varying the conditions of heat removal, which depend on the material, quality, and thickness of the substrate (k_s, D_s), as well as on the heat production conditioned by the material of the superconductor, i.e., by the parameters T_c, J_c, ρ_n, and d_f. By varying the parameter η by choosing various materials and changing the quality and the width of the substrate and the film, one can create and change the width of a bistable region of the superconductor and also change the region of stability of uniform states.

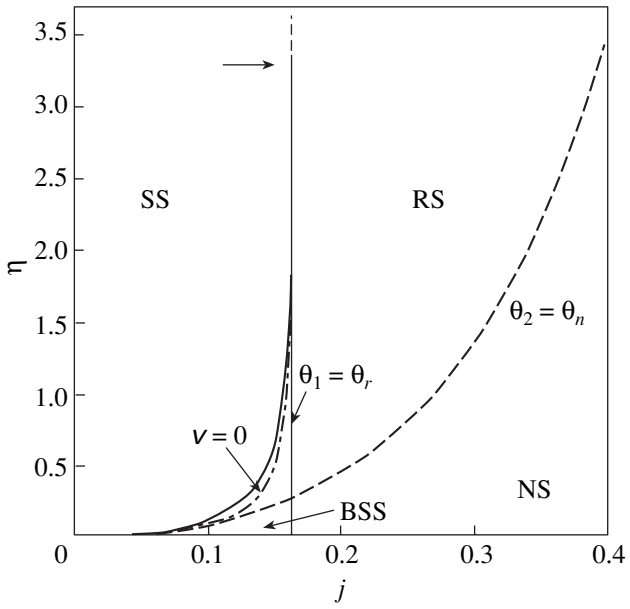

Fig. 1. Phase diagram of a wide superconducting film carrying a current constructed in the plane of the thermal balance coefficient η and the average current density j.

In calculations, we assumed the temperature dependence of the critical current to have the form $j_c(\theta) = (1 - \theta)$ (see [14, 15]) and the temperature dependence of the dispairing current to be $j_{GL}(\theta) = 10(1 - \theta)^{3/2}$ [16]. The temperature of the thermostat was taken to be $\theta_0 = 0.837$.

Figure 1 illustrates the phase diagram of the superconductor in the space of parameters η and j for the model considered. This diagram shows the regions of existence of all stable stationary uniform and nonuniform states of the wide superconducting film. The film can be in a uniform superconducting (SS), resistive (RS), or normal (NS) state. The solid lines bound the region of a bistable state (BSS) with a uniform or nonuniform temperature distribution. With an increase in the effective coefficient of thermal balance, the right and left boundaries of the BSS region approach each other and merge together at $\eta \approx 3.29$. This point is indicated in Fig. 1 by a horizontal arrow. Outside this region, only uniform states of the superconducting film

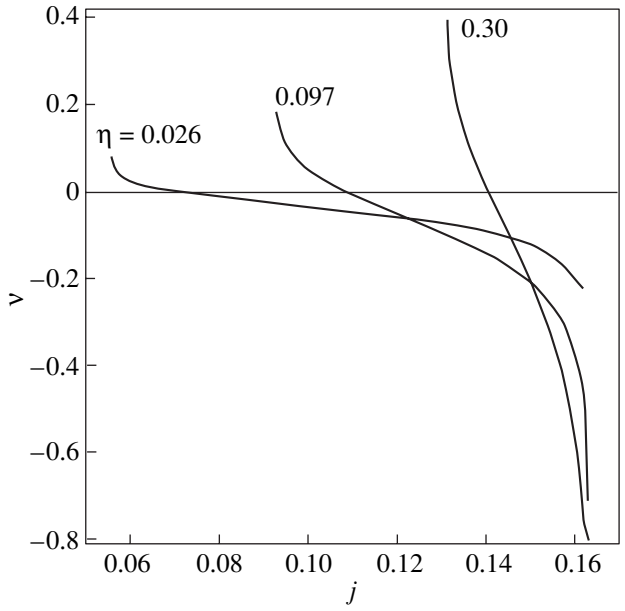

Fig. 2. The velocity of switching wave ν as a function of average current density j at various values of thermal balance coefficient η.

carrying a current can be stable. Dashed lines separate SS and RS regions ($\theta_1 = \theta_r$), as well as the RS and NS regions ($\theta_2 = \theta_n$).

Two nonuniform solutions (S–R and S–N switching waves) can exist in the BSS region. The region at the bottom of the diagram corresponding to the temperature θ_1 is always superconducting. The region at the top (θ_2) can be resistive above the dashed line $\theta_2 = \theta_r$ and normal below this line. The dot-and-dashed line corresponds to the values of the thermal balance coefficient and current density for which the velocity of the switching wave is equal to zero. To the left of this line, the wave moves towards the resistive or normal state and switches the whole sample to the superconducting state. This is the region of absolute stability of the superconducting state of the wide film. To the right of this line, the switching wave sets the sample either in the resistive or in the normal state. Here, inside the BSS region, the uniform superconducting state is metastable.

4. THERMAL STABILITY OF THE SUPERCONDUCTING STATE

In this section, nonuniform stationary solutions of Eq. (6) are considered. Such solutions can exist within the range of model parameters where Eq. (7) has three roots. In this case, the two edge singular points (θ_1, θ_2) in the phase plane are stable saddles, while the third one (θ_3) is an unstable node [17]. Let us consider the stationary solutions to Eq. (6) in the form $\theta(l, \tau) = \theta(l - v\tau)$ with the boundary conditions

$$\theta(l = -\infty, \tau) = \theta_1, \quad \theta(l = +\infty, \tau) = \theta_2,$$

$$\frac{\partial\theta}{\partial l}(l = \pm\infty, \tau) = 0.$$

According to [17, 18], the only stable stationary solution of this type is the solution corresponding to a separatrix going from one saddle to the other. This solution corresponds to a nonuniform temperature distribution moving with a constant velocity ν. The lowest temperature region of this solution always corresponds to a superconducting state. A high-temperature region can be either resistive or normal depending on the values of the current and parameters of the model.

The dependence of the propagation velocity of the wave in the nonuniform state on the current density in the film at various values of thermal balance coefficient η is shown in Fig. 2. At small values of the current, the boundary moves in the positive direction of the l axis from the superconducting to the normal phase. In the course of this motion, the superconducting region expands. This means that the superconducting phase is absolutely stable at small values of the current; that is, a fluctuation region of the normal (resistive) phase collapses in the course of time. At a certain value of the current, the velocity of boundary motion changes sign, which means that the switching wave begins to move towards the superconducting phase, thus switching the sample to the normal (resistive) state. Figure 1 shows how the thermal balance coefficient affects the magnitude of the current at which the wave velocity v is zero. The dimensionless velocity ν is related to the dimensional velocity ν by the expression $v = (k_s/C_sD_s)\nu$.

It can be seen from the curves in Fig. 2 that, with increasing the effective coefficient of heat removal $h = k_s/D_s$, as well as with decreasing the quantity $d_f\rho_n J_c^2(0)/T_c$, the interval of currents corresponding to the existence of nonuniform solutions narrows (Fig. 1) and the maximum velocity of the switching wave at the bounds of the current interval increases.

5. CONCLUSION

In conclusion, we note that the nonuniform states in the wide-film model differ from the analogous states in the model of a layered superconductor [11, 12]. In the latter case, the lower θ_1 state can be either superconducting or resistive. In our wide-film model, this state can be only superconducting. Formally, this can be explained by the fact that the derivative $\partial\dot{q}/\partial\theta$ in our model has a discontinuity at the temperature θ_r at which the film transforms into a resistive state. In this case, the line separating the superconductive and resistive states on the phase diagram ($\theta_1 = \theta_r$ line in Fig. 1) merges with the right-hand boundary of the BSS region. The exper-

imental study of this peculiarity is hampered, since the voltage across the sample near the resistivity threshold is so small that it is below the level of thermal noise. Therefore, an unambiguous solution of this problem requires additional theoretical and experimental studies of the current states of superconducting films.

ACKNOWLEDGMENTS

This study was supported by the Ministry of Education and Science of Ukraine, project no. 2M/71-2000.

REFERENCES

1. R. G. Mints and A. L. Rakhmanov, *Instabilities in Superconductors* (Nauka, Moscow, 1984).
2. Yu. M. Ivanchenko and P. N. Mikheenko, Zh. Éksp. Teor. Fiz. **82** (2), 488 (1982) [Sov. Phys. JETP **55**, 281 (1982)].
3. Yu. M. Ivanchenko and P. N. Mikheenko, Zh. Éksp. Teor. Fiz. **83** (2), 684 (1982) [Sov. Phys. JETP **56**, 380 (1982)].
4. I. M. Dmitrenko, Fiz. Nizk. Temp. **22** (8), 849 (1996) [Low Temp. Phys. **22**, 648 (1996)].
5. V. G. Volotskaya, I. M. Dmitrenko, L. E. Musienko, and A. G. Sivakov, Fiz. Nizk. Temp. **7** (3), 383 (1981) [Sov. J. Low Temp. Phys. **7**, 188 (1981)].
6. I. M. Dmitrenko, V. G. Volotskaya, I. E. Musienko, and A. G. Sivakov, Physica B & C (Amsterdam) **108** (1–3), 783 (1981).
7. N. A. Buznikov and A. A. Pukhov, Pis'ma Zh. Tekh. Fiz. **24** (2), 22 (1998) [Tech. Phys. Lett. **24**, 51 (1998)].
8. A. A. Elistratov and I. L. Maksimov, Fiz. Tverd. Tela (St. Petersburg) **42**, 196 (2000) [Phys. Solid State **42**, 201 (2000)].
9. N. A. Taĭlanov and U. T. Yakhshiev, Fiz. Tverd. Tela (St. Petersburg) **43**, 396 (2001) [Phys. Solid State **43**, 413 (2001)].
10. N. A. Taĭlanov and U. T. Yakhshiev, Fiz. Tverd. Tela (St. Petersburg) **44**, 17 (2002) [Phys. Solid State **44**, 16 (2002)].
11. I. L. Maksimov and D. Yu. Vodolazov, Pis'ma Zh. Tekh. Fiz. **24** (21), 1 (1998) [Tech. Phys. Lett. **24**, 829 (1998)].
12. A. N. Artemov and Yu. V. Medvedev, Fiz. Nizk. Temp. **28**, 349 (2002) [Low Temp. Phys. **28**, 242 (2002)].
13. S. V. Lempitskiĭ, Zh. Éksp. Teor. Fiz. **90** (2), 793 (1986) [Sov. Phys. JETP **63**, 462 (1986)].
14. R. Glover and H. Coffey, Rev. Mod. Phys. **36**, 299 (1964).
15. A. Yu. Larkin and Yu. N. Ovchinnikov, Zh. Éksp. Teor. Fiz. **61**, 1221 (1971) [Sov. Phys. JETP **34**, 651 (1971)].
16. V. L. Ginzburg, Dokl. Akad. Nauk SSSR **118**, 464 (1958) [Sov. Phys. Dokl. **3**, 102 (1958)].
17. V. A. Vasil'ev, Yu. M. Romanovskiĭ, and V. G. Yakhno, *Auto-Wave Processes* (Nauka, Moscow, 1987).
18. Ya. I. Kanel', Mat. Sb. **59**, 245 (1962).

Translated by A. Zalesskiĭ

Physics of the Solid State, Vol. 45, No. 3, 2003, pp. 414–418. Translated from Fizika Tverdogo Tela, Vol. 45, No. 3, 2003, pp. 390–394.

SEMICONDUCTORS AND DIELECTRICS

Impurity Bands in the CdI_2–PbI_2 Crystal System

A. V. Gloskovskiĭ, M. R. Panasyuk, L. I. Yaritskaya, and N. K. Gloskovskaya

Franko L'vov State University, L'vov, 79005 Ukraine

e-mail: nglos@bigfoot.com

Received April 16, 2002

Abstract—The absorption spectra and photo- and dark conductivity of the CdI_2–PbI_2 system are investigated in the temperature range 4.2–300 K. The temperature dependence of the photoluminescence and the IR stimulation spectra of luminescence and induced photoconductivity at 4.2 K are also studied. The results are interpreted by considering microphase inclusions of PbI_2 into the CdI_2 crystal lattice as activator centers. An energy-level diagram in which the narrow band of the PbI_2 microphase genetically related to the metastable $^3P_0$ level of lead plays a significant role is presented for this crystal system. © *2003 MAIK "Nauka/Interperiodica".*

1. INTRODUCTION

Layered systems are a subject of special attention in the physics of semiconductors. Artificial layered systems, whose properties are relatively easily controlled by external influences, are used in integrated electronics. Natural layered systems are particularly interesting from the scientific and applied viewpoints.

The CdI_2–PbI_2 crystal system is produced from layered compounds of the same structure type with similar lattice parameters: a = 4.24 Å and c = 6.84 Å for CdI_2 and a = 4.56 Å and c = 6.96 Å for PbI_2.

Starting with the first investigations of CdI_2 crystals, the absorption band in the vicinity of 3.23 eV characterized by a small half-width and temperature stability of its spectral position has attracted attention. This band was attributed in [1] to electron transitions in one of the polymorphic modifications of CdI_2. Later [2], the relationship between the lead impurities in CdI_2 crystals and the band at 3.23 eV was proved and a model was proposed for the $A_{1g} \longrightarrow A_{2u}$, E_u transition, which occurs in lead ions that isomorphically replace cadmium in the regular sites of the CdI_2 crystal lattice and is genetically related to the $^1S_0 \longrightarrow {}^1P_1$ transition in the free Pb^{2+} ion. Later on, this band was attributed to the ^3E_u and $^3A_{2u}$ low-energy states of the lead ion corresponding to the $^3P_1$ level of the free Pb^{2+} ion [3]. In addition, the model of the donor–acceptor pair was proposed in [4] and the relationship between this band and line defects of the crystal structure was established [5].

Investigations of the Raman scattering spectra [6] led to the conclusion that, for $0.1 < x < 1$, the $Pb_xCd_{1-x}I_2$ crystal system is formed in such a way that the CdI_2 and PbI_2 layers are built in without mixing; moreover, this property is typical of most layered systems. For $x < 0.1$, we suggested a model of the island center in the form of an interlayer of a phase inclusion of $2H$-PbI_2 into the $4H$-CdI_2 crystal lattice [7, 8]; for the band at 3.23 eV, we proposed a model of the $A_4^+ \longrightarrow A_{5+6}^-$ excitonic transition in PbI_2 disturbed by the crystal field of the CdI_2 lattice.

In this paper, we continue the investigations reported in [7–9]. We study the absorption spectra and photo- and dark conductivities of the CdI_2–PbI_2 system in the temperature range 4.2–300 K, the temperature dependence of the photoluminescence, and the IR stimulation spectra of photoluminescence and induced conductivity at 4.2 K. An energy-level diagram of the CdI_2–PbI_2 crystal system at this temperature is proposed.

2. EXPERIMENTAL TECHNIQUE

The crystals to be investigated were grown using the Stockbarger method in evacuated sealed ampules. PbI_2 impurities were introduced into a CdI_2 batch in an amount not exceeding 10 mol %. Samples $5 \times 10 \times 0.15$ mm in size were cut from the grown crystals along the cleavage plane.

The absorption spectra of the crystals were recorded in the temperature range 4.2–300 K using a MDR-12 monochromator. To measure the photoconductivity of the CdI_2–PbI_2 crystals, a xenon DKsSh-1000 lamp was used as an excitation source; exciting light of the necessary wavelength was separated using an SF-4 monochromator. Gallium–indium contacts were deposited on the crystal surface; the applied voltage was varied from 100 to 250 V. The photocurrent was detected in the direction perpendicular to the crystallographic axis using a V7-30 electrometer.

To investigate the IR stimulation spectra of photoluminescence and induced conductivity, the exciting light was decomposed into a spectrum using the monochromator of an SF-4 spectrophotometer and a 300-W

quartz incandescent lamp was used as a light source; the spectrum was normalized by a thermopile.

3. EXPERIMENTAL RESULTS

Figure 1 shows the absorption spectra of a crystal of CdI_2–10^{-3} mol % PbI_2 (in the batch) at temperatures 4.2, 77, 108, and 208 K (curves *1–4*, respectively). The fundamental absorption edge of CdI_2 is associated with indirect interband transitions. The absorption band in the vicinity of 3.23 eV has a structure; the position and the halfwidth of its maximum are temperature-dependent. It can be seen from Fig. 1 that, at 208 K, the activator band overlaps with the fundamental absorption edge of CdI_2 (curve *4*) and, in the temperature range 4.2–108 K (curves *1–3*), the overlapping is absent.

When CdI_2–PbI_2 crystals are irradiated in the vicinity of the impurity absorption band at 3.23 eV, both photoluminescence and photoconductivity are observed. The spectral distribution of the photoluminescence is temperature-dependent. At room temperature, the long-wavelength emission band in the vicinity of 2.07 eV is mainly excited; its intensity attains a maximum at the liquid-nitrogen temperature. With decreasing temperature, an emission band with a maximum at 2.38 eV appears; the intensity of the band sharply increases in the temperature range 36–38 K. As the temperature is decreased further to the liquid-helium temperature, the intensity of the narrow emission band in the vicinity of 3.13 eV grows. The temperature dependence of the photoluminescence intensity of CdI_2–PbI_2 crystals excited at E = 3.23 eV is shown in Fig. 2b for different emission bands.

For comparison, the temperature dependence of the photoconductivity of a CdI_2–0.1 mol % PbI_2 crystal (in the batch) excited at E = 3.23 eV is shown in Fig. 2a: the decrease in the photoconductivity at 100 K changes to photocurrent activation at 60 K; the photoconductivity increases by more than three times and then decreases at $T < 20$ K. For the crystals under investigation, the magnitude of the dark current in the temperature range 4.2–100 K is 10^{-13} A.

Figure 3 shows the stimulation spectra of luminescence (curve *2*) and induced conductivity (curve *1*) at 4.2 K after preliminary excitation of the crystals at E = 3.23 eV. The maxima of these spectra are at 0.85 and 1.25 eV; steps are pronounced at the excitation energies 1.6–1.75 and 1.8 eV (curve *1*). The IR stimulation spectrum of luminescence exhibits a minimum at 0.9 eV and a wide band in the range 1.2–1.8 eV (curve *2*). A comparison of curves *1* and *2* shows that the same trapping centers are obviously revealed in the IR stimulation spectra of luminescence and induced conductivity. The induced conductivity is mainly due to the charge carriers released by radiation at 0.85 and 1.25 eV, while the stimulated luminescence is due to the charge carriers released by radiation in the range 1.2–1.8 eV.

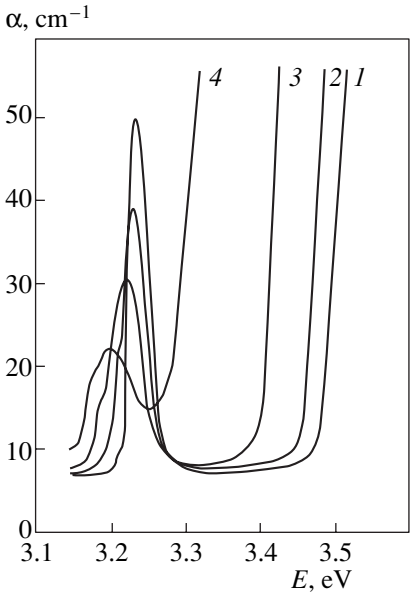

Fig. 1. Absorption spectra of a CdI_2–10^{-3} mol % PbI_2 crystal at different temperatures: (*1*) 4.2, (*2*) 77, (*3*) 108, and (*4*) 208 K.

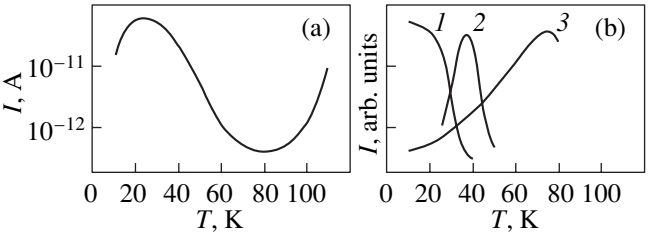

Fig. 2. Temperature dependence of (a) photoconductivity and (b) photoluminescence of a CdI_2–PbI_2 crystal at excitation energy E = 3.23 eV for luminescence bands at (*1*) 3.13, (*2*) 2.38, and (*3*) 2.07 eV.

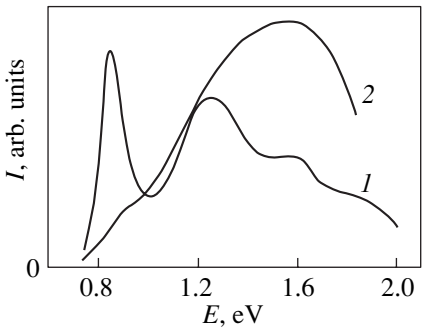

Fig. 3. IR stimulation spectra of (*1*) conductivity and (*2*) luminescence of a CdI_2–PbI_2 crystal after its preliminary excitation in the vicinity of 3.23 eV.

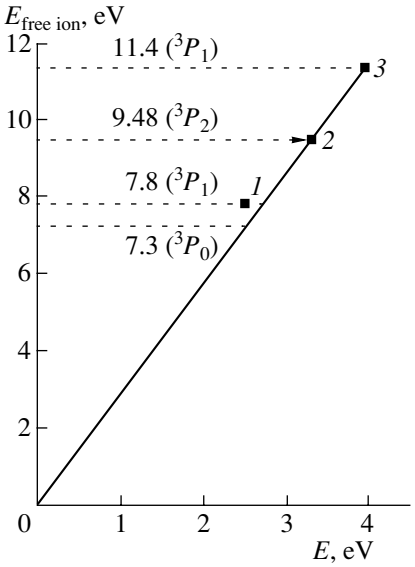

Fig. 4. Relationship between the energy of the low-energy cation excitons of PbI_2 and the energy of the corresponding electronic states of the free lead ion.

4. DISCUSSION

Most of the published results indicate that lead is present even in the most carefully purified CdI_2 crystals: the optical absorption spectra and, particularly, the stimulation spectrum of luminescence contain a band at 3.23 eV, which arises due to lead [1–5]. An x-ray structure analysis of CdI_2 crystals containing less than 10% PbI_2 established [8] that from one to two thirds of the lead introduced into a crystal is in the form of the compound PbI_2 and that the rest is in the form of atoms or ions [8]. Since the lead introduced into the crystal can be in different forms, the model describing the lead luminescence center in the CdI_2–PbI_2 crystal system is open to question.

The possible formation of PbI_2 microphase inclusions in the CdI_2 crystal lattice follows from both the crystal-growth technique used and the physicochemical parameters of these compounds. In CdI_2–PbI_2 crystals grown from a melt using the Stockbarger method, the lead can form complexes. Due to the large density of the PbI_2 compound (in comparison with CdI_2), it concentrates in the vicinity of the crystallization front, and the higher crystallization temperature of the PbI_2 compound (685 K) in comparison with that for CdI_2 (661 K) should cause PbI_2 to precipitate first in the form of microcrystal inclusions in the growing CdI_2 crystal. Moreover, the differences in the electron configurations of Pb^{2+} and Cd^{2+} ($6s^2$ and $5p^6$) and in their ionic radii (1.2 and 0.98 Å, respectively) also do not correspond to the conditions of isomorphic substitution for these ions.

At the same time, a number of characteristics of the band at 3.23 eV do not make it possible to relate this band to the classical model of the lead ion isomorphically replacing the cation in the regular site of the CdI_2 crystal lattice. Among these characteristics are the small half-width of the band, the negligible temperature shift of its maximum, and the predominance of 100 cm^{-1} PbI_2 phonons in the electron–phonon structure of this band [2]. In addition, the increase in the photoluminescence of the CdI_2–PbI_2 system observed in this work in the temperature range 20–60 K cannot be explained in terms of the classical model of an isolated activator center.

At the same time, it is known that the localization of electrons and holes in the same crystal layer can lead to very significant excitonic effects [10]. In developing the model of exciton transition for the band at 3.23 eV [7], the increase in the photoluminescence of the CdI_2–PbI_2 system at very low temperatures may be attributed to the strong exciton–phonon interaction typical of CdI_2. In CdI_2 and PbI_2 layered crystals, the efficiency of the exciton scattering on lattice deformations associated with bending vibrations increases in this low-temperature range. At temperatures from 4.2 to 45 K, for example, the interaction of free PbI_2 excitons with bending vibrations of the lattice was observed in [11]. For $T <$ 50 K, it was established that the bending vibrations in 2*H*- and 4*H*-PbI_2 and 4*H*-CdI_2 play an important role in the NQR spin–lattice relaxation for the halogen nuclei in these layered crystals [12].

In addition, a sharp change in the spectral distribution of the photoluminescence in the CdI_2–PbI_2 crystals investigated is revealed in this temperature range (Fig. 2b). The absorption band at 2.43 eV exhibited at temperatures from 36 to 38 K is also interpreted in [3] in terms of the model of radiative exciton decay, though the nature of the decay is related to the excitation of the CdI_2 crystal lattice in the vicinity of the lead ion.

We suppose that the results of the investigation of the temperature dependence of the photoconductivity and photoluminescence support the interpretation of the absorption band at 3.23 eV in the CdI_2–PbI_2 crystal system being a manifestation of the cation exciton in the PbI_2 interlayer built into the 4*H*-CdI_2 crystal lattice. The lowest energy excitonic states of the PbI_2 crystal have been well investigated, and their cation nature has been reliably established [13]. The origin of the three lowest energy exciton series (2.5, 3.31, 3.9 eV) is attributed to transitions from the highest valence band to the three lowest bands genetically related to the 6*P* orbitals of lead. Based on these literature data, the relationship between the energy of low-energy cation excitons of PbI_2 and the energy of the corresponding electronic states of the free lead ion is shown in Fig. 4. It is seen that the positions of the two higher energy excitons correspond to a linear dependence (points *2*, *3*), while the position of the lower energy band at 2.5 eV is slightly inconsistent (point *1*). By analogy with the impurity centers in alkali halide crystals, we can introduce the

coefficient of energy-level compression of the lead ions by the crystal field, $\rho = E_0/E_{ex}$ (E_0 is the transition energy in the free ion, E_{ex} is the exciton transition energy in the crystal); for PbI_2, the compression ratio is $\rho = 2.87$.

Since the properties of PbI_2 phase inclusions into the layered crystal lattice of CdI_2 should be consistent with the properties of the bulk crystal, we associated the band at 3.23 eV, which is due to lead impurities in the CdI_2–PbI_2 system, with the high-energy cation exciton of the PbI_2 microphase related to the $^3P_2$ state of the free lead ion [7] (its position is marked by a cross in Fig. 4). In this case, the coefficient of lead energy-level compression by the CdI_2 crystal field is 2.93. At such a compression, the cation high-energy exciton of PbI_2 (genetically related to the $^1P_1$ state of the lead ion) has an energy of 3.89 eV, which falls within the fundamental absorption range of CdI_2. The calculated energy of the low-energy PbI_2 exciton (genetically related to the $^3P_1$ state of the free lead ion) in the CdI_2 crystal lattice is 2.66 eV, which is consistent with the energy of the corresponding exciton in ultrathin PbI_2 layers consisting of two PbI_2 layer packs [14]. At the same time, the experimentally observed absorption spectra of CdI_2 with a small content of PbI_2 do not reveal activator bands at energies lower than 3.23 eV, which makes them similar to the absorption spectra of clusters containing five PbI_2 molecules [15].

Figure 5 shows the energy-level diagram of the CdI_2–PbI_2 system at 4.2 K. Since the layers of the initial crystals in the system under investigation are not mixed [6], the width of the CdI_2 indirect band (3.48 eV) is shown (curve *1* in Fig. 1); the width of the direct band is estimated as 3.88 eV [16]. The positions of the lead energy states with respect to the CdI_2 valence band were estimated from the measured photoconductivity of the CdI_2–PbI_2 crystals.

We showed in [9] that, at room temperature, the photoconductivity due to PbI_2 impurities is electronic in character and associated with the photothermal ionization of the state described by the band at 3.23 eV. This process stops at 100 K (Fig. 2a). We assumed that the excited state of the lead center in this case coincides with the bottom of the indirect conduction band, whose width at this temperature is 3.39 eV. Since the maximum of the impurity band at 100 K is at 3.22 eV, we established that the position of the ground level of the lead center is 0.17 eV away from the top of the valence band, which is consistent with the energy 0.166 eV at room temperature given by *ab initio* calculations [9]. We retained the 0.17-eV gap in the energy-level diagram of the CdI_2–PbI_2 system at 4.2 K; in the framework of the model of PbI_2 phase inclusion into the CdI_2 crystal lattice, this state should correspond to the valence band of the PbI_2 microphase genetically related to the $^1S_0$ state of the lead ion. At distances 2.66, 3.23, and 3.89 eV away from this state, there are narrow exciton bands corresponding to excitation of the lead into the $^3P_1$, $^3P_2$, and $^1P_1$ states.

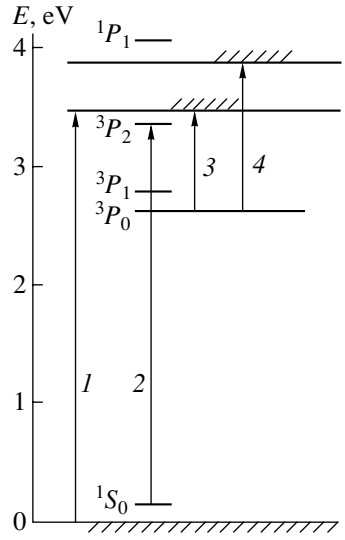

Fig. 5. Energy-level diagram of the CdI_2–PbI_2 system at 4.2 K.

In order to interpret the IR stimulation spectra of photoluminescence and of induced photoconductivity (Fig. 3), we introduced the state corresponding to the $^3P_0$ level of the Pb^{2+} ion into the energy-level diagram. At the compression ratio $\rho = 2.93$, the state is 2.49 eV away from the valence band of the PbI_2 microphase and corresponds to a narrow band, which is a deep trap for electrons. After preliminary irradiation of the crystal by light in the fundamental absorption range (transition *1*) or in the range of the maximum at 3.23 eV (transition *2*), not all the electrons are involved in the radiative transitions: some electrons fill this "metastable" band and remain there after the irradiation has been stopped. Additional IR illumination transfers these electrons to the indirect (0.81 eV) or direct (1.22 eV) conduction band, which is revealed in the form of the induced photoconductivity (transitions *3* and *4*, respectively). With due regard for the density of the energy states at the band edges, the energies obtained are in good agreement with the experimentally obtained energies 0.85 and 1.25 eV (curve *1* in Fig. 3). The wide nonelementary maximum of the stimulated photoluminescence in the vicinity of 1.5 eV transfers the electrons to the fundamental absorption range of CdI_2, which overlaps with the high-energy states of the PbI_2 microphase originating from the $^1P_1$ states of the Pb^{2+} ion.

The energy-level diagram suggested and the interpretation of the induced impurity conductivity are in agreement with the conclusion drawn in [17] that the centers producing the polarization of a sample after its preliminary irradiation are of a recombination nature and are associated with the impurity substituting for

cadmium at the regular sites of the CdI_2 lattice, although it was assumed in [17] that these impurities are uncontrolled copper atoms. Obviously, the occurrence of the long-term relaxation and residual conductivity of the CdI_2–PbI_2 system in the temperature range 130–270 K is also explained by the influence of the $^3P_0$ band of PbI_2 microphase inclusions [18].

5. CONCLUSIONS

Thus, the interpretation of the absorption band at 3.23 eV as a high-energy excitonic state of the PbI_2 microphase (genetically related to the $^3P_2$ states of the free lead ion) in the CdI_2 crystal lattice allows a unified explanation of all features in the earlier suggested models: the relationship to the polytypic modification of the CdI_2 [1], the transitions in the lead ions [2, 3], the excitonic model [19], the donor–acceptor pair model [4], the model of size defects in the crystal lattice [5], and the recombination nature of the trapping centers arising due to photochemical processes [17]. Based on the model treating the luminescence center as a PbI_2 microphase inclusion into the CdI_2 crystal lattice, we have constructed the energy-level diagram of this crystal system and estimated the influence of the metastable band (genetically related to the $^3P_0$ states of the lead ions) as a deep trapping center on the charge transfer in the system under investigation.

ACKNOWLEDGMENTS

We are grateful to M.V. Fock for discussion of the model proposed and to A.S. Voloshinovskiĭ for his participation in the analysis of the results.

REFERENCES

1. E. F. Gross and A. P. Kaplyanskiĭ, Zh. Tekh. Fiz. **25** (12), 2061 (1955).
2. T. Goto and M. Ueta, J. Phys. Soc. Jpn. **29** (6), 1512 (1970).
3. T. Hayashi, T. Ohata, M. Watanabe, and S. Koshino, J. Phys. Soc. Jpn. **63** (12), 4629 (1994).
4. V. D. Bondar', O. B. Kushnir, A. B. Lyskovich, *et al.*, Fiz. Tverd. Tela (Leningrad) **23** (11), 3479 (1981) [Sov. Phys. Solid State **23**, 2024 (1981)].
5. A. B. Lyskovich, N. K. Gloskovskaya, and I. M. Bolesta, Ukr. Fiz. Zh. **20**, 912 (1975).
6. V. V. Artamonov, M. Ya. Valakh, V. A. Korniĭchuk, *et al.*, Ukr. Fiz. Zh. **27** (7), 1046 (1982).
7. N. K. Gloskovskaya, L. I. Yaritskaya, and R. M. Turchak, Ukr. Fiz. Zh. **35** (3), 364 (1990).
8. N. K. Gloskovskaya, I. V. Kityk, and L. I. Yaritskaya, Fiz. Tverd. Tela (St. Petersburg) **36** (7), 1968 (1994) [Phys. Solid State **36**, 1075 (1994)].
9. L. I. Yarits'ka, I. V. Kitik, O. B. Kushnir, and A. V. Gloskovs'kiĭ, Visn. L'viv. Derzh. Univ., Ser. Fiz. **30**, 81 (1998).
10. T. Ando, A. B. Fowler, and F. Stern, in *Electronic Properties of Two-Dimensional Systems* (Am. Phys. Soc., New York, 1982; Mir, Moscow, 1985).
11. M. S. Brodin, I. V. Blonskiĭ, A. S. Krochuk, *et al.*, Fiz. Tverd. Tela (Leningrad) **24** (3), 681 (1982) [Sov. Phys. Solid State **24**, 383 (1982)].
12. B. E. Vugmeĭster, M. D. Glinchuk, I. M. Zaritskiĭ, *et al.*, Zh. Éksp. Teor. Fiz. **69** (5), 1756 (1975) [Sov. Phys. JETP **42**, 892 (1975)].
13. G. Harbeke, E. Tosatti, and F. Bassani, in *Proceedings of International Conference on Physics of Semiconductors, Warshawa* (Pergamon, New York, 1972), p. 302.
14. T. Goto and J. Maeda, J. Phys. Soc. Jpn. **56** (10), 3710 (1987).
15. Z. K. Tang, Y. Nozue, and T. Goto, J. Phys. Soc. Jpn. **61** (8), 2943 (1992).
16. H. Matsumoto, M. Nakagawa, and S. Kondo, Sci. Rep. Rev. Inst. Tehor. Phys. Univ. A **27** (1), 15 (1979).
17. S. A. Piroga and I. D. Olekseyuk, Neorg. Mater. **26** (11), 2402 (1990).
18. S. A. Piroga, I. D. Olekseyuk, and I. V. Kityk, Ukr. Fiz. Zh. **42** (4), 474 (1997).
19. A. B. Lyskovich, S. K. Zherebetskiĭ, G. M. Pentsak, and Z. P. Chorniĭ, Izv. Akad. Nauk SSSR, Ser. Fiz. **33** (6), 1029 (1969).

Translated by A. Pushnov

Physics of the Solid State, Vol. 45, No. 3, 2003, pp. 419–425. Translated from Fizika Tverdogo Tela, Vol. 45, No. 3, 2003, pp. 395–402.

SEMICONDUCTORS AND DIELECTRICS

Intrinsic and Zn-, Ce-, Tb-, Er-, Sm-, and Eu-Activated Photoluminescence of Pseudoamorphous GaN and InGaN Thin Films

A. A. Andreev

Ioffe Physicotechnical Institute, Russian Academy of Sciences, Politekhnicheskaya ul. 26, St. Petersburg, 194021 Russia

Received June 10, 2002

Abstract—Thin films of pseudoamorphous GaN (*a-nc*-GaN), as well as of its alloys with indium, $In_xGa_{1-x}N$ ($x = 0.04, 0.16$), were prepared by magnetron sputtering of a metallic target in the plasma of a reactive nitrogen and argon mixture. The *a-nc*-GaN films were codoped by the Zn acceptor impurity and a set of rare-earth metal (REM) dopants, namely, Ce, Tb, Er, Sm, and Eu. Photoluminescence (PL) spectra excited by a nitrogen laser with wavelength $\lambda = 337$ nm at room temperature and 77 K were measured for all compositions and a set of impurities. It was shown that the high-energy PL edge of the pseudoamorphous (*a-nc*) GaN matrix lies at the same energy as that of the crystalline (epitaxial) *c*-GaN. As in *c*-GaN, the Zn acceptor impurity stimulates blue luminescence; however, the PL spectrum is substantially more diffuse, with practically no temperature quenching of the PL present. Indium doping in an amount of 16 at. % results in strong PL with a diffuse peak at 2.1–2.2 eV; the PL of the alloy exhibits temperature quenching as high as a factor of three to four in the interval 77–300 K. The decay time of the PL response increases up to 50 μs. RE impurities enter the amorphous GaN host as trivalent ions and produce narrow-band (except Ce) high-intensity spectra, thus indicating both a high solubility of RE impurities in *a-nc*-GaN and the generation of an effective crystal field (by the GaN anion sublattice) whose local symmetry makes the intracenter *f–f* transitions partly allowed. © *2003 MAIK "Nauka/Interperiodica".*

1. INTRODUCTION

Gallium nitride (*c*-GaN) is a wide-band-gap semiconductor material ($E_g = 3.45$ eV) which enjoys considerable attention, primarily in connection with the development of quantum-dot lasers based on multilayer GaN–InGaN structures and operating in the blue region of the spectrum [1]. Further investigation of these materials stirred by this discovery showed them to have considerable application potential in the area of optoelectronics [2]. It is thus of interest to study the amorphous phase of GaN and InGaN, which can be prepared in the form of thin films. Modification of the structural network, i.e., its partial disordering, which occurs at amorphization, may give rise to substantial changes in radiative recombination because of electronic-state localization in the band tails. The localization impedes energy exchange between states and, accordingly, reduces energy losses through the competing nonradiative recombination channels. As a result, amorphous materials exhibit a strong suppression of temperature quenching of radiative recombination.

This study was aimed at estimating the efficiency of radiative recombination at room and liquid-nitrogen temperatures in amorphous (or, to be more specific, as will be seen in what follows, in pseudoamorphous) gallium nitride films in the following cases: (i) photoluminescence (PL) of the intrinsic material and the PL induced by doping it with a Zn acceptor impurity, which activates the high-energy wing of the intrinsic PL by enhancing the intensity of the donor–acceptor radiative transitions, (ii) PL in $In_xGa_{1-x}N$ solid solutions ($x = 0.04, 0.16$), which exhibit a shift of photoluminescence to the visible region in the crystalline state, and (iii) PL of rare-earth metal (REM) impurities, namely, Ce, Tb, Er, Sm, and Eu, which make up a specific class of intracenter narrow-band emitters. The wide-band-gap GaN matrix is transparent to REM impurity radiation in the visible range. The characteristic energies of the REM impurity emission cover nearly the total visible range. This opens up the possibility of tuning the PL wavelength through proper selection of the impurity. The specific features of the PL generated by REM impurities in semiconductor matrices are still not adequately studied, and even less so in amorphous GaN.

As follows from the above, this paper addresses, in an implicit form, one more problem, namely, investigation of the possibilities of controlling light emission from an amorphous GaN matrix by various means; this suggests that an analysis of the results obtained in diverse studies in terms of a common problem is a reasonable approach.

1063-7834/03/4503-0419$24.00

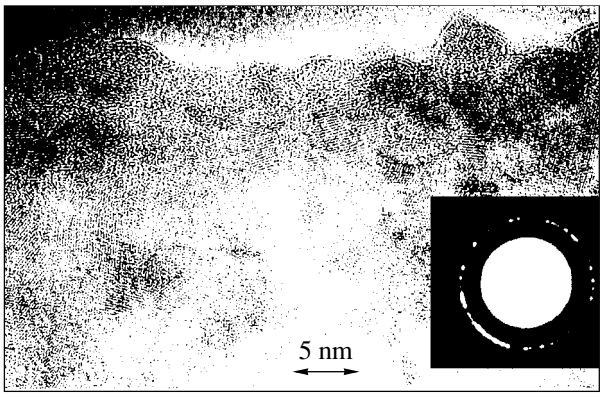

Fig. 1. Photograph of the microstructure of pseudoamorphous (*a-nc*) GaN obtained using high-resolution transmission electron microscopy (HRTEM). The regions with ordered atomic planes correspond to nanocrystals. Inset shows an electron diffraction pattern for ordered regions. The electron diffraction pattern for the amorphous matrix is a halo without reflections.

2. EXPERIMENTAL

Thin films of amorphous gallium nitride were prepared by dc magnetron sputtering. Earlier studies showed cathode sputtering to produce acceptable GaN films [3]. Magnetron sputtering ensures lower ion bombardment exposures during film deposition, which makes this method preferable. A metallic target of liquid gallium was contained in a concentric boat of graphite or stainless steel whose surface was coated preliminarily by titanium nitride as a diffusion barrier. The shape of the boat (and, hence, of the gallium melt) was chosen according to the magnetron magnetic field configuration so as to position the zone of most intense plasma discharge (and, hence, of sputtering) directly above the liquid gallium surface. To suppress possible sources of contamination, the target edge regions were masked and screened electrostatically. To optimize the film growth regimes, various combinations of magnetron discharge parameters were tried. Finally, we chose the low-pressure regime in which the mean free path of a gallium atom knocked out of the target was approximately equal to the target–substrate distance. This regime corresponded to a pressure of the Ar + N_2 mixture equal to or less than 7.0×10^{-4} Torr, with the partial pressure ratio Ar/N_2 = 3/2. The discharge power employed was that which was the lowest for which plasma burning was still stable. The growth process was monitored with a laser interferometer. The film growth rate did not exceed 3–4 Å/s. Fused quartz and silicon plates were used as substrate material. The maximum film thickness reached 5 μm. The dependence of the film structural properties on substrate temperature T_s was studied in the range 300–480°C. Films prepared at $T_s \cong 300$–330°C were experimentally established to be most stable to spontaneous crystallization. This is why all the growth processes were carried out at these values of T_s.

The Zn and REM impurities were introduced by extending small, elongated plates of the required area to a controllable distance into the discharge zone above the liquid-gallium surface. Because of Zn being characterized by a high sputtering coefficient, its plates were positioned in the zone of low-current discharge. Films of composition $In_xGa_{1-x}N$ were prepared by replacing the Ga melt with the corresponding In–Ga melt. Because of the melt becoming depleted in In in the course of film growth, the target was employed for a limited time only. This made it possible to bring the errors in the alloy composition to a minimum.

The actual amount of impurity to be introduced was chosen so as to obtain an optimum manifestation of impurity in the luminescence spectra, i.e., the maximum luminescence intensity at room temperature. Estimates showed the absolute Er concentration to be 5.0×10^{20} cm^{-3} [4], which corresponds to 1 at. %. The other REM impurities were sputtered under approximately the same conditions. In view of the REM sputtering coefficients being similar, one could expect the concentrations of the above REM impurities also to be of the same order of magnitude. Such a high solubility of the REM impurities is due to the following two factors:

(1) The cation radius of the REM impurities (as well as that of Zn) only slightly exceeds that of Ga, which may account for their efficient substitution for Ga [5].

(2) The solubility in an amorphous matrix is always higher than that in a crystalline one because of the structural network of amorphous materials being labile.

To optimize the film properties and optically activate the impurities, the films were thermally annealed in vacuum and in nitrogen–argon and nitrogen–oxygen atmospheres. In one-step annealing, T_{ann} was set at 650°C, and in repeated annealing, at 750°C. It should be stressed that annealing was not a regular technological step and was attempted only in the cases where it improved the PL response.

The structural properties of the films were checked with x-ray and electron diffraction, high-resolution transmission electron microscopy (HRTEM), and Raman spectroscopy. The relevant data obtained in these studies having been reported elsewhere [6], this communication only sums up their main results. As seen from Fig. 1, which presents an HRTEM image of the microstructure,[1] the films actually represent a continuous amorphous matrix with inclusions of randomly oriented, nanosized regions with crystal ordering. The electron diffraction pattern of these regions shown in the inset permits one to determine the interplanar distances in the nanocrystallite lattice, which were found to coincide, to within sufficient accuracy, with those of hexagonally packed GaN. The volume fraction of *nc*-GaN reaches 10% for as-prepared samples and

[1] Courtesy of H.P. Strunk of the Erlangen University, Germany.

increases to 35% after annealing. The amorphous character of the structure and the tendency to crystallization revealed under annealing agree fully with the Raman spectra reported by Davydov [6, 7].

The intrinsic optical absorption measurements presented in Fig. 2 corroborate the results of structural studies. We readily see that the absorption edge, determined at the level $\alpha = 2.0 \times 10^4$ cm^{-1}, corresponds to approximately the same energy for *c*-GaN and *a-nc*-GaN,[2] which is possible only if these materials sustain a common short-range order. The absorption tail extending to the low-energy domain in *a-nc*-GaN obeys the Urbach rule [$\alpha \sim \exp(h\nu/E_0)$] with $E_0 \approx 170$ meV. The Urbach absorption tail is a phenomenon common to amorphous solids. In the $In_{0.04}Ga_{0.96}N$ alloy, the Urbach constant increases ($E_0 \approx 190$ meV), while the shift of the absorption edge is practically imperceptible. The optical absorption in the $In_{0.16}Ga_{0.84}N$ alloy becomes still more diffuse. The estimate of the position of the absorption edge appears little more than tentative. The increase in the Urbach constant initiated by high-temperature annealing (650°C) comes as a surprise. In classical cases, annealing heals defects and the Urbach constant decreases. The steepness of the edge in *a*-InN, which was prepared for comparison, rises again. The optical data are discussed below.

The PL spectra were measured with an SPM quartz-prism monochromator equipped with a FÉU-79 PM tube. An LGI-21 pulsed nitrogen laser ($\tau = 10$ ns, $\lambda = 337$ nm) was used for excitation. The signal detection equipment consisted of a wide-band low-noise amplifier, a pulsed phase detector unit, and a system to measure spectral variations in time.

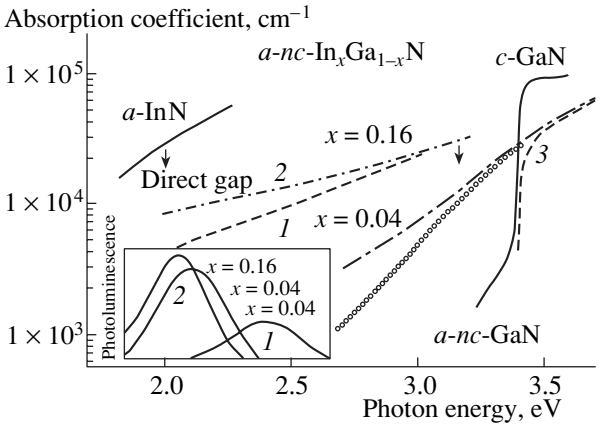

Fig. 2. Optical absorption in pseudoamorphous GaN and $In_xGa_{1-x}N$ ($x = 0.04$, 0.16) (*1*) before and (*2*) after annealing at 650°C and in InN. Shown for comparison are the edge absorption for *c*-GaN and absorption curve *3*, calculated from the formula $\alpha = \alpha_0(h\nu - E_g)^{0.5}$, where $\alpha_0 = 1.1 \times 10^5$ cm^{-1} and $E_g = 3.4$ eV. Inset presents the position of photoluminescence peaks for alloys with indium (*1*) before and (*2*) after annealing at 650°C.

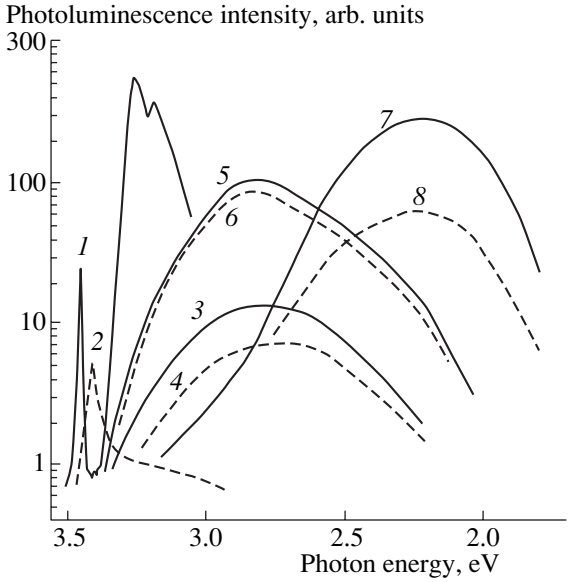

Fig. 3. Photoluminescence spectra of (*1*, *2*) crystalline (epitaxial) *c*-GaN, (*3*, *4*) intrinsic *a-nc*-GaN, (*5*, *6*) Zn-doped *a-nc*-GaN, and (*7*, *8*) an $In_{0.16}Ga_{0.84}N$ alloy measured at 77 K (solid lines) and room temperature (dashed lines). Pumping was performed with a nitrogen laser ($\lambda = 337$ nm).

3. INTRINSIC AND Zn-STIMULATED PHOTOLUMINESCENCE

Figure 3 presents PL spectra of intrinsic and Zn-doped *a-nc*-GaN and of an $In_xGa_{1-x}N$ alloy ($x = 0.16$) measured at room and liquid-nitrogen temperatures. A large set of samples were studied. The results obtained on such sets of samples do not differ qualitatively; therefore, Fig. 3 shows only the most typical relations measured on specific samples rather than those derived by averaging.

To reveal the changes in PL spectra associated with the network amorphization, we measured PL spectra of a high-quality epitaxial *c*-GaN sample, which are also displayed in Fig. 3. A comparison of PL spectra of epitaxial and pseudoamorphous GaN, both intrinsic and Zn-doped, suggests the following conclusions.

(1) The high-energy endpoints of the PL spectra of the crystalline and amorphous phases coincide in the first approximation. Considered together with optical and direct structural data, this result indicates that the local atomic structure of GaN is preserved upon amorphization.

(2) The crystalline and amorphous samples differ, however, substantially in the PL edge structure. The PL spectrum of *c*-GaN exhibits a distinct fine structure formed by exciton emission (the edge band at 3.45 eV

[2] The 2.0×10^4 cm^{-1} level provides better agreement with the edge absorption as found from approximating direct optical transitions $\alpha \approx \alpha_0(h\nu - E_g)^{0.5}$, where $\alpha_0 = 1.1 \times 10^5$ cm^{-1} and $E_g = 3.4$ eV.

at 77 K and 3.4 eV at 300 K) and by two broader related peaks, which are assigned in the literature to a donor–acceptor transition and its phonon replica [8]. In the amorphous phase, neither the amorphous nor the Zn-doped material permits isolation of the fine structure. The loss of this structure is a fundamental consequence of amorphization. Due to structural disorder, the electronic state distribution near the band edge is strongly broadened; this brings about the falling off of the fairly intense PL tail smoothly away into the low-energy region. One may even conceive of the observed PL spectrum, or, more specifically, of its high-energy wing, as a remnant of the crystal PL fine structure, that has been broadened to such an extent that it loses all fine details. At the same time, the integrated PL intensity remains high, because the band tail states are strongly localized and preclude electron migration to nonradiative recombination channels. This fundamental property of the amorphous structure results in a sharp weakening or even a complete disappearance of the PL temperature quenching. This effect appears particularly important for device applications, because it makes *a-nc*-GaN a material that efficiently emits light at room temperature.

(3) What has been said above about intrinsic GaN is fully applicable to the Zn-doped material. Zinc in *c*-GaN usually forms a broad and intense blue emission peak ($\lambda \approx 450$ nm). This peak is difficult to distinguish in an amorphous matrix, because, first, it is strongly broadened and, second, it is masked by the tailing edge emission. As is evident from a comparison of the data presented for the intrinsic and doped materials, introducing the Zn impurity enhances the high-energy PL wing by approximately an order of magnitude. This implies that Zn does not damage the GaN structural network substantially and, hence, does not nucleate defects. This is possible if zinc replaces gallium through substitution. In this case, being a Group-II element, zinc acts as an acceptor and stimulates donor–acceptor transitions, which accounts for the increasing PL brightness.

(4) Annealing at $T = 650$°C reduces the radiation efficiency in the PL high-energy wing. Whence it follows that annealing destroys the continuous amorphous network and introduces defects, although not to the extent where the GaN nanocrystals thus formed could play an even somewhat noticeable role in the luminescence. Hence, both the intrinsic and the zinc-doped PL are specific properties of the amorphous matrix.

4. PHOTOLUMINESCENCE IN $In_{0.04}Ga_{0.96}N$ AND $In_{0.16}Ga_{0.84}N$ ALLOYS

A specific feature of the alloy PL spectra is a sharp drop in the PL high-energy wing and the appearance of intense radiation with a clearly pronounced maximum at 2.1–2.2 eV, i.e., considerably below the edge. It should be stressed that, in the $x = 0.04$ alloy, the radiation peaking at 2.1 eV appears only following a high-temperature anneal. Before the anneal, a weak maximum can be seen at 2.4 eV (inset to Fig. 2). In the alloy with $x = 0.16$, annealing increases the PL intensity by more than an order of magnitude. As a result, the PL intensity of the alloy exceeds that of the intrinsic *a*-GaN sample by nearly two orders of magnitude. When viewed directly, the PL of the alloy with $x = 0.16$ pumped at 3 mW is barely distinguishable from the white luminescence of the incandescent microlamp. We may add that while the annealing of amorphous GaN films also brings about PL enhancement in the low-energy region (2.3–2.0 eV), which is assigned to the radiation of native defects, the intensity of this PL does not ever reach such a high level.

Another specific feature of the PL of the alloys with indium is the substantial increase in the PL decay time after the excitation removal (τ may become as high as 50 μs). For *a-nc*-GaN, the PL decay time is so short that it cannot be resolved with our instrumentation. Finally, alloys with indium exhibit noticeable temperature quenching of the PL, which becomes fourfold in the region 77–333 K.

The totality of the experimental data suggests that we are confronted here with a new phenomenon. This suggestion rests on the following reasoning. Within a certain range of x values, immiscibility of the components (InN and GaN) or phase separation, i.e., a eutectic-type compositional segregation of the material, takes place in the $In_xGa_{1-x}N$ alloy system [9, 10]. This separation results in nucleation of structural formations, "drops" (or islands), which are enriched in In to a larger extent than is the matrix in which these islands are embedded. In the case of thermodynamic equilibrium, the composition of the drops should be that of InN enriched in Ga at the limit of solubility and the composition of the matrix should be that of GaN also enriched in In to the solubility limit. Because the band gap width E_g of such drops is less than that of the matrix, the drops should be identified, in the energy diagram of the alloys, with deep potential wells ($\approx$0.5 eV for both the electrons and the holes). The potential wells are sinks for nonequilibrium electrons excited by a laser with $h\nu > E_g$ of the matrix; therefore, radiative recombination should primarily occur in such wells, i.e., within the InN drops (islands). For InN, $E_g \approx$ 2.0 eV; therefore, the PL maximum should also lie at this energy. The model of phase segregation and InN drop nucleation is also argued for by the fact that the PL maximum in alloys of different composition ($x = 0.04$, 0.16) is located at the same energy after annealing. The difference between these two cases consists in the density of the drops. For $x = 0.04$, this density should be lower and the PL should be weaker; this exactly is observed experimentally. It is possible that the InN drops also account for the additional light absorption at low energies (Fig. 2). The same effect of annealing was also observed to occur in *c*-InGaN [11].

As follows from the density-of-states curve of amorphous GaN [12], the energy gap in an InN drop corresponds to the minimum density of states in the band gap of the GaN matrix. As a result, radiative recombination through the InN drops occurs practically without losses in energy, which accounts for the high luminescence intensity.

Temperature quenching is apparently due to high-temperature transfer of part of the nonequilibrium carriers to nonradiative recombination channels.

The increase in the PL decay time, i.e., the longer lifetime in potential wells, may be associated with the relatively large size of the InN drops (beyond the size quantization limits). In this case, the perturbation of the potential-well bottom by structural disorder can no longer be neglected. The relation for the radiative recombination lifetime for direct transitions becomes inapplicable. Optical transitions should presumably be indirect and zero-phonon [13]. While no theoretical analysis of the radiative lifetime has thus far been carried out for such transitions, one can, however, visualize the following physical picture. Simultaneous deformation (bending) of the conduction and valence band edges caused by field fluctuations may be expected to separate an electron and a hole in space within a well. This should reduce the probability of radiative annihilation of an electron–hole pair captured by an InN drop. The PL decay time should increase accordingly. This situation is similar, to a certain extent, to donor–acceptor recombination at compact impurity-center pairs, a process that is well studied in semiconductors [14]. The parameters of this process, namely, the radiative lifetime and temperature quenching (see, e.g., [15]), are very close to those observed in this study.

The heterogeneous model of InN drops in GaN obviously requires additional corroborative evidence; here, we consider this model as a possibility.

5. REM IMPURITIES Ce, Tb, Er, Sm, AND Eu IN THE *a-nc*-GaN MATRIX

REM impurities make up a qualitatively new class of radiative centers in semiconductor matrices. They are specific in that radiative transitions in REM ions may take place within the filled 4*f* shell, which is screened from the matrix by the outer $5s^2 5p^6$ shell. As a result, the 4*f*–4*f* transitions form narrow luminescence lines of width $\Delta \cong 5$–15 nm whose position may be considered, in a first approximation, to be temperature-independent. REM impurities can produce efficient luminescence only under certain conditions, namely, (i) when electron transitions within a closed electron shell are at least partially allowed, (ii) there exist efficient enough paths for excitation energy transfer from the matrix to the REM ions, and (iii) the concentration of optically active centers is be high.

Forbiddenness of intracenter 4*f* transitions can be partially lifted by properly selecting the symmetry and strength of the crystal field acting on an REM ion in the matrix. The crystal field brings about Stark splitting of the 4*f* levels and, as a consequence, causes a weak mixing of wave functions of the 4*f* multiplets, which partially lifts the selection rules. The crystal field itself is generated by the electrically negative ions on the anion sublattice (ligands). The nitrogen ion is second in electronegativity to the oxygen ion. For this reason, one may assume that matrices with a nitrogen anion sublattice should, in principle, create a strong electric field. The problem of the ligand field symmetry, in particular, the requirement of no inversion site symmetry, is extremely important for removal of the selection rules. The problem of crystal field symmetry can be solved to some extent by properly selecting a matrix with the corresponding structure and by choosing growth conditions favoring REM ion arrangement in the corresponding positions. For instance, doping followed by annealing may create conditions conducive to cation substitution or interstitial arrangement of the impurity. One can also change the ion environment of the impurity ion through proper codoping with other anions, for instance, oxygen.

Finally, to achieve a high impurity concentration, the process of solution must be affected. This can be done, for example, through amorphization of the matrix. The solubility of foreign atoms in an amorphous matrix is always higher due to the absence of stringent requirements on structural organization imposed by long-range order in crystals. However, the impurity concentration can be increased only up to a certain limit, because an excess density of impurity centers may bring about concentration-induced quenching as a result of their interacting.

In the present study, an attempt was made for solve all of the above problems by doping *a-nc*-GaN with such REMs as Ce, Tb, Er, Sm, and Eu. These REMs were chosen so as to obtain emission in various regions of the visible spectrum, namely, in the blue (Ce), in the green (Tb, Er), and in the red and red-orange regions (Eu, Sm). After experimentally choosing the optimum concentration and, when required, achieving optical activation through anneals in various environments (vacuum, nitrogen, nitrogen plus oxygen), cumulative annealing (multistep annealing at progressively increasing temperatures), or properly varying the growth process parameters and introducing sensitizers, we succeeded in reaching PL intensities high enough to be observable by eye under excitation of the matrix by photons with energies above the band edge and at an average laser power of 3 mW. Figure 4 displays normalized luminescence spectra. In all the spectra, the wide band gap PL of the matrix itself was subtracted by decomposing each spectrum into Gaussians. In cases where the intrinsic PL noticeably distorted the REM ion spectrum, time-resolved measurements were carried out; i.e., the REM ion spectrum was measured with a time delay under conditions where the matrix PL intensity had decreased markedly because of the inter-

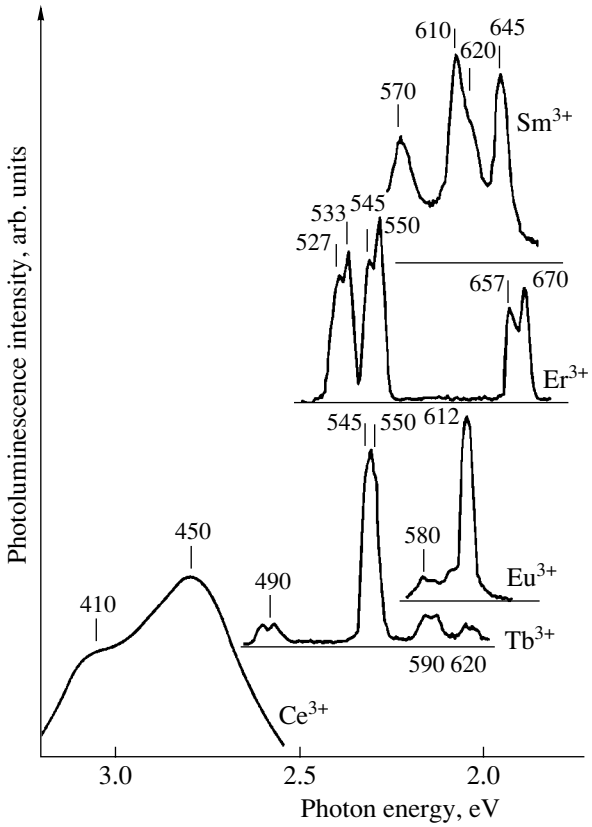

Fig. 4. Visible photoluminescence spectra of REM impurities in an *a-nc*-GaN matrix. The spectra are normalized against the maximum intensity peak for each REM ion.

band radiative transitions decaying faster than the partially forbidden *f–f* transitions, which, thus, followed slower decay kinetics. The luminescence spectra could be unambiguously identified as belonging to trivalent REM ions [16].

The highest energy PL peaks (at 410 and 450 nm) are due to Ce^{3+} and are produced in the $^2D(5d) \longrightarrow {}^2F_{5/2}$, $^2F_{7/2}(4f)$ transitions. Ce^{3+} is the only REM ion in which intershell *d–f* transitions are dominant. In the free ion, these transitions correspond to $\lambda \cong 320$–340 nm. The shift to lower energies and the relatively large peak width ($\Delta = 40$ nm) are most likely due to the high density of the cerium impurity in the matrix and, hence, to the interaction of ions, which does not, however, result in concentration quenching. A lowering of the *d–f* transition energy at a high cerium density was observed earlier in the II–VI semiconductor matrices [17] or in CeF_2, where Ce makes up the bulk of the material. It should also be pointed out that Ce affects the intensity enhancement in the high-energy PL wing in *a-nc*-GaN even more strongly than the substitutional Zn impurity does. It may be conjectured that Ce enters the GaN structural network without destroying it. This is possible, in principle, if trivalent cerium substitutes for gallium. In this process, the problem of charge compensation does not arise; this factor likewise increases the PL intensity. It is also essential that the 5*d*–4*f* transitions in Ce^{3+} occur between different electronic shells and, hence, are allowed. This factor does not pose additional requirements on the ligand field symmetry.

The main peak in the Tb^{3+} spectrum ($\Delta = 10$ nm) falls in the green region (545–550 nm); this spectrum also contains a number of distinct satellite peaks of a considerably lower intensity and originates from transitions within the 4*f* shell between the lowest nonexcited state of the 5*D* multiplet, $^5D_4$, and the $^4F_{6,5,4,3}$ states of the 4*F* multiplet (490, 545, 585, and 620 nm, respectively). The intracenter transitions in Tb^{3+} are partially forbidden and have a lifetime $\tau \approx 500$ μs.

The highest intensity PL peak of Eu^{3+} lies in the red region at 612 nm ($\Delta = 10$ nm) and originates from the $^5D_0 \longrightarrow {}^7F_2$ transition with $\tau \approx 200$ μs. It was experimentally found that the optical transition intensity in both Tb^{3+} and Eu^{3+} is not critical to the annealing process. It thus follows that the ion positions with a ligand field symmetry providing optical activity of the ions form already in the course of film growth.

The situation with the Er^{3+} ions is radically different. This ion becomes optically active only after multistep annealing. This is possibly due to the fact that the *f–f* transitions in the Er^{3+} ion are predominantly parity-forbidden (whereas in the Tb^{3+} and Eu^{3+} ions, they are spin-forbidden), so that partial lifting of this forbiddenness poses more stringent requirements on the ligand field symmetry. In view of the fact that prolonged high-temperature anneals favor diffusion of residual oxygen in the matrix and that REM ions, including Er^{3+}, are highly active oxygen getters, it may be conjectured that the Er^{3+} ligand field is generated by the oxygen environment. The Er^{3+} spectrum, as seen from Fig. 4, contains a group of peaks at 523, 527, 533, 545, 555, 657, and 670 nm, which correspond to transitions from the $^2H_{11/2}$, $^4S_{3/2}$, and $^4F_{9/2}$ excited states to the $^4I_{15/2}$ ground state ($\tau < 10$ μs). Erbium luminescence appears to the eye to be light green. The erbium luminescence in the visible range was studied in [4].

The PL spectrum of Sm^{3+} is a group of three relatively broad peaks at 570, 610, and 645 nm, which are similar in amplitude and correspond to the $^4S_{5/2} \longrightarrow {}^6H_{5/2,7/2,9/2}$ transitions ($\tau \approx 40$ μs). The Sm^{3+} luminescence is seen as red orange.

The radiating capacity of the REM impurities in *a-nc*-GaN is high. Because the nitrogen laser used for pumping cannot transfer the pump photon energy directly to the REM ion, as these ions do not have absorption levels resonant with the laser frequency, one may conclude that the semiconductor matrix absorbing the laser energy through interband electron transitions to the conduction band acts so as to transform the pump energy and transfer it to the impurity ion. Obviously enough, the nitrogen laser pump energy thermalizes to

the band edge and is subsequently transferred to the band tail localized states. The energies of localized states in a broad band tail distribution likely coincide with resonant absorption levels of the REM ions. This makes it possible to transfer the pump energy from the laser to the ion.

6. CONCLUSIONS

The major results obtained in this study can be summed up as follows.

(1) Gallium nitride can be prepared in the amorphous state in the form of thin films on quartz and silicon substrates. A detailed analysis of the microstructure shows that the amorphous phase contains randomly oriented nanocrystallites 5–7 nm in size, which make up a volume fraction of 10%. For this reason, the term "pseudoamorphous" (*a-nc*-GaN) is more adequate for characterization of these films.

(2) Studies into the optical absorption and edge PL show that the band gap width of the amorphous and crystalline materials is approximately the same.

(3) The fine structure in the edge PL is lost in amorphization. The exciton lines disappear. At the same time, the intensity of the high-energy wing, including the blue region of the spectrum, increases. This rise in the PL is particularly well seen in Zn-doped samples. There is practically no temperature quenching of the PL.

(4) Doping with In to 16 at. % brings about a decrease in E_g and the appearance of a broad and intense PL peak at 2.1–2.3 eV. The strength of this peak exceeds that of the intrinsic-material PL by more than an order of magnitude. At a pump power of 3 mW (λ = 337 nm), this luminescence is seen to be of a white color practically indistinguishable from the glow of an incandescent lamp.

(5) Films of *a-nc*-GaN are an excellent matrix for REM impurities. The REM solubility can be as high as 5.0×10^{20} cm^{-3}. The impurity enters the matrix in the form of trivalent ions. The nitrogen anion sublattice generates a crystal field strong enough to ensure optical activation of the intracenter *f–f* transitions. In the case of Er^{3+}, optical activity is reached only after multistep annealing. This experimental finding gives one grounds to suggest that the ligand environment of the required symmetry is formed, in the case of erbium, by diffusion of residual oxygen.

Ce^{3+} provides a relatively broad PL spectrum (390–480 nm), which is perceived by the eye as blue. The Ce^{3+} luminescence is due to the 5*d*–4*f* transitions and is possible in the blue region only at very high concentrations.

The *f–f* transitions in Tb^{3+} and Eu^{3+} produce narrow (10–15 nm) peaks at λ = 545–550 and 610–615 nm, respectively. The lines of terbium (green) and europium (red) are strong enough to be seen in a lighted room.

Er^{3+} and Sm^{3+} have spectra of complex structure with peaks spread over a broad wavelength range that are light green and red-orange, respectively, to the eye.

REFERENCES

1. S. Nakamura and G. Fasol, *The Blue Laser Diode: GaN Based Light Emitters and Lasers* (Springer, Berlin, 1997), p. 129.
2. A. J. Steckl, J. Heikenfeld, M. Garter, *et al.*, Compd. Semicond. **6** (1), 48 (2000).
3. K. Kubota, Y. Kobayashi, and K. Fujimoto, J. Appl. Phys. **66** (7), 2984 (1989).
4. A. A. Andreev, Fiz. Tverd. Tela (St. Petersburg) **44** (2), 239 (2002) [Phys. Solid State **44**, 248 (2002)].
5. P. H. Citrin, P. A. Northrap, R. Birkhalm, and A. J. Steckl, Appl. Phys. Lett. **76** (20), 2865 (2000).
6. S. B. Aldabergenova, M. Albrecht, A. A. Andreev, *et al.*, J. Non-Cryst. Solids **283** (1–3), 173 (2001).
7. V. Yu. Davydov, Yu. E. Kitaev, J. N. Goncharuk, *et al.*, J. Cryst. Growth **189/190**, 656 (1998).
8. T. Matsumoto and M. Aoki, Jpn. J. Appl. Phys. **13** (11), 1804 (1974).
9. K. Osamura, S. Naka, and Y. Murakami, J. Appl. Phys. **46** (8), 3432 (1975).
10. A. Wakahara, T. Tokuda, X. Z. Dang, *et al.*, Appl. Phys. Lett. **71** (18), 906 (1997).
11. M. D. McCluskey, L. T. Romano, B. S. Krusor, *et al.*, Appl. Phys. Lett. **72** (14), 1730 (1998).
12. P. Stumm and D. A. Drabold, Phys. Rev. Lett. **79** (4), 677 (1997).
13. N. F. Mott and E. A. Davis, *Electron Processes in Non-Crystalline Materials*, 2nd ed. (Clarendon, Oxford, 1979; Mir, Moscow, 1982), Vol. 1.
14. T. S. Moss, G. J. Burrell, and B. Ellis, *Semiconductor Opto-Electronics* (Butterworth, London, 1973; Mir, Moscow, 1976).
15. A. L. Gurskiĭ, E. V. Lutsenko, N. K. Morozova, and G. P. Yablonskiĭ, Fiz. Tverd. Tela (St. Petersburg) **34** (11), 3530 (1992) [Sov. Phys. Solid State **34**, 1890 (1992)].
16. A. A. Kaminskiĭ, *Laser Crystals* (Nauka, Moscow, 1975), p. 14.
17. Y. Tamura, J. Ohwaki, H. Kozawaguchi, and B. Tsujiyama, Jpn. J. Appl. Phys. **26** (2), 105 (1986).

Translated by G. Skrebtsov

Physics of the Solid State, Vol. 45, No. 3, 2003, pp. 426–432. Translated from Fizika Tverdogo Tela, Vol. 45, No. 3, 2003, pp. 403–408.

SEMICONDUCTORS AND DIELECTRICS

Analysis of the Charge Transfer Mechanisms Responsible for the Current–Voltage Characteristics of $Ca_4Ga_2S_7 : Eu^{3+}$ Single Crystals

B. G. Tagiev, U. F. Kasumov, N. N. Musaeva, and R. B. Dzhabbarov

Institute of Physics, Academy of Sciences of Azerbaijan, pr. Dzhavida 33, Baku, 370143 Azerbaijan
e-mail: ulvi@azintex.com, e-mail: ulwi@mail.ru

Received June 27, 2002

Abstract—The current–voltage characteristics of $Ca_4Ga_2S_7 : Eu^{3+}$ single crystals are measured for the first time, and the processes affecting these characteristics are analyzed theoretically. It is demonstrated that $Ca_4Ga_2S_7 : Eu^{3+}$ single crystals are high-resistance semiconductors with a resistivity of ~10^9 Ω cm and a relative permittivity of 10.55. The electrical properties of the studied materials are governed by traps with activation energies of 0.13 and 0.19 eV and a density ranging from 9.5×10^{14} to 2.7×10^{15} cm^{-3}. The one-carrier injection is observed in weak electric fields. In electric fields with a strength of more than 4×10^3 V/cm, traps undergo thermal field ionization according to the Pool–Frenkel mechanism. At low temperatures and strong fields (160 K and 5×10^4 V/cm), the electric current is most likely due to hopping conduction by charge carriers over local levels in the band gap in the vicinity of the Fermi level. *© 2003 MAIK "Nauka/Interperiodica".*

1. INTRODUCTION

It is known that local levels in the band gap of semiconductors can substantially affect the injection currents and, consequently, the current–voltage characteristics of the material. In this respect, investigation into the current–voltage characteristics of semiconductors over a wide range of applied electric fields makes it possible to reveal traps of different types, to determine the most important characteristics of the traps, to elucidate the mechanism of charge transfer, and to evaluate a number of microscopic parameters of the studied compounds.

In this work, the current–voltage characteristics of $Ca_4Ga_2S_7 : Eu^{3+}$ single crystals were studied for the first time. The measurements were performed in the electric field range $0–8 \times 10^4$ V/cm at temperatures from 160 to 365 K.

The $Ca_4Ga_2S_7 : Eu^{3+}$ compound belongs to the family of high-efficiency phosphors of the general formula $Ca_mGa_2S_n$: REE (where $n = 4, 5, 6, \ldots$; $m = n - 3$; and REE is a rare-earth element). The distinguishing features of these compounds are as follows: (i) the absence of concentration quenching for a number of dopants involved in the excitation of luminescence and (ii) high-efficiency luminescence (specifically in the infrared spectral range) suitable for use in fiber-optic communication lines. Under ultraviolet and visible radiation, as well as upon exposure to electric fields, $Ca_4Ga_2S_7$: REE compounds can be efficiently excited and convert the excitation into visible light. Among the $Ca_4Ga_2S_7$: REE phosphors, $Ca_4Ga_2S_7$ doped with 2 mol % EuF_3 is the most interesting compound. A mixture of $Ca_4Ga_2S_7 : Eu^{3+}$ with a commercial phosphor was used to manufacture an experimental batch of high-efficiency electroluminescent lamps [1–5]. It was expedient to investigate the electrical properties of the $Ca_4Ga_2S_7 : Eu^{3+}$ semiconductor and to determine its characteristics.

2. SAMPLE PREPARATION AND EXPERIMENTAL TECHNIQUE

Single crystals of $Ca_4Ga_2S_7 : Eu^{3+}$ in the form of cylindrical ingots 15–17 mm in height and 8–10 mm in diameter were grown using the Bridgman–Stockbarger technique. Earlier [6], we examined the fundamental absorption edge for the $Ca_4Ga_2S_7 : Eu^{3+}$ compound and revealed that indirect and direct (both forbidden and allowed) optical transitions occur in the energy ranges 2.2–2.6 and 2.6–3.0 eV. The band gaps corresponding to these transitions were determined to be E_{gi} = 1.88 eV, E_{gdf} = 2.32 eV, and E_{gda} = 2.45 eV at T = 300 K.

The experiments were performed with 70-μm-thick samples prepared by grinding single-crystal ingots. The sample thickness was checked at all stages of treatment. For this purpose, we used an indicating micrometer for thicknesses larger than 100 μm and an optomechanical indicator for smaller thicknesses. Indium sandwich contacts (area, 0.25 mm^2) were applied through evaporation. All the measurements with $Ca_4Ga_2S_7 : Eu^{3+}$ single-crystal samples were carried out in a shielded vacuum thermostat. The error in measurements of the current with the use of an electrometric amplifier did not

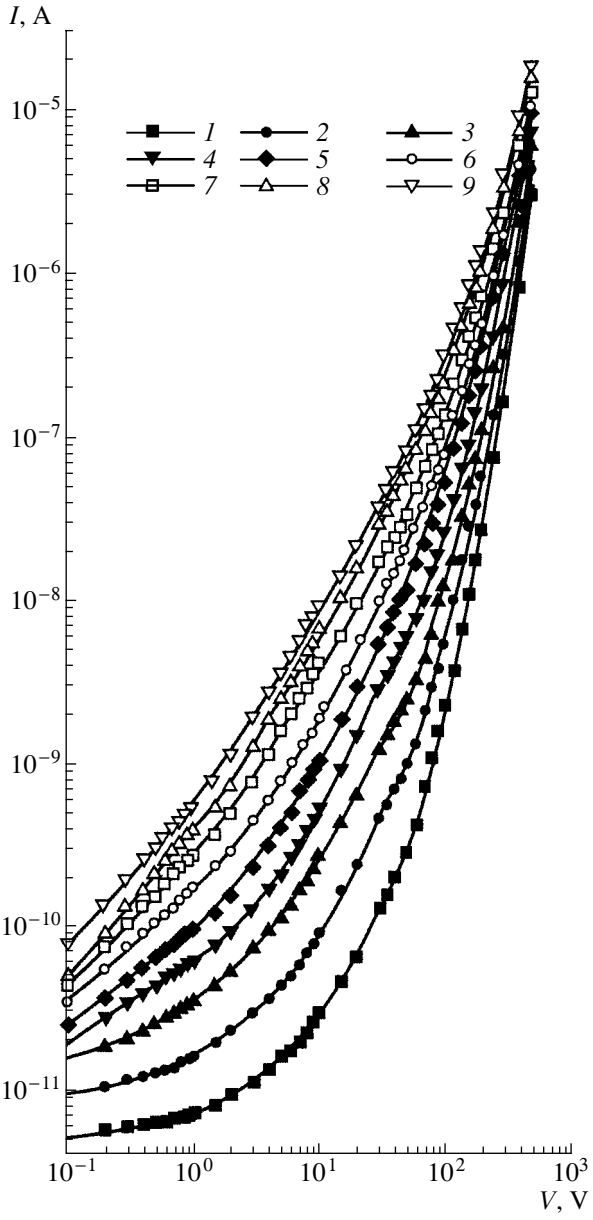

Fig. 1. Current–voltage characteristics of the $Ca_4Ga_2S_7$: Eu^{3+} single crystal at different temperatures. *T*, K: (*1*) 160, (*2*) 185, (*3*) 205, (*4*) 227, (*5*) 260, (*6*) 293, (*7*) 318, (*8*) 342, and (*9*) 365.

exceed 10% for the most sensitive subband (10^{12} Ω) of output resistances. The voltage was measured accurate to within 0.1%.

The data presented in this paper refer to the $Ca_4Ga_2S_7$ compound doped with 2 mol % EuF_3.

3. RESULTS AND DISCUSSION

The current–voltage characteristics of the $Ca_4Ga_2S_7$: Eu^{3+} single crystal are shown in Fig. 1. The *I–V* curves can be separated into four portions: quasi-linear portion

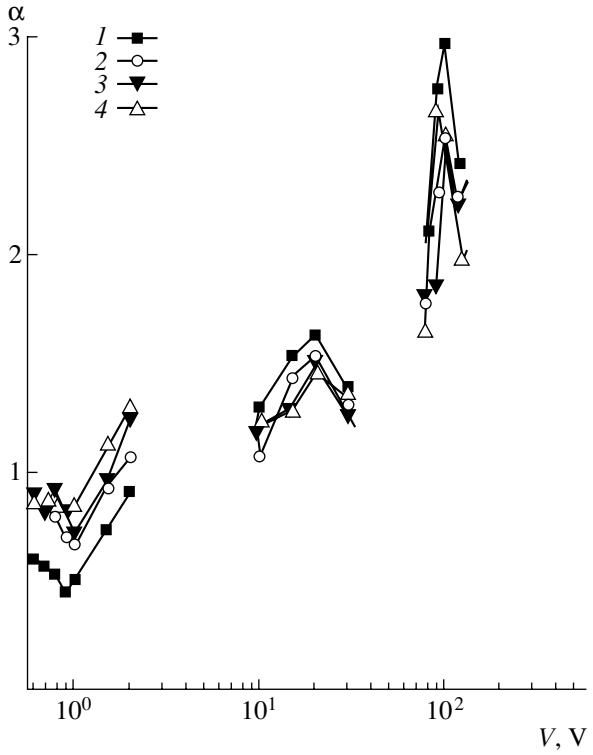

Fig. 2. Dependences of the nonlinearity exponent α on the voltage *V* at different temperatures. *T*, K: (*1*) 260, (*2*) 318, (*3*) 342, and (*4*) 365.

I, which is observed at relatively low temperatures; linear portion **II**; quadratic portion **III** ($I \sim V^{1.5–2}$); and portion **IV**, which is characterized by a rapid increase in the current ($I \sim V^{2.5–4.5}$ or $I \sim V^{6–7}$ at low temperatures). It should be noted that a decrease in the temperature leads to a shift of the *I–V* curves toward the high-field range. The current–voltage characteristics of $Ca_4Ga_2S_7$: Eu^{3+} single crystals were analyzed in terms of the generalized approximate theory of contact injection phenomena in semiconductors, the Pool–Frenkel theory, and the activationless-conduction theory.

In the framework of the generalized approximate theory of contact injection phenomena, different approximations of the current–voltage characteristic of a quasi-monopolar semiconductor with a finite injecting junction and an arbitrary band structure in the bulk are used depending on the contact injection regimes. Within this theory, the extrema of the nonlinearity exponent α, which is defined by the formula

$$\alpha = \frac{d\log I}{d\log V} = \frac{V}{I}\frac{dI}{dV}, \quad (1)$$

can be related to the relevant injection regimes and the macroscopic and microscopic parameters [7–14].

Table 1. Parameters determined from the minimum in the dependence $\alpha(V, I)$

T, K	α_m	V_m, V	I_m, $\times 10^{-10}$ A	n_{k0}, $\times 10^{12}$ cm^{-3}	D_k^*, $\times 10^{-8}$	s_k, $\times 10^{-5}$ cm/s	τ, $\times 10^{-7}$ s	E_F, eV
260	0.45	1	0.91	1.72	1.03	3.70	1.49	0.35
318	0.67	1	2.75	2.96	2.02	7.90	4.19	0.41
342	0.72	1	3.90	3.74	2.37	9.60	5.99	0.44
365	0.79	1	5.10	4.31	2.95	12.40	9.94	0.46

Note: Here, T is the absolute temperature; α_m is the minimum nonlinearity exponent; V_m and I_m are the voltage and the current strength at the minimum nonlinearity exponent α_m, respectively; n_{k0} is the carrier concentration in the vicinity of the cathode; D_k^* is the cathode transparency; s_k is the rate of surface recombination; τ is the carrier recombination lifetime; and E_F is the energy at the Fermi quasi-level.

Table 2. Parameters determined from the maximum in the dependence $\alpha(V, I)$

T, K	α_M	I_M, $\times 10^{-7}$ A	V_M, V	Q_M	σ_M, $\times 10^9$ Ω^{-1} cm^{-1}	ρ_M, $\times 10^4$ C cm^{-3}	μ_M, cm^2/V s
260	2.97	3.22	100	3.05	5.42	5.64	9.85
318	2.66	2.14	100	2.31	3.69	4.63	5.54
342	2.53	1.39	100	2.02	2.43	4.22	3.32
365	2.45	0.54	100	1.85	0.96	3.97	1.23

Note: Here, T is the absolute temperature; α_M is the maximum nonlinearity exponent; V_M and I_M are the voltage and the current strength at the maximum nonlinearity exponent α_M, respectively; Q_M is the discrimination coefficient; σ_M is the electrical conductivity; ρ_M is the charge density; and μ_M is the drift mobility in strong electric fields.

The dependences of the nonlinearity exponent $\alpha(V, I)$ on the voltage at different temperatures (Fig. 2) were calculated from the experimental data presented in Fig. 1.

As can be seen from Fig. 2, the dependences $\alpha(V)$ exhibit minima α_m and maxima α_M. With knowledge of these extrema, it is possible to calculate a number of microscopic parameters from the formulas derived in [7–14]. The calculated microscopic parameters are listed in Tables 1 and 2.

It is worth noting that different physical phenomena occurring in semiconductors in response to external electric fields below the breakdown (for example, one-carrier and two-carrier injection, barrier electrical conduction, and field ionization of traps) are characterized by similar current–voltage curves [8, 11]. For this reason, when analyzing the current–voltage characteristics, special attention should be focused on identifying the dominant mechanisms of the processes involved.

It is established that the discrimination coefficient Q_M and the nonlinearity exponent α_M obey the following relationships: $Q_M \le 4\alpha_M$ for field ionization of traps, $Q_M \ge 1$ for one-carrier injection, and $Q_M \le 1$ for two-carrier injection. In the case of field ionization (FI), the discrimination coefficient can be represented in the form [15]

$$(Q_M)_{FI} = \frac{(2\alpha_M - 1)^2(\alpha_M - 1)}{(\alpha_M + 1)}. \qquad (2)$$

The discrimination coefficients calculated for $Ca_4Ga_2S_7 : Eu^{3+}$ single crystals at different temperatures are given in Table 2.

As follows from Table 2, the conditions for one-carrier injection and field ionization of traps are satisfied for the single crystals under investigation.

The experimental data obtained for the *I–V* portion in the electric field range 6×10^3–7.2×10^4 V/cm, which is characterized by a rapid increase in the current and is preceded by the quadratic portion, were processed in accordance with the Pool–Frenkel theory of thermal electron ionization.

According to the Pool–Frenkel theory [16–18], we can write the relationship

$$j = \sigma_0 F \exp(\beta\sqrt{F}), \qquad (3)$$

where

$$\beta = \frac{\sqrt{e^3}}{kT\sqrt{\pi\varepsilon\varepsilon_0}} \quad (4)$$

is the Frenkel coefficient. Here, F is the electric field strength, j is the current density in strong electric fields, σ_0 is the conductivity in the ohmic region, e is the elementary charge, ε is the permittivity of the material, ε_0 is the permittivity of free space, k is the Boltzmann constant, and T is the absolute temperature.

Figure 3 shows the dependences of $\log\sigma$ on the electric field strength $F^{1/2}$ for nine temperatures. As is clearly seen from Fig. 3, the experimental points fall on straight lines with different slopes. The slopes increase with a decrease in the temperature. This is in excellent agreement with the Pool–Frenkel theory and suggests an increase in the probability of field ionization of local levels.

The Frenkel coefficients β at different temperatures were determined from the slopes of the straight lines. According to expression (4), the Frenkel coefficient β linearly depends on the reciprocal of the temperature $1/T$ and the extrapolated curve for $\beta \sim 1/T$ should pass through the origin of the coordinates. As can be seen from Fig. 4, our experimental results agree well with the theoretical predictions.

From the calculated Frenkel coefficients, we determined the permittivity $\varepsilon = 10.55$, which is in good agreement with the permittivity obtained by the capacitance method.

The temperature dependences of the electrical conductivity of the $Ca_4Ga_2S_7 : Eu^{3+}$ single crystal in electric fields ranging from 1.4×10^3 to 5.7×10^4 V/cm are plotted in Fig. 5.

It can be seen from Fig. 5 that the experimental points in the $10^3/T$–$\log\sigma$ coordinates fall on two straight lines with different slopes. These straight lines correspond to two temperature ranges, namely, the low-temperature range 160–270 K and the high-temperature range 270–365 K. Analysis of the curves obtained demonstrates that the trap activation energy E_t determined by the slope of the straight-line portions decreases with an increase in the applied electric field. In the framework of the Pool–Frenkel theory, the decrease in the trap activation energy E_t with a change in the electric field strength F is adequately described by the expression [18]

$$E_t(F) = E_t(0) - \sqrt{\frac{e^3F}{\pi\varepsilon_0\varepsilon}}, \quad (5)$$

where $E_t(F)$ is the trap activation energy in strong electric fields and $E_t(0)$ is the trap activation energy at $F = 0$ (for other designations, see above).

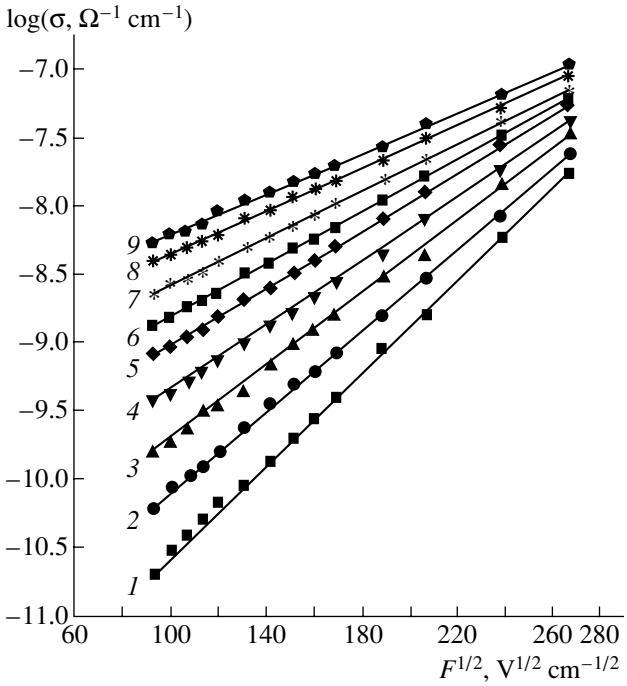

Fig. 3. Dependences of the electrical conductivity of the $Ca_4Ga_2S_7 : Eu^{3+}$ single crystal on the square root of the electric field strength F at different temperatures. T, K: (*1*) 160, (*2*) 185, (*3*) 205, (*4*) 227, (*5*) 260, (*6*) 293, (*7*) 318, (*8*) 342, and (*9*) 365.

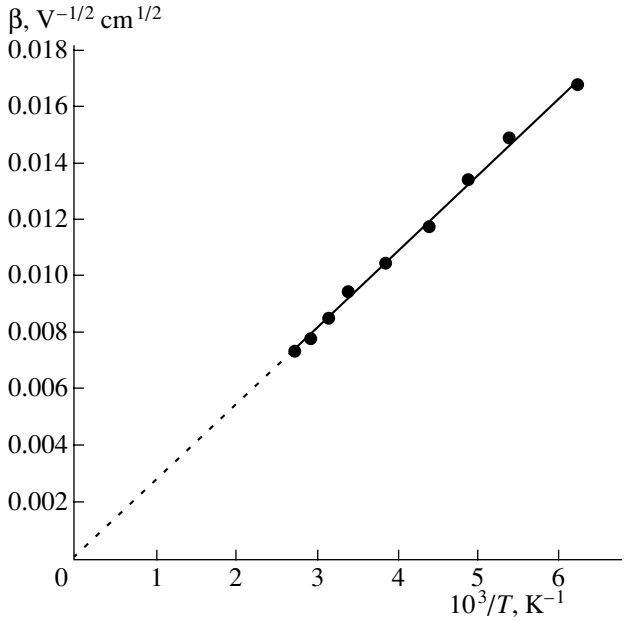

Fig. 4. Dependence of the Frenkel coefficient β on the reciprocal of the temperature $10^3/T$.

Figure 6 depicts the dependences of $\log[\sigma(F)/\sigma(0)]$ on the reciprocal of the temperature $10^3/T$ in applied electric fields in the range from $0.1 \times$

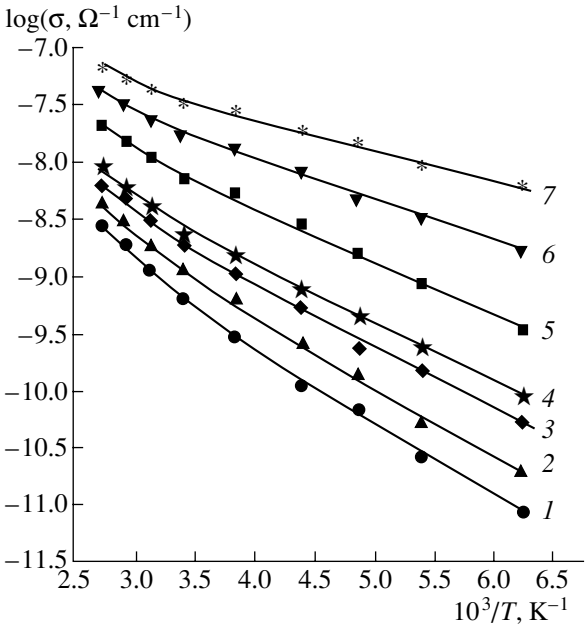

Fig. 5. Dependences of the electrical conductivity on the reciprocal of the temperature at different applied electric fields. *F*, 10^3 V/cm: (*1*) 1.4, (*2*) 5.7, (*3*) 8.75, (*4*) 14.3, (*5*) 28.6, (*6*) 43.0, and (*7*) 57.0.

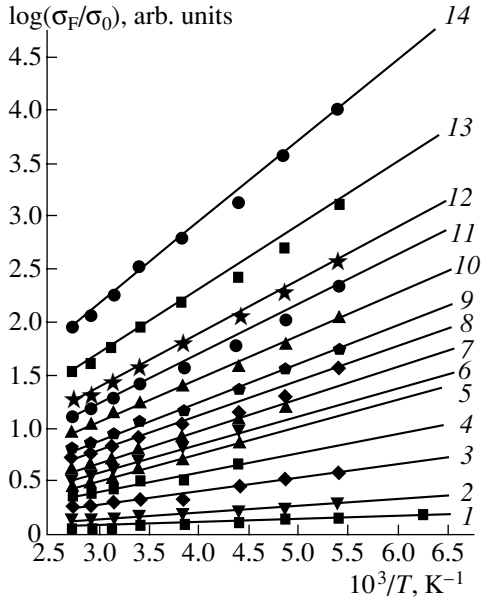

Fig. 6. Dependences of $\log(\sigma_F/\sigma_0)$ on the reciprocal of the temperature at different applied electric fields. *F*, 10^3 V/cm: (*1*) 0.1, (*2*) 0.4, (*3*) 0.9, (*4*) 1.2, (*5*) 2.86, (*6*) 5.0, (*7*) 7.14, (*8*) 10.0, (*9*) 12.86, (*10*) 17.14, (*11*) 22.86, (*12*) 22.57, (*13*) 28.57, and (*14*) 71.4.

10^3 to 71.4×10^3 V/cm. It can be seen that an increase in the electric field leads to an increase in the slope of the straight lines. This indicates a change in the activation energy at impurity levels.

A decrease in the trap activation energy by $(e^3F/\pi\varepsilon\varepsilon_0)^{1/2}$ in an electric field is a necessary but not sufficient condition for an electron to leave the Coulomb center. The Pool–Frenkel effect can be observed only in the case when a charge carrier has retained an energy higher than $E_t - (e^3F/\pi\varepsilon\varepsilon_0)^{1/2}$ after it colliding with phonons and overcoming the potential barrier. This condition is satisfied at $\lambda > r_m$ [15]. Otherwise, the role of the electric field in the release of electrons from the Coulomb centers consists only in facilitating diffusion of charge carriers from the centers. The changes in the activation energy at impurity levels ΔE_i were calculated from the data presented in Fig. 6. Then, we constructed the dependence of ΔE_i on the external electric field in the F–ΔE_i coordinates. It turned out that the dependence obtained is characterized by an inflection point corresponding to the critical electric field F_{cr} in which the Pool–Frenkel effect manifests itself. Knowing the critical field, we can compare the mean free path of charge carriers $\lambda = \beta kT/2e(F_{cr})^{1/2} = 1.73 \times 10^{-5}$ cm with the distance from the trap to the potential barrier at the maximum $r_m = (e/4\pi\varepsilon\varepsilon_0F_{cr})^{1/2} = 1.46 \times 10^{-5}$ cm. As can be seen, the aforementioned two necessary conditions for the Pool–Frenkel effect to manifest itself are satisfied for the single crystals under investigation. The possibility of thermal field ionization occurring through the Pool–Frenkel mechanism in the studied semiconductors is confirmed by the effective sizes of the trap potential well. We calculated the shape of the trap potential well from the dependence of the trap activation energy on the electric field according to the technique proposed by Georgobiani *et al.* [19].

The trap density can be calculated from the formula [15]

$$N_t = \frac{3}{4\pi}\frac{e^3F_{cr}^{3/2}(F_2^{1/2} - F_1^{1/2})^3}{[E_t(F_1) - E_t(F_2)]^3}. \quad (6)$$

This formula makes it possible, without knowledge of the permittivity, to estimate the trap density from the experimental data on the electrical conductivity measured in strong electric fields. After substitution of the critical electric field into formula (6), we obtained $N_t = 2.7 \times 10^{15}$ cm^{-3} at $E_t = 0.13$ eV and $N_t = 9.5 \times 10^{14}$ cm^{-3} at $E_t = 0.19$ eV.

Moreover, we examined the current–voltage characteristics of the $Ca_4Ga_2S_7 : Eu^{3+}$ single crystals in terms of the injection current theory developed in [20].

The critical current and critical voltage at which the quadratic portion of the current–voltage characteristic transforms into the *I*–*V* portion characterized by a sharp

increase in the current can be represented by the following relationships:

$$I_2 = \frac{e^2 n_0^2 \mu L B C}{\varepsilon}, \quad (7)$$

$$V_2 = \frac{e n_0 L^2 B}{2\varepsilon} = \frac{e N_t L^2}{2\varepsilon}. \quad (8)$$

In relationships (7) and (8), we used the following designations: e is the elementary charge, n_0 is the concentration of free charge carriers, L is the distance between the electrodes (the sample thickness), ε is the permittivity of the semiconductor, θ is the trapping coefficient, and N_t is the trap density. The quantities $C = N/gn_0$ (where $N = n_i$ is the concentration of charge carriers injected from an electrode) and $B = N_t/n_0$ are related to the trapping coefficient through the expression $\theta = C/B \ll 1$.

The concentration of free charge carriers, which was determined from the above relationships, falls in the range from 8.6×10^{16} cm^{-3} at $T = 260$ K to 5.2×10^{17} cm^{-3} at $T = 365$ K. The trap density $N_t = 2.5 \times 10^{13}$ cm^{-3} proved to be less than that estimated using other methods (9.5×10^{14} cm^{-3}). This difference can be explained by the fact that, in $Ca_4Ga_2S_7 : Eu^{3+}$ single crystals, the activation energy of traps with respect to the Fermi level is insufficiently low to satisfy the assumptions made in deriving relationships (7) and (8).

When analyzing the low-temperature current–voltage characteristics of the $Ca_4Ga_2S_7 : Eu^{3+}$ single crystals, we found that the electric current drastically increases with an increase in the temperature at field strengths of approximately 10^4 V/cm. Differential analysis of the current–voltage characteristics at a temperature of 160 K revealed a maximum in the dependence of $\alpha(V, I)$ on the voltage V in strong electric fields. In this case, the nonlinearity exponent α takes on the largest values ($I \sim V^7$). The calculations of the discrimination coefficient showed that the field ionization condition is violated ($Q_M = 126.75 \gg 4\alpha_M$). As follows from observations, such a sharp increase in the current in strong electric fields at relatively low temperatures can be associated with the high density of localized states in the band gap. This assumption can be explained in terms of the Shklovskiĭ theory of hopping conduction in crystalline and amorphous compensated semiconductors [21]. The basic idea of this theory lies in the fact that, at low temperatures, charge carriers can occupy only the deepest impurity levels and the separation between the Fermi level and the nearest allowed band considerably exceeds the binding energy of an isolated impurity. As a consequence, nonohmic hopping conduction can be observed over a wide range of electric fields.

The above treatment in terms of the Shklovskiĭ theory allowed us to calculate a number of parameters characterizing nonohmic hopping conduction. The density of states in the vicinity of the Fermi level is found to be 6.4×10^{19} eV^{-1} cm^{-3}. This value of N_F suggests a high density of localized states in the band gap. The mean hopping length is determined to be $\bar{r}_j = 7.4 \times 10^{-7}$ cm. Moreover, we estimated the density of states n_F through which hopping conduction can occur. It can be assumed that hopping conduction through these states gives rise to relaxation currents. Note that the relaxation currents were actually revealed and studied experimentally. The density of these states was calculated to be $n_F = 2.3 \times 10^{19}$ cm^{-3}, which is in agreement with the density of states determined from the available data on relaxation currents (2.6×10^{19} cm^{-3}).

4. CONCLUSIONS

Thus, the current–voltage characteristics of $Ca_4Ga_2S_7 : Eu^{3+}$ single crystals were examined for the first time. The differential analysis of the I–V curves demonstrated that the electrical properties of the high-resistance semiconductors under investigation are governed by trapping levels with activation energies of 0.13 and 0.19 eV and a trap density of 9.5×10^{14}–2.7×10^{15} cm^{-3}. It was established that the traps in strong electric fields undergo thermal field ionization. The inference was made that, at relatively low temperatures and strong fields, the current flow predominantly occurs through the mechanism of activationless conduction.

ACKNOWLEDGMENTS

We would like to thank S.N. Mustafaeva (Institute of Physics, Academy of Sciences of Azerbaijan) for her participation in discussions of the experimental results and helpful remarks.

REFERENCES

1. B. G. Tagiev, R. B. Jabbarov, U. F. Kasumov, *et al.*, New Technol. 21st Century, No. 2, 58 (1999).
2. A. N. Georgobiani, B. G. Tagiev, O. B. Tagiev, *et al.*, Jpn. J. Appl. Phys. **39-1**, 434 (2000).
3. B. G. Tagiev, U. F. Kasumov, R. B. Dzhabbarov, *et al.*, Neorg. Mater. **36** (1), 7 (2000).
4. B. G. Tagiev, U. F. Kasumov, R. B. Dzhabbarov, *et al.*, Neorg. Mater. **37** (12), 1430 (2001).
5. B. G. Tagiev, A. N. Georgobiani, O. B. Tagiev, *et al.*, Neorg. Mater. (in press).
6. B. G. Tagiev, U. F. Kasumov, R. B. Dzhabbarov, *et al.*, Fiz. Tekh. Poluprovodn. (St. Petersburg) **34**, 1170 (2000) [Semiconductors **34**, 1120 (2000)].
7. A. N. Zyuganov and S. V. Svechnikov, *Contact Injection Phenomena in Semiconductors* (Naukova Dumka, Kiev, 1981).

8. A. N. Zyuganov, S. V. Svechnikov, and Yu. G. Pis'mennyĭ, in *Semiconductor Technology and Microelectronics* (Naukova Dumka, Kiev, 1973), No. 11, p. 96.
9. A. N. Zyuganov, S. V. Svechnikov, and E. P. Shul'ga, Ukr. Fiz. Zh. **23**, 291 (1978).
10. A. N. Zyuganov, S. V. Svechnikov, A. Yu. Tkhorik, and E. P. Shul'ga, Ukr. Fiz. Zh. **21**, 370 (1977).
11. A. N. Zyuganov, S. V. Svechnikov, and E. P. Shul'ga, in *Semiconductor Technology and Microelectronics* (Naukova Dumka, Kiev, 1979), No. 29, p. 48.
12. A. N. Zyuganov and S. V. Svechnikov, Mikroélektronika **10** (2), 99 (1981).
13. Yu. G. Gusev, A. M. Ivanov, A. N. Zyuganov, *et al.*, in *Optoelectronics and Semiconductor Technology* (Naukava Dumka, Kiev, 1988), No. 14, p. 26.
14. A. N. Zyuganov, Ukr. Fiz. Zh. **15**, 45 (1974).
15. O. B. Tagiev and G. H. Kasimova, Phys. Status Solidi A **128**, 167 (1981).
16. Ya. I. Frenkel, Phys. Rev. **54**, 657 (1938).
17. P. N. Murgatroud, J. Phys.: Condens. Matter **3** (2), 151 (1970).
18. R. M. Hill, Thin Solid Films **8**, R21 (1971).
19. A. N. Georgobiani, V. I. Demin, and E. S. Logazinskaya, Tr. Fiz. Inst. im. P.N. Lebedeva, Akad. Nauk SSSR **182**, 69 (1987).
20. M. A. Lampert and P. Mark, *Injection Current in Solids* (Academic, New York, 1970; Mir, Moscow, 1973).
21. B. I. Shklovskiĭ, Fiz. Tekh. Poluprovodn. (Leningrad) **6**, 2335 (1972) [Sov. Phys. Semicond. **6**, 1964 (1972)].

Translated by O. Borovik-Romanova

Physics of the Solid State, Vol. 45, No. 3, 2003, pp. 433–437. Translated from Fizika Tverdogo Tela, Vol. 45, No. 3, 2003, pp. 409–412.

SEMICONDUCTORS AND DIELECTRICS

Structural and Physical Properties of Cobalt-Intercalated Titanium Diselenide and Ditelluride Compounds

V. G. Pleshchev*, A. N. Titov*, and S. G. Titova**

** Ural State University, pr. Lenina 51, Yekaterinburg, 620083 Russia*

*** Institute of Metallurgy, Ural Division, Russian Academy of Sciences, Yekaterinburg, 620016 Russia*

e-mail: Valery.Pleschov@usu.ru

Received April 9, 2002

Abstract—A complex investigation of the structural, electrical, and magnetic properties of cobalt-intercalated titanium diselenide and ditelluride compounds at different intercalant concentrations and temperatures is performed for the first time. The influence of the matrix on the physical characteristics of the intercalation materials is analyzed. © *2003 MAIK "Nauka/Interperiodica".*

1. INTRODUCTION

The considerable interest expressed by researchers in compounds prepared through intercalation of transition elements into titanium dichalcogenides is associated with the possibility of producing structures with alternating layers of magnetic and nonmagnetic atoms [1, 2]. These materials, unlike artificial two-dimensional magnetic structures, consist of layers whose thicknesses can be comparable to interatomic distances. In this case, the two-dimensional character of the structure manifests itself in the properties of the material to a maximum degree.

The initial matrices (TiS_2, $TiSe_2$, $TiTe_2$) used for intercalation have similar crystal structures and belong to the CdI_2 structure type [3]. As was shown earlier in [4, 5], the intercalation of 3*d* transition metals leads to hybridization of the 3*d* states of intercalated atoms with the band states of the $TiSe_2$ matrix. The contribution of intercalated atoms to the formation of new molecular orbitals depends on the nature of these atoms. The formation of the new states is accompanied by a distortion of the crystal lattice and a decrease in the electrical conductivity and the effective magnetic moment. Similar features have been observed for a number of intercalation materials based on titanium diselenide, especially for compounds in the Co_xTiSe_2 system [6].

To the best of our knowledge, intercalation compounds based on titanium ditelluride have not been studied. In this work, the experimental data on the structural, electrical, and magnetic characteristics of compounds in the Co_xTiTe_2 system were obtained for the first time. In order to gain detailed information on the mechanisms responsible for the physical properties of these compounds, it is necessary to elucidate the role played not only by intercalated unlike atoms that differ in the electronic structure of the *d* orbitals but also by the crystal matrix upon intercalation of like atoms. The results of our investigation make possible a comparative analysis of the structure parameters and physical properties of Co_xTiSe_2 and Co_xTiTe_2 compounds.

2. SAMPLES AND EXPERIMENTAL TECHNIQUE

Samples of the compositions Co_xTiSe_2 and Co_xTiTe_2 were prepared according to the two-stage procedure described earlier in [5]. At the first stage, we synthesized $TiSe_2$ and $TiTe_2$ compounds. Then, we performed x-ray diffraction analysis of these compounds and examined their physical properties. The unit cell parameters of the synthesized compounds are in reasonable agreement with those available in the literature. For both systems, the concentrations of intercalated cobalt atoms fall in the range $0 < x \le 0.5$. X-ray diffraction analysis and the determination of the structure parameters were carried out using a DRON-3M x-ray diffractometer. The errors in the determination of the lattice parameters *a* and *c* were equal to 1×10^{-4} and 4×10^{-4} nm, respectively.

The magnetic susceptibility was measured by the Faraday method in the temperature range 80–295 K. The electrical conductivity and the Seebeck coefficient were determined according to standard methods with the use of cylindrical sintered samples.

3. RESULTS AND DISCUSSION

In this work, we performed a combined analysis of the experimental results obtained for the above compounds and elucidated how the matrix used for intercalation affects the physical properties of the compounds under investigation. For this purpose, we compared the available data on the structural features of $TiSe_2$ and $TiTe_2$. Table 1 presents the main structural and crystal chemical characteristics of these compounds [7, 8].

Table 1. Unit cell parameters, the distances d_{x-x} between TiX_2 layers, and the radii r_x of X^{-2} chalcogen ions

Compound	a_0, nm	c_0, nm	c_0/a_0	d_{x-x}, nm	r_x, nm
$TiSe_2$	0.3542	0.6004	1.69	0.2964	0.182
$TiTe_2$	0.3766	0.6491	1.72	0.3121	0.211

Table 2. Structural characteristics of samples in the Co_xTiSe_2 and Co_xTiTe_2 systems

Co_xTiSe_2				Co_xTiTe_2			
x	a, nm	c, nm	c/a	x	a, nm	c, nm	c/a
0	0.3540	0.6004	1.69	0	0.3766	0.6491	1.72
0.1	0.3542	0.5962	1.68	0.05	0.3771	0.6468	1.71
0.2	0.3548	0.5934	1.67	0.15	0.3804	0.6397	1.682
0.25	0.3548	0.5901	1.66	0.25	0.3822	0.6400	1.674
0.33	0.3554	0.5890	1.65	0.4	0.3836	0.6442	1.679
0.5	0.3565	0.5883	1.64	0.5	0.3838	0.6453	1.681

As can be seen from the Table 1, the d_{x-x} distance (specifying the van der Waals gap) between chalcogen atoms located in the adjacent layers in $TiTe_2$ is larger than that in $TiSe_2$. The relative increase in the d_{x-x} distance is determined to be $\Delta d_{x-x}/d = 0.054$. This can indicate, at first glance, an increase in the degree of two-dimensionality of the crystal structure and, hence, a weakening of the interaction between TiX_2 layers and an increase in the compressibility in the order $TiSe_2 \longrightarrow TiTe_2$. However, the d_{x-x} distances given in Table 1 can serve only as a measure of the geometric width of the van der Waals gap. The final conclusion regarding the change in the degree of two-dimensionality of the crystal structure can be drawn with due regard for the fact that the radius of Te^{2-} ions exceeds the radius of Se^{2-} ions due to a larger size of the Te 4*p* orbitals. Indeed, when changing over from Se^{2-} to Te^{2-} ions, the relative increase in the ionic radius $\Delta r_x/r_{Se} = 0.093$ appears to be nearly twice as large as that in the interlayer distance. This estimate demonstrates that the "physical" width of the van der Waals gap in $TiTe_2$ is smaller than that in $TiSe_2$. Consequently, the interaction between layers in the former compound should be stronger than the interlayer interaction in the latter compound. The above inference is confirmed by the compressibilities determined from the pressure dependences of the unit cell parameters of these compounds. According to the data obtained in our previous work [9], the compressibility dc/c_0dp in the direction perpendicular to the layers is equal to 0.73×10^{-11} Pa^{-1} for titanium ditelluride and 1.53×10^{-11} Pa^{-1} for titanium diselenide. The larger size of the Te 4*p* orbitals should also affect their interaction with 3*d* electrons of intercalant atoms. Therefore, it can be expected that, under the same conditions, the behavior of the structural characteristics for compounds in the Co_xTiTe_2 system should differ from that in the Co_xTiSe_2 system.

The structural data obtained for Co_xTiTe_2 and Co_xTiSe_2 intercalation compounds are presented in Table 2.

Analysis of the structural data shows that, as the cobalt content increases, the lattice parameter *a* increases monotonically in both systems, whereas the behavior of the lattice parameter *c* and the ratio *c*/*a* for compounds in these systems differs significantly. From the structural data presented in Table 2, we calculated the relative changes in the unit cell parameters *a* and *c* for the compounds under investigation (Fig. 1). It can be seen from Fig. 1 that the parameter *a* characterizing the distance between cobalt atoms in a layer increases monotonically in both systems; however, its variation is more pronounced for Co_xTiTe_2 compounds. The degree of contraction of the unit cell along the *c* axis for the Co_xTiTe_2 crystals is larger than that for the Co_xTiSe_2 crystals at the initial stage of cobalt intercalation but turns out to be noticeably smaller as the cobalt concentration increases. This difference in the behavior of the unit cell parameter *c* can be associated with the following two factors. (1) The Te–Co–Te covalent bonds become stronger due to an increase in the overlap of orbitals. (2) As the $TiTe_2$ layers approach each other, the electron–electron repulsion increases and hinders further distortion of the unit cell in the Co_xTiTe_2 crystals. In the Co_xTiSe_2 crystals, which, as was noted above, are characterized by a larger physical width of the van der Waals gap, the degree of contraction of $TiSe_2$ layers continues to increase at higher cobalt concentrations.

Our data on the magnetic susceptibility χ for Co_xTiSe_2 [6] and Co_xTiTe_2 (Fig. 2) compounds indicate that the magnitudes of χ and its temperature dependences correspond to a paramagnetic state. As the cobalt content increases, the magnetic susceptibility χ increases in both systems but remains substantially smaller for compounds based on titanium ditelluride at the same intercalant content. These findings should be interpreted with due regard for the change in the electronic structure of the matrix and the possible transformation of the electronic configuration of intercalant atoms.

The effective magnetic moments of cobalt atoms in the studied compounds (Fig. 3) were determined from the experimental magnetic susceptibilities after elimination of the temperature-independent contributions caused by paramagnetism of the free charge carriers and diamagnetism of the filled electron shells of the atoms involved.

It can be seen from Fig. 3 that the effective magnetic moments of cobalt atoms in the Co_xTiTe_2 compounds are smaller than those in the Co_xTiSe_2 compounds. This difference accounts for the lower magnetic susceptibility of the former compounds as compared to that of the latter compounds. Analysis of the results obtained in previous studies of titanium diselenides intercalated with transition elements demonstrates that the effective magnetic moments determined in this work are close to those of cobalt atoms in the $3d^7$ configuration. As was shown earlier in [5], the filling of the cobalt *d* orbitals in the titanium diselenide corresponds, to a greater extent, to a high-spin state and the decrease in the effective magnetic moment, as compared to μ_{eff} for a free ion, is associated with the delocalization of the 3*d* electrons involved in the formation of covalent bonds. This can also be responsible in part for the smaller values of μ_{eff} for the Co_xTiTe_2 compounds. However, the decrease in the physical width of the van der Waals gap and the increase in the electron–electron repulsion should enhance the effect of the crystal field of ligands surrounding the intercalant atom. Consequently, the electronic configuration of cobalt atoms can transform into a low-spin state. In this case, the theoretical spin moment of the Co^{2+} ion is equal to $1.73\mu_B$, which is in better agreement with the effective magnetic moment determined for the Co_xTiTe_2 compounds.

The experimental investigation of the kinetic properties revealed that all the Co_xTiTe_2 compounds, like the Co_xTiSe_2 compounds [6], possess metallic conductivity in the temperature range covered (Fig. 4). However, the concentration dependences of the electrical conductivity of the former compounds exhibit a qualitatively different behavior as compared to that of the latter compounds (Fig. 5). Upon intercalation of small amounts of cobalt into $TiSe_2$, the electrical conductivity of the Co_xTiSe_2 intercalation compounds, unlike the conductivity of the matrix [6] (for $TiSe_2$, $\sigma \approx 10^5$ S/m

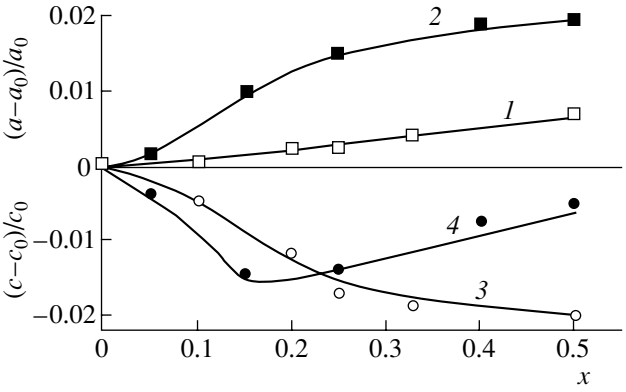

Fig. 1. Relative changes in the unit cell parameters (*1, 2*) *a* and (*3, 4*) *c* as functions of the cobalt content in (*1, 3*) Co_xTiSe_2 and (*2, 4*) Co_xTiTe_2 compounds.

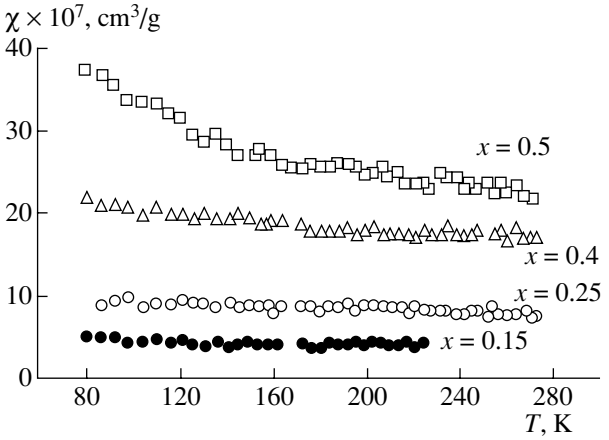

Fig. 2. Temperature dependences of the magnetic susceptibility for Co_xTiTe_2 compounds at different cobalt contents.

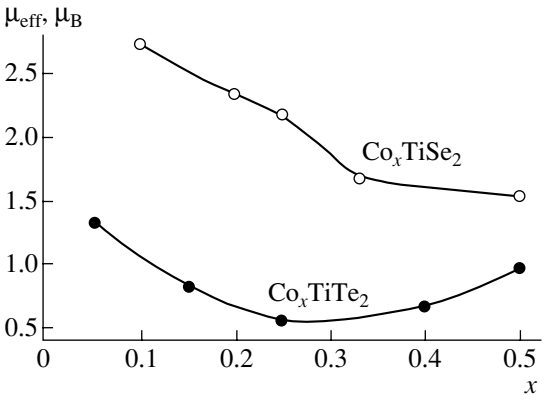

Fig. 3. Concentration dependences of the effective magnetic moment of cobalt for Co_xTiSe_2 and Co_xTiTe_2 compounds.

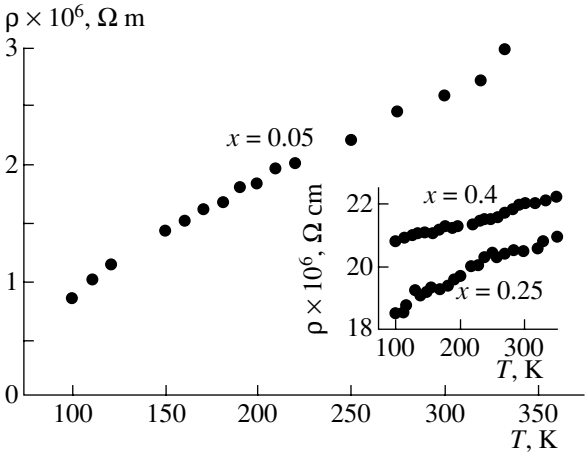

Fig. 4. Temperature dependences of the electrical resistivity of Co_xTiTe_2 compounds at different cobalt contents.

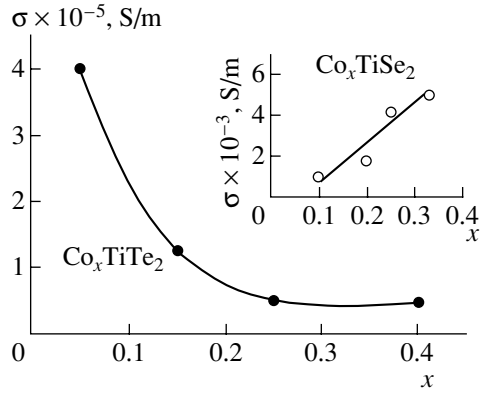

Fig. 5. Dependences of the electrical conductivity for Co_xTiSe_2 (inset) and Co_xTiTe_2 compounds on the cobalt content (T = 295 K).

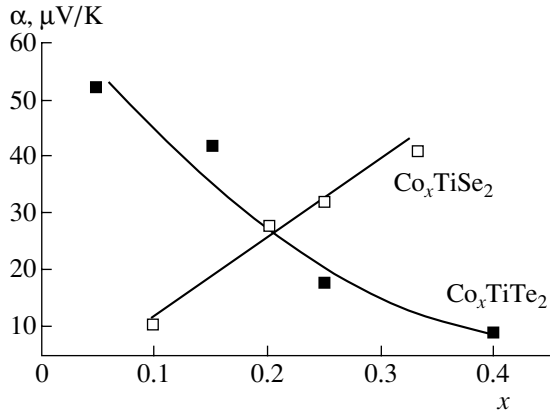

Fig. 6. Dependences of the Seebeck coefficient for Co_xTiSe_2 and Co_xTiTe_2 compounds on the cobalt content (T = 295 K).

[10]), first rapidly decreases and then begins to increase. In contrast, the electrical conductivity of the Co_xTiTe_2 compounds appreciably decreases with an increase in the intercalant content. For compounds in both systems, the concentration dependences of the Seebeck coefficient (Fig. 6) are qualitatively similar to those of the electrical conductivity. This suggests that the intercalation of cobalt into titanium diselenides and ditellurides is attended primarily by a change in the mobility of charge carriers. An increase in the mobility of charge carriers in the Co_xTiSe_2 compounds can be associated both with the overlap of the wave functions of electronic states of cobalt atoms due to the distances between them being shorter and with the formation of a partly filled impurity band. For the Co_xTiTe_2 compounds, the temperature and concentration dependences of the electrical conductivity and the Seebeck coefficient indicate that the mobility of charge carriers decreases. Note that, in this case, the mobility is governed by lattice-vibration scattering and scattering by intercalated atoms, which play the role of scattering centers. The wave functions of the electronic states of cobalt atoms within one layer overlap to a smaller extent owing to the larger cobalt–cobalt distance determined by the unit cell parameter a, which, in the Co_xTiTe_2 compounds, more substantially increases upon intercalation.

4. CONCLUSIONS

Thus, the results obtained in the above investigation demonstrated that, although different titanium dichalcogenides have similar crystal structures, more rigorous analysis of the mechanisms responsible for the physical properties of intercalation compounds should include not only the differences in the electronic structure of intercalated 3*d* transition metal atoms but also the specific features of the matrices used for intercalation.

ACKNOWLEDGMENTS

This work was supported by the US Civilian Research and Development Foundation for the Independent States of the Former Soviet Union (CRDF) (project no. REC-005), the Russian Foundation for Basic Research (project no. 01-03-32620), and the Scientific Program “Russian Universities” (project no. UR.01.01.005).

REFERENCES

1. G. Calvarin, J. Calvarin, M. Buhannic, *et al.*, Rev. Phys. Appl. **22**, 1131 (1987).
2. M. Inoue and H. P. Hughes, Adv. Phys. **38**, 565 (1989).

3. T. Hibma, in *Intercalation Chemistry*, Ed. by M. Stanley Whittingham and A. J. Jacobson (Academic, London, 1982), pp. 285–313.
4. Yu. Tazuke and T. Takeyama, J. Phys. Soc. Jpn. **66**, 827 (1997).
5. A. V. Kuranov, V. G. Pleshchev, A. N. Titov, *et al.*, Fiz. Tverd. Tela (St. Petersburg) **42** (11), 2029 (2000) [Phys. Solid State **42**, 2089 (2000)].
6. V. G. Pleshchev, A. N. Titov, and A. V. Kuranov, Fiz. Tverd. Tela (St. Petersburg) **39** (9), 1618 (1997) [Phys. Solid State **39**, 1442 (1997)].
7. F. R. Gamble, J. Solid State Chem. **9**, 358 (1974).
8. M. P. Shaskol'skaya, *Crystallography* (Vysshaya Shkola, Moscow, 1984), p. 133.
9. A. N. Titov, A. V. Dolgoshein, I. K. Bdikin, and S. G. Titova, Fiz. Tverd. Tela (St. Petersburg) **42** (9), 1567 (2000) [Phys. Solid State **42**, 1610 (2000)].
10. J. A. Wilson, Phys. Status Solidi B **86**, 11 (1978).

Translated by O. Borovik-Romanova

Physics of the Solid State, Vol. 45, No. 3, 2003, pp. 438–440. Translated from Fizika Tverdogo Tela, Vol. 45, No. 3, 2003, pp. 413–415.

SEMICONDUCTORS AND DIELECTRICS

Electronic Structure of Crystalline Sulfites

Yu. N. Zhuravlev, L. V. Zhuravleva, and A. S. Poplavnoĭ

Kemerovo State University, ul. Krasnaya 6, Kemerovo, 650043 Russia

e-mail: zhur@phys.kemsu.ru

Received April 15, 2002

Abstract—The band spectra, densities of states, and distributions of the valence and difference densities in Na_2SO_3 and K_2SO_3 crystals with a hexagonal lattice are calculated in terms of the local-density functional theory. It is found that the absorption edge of these crystals is curvilinear. The partial compositions of the bundles of valence bands are determined. It is shown that the polarizing effect of the cations on the anions substantially depends on the symmetry and the number of metal sublattices. © *2003 MAIK "Nauka/Interperiodica".*

1. INTRODUCTION

It is known that crystals of oxyanion compounds are characterized by a complex distribution of the valence electron density. In particular, the deformation electron density of magnesium and calcium carbonates [1], sodium nitride [2], potassium perchlorate [3], and a large variety of other compounds exhibits maxima not only along the *A*–O bond in an AO_n^{m-} anionic complex but also in the region behind the nuclei of terminal oxygen atoms. By using an NO_2^- ion as an example, Kikkawa *et al.* [4] demonstrated that these additional maxima are symmetric with respect to the *A*–O bond and result from the electron charge redistribution due to interaction between nitrogen and oxygen atoms. Bats and Fuess [3] proved that the magnitudes of these two maxima differ for $KClO_4$ and are equal to each other for $MgCO_3$ and $CaCO_3$ [1]. In this respect, it is of interest to elucidate the role played by the metal atom in the formation of the aforementioned maxima of the electron density.

In our recent works [5, 6], the difference density was calculated by subtracting the valence electron densities of the sublattices constituting the crystal from the valence electron density of the crystal. It turned out that the difference density is in qualitative agreement with the experimental deformation electron density. In the present work, the sublattice method was applied to an analysis of the interlattice electron transfer in sodium and potassium sulfites.

2. OBJECTS OF INVESTIGATION AND COMPUTATIONAL METHOD

The choice of sodium and potassium sulfites as the objects of our investigation was motivated by the fact that, unlike the crystal lattices studied in [5, 6], the Na_2SO_3 and K_2SO_3 lattices consist of oxygen and sulfur sublattices and three nonequivalent metal sublattices. Sodium and potassium sulfites have a hexagonal structure with the lattice parameters determined by Larsson and Kierkegard [7] and Andersen and Stroemberg [8], respectively.

Until recently, the electronic structure of alkali metal sulfite crystals had not been investigated theoretically. In this work, we calculated the band spectrum $E(\mathbf{k})$, the densities of states $N(E)$, the distributions of the valence electron charge $\rho(\mathbf{r})$, and the difference density $\Delta\rho(\mathbf{r})$ in different crystallographic planes of M_2SO_3 (M = Na, K). The calculations were performed in the framework of the local electron density functional theory within the pseudopotential approximation in the basis set of $s^1p^3d^5$ atomic pseudoorbitals with the use of the program described earlier in [9].

3. RESULTS AND DISCUSSION

Figure 1 shows the band spectrum of Na_2SO_3 and the densities of states of Na_2SO_3 and K_2SO_3. The energy is reckoned from the last occupied state. The points of the Brillouin zone are designated according to [10]. In Fig. 1, the two lower weakly disperse bundles of electron energy bands are omitted. In the density of states $N(E)$, these bundles correspond to maxima at –27.3 and –24.5 eV for Na_2SO_3 and at –27.9 and –25.3 eV for K_2SO_3.

The band spectrum of K_2SO_3 is qualitatively similar to that of Na_2SO_3. This similarity is primarily associated with the anionic nature of the valence states of these compounds. The location of the energy bands in the spectra is in reasonable agreement with the energies of the molecular orbitals of the SO_3^{2-} ion. The upper part of the valence band is separated into two subbands, which is characteristic of the majority of oxyanion crystals [11]. The contribution to the highest subband is made predominantly by the O p_{xy} and O p_z ($\mathbf{z} \parallel \mathbf{C}_3$) orbitals, whereas the lower subband is governed by the

1063-7834/03/4503-0438$24.00

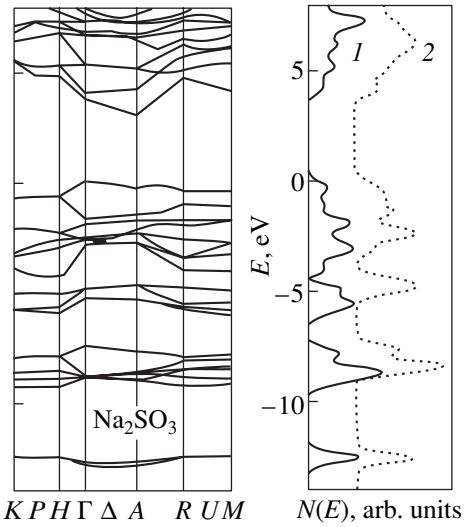

Fig. 1. Band spectrum of Na_2SO_3 and the densities of states $N(E)$ for (*1*) Na_2SO_3 and (*2*) K_2SO_3.

O p_{xy} and S p_{xy} orbitals. For M_2SO_3, the absorption edge is curvilinear, because the valence band top and the conduction band bottom correspond to the Γ ($\mathbf{k} = 0$) and *A* points of the Brillouin zone, respectively. According to our data, the band gaps E_g in Na_2SO_3 and K_2SO_3 are equal to 3.1 and 3.3 eV, respectively. It should be noted that the local-density approximation, as applied to the band calculation, always leads to underestimated values of the band gap E_g.

Let us now consider the spatial distribution of the electron charge. The valence charge is predominantly localized at the anion, specifically at the oxygen ions. There exist contours of the density $\rho(\mathbf{r})$ that envelope the anion atoms and the anions as a whole. This leads to the formation of a layered structure consisting of anions and cations.

Figure 2 represents the distribution of the difference density $\Delta\rho(\mathbf{r})$ for Na_2SO_3, which characterizes the charge transfer between the sublattices. In this figure, the *XY* plane at the left corresponds to oxygen atoms and the *YZ* plane at the right involves the metal and sulfur atoms. The oxygen atom is located at a distance of 0.33 Å from the latter plane. Here, the distances are given in Å and the distributions of the difference density $\Delta\rho(\mathbf{r})$ are expressed in $e\text{Å}^{-3}$, where e is the elementary charge. The contours of the distribution of the difference density $\Delta\rho(\mathbf{r})$ are drawn at intervals of 0.05 $e\text{Å}^{-3}$. In both planes, the difference density is negative at the atomic nuclei and in the vicinity of the metal atom. In the *YZ* plane, the difference density is positive both in the region between sulfur and oxygen atoms with a maximum of 0.045 $e\text{Å}^{-3}$ and in the region behind the nuclei of oxygen atoms. The maxima revealed in the distribution of the difference density $\Delta\rho(\mathbf{r})$ behind the oxygen nuclei differ in magnitude. In the *YZ* plane, the larger maximum is equal to 0.045 $e\text{Å}^{-3}$ and corresponds to the oxygen atom nearest to the Na_2 and Na_3 atoms. The distances between these atoms and the oxygen atom are equal to 2.33 and 2.45 Å, respectively. The Na_1–O bond length is 2.47 Å. The distribution of the difference density $\Delta\rho(\mathbf{r})$ shown in Fig. 2 differs fundamentally from both the experimental deformation electron density [1] and the electron density calculated [6] for $MgCO_3$, in which the maxima in the electron density behind the oxygen nuclei have a symmetric form and are equal in magnitude. Thus, the change in the electron density of the anion occurs due to the different polarizing effects of the crystallographically nonequivalent sodium atoms.

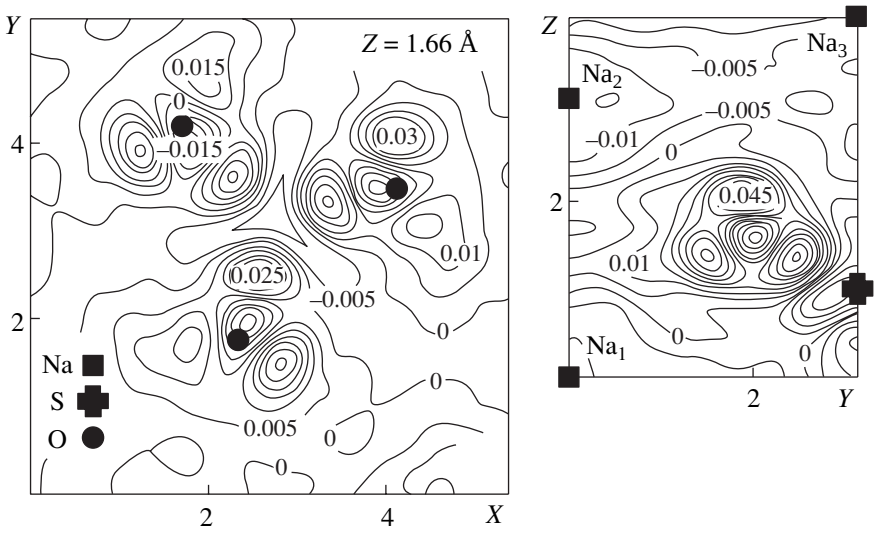

Fig. 2. Distribution of the difference density in Na_2SO_3.

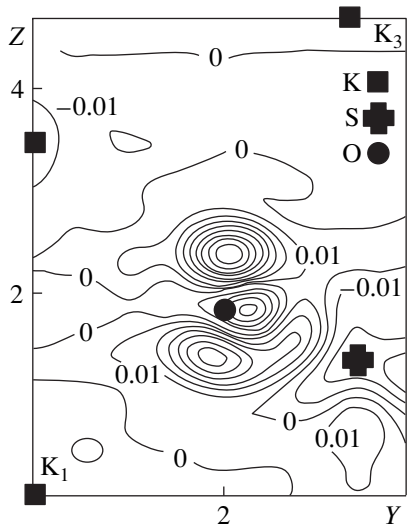

Fig. 3. Distribution of the difference density in K_2SO_3.

The replacement of the cation upon changing over to K_2SO_3 leads to the rotation of the anion with respect to the C_3 axis. Consequently, the oxygen atom is located in the *YZ* plane and the K_1–O distance becomes shorter than the K_3–O distance. This manifests itself in the distribution of the difference density for K_2SO_3. The map of the difference density in the *YZ* plane is depicted in Fig. 3. As before, the positive maxima in the difference density in the region behind the oxygen nuclei differ from each other and are equal to 0.08 and 0.06 eÅ^{-3}, whereas the maximum in the distribution of the difference density $\Delta\rho(\mathbf{r})$ along the S–O bond is 0.03 Å^{-3}. This value stems from the smaller maximum, as was experimentally demonstrated by Gonda *et al.* [2].

4. CONCLUSIONS

Thus, the results of our investigation allowed us to make the following inferences. Upon interaction of the sublattices, the electron charge is redistributed from the sulfur atoms toward the midpoint of the S–O bond, thus providing the covalent component of the chemical bond inside the anion, and also from the metal atom to the anion, which leads to the ionic bond between them. The crystallographically nonequivalent cations have different polarizing effects on the anion. As a result, there occurs a charge redistribution in the region behind the nuclei of oxygen atoms. In this case, the maxima observed in the difference density differ in magnitude, which leads to a change in the chemical activity. The excess charge at the S–O bond depends on the cation nature, which can also affect the stability of the anion.

ACKNOWLEDGMENTS

This work was supported by the Scientific Program "Russian Universities," project no. UR.01.01.47.

REFERENCES

1. E. N. Maslen, V. A. Streltsov, N. R. Streltsova, and N. Ishizawa, Acta Crystallogr. B **51**, 929 (1995).
2. T. Gohda, M. Ichikawa, T. Gustafsson, and I. Olovsson, Acta Crystallogr. B **56**, 111 (2000).
3. J. W. Bats and H. Fuess, Acta Crystallogr. B **38**, 2116 (1982).
4. T. Kikkawa, S. Ohba, Y. Saito, *et al.*, Acta Crystallogr. B **43**, 83 (1987).
5. Yu. N. Zhuravlev and A. S. Poplavnoĭ, Zh. Strukt. Khim. **42** (5), 860 (2001).
6. Yu. N. Zhuravlev and A. S. Poplavnoĭ, Fiz. Tverd. Tela (St. Petersburg) **43** (11), 1984 (2001) [Phys. Solid State **43**, 2067 (2001)].
7. L. O. Larsson and P. Kierkegard, Acta Chem. Scand. **23**, 2253 (1969).
8. L. Andersen and D. Stroemberg, Acta Chem. Scand. **40**, 479 (1986).
9. Yu. N. Zhuravlev, Yu. M. Basalaev, and A. S. Poplavnoĭ, Izv. Vyssh. Uchebn. Zaved., Fiz., No. 3, 96 (2000).
10. O. V. Kovalev, *Irreducible and Induced Representations and Corepresentations of Fedorov Groups* (Nauka, Moscow, 1986).
11. Yu. N. Zhuravlev and A. S. Poplavnoĭ, Izv. Vyssh. Uchebn. Zaved., Fiz., No. 4, 53 (2001).

Translated by O. Moskalev

Physics of the Solid State, Vol. 45, No. 3, 2003, pp. 441–443. Translated from Fizika Tverdogo Tela, Vol. 45, No. 3, 2003, pp. 416–418.

SEMICONDUCTORS AND DIELECTRICS

Thermal Properties of $K_3Li_{2-x}Nb_{5+x}O_{15\pm\delta}$ Crystals

A. U. Sheleg, E. M. Zub, T. I. Dekola, N. P. Tekhanovich, S. A. Guretskiĭ, and A. M. Luginets

Institute of Solid-State and Semiconductor Physics, Belarussian Academy of Sciences, ul. Brovki 17, Minsk, 220072 Belarus

e-mail: sheleg@ifttp.bas-net.by

Received June 4, 2002

Abstract—The unit-cell parameters of the nonlinear crystal $K_3Li_{1.88}Nb_{5.12}O_{15\pm\delta}$ were measured with x-ray diffraction in the temperature region 80–300 K. The room-temperature parameters of the crystal of this composition are $a = 12.599 \pm 0.001$ and $c = 4.018 \pm 0.001$ Å. The temperature dependences of the thermal expansion coefficients (TECs) along the [100] and [001] crystallographic directions were determined. A small TEC anisotropy was established. The specific heat of this crystal was measured using adiabatic calorimetry in the temperature interval 80–300 K. The experimental data on the specific heat were used to calculate the changes in the thermodynamic functions. © *2003 MAIK "Nauka/Interperiodica".*

1. INTRODUCTION

$K_3Li_{2-x}Nb_{5+x}O_{15\pm\delta}$ (KLN) crystals are promising materials for use as nonlinear-optical, electrooptical, and piezoelectric devices due to their broad transparency region, high radiation strength, and extremely good nonlinear-optical and electrooptical characteristics. The ferroelectric KLN crystals are tetragonal, with the room-temperature unit-cell parameters $a = 12.5764 \pm 0.0002$ Å and $c = 4.0149 \pm 0.0001$ Å [1]. Note, however, that stoichiometric KLN crystals are unstable. Stable crystals can be prepared only if the melt contains an Nb excess, i.e., has a nonstoichiometric composition $K_3Li_{2-x}Nb_{5+x}O_{15\pm\delta}$. By properly varying the melt composition, growth of KLN crystals with cell parameters in the range $a = 12.49$–12.60 Å and $c = 4.01$–4.06 Å was performed in [2]. It is common knowledge that the melt composition affects not only the crystallographic parameters but also a number of other physical properties, such as the Curie temperature and the wavelength at noncritical phase matching. Because the KLN crystal is known to be a nonlinear optical material, the information published on it relates primarily to optical properties. Moreover, any practical application would require knowledge of its thermal and thermodynamic characteristics. This communication reports on a study of the unit-cell parameters, thermal expansion, and specific heat of KLN crystals in the temperature region 80–300 K.

2. GROWTH OF $K_3Li_{2-x}Nb_{5+x}O_{15\pm\delta}$ CRYSTALS

The KLN single crystals were grown, using the Kyropoulos method, from a melt with different ratios of the starting oxides K_2O, Li_2O, and Nb_2O (30.0, 22.5–26, and 47.5–44.0 mol %, respectively). The batch was prepared by successively adding the starting OSCh-grade components to the melt, with weighing performed after each stage of preparation. The melt volume was 60–100 cm^3. The setup employed was equipped with a resistive heater. The temperature was maintained to within ±0.2 K. The crucible was placed into a vertical growth chamber. After the melt homogenization, a seed crystal was lowered into the surface zone of the melt. Two seed orientations, [001] and [100], were used. The best results were obtained with a [100]-oriented seed; the effect became more pronounced with increasing Li_2O concentration. The seed crystal rotation speed was 40–60 rpm. The crystallization onset temperature varied from 1273 to 1303 K. The temperature was lowered at a rate of 1.0 to 6.0 K/day. The crystals obtained were yellowish in color and transparent over the wavelength range from 0.4 to 50.0 μm. Sometimes, the crystals had cracks parallel to the (001) cleavage plane; these cracks formed in the course of crystal cooling from the growth temperature to room temperature.

It is known that the nonlinear optical properties of an KLN crystal depend on its chemical composition [2]. For this reason, the lithium ion concentration in the crystal matrix was determined from measuring the wavelength at which the KLN crystal of a given composition exhibited 90° phase matching at room temperature. The thermal expansion and specific heat were studied on KLN crystals of composition $K_3Li_{1.88}Nb_{5.12}O_{15\pm\delta}$.

3. EXPERIMENTAL TECHNIQUE AND RESULTS

The unit-cell measurements on KLN crystals were performed on a TUR-M62 double-crystal diffractometer (with CuK_α monochromatic radiation) equipped with an SG-9 goniometer and a Rigaku low-temperature x-ray chamber. The KLN samples were used in the form plates measuring $\sim 5 \times 7 \times 1$ mm cut from single-

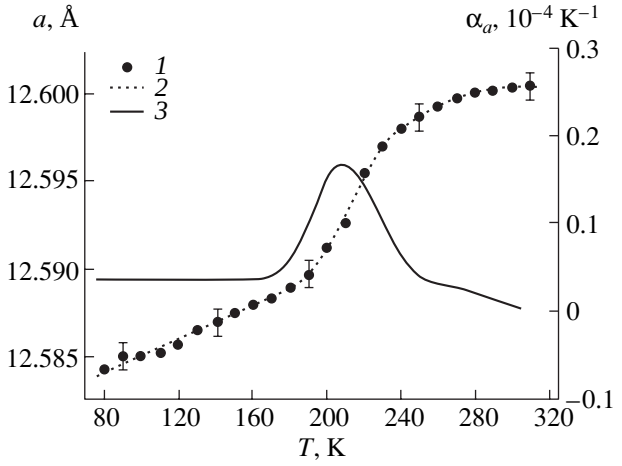

Fig. 1. Temperature dependence of the unit-cell parameter *a*: (*1*) experimental points, (*2*) fit to experimental data, and (*3*) temperature dependence of the TEC α_a.

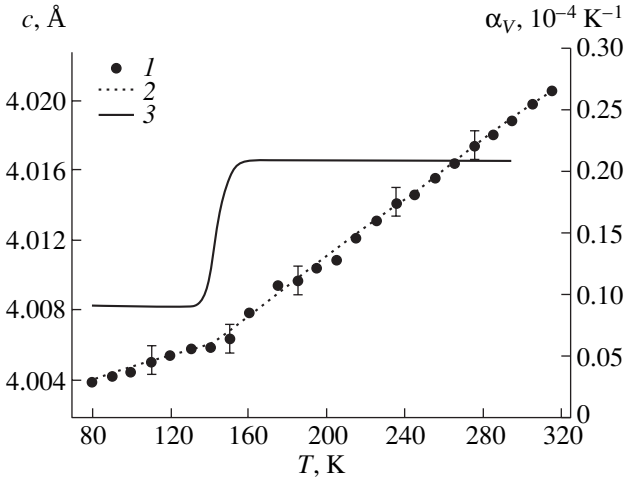

Fig. 2. Temperature dependence of the parameter *c*: (*1*) experimental points, (*2*) fit to experimental data, and (*3*) temperature dependence of the TEC α_c.

crystal ingots. The (00*l*) and (*hh*0) planes were used for reflection. The (00*l*) plane was fitted to the cut surface to an accuracy of 3′–8′, and the growth surface coincided with the (*hh*0) plane. Prior to exposure, the sample was thermostated at the given temperature for 10–15 min. The diffraction spectra were obtained by θ–2θ continuous scanning, with the reflection intensity profiles recorded once every 2–4 K at a counter rotation rate of 1/4 deg/min. The diffraction angles were determined from the positions of the centers of gravity of the (006) and (660) reflections to within 0.2′–0.4′. The parameter *c* was derived from the experimentally measured interplanar distance d_{00l}, and the parameter *a* was calculated from the values of d_{00l} and d_{hh0}.

The heat capacity of KLN crystals was studied in a vacuum adiabatic calorimeter with discrete heat injection at intervals of 1.4–1.9 K. Samples 5.794 g in mass were heated during measurements at a rate of 0.07–0.10 K/min. The error in heat capacity measurements, estimated from Grade-1 KV-quartz as a reference, did not exceed 0.3% within the temperature interval covered. The experimental data on the specific heat were least-squares fitted with a polynomial $C_i = \sum_{i=0}^{3} A_i T^i$.

The room-temperature unit-cell parameters of the KLN crystal determined by us are $a = 12.599 \pm 0.001$ Å and $c = 4.018 \pm 0.001$ Å.

Figures 1–3 display temperature dependences of the lattice parameters *a* and *c* and of the unit-cell volume *V*, respectively, for the KLN crystal measured in the temperature range 80–300 K. The values of *a* and *c* are seen to increase with temperature. However, these parameters vary differently with temperature. The parameter *c* varies linearly, with a break in the $c = f(T)$ curve appearing at $T \approx 140$ K. At the same time, the $a = f(T)$ curve exhibits a linear segment only in the temperature range 80–180 K and a strong rise in the interval ≈180–240 K. The unit-cell volume also grows with increasing temperature, with a break forming in the $V = f(T)$ curve at $T \approx 225$ K. The $a = f(T)$, $c = f(T)$, and $V = f(T)$ relations were fitted by a polynomial of the type of $L = L_0 + \sum_{i=1}^{n} A_i T^i$, where L_0 and A_i are coefficients. As seen from Figs. 1–3, the temperature dependences of the experimental values of the parameters *a* and *c* and volume *V* (points) can be well fitted by polynomials of this type (dashed curves). The linear segments of the $a = f(T)$, $c = f(T)$, and $V = f(T)$ curves were approximated by linear polynomials. The nonlinear $a = f(T)$ relation was fitted by an eighth-degree polynomial; the part of the $V = f(T)$ curve extending from 80 to 255 K, by a polynomial of third degree. The thermal expansion coefficients (TECs) α_a and α_c along the principal crystallographic axes, as well as the volume TEC α_V, were

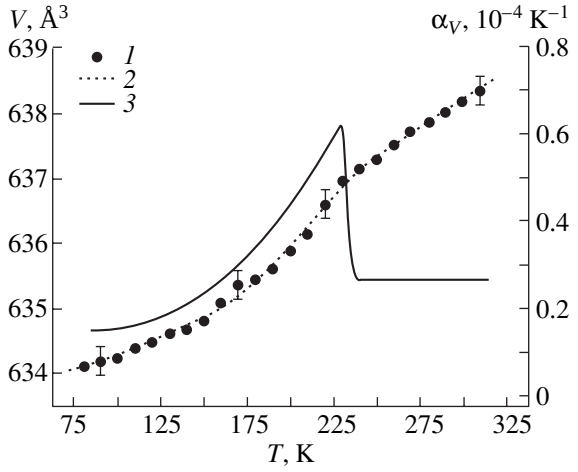

Fig. 3. Temperature dependence of unit-cell volume *V*: (*1*) experimental points, (*2*) fit to experimental data, and (*3*) temperature dependence of the TEC α_V.

Fitted values of the specific heat and the changes in thermodynamic functions of KLN

T, K	$C_p(T)$	$S(T)$–S(80 K)	$\Phi(T)$–Φ(80 K)	$H(T)$–H(80 K)
	J/(K mol)			J/mol
80	169.94	0.000	0.000	0.0
100	218.57	43.10	9.956	3885
120	262.88	86.86	24.70	8700
140	303.01	130.4	42.00	14359
160	339.13	173.3	60.71	20780
180	371.49	215.1	80.21	27886
200	400.16	255.7	100.1	35603
220	425.35	295.1	120.1	43858
240	447.20	333.0	140.1	52583
260	465.91	369.6	159.9	61714
280	481.64	404.7	179.6	71190
300	494.55	438.4	198.9	80952

derived from the relation $\alpha_L = \Delta L/(\Delta T L)$, where $L = a$, c, V correspond to the midpoint of the segment ΔT for which the TEC is determined and ΔL is the change in the parameters within this segment.

Figures 1–3 (solid curves) present temperature dependences of the TECs $\alpha_a = f(T)$ and $\alpha_c = f(T)$ along the [100] and [001] directions, as well as of the volume TEC $\alpha_V = f(T)$. As seen from Figs. 1 and 2, the KLN crystal exhibits a small anisotropy in thermal expansion, with the values of the TEC along the [001] direction being somewhat larger than those along [100] throughout the temperature range covered. The $\alpha_a = f(T)$ curve shows a maximum near ~210 K, whereas in the other temperature ranges, the values of α_a do not exceed 0.05×10^{-4} K^{-1}. The $\alpha_c = f(T)$ dependence (Fig. 2) behaves differently. At $T \approx 140$ K, the $\alpha_c = f(T)$ curve undergoes a jump, while above and below 140 K, the TEC remains at a constant level. The volume TEC α_V grows with increasing temperature and then, at $T \approx 225$ K, falls off sharply and no longer varies with a further increase in temperature (Fig. 3).

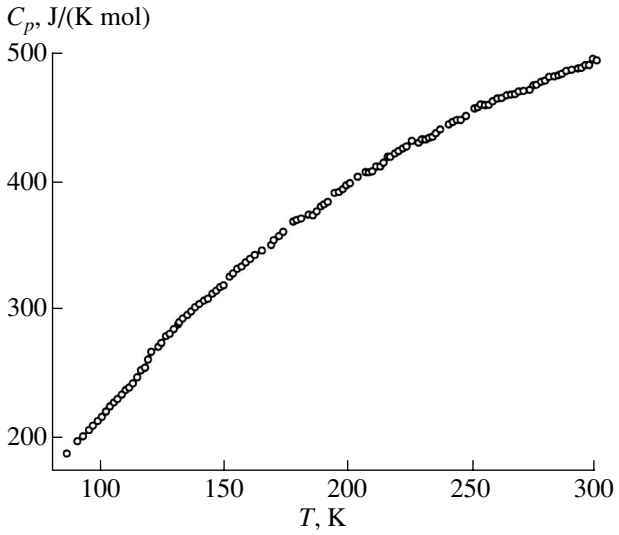

Fig. 4. Temperature dependence of the specific heat of the KLN crystal.

Figure 4 shows the experimental data on the specific heat of the crystal plotted as a function of temperature in the range 80–320 K. It is seen that the specific heat C_p of the KLN crystal grows smoothly with increasing temperature; however, no saturation is achieved. The $C_p(T)$ curve constructed by smoothing the experimental data was used to calculate, through numerical integration, the changes in the thermodynamic functions of the KLN crystal, namely, the entropy, enthalpy, and reduced Gibbs energy. The fitted values of the specific heat and the corresponding changes in the thermodynamic functions are listed in the table.

4. CONCLUSION

Thus, we have determined the TECs along the principal crystallographic axes, the specific heat, and the changes in the thermodynamic functions for an KLN crystal over a broad temperature range, which may prove very useful in applications of these crystals as nonlinear-optical, electrooptical, or piezoelectric devices below room temperature.

REFERENCES

1. S. C. Abrahams, P. B. Jamilson, and J. L. Bernstein, J. Chem. Phys. **54**, 2355 (1971).
2. Lian Li, T. C. Chong, X. W. Xu, *et al.*, J. Cryst. Growth **211**, 281 (2000).

Translated by G. Skrebtsov

Physics of the Solid State, Vol. 45, No. 3, 2003, pp. 444–448. Translated from Fizika Tverdogo Tela, Vol. 45, No. 3, 2003, pp. 419–423.

SEMICONDUCTORS AND DIELECTRICS

Variation of Spontaneous Emission in the Opal Stop-Band with an Enhanced Refractive-Index Contrast

S. G. Romanov and A. V. Fokin

Ioffe Physicotechnical Institute, Russian Academy of Sciences, Politekhnicheskaya ul. 26, St. Petersburg, 194021 Russia

Received June 6, 2002

Abstract—Photoluminescence spectra of an opal with an anatase layer grown on its inner surface were studied. Measurements were carried out with a high angular resolution at various pump power levels and detection angles. The intensity and probability of emission were found to acquire an anisotropy corresponding to the frequency and angular dispersion of the first opal photonic band gap. As the pump power increases, the suppression of spontaneous emission in the photonic band gap is shown to be replaced by its amplification. The amplification of spontaneous emission is tentatively assigned to the existence of localized defect optical modes in the photonic band gap. *© 2003 MAIK "Nauka/Interperiodica".*

1. INTRODUCTION

Light sources based on photonic crystals (PhCs) can presumably exhibit a high efficiency through suppression of spontaneous emission in the broad spectral region referred to as the photonic band gap (PBG) and narrow-band amplification of the emission in the region of a sharp drop in the density of photon states [1–3].

Of most interest are three-dimensional (3D) PhCs, where the PBG does not depend on direction. However, no 3D PhCs with an omnidirectional PBG in the visible region have been developed thus far; therefore, the best studied 3D PhCs in the optical range are anisotropic PhCs, in particular, conventional and inverted opals [4]. Because of the PBG anisotropy and of the PhCs being of finite size, the optical-mode density spectra contain a considerable fraction of propagation modes at the PBG frequencies. We shall call such a PBG a stop band in what follows. The high density of photon states in the region of the stop band accounts primarily [5] for the insignificant variation of the radiative recombination probability in opals with a low refractive-index contrast [6, 7].

Despite the absence of PhCs with a complete PBG, the effect of the photonic band gap on the light source emission is fairly large in the angular region corresponding to the Bragg cone, i.e., in the angular space region inaccessible for propagation of electromagnetic (EM) waves with frequencies in the stop band. The emission intensity is observed to decrease in the stop band region in practically all well-ordered opals [8]. Until recently, however, the variation in the emission probability associated with the existence of the stop band was a subject of debate [9]. Alternative mechanisms capable of varying the spontaneous emission rate involve distributed feedback in a periodically modulated scattering medium and photon localization in an irregular scattering medium, in which the phase coherence condition can be satisfied randomly in certain regions [10]. Both mechanisms operate in opals with a very low refractive-index contrast to produce lasing, whose parameters are either associated with the structure [11] or originate from diffuse scattering [12].

Opals contain a considerable number of uncontrollable defects [13] with modes that differ from those of a crystalline PhC. Obviously enough, radiation can be supported by modes of either type, with the probability of spontaneous emission in a given mode depending on the actual type of EM field mode employed (the Parcell effect [3]). Thus, it appears natural to look for a possible modification of spontaneous emission in opals where there are no ideal PhC modes, i.e., in the Bragg cone. A distinctive feature of this modification of radiation will be the occurrence of an anisotropy in correspondence with the PhC symmetry. Photoluminescence (PL) measured with a high angular resolution could be used as a possible tool in this search.

The position of the emitter in the PhC unit cell is an important factor in the amplification of spontaneous emission, because the larger the electric field amplitude of an optic mode at the emitter site, the higher the emission probability. As shown earlier, in polymer opals with a refractive-index contrast of about 1.5 to 1 that have a light source inside the spheres, the PL intensity in the stop band region grows ~10% slower with increasing pump power [14]. As the refractive-index contrast increases, the EM field concentration in the spheres is amplified, which may increase the efficiency of excitation transformation into emission. This communication reports on an experimental increase in the contrast reached by coating the inner opal surface with TiO_2.

1063-7834/03/4503-0444$24.00

2. MATERIAL AND EXPERIMENTAL TECHNIQUE

The samples employed in this study were prepared from SiO_2 opals with a pore volume fraction of 13%. The porosity was reduced by sintering and burying the opal pores with amorphous silica to strengthen the opal following sedimentation. The accessible porosity was determined from the diffraction resonance frequency shift of the opal in the [111] direction of its fcc lattice after filling it with oil with a known refractive index. The inner surface of the opal was coated by a thin layer of TiO_2 in a 26-fold molecular layering procedure; this process is described in considerable detail in [15]. The Ti content in the opal, as derived from x-ray microprobe analysis, was about 6.4%. The Raman scattering spectrum of the composite thus obtained is dominated by a band at 141 cm^{-1} characteristic of crystalline TiO_2 (anatase). Electron microscopy yielded 234 nm for the opal sphere diameter and about 100 μm for the crystallites making up the opal. Light is emitted in this sample by oxygen defects present in the amorphous silica.

The sample used was in the form of a plate about 0.3 mm thick, with the wide face oriented along the (111) opal plane. The PL was excited optically by a cw argon-laser line (351.4 nm). The radiation was collected within a solid angle of about $\Omega = 0.35°$ from the sample side opposite to the illuminated face (Fig. 1) and measured with a PM tube with a photon counter located near the double-grating monochromator. The reflection spectra were obtained with halogen incandescent lamp radiation after dispersion in a monochromator. The reflected intensity was measured with a PM tube in a solid angle of about 1° at a reflection angle equal to the angle of incidence.

3. EXPERIMENTAL RESULTS

The TiO_2 coating increased the average refractive index by 0.07, which shifted the Bragg resonance from 2.33 to 2.2 eV. In the effective-medium approximation,

$$n^2_{\text{sample}} = n^2_{SiO_2} f_{SiO_2} + n^2_{TiO_2} f_{TiO_2} + f_{\text{air}},$$

where n_i is the refractive index and f_i is the relative filling of the opal by a substance with the corresponding refractive index; this shift corresponds to a 4.6% filling of the total volume of the starting opal by anatase. Thus, the PhC studied consists of SiO_2 spheres coated by a layer of anatase about 7 nm thick, with the pores occupying approximately 8% of the total volume.

Figure 1a presents sample reflectance spectra measured at angles 0°, 20°, and 40° with respect to the [111] opal lattice axis. The relative FWHM of the Bragg peak in the reflectance spectrum is $\Delta E/E_B \approx 0.05$, where E_B is the resonance frequency. This figure is slightly smaller than the band width calculated for an opal with 26% porosity [16], which is in agreement with the data on the stop band narrowing along the [111] direction with increasing the fraction of dielectric in the opal [17].

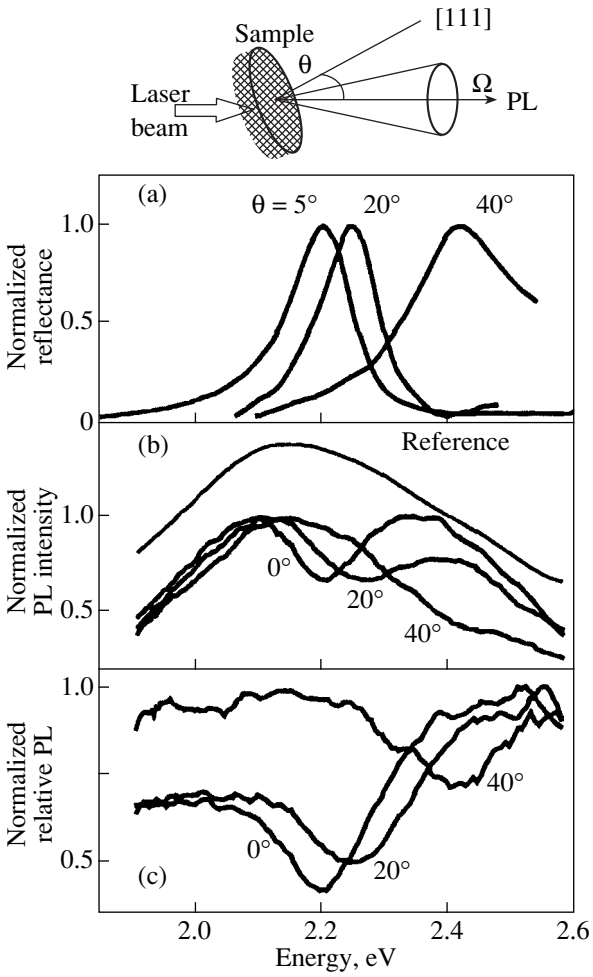

Fig. 1. Optical spectra of an opal with TiO_2. (a) Sample reflectance spectra plotted vs. incidence angle. The angles are specified near the curves. θ = 0° corresponds to the [111] axis in the opal fcc lattice. (b) PL spectra for the same directions. The spectrum for θ = 80° used as a PL reference for a sample without a stop band is translated vertically. (c) Relative PL spectra derived from PL spectra for θ = 0°, 20°, and 40° by dividing them by the reference spectrum. The spectra are normalized against their maxima. The inset on top explains the photoluminescence measurement scheme.

The opal PL spectra (Fig. 1b) contain a minimum that coincides in position with the Bragg peak in the reflectance. As the angle of observation increases to 40°, the minimum in the PL spectrum shifts toward higher frequencies and washes out both because of disorder in the opal lattice and as a result of approaching the edge of the PL band.

Figure 1c displays the relative PL (RPL) spectra obtained by dividing the PL spectra by the PL spectrum measured at an angle θ = 80° to the [111] axis. The latter spectrum is accepted as a reference, because it contains all the characteristic spectral features of the light source used, except the photon band gap effect. RPL

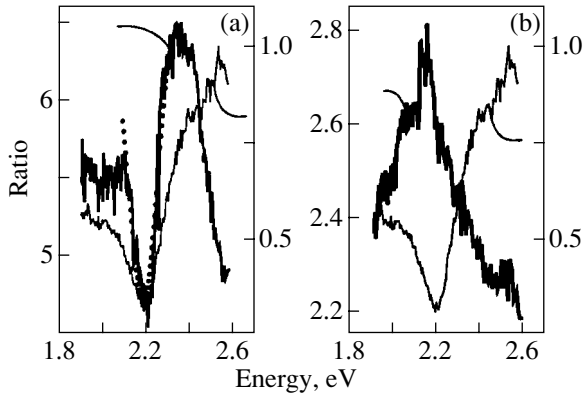

Fig. 2. (a) Ratio of PL spectra obtained under 100- and 10-mW pumping (thick line) and fitting a Gaussian to the RS (points). The relative PL spectrum (thin line) for θ = 0° is shown for comparison. (b) An RS derived from PL spectra measured at pump powers of 450 and 100 mW. The RS presented was obtained by averaging over several measurements.

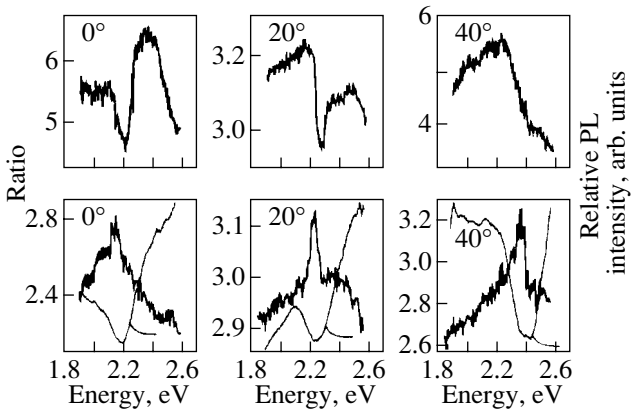

Fig. 3. RS for θ = 0°, 20°, and 40° measured for pump power increments of 100 mW/10 mW (top row) and 450 mW/100 mW (bottom row). The angles are specified for each graph. The RSs were averaged over several measurements. Relative PL spectra are represented by thin lines in the bottom row to indicate the stop band position.

spectra permit one to determine the central frequency and the width of the stop band in the emission. The stop band in the emission, $E_c(\theta = 0°) = 2.2$ eV, is seen to be centered at the diffraction resonance frequency, its relative width being $\Delta E/E_c = 0.07$. The PL intensity in the stop band is 40–50% suppressed. The RPL spectrum apparently differs from the transmittance spectrum in the fact that the contribution to the radiation comes from the near-surface sample region, where the effect of the stop band is comparatively weaker than in the bulk of the opal, and in the radiation source being noncollimated. The Bragg attenuation length in the [111] direction can be estimated from the width of the resonance peak as

$$L_B = 2d\lambda_B/\pi\Delta\lambda \approx 2280 \text{ nm},$$

where $d = 0.816D$ is the lattice period in this direction. Thus, the RPL spectra obtained give one an idea of the relative decrease in the number of optic modes in the stop band.

The PL spectra were taken at various pump power levels. To reveal weak changes in the PL spectrum shape more clearly, the ratios of two spectra measured at different pump intensities were plotted. As seen from Fig. 2a, for θ = 0°, the ratio of the two PL spectra obtained at pump powers of 10 and 100 mW passes through a minimum centered at the Bragg frequency. The amplitude of the ratio is ~6.5, which is less than the increment of the pump power, apparently due to nonradiative recombination. A Gaussian fit to the minimum in the ratio spectrum (RS) permits one to estimate the relative FWHM of the minimum as 0.04 and its relative depth as ~20% (Fig. 2a). The corresponding attenuation length for this line is about twice the Bragg attenuation length.

As the pump power is increased from 100 to 450 mW, the minimum at the Bragg frequency in the RS is replaced by a maximum (Fig. 2b). The band in this spectrum is shifted by 0.05 eV toward lower frequencies with respect to the central frequency of the stop band. Figure 3 displays PL ratio spectra for θ = 0°, 20°, and 40° measured at the same pump power increments. The minima and maxima in the ratio spectra are locked in frequency to the Bragg resonance and shift in accordance with its angular dispersion. The red shift of the peak band relative to the Bragg gap remains the same for all directions.

4. DISCUSSION OF RESULTS

To interpret the experimental data correctly, we consider the emission in opal. The wide-band emission in the SiO_2 opal is known to be produced by the oxygen vacancies in silicon dioxide [15]. The PL intensity of an unstructured sample is distributed spectrally in accordance with the occupation probability of the oxygen vacancy excited states; note that because the emitting dipoles are randomly oriented, the light sources can be considered to be points. By contrast, in ordered opal, there is a band structure for the allowed modes. Because the photon band gap is strongly dispersed, an ideal opal has no eigenmodes of a given frequency only for certain values of the wave vector and, accordingly, in the region of the Bragg cone in real space. However, if an opal lattice defect mode does exist in the photon band gap, this mode can also propagate in the direction of the diffraction resonance. In the case of low defect density, the EM modes of a nonideal PhC can be conventionally divided in two reservoirs, namely, modes of an ideally packed PhC and those of defects. The density of defect modes in allowed bands is low in comparison with that of the eigenmodes of a defect-free PhC; therefore, the only regions where defect modes can notice-

ably affect the PhC optical properties are the stop bands.

According to Fermi's golden rule, the probability of spontaneous emission depends on the optical-state density and on the EM field structure of the modes associated with the emitter. Because the opal under study does not differ strongly in its properties from an ideal fcc sphere packing, the minimum in the total density of states in the region of its Bragg photonic band gap is only a few percent [18]. Accordingly, theory (see, e.g., [7] for the opal) predicts an insignificant decrease in the emission probability for a source in the opal.

In the case of an opal with defects, this consideration should be apparently modified because of the emission being connected either with the modes of an ideal lattice in an allowed band or with the modes of defects in the Bragg cone. It may be expected that, first, the radiative recombination probabilities outside and inside the stop band will be different due to the Parcell effect [3] and, second, the effective recombination probability will inherit an anisotropy from the opal Bragg stop band.

Radiation in the opal is transported both ballistically and through diffusion. Ballistic photons exit the opal without scattering; i.e., they belong to the modes involved in a recombination event. By contrast, photons which have undergone multiple scattering lose information about their origin. The photon mean free path in opals is 7–10 μm [19], which is larger than the Bragg attenuation length. It is this length that determines the escape depths of ballistic photons. Note that the relative fraction of diffusely scattered photons is determined by the defect density and is independent of the pump power; therefore, the RS reflects the ballistic radiation component only.

Because a defect is enclosed in a Bragg resonator, those of its modes whose frequencies and wave vectors lie in the stop band are localized; i.e., these modes are similar to those of a resonator with a Q factor determined by the coupling of a given mode with free-space propagating modes. In the case of optical pumping, localization of a mode results in amplification of the emission in proportion to the mode Q factor. Thus, as the pump power is increased, the occupation of all modes increases, but this increase is superlinear for the localized modes only.

The spontaneous emission probability in the stop band is a composite function of both the number of modes and their Q factor; therefore, this probability can be both lower and higher than that of emission in the allowed bands, depending on the pump level. The evolution of an RS with pump intensity reflects the balance of competing processes; more specifically, at low pumping powers, spontaneous emission in the stop band is suppressed, while at higher pump intensities, amplification prevails. The red shift of the emission gain band relative to the central frequency of the stop band is caused by the EM wave field being concentrated in the dielectric component of the opal. This observation argues for the proposed description of the role of defects as a weak perturbation of the EM field distribution in an opal.

5. CONCLUSION

Thus, in order to estimate the relative suppression/amplification of spontaneous emission in the stop band, we analyzed the PL spectrum distortion of ballistically propagating modes by constructing ratio spectra. It has been found that the RS has a feature at the stop band frequencies as a result of the emitter coupling with the PhC eigenmodes beyond the stop band and with defect modes in the stop band being different. The RS minimum in the stop band observed at low pump powers is a consequence of the small number of modes which can couple with the emitter. By contrast, the RS maximum, which occurs at a higher pump intensity, is apparently due to the emitter being more efficiently coupled to the localized defect modes than to the free-space propagating PhC modes. The method used here to construct the RS is a facilitated version of a more general method for obtaining a spectrum of the exponent in the dependence of the emission intensity on pump power, which will be described in a later publication. Summing up the results obtained in this study, we can say that while stop band dispersion in opal gives rise to a clearly pronounced emission directivity pattern [20], the same dispersion results in an anisotropy of the effective spontaneous emission probability in the presence of two types of optical modes.

ACKNOWLEDGMENTS

The authors are indebted to M. Kalitievskiĭ and D. Chigrin for stimulating discussions.

This study was supported by the Russian Foundation for Basic Research, project no. 02-02-17685.

REFERENCES

1. V. P. Bykov, Zh. Éksp. Teor. Fiz. **63** (4), 1226 (1972) [Sov. Phys. JETP **36**, 646 (1973)].
2. E. Yablonovitch, Phys. Rev. Lett. **58**, 2059 (1987).
3. E. M. Parcell, Phys. Rev. **69**, 681 (1946).
4. Special issue of Photonic Crystals, Adv. Mater. **13** (6) (2001).
5. Zhi-Yuan Li and Zhao-Qing Zhang, Phys. Rev. B **63**, 125106 (2001).
6. E. P. Petrov, V. N. Bogomolov, I. I. Kalosha, and S. V. Gaponenko, Phys. Rev. Lett. **81**, 77 (1998).
7. M. Megens, J. E. G. J. Wijnhoven, A. Lagendijk, and W. L. Vos, Phys. Rev. A **59**, 4727 (1999).
8. S. G. Romanov, A. V. Fokin, V. I. Alperovich, *et al.*, Phys. Status Solidi **163**, 169 (1997); S. G. Romanov, A. V. Fokin, and R. M. De La Rue, Appl. Phys. Lett. **74**, 1821 (1999); Y. A. Vlasov, M. Deutsch, and D. J. Norris, Appl. Phys. Lett. **76**, 1627 (2000).

9. S. G. Romanov, A. V. Fokin, V. V. Tretijakov, *et al.*, J. Cryst. Growth **159**, 857 (1996); Yu. A. Vlasov, K. Literova, I. Pelant, *et al.*, Appl. Phys. Lett. **71**, 1616 (1997).
10. M. N. Shkunov, Z. Valy Vardeny, M. C. DeLong, *et al.*, Adv. Funct. Mat. **12**, 21 (2002).
11. S. V. Frolov, Z. V. Vardeny, K. Yoshino, *et al.*, Phys. Rev. B **59**, R5284 (1999).
12. H. Cao, J. X. Xu, Y. Ling, *et al.*, in *Photonic Crystals and Light Localization in the 21st Century*, Ed. by C. M. Soukoulis (Kluwer Academic, Dordrecht, 2001); NATO ASI Ser. **563**, 389 (2001).
13. Yu. A. Vlasov, M. A. Kaliteevski, and V. V. Nikolaev, Phys. Rev. B **60**, 1555 (1999).
14. S. G. Romanov, T. Maka, C. M. Sotomayor Torres, *et al.*, J. Appl. Phys. **91**, 9426 (2002).
15. S. G. Romanov, F. V. Fokin, V. Yu. Butko, *et al.*, Fiz. Tverd. Tela (St. Petersburg) **38**, 3347 (1996) [Phys. Solid State **38**, 1825 (1996)].
16. A. Reynolds, F. López-Tejeira, D. Cassagne, *et al.*, Phys. Rev. B **60**, 11 422 (1999).
17. S. G. Romanov, H. M. Yates, M. E. Pemble, and R. M. De La Rue, J. Phys.: Condens. Matter **12**, 339 (2000); A. L. Reynolds, D. Cassagne, C. Jouanin, and J. M. Arnold, Synth. Met. **116**, 453 (2001).
18. K. Busch and S. John, Phys. Rev. E **58**, 3896 (1998).
19. J. Huang, N. Eradat, M. E. Raikh, *et al.*, Phys. Rev. Lett. **86**, 4815 (2001).
20. S. G. Romanov, T. Maka, C. M. Sotomayor Torres, *et al.*, J. Lightwave Technol. **17**, 2121 (1999).

Translated by G. Skrebtsov

Physics of the Solid State, Vol. 45, No. 3, 2003, pp. 449–452. Translated from Fizika Tverdogo Tela, Vol. 45, No. 3, 2003, pp. 424–428.

SEMICONDUCTORS AND DIELECTRICS

Thermal Conductivity of Polycrystalline Zinc Selenide

N. V. Lugueva*, S. M. Luguev*, and A. A. Dunaev**

** Institute of Physics, Dagestan Scientific Center, Russian Academy of Sciences, ul. Dvadtsati Shesti Bakinskikh komissarov 94, Makhachkala, 367003 Russia*

e-mail: luguev.if@mail.ru

*** Research Institute of Optical Materials Technology, Vavilov State Optical Institute All-Russia Scientific Center, Birzhevaya liniya 14, St. Petersburg, 193131 Russia*

Received May 14, 2002; in final form, June 19, 2002

Abstract—The thermal conductivity of optically transparent zinc selenide polycrystals fabricated by vapor deposition was experimentally studied in the temperature range 80–400 K in the as-deposited state and after deformation along the crystal growth direction followed by recrystallization. In the low-temperature range, textured ZnSe samples exhibit anisotropy of the thermal conductivity, which also persisted after their deformation and recrystallization. The anisotropy of the thermal conductivity is caused by phonon scattering by dislocations oriented along the crystal growth direction. The thermal conductivity of ZnSe at $T > 270$ K is shown to be limited by the scattering of acoustic phonons by optical phonons. © *2003 MAIK "Nauka/Interperiodica".*

Zinc selenide is a wide-spectrum optical material used as elements of structural optics in infrared systems and laser setups. Apart from having to be transparent in a wide spectral range, materials applied in IR engineering must have high mechanical strength and exhibit isotropic properties. Polycrystalline optical materials are best suited to these requirements [1]. Vapor deposition methods have been extensively used in recent years to fabricate them. Polycrystals grown using such methods have a low amount of impurities and other defects, which substantially improves the optical properties of samples; however, texture appearing during the growth of crystals can significantly affect the thermal and mechanical properties of materials. The negative effect of texture on the thermal and mechanical properties of samples can be reduced by subjecting them to deformation and recrystallization.

Operation of the elements of structural optics under varying thermal conditions and high thermal loads requires knowledge of the thermal conductivity κ of a given optical material. The thermal conductivity of single-crystal ZnSe was studied in [2]. Data on κ of polycrystalline ZnSe as a function of texture and deformation are not available in the literature. The investigation of the thermal conductivity of ZnSe polycrystals prepared by vapor deposition will allow one not only to obtain data on κ required for engineering calculations but also to gain insight into the mechanisms of heat transfer in texturized samples and samples subjected to deformation and recrystallization.

The purpose of this work is to experimentally study the thermal conductivity of polycrystalline ZnSe and its temperature dependence, as well as to study the variation of κ with the ZnSe structure. The investigation of the effect of the phonon spectrum of ZnSe on the value and temperature dependence of κ is also of interest.

Samples for investigation were cut from zinc selenide blocks having different technological histories. The material from which samples *1* and *2* were cut was fabricated by vapor deposition onto a heated substrate in a closed container at a temperature of 1250 K and a deposition rate of 0.8 mm/h. The polycrystalline material obtained under these conditions had a pronounced columnar structure with the preferred $\langle 111 \rangle$ orientation of crystallites. The mean grain size in the deposition plane is 2 mm. A micrograph of the as-deposited ZnSe polycrystal is shown in Fig. 1a. Samples *3* and *4* were cut from the same blocks as samples *1* and *2*, but the blocks were additionally subjected to deformation under pressure in the direction parallel to the direction of crystal growth and to recrystallization. The deformation and recrystallization of the polycrystalline blocks were carried out sequentially at a temperature of 1150 K and a pressure of 150 MPa for 15 min and followed by annealing at 1450 K for 20 min. The ZnSe polycrystals subjected to deformation and recrystallization consisted of crystallites without any preferred orientation (Fig. 1b). Workpieces fabricated by the technique described above were used to cut samples measuring $15 \times 6 \times 6$ mm in two mutually perpendicular directions (Fig. 2). According to x-ray diffraction analysis, the samples had a cubic (sphalerite) structure.

We measured the absolute values of κ in the temperature range 80–400 K in vacuum using a stationary method on a device similar to the "A"-type device described in [3]. The schematic of the heat-flow directions in the measuring cell of the device with respect to the sample texture and the pressure applied for deformation is shown in Fig. 2. We measured κ in the geom-

1063-7834/03/4503-0449$24.00

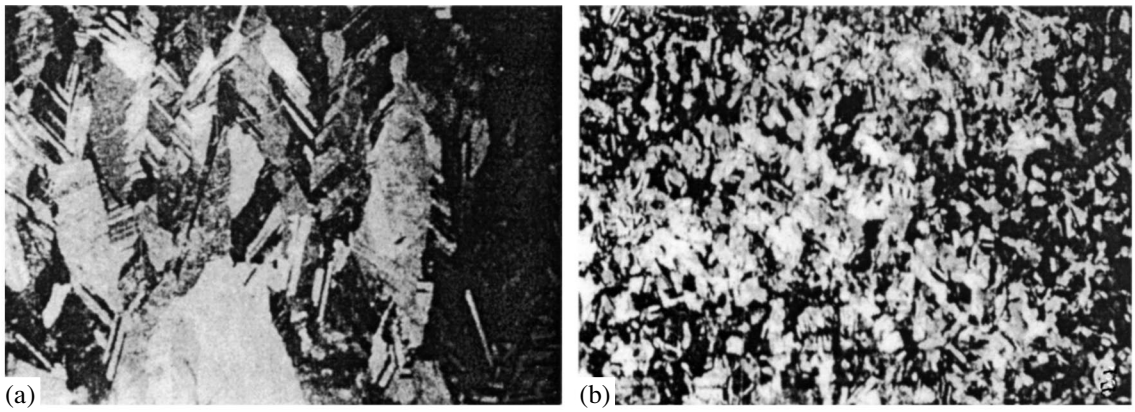

Fig. 1. Micrographs of ZnSe polycrystals: (a) an as-deposited sample and (b) the same sample but after deformation and recrystallization.

etry where the heat flow through a sample was either coincident with the preferred growth direction of crystallites or normal to it. The margin of relative error of measuring κ was smaller than 2% over the whole temperature range studied.

The experimental data on the thermal conductivity of ZnSe samples with various technological histories and heat-flow directions with respect to the texture are shown in Fig. 3. The numerals on the curves in Fig. 3 correspond to the numbers of samples in Fig. 2. The κ data for single-crystal ZnSe from [2] are also given in Fig. 3. As is seen, the κ values and its temperature dependences for polycrystalline ZnSe samples are close to those presented in [2] for a single-crystal ZnSe.

The temperature dependences of $\kappa(T)$ for samples *1*–*4* at $T > 300$ K are virtually coincident. In the low-temperature range, the experimental results exhibit κ anisotropy in the polycrystalline ZnSe with respect to the crystallite growth direction. At 80 K, the thermal conductivity of sample *1*, for which the heat-flow direction coincided with the crystal growth direction, is 14% higher than that of sample *2*, for which the heat-flow direction was normal to the crystal growth direction (curves *1*, *2* in Fig. 3, respectively,). The thermal conductivities of polycrystalline samples additionally subjected to deformation and recrystallization (samples *3*, *4*) also exhibit anisotropy, depending on the heat-flow direction through the sample.

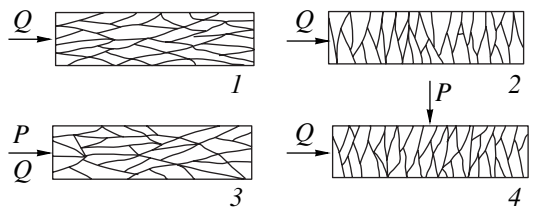

Fig. 2. Schematic of the texture and the directions of a heat flux Q and an applied stress P in samples *1*–*4* during measurements of κ.

Consider possible contributions to the total thermal conductivity of the samples studied. Since the electrical resistivity of ZnSe is high, the electronic component of the thermal conductivity is negligible. The high optical transparency of ZnSe suggests that heat transfer can proceed in it via electromagnetic radiation. We estimated the photon component κ_{phot} of the thermal conductivity in the samples using the Genzel formula [4]. When calculating κ_{phot}, we used the absorption coefficients calculated from the experimental data on the transparency of the samples studied. The refraction indices were taken from [5]. Our estimation showed that κ_{phot} is insignificant in the low-temperature range, is equal to 2% of the total thermal conductivity at 300 K, and is equal to 6% at 400 K. Thus, in the temperature range studied, heat transfer in the ZnSe crystals is due mainly to lattice vibrations; the κ_{phot} contribution to κ should be taken into account only in the range 300–400 K.

Since the ZnSe samples have cubic structure, the anisotropy of κ experimentally observed in the low-temperature range cannot be explained in terms of the anisotropic elastic properties of the crystal lattice. The κ anisotropy in the polycrystalline ZnSe samples can be due to the presence of a preferred direction of intercrystalline boundaries and oriented dislocations. To reveal the role of boundaries in phonon scattering and in decreasing κ in the polycrystalline ZnSe, we calculated the mean free path of phonons in this material. According to the Debye kinetic relation, the lattice thermal conductivity κ_{ph} of a dielectric crystal is

$$\kappa_{ph} = \frac{1}{3} C_v v l, \tag{1}$$

where C_v is the specific heat (per unit volume) of the crystal, v is the mean velocity of sound, and l is the mean free path of phonons. The experimental κ_{ph} data for zinc selenide allow us to estimate the mean free path of phonons at various temperatures using Eq. (1). In

order to calculate l, we took the C_v values for ZnSe from [6] and the v values from [7]. The mean free path of phonons in the ZnSe polycrystals is found to be $l = (1.3–11) \times 10^{-7}$ m at 80 K, depending on the heat-flow direction with respect to the crystallite growth direction, and 2.2×10^{-9} m for all samples at 400 K. A comparison of l in the polycrystalline ZnSe with the crystallite size (2 mm) shows that scattering by boundaries does not affect κ in the temperature range covered.

Now, we analyze the dislocation structure of the samples. Crystals of II–VI compounds are known to grow via screw dislocations whose axes coincide with the growth direction [8]; therefore, the samples studied contain screw dislocations with a preferred orientation along the crystal growth direction.

According to [9], the lattice thermal resistance W due to phonon scattering by dislocations can be represented as

$$W_d = kL\sigma\sin\alpha, \quad (2)$$

where L is the dislocation length, σ is the dislocation scattering cross section, α is the angle between the dislocation axis and the temperature gradient direction, and k is a constant depending on the phonon frequency. It follows from Eq. (2) that the phonon scattering by dislocations decreases with decreasing angle between the dislocation axis and the temperature gradient direction. When measuring κ, we oriented polycrystalline ZnSe samples so that the direction of screw dislocations that appear during the growth of the samples was coincident with the heat-flow direction (sample *1*) or was normal to this direction (sample *2*). The thermal conductivity of sample *1*, in which dislocations were oriented along the heat-flow direction, is higher than that of sample *2*, in which dislocation axes were normal to the heat flow direction. Thus, the anisotropy of the thermal conductivity in the polycrystalline ZnSe can be related to dislocations oriented along the crystal growth direction. The contribution to the thermal resistance from dislocations can be determined from the experimental thermal resistances of samples *1* and *2*: $W_d = W_2 - W_1$, where W_1 and W_2 are the thermal resistances of samples *1* and *2*, respectively. In the temperature range 80–400 K, W_d is found to be constant for the ZnSe samples.

In the ZnSe polycrystals additionally subjected to deformation and recrystallization, κ decreases in the same manner for both the samples in which the heat-flow direction coincides with the applied stress and the samples in which these directions are perpendicular to each other. Hence, deformation of polycrystals creates defects that reduce the thermal conductivity irrespective of the orientation of the heat flow through the sample with respect to the applied-stress direction. The anisotropy of the thermal conductivity with respect to the crystal growth direction remains even after deformation and recrystallization, which may be considered an indication that the preferred dislocation orientation is retained after deformation and recrystallization of the samples.

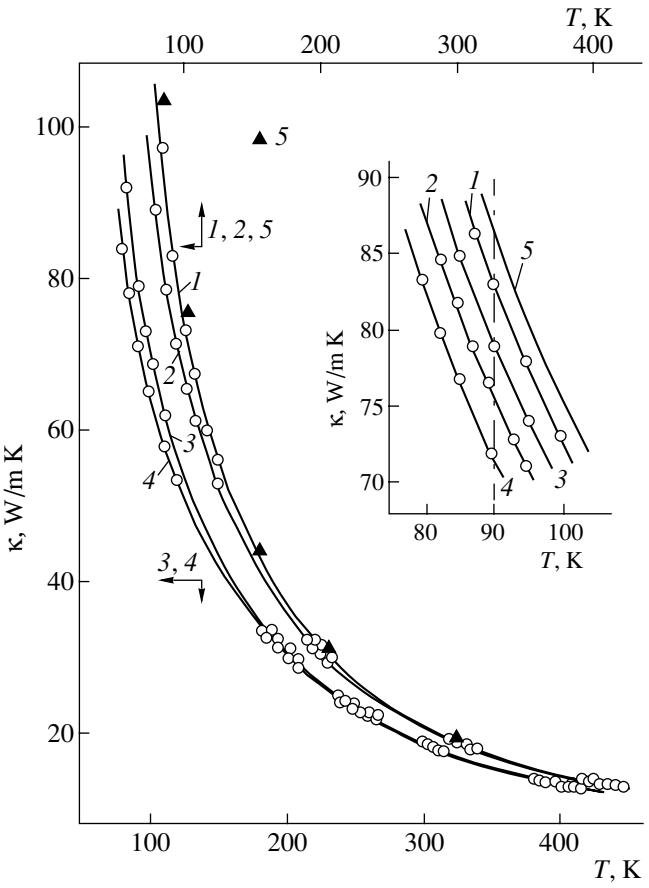

Fig. 3. Temperature dependences of the thermal conductivity κ in polycrystalline ZnSe samples. Numerals *1–4* on the curves correspond to the numbers of samples in Fig. 2. Curve *5* shows the κ data for single-crystalline ZnSe from [2].

Figure 4 shows the temperature dependence of the lattice thermal resistance of the polycrystalline ZnSe (sample *1*). As is seen, the slope of the $W(T)$ dependence changes near 270 K. Similar temperature dependences of W are also observed for samples *2–4*. It is well known that the temperature dependence of the thermal resistance of real crystals can be represented as

$$W = BT + C. \quad (3)$$

The coefficient B, which determines the slope of the $W(T)$ straight line, characterizes the material, and the coefficient C depends on impurities. Since $B \sim \gamma^2/\theta^3$ (γ is the Güneisen parameter, θ is the Debye temperature) [10], a change in the quantity γ^2/θ^3 specifies a change in the slope of the temperature dependence of the thermal resistance. The values of γ and θ for longitudinal (LA) and transverse (TA) acoustic phonons are different. Therefore, the ratio γ^2/θ^3 (and, hence, B) can change when the contributions from LA and TA acoustic phonons to the heat transfer vary.

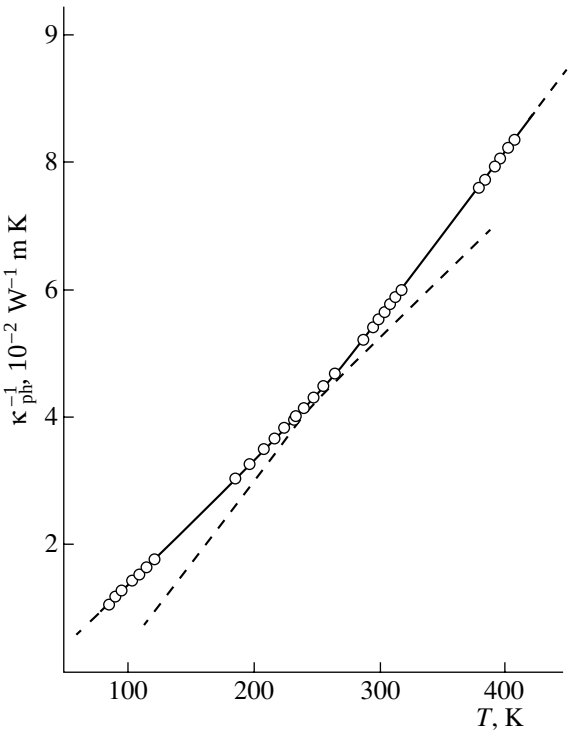

Fig. 4. Temperature dependence of the lattice thermal resistance ($W = \kappa_{ph}^{-1}$) of the polycrystalline ZnSe (sample *1*).

A change in the $W(T)$ slope caused by changes in the contributions from LA and TA acoustic phonons to heat transfer was observed in ZnS, which is similar to ZnSe, in a temperature range in which all TA phonons were excited and the number of LA phonons continued to increase with temperature [11]. The phonon spectrum of ZnSe [12] suggests that a similar change in the fraction of LA phonons participating in the heat transfer in ZnSe can occur in the range 100–250 K. However, as is seen from Fig. 4, the slope of the $W(T)$ dependence in this temperature range remains unchanged. The absence of specific features in the $W(T)$ dependence at $T < 270$ K becomes clear if we calculate the magnitude of γ^2/θ^3 for LA and TA phonons. Using the γ and θ values from [12], we found that the values of γ^2/θ^3 for TA and LA phonons in ZnSe differ from each other by a factor of 1.2. Because of this small difference, the involvement of an additional number of LA phonons in the heat transfer does not affect B noticeably, as opposed to ZnS, where the ratios γ^2/θ^3 for TA and LA phonons differ from each other by a factor of more than three.

At 280 K, TA and LA phonon branches in ZnSe are completely excited (the values of θ for TA and LA phonons are 101 and 280 K, respectively [12]). In this temperature range, optical phonons, for which the characteristic temperatures of the transverse and longitudinal branches are 300 and 330 K, respectively, become excited [12]. Having low dispersion, optical phonons contribute only slightly to the heat transfer. Since the energy gap between the acoustic and optical branches of ZnSe is small, acoustic phonons can be scattered by optical phonons, which can cause an increase in the lattice thermal resistance and in the slope of the $W(T)$ dependence observed at $T > 270$ K in the samples studied.

Thus, we experimentally determined the temperature dependence of the thermal conductivity of polycrystalline zinc selenide fabricated through vapor deposition. We found that, in the temperature range studied, κ of the polycrystalline ZnSe is not affected noticeably by phonon scattering by the boundaries of crystallites with a mean size of 2 mm. At 80–200 K, textured polycrystalline ZnSe samples exhibit significant anisotropy in their thermal conductivity, which is explained by phonon scattering by screw dislocations oriented along the crystal growth direction. Additional deformation and recrystallization reduce the thermal conductivity of polycrystalline ZnSe samples, irrespective of the angle between the heat-flow and applied-stress directions. A change in the slope of the $W(T)$ dependence detected at 270 K is caused by scattering of acoustic phonons by optical phonons, which becomes significant in the high-temperature range.

REFERENCES

1. F. K. Volynets, Opt. Mekh. Prom., No. 11, 39 (1978).
2. G. A. Slack, Phys. Rev. B **6** (10), 3791 (1972).
3. E. D. Devyatkova, A. V. Petrov, I. A. Smirnov, and B. Ya. Moĭzhes, Fiz. Tverd. Tela (Leningrad) **2** (4), 738 (1960) [Sov. Phys. Solid State **2**, 681 (1960)].
4. L. Genzel, Z. Phys. **135** (2), 177 (1953).
5. *Acoustical Crystals*, Ed. by M. P. Shaskol'skaya (Nauka, Moscow, 1982).
6. H. M. Kagaya and T. Soma, Phys. Status Solidi B **134** (1), K101 (1986).
7. B. H. Lee, J. Appl. Phys. **41** (7), 2988 (1970).
8. *Physics and Chemistry of II–VI Compounds*, Ed. by M. Aven and J. S. Prener (North-Holland, Amsterdam, 1967; Mir, Moscow, 1970).
9. V. S. Oskotskiĭ and I. A. Smirnov, *Defects in Crystals and Thermal Conductivity* (Nauka, Leningrad, 1972).
10. G. A. Slack, *Solid State Physics* (Academic, New York, 1979), Vol. 34, p. 1.
11. N. V. Lugueva and S. M. Luguev, Fiz. Tverd. Tela (St. Petersburg) **44** (2), 251 (2002) [Phys. Solid State **44**, 260 (2002)].
12. D. N. Talwar, M. Vandevyver, K. Kunc, and M. Zigone, Phys. Rev. B **24** (2), 741 (1981).

Translated by K. Shakhlevich

Physics of the Solid State, Vol. 45, No. 3, 2003, pp. 453–458. Translated from Fizika Tverdogo Tela, Vol. 45, No. 3, 2003, pp. 429–433.

SEMICONDUCTORS AND DIELECTRICS

On the Born Relation for Crystals with Diamond and Sphalerite Structure

V. P. Mikhal'chenko

Institute of Thermoelectricity, National Academy of Sciences of Ukraine, Chernovtsy, 58002 Ukraine

e-mail: mikhalchenko@ite.cv.ua

Received May 27, 2002; in final form, July 11, 2002

Abstract—The experimental data on the elastic constants C_{ij} for crystals with diamond and sphalerite structure at $T = 293$ K were used to check the Born relation $\Lambda = 4C_{11}(C_{11} - C_{44})/(C_{11} + C_{12})^2 = 1$. The relation was shown to be satisfied with a low accuracy for diamond due to a large scatter in the C_{ij} experimental values and with accuracies of 8.3, 7.6, 1.6, and 1.0% for Si, SiC, Ge, and α-Sn, respectively. For II–VI, III–V, and I–VII compounds with sphalerite structure, Λ was found to systematically deviate from unity toward lower values, and it was shown that the quantity $(1 - \Lambda)$ can be used to estimate the bond ionicity in these crystals. The effect of anharmonicity on the Λ values for Ge, Si, GaAs, InAs, and ZnSe was estimated; this effect was found to be insignificant. © *2003 MAIK "Nauka/Interperiodica".*

1. INTRODUCTION

The relation between the elastic constants C_{ij} of cubic crystals with diamond structure derived by Born in 1914 [1] has the form

$$\Lambda = \frac{4C_{11}(C_{11} - C_{44})}{(C_{11} + C_{12})^2} = 1. \quad (1)$$

The constants C_{ij} of diamond were measured using an ultrasonic technique only 32 years later [2], and Born noted satisfactory agreement between Eq. (1) and experiment ($\Lambda_{exp} = 1.1$) in his report at the *International Conference on Lattice Dynamics* in 1964 [3]. Then, five more papers were published [4–8] in which the constants C_{ij} of natural diamond single crystals were measured using x-ray diffraction and precision acoustic methods (Table 1).

It follows from Table 1 that relation (1) holds only for the data from [2, 4], whereas the more recent C_{ij} data obtained in [6, 8] using precision methods show that this relation is not actually true. This discrepancy is caused by a large scatter in the values of the off-diagonal component C_{12} (measured with a lower accuracy than C_{11} and C_{44}, which also substantially differ) rather than by disadvantages inherent to the two-parameter Born force model.

Thus, natural diamond single crystals are rather unreliable objects in precision measurements of their elastic properties when acoustic methods are used because of their small sizes, varying density, differing defect and impurity levels depending on the diamond deposit, etc. (see, e.g., [7, 9]).

These circumstances stimulated further investigations, in which Eq. (1) was modified by various authors to make the Born model more complex in order to describe diamond-like structures [10, 11].

Nevertheless, Huntington [10, Table XIII] emphasized that Eq. (1) suits Ge, Si, ZnS, InSb, and InAs much more accurately than does the equation modified by Harrison.

Relation (1) modified by Keating [12] is accurate within 0.6% for diamond and 1% for Si; however, the accuracy for Ge is only 9%, which is significantly worse than the accuracy to which the original Born

Table 1. Elastic constants C_{ij} (in 10^{11} dyn/cm^2) and Λ values for diamond

T, K	C_{11}	C_{12}	C_{44}	Λ	Reference	Experimental technique
293	95.0	39.0	43.0	1.10	[2]	Acoustic
298	93.2	41.1	41.6	1.06	[4]	Acoustic
573	110.0	33.0	44.0	1.42	[5]	X-ray diffraction
300	107.6	12.5	57.6	1.49	[6]	Precision acoustic
298	107.6	27.5	51.9	1.31	[7]	Precision acoustic
298	107.9	12.4	57.8	1.494	[8]	Precision acoustic

1063-7834/03/4503-0453$24.00 © 2003 MAIK "Nauka/Interperiodica"

Table 2. $\Lambda(293)/\Lambda(0)$ values with allowance made for anharmonicity

Crystal	γ	β	$\gamma\beta$	$\Lambda(293)$	$\Lambda(0)$	$\Lambda(293)/\Lambda(0)$
Ge	0.72	17.4	12.53	1.016	1.018	0.998
Si	0.45	7.5	3.37	1.083	1.089	0.994
InAs	0.58	13.23	7.67	0.882	0.880	1.002
GaAs	0.52	17.4	9.05	0.940	0.941	0.998
ZnSe	0.65	21.42	13.92	0.825	0.826	0.998

Table 3. Elastic constants C_{ij} (in 10^{10} Pa), deviations $C_{12} - C_{44}$ from the Cauchy relation, Λ values, and ionicities measured on the Phillips (f_i) and Bazhenov (f_i^B) scales for crystals with the diamond and sphalerite structures at $T = 293$ K

Crystal	C_{11}	C_{12}	C_{44}	$C_{12} - C_{44}$	Λ	$1 - \Lambda$	f_i	f_i^B
Ge	12.60	4.40	6.77	–2.33	1.016		0	0
Si	16.01	5.78	8.00	–2.22	1.083		0	0
β-SiC	41.05	16.43	19.38	–2.95	1.076		0	0
α-Sn	7.45	3.48	3.40	+0.080	1.01		0	0
AlP	13.82	6.065	6.90	–0.835	0.967	0.033	0.307	0.321
AlSb	8.939	4.427	4.155	+0.27	0.795	0.205	0.426	0.214
GaP	14.11	6.349	7.034	–0.685	0.9545	0.046	0.374	0.347
GaAs	11.76	5.268	5.965	–0.697	0.940	0.060	0.310	0.314
GaSb	8.839	4.033	4.316	–0.283	0.9651	0.032	0.261	0.270
InP	10.22	5.76	4.60	+1.16	0.899	0.101	0.421	0.414
InAs	8.337	4.538	3.952	+0.586	0.882	0.118	0.367	0.381
InSb	6.472	3.265	3.071	+0.194	0.929	0.071	0.321	0.360
β-ZnS	9.76	5.90	4.51	+1.39	0.829	0.171	0.623	0.668
ZnSe	8.029	4.509	3.985	+0.524	0.827	0.173	0.676	0.666
ZnTe	7.11	4.07	3.13	+0.94	0.905	0.095	0.546	0.630
CdS	7.33	5.09	3.02	+2.07	0.819	0.181	0.685	0.711
CdTe	5.350	3.681	1.994	+0.687	0.881	0.119	0.675	0.691
HgSe	6.05	4.50	2.24	+2.26	0.828	0.172	0.680	–
HgTe	5.08	3.58	2.05	+1.53	0.790	0.210	0.650	–
CuCl	4.25	3.90	2.10	+1.80	0.550	0.440	0.746	–
CuBr	3.91	3.26	1.95	+1.31	0.560	0.446	0.735	–
CuI	4.05	3.05	1.58	+1.47	0.793	0.207	0.692	–

relation (1) is satisfied (1.6%, see below). Keating's remark that the Born model is inadequate because it leads to a negative value of the elastic dilatation compliance S_{11} cannot be accepted, since S_{11} is negative only under the condition that the central-force constant α' in the diamond lattice is smaller than the noncentral-force constant β'; however, the inequality $\alpha' < \beta'$ is not realistic for any parameter-free crystal lattice. The second disadvantage of the Born model (the dependence of the bulk modulus B on β') cannot be considered as substantial, since even in the modified, more complex Keating model, B is also a function of the force constant β for the noncentral interaction with the next-to-nearest neighbors. Therefore, Keating's assumption that the noncentral interaction between the nearest neighbors should be absent in all nonmetallic crystals does not appear natural.

When generalizing the Keating model to the case of sphalerite, Martin [13] had to introduce additional force constants. The Born relation modified in [13] is accurate to within 7.4, 11.3, and 13.1% for GaAs, InAs, and ZnSe, respectively. At the same time, the original version of relation (1) is satisfied for these compounds virtually with the same accuracy (see Table 3 below).

Thus, in the long-wavelength limit of lattice dynamics, the original Born relation (1) is seen to be no worse than its various modifications, and comprehensive verification of it is of interest.

It is slightly surprising that the authors of the thorough monograph [11], in which several modifications of the original Born relation (1) for diamond-type lattices were analyzed and compared in detail, did not check the original relation (1) as applied to sphalerite-type lattices.

In this work, we checked relation (1) for II–VI, III–V, and I–VII compounds with a mixed ionic and covalent bond, including the covalent Ge, Si, SiC, and α-Sn crystals considered earlier in [11]. Moreover, unlike [11], we estimated the effect of anharmonicity on Λ for some of these crystal. We also showed that, even without regard for the contribution from anharmonicity to Λ, a systematic deviation of Λ from unity toward lower values for sphalerite-type compounds can be used to estimate bond ionicity in these crystals.

2. RESULTS OF CHECKING THE BORN RELATIONS AND DISCUSSION

Strictly speaking, to correctly check relation (1), we need the $\tilde{C}_{ij}$ harmonic values obtained with a linear extrapolation of the $C_{ij}(T)$ temperature dependences from the classical temperature range $T > \Theta_D$ (Θ_D is the Debye temperature) to $T = 0$ K [14]. Using the $\tilde{C}_{ij}$ and C_{ij} values for Ge, Si, InAs, GaAs, and ZnSe from [11] at $T = 293$ K, which contain the anharmonicity contribution, we can estimate the effect of anharmonic lattice vibrations on Λ.

For these crystals, Table 2 gives the values of Λ(293) at $T = 293$ K and Λ(0) at $T = 0$ K, as well as the Grüneisen parameters γ and the coefficients of volumetric expansion β (in 10^{-6} K^{-1}) at 293 K taken from [15]. The product γβ is a measure of the anharmonicity of lattice vibrations [16].

The data in Table 2 show that the anharmonicity virtually does not affect Λ, which is likely due to the fact that in covalent crystals at $T > \Theta_D$, all three independent coefficients C_{ij}, as a rule, decrease with increasing temperature, i.e., $dC_{ij}/dT < 0$, with slightly different slopes [11].

However, some crystals with an ion-covalent bond may exhibit anomalous $C_{ij}(T)$ dependences (softening of some C_{ij}, usually of the off-diagonal C_{12} component, and $dC_{12}/dT > 0$). Therefore, the anharmonicity in such crystals should be taken into account in calculating Λ.

An analysis of the data in Table 2 relative the surprising fact that the maximum deviation of Λ(293)/Λ(0) from unity was observed for Si having a minimum value of γβ, i.e., the minimum anharmonicity. This fact can be not only due to differences in the dC_{ij}/dT slopes between Si and the other crystals listed in Table 2 but also due to a somewhat arbitrary procedure of linear interpolation of $C_{ij}(T)$ from high temperatures $T > \Theta_D$ to $T = 0$ because of a weak $C_{ij}(T)$ nonlinearity in the range $T < \Theta_D$ (Si has the maximum value of Θ_D among the crystals listed in Table 2). On the other hand, the Cauchy relation $C_{12} = C_{44}$ is violated even for the central-force interaction of the nearest neighbors if anharmonicity is included. Ludwig [14, Eq. (15.27)] showed that the difference $C_{12} - C_{44}$ for cubic parameter-free crystals is

$$C_{12} - C_{44} = -\frac{27s}{V_Z}\gamma^2 kT, \qquad (2)$$

where γ is the Grüneisen parameter, s is the number of atoms in the unit cell, k is the Boltzmann constant, and V_Z is the unit-cell volume. It should be noted that the assumptions that were taken to derive Eq. (2) do not affect either the sign or the temperature dependence of the quantity $C_{12} - C_{44}$.

From this point of view, the contribution from central-force interaction to C_{ij} for the Si lattice is smaller than that for the other crystals listed in Table 2, which can influence the slopes dC_{ij}/dT and, hence, Λ.

Thus, an analysis of the data in Table 2 shows that the Born relation (1) can be checked using the experimental data on C_{ij} at $T = 293$ K, although it is not inconceivable that possible $C_{ij}(T)$ anomalies can affect Λ(293)/Λ(0) more significantly for some of the II–VI, III–V, and I–VII compounds.

Table 3 gives the experimental data on C_{ij} at $T = 293$ K for Ge, Si, α-Sn, and SiC, as well as for II–VI, III–V, and three I–VII sphalerite-structure compounds with a mixed ionic and covalent bond, taken from [11], and the values of Λ calculated from these data. Table 3 also contains the values of $C_{12} - C_{44}$, characterizing the deviation from the Cauchy relation; $C_{12} - C_{44} < 0$ for crystals with a pure covalent bond or with a significant overlap of electron shells of atoms (ions), while $C_{12} - C_{44} > 0$ for metals and most of the ionic and quantum crystals [17]. To comprehensively discuss the results of checking Eq. (1), we also give the ionicities after Phillips f_i and Bazhenov f_i^B taken from [11] (Table 3).

As follows from Table 3, Eq. (1) is fairly accurate for Ge and α-Sn; slightly higher values of Λ may be caused by a scatter in the C_{ij} values for these crystals. For Si and SiC, relation (1) is accurate to within 8.3 and 7.6%, respectively, and, hence, is not worse than some of the modified relations (see above). The values of $\Lambda \geq 1$ observed for typical covalent crystals Ge, Si, and β-SiC are in accord with the negative difference $C_{12} - C_{44} < 0$. The positive difference $C_{12} - C_{44} > 0$ for α-Sn is likely due to an increase in the metallic fraction of the bond in its lattice.

In this regard, the opposite, unique example is chromium, which is the only metal of the cubic crystal sys-

Table 4. Series of compounds satisfying the inequality C_{12}–$C_{44} < 0$ arranged in order of increasing ionicity on the $(1 - \Lambda)$, f_i, and f_i^B scales

Scale	Compound			
$(1 - \Lambda)$	AlP (0.033)	GaSb (0.035)	GaP (0.046)	GaAs (0.060)
f_i	GaSb (0.261)	AlP (0.307)	GaAs (0.310)	GaP (0.374)
f_i^B	GaSb (0.270)	GaAs (0.314)	AlP (0.321)	GaP (0.374)

tem for which the inequality $C_{12} - C_{44} < 0$ is true. This means that the covalent component of the bond in the Cr lattice is predominant, which manifests itself in its mechanical properties: chromium is a relatively brittle material among plastic materials with fcc and bcc lattices, which causes the well-known problem of chromium plasticity. Interestingly, a check of relation (1) for chromium using the C_{ij} data at 293 K taken from [18] ($C_{11} = 3.500$, $C_{12} = 0.678$, $C_{44} = 1.008$ in 10^{10} Pa) yields $\Lambda = 1.998$, which gives $\Lambda/2 = 0.999 \approx 1$ with allowance for the fact that each atom on a bcc lattice has eight nearest neighbors.

Taking this curious finding not very seriously, we may state that such a closeness of Λ to unity for chromium unambiguously indicates that there is a covalent bond and that there is a significant overlap of 3*d* orbitals oriented along the $\langle 111 \rangle$ directions in its bcc lattice [19]. Moreover, chromium is the only cubic metal whose thermal expansion coefficient is negative at low temperatures, $T < 40$ K, which is a characteristic feature of crystals with covalent bonds [15].

The most interesting and unambiguous result of checking the Born relation (1) is that the values of Λ are less than unity for all of the II–VI, III–V, and I–VII compounds listed in Table 3. This means that these crystals have a certain bond ionicity, which can be characterized by the difference $1 - \Lambda$ ($\Lambda = 1$ for a purely covalent bond).

On the whole, the ionicity values given on the $(1 - \Lambda)$ scale in Table 3 agree with the values of f_i and f_i^B on the Phillips and Bazhenov scales, respectively, although there are some discrepancies between them, which may be due both to the insufficient accuracy of determining $(1 - \Lambda)$, f_i, and f_i^B and to a possible scatter in the C_{ij} experimental values of the compounds in question.

The determination of Λ is four times less accurate than that of C_{ij} when modern precision methods of physical acoustics are used and can reach 2–3%. The estimation of the accuracy of determining f_i and f_i^B is not as unambiguous as that for Λ. Indeed, by definition, $f_i = E_c^2/E_g^2$, where E_g is the mean energy gap width and E_c is the heteropolar contribution to E_g; that is, the margin of error within which f_i is determined is at least twice that for E_g (0.1–0.2%), whereas estimation of the accuracy of determining E_c is rather difficult. Nevertheless, it is of interest to determine the limiting ionicity values for the crystals listed in Table 3 using the following two methods.

(1) The covalent crystals for which the deviation from the Cauchy relation is negative, $C_{12} - C_{44} < 0$, are arranged in order of increasing ionicity;

(2) The metals and ionic crystals, for which $C_{12} - C_{44} > 0$ are arranged in order of decreasing ionicity.

In the first case, we can arrange the compounds in the series presented in Table 4 (the ionicity is given in parentheses). It is easy to see that for AlP, GaSb, GaP, and GaAs, whose ionicity values differ only slightly, the ionicities determined on the $(1 - \Lambda)$ scale, as well as on the f_i or f_i^B scale, are close to each other. Thus, gallium antimonide, aluminum phosphide, gallium phoshpide, and gallium arsenide (which are covalent, according to the inequality $C_{12} - C_{44} < 0$) have the minimum ionicity among the compounds given in Table 3, irrespective of the method of determining the ionicity.

For values of $(1 - \Lambda) > 0.060$, positive deviations $C_{12} - C_{44}$ are observed for all the compounds in Table 3. The same situation is observed for $f_i > 0.374$ [except for InSb ($f_i = 0.321$) and InAs ($f_i = 0.337$)] and $f_i^B > 0.374$ [except for AlSb ($f_i^B = 0.2141$)].

Thus, the comparison of the data of Table 4 arranged on the $(1 - \Lambda)$, f_i, and f_i^B scales indicates that relation (1) makes it possible to estimate the bond ionicity in sphalerite-type lattices on the $(1 - \Lambda)$ scale not worse (or, with allowance for changes in the sign of $C_{12} - C_{44}$, maybe even better) than on the f_i or f_i^B scale.

On the other hand, the closeness of the ionicity values of the compounds with the negative deviation $C_{12} - C_{44}$ (Table 3) requires their refinement with a higher resolution as compared to that yielded by the three scales. Apparently, there is no other method here that x-ray diffraction measurement of the Fourier components of structure amplitudes and determination of the electron-density distributions for these crystals.

Table 5. Series of compounds satisfying the inequality $C_{12} - C_{44} > 0$ arranged in order of decreasing ionicity on the $(1 - \Lambda)$, f_i, and f_i^B scales

Scale	Compound						
$(1 - \Lambda)$	CuBr (0.446)	CuCl (0.440)	HgTe (0.210)	CuI (0.207)	AlSb (0.205)	CdS (0.181)	ZnSe (0.173)
f_i	CuCl (0.746)	CuBr (0.735)	CuI (0.692)	CdS (0.685)	HgSe (0.680)	ZnSe (0.676)	CdTe (0.675)
f_i^B	–	–	–	CdS (0.711)	–	CdTe (0.691)	ZnS (0.668)
Scale	Compound						
$(1 - \Lambda)$	HgSe (0.172)	ZnS (0.171)	CdTe (0.119)	InAs (0.118)	InP (0.101)	ZnTe (0.095)	InSb (0.071)
f_i	HgTe (0.650)	ZnS (0.623)	ZnTe (0.546)	AlSp (0.426)	InP (0.421)	InAs (0.367)	InSb (0.321)
f_i^B	–	ZnS (0.666)	ZnTe (0.630)	InP (0.414)	InAs (0.381)	InSb (0.360)	AlSb (0.214)

In the second case, the other fourteen compounds listed in Table 3 are arranged in series (Table 5). It can be seen from Table 5 that the $(1 - \Lambda)$ and f_i scales are uniquely calibrated against ionicity at the beginning and end of each of them. Detailed consideration reveals an exact coincidence for ZnS (middle of the scales), as well as for InP and InSb (right end of the scales). At the beginning of the scales, the values are rather close for copper chloride and bromide, although the difference in the values for CuI is slightly larger (because of the underestimated C_{44} value in comparison with those for CuCl and CuBr). At the center of the scales, the related compounds CdTe, ZnTe, HgSe, and HgTe demonstrate reasonable agreement.

Such agreement between the $(1 - \Lambda)$ and f_i scales is not incidental, since the ionicity decreases monotonically in each series formed on the basis of the scales (including the f_i^B scale).

Thus, we may conclude that, in both the $(1 - \Lambda)$ and f_i scales, the maximum ionicity can be assigned to copper halides; the intermediate ionicity is assigned to Hg, Cd, and Zn selenides, sulfides, and tellurides, and the minimum ionicity is assigned to indium antimonide, phosphide, and arsenide. Approximately the same situation is observed for the f_i^B scale (although copper halides are absent here).

Without analyzing the possible causes for the rather large differences in the ionicities of ZnTe and HgSe measured on the $(1 - \Lambda)$ and f_i scales and in the ionicities of AlSb and ZnSe measured on the f_i and f_i^B scales, we may conclude that the estimation of the ionicity on the $(1 - \Lambda)$ scale for a number of compounds arranged in order of decreasing ionicity and satisfying the inequality $C_{12} - C_{44} > 0$ is as valid as that performed on the f_i and f_i^B scales.

Moreover, the analysis of the ionicity shows that its determination on the $(1 - \Lambda)$ scale is more rigorous and, above all, more unambiguous than a qualitative estimation of ionicity as a deviation from the Cauchy ratio (e.g., $C_{12} - C_{44} < 0$ for some lithium halides [11]).

From the gnosiological point of view, the Born atomistic two-parameter force model of diamond-type crystal lattices, along with relation (1), is at least as useful as, for example, the Debye one-parameter continuum model of solids, which is still widely used in studying heat capacity. Unfortunately, the Born model and relation (1) are rarely referred to in the literature and actually are not considered in the well-known textbooks and manuals on solid-state physics.

In conclusion, we note that the Born relation (1) can be generalized to the case of crystals of other crystal systems by analogy with [17], where deviations from the Cauchy relation are strictly shown to form a symmetrical second-rank tensor.

ACKNOWLEDGMENTS

The author is grateful to L.I. Anatychuk and O.J. Luste for useful discussions on the work.

REFERENCES

1. M. Born, Ann. Phys. (Leipzig) **44** (8), 605 (1914).
2. S. Bhagavantam and J. Bhimuassenachar, Proc. R. Soc. London, Ser. A **187**, 381 (1946).
3. M. Born, in *Proceedings of International Conference on Lattice Dynamics* (Copenhagen, 1964).
4. R. F. S. Hearmon, Rev. Mod. Phys. **18** (4), 409 (1946).
5. E. Prince and W. A. Wooster, Acta Crystallogr. **6** (450), 1717 (1953).
6. H. J. McSkimin and W. L. Bond, Phys. Rev. **105** (1), 116 (1957).
7. E. W. J. Mitchell, in *Physical Properties of Diamond*, Ed. by R. Berman (Clarendon, Oxford, 1965).

8. H. J. McSkimin, P. Andreatch, and P. Geyrn, J. Appl. Phys. **43** (3), 985 (1972).
9. *Physical Properties of Diamond*, Ed. by N. V. Novikov (Naukova Dumka, Kiev, 1987).
10. H. B. Huntington, in *Solid State Physics*, Ed. by F. Seitz and D. Turnbull (Academic, New York, 1958), Vol. 7, p. 214.
11. S. P. Nikanorov and B. K. Kardashev, *Elasticity and Dislocation Inelasticity of Crystals* (Nauka, Moscow, 1985).
12. P. N. Keating, Phys. Rev. **145** (4), 637 (1966).
13. R. M. Martin, Phys. Rev. B **1** (1), 1005 (1970).
14. W. Ludwig, Springer Tracts Mod. Phys. **43**, 1 (1967).
15. S. I. Novikova, *Thermal Expansion of Solids* (Nauka, Moscow, 1974), p. 292.
16. V. P. Mikhal'chenko, Zh. Fiz. Khim. **53** (2), 476 (1979).
17. S. Haussuhl, Phys. Condens. Mater. **6** (3), 181 (1967).
18. V. M. Nadutov, in *Encyclopedic Dictionary*, Vol. 2: *Solid-State Physics*, Ed. by V. G. Bar'yakhtar (Naukova Dumka, Kiev, 1998), p. 483.
19. V. K. Grigorovich, *Metallic Bonding and Structure of Metals* (Nauka, Moscow, 1988).

Translated by K. Shakhlevich

Physics of the Solid State, Vol. 45, No. 3, 2003, pp. 459–471. Translated from Fizika Tverdogo Tela, Vol. 45, No. 3, 2003, pp. 434–445.

SEMICONDUCTORS AND DIELECTRICS

Bragg Diffraction of Light in Synthetic Opals

A. V. Baryshev, A. A. Kaplyanskiĭ, V. A. Kosobukin, M. F. Limonov, K. B. Samusev, and D. E. Usvyat

Ioffe Physicotechnical Institute, Russian Academy of Sciences, Politekhnicheskaya ul. 26, St. Petersburg, 194021 Russia

e-mail: alex.baryshev@pop.ioffe.rssi.ru

Received July 16, 2002

Abstract—Three-dimensional light diffraction from the crystal structure, formed by closely packed *a*-SiO_2 spheres of submicron size, of samples of synthetic opals was visualized. The diffraction pattern of a monochromatic light beam was established to consist of a series of strong maxima whose number and angular position depend on the wavelength and mutual orientation of the incident beam and the crystallographic planes of the sample. The diffraction patterns were studied under oblique incidence on the (111) growth surface of the sample and with light propagated in the (111) plane in various directions perpendicular to the sample growth axis. The spectral and angular relations of diffracted intensity were studied in considerable detail in both scattering geometries. The experimental data are interpreted in terms of a model according to which the major contribution to the observed patterns is due to Bragg diffraction of light from (111)-type closely packed layers of the face-centered cubic opal lattice. The model takes into account the disorder in the alternation of the (111) layers along the sample growth axis; this disorder gives rise, in particular, to twinning of the fcc opal lattice. © *2003 MAIK "Nauka/Interperiodica"*.

1. INTRODUCTION

Scattering of light waves from periodic structures (diffraction gratings), known as Bragg diffraction, has been attracting attention recently in connection with the problem of developing photonic crystals [1, 2]. Photonic crystals are unique in that they have spectral band gaps in which electromagnetic waves cannot propagate. These band gaps result from Bragg diffraction of waves from a periodically modulated dielectric structure with a period comparable with the wavelength of light. Depending on the permittivity modulation amplitude and the actual lattice symmetry of a photonic crystal, the crystal may have either a complete photonic band gap (forbidding light propagation in any direction in three-dimensional space) or stop bands (for propagation of light in certain crystallographic directions). Both possibilities are considered extremely promising for the development of optical filters, switches, etc. [2].

Among the materials most promising for developing photonic crystals are synthetic opals made up of close-packed *a*-SiO_2 spheres [3–5], as well as opal-based structures with pores filled by various dielectrics [3, 4], inverted opals [5], etc. In opals whose dielectric properties are modulated with a period (determined by the size of the close-packed *a*-SiO_2 particles) close to the wavelength of visible light, stop bands appear, which can be detected directly in optical spectra. Most of the published optical studies of stop bands in opals have been made using methods based on the reflection or transmission of light [3, 6–15]. It is noteworthy that the experimental material presented in these publications is limited in quantity. For instance, the measurements reported in [6, 9–12, 15] were performed only in reflection from the (111) growth plane, where the direction of the mirror reflection of light from the sample surface and the direction of diffraction from a periodic structure coincide; in [7], the reflectance was integrated over a spatial angle; and in [14], the scattering geometry was not specified at all (the same also relates to the study performed in [8] on TiO_2-based photonic structures). One should make a point of the comprehensive studies performed in [16] on the diffraction of light from a large number of samples of natural opals; however, the structure and orientation of these samples were not determined and the publications were largely of a descriptive nature and did not culminate in construction of the theory of light diffraction in opals. To sum up, most of the studies published until recently focused attention on light reflection (transmission) from the (111) growth plane of opals, while the three-dimensional pattern of electromagnetic-wave diffraction in opals has not been observed at all thus far (such studies of periodically modulated layered colloidal systems were reported in [17, 18]).

This study primarily deals with three-dimensional light diffraction from the crystal structure of synthetic opals. Diffraction reflections (spots) were observed visually in the backscattering geometry in the total solid angle (hemisphere) and photographed, with subsequent analysis of the spectral response and angular distribution of diffracted light. It was shown that the hexagonal close-packed (111) layers in opals were fairly perfect and, therefore, allowed Bragg diffraction,

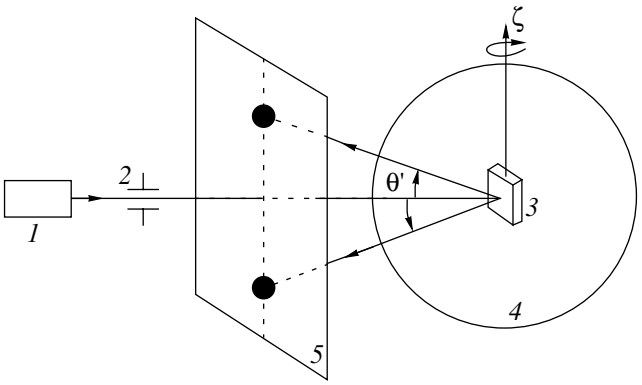

Fig. 1. Experimental setup: (*1*) light source, (*2*) collimator, (*3*) opal sample, (*4*) spherical vessel, and (*5*) screen. The schematic relates to the specific case of a monochromatic light beam propagating in the $[\bar{2}11]$ direction in the (111) sample growth plane (see text).

which was responsible for the visually observed light scattering patterns. In the case of light-beam incidence perpendicular to the sample growth axis, the diffraction pattern qualitatively changed depending on the beam incidence direction in the plane perpendicular to this axis. Three-dimensional diffraction patterns from opals clearly reveal the presence of a twinned fcc structure complicated by disorder in the alternation of the (111) layers, which are perpendicular to the growth axis.

In Section 2, we consider the structure of synthetic opals; Section 3 reports on the investigation of light diffraction from opals using photography and optical spectroscopy; in Section 4, fundamentals of the theory of light diffraction from opals are put forward; and Section 5 compares theory with experiment and discusses the results obtained.

2. SAMPLE CHARACTERIZATION

Synthetic opals, like their natural counterparts [16], consist of spherical *a*-SiO_2 particles, which form hexagonal close-packed layers perpendicular to the growth axis. A three-dimensional close-packed structure allows three possible arrangements of such layers, denoted conventionally by *A*, *B*, and *C* [19]. In three-dimensional close packing, any two adjacent layers may occupy different positions in this set. Periodic layer alternation in a three-dimensional close-packed structure arranged in the *ABCABC*… order corresponds to the fcc lattice, and the sequence *ABABAB*… corresponds to the hcp structure. In practice, synthetic opals are grown through gravity-controlled sedimentation of colloidal *a*-SiO_2 particles with their subsequent self-organization and the actual sequence in which the layers alternate along the growth axis follows the probability law. The one-dimensionally disordered close-packed structure thus obtained (the so-called random close packing) features arbitrarily alternating hexagonal layers, for instance, *ABACBACA*… . Therefore, the structure of real opals is neither an ideal fcc nor an ideal hcp lattice (for a close-packed structure of noninteracting spheres, the fcc lattice is believed to be thermodynamically preferable [20]). In a real opal crystal structure, the system of the (111) growth planes (in terms of an fcc lattice) perpendicular to the growth axis ζ differs radically from the other three fcc lattice planes: $(\bar{1}11)$, $(1\bar{1}1)$, and $(11\bar{1})$. This is a result of the layers in synthetic opals being randomly stacked along the growth axis ζ, which makes the latter structurally preferable over the other three axes, $[\bar{1}11]$, $[1\bar{1}1]$, and $[11\bar{1}]$, defined in the fcc lattice.

In our study, we used synthetic opal samples grown employing the technology put forward in [21]. The samples measured a few cm on the base and up to 1 cm in height. Characterization of these samples with atomic-force microscopy and optical transmission was described in our previous publication [22], where it was shown that the parts of a sample that form in the later stages of growth are the most uniform. Therefore, we first chose the most uniform samples, cut them perpendicular to the growth axis ζ in the form of plates, and finally selected, for optical studies, the most uniform plates, which formed in the last growth stage. Next, we established the position of the crystallographic axes of these plates relative to their geometry using atomic-force microscopy and determined the lattice parameters. The samples used in the study are made up of close-packed monodisperse *a*-SiO_2 spherical particles with an average diameter varying from 200 to 400 nm, depending on the sample. With such opal crystal lattice parameters, the conditions of Bragg diffraction are satisfied in the visible range. The images of the (111) growth layers obtained with atomic-force microscopy reveal a high degree of *a*-SiO_2 sphere ordering in the hexagonal layers, i.e., the existence of long-range order in each layer on a macroscopic scale of up to hundreds of microns.

3. EXPERIMENTAL RESULTS

3.1. Experimental Technique

Light diffraction patterns obtained in the backscattering geometry and spectra of the light diffracted from opals were measured on the setup shown schematically in Fig. 1 (this scheme illustrates the particular experimental geometry in which the incident ray of light lies in the (111) growth layer plane of the sample and is perpendicular to its growth axis ζ). The source of light *1* was an He–Ne, Ar, or a Cu laser or an incandescent lamp. In the latter case, the beam was collimated with a diaphragm and a lens *2*. After this, the narrow beam of light impinged on the opal sample *3* placed at the center of spherical vessel *4*, which was 5 cm in diameter. The vessel with a sample was filled with an immersion liquid to attain the minimum incoherent (diffuse) scatter-

ing of light by the sample surface. This was accomplished by choosing a liquid with a refractive index close to the average refractive index of the opal. As a consequence, there was practically no reflection and refraction of light at the sample surface in our experiments and the actual shape of a sample and its surface relief were inessential. Using a vessel of spherical shape permitted us to exclude the additional factor capable of degrading three-dimensional diffraction patterns that originates from possible refraction of light at the immersion-liquid/vessel and wall/air interfaces.

To study light scattering in crystal structures oriented differently relative to the incident beam, facilities were provided for rotating the sample around the growth axis ζ. When illuminated with white light, the beam cross-sectional area on the sample surface was 1–1.5 mm^2. To reduce the beam size, an additional focusing lens with a 5-cm focal length was used in some experiments. Three-dimensional diffraction was studied in the backscattering geometry within a large solid angle of the back hemisphere. The diffraction reflections were observed visually and photographed from screen *5*, which was placed 5 cm from the sample and was provided with a square measuring grid having a 1-cm period. In addition, the diffracted light was directed onto the entrance slit of a DFS-12 spectrometer through a fiber 2 mm in diameter. As a result, the diffracted light intensity was measured with an angular resolution of about 1°.

3.2. Formulation of the Problem

Our purpose was to investigate the angular and spectral responses of the diffracted intensity under excitation with monochromatic and white light. The measurements were conducted in two scattering geometries, which are displayed schematically in Fig. 2 under the assumption of the opal having an ideal fcc lattice. The diagrams in Fig. 2 are presented in the form of vector triangles corresponding to the Laue equations [23]

$$\mathbf{K}' = \mathbf{K} + \mathbf{b}, \qquad (1)$$

which define the directions of the principal maxima of Bragg diffraction from a crystal structure. Here, **K** and **K**' are the wave vectors of the incident and scattered waves in the crystal, respectively, and **b** is the reciprocal lattice vector perpendicular to the system of atomic planes responsible for the Bragg diffraction. It is essential for what follows that in the case of elastic scattering, i.e., for $|\mathbf{K}'| = |\mathbf{K}|$, Bragg diffraction on the atomic plane defined by vector **b** occurs through mirror reflection from this plane. The diagrams in Fig. 2 illustrate all processes of light diffraction occurring in the backscattering geometry from the system of closest packed fcc lattice planes, the four (111)-type planes. Our experiments studied diffraction from these planes, more specifically, from the system of the (111) growth planes

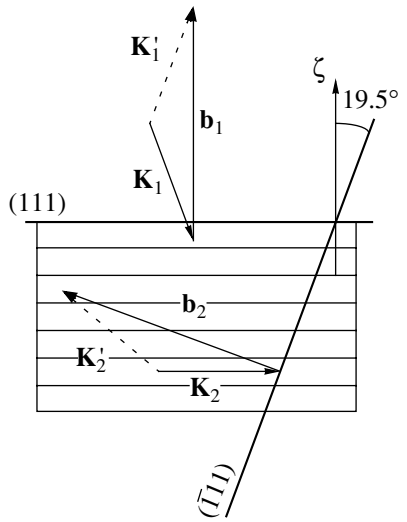

Fig. 2. Scattering diagrams for the Bragg diffraction of light from the {111} planes of the opal fcc lattice. The $\mathbf{K}_1 \longrightarrow \mathbf{K}_1'$ process corresponds to diffraction from the system of (111) growth layers with vector $\mathbf{b}_1 \equiv \mathbf{b}_{(111)} \parallel [111]$; the $\mathbf{K}_2 \longrightarrow \mathbf{K}_2'$ process, to scattering from the $(\bar{1}11)$ plane system with vector $\mathbf{b}_2 \equiv \mathbf{b}_{(\bar{1}11)} \parallel [\bar{1}11]$.

and three other fcc plane systems: $(\bar{1}11)$, $(1\bar{1}1)$, and $(11\bar{1})$.

The first diagram in Fig. 2 relates to the scattering experiment in which light impinged normally or at an angle on the (111) opal growth plane perpendicular to vector $\mathbf{b}_1 = \mathbf{b}_{(111)}$ and the $\mathbf{K}_1 \longrightarrow \mathbf{K}_1'$ backscattering was studied. In the second case, the incident light propagated in the (111) growth plane (the wave vector $\mathbf{K}_2$ was perpendicular to the opal growth axis ζ). The corresponding diagram in Fig. 2 refers to the specific case of diffraction of an incident beam with its wave vector $\mathbf{K}_2$ is parallel to the $[\bar{2}11]$ direction lying in the growth plane and the Bragg reflection $\mathbf{K}_2 \longrightarrow \mathbf{K}_2'$ in the $(\bar{1}11)$ plane with vector $\mathbf{b}_2 = \mathbf{b}_{(\bar{1}11)}$ observed in the backscattering. By rotating the crystal about the ζ axis in this arrangement, three-dimensional diffraction $\mathbf{K}_2 \longrightarrow \mathbf{K}_2'$ on both the $(\bar{1}11)$ plane and the equivalent planes $(1\bar{1}1)$ and $(11\bar{1})$ was studied experimentally. Consider the results obtained in the measurements for each of these two cases.

3.3. Light Diffraction from the (111) Opal Growth Plane

When white light impinges obliquely at angles of incidence up to about 60° on the (111) growth plane of

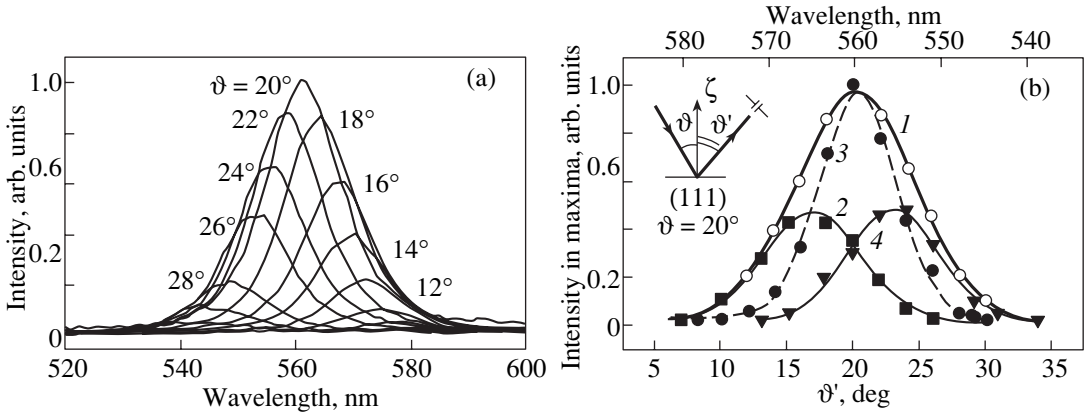

Fig. 3. (a) Spectra of diffraction scattering from a system of (111) growth planes measured at a fixed angle of white-light incidence $\vartheta = 20°$ and at different reflection angles ϑ'. (b) Spectral–angular response of diffracted intensity obtained under illumination by white light (curve *1*) and angular dependences of the scattered intensity of monochromatic light with wavelength λ equal to (*2*) 550, (*3*) 560, and (*4*) 570 nm. The experimental points on curve *1* (open circles) in panel (b) correspond to the maxima in the spectral curves shown in panel (a): the bottom scale indicates the angular positions of the maxima, while the top wavelength scale shows the spectral positions of the maxima and refers only to spectral–angular response *1*. Inset specifies the experimental geometry.

opal with a *a*-SiO_2 sphere diameter of 270 nm, our experiments reveal a strong diffraction reflection in the direction of mirror reflection. When light strikes the sample growth plane, diffraction takes place from the (111) system of atomic planes. This system can be identified with the reciprocal lattice vector $\mathbf{b}_{(111)}$ parallel to the direction from the Γ point of the Brillouin zone for the fcc lattice to the L point, i.e., along the [111] normal to the (111) surface. Bragg diffraction is caused by the interaction of light with periodic components of the dielectric permittivity; mirror reflection, by the interaction with the uniform (spatially averaged) dielectric background. As seen from the diagram of the $\mathbf{K}_1 \longrightarrow \mathbf{K}_1'$ scattering process (Fig. 2), if the sample surface is identified with the (111) opal growth plane, the directions of Bragg diffraction from the (111) planes and of mirror reflection from the sample surface coincide; i.e., in general, mirror reflection is superposed on the observed diffraction maximum. The immersion liquid with a dielectric permittivity close to that of the opal used in our experiments substantially suppressed the mirror component.

The geometry of the experiment is shown in the inset to Fig. 3b, with the angles of incidence ϑ and reflection ϑ' being reckoned from the normal to the sample growth plane. To characterize the spot due to the primary beam incident at $\vartheta = 20°$ being diffracted from the (111) plane system, we measured a series of spectra of light diffracted to various angles ϑ' close to the mirror reflection angle, $\vartheta' = \vartheta$. The angle $\vartheta = 20°$ of the beam incidence was chosen because it simplifies comparison of the results obtained in different scattering geometries (Section 5). Figure 3a presents diffracted intensity spectra measured in reflection under sample illumination by white light. The angular responses of diffracted intensity derived from these spectra are shown in Fig. 3b. Curve *1* in Fig. 3b relates light intensity at the maxima of reflection bands displayed in Fig. 3a to angle ϑ'. We readily see that the backscattered diffracted intensity is the strongest at the wavelength of 560 nm in the direction $\vartheta' = \vartheta = 20°$, which corresponds to mirror reflection. Curves *2–4* display a diffracted intensity of monochromatic light of different wavelengths λ as a function of angle ϑ'; these curves were derived from the experimental data in Fig. 3a.

3.4. Diffraction of Light Incident Perpendicular to the Growth Axis ζ

Monochromatic light propagating in the (111) opal hexagonal layer plane perpendicular to the growth axis ζ (as shown in Fig. 1) produces a number of diffraction spots. The simplest diffraction pattern is observed in the so-called $[\bar{2}11]$ geometry, in which the beam falling on the (111) plane is aligned with the $[\bar{2}11]$ direction lying in this plane (the indices relate to the fcc lattice). The diffraction pattern obtained in the $[\bar{2}11]$ geometry consists of two spots displaced symmetrically along the ζ axis with respect to the incident beam (Figs. 1, 4). The angular deflection $|\theta'|$ of the centers of the two symmetrical spots is the larger, the smaller the wavelength of incident light. This is illustrated in Fig. 4 by photographs of the diffraction pattern obtained on the screen under illumination of the sample by monochromatic light of He–Ne, Cu, and Ar lasers. When the sample is rotated around the ζ axis, the number and position of the diffraction spots seen in the $[\bar{2}11]$ geometry vary with a period of 60°. The two-spot pattern repeats every 60°, when the direction of the beam

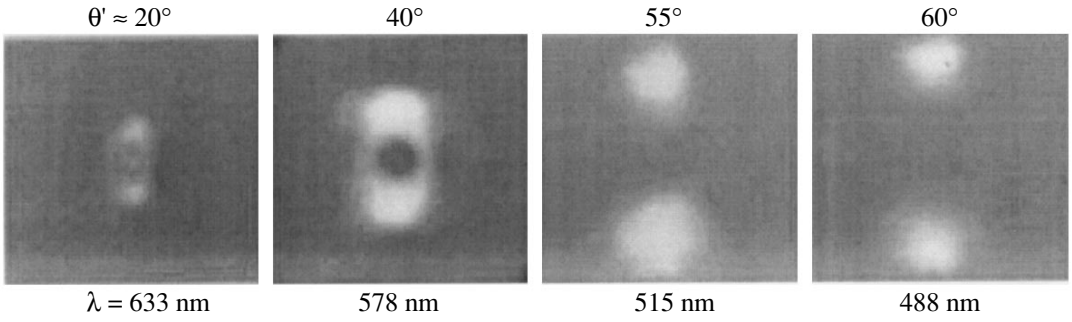

Fig. 4. Photographic image of diffraction patterns on the screen (Fig. 1) obtained with monochromatic light of wavelengths λ = 633, 578, 515, and 488 nm falling in the [$\bar{2}$11] direction. The observation angles θ' corresponding to these wavelengths are identified.

incidence coincides with one of the directions [$2\bar{1}\bar{1}$], [$11\bar{2}$], [$\bar{1}\bar{1}2$], [$1\bar{2}1$], and [$\bar{1}2\bar{1}$] lying in the (111) growth plane and equivalent to the [$\bar{2}$11] direction. If the monochromatic beam is oriented along the high-symmetry directions of the [$0\bar{1}1$] type, which lie in the (111) growth plane, the diffraction pattern contains four reflections at the corners of the rectangle whose sides are parallel or perpendicular to the growth axis. In this study, we shall limit ourselves to experimental data obtained in [$\bar{2}$11] diffraction, because they will suffice to understand the general pattern of light diffraction in opals (see Section 5).

3.5. Spectral and Angular Responses of the Diffracted Radiation

The Bragg diffraction intensity is related to the wavelength of light and the scattering angle through Eq. (1). Therefore, in considering the spectral and angular characteristics of diffraction obtained under illumination by white light we shall call them the spectral–angular response in what follows. In accordance with the above study of diffraction in monochromatic light in the [$\bar{2}$11] geometry, illumination of an opal sample with white light (continuous spectrum) produces, on the screen, a vertically extended colored stripe (10° in angular width) of diffracted light, which is oriented in space parallel to the sample growth axis ζ (Fig. 1). The visually observed colored stripe displays spectral decomposition of white light in two symmetrical directions relative to the incident beam. For our sample, with *a*-SiO_2 spheres 270 nm in diameter, backscattering at small angles $|\theta'| \longrightarrow 0$ corresponds to the red color, the wavelength of diffracted light decreasing with increasing angle |θ'|.

The spectral composition of white light diffracted in the [$\bar{2}$11] geometry was studied in considerable detail as a function of angle θ' (in the experiment illustrated schematically in Fig. 1, this angle was varied by properly displacing the fiber through which the signal was fed to the spectrometer). The reflectance spectra measured at different angles ±θ' are displayed in Figs. 5a and 5b. The spectra of Fig. 5a relate to light scattering into the lower part of the back hemisphere within the angular interval $-60° < \theta' < 0°$, and those in Fig. 5b relate to light scattered into the upper part of the same hemisphere in the symmetric interval of angles, $0° < \theta' < 60°$. In both cases, Figs. 5a and 5b, the strongest reflection bands are observed at angles $\theta' = \pm 40°$, the absolute maximum in these spectra being at $\lambda \approx 570$ nm (yellow region). Figure 5c shows the spectral–angular response of the intensity at the maxima of the reflection bands presented in Figs. 5a and 5b. One clearly sees two intensity maxima at $\theta' = \pm 40°$ in this figure.

3.6. Preliminary Discussion

It appears of interest to compare the spectral–angular response of the diffracted light intensity obtained in the two scattering geometries shown in Fig. 2. Both dependences are characterized by maxima in the angular distribution of the diffracted intensity; indeed, in the case of a beam of white light striking the (111) growth surface, there is one maximum (Fig. 3b) and for a beam propagating in the (111) plane in the [$\bar{2}$11] direction there are two maxima (Fig. 5c). The angular position of each maximum defines the direction in which the major part of diffracted radiation escapes out of the sample. According to Fig. 3b, the spectral width of the diffraction spot is approximately 20 nm and the total angular width of the diffraction maximum is ≈10° under white-light illumination and ≈5° for monochromatic light. As follows from Fig. 5c, the spectral width of the stripe of diffracted light propagating into the upper and lower parts of the hemisphere is about 100 nm and the width of the angular dependence of distribution of the diffracted intensity constitutes ≈20°. The noticeable difference in the values of both spectral and angular width of diffraction maxima between the two scattering geometries under discussion (Fig. 2) is evidence that

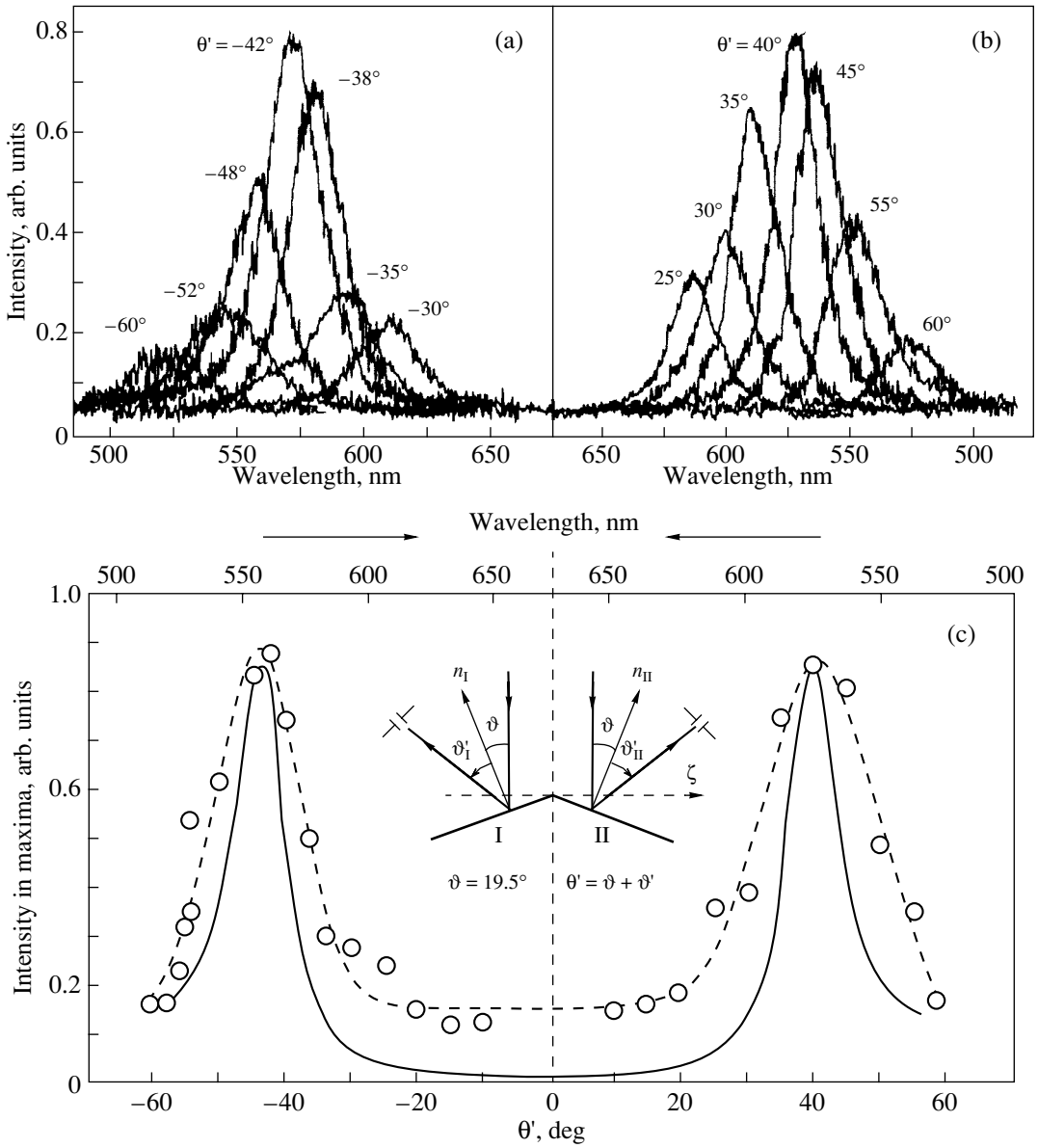

Fig. 5. (a, b) Scattering spectra measured at different observation angles θ' with the sample illuminated by white light in the $[\bar{2}11]$ direction. (c) Spectral–angular response of intensity at the maxima of white-light scattering spectra displayed in panels (a) and (b). The experimental data are identified by circles and a dashed line, and the calculation is indicated by a solid line. Inset shows the geometry of light scattering from two $(\bar{1}11)$-type plane systems belonging to the fccI and fccII lattices of a twinned fcc structure.

the conditions of diffraction are different in these two cases.

As already mentioned, the $\mathbf{K}_1 \longrightarrow \mathbf{K}_1'$ diffraction (Fig. 2) should manifest itself in the direction of mirror reflection from the (111) growth plane. Practically all earlier studies into the photonic stop bands in opals deal with diffraction of this type. The results discussed above (Fig. 3) substantially complement the data reported in those publications, because they contain detailed information on the spectral composition and angular characteristics of the diffracted beam. Due to the use of an immersion liquid, the diffracted component of radiation in our measurements is not masked by the conventional mirror reflection. This is important, in particular, for further determination of the optical characteristics of a sample based on the Bragg law.

According to Fig. 2, Bragg diffraction $\mathbf{K}_2 \longrightarrow \mathbf{K}_2'$ from the $(\bar{1}11)$ plane should produce a diffraction maximum in the scattering plane which includes vectors $\mathbf{K}_2$ and $\mathbf{b}_2 = \mathbf{b}_{(\bar{1}11)}$. In the case of the fcc lattice, this diffraction pattern should repeat if the crystal is rotated

around the ζ axis by 120° or 240° (in the fcc lattice, the ζ axis is a threefold rotation axis). In actual fact, the diffraction pattern observed in the case of $\mathbf{K} \parallel [\bar{2}11]$ under illumination with monochromatic light (Fig. 4) is substantially more complex; namely, it consists of two spots arranged symmetrically on the ζ growth axis and repeats every 60° as the crystal is rotated about the ζ axis. Thus, the experimental diffraction patterns obtained for $\mathbf{K} \perp \zeta$ cannot be explained based on the model of an ideal fcc structure.

We will show in Sections 4 and 5 that the observed doubling of the number of diffraction reflections is caused by disorder in the alternation of close-packed (111) layers along the growth axis, which gives rise to the formation of growth twins of the fcc lattice. The disorder in the alternation of the (111) growth layers in synthetic opals turns out to be also responsible for the observed features in the spectral–angular relations of diffraction, which should not occur in regular crystal lattices.

4. SPECIFIC FEATURES OF LIGHT DIFFRACTION IN OPALS: THEORY

4.1. General Relations

Bragg diffraction of electromagnetic waves in the visible region is similar in general features to x-ray diffraction [24, 25]. In the Born approximation, the intensity of elastic scattering (diffraction) of a monochromatic light wave with frequency ω from a half-space of a scattering medium can be written as

$$I(\mathbf{Q} \longrightarrow \mathbf{Q}') = CS(\mathbf{K}' - \mathbf{K})|\varepsilon_{\mathbf{K}'-\mathbf{K}}|^2. \quad (2)$$

Here, **Q** and **Q'** are the wave vectors of the incident and diffracted waves, respectively, measured in vacuum; **K** and **K'** are the corresponding vectors inside the scattering medium; and coefficient *C* describes the light wave transformation, $\mathbf{Q} \longrightarrow \mathbf{K}$ and $\mathbf{K}' \longrightarrow \mathbf{Q}'$, at the sample boundary. In Eq. (2), the structure factor

$$S(\mathbf{K}' - \mathbf{K}) = \left|\frac{1}{\sqrt{N}}\sum_l \exp[-i(\mathbf{K}' - \mathbf{K})\mathbf{R}_l]\right|^2 = \frac{1}{N}\sum_{l,l'} \exp[-i(\mathbf{K}' - \mathbf{K})(\mathbf{R}_l - \mathbf{R}_{l'})] \quad (3)$$

depends on the position vectors $\mathbf{R}_l$ of the scatterers (*a*-SiO_2 spheres in the opal); it is this factor that, in accordance with Eq. (2) for the intensity, determines the diffraction patterns.

The nonuniform dielectric permittivity $\varepsilon(\mathbf{r})$ of the scattering volume enters Eq. (2) through its Fourier components $\varepsilon_{\mathbf{K}'-\mathbf{K}}$. In photonic crystals, the dielectric permittivity is a periodic function varying with the period of the lattice translation vector **a**; i.e., $\varepsilon(\mathbf{r}) = \varepsilon(\mathbf{r} + \mathbf{a})$. It can be expanded in a Fourier series

$$\varepsilon(\mathbf{r}) = \sum_{\mathbf{b}} \varepsilon_{\mathbf{b}} \exp(i\mathbf{b}\mathbf{r}),$$
$$\varepsilon_{\mathbf{b}} = \frac{1}{\Omega_0}\int_{\Omega_0} d\mathbf{r}\varepsilon(\mathbf{r})\exp(-i\mathbf{b}\mathbf{r}) \quad (4)$$

in reciprocal lattice vectors **b**, with $\varepsilon_{-\mathbf{b}} = \varepsilon_{\mathbf{b}}^*$ for the real function $\varepsilon(\mathbf{r})$. Note that $\varepsilon_{\mathbf{K}'-\mathbf{K}}$ in Eq. (2) are the Fourier amplitudes $\varepsilon_{\mathbf{b}}$, which are expressed through the integral in Eq. (4) over the unit-cell volume Ω_0 and depend on the size and shape of the scattering volumes.

As a zero approximation, we shall consider a half-space with uniform dielectric permittivity ε_0, which corresponds to $\mathbf{b} = 0$. As seen from Eq. (4),

$$\varepsilon_0 = \varepsilon_s f + \varepsilon_v(1 - f), \quad (5)$$

where ε_s and ε_v are the dielectric constants inside and outside the *a*-SiO_2 spheres and *f* is the volume filling of the lattice ($f = 0.74$ for the fcc lattice). This permittivity determines the wave vector

$$\mathbf{K} = \sqrt{\varepsilon_0}\frac{\omega}{c}\{(\mathbf{e}_x\cos\varphi + \mathbf{e}_y\sin\varphi)\cos\theta + \mathbf{e}_z\sin\theta\} \quad (6)$$

of the incident wave, with $\mathbf{e}_x$, $\mathbf{e}_y$, and $\mathbf{e}_z$ being mutually orthogonal unit vectors. The vector **K'** of the backscattered wave differs from Eq. (6) in its polar, $\pi - \theta'$, and azimuthal, φ', angles, with $|\mathbf{K}| = |\mathbf{K}'|$ in the case of elastic scattering.

In the case of an ideal three-dimensional lattice with basis vectors $\mathbf{a}_i$ ($i = 1, 2, 3$), the sum in Eq. (3) is taken over sites $\mathbf{R}_l = \sum_{l_i} \mathbf{a}_i l_i$, where l_i are integers. Summation of Eq. (3) shows [23] that the main intensity maxima (2) for diffracted radiation appear in the **K'** directions satisfying Eq. (1). The atomic plane responsible for diffraction is determined by the reciprocal lattice vector $\mathbf{b} = \sum_{i=1,2,3} \mathbf{b}_i m_i$ perpendicular to it, with the basis vectors $\mathbf{b}_i$ and indices (m_1, m_2, m_3). As follows from Eqs. (1)–(3) [26], illumination of an ideal three-dimensional lattice by white light produces diffraction maxima only at certain wavelengths. The diffraction spots obtained with opals have an essentially different structure (Figs. 4, 5); namely, each of them represents a spectral decomposition of white light in a diffraction angle. This structure of the observed reflections is, in principle, compatible with predictions of the theory of diffraction from a two-dimensional (plane) grating [26]. To make this correspondence more revealing, we consider the diffraction of light in opals in stages, starting from a single-layer model.

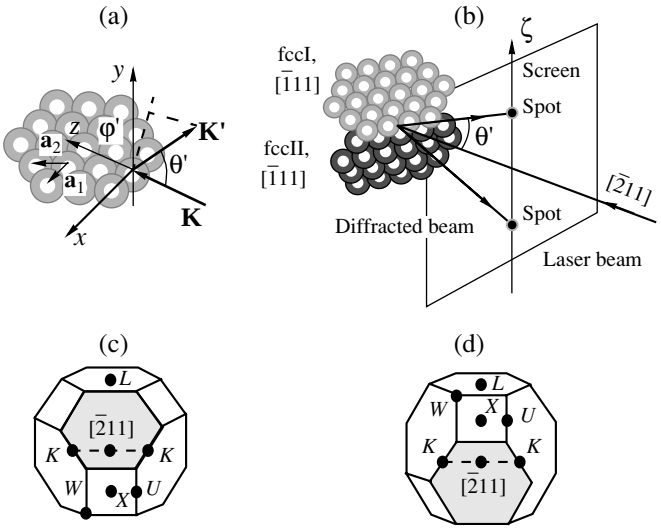

Fig. 6. Bragg diffraction of light with the sample illuminated in the [$\bar{2}11$] direction. (a) Geometry of the **K** ⟶ **K'** backscattering and a fragment of a hexagonal layer with basis lattice vectors $\mathbf{a}_1$ and $\mathbf{a}_2$. (b) Scheme of light diffraction from the sample illuminated along the [$\bar{2}11$] direction; the ($\bar{1}11$) planes of the fccI and fccII lattices making up the twin are shown. (c, d) Brillouin zones of the fccI and fccII structures.

Our subsequent discussion will take into account the following specific features of opal structure. In real opals, the close-packed growth layers are ordered but alternate along the sample growth axis ζ in a random manner by occupying, one after another, positions *A*, *B*, and *C*, which are defined in Section 2. In layer-by-layer summation, the structure factor in Eq. (3) can be represented as the product of a regular intralayer factor $S_\parallel$ and an irregular interlayer factor $S_\perp$:

$$S(\mathbf{\Delta K}, p) = S_\parallel(\Delta\mathbf{K})S_\perp(\Delta\mathbf{K}, p), \quad (7)$$

where $\mathbf{\Delta K} = \mathbf{K}' - \mathbf{K}$ is the scattering vector and p is a parameter identifying the random stacking of layers along the growth axis ζ.

4.2. Light Diffraction from a Single Layer

The intralayer structure factor $S_\parallel$ is defined by two basis vectors $\mathbf{a}_1$ and $\mathbf{a}_2$ of the hexagonal layer (Fig. 6a); i.e., $S_\parallel$ describes diffraction from a two-dimensional structure indexed (m_1, m_2). Summation over sites of a plane hexagonal lattice yields

$$S_\parallel(\mathbf{\Delta K}) = \prod_{i=1,2} S_i(\mathbf{\Delta K}) = \prod_{i=1,2} \frac{1}{N_i}\frac{\sin^2(N_i\mathbf{\Delta K}\mathbf{a}_i/2)}{\sin^2(\mathbf{\Delta K}\mathbf{a}_i/2)}, \quad (8)$$

where N_i is the number of unit cells along the $\mathbf{a}_i$ vector. In the limit as $N_i \longrightarrow \infty$, each of the two functions $S_i(\mathbf{\Delta K})$ in Eq. (8) assumes the form

$$\lim_{N_i\to\infty}\frac{1}{N_i}\frac{\sin^2(N_i\mathbf{\Delta K}\mathbf{a}_i/2)}{\sin^2(\mathbf{\Delta K}\mathbf{a}_i/2)} = 2\pi\sum_{m_i}\delta(\mathbf{\Delta K}\mathbf{a}_i - 2\pi m_i), \quad (9)$$

where $i = 1, 2$ and m_1 and m_2 are integers. As follows from Eqs. (2) and (7)–(9), the delta functions in Eq. (9) correspond to Bragg diffraction intensity maxima. In the case of a single hexagonal layer, these maxima appear at the values of the scattering vector **ΔK** satisfying the conditions

$$\mathbf{\Delta K}\mathbf{a}_i = 2\pi m_i. \quad (10)$$

If the angles θ and φ of the incident beam are given, Eqs. (10) can be recast, in view of Eqs. (5) and (6), in the form of the following equations for angles θ' and φ', which define the direction of light diffraction:

$$\begin{cases} \cos\varphi'\sin\theta' - \cos\varphi\sin\theta = m_1\dfrac{\lambda}{\sqrt{\varepsilon_0}a}, \\ (\cos\theta' + \cos\theta) = \left(\dfrac{m_1}{2} - m_2\right)\dfrac{2}{\sqrt{3}}\dfrac{\lambda}{\sqrt{\varepsilon_0}a}. \end{cases} \quad (11)$$

Here, $\lambda = 2\pi c/\omega$ is the wavelength of light in vacuum and $a = 2R$ is the distance between neighboring sites in a close-packed layer of *a*-SiO_2 spheres of radius *R* in opal.

For the experiment in the [$\bar{2}$ 11] geometry described in Subsection 3.4 (Fig. 6a), where $\varphi = 0$ and $\theta = 0$, the set of coupled equations (11) can be solved to yield $\varphi' = \pi/2$ and $\theta'(\lambda)$ for the pair $m_1 = 0$, $m_2 = -1$, which defines the (0, $\bar{1}$) diffraction reflection. This solution is unique for any wavelength λ within the interval $R\sqrt{3\varepsilon_0} < \lambda \le 2R\sqrt{3\varepsilon_0}$. In the visible region of the spectrum, these inequalities can be met if the *a*-SiO_2 spheres in opal are a few hundred nanometers in diameter ($250 < 2R < 500$ nm). This condition is also upheld for the opals we studied ($2R = 270$ nm). For $m_1 = 0$ and $m_2 = -1$, Eqs. (11) yield the following expression relating the wavelength of light to the angle θ' (an analog of the Bragg condition for the case of two-dimensional diffraction):

$$\lambda(\theta') = R\sqrt{3\varepsilon_0}(1 + \cos\theta'), \quad (12)$$

which describes the spectral decomposition of white light in angle θ'. In general, as the wavelength decreases (for $\lambda < R\sqrt{3\varepsilon_0}$), solutions to Eqs. (11) with other indices (m_1, m_2) arise: ($\bar{1}$, 0), (0, $\bar{2}$), (1, $\bar{1}$), etc.; however, in the case of spheres with $2R = 270$ nm, the wavelengths for these diffraction reflections lie beyond the

violet boundary of the visible range. Thus, in our experiments, which are performed in visible light, one can expect the appearance of diffraction reflections with $m_1 = 0$ and $m_2 = -1$ only.

4.3. Diffraction from Randomly Stacked Layers

Let us turn our consideration from diffraction by one layer to Bragg diffraction of light from a system of growth layers. In the general case of a disordered close-packed structure, the observed quantities should be averaged over an infinite random sequence of the *A*, *B*, and *C* hexagonal layers defined above. In view of the strongly pronounced interlayer disorder, the intensity given by Eq. (2) should be averaged in our case, which reduces to calculating the mean value $\langle S(\mathbf{K}' - \mathbf{K})\rangle$ of the structure factor in Eq. (3). For a random sequence of layers *A*, *B*, and *C*, one may conveniently choose as the parameter in Eq. (7) the stacking correlation coefficient *p* [27]. This is actually the probability of three adjacent layers being located in three different positions defined by the set *A*, *B*, and *C*. If the first layer of spheres occupies position *A* and the second, *B*, then the third layer may be found in position *C* with a probability *p* or *A* with a probability $1 - p$, and so on. For $0 < p < 1$, such a stacking turns out to be irregular; for $p = 1$, it transfers to a perfect fcc lattice, and for $p = 0$, it becomes a perfect hcp structure.

Let us analyze the averaged structure factor $\langle S(\mathbf{\Delta K})\rangle$ for a given correlation coefficient *p* of random growth-layer stacking in the opal. In [27], a method was proposed for calculating the quantity $\langle S\rangle$ for various pairs of indices (m_1, m_2) in terms of the random-stacking model in the limit of a large number of layers $N_3 \longrightarrow \infty$, where self-averaging occurs. Following [27], the averaged structure factor corresponding to diffraction in our $[\bar{2}11]$ geometry with indices $m_1 = 0$ and $m_2 = -1$ for $0 < p < 1$ can be found to be

$$\langle S\rangle = \frac{3p(1-p)}{G}, \qquad (13)$$

where $G = 2\left\{p^2\left[2\cos\left(\frac{4\pi\sqrt{2}}{3}\cot\frac{\theta'}{2}\right) + \frac{5}{2}\right] + (2p - 1)\left[\cos\left(\frac{8\pi\sqrt{2}}{3}\cot\frac{\theta'}{2}\right) - 1\right]\right\}$. This expression was derived with due account of Eq. (12), relating the wavelength of light λ to angle θ' for the $(0, \bar{1})$ diffraction. Significantly, the same $\lambda(\theta')$ relation determines the angular position of spots at different wavelengths, which is observed in experiments on the diffraction of monochromatic light (Fig. 4).

We used Eq. (13) to perform a numerical analysis of the mean structure factor $\langle S\rangle$ as a function of reflection angle θ' in terms of the random opal-stacking model for the case of $p \geq 0.6$, where the fcc structure forms predominantly. The calculations of the spectral–angular response of the structure factor (13) are presented graphically in Fig. 7, and Fig. 5c compares the theoretical relation for $\langle S\rangle$ with the observed spectral–angular response of the diffracted intensity. The theoretical dependences of $\langle S\rangle$ on angle θ' (Fig. 7) predict the presence of two diffracted intensity maxima symmetric in θ' (rather than one, as would be the case for a perfect fcc lattice) within the angular range $|\theta'| < 60°$ studied by us. These two maxima are seen clearly to exist at values of the random-stacking correlation coefficient sufficiently close to unity ($p > 0.8$). For such values of *p*, these are regions of a regular fcc structure which include several hexagonal layers (for $p \longrightarrow 1$, their number tends to infinity). The model of random layer stacking also predicts coexistence of fcc structures of two types, characterized by mutually reverse layer stacking order, namely, *ABCABC*… and *CBACBA*…. This configuration is known in crystallography as a growth twin for fcc lattices [28]; the part it plays in light diffraction is discussed in considerable detail in Subsection 5.2 on the basis of our experimental data.

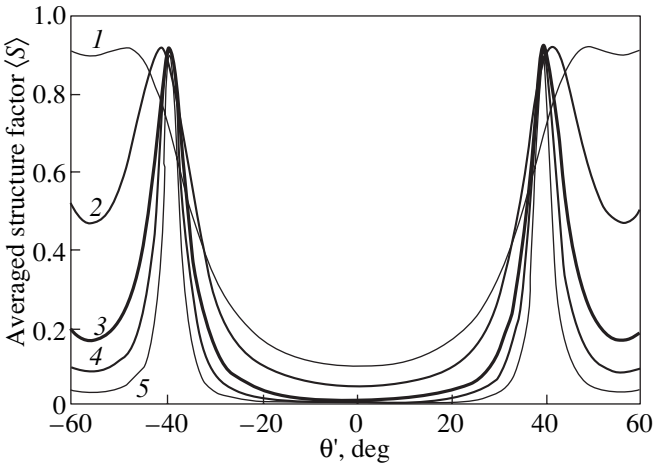

Fig. 7. Averaged structure factor $\langle S\rangle$ vs. angle ϑ' relation calculated for the $[\bar{2}11]$ scattering geometry in the model of random close stacking of opal growth layers with *a*-SiO_2 spheres 270 nm in diameter. The curves correspond to the following values of the random-stacking correlation coefficient *p*: (*1*) 0.6, (*2*) 0.7, (*3*) 0.8, (*4*) 0.85, and (*5*) 0.9.

5. DISCUSSION OF EXPERIMENTAL RESULTS

5.1. Dielectric Parameters of Opals

In accordance with Eq. (1) and Fig. 2, the condition of Bragg diffraction in a crystal can be written as $\tilde{\lambda}_B = 2d\sqrt{\varepsilon_0}\cos(\tilde{\theta}_B/2)$, where $\tilde{\lambda}_B$ and $\tilde{\theta}_B/2$ are the Bragg wavelength and angle in the crystal, respectively, and *d* is the distance between the atomic planes responsible for diffraction. Therefore, we can recast the diffraction

condition through the quantities λ_B and ϑ_B measured outside as [22]

$$\lambda_B = 2dn_{\text{eff}}\cos\vartheta_B, \quad (14)$$

where n_{eff} is an effective refractive index determined empirically and ϑ_B is the Bragg angle of light reflection outside the crystal. By using the spectral position of the transmission band minimum which corresponds to the Bragg diffraction condition (14) and is measured under normal incidence of white light on the (111) growth plane ($\cos\vartheta_B = 1$), we found $d_{(111)}n_{\text{eff}} = R\sqrt{8/3}\,n_{\text{eff}} \simeq 300$ nm for our opal samples. In the case of oblique incidence, $2\vartheta_B = 40°$ and Eq. (14) yields $\lambda_B \simeq 560$ nm for the Bragg wavelength for our samples (yellow light). It is this wavelength $\lambda_B = 560$ nm that corresponds to maximum scattered light in the direction of mirror reflection in our experiments on white light diffraction from the (111) growth plane for $\vartheta' = \vartheta = 20°$ (Fig. 3a). Thus, Eq. (14) agrees well with the experimental data on Bragg diffraction from the (111) growth planes. Assuming $2R = 270$ nm for the sphere diameter in our samples [22], i.e., $d_{(111)} = 220$ nm, the above experimental data obtained on an opal with filler suggests $n_{\text{eff}} = 1.36$, whereas Eq. (5) yields $n_{\text{eff}} = 1.37$ for the background light reflection coefficient for our samples [22].

5.2. Light Diffraction from a Twinned FCC Opal Lattice

In our opinion, the optical phenomena in opals described in Section 3 are due to Bragg diffraction of light from the (111)-type high-symmetry planes of the fcc lattice (Fig. 2). For instance, illumination of an fcc lattice by a beam propagating in the (111) plane in the $[\bar{2}11]$ direction can, in principle, undergo diffraction on three $(\bar{1}11)$ type plane systems. When illuminated by a $[\bar{2}11]$ white-light beam, the generalized condition of Bragg diffraction (14) from a system of $(\bar{1}11)$ planes is satisfied for the angle $2\vartheta_B = 39°$ between the $[\bar{2}11]$ and $[\bar{1}11]$ directions in an fcc lattice for a wavelength $\lambda_B = 565$ nm (if $d_{(\bar{1}11)}n_{\text{eff}} = 300$ nm). In the case of the $[\bar{2}11]$ beam, the Bragg reflections from the two other plane systems, $(1\bar{1}1)$ and $(11\bar{1})$, which meet condition (14), are outside the backscattering hemisphere.

As already mentioned, the diffraction pattern observed under illumination with monochromatic light in the visible region consists not of one but rather of two spots arranged symmetrically on the ζ axis (Fig. 4). The experimentally observed diffraction direction ($\vartheta' = \pm 40°$) and the light wavelength corresponding to maximum scattering into the back hemisphere satisfy condition (14) for Bragg reflection from the system of $(\bar{1}11)$ planes. However, such a pattern cannot be explained assuming the opal structure to be ideally fcc. Indeed, for the second spot to appear on the ζ axis, the structure has to have a horizontal reflection plane perpendicular to the ζ axis or a twofold rotation axis parallel to the $[\bar{2}11]$ direction; a perfect fcc structure does not, however, have such symmetry elements. At the same time, the diffraction of light observed for $\mathbf{K} \perp \zeta$ corresponds to a superposition of diffraction patterns from two fcc lattices with mutually reverse stacking order of the close-packed (111) layers along the ζ axis. Two types of fcc layer stacking may coexist in real opals in the case of random growth layer alternation. Two such fcc lattices form a structure …*ABCABC***A***CBACBA*… involving mirror reflection through a plane denoted here by **A**. This enantiomorphic structure represents a growth twin known in crystallography to exist for the fcc lattice (in general, the growth twin may have a multilayer boundary [28]). Thus, The Bragg diffraction data displayed in Figs. 4 and 5 indicate the presence of a twin fcc structure in synthetic opals.

The twin structure of synthetic opals is due to random stacking of growth hexagonal layers, for which we earlier introduced the correlation coefficient p. For values of p close to unity ($1 - p \ll 1$), the samples consist of fairly extended sequences of hexagonal layers stacked regularly along the ζ axis to form an fcc lattice. As already mentioned, two types of such stacking are possible, *ABCABC*… and *CBACBA*… (denoted by fccI and fccII in Fig. 6b and in what follows). If the alternating fragments of type I and II fcc structures have many layers, this is the case of many twins with boundaries parallel to the (111) plane. Each of the fccI and fccII lattices making up a twin can be characterized by its Brillouin zone, shown in Figs. 6c and 6d, respectively. We readily see that one of these Brillouin zones transforms into the other either when rotated by 60° around the vertical axis or under mirror reflection in a horizontal plane parallel to the fcc (111) plane.

Each of fccI and fccII lattices, making up a twin, is characterized by a system of planes equivalent to the $(\bar{1}11)$ plane system. In our experiment, the $[\bar{2}11]$ incident beam direction lies in the (111) plane of both fcc lattices (Fig. 2). Because of the above symmetry of the Brillouin zones of the fccI and fccII lattices, the $[\bar{2}11]$ direction coincides with the twofold axis about which the Brillouin zone of one of these fcc structures should be rotated to be taken into the Brillouin zone of the other (fccI transfers to fccII and *vice versa*). This accounts for the appearance of two spots symmetrical with respect to the $[\bar{2}11]$ direction in diffraction from a twinned fcc structure; indeed, each of these spots is caused by diffraction of light from the $(\bar{1}11)$ plane system of its structure, fccI or fccII (this kind of diffraction pattern is illustrated in Fig. 6b).

We readily see that the totality of calculated dependences of the average structure factor (13) on angle θ' obtained for a randomly stacked layer structure (Fig. 7) is in qualitative agreement with the "two-spot" diffraction pattern. Figure 5c quantitatively compares the theoretical dependence of $\langle S \rangle$ on θ' with an experimental spectral–angular response of scattered intensity $I_{max}(\theta')$ at the maxima. For this purpose, Fig. 5c presents the calculated $\langle S \rangle$ vs. θ' dependence from those displayed in Fig. 7 that fits the experiment best of all; this curve corresponds to the stacking correlation coefficient p = 0.8. This value of the coefficient p is quite large, which suggests that the opal samples studied by us are dominated by the fcc structure. As seen from Fig. 5c, the maxima in the spectral–angular response of the intensity correspond to the angle $2\vartheta = \pm 40°$ and wavelength λ = 570 nm. These values are close to the figures $2\vartheta_B$ = 39° and λ_B = 565 nm derived above from condition (14) for Bragg diffraction from (111)-type planes of a perfect fcc lattice and from the experimental data on white-light diffraction on the (111) growth layer system. Thus, the maxima in the $I_{max}(\theta')$ relation are explained as being due to Bragg diffraction of light from the $(\bar{1}11)$ plane system of a twinned opal fcc lattice. The angular width of the corresponding peaks is due to the finite size of the fccI or fccII fragment, which forms the $(\bar{1}11)$ plane system responsible for diffraction in the $[\bar{2}11]$ geometry. Estimates show that the twins forming at p = 0.8 are most likely to be those in which parts of a regular fcc structure include about ten hexagonal layers.

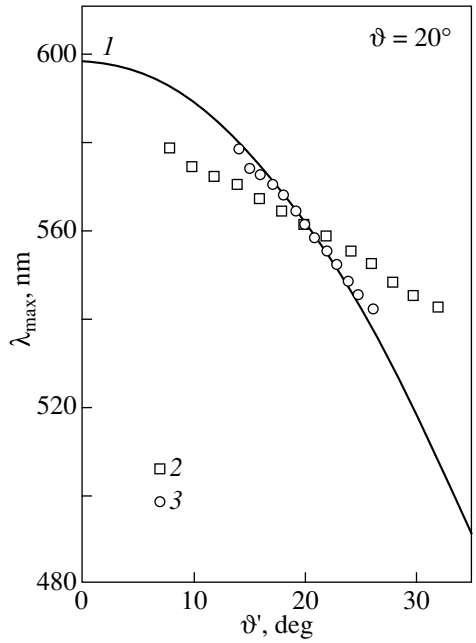

Fig. 8. Comparison of the Bragg wavelength given by Eq. (14) with the wavelengths λ_{max} corresponding to the maxima of measured diffraction reflection spectra (Fig. 3a) plotted vs. reflection angle ϑ'. (*1*) Function $2dn_{eff}\cos\vartheta'$ calculated for $d_{(111)}n_{eff}$ = 300 nm, (*2*) wavelengths $\lambda_{max}(\vartheta')$ corresponding to the maxima in the experimental spectra of the diffracted intensity, and (*3*) wavelengths λ_B calculated from Eq. (14) for the Bragg angles $\vartheta_B = (\vartheta + \vartheta')/2$. The results correspond to white light striking the sample growth surface at an angle ϑ = 20°.

5.3. Angular Broadening of Diffraction Spots

In conclusion, we discuss the mechanism of angular diffraction spot broadening observed to occur in the scattering geometry where a beam of white light falls on the (111) opal growth plane. Let us address the measured spectral–angular response of diffracted intensity $I_{max}(\vartheta')$ (curve *1* in Fig. 3b). The inset to Fig. 3b shows that the angles of incidence ϑ and reflection ϑ', determining the $I_{max}(\vartheta')$ function, are reckoned from the direction accepted in the experiment as the sample growth axis ζ. If this direction is perpendicular to the system of (111) scattering planes, then the relation $\vartheta' = \vartheta = \vartheta_B$, corresponding to the Bragg diffraction scheme $\mathbf{K}_1 \longrightarrow \mathbf{K}_1'$ shown in Fig. 2 holds. In this case, the Bragg wavelength in Eq. (14) measured in vacuum as a function of angle ϑ' is given by the relation $\lambda_B(\vartheta') = 2dn_{eff}\cos\vartheta'$, which is presented by solid curve *1* in Fig. 8.

For comparison, curve *2* in Fig. 8 shows the wavelengths $\lambda_{max}(\vartheta')$ at the spectral maxima [the points of the $I_{max}(\vartheta')$ curve] measured at different reflection angles ϑ'. It is seen that at, an angle of incidence ϑ = 20° corresponding to Fig. 3, condition (14) for a sample with $d_{(111)}n_{eff}$ = 300 nm is satisfied at the point of maximum in the $I_{max}(\vartheta')$ relation, namely, at an angle ϑ' = 20° and wavelength $\lambda_{max}(20°)$ = 560 nm; these figures thus have the meaning of the Bragg quantities ϑ_B and λ_B. However, for the points of the experimental $I_{max}(\vartheta')$ relation for which $\vartheta' \neq \vartheta = 20°$ the function $\lambda_{max}(\vartheta')$ deviates strongly from curve *1*, which implies that Bragg condition (14) does not hold for the corresponding pairs of quantities $\{\vartheta', \lambda_{max}(\vartheta')\}$, namely, $\lambda_{max}(\vartheta') \neq 2dn_{eff}\cos\vartheta'$. This means that the simple $\mathbf{K}_1 \longrightarrow \mathbf{K}_1'$ scattering scheme that assumes the sample growth axis ζ to coincide with the normal to the (111) Bragg plane is applicable only at the maximum of the spectral–angular response $I_{max}(\vartheta')$ where $\vartheta' = \vartheta$ but not at the points where $\vartheta' \neq \vartheta$.

To settle this controversy, we assume that, in different regions of the opal, the normals to the (111) plane system are oriented differently relative to the growth axis ζ [22]. In each of such regions, Bragg diffraction of light occurs in accordance with the scheme $\mathbf{K}_1 \longrightarrow \mathbf{K}_1 + \mathbf{b}_{(111)}$, but vector $\mathbf{b}_{(111)}$ is directed differently in different regions. Then, reflected radiation observed at an angle ϑ' at a fixed angle of incidence ϑ arrives from the opal regions in which the normal to the (111) plane

(vector $\mathbf{b}_{(111)}$) deviates from the ζ axis by an angle $|\vartheta' - \vartheta|/2$. In the case of $\mathbf{K}_1 \longrightarrow \mathbf{K}_1'$ diffraction from the (111) plane system in such a region, the quantity $(\vartheta + \vartheta')/2$ plays the part of the Bragg angle ϑ_B in Eq. (14). In Fig. 8, curve *3* plots the $\lambda_{max}((\vartheta + \vartheta')/2)$ relation, which is seen to fit the $\lambda_B((\vartheta + \vartheta')/2)$ relation calculated using Eq. (14). The good agreement between curves *1* and *3* corroborates the conjecture that while Bragg condition (14) is met for any angle ϑ', the quantity $I_{max}(\vartheta')$ at each ϑ' is associated with light diffraction in regions with specific orientations of vector $\mathbf{b}_{(111)}$ with respect to the sample axis ζ. Viewed from this standpoint, the angular broadening of the diffraction spot may be attributed to different regions of the sample being distributed in the angle of orientation of their (111) growth planes relative to the ζ axis. This mechanism of nonuniform angular broadening of the diffraction spot is in accord with data obtained with atomic-force microscopy, which suggest that the angle between the normal to the (111) close-stacked hexagonal layers in different regions of the sample surface and the growth axis ζ may become as high as 5° [29].

6. CONCLUSION

Thus, we have reported on a first observation of three-dimensional light diffraction from the crystal lattice of synthetic opals. The optical patterns reveal, similar to x-ray diffraction patterns, symmetric systems of diffraction reflections. The diffraction patterns observed in our fairly perfect opals are accounted for by Bragg diffraction from (111)-type planes of a twinned fcc structure. A comparison of the results obtained in a theoretical analysis of the model assuming random stacking of hexagonal layers with the experimental data for our samples yielded the stacking correlation coefficient $p = 0.8$; the large value of this coefficient indicates the predominant formation of a twinned fcc lattice in opals. It has been shown that the angular broadening of the diffraction spots originates from the following two mechanisms: (i) one-dimensional (interlayer) disorder in the alternation of close-packed layers along the sample growth axis ζ, which gives rise to the formation of regions with a regular fcc structure of finite size, and (ii) deflection of the normal to the (111) growth hexagonal layers in different regions of the sample from the averaged axis of its growth. Our studies of diffraction spots permit visualization of the spectral (color) interval and the spatial direction that characterize the corresponding photonic stop band in an opal.

ACKNOWLEDGMENTS

The authors are indebted to S.M. Samoĭlovich for providing the samples, to A.V. Ankudinov for their characterization with atomic-force spectroscopy, and to Yu.É. Kitaev for helpful discussions.

This study was supported by the Russian Foundation for Basic Research, project nos. 02-02-17689 and 02-02-17601.

REFERENCES

1. E. Yablonovich, Phys. Rev. Lett. **58**, 2059 (1987); S. John, Phys. Rev. Lett. **58** (23), 2486 (1987).
2. J. D. Joannopoulos, R. D. Mead, and J. N. Winn, *Photonic Crystals* (Princeton Univ. Press, Princeton, NJ, 1995).
3. V. N. Astratov, V. N. Bogomolov, A. A. Kaplyanskii, *et al.*, Nuovo Cimento D **17**, 1349 (1995).
4. Yu. A. Vlasov, V. N. Astratov, O. Z. Karimov, *et al.*, Phys. Rev. B **55** (13), 357 (1997); S. G. Romanov, A. V. Fokin, V. I. Alperovich, *et al.*, Phys. Status Solidi A **164**, 169 (1997).
5. A. A. Zakhidov, R. H. Baughman, Z. Iqbal, *et al.*, Science **282**, 897 (1998); V. G. Golubev, V. A. Kosobukin, D. A. Kurdyukov, *et al.*, Fiz. Tekh. Poluprovodn. (St. Petersburg) **35** (6), 710 (2001) [Semiconductors **35**, 680 (2001)].
6. V. N. Bogomolov, S. V. Gaponenko, I. N. Germanenko, *et al.*, Phys. Rev. E **55** (6), 7619 (1997).
7. S. G. Romanov, N. P. Johnson, A. V. Fokin, *et al.*, Appl. Phys. Lett. **70** (16), 2091 (1997).
8. J. Wijnhoven and W. L. Vos, Science **281**, 802 (1998).
9. V. N. Bogomolov, A. V. Prokof'ev, and A. I. Shelykh, Fiz. Tverd. Tela (St. Petersburg) **40** (4), 648 (1998) [Phys. Solid State **40**, 594 (1998)].
10. A. Reynolds, F. López-Tejeira, D. Cassagne, *et al.*, Phys. Rev. B **60**, 11422 (1999).
11. M. S. Thijssen, R. Sprik, J. J. Wijnhoven, *et al.*, Phys. Rev. Lett. **83**, 2730 (1999).
12. H. Míguez, A. Blanco, F. Meseduer, *et al.*, Phys. Rev. B **59** (3), 1563 (1999).
13. Yu. A. Vlasov, V. N. Astratov, A. V. Baryshev, *et al.*, Phys. Rev. E **61** (5), 5784 (2000).
14. A. Blanco, E. Chomski, S. Grabtchak, *et al.*, Nature **405**, 437 (2000).
15. J. Huang, N. Eradat, M. E. Raikh, *et al.*, Phys. Rev. Lett. **86**, 4815 (2001).
16. J. V. Sanders, Nature **204**, 1151 (1964); Nature **209**, 13 (1966); Acta Crystallogr. A **24**, 427 (1968).
17. C. Dux and H. Versmold, Phys. Rev. Lett. **78** (9), 1811 (1997).
18. R. M. Amos, J. G. Rarity, and S. C. Kitson, Phys. Rev. B **61** (3), 2929 (2000).
19. C. Kittel, *Introduction to Solid State Physics*, 6th ed. (Wiley, New York, 1986; Nauka, Moscow, 1978).
20. L. V. Woodcock, Nature **385**, 141 (1997); A. D. Bruce, N. B. Wilding, and G. J. Ackland, Phys. Rev. Lett. **79**, 3002 (1977); S.-C. Mau and D. A. Huse, Phys. Rev. E **59**, 4396 (1999).
21. N. D. Deniskina, D. V. Kalinin, and L. K. Kazantseva, *Precious Opals, Their Synthesis and Natural Genesis* (Nauka, Novosibirsk, 1988), p. 353.

22. A. V. Baryshev, A. V. Ankudinov, A. A. Kaplyanskiĭ, *et al.*, Fiz. Tverd. Tela (St. Petersburg) **44** (9), 1573 (2002) [Phys. Solid State **44**, 1648 (2002)].
23. L. D. Landau and E. M. Lifshitz, *Course of Theoretical Physics*, Vol. 8: *Electrodynamics of Continuous Media*, 3rd ed. (Nauka, Moscow, 1982; Pergamon, New York, 1984).
24. J. M. Ziman, *Models of Disorder: The Theoretical Physics of Homogeneously Disordered Systems* (Cambridge Univ. Press, Cambridge, 1979; Mir, Moscow, 1982).
25. J. C. Slater, *Insulators, Semiconductors, and Metals* (McGraw-Hill, New York, 1967; Mir, Moscow, 1969).
26. N. I. Kaliteevskiĭ, *Wave Optics*, 2nd ed. (Vysshaya Shkola, Moscow, 1995), p. 344.
27. W. Loose and B. J. Ackerson, J. Chem. Phys. **101** (9), 7211 (1994).
28. B. K. Vaĭnshteĭn, V. M. Fridkin, and V. L. Indenbom, *Modern Crystallography*, Vol. 2: *Structure of Crystals* (Nauka, Moscow, 1979; Springer, Berlin, 1982).
29. A. V. Ankudinov, private communication.

Translated by G. Skrebtsov

Physics of the Solid State, Vol. 45, No. 3, 2003, pp. 472–476. Translated from Fizika Tverdogo Tela, Vol. 45, No. 3, 2003, pp. 446–450.

DEFECTS, DISLOCATIONS, AND PHYSICS OF STRENGTH

Effect of Electric Current on the Migration of Hydrogen Interstitial Atoms in the Region of a Crack Tip in a Crystal

D. N. Karpinskiĭ and S. V. Sannikov

Institute of Mechanics and Applied Mathematics, Rostov State University, pr. Stachki 200/1, Rostov-on-Don, 344090 Russia

e-mail: karp@math.rsu.ru

Received April 8, 2002

Abstract—The effect of a constant electric current on the migration of interstitial atoms dissolved in a crystal in the region of a tensile crack tip is estimated. The calculation takes into account plastic deformation that is produced in the vicinity of the crack tip in the loaded sample by dislocation motion in active slip planes of the crystal under the action of mechanically and electrically induced shear stresses, Joule heat release, the Thomson effect, and ponderomotive forces and allows for the effect of gas exchange near the crack edges on the evolution of the distribution of interstitial impurity atoms. The time dependence of the stress intensity factor is found for both the cases of the presence and absence of a constant electric current near the crack tip. Numerical calculations are performed for an α-Fe crystal. © *2003 MAIK "Nauka/Interperiodica".*

A high-density electric current has been recently established to sharply decrease the strain resistance of metals and to increase their plasticity [1–3]. Therefore, the investigation of the evolution of point defects near a crack tip under the joint action of mechanical and electrical forces is of great interest. From the practical point of view, the study of the penetration of hydrogen atoms into loaded samples with defects is of particular interest. An interrelation between the processes of fracture and hydrogenation was detected in [4]. The time evolution of the point-defect distribution in the absence of an electric current was considered in [5]. However, in order to develop methods of electrochemical hydrogenation [6] and to solve other relevant problems, it is important to understand the effect of an electric current on sample strength, which substantially depends on the migration of points defects in them. In this line of inquiry, we know only one work [7], in which the evolution of the distribution of hydrogen atoms dissolved near a notch in a current-carrying rod was calculated. However, Ugodchikov and Berendeeva [7] assumed that an applied load did not induce plastic deformation and that gaseous impurities were not accumulated in the notch space. In [8], we studied three mechanisms of transport of hydrogen interstitials near a crack tip in the absence of an electric current: (1) lattice diffusion, (2) dislocation-induced "sweeping out" of point defects, and (3) transport of impurity atoms in dislocation cores moving in a plastic zone. The calculations performed in [5, 8, 9] showed that the first mechanism of impurity atom transport (lattice diffusion) makes the main contribution to the flux of impurity atoms flowing towards the crack space.

Consider a crack of length $2l$ located in the (010) cleavage plane (along the negative semiaxis x) of a bcc crystal H thick and infinite in the other two dimensions (Fig. 1). The crystal planes $y \longrightarrow \pm\infty$ are loaded with a uniform tensile stress $\sigma_a(t)$ (mode *1*) monotonically increasing to the maximum value $\sigma_{\max}$ sufficient for plastic deformation of the crystal to occur but insufficient to cause crack growth. As in [10], we assume that the plastic deformation of the bcc crystal proceeds via the motion of perfect dislocations with Burgers vector

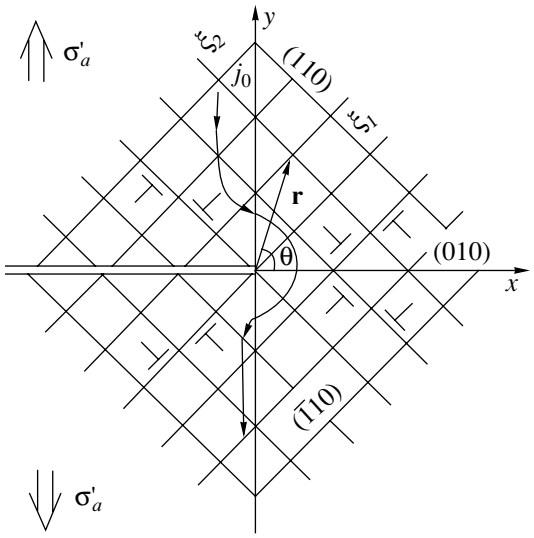

Fig. 1. Crystallographic schematic of the {110} easy-slip planes at the tip of a {001} cleavage crack under tension at stress σ. Lines of a constant electric current are shown.

1063-7834/03/4503-0472$24.00 © 2003 MAIK "Nauka/Interperiodica"

$\mathbf{b} = (1/2)\langle 111\rangle$ along the {110} planes of easy slip. The {110} planes intersect the *xy* plane to form two families of slip lines, whose directions are defined by vectors ξ_j ($j = 1, 2$). Dislocation sources that emit rectangular loops lying in the easy-slip planes are uniformly distributed in the crystal. Then, according to [10, 11], the rate of plastic deformation induced by the motion of dislocations near the crack tip is

$$\frac{d\varepsilon^j(\mathbf{r}, t)}{dt} = \dot{\varepsilon}_0 \exp\left[-\frac{U_0\{1 - [\sigma_e^j(\mathbf{r}, t)/\tau_0]^{1/2}\}}{k_B T(\mathbf{r}, t)}\right] \times \operatorname{sgn}\sigma_e^j(\mathbf{r}, t), \quad (1)$$

where U_0 is the activation energy, $\dot{\varepsilon}_0$ and τ_0 are constants, and σ_e^j is the effective shear stress in the easy-slip planes,

$$\sigma_e^j(\mathbf{r}, t) = \begin{cases} \sigma^j(\mathbf{r}, t) - \sigma_s(\mathbf{r}, t)\operatorname{sgn}\sigma^j(\mathbf{r}, t), & |\sigma^j| > |\sigma_s| \\ 0, & |\sigma^j| < |\sigma_s|. \end{cases} \quad (2)$$

In Eq. (2), the shear stress $\sigma^j(\mathbf{r}, t) = \sigma_j^c(\mathbf{r}, t) + \sigma_j^l(\mathbf{r}, t)$, where $\sigma_j^c(\mathbf{r}, t)$ is the Westergaard stress,

$$\sigma_j^c(\mathbf{r}, t) = \frac{K^c}{\sqrt{2\pi r}}\Psi(\varphi), \quad (3)$$

and $\sigma_j^l(\mathbf{r}, t)$ is the long-range elastic stress created by dislocations of the same sign in the plastic zone,

$$\sigma_j^l(\mathbf{r}, t) = \sum_{k=1}^{2}\int_{D_k}\hat{\sigma}_j(z_k')\Delta\rho_k(z', t)dz'. \quad (4)$$

In Eq. (3), K^c is the stress intensity factor (SIF) for a brittle crack under the action of a mechanical tensile load,

$$K^c = \sigma_a'(t)\sqrt{\pi l}, \quad (5)$$

and $\Psi(\varphi)$ is a function of the vectorial angle φ. In Eq. (4), $\Delta\rho_k(z', t)$ is the density of effective dislocations connected with the strain $\varepsilon(\mathbf{r}, t)$by the relationship

$$\Delta\rho_k(\mathbf{r}, t) = -\frac{1}{b}\frac{d}{d\xi_k}\varepsilon^k(\mathbf{r}, t) \quad (6)$$

and $\hat{\sigma}_j(z_k')$ specifies the stresses created by a dislocation in an elastic plane with a semi-infinite notch.

The method of calculating the evolution of plastic deformation in the region of a crack tip is described in detail in [10, 11].

Additionally to [10, 11], we assume that a constant electric current with a density j_0 ($j_x(\mathbf{r}) = 0$, $j_y = j_0$ at $|\mathbf{r}| \longrightarrow \infty$) passes through the crystal normally to the crack plane in a portion of the crystal far from the crack. In this work, we take into account three mechanisms of the effect of an electric current on dislocations in the plastic zone of the crack: (1) the Joule heat, (2) the Thomson effect (the shift of a region heated by the Joule heat along the drift of conduction electrons), and (3) ponderomotive forces (the forces caused by the interaction between an electric current and its magnetic field) [12].

It seems topical to refine the results of [5, 9] with allowance for the joint effect of mechanical and electric fields on hydrogen atoms dissolved in the crystal. The effect of an electric current on the atoms is both direct and indirect (through changes in the character of dislocation motion). In [13], we took into account only the first and second mechanisms of the effect of an electric current; in this work, we also take into account the third mechanism.

Consider the contribution of ponderomotive forces to the evolution of the plastic deformation at the crack tip [14]. According to the Biot–Savart–Laplace law, an electric current produces a magnetic field in the crystal; in the problem in question, the magnetic induction $\mathbf{B}(\mathbf{r})$ has one nonzero component,

$$B_z(\mathbf{r}, t) = \frac{\mu H}{4\pi}\int_S \frac{J_x(\mathbf{r}', t)R_y - J_y(\mathbf{r}', t)R_x}{R^3}dS'. \quad (7)$$

Here, μ is the magnetic permeability of the crystal; $\mathbf{R} = \mathbf{r} - \mathbf{r}'$; R_x and R_y are the projections of $\mathbf{R}$ onto the *x* and *y* axes, respectively, and integration is performed over the region *S*' occupied by the electric current. According to [12], the current density vector $\mathbf{J}(\mathbf{r}, t)$ near the crack tip in the polar coordinates has the form $J_x(\mathbf{r}, t) = J_0'(t)\sqrt{l/2r}\sin(\theta/2)$ and $J_y(\mathbf{r}, t) = J_0'(t)\sqrt{l/2r}\cos(\theta/2)$.

In our case, the density of the ponderomotive forces is given by

$$\mathbf{b}(\mathbf{r}, t) = \mathbf{J}(\mathbf{r}, t)\times\mathbf{B}(\mathbf{r}, t) = B_z(\mathbf{r}, t)[J_y(\mathbf{r}, t)\mathbf{i} - J_x(\mathbf{r}, t)\mathbf{j}]. \quad (8)$$

Body forces (8), acting along the easy-slip planes in the crystal, induce an additional shear stress σ_j^{pm}, which can be taken into account by replacing the SIF of the crack $K^c(t) = [\sigma_a'(t) + P(t)]\sqrt{\pi l}$ [9], disregarding the effect of the plastic deformation on this crack, with

$$K^{cb} = K^c + K^b, \quad (9)$$

where K^b is determined by solving the problem in the elasticity theory on the equilibrium of an elastic plane with a semi-infinite notch subjected to body forces (8).

Consider the heat release caused by the Joule heat in the plastic zone near the crack tip. The temperature

field in the upper half-plane at instant t is determined by solving the heat-conduction problem:

$$\frac{\partial T}{\partial t} = \alpha\Delta T + F(x, y, t), \quad -\infty, x < \infty, \quad 0 \le y < \infty, \tag{10}$$

$$\left.\frac{\partial T}{\partial y}\right|_{y=0} = \Phi(x, t), \tag{11}$$

$$T|_{t=0} = T_0(x, y), \quad 0 < t < \infty. \tag{12}$$

In Eq. (10), $a = \lambda/\rho C$ is the thermal diffusivity of the crystal, λ is the thermal conductivity, ρ is the density, C is the specific heat, and

$$F(x, y, t) = \varrho j^2(x, y, t) + L j_i(x, y, t)\nabla_i T(x, y, t). \tag{13}$$

In Eq. (13), $\varrho = \varrho_0[1 + \alpha(T - 273\ \text{K})]$ is the resistivity of the crystal, ϱ_0 is the resistivity at $T = 273$ K, α is the temperature coefficient of resistance, and L is the Thomson coefficient [12]. Using the symmetry of the problem for $y = 0$, we obtain the boundary condition $\Phi(x, t) = 0$. Equation (10) for $T(x, y, t)$ is solved using the method described in detail in [11].

In our calculations, we assumed that the crack SIF can be represented as [9, 10]

$$K(t) = K^{cb}(t) + K^p(t), \tag{14}$$

where the correction $K^p(t)$ takes into account the effect of plastic deformation on the SIF,

$$K^p(t) = \sum_{j=1}^{2}\int_{D_j}\hat{K}_j^p(z)\Delta\rho_j(z, t)dz, \quad z = x + iy. \tag{15}$$

The quantity $\hat{K}_j^p(z) = \hat{K}_\text{I}^p - i\hat{K}_\text{II}^p$ was found in [10].

The rate of loading the crystal is chosen so that the condition $\max|\dot{\varepsilon}^j(\mathbf{r}, t)| \le 0.1\ \text{s}^{-1}$ is met at the maximum strain rate in Eq. (1) [9]. The mechanical loading of the crystal is terminated when $K^{cb}(t)$ reached its maximum, $K_{\max}^{cb}$. The current density is monotonically increased with time up to a given value j_0 such that the relation $K_b = K_c/10$ is valid in Eq. (9).

In calculating the evolution of the plastic deformation near the crack tip in an α-Fe crystal under the action of an applied mechanical load and an electric current, we used the following constants: $H = 10^{-2}$ m, $2l = 10^{-3}$ m, $\rho = 7800$ kg/m^3, $\lambda = 78.2$ W/(m K), $C = 460$ J/(kg K), $T_0 = 300$ K, $\varrho_0 = 8.6 \times 10^{-8}\ \Omega$ m, $L = -22.8 \times 10^{-6}$ V/K, $\mu = 4\pi \times 10^{-7}$ H/m, $\alpha = 3.3 \times 10^{-3}$ K^{-1}, $J_0 = 8 \times 10^8$ A/m^2, and $K_{\max}^{cb} = 0.2$ MPa m$^{1/2}$. The other constants were chosen as in [9].

Now, we analyze the equation of electromechanical diffusion (see, e.g., [7])

$$\frac{\partial c(\mathbf{r}, t)}{\partial t} = D\nabla^2 c(\mathbf{r}, t) + \frac{Dc(\mathbf{r}, t)}{k_\text{B}T(\mathbf{r}, t)}\nabla c(\mathbf{r}, t)\nabla V(\mathbf{r}, t), \tag{16}$$

where D is the diffusion coefficient, $V(\mathbf{r}, t) = \Delta\upsilon\sigma_{ii}^e(\mathbf{r}, t) - eZ^*\bar{\varphi}(r, t)$, $\Delta\upsilon$ is the change in the unit-cell volume caused by an interstitial atom in it, $\sigma_{ii}^e(\mathbf{r}, t)$ is the spherical component of the effective stress tensor at the crack tip [9], e is the elementary charge, Z^* is the effective charge number, and $\bar{\varphi}(\mathbf{r}, t)$ is the electric potential of the current in the crystal. It follows from [12] that $\bar{\varphi} = -\rho j_0\sqrt{2l}\sin(\theta/2)$ at $|\mathbf{r}|/l \longrightarrow 0$. Equation (16) was derived for a dilute solution of impurities ($c \ll 1$) with allowance for the condition $\Delta V = 0$.

We assume that hydrogen interstitials with a concentration c_0 are uniformly distributed in the crystal prior to loading. Then, the initial condition is $c = c_0$ at $t = 0$. The boundary conditions are as follows: at $y = 0$ and $x > 0$,

$$\frac{\partial c(x > 0, 0, t)}{\partial y} = \frac{eZ^* c j_0 \rho}{k_\text{B}T}\sqrt{l/2r}; \tag{17}$$

at $y = 0$ and $x < 0$,

$$D\frac{\partial c(x < 0, 0, t)}{\partial y} = k_m[c^2 - (\Gamma')^{-1}P(t)] \tag{18}$$

(the Sieverts law [5]); and at $|\mathbf{r}| \longrightarrow \infty$, $c = c_0$. In Eq. (18), k_m is the constant of mass transfer at the gas–solid phase interface, $P(t)$ is the gas pressure in the crack space, and Γ' is a modified Henry constant [5].

We also assume that the gas in the crack space can be treated as an ideal gas; then, its pressure $P(t)$ inside the crack is [5]

$$P(t) = \frac{1}{2}\sigma_a'(t)\left\{\left[1 + \frac{4Gk_\text{B}TN(t)}{\pi(1-\nu)(2l)^2\sigma_a'^2(t)}\right]^{1/2} - 1\right\}, \tag{19}$$

where G is the shear modulus and ν is the Poisson ratio in the crystal. As in [9], we assume that the main flow of gas dissolved in the bulk of the crystal enters the crack space through its edges. In this case, the number of hydrogen molecules in the crack space is $N(t) = \int_0^t J(t)dt$, where

$$J(t) = k_m\int_{-\infty}^{0}[c^2(x, 0, t) - (\Gamma')^{-1}P(t)]dx$$

is the gas atom flux through the crack edges. The method of solving Eqs. (16)–(19) is similar to that used in [5, 9].

We take into account the plasticizing effect of the dissolved hydrogen by introducing a correction to the yield stress σ^τ [9, 15]:

$$\sigma^\tau = \frac{2\pi\beta^2 c(\mathbf{r}, t)}{3\sqrt{3} r_0 b k_B T}, \quad \beta = \frac{Gb(1+\nu)}{3\pi(1-\nu)}\Delta\upsilon, \qquad (20)$$

where r_0 is the dislocation core radius.

To calculate the migration of hydrogen interstitials in an α-Fe crystal, we used the following constants: $b = 2.48 \times 10^{-4}$ μm, $D = 4.88 \times 10^{-12}$ m^2 s^{-1}, $k_m = 4.88 \times 10^{-9}$ m^2 s^{-1}, $r_0 = 2b$, $G = 83$ GPa, $\nu = 0.28$, and $\Delta\upsilon = 3 \times 10^{-30}$ m^3.

Now, we discuss the effect of the electric current on the evolution of the distribution of point defects in the region of the crack tip. The direct effect of the electric current on hydrogen atoms is caused by its electric potential, the Joule heat, and the Thomson effect. The indirect effect of the electric current on dissolved hydrogen atoms is caused by a change in the hydrostatic component of the mechanical stress tensor at the crack tip due to an additional extension of the crack induced by the ponderomotive forces. This change leads to a dislocation redistribution in the plastic zone. The additional Westergaard stress field, in combination with the elastic field created by dislocations in the plastic zone, affects the migration of point defects. The electric current can also indirectly affect the migration of hydrogen atoms to the crack space and, consequently, change the gas pressure in it.

Figure 2 shows the time dependences of the SIF in the crystal containing hydrogen interstitials with concentrations $c_0 = 10^{-5}$ (curve *2*) and 10^{-4} (curve *3*). Curve *1* in Fig. 2 corresponds to the concentration $c_0 = 10^{-5}$ in the case when the Joule heat and Thomson effect are neglected. The end points of these curves correspond to the instants the evolution of plastic deformation ε^j was terminated when the effective stress σ_e^j decreased below the yield stress. A comparison of curves *1* and *2* demonstrates that the neglect of the thermal effect of the electric current considerably (by ~3%) decreases the stress relaxation at the crack tip and increases the time it takes for the termination of the plastic deformation from 1.34 to 1.4 s. The results of SIF calculation at a concentration of $c_0 = 10^{-4}$ showed an insignificant decrease in the SIF (by ~1%) in comparison with the calculated value at $c_0 = 10^{-5}$ and a considerable decrease in the time for termination of the evolution of plastic deformation (down to 1.01 s). This effect may be due to a noticeable decrease in the yield stress resulting from the nonlinear dependence of σ^τ on the concentration c.

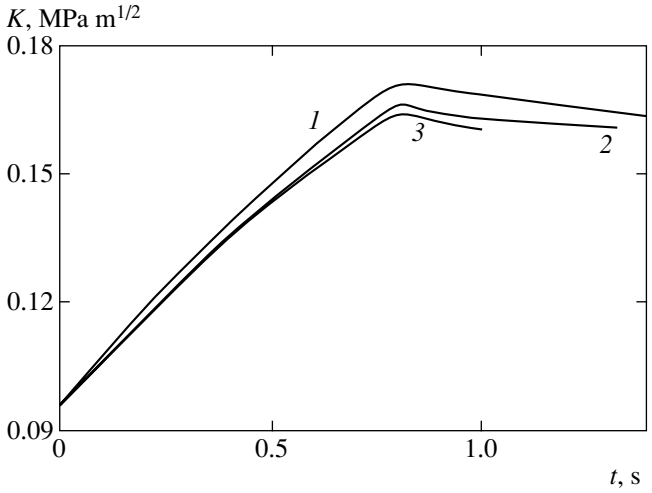

Fig. 2. Calculated time dependences of stress intensity factors for a plastic tensile crack in a bcc crystal containing hydrogen interstitials with initial concentration c_0: (*1*) without regard for the heating of the crystal due to the Joule heat, $c_0 = 10^{-5}$; (*2*) with allowance for all mechanisms of the effect of an electric current, $c_0 = 10^{-5}$; and (*3*) the same as for curve *2*, but with $c_0 = 10^{-4}$.

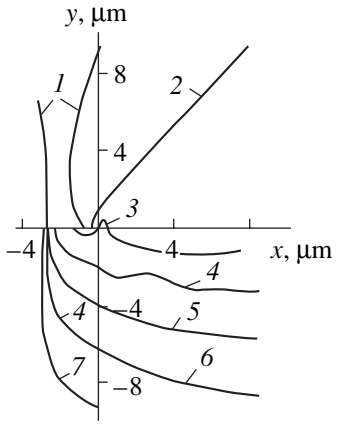

Fig. 3. Level lines of the dimensionless concentration $c(\mathbf{r}, t)/c_0$ of hydrogen interstitial impurity atoms in the region of the crack tip for the initial concentration $c_0 = 10^{-5}$ at the instant $t = 1.34$ s: (*1*) 0.919, (*2*) 0.944, (*3*) 0.969, (*4*) 0.994, (*5*) 1.02, (*6*) 1.04, and (*7*)1.07.

It is important to note that the continuous decrease in the SIF in Fig. 2 (curves *1*–*3*) is caused by the competition of mechanisms that accelerate the development of plastic deformation, which leads to an additional stress relaxation at the crack tip due to the Joule heat (curves *1*, *2*) and to a decrease in the yield stress with increasing hydrogen concentration (curves *2*, *3*). At the same time, an increase in the gas pressure in the crack space due to a rise in hydrogen migration to the crack sink caused by a higher mobility of dissolved hydrogen interstitials upon heating and due to an increase in the

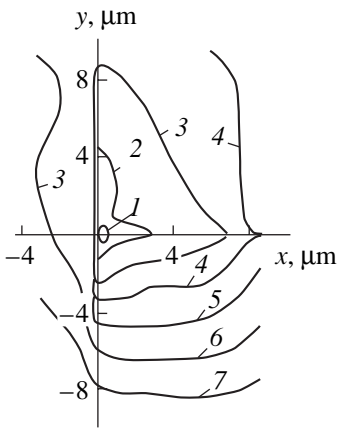

Fig. 4. Level lines of the dimensionless concentration $c(\mathbf{r}, t)/c_0$ of hydrogen interstitial impurity atoms in the region of the crack tip for the initial concentration $c_0 = 10^{-4}$ at the instant $t = 1.01$ s: (*1*) 0.833, (*2*) 0.865, (*3*) 0.896, (*4*) 0.927, (*5*) 0.958, (*6*) 0.990, and (*7*)1.02.

initial hydrogen concentration results in a higher stress level at the crack tip. Heating of gas in the crack space caused by the Joule heat leads to an increase in the pressure P in Eq. (19) and in the modified Henry constant $\Gamma'(T)$ [5, 9], which are involved in boundary conditions (18). These changes result in a decrease in the crack-edge permeability to hydrogen. The calculations performed with the constants chosen showed a predominant contribution from relaxation mechanisms to the SIF evolution.

Figure 3 shows the concentration distribution of hydrogen interstitials in the region of the crack tip that corresponds to the end point of curve *2* in Fig. 2. The concentration distribution is seen to be asymmetric about the crack line. The concentration distribution of point defects in Fig. 4 corresponds to the end point of curve *3* in Fig. 2; in this case, however, there is a region with a lower concentration (concentration "dip") in front of the crack tip. It should be noted that the hydrogen flux through the upper crack edge (Fig. 1) is smaller than that through the lower ("shadow") one (by less than 1%), except in the initial loading stage. However, the total hydrogen flux flowing towards the crack space is the same in both the absence and presence of the electric current in the crystal. In other words, the electric current cannot decrease the flow of hydrogen dissolved in the crystal to the crack space. However, the effect of the electric current on the hydrogen distribution in the region of the crack tip is noticeable as compared to the current-free loading mode [5].

In conclusion, we note the following.

(1) The relaxation mechanisms of the effect of an electric current on the evolution of plastic deformation dominate over the mechanisms that raise the concentration of mechanical stresses at a crack tip in a crystal with dissolved hydrogen.

(2) The Joule heat is the main mechanism of the direct and indirect effect of an electric current on the migration of hydrogen interstitials and on the relaxation of mechanical stresses at the crack tip.

(3) The distribution of point defects near the crack tip depends substantially on their initial concentration and the current density. At the available current densities, the current cannot decrease the flow of dissolved hydrogen to the crack space.

REFERENCES

1. V. E. Gromov, L. B. Zuev, and É. V. Kozlov, *Electric-Current-Stimulated Plasticity of Metals and Alloys* (Nedra, Moscow, 1997).
2. V. I. Spitsin and O. A. Troitskiĭ, *Electroplastic Deformation of Metals* (Nauka, Moscow, 1985).
3. A. F. Sprecher, S. L. Mannan, and H. Conrad, Acta Metall. **34** (7), 1145 (1986).
4. Yu. A. Khrustalev, Vestn. Tambov. Gos. Univ. **5** (2–3), 234 (2000).
5. D. N. Karpinskiĭ and S. V. Sannikov, Fiz. Met. Metalloved. **85** (2), 121 (1998).
6. S. M. Beloglazov, *Hydrogenation of Steel under Electrochemical Processes* (Leningr. Gos. Univ., Leningrad, 1975).
7. N. A. Ugodchikov and A. G. Berendeeva, in *Applied Problems of Strength and Plasticity. Methods of Solution* (KMK, Moscow, 1997), p. 69.
8. D. N. Karpinskiĭ and S. V. Sannikov, Fiz. Tverd. Tela (St. Petersburg) **39** (9), 1580 (1997) [Phys. Solid State **39**, 1407 (1997)].
9. D. N. Karpinskiĭ and S. V. Sannikov, Fiz. Tverd. Tela (St. Petersburg) **42** (12), 2171 (2000) [Phys. Solid State **42**, 2236 (2000)].
10. D. N. Karpinskiĭ and S. V. Sannikov, Prikl. Mekh. Tekh. Fiz. **34** (3), 154 (1993).
11. D. N. Karpinskiĭ and S. V. Sannikov, Fiz. Tverd. Tela (St. Petersburg) **37** (2), 505 (1995) [Phys. Solid State **37**, 273 (1995)].
12. L. D. Landau and E. M. Lifshitz, *Course of Theoretical Physics*, Vol. 8: *Electrodynamics of Continuous Media*, 4th ed. (Nauka, Moscow, 1995; Pergamon, New York, 1984).
13. D. N. Karpinskiĭ and S. V. Sannikov, Vestn. Tambov. Gos. Univ. **5** (2–3), 236 (2000).
14. G. X. Cai and F. G. Yuan, Adv. Eng. Softw. **29** (3–6), 297 (1998).
15. N. M. Vlasov and V. A. Zaznoba, Fiz. Tverd. Tela (St. Petersburg) **41** (3), 451 (1999) [Phys. Solid State **41**, 404 (1999)].

Translated by K. Shakhlevich

Physics of the Solid State, Vol. 45, No. 3, 2003, pp. 477–481. Translated from Fizika Tverdogo Tela, Vol. 45, No. 3, 2003, pp. 451–455.

DEFECTS, DISLOCATIONS, AND PHYSICS OF STRENGTH

Internal Friction and Young's Modulus of Si_3N_4/BN Fibrous Monoliths at Various Vibrational Strain Amplitudes

B. K. Kardashev*, B. I. Smirnov*, D. Singh, K. C. Goretta**, and A. R. de Arellano-López*****

** Ioffe Physicotechnical Institute, Russian Academy of Sciences, Politekhnicheskaya ul. 26, St. Petersburg, 194021 Russia*
e-mail: b.kardashev@mail.ioffe.ru
*** Argonne National Laboratory, Argonne, Illinois, 60439 USA*
**** Universidad de Sevilla, Sevilla, 41080 Spain*
Received May 30, 2002

Abstract—The effect of temperature and vibrational strain amplitude on Young's modulus and an ultrasound damping (internal friction) of ceramic boron nitride samples and silicon nitride/boron nitride fibrous monoliths was studied. It was shown that the elastic moduli and the elastic vibration decrement of the low-modulus BN ceramic and of the high-modulus Si_3N_4/BN monoliths measured at small strain amplitudes (in the region of amplitude-independent internal friction) exhibit a noticeable temperature hysteresis. Temperature exerts the smallest effect on the amplitude-independent decrement and on the amplitude-dependent damping and Young's modulus defect of a monolith whose filaments are arranged both along and perpendicular to the axis of a rod-shaped sample. These parameters behave in the most complicated way in a sample with all its filaments aligned with the rod axis. The observed relations can be assigned to structural features of the monoliths and the considerable influence of transverse strain on the evolution of defect structure in the materials studied. © *2003 MAIK "Nauka/Interperiodica".*

1. INTRODUCTION

The present study is a continuation of the investigation [1, 2] into the elastic and inelastic characteristics of ceramic boron nitride (BN) and silicon nitride/boron nitride fibrous monoliths (Si_3N_4/BN). The original publication [1] dealt primarily with the high-temperature elastic properties of boron nitride ceramics fabricated employing different technologies. Similar studies were carried out on Si_3N_4/BN fibrous monoliths [2]. These monoliths are fabricated by pressing ceramic filaments coated by an appropriate binder and compare favorably with conventional high-strength ceramic-based composites in that their structure precludes catastrophic crack propagation at high stresses [3–7].

This study focuses attention on the behavior of the acoustic characteristics (Young's modulus E, vibrational decrement δ) of boron nitride and Si_3N_4/BN fibrous monoliths over a broad range of vibrational strain amplitudes at moderate temperatures (100–390 K).

2. EXPERIMENTAL

The fibrous monoliths were fabricated in the USA (Advanced Research, Tucson, AZ) from polymer-bound Si_3N_4/BN filaments ~325 μm in diameter, which represented Si_3N_4 cores (85 vol %) coated by a BN layer (15 vol %). Detailed information on the technology of fabrication and structure of the materials used in this study is given in [2] and the references therein (see also [8, 9]). We only note here that after the binding pyrolysis and pressing of the monoliths, the filaments were approximately 100×200 μm^2 in cross section. Monolithic Si_3N_4 and BN ceramics were also prepared employing the same technology for comparison.

Acoustic measurements were carried out on rod-shaped specimens of rectangular cross section (~10–20 mm^2) and about 25 mm in length. Rods of three types, with differently arranged filaments (fiber architecture), were used; more specifically, the filaments were arranged along (sample notation [0]), across [90], and along and across [0/90] the main rod axis. In the latter case, layers with mutually perpendicular filament arrangement were stacked alternately. Schematics of the structure of these fibrous monoliths and their SEM micrographs can be found in [2].

The acoustic characteristics at various temperatures T and vibrational strain amplitudes ε were studied using the resonance method of a composite piezoelectric oscillator on samples vibrating longitudinally at frequencies of about 100 kHz. This method is described in considerable detail in [10]. This method permits one to perform acoustic measurements over a broad range of strain amplitudes (spanning about three decades), including the range of amplitude-independent ultrasound damping where a material behaves linearly and the range of nonlinear amplitude-dependent damping where inelastic (microplastic) deformation becomes noticeable.

1063-7834/03/4503-0477$24.00 © 2003 MAIK "Nauka/Interperiodica"

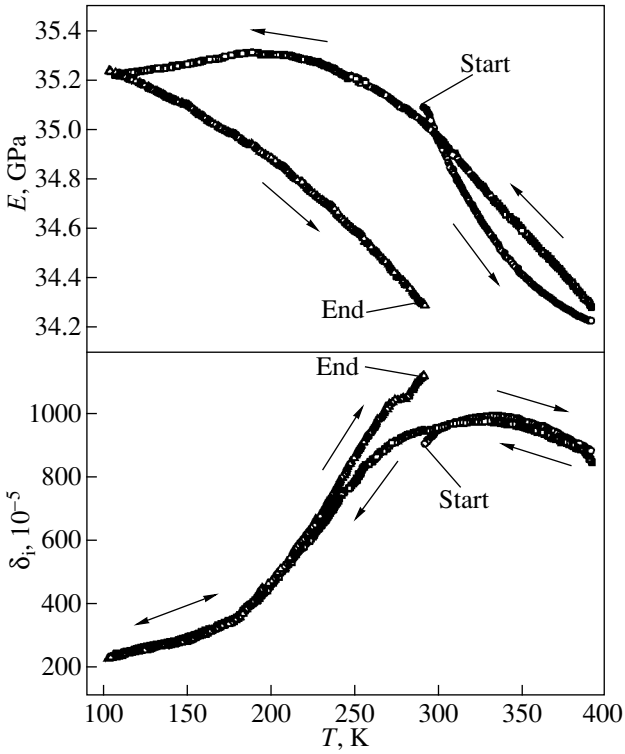

Fig. 1. Young's modulus E and elastic vibration decrement δ_i of a BN sample measured in the temperature range 100–390 K at a strain amplitude $\varepsilon = 1.0 \times 10^{-6}$; arrows indicate the direction of temperature variation.

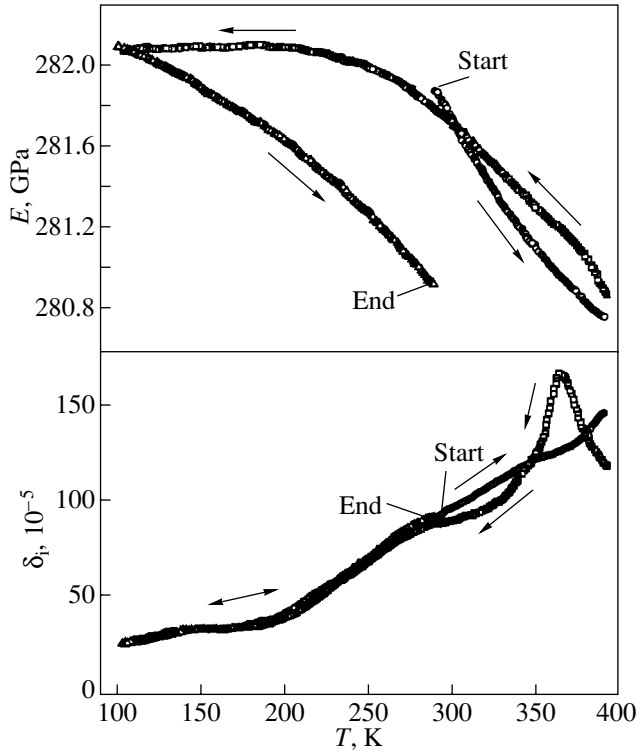

Fig. 2. Young's modulus E and elastic vibration decrement δ_i of a sample of fibrous monolith Si_3N_4/BN [0] measured in the temperature range 100–390 K at a strain amplitude $\varepsilon = 1.0 \times 10^{-6}$; arrows indicate the direction of temperature variation.

The inelastic properties become manifest at sufficiently large strain amplitudes. As a measure of inelasticity, one may use the amplitude-dependent Young's modulus defect $(\Delta E/E)_h = [E(\varepsilon) - E_1]/E_1$, where E_1 is the modulus determined in the amplitude-independent region at the smallest ε used in a given experiment. The elastic-modulus defect $(\Delta E/E)_h$ is approximately equal to the ratio of inelastic to elastic strain [10]. The amplitude-dependent decrement $\delta_h = \delta(\varepsilon) - \delta_i$ also reflects the nonlinear behavior of a material (here, δ_i is the decrement measured at a small strain amplitude in the amplitude-independent region).

3. RESULTS AND DISCUSSION

Figures 1 and 2 illustrate the experimental temperature dependences of Young's modulus $E(T)$ and elastic vibration decrement $\delta_i(T)$ measured at $\varepsilon = 1.0 \times 10^{-6}$ (region of amplitude-independent damping) on the BN ceramic and Si_3N_4/BN [0] monolith samples under thermal cycling in the range 100–390 K. The measurements were started by heating a sample from room temperature to ~390 K, followed by cooling to approximately 100 K, and then heating again to 290 K. The heating and cooling rates were about 2 K/min. As seen from the figures, both samples exhibit a temperature hysteresis in both the elastic modulus and the decrement. The relations demonstrated by fibrous monoliths of [90] and [0/90] architecture in similar experiments are qualitatively similar to the $E(T)$ and $\delta_i(T)$ dependences obtained on boron nitride (Fig. 1). The behavior of Young's modulus in the [0] architecture (Fig. 2) is qualitatively indistinguishable from $E(T)$ of BN (Fig. 1), despite the nearly order-of-magnitude differences in the absolute value of the modulus. This suggests that the low-modulus component of boron nitride is primarily responsible for the changes in Young's modulus effected under thermal cycling.

The behavior of the decrement in these experiments is also dominated by damping in the boron nitride. This is particularly well seen from Fig. 3, which compares the values of the decrement δ_i and the relative variation of Young's modulus E observed under cooling from 390 to 100 K for all the samples studied in this work. The damping in the Si_3N_4 sample with no boron nitride present is very low (curve *5* in Fig. 3). The presence of Si_3N_4 filaments in the monolith noticeably reduces the decrement, the drop in δ_i being the largest in the sample with the [0] architecture, where the filaments are arranged along the main rod axis. This sample exhibits, however, as evident from Figs. 2 and 3, a very well-pronounced damping peak at 365 K; in the samples with

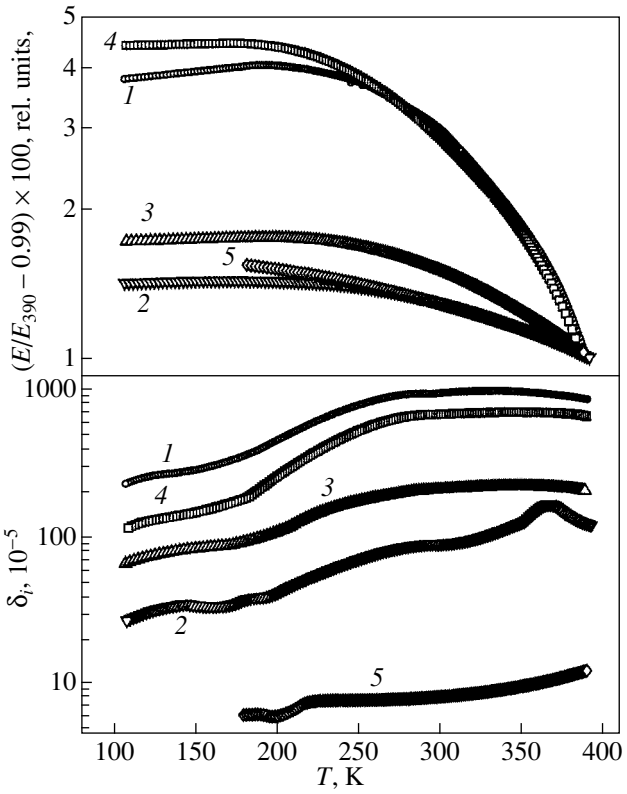

Fig. 3. Temperature dependences of Young's modulus E and decrement δ_i of samples of (*1*) BN and (*5*) Si_3N_4 and of Si_3N_4/BN fibrous monoliths with filament orientation (*2*) [0], (*3*) [0/90], and (*4*) [90] measured under cooling from 390 to 100 K at a strain amplitude $\varepsilon = 1.0 \times 10^{-6}$.

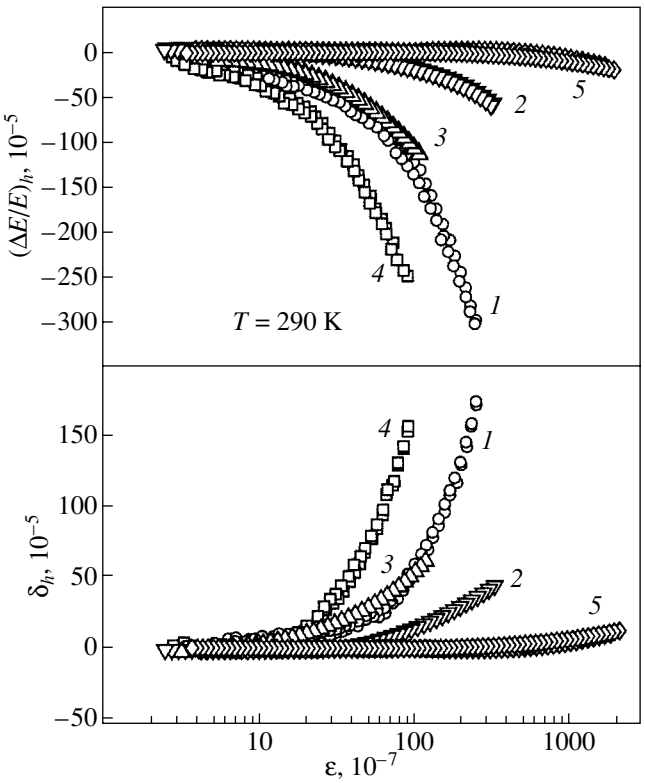

Fig. 4. Amplitude-dependent Young's modulus defect $(\Delta E/E)_h$ and elastic vibration decrement $\delta_h = (\delta - \delta_i)$ measured as functions of vibrational strain amplitude under increasing and decreasing ε for samples of (*1*) BN, (*2*) Si_3N_4/BN [0], (*3*) Si_3N_4/BN [0/90], (*4*) Si_3N_4/BN [90], and (*5*) Si_3N_4. T = 290 K.

the [90] and [0/90] architecture, as well as in the BN matrix, this peak is either very broad or absent altogether. Interestingly, temperature affects least of all the decrement δ_i of the [0/90] sample.

The inelastic properties were studied in two ways: (i) the strain amplitude dependences of the modulus $E(\varepsilon)$ and the decrement $\delta(\varepsilon)$ were measured at some fixed temperatures and (ii) the $E(T)$ and $\delta(T)$ dependences were determined at two fixed strain amplitudes, one of which was in the region of amplitude-independent ($\varepsilon = 1.0 \times 10^{-6}$) and the other, in that of amplitude-dependent ultrasound damping; in the latter experiment, the sample was subjected mainly to a large-strain amplitude ultrasound, after which a low strain amplitude was set for a short time (about 1 s, a time long enough for the value of ε to stabilize and the measurements to be made). In these experimental conditions, we were able to obtain detailed information on temperature spectra of the amplitude-dependent Young's modulus defect $(\Delta E/E)_h$ and decrement δ_h.

Figures 4–6 present graphs of the amplitude-dependent decrement and Young's modulus defect measured at three fixed temperatures: 290, 390, and 102 K. The measurements showed that experimental curves obtained with increasing and subsequently decreasing strain amplitude coincide, which shows that the materials are of good quality. These curves illustrate the ability of a sample to inelastically (microplastically) deform. Data on $(\Delta E/E)_h$ (Figs. 4–6) permit one to derive information on the level of inelastic strain for the materials studied by constructing stress-inelastic-strain graphs. This was done [2] for room-temperature data. It was shown that the level of stresses required for initiation of the same microplastic deformation decreases on going along the series Si_3N_4, Si_3N_4/BN [0], Si_3N_4/BN [0/90], Si_3N_4/BN [90], and BN and that the inelastic strain reached in acoustic experiments at the highest strain amplitudes used on all the materials does not exceed 10^{-7}. The data displayed in Figs. 5 and 6, which were obtained at 390 and 102 K, likewise indicate that microplastic strain, both above and below room temperature, changes neither this series nor the strain level (10^{-7}). The only feature, seen as a maximum in the $\delta_h(\varepsilon)$ curve obtained at 390 K, is observed in Fig. 5 for the Si_3N_4/BN [0] sample (curve *2*); furthermore, curves *2* and *3* for $(\Delta E/E)_h$ in Fig. 5 lie substantially closer to

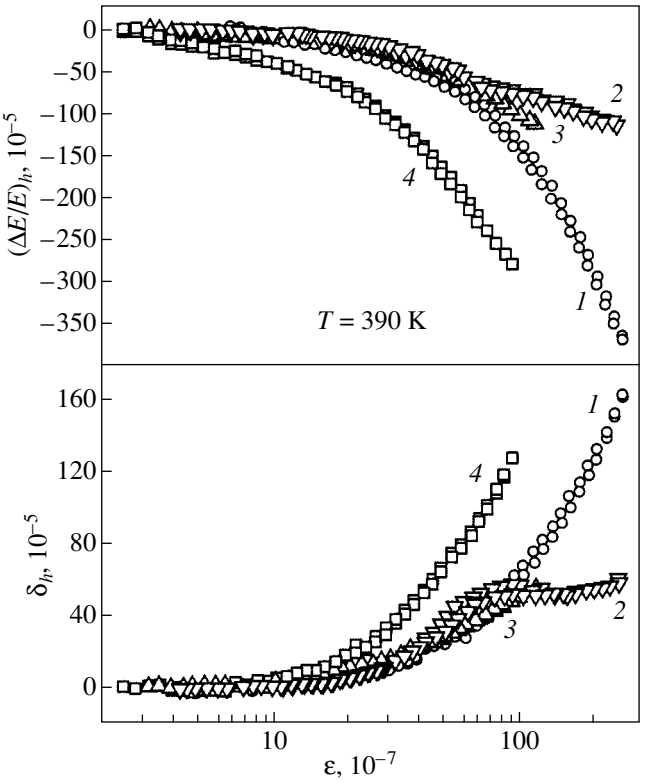

Fig. 5. Amplitude-dependent Young's modulus defect $(\Delta E/E)_h$ and elastic vibration decrement $\delta_h = (\delta - \delta_i)$ measured as functions of vibrational strain amplitude under increasing and decreasing ε for samples of (*1*) BN, (*2*) Si_3N_4/BN [0], (*3*) Si_3N_4/BN [0/90], and (*4*) Si_3N_4/BN [90]. T = 390 K.

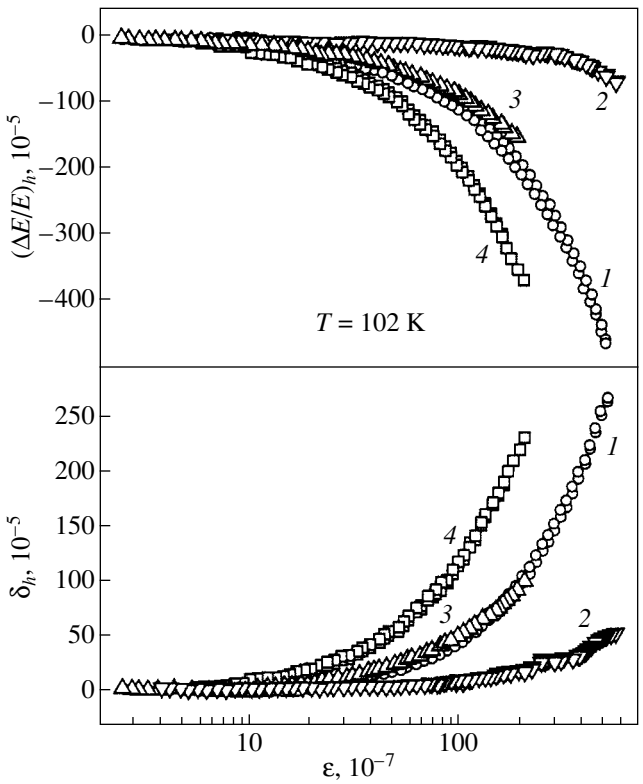

Fig. 6. Same as in Fig. 5 but for T = 102 K.

each other than the similar curves in Figs. 4 and 6, which were taken at room temperature and at 102 K, respectively.

Figure 7 illustrates the effect of temperature on the nonlinear characteristics of the BN and Si_3N_4/BN samples in more detail. In these experiments, the stabilization strain amplitude was different for all samples. Based on the data presented in Figs. 4–6, the amplitude was chosen such that, on the one hand, the measured δ_h and $(\Delta E/E)_h$ were large enough to be determined with acceptable accuracy throughout the temperature range covered, while on the other, were not so large as to make stabilization of the chosen value of ε technically impossible (to satisfy these requirements, the stabilization strain amplitude should be, as a rule, in the central part of the range covered by the strain amplitude dependences). As seen from Fig. 7, the behavior of the parameters measured for the BN and Si_3N_4/BN [90] samples differ little in character (curves *1*, *4*). By contrast, curves *2* and *3*, which display the behavior of δ_h and $(\Delta E/E)_h$ of two other samples, differ qualitatively from curves *1* and *4* and from each other. The sample with the [0] architecture exhibits distinct amplitude-dependent internal friction peaks at comparatively high temperatures. The [0/90] sample is remarkable for a very weak dependence on temperature in both its decrement (there is a weakly pronounced maximum in the region of 240 K) and its modulus defect.

The specific features of the experimental relations observed in different fibrous monoliths are apparently due to different strengths of bonding between the fiber core (Si_3N_4) and the coating (BN), as well as to fibers in samples of different architecture being differently stressed.

In [0] samples, imperfect bonding of filaments aligned with the main rod axis is apparently more conspicuous in the chosen experimental conditions against the comparatively low δ_h level. In samples with filaments arranged across the sample axis (the [90] architecture), this background is very high (curve *4* in Fig. 7) and features in the form of peaks or dips are not so distinct. In addition, the stressed state here is completely different and bonding defects may produce similar peaks in δ_h at other (higher) temperatures. Figure 7 (curves *2*) suggests the existence of a whole spectrum of defects, which become manifest in the presence of well-pronounced maxima in the temperature dependence of the amplitude-dependent decrement δ_h and fairly high absolute values of the modulus defect $(\Delta E/E)_h$ above room temperature. The presence of defects becoming active at temperatures of 300 K and

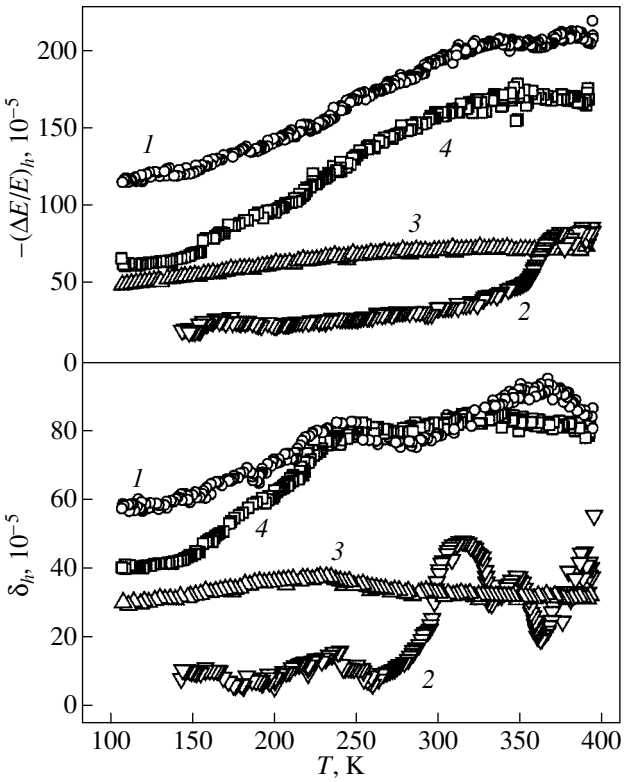

Fig. 7. Amplitude-dependent Young's modulus defect $(\Delta E/E)_h$ and elastic vibration decrement $\delta_h = (\delta - \delta_i)$ measured as functions of T for samples of (*1*) BN, (*2*) Si_3N_4/BN [0], (*3*) Si_3N_4/BN [0/90], and (*4*) Si_3N_4/BN [90] under cooling from 390 to 100 K; the vibrational strain amplitude in each experiment was maintained constant at a level (*1*) 1.3×10^{-5}, (*2*) 1.5×10^{-5}, (*3*) 0.70×10^{-5}, and (*4*) 0.50×10^{-5}.

higher in [0] samples also accounts for the appearance of a well-pronounced maximum in the amplitude-independent decrement (see Figs. 2, 3). There can hardly be any doubt that the features in the behavior of δ_i and δ_h are related. However, the sensitivity of nonlinear inelastic effects to the presence of defects and to the possible evolution of defect structure is apparently much higher.

In connection with the above observations, mention should be made of the structural perfection of the sample with [0/90] architecture, which is reflected in the very weak temperature dependences of δ_i, δ_h, and $(\Delta E/E)_h$. An important role may play here not only the almost total absence of mobile defects but also the substantially suppressed transverse deformation in this material (in the case of longitudinal vibrations), which is due to high-modulus filaments being arranged across the main rod axis.

4. CONCLUSIONS

Thus, our studies convincingly showed that transverse filaments play an important stabilizing part in a composite. The sample with the [0/90] architecture apparently ensures the required strength of bonding between Si_3N_4 and BN and, hence, a small concentration and low mobility of defects. The experience gained in this study suggests that nonlinear acoustic parameters provide the most complete characterization of the defect structure and can be employed in studying and estimating the quality of bonding between a filament and the matrix in a composite material.

ACKNOWLEDGMENTS

This study was supported by the Russian Foundation for Basic Research (project no. 00-01-00482), NATO (grant no. PST.CLG.977016), and DOE, USA (contract no. W-31-109-Eng.38).

REFERENCES

1. B. K. Kardashev, Yu. A. Burenkov, B. I. Smirnov, *et al.*, Fiz. Tverd. Tela (St. Petersburg) **43** (6), 1048 (2001) [Phys. Solid State **43**, 1084 (2001)].
2. B. I. Smirnov, Yu. A. Burenkov, B. K. Kardashev, *et al.*, Fiz. Tverd. Tela (St. Petersburg) **43** (11), 2010 (2001) [Phys. Solid State **43**, 2094 (2001)].
3. D. Kovar, B. H. King, R. W. Trice, and J. W. Halloran, J. Am. Ceram. Soc. **80** (10), 2471 (1997).
4. G. A. Danko, G. E. Hilmas, J. W. Halloran, and B. King, Ceram. Eng. Sci. Proc. **18** (3), 607 (1997).
5. J. L. Routbort, K. C. Goretta, E. T. Park, *et al.*, Ceram. Eng. Sci. Proc. **20** (3), 427 (1999).
6. M. Tlustochowicz, D. Singh, W. A. Ellingson, *et al.*, Ceram. Trans. **103**, 245 (2000).
7. D. Singh, T. A. Cruse, D. J. Hermanson, *et al.*, Ceram. Eng. Sci. Proc. **21** (3), 597 (2000).
8. R. W. Trice and J. W. Halloran, J. Am. Ceram. Soc. **82**, 2502 (1999).
9. R. W. Trice and J. W. Halloran, J. Am. Ceram. Soc. **83**, 311 (2000).
10. S. P. Nikanorov and B. K. Kardashev, *Elasticity and Dislocation Inelasticity of Crystals* (Nauka, Moscow, 1985).

Translated by G. Skrebtsov

Physics of the Solid State, Vol. 45, No. 3, 2003, pp. 482–485. Translated from Fizika Tverdogo Tela, Vol. 45, No. 3, 2003, pp. 456–459.

DEFECTS, DISLOCATIONS, AND PHYSICS OF STRENGTH

Temperature Dependences of Young's Modulus of Biomorphic Silicon Carbide Ceramics

B. I. Smirnov*, Yu. A. Burenkov*, B. K. Kardashev*, F. M. Varela-Feria, J. Martínez-Fernández**, and A. R. de Arellano-López****

** Ioffe Physicotechnical Institute, Russian Academy of Sciences, Politekhnicheskaya ul. 26, St. Petersburg, 194021 Russia*
e-mail: smir.bi@mail.ioffe.ru
*** Universidad de Sevilla, Sevilla, 41080 Spain*
Received June 21, 2002

Abstract—Temperature dependences of the Young's modulus *E* of wood-derived biomorphic SiC ceramics fabricated through pyrolysis of eucalyptus and oak with subsequent silicon infiltration were studied using electrostatic resonance excitation of longitudinal vibrations. The decrease in *E* with increasing temperature observed to occur in eucalyptus SiC in the temperature interval 20–1000°C was found to be accompanied by several jumps (splittings) in the resonance frequency, which persist after the sample is heated to 1000°C. The oak-SiC ceramic exhibits only one jump, which vanishes after heating to 1000°C. The observed anomalies are assigned to the presence of defects (including pores) in the materials studied. © *2003 MAIK "Nauka/Interperiodica".*

1. INTRODUCTION

Investigation of the physicomechanical properties of present-day composite ceramics is of considerable research and applied interest, because they combine a high strength with a great resistance to high-temperature creep [1–3]. On the other hand, considerable difficulties related to the technological nature involved in the fabrication and mechanical treatment of products are present in these properties. This problem becomes particularly acute if the electrical conductivity of these materials is not high enough to permit the use of the spark-cutting technique.

At the same time, wood-derived biomorphic silicon carbide ceramics, which are presently enjoying increasing interest [4–9], are not plagued by this shortcoming.

The ceramics mentioned above are prepared through fast and controlled mineralization of the chosen wood in two stages; namely, it is first pyrolyzed (carbonized), after which silicon is infiltrated to obtain silicon carbide, with the wood structure preserved. Nature offers a rich variety of various wood structures differing in density and property anisotropy, thus facilitating proper choice of an object.

This approach possesses a number of advantages over other methods of fabrication of SiC ceramics. The advantages are, in particular, a possibility of preparing any desired preform, fast preparation and low density of the material, and a lower processing temperature. The experiments performed thus far on the above-mentioned SiC materials indicate that they have very good mechanical properties at high temperatures [4–9].

This communication reports on a first study of Young's modulus of biomorphic SiC ceramics carried out over a broad temperature range (up to 1000°C). The results obtained are compared with information on the structure of these ceramics.

2. SAMPLES AND EXPERIMENTAL TECHNIQUE

Biomorphic SiC was obtained by vacuum infiltration of molten silicon into porous carbonaceous preforms prepared through the pyrolysis of wood (white Eucalyptus and Spanish Oak) in an argon environment at 1000°C [7]. The final product was a cellular SiC structure extended along the tree growth direction. Following the infiltration, the samples were cut parallel and perpendicular to the growth axis and polished for metallographic measurements. The sample microstructure was studied with a scanning electron microscope (Philips XL30, Microscopy Service, University of Seville, Spain). The sample density ρ was determined by hydrostatic weighing at room temperature.

The initial densities of eucalyptus and oak were 0.84 and 0.88 g/cm^3, which changed after the pyrolysis to 0.67 and 0.78 g/cm^3, respectively. If the carbon of the wood reacted completely with molten silicon and there was no excess of the latter, the expected densities of biomorphic SiC of the above origins would be 2.23 and 2.6 g/cm^3, respectively. The experimentally produced material was found to have $\rho = 2.37$ g/cm^3 for the eucalyptus SiC and 2.28 g/cm^3 for the oak SiC. These figures indicate the presence of excess silicon (≈6 vol %) in the eucalyptus-SiC samples and of unreacted carbon in the Oak SiC. The presence of Si in the former is corroborated by x-ray diffraction data. Density measure-

1063-7834/03/4503-0482$24.00

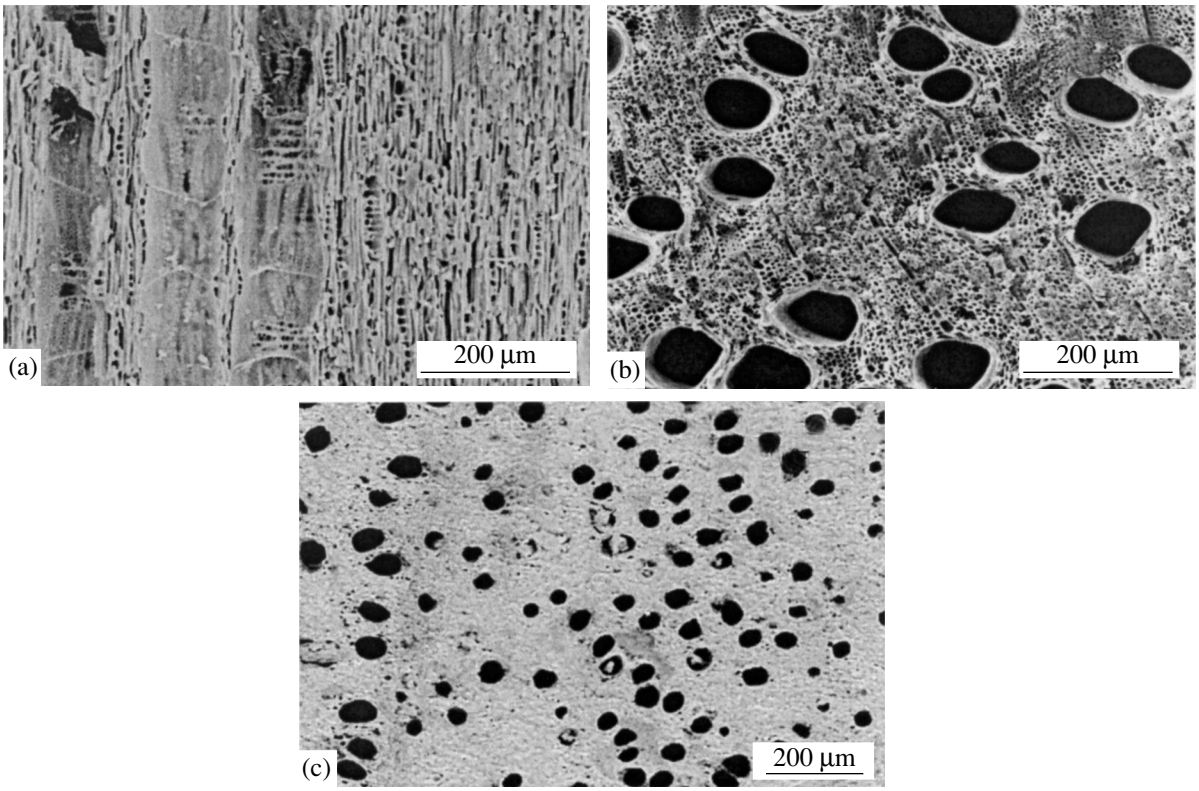

Fig. 1. SEM micrographs of the structure (a, b) of white eucalyptus after pyrolysis and (c) of biomorphic eucalyptus SiC, which were obtained (a) along and (b, c) across the tree growth direction.

ments show both samples to have porosities of about 15–20 vol %.

Figure 1 presents SEM micrographs of the eucalyptus structure after the pyrolysis and of the biomorphic eucalyptus SiC. Figure 1a reveals a clearly pronounced axially extended cellular structure; Figs. 1b and 1c, individual pores measuring up to 100 μm.

Samples prepared for acoustic measurements were rods with a rectangular cross section 10–20 mm^2 and length $l \approx$ 20–40 mm oriented along the tree growth direction. Young's modulus was determined, using electrostatic resonance excitation of longitudinal vibrations in the sample [10, 11], from the formula $E = 4\rho l^2 f^2 n^{-2}$, where f is the resonance vibration frequency and n is the number of the excited harmonic (in our case, $n = 1$). The experiments were performed in the temperature range T = 20–1000°C in a helium-filled chamber. The average heating rate was ~2 deg/min.

3. RESULTS AND DISCUSSION

Figure 2 illustrates two successive measurements of the temperature dependence of the resonance frequency made on a rod sample of the biomorphic eucalyptus-SiC ceramic within the range 20–1000°C and plotted in f^2–T coordinates. The first measurement (Fig. 2a) was performed on an as-fabricated sample; the second

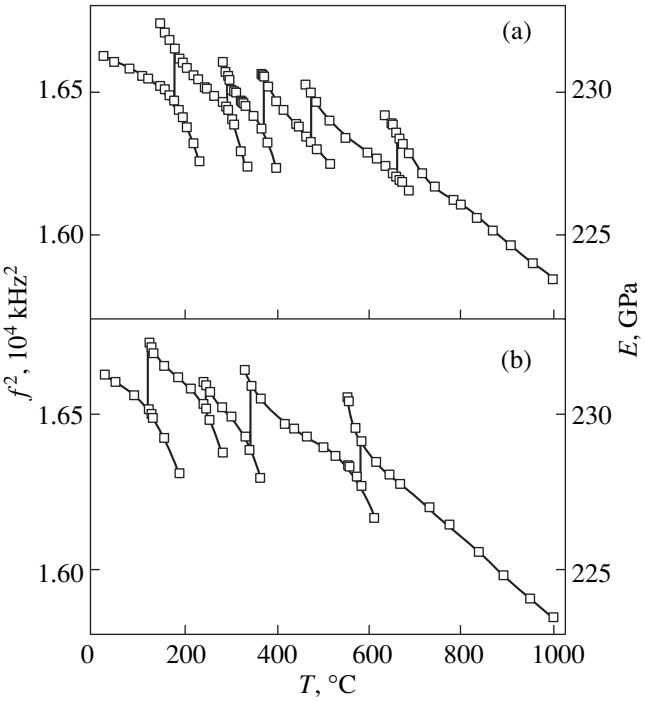

Fig. 2. Temperature dependences of the resonance frequency squared and of the calculated Young modulus of an eucalyptus-SiC sample obtained in two measurements, (a) before and (b) after annealing at 1000°C for two hours.

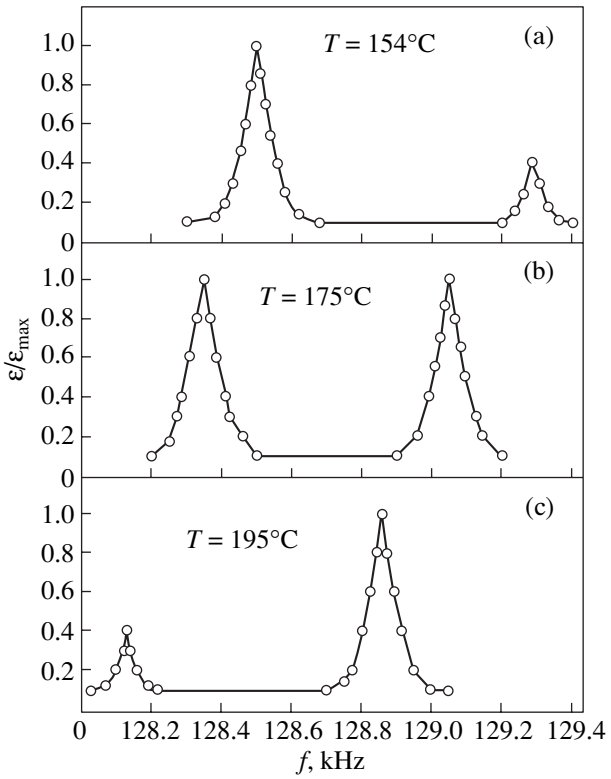

Fig. 3. Variation of the amplitude vs. frequency characteristic of the eucalyptus-SiC sample obtained under heating in the region of the resonance frequency splitting.

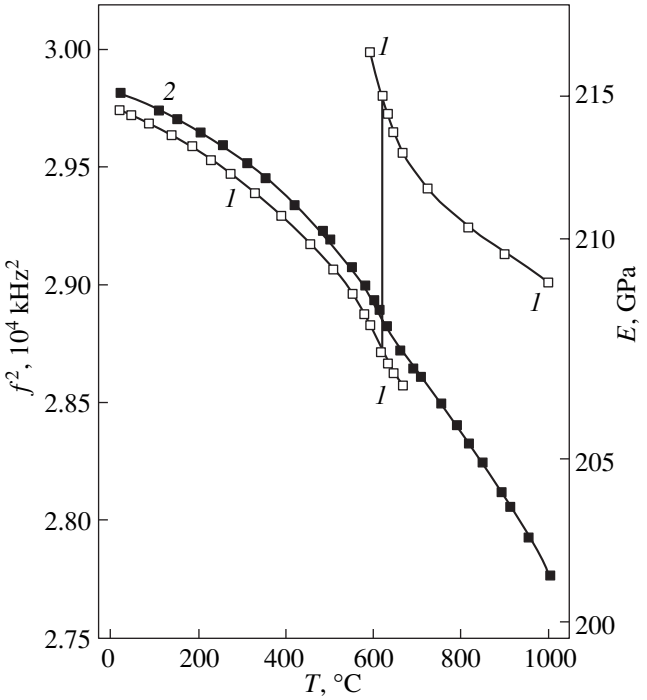

Fig. 4. Temperature dependences of the resonance frequency squared and of the calculated Young modulus of an oak-SiC sample obtained in two measurements, (*1*) before and (*2*) after annealing at 1000°C.

(Fig. 2b), after maintaining the sample at 1000°C for two hours. We readily see that as the temperature is increased, the monotonic decrease in f is accompanied by jumps in the sample resonance frequency, which are specified in the $f^2(T)$ plots by vertical lines.

An essential experimental finding is the resonance frequency splitting, i.e., the presence of two closely spaced resonance frequencies for the same sample in some temperature intervals. The second (extra) frequency f_2 appears at some value of T, and the amplitude ε at this frequency (the resonance line intensity) grows gradually with increasing temperature. At the same time, the sample vibration amplitude at f_1 that was the main resonance frequency at lower temperatures decreases gradually and the maximum in the $\varepsilon(f)$ dependence observed at f_1 disappears completely. The evolution of the amplitude vs. frequency characteristic of the eucalyptus-SiC sample at temperatures from 154 to 195°C is illustrated for one of the jumps in Fig. 3. The temperatures at which the jumps occur (identified in Fig. 2 by vertical lines) correspond to the times at which the intensities of the two resonance lines become equal (Fig. 3b). The resonance frequency splitting at a jump is observed to exist within a temperature interval $\Delta T > 40$°C.

The positions and number of resonance frequency jumps for a rod of a given material were found to be sensitive to the period of time over which the sample was maintained at 1000°C (cf. Figs. 2a, 2b). This suggests that the observed phenomena are associated with the defect structure of the material, which undergoes noticeable changes during the anneal. These effects apparently have a dynamic character and originate from the dynamic (ultrasound) method employed in measuring of the elastic modulus. The values of E plotted on the right-hand vertical axis in Fig. 2 give an idea of the magnitude of Young's modulus at the temperatures where no jumps are observed. The absolute value of the modulus $E \approx 230$ GPa for the eucalyptus SiC at room temperature is lower than the value $E \approx 297$ GPa for the SiC ceramic.

Similar relations were observed to hold for the oak-SiC biomorphic ceramic (Fig. 4). This material differs from the eucalyptus-SiC biomorphic ceramic in that it exhibited only one resonance frequency jump, which transformed, after the annealing at 1000°C, to a barely distinguishable kink at about the same temperature (about 600°C).

The large number of jumps in the resonance frequency observed under sample heating can be assigned to the presence of a spectrum of defects of different nature in a material. The existence of cavities and/or weak bonding between the structural elements making up the sample material may excite additional degrees of

freedom of the vibrating system under specific external conditions (two degrees of freedom should produce two maxima in the amplitude vs. frequency characteristic of a vibrator [12]). In particular, defects of different origin may become activated at different temperatures, which will show up in the measurements.

The splitting of the resonance frequency of a vibrating system was also observed earlier in resonance measurements of the temperature dependences of elastic constants and of the internal friction of various materials [13–15]. For instance, studies of potassium nitrite [13, 14] showed that the resonance frequency splitting temperature for this compound coincides with the temperature of the KNO_2III $\longrightarrow$ KNO_2II phase transition, and it was suggested that this effect is caused by the coexistence of structural forms III and II of this nitrite. Such a manifestation of additional degrees of freedom of a vibrating system was attributed in [15] to specific features in the structure of the materials studied [Y(Er)$Ba_2Cu_4O_{7-\delta}$ HTSC ceramics]. A jump in the resonance frequency was reported in [16] to occur under loading (deformation) of silicon bronze and was assigned to the presence of precipitates of a second phase in the samples studied.

A comparison of the above two materials convincingly showed the eucalyptus-SiC ceramic to be more defective and less stable, because it revealed many more features in the $f(T)$ curves. This may be due to the presence of excess silicon in the material. In addition, the appearance of a splitting of resonance frequency in a SiC ceramic may be associated with specific features in the cellular structure of the original wood, in particular, of its porosity.

4. CONCLUSION

Thus, we have studied the behavior of the elastic characteristics of novel ceramic materials, biomorphic silicon carbide ceramics, by using the dynamic ultrasound method. The defect structure of these materials has been shown to dominate the character of the temperature dependences of the amplitude vs. frequency characteristics obtained. However, it appears impossible at present to identify the structural elements responsible for the individual features in the experimental curves. Such identification would require further work combining acoustic, technological, and structural studies.

ACKNOWLEDGMENTS

This study was supported by the Russian Foundation for Basic Research, project no. 00-01-00482.

REFERENCES

1. J. B. Wachtman, *Mechanical Properties of Ceramics* (Wiley, New York, 1996).
2. D. Kovar, B. H. King, R. W. Trice, and J. W. Halloran, J. Am. Ceram. Soc. **80** (10), 2471 (1997).
3. R. Naslain, Adv. Compos. Mater. **8** (1), 3 (1999).
4. P. Greil, T. Lifka, and A. Kaindl, J. Eur. Ceram. Soc. **18**, 1961 (1998).
5. H. Sieber, C. Hoffmann, A. Kaindl, and P. Greil, Adv. Eng. Mater. **2** (3), 105 (2000).
6. J. Martínez-Fernández, F. Varela-Feria, and M. Singh, Scr. Mater. **43**, 813 (2000).
7. M. Singh, Ceram. Eng. Sci. Proc. **21** (4), 39 (2000).
8. J. Martínez-Fernández, F. Varela-Feria, S. López Pombero, *et al.*, Ceram. Eng. Sci. Proc. **22** (3), 135 (2001).
9. F. M. Varela-Feria, J. Martínez-Fernández, and A. R. de Arellano-López, J. Eur. Ceram. Soc. (2002) (in press).
10. Yu. A. Burenkov, S. P. Nikanorov, and A. V. Stepanov, Izv. Akad. Nauk SSSR, Ser. Fiz. **35**, 525 (1971).
11. B. I. Smirnov, Yu. A. Burenkov, B. K. Kardashev, *et al.*, Fiz. Tverd. Tela (St. Petersburg) **43** (11), 2010 (2001) [Phys. Solid State **43**, 2094 (2001)].
12. F. S. Crawford, Jr., *Waves* (McGraw-Hill, New York, 1968; Nauka, Moscow, 1974).
13. V. N. Belomestnykh, Neorg. Mater. **29** (2), 210 (1993).
14. V. N. Belomestnykh and Yu. I. Paskal', Izv. Vyssh. Uchebn. Zaved., Fiz. **38** (6), 22 (1995).
15. V. A. Melik-Shakhnazarov, N. L. Arabadzhyan, and V. M. Tavkhelidze, Sverkhprovodimost: Fiz., Khim., Tekh. **3** (9), 2054 (1990).
16. K. V. Sapozhnikov, S. B. Kustov, P. Kopanya, and Sh. Piletski, Fiz. Tverd. Tela (St. Petersburg) **35** (1), 83 (1993) [Phys. Solid State **35**, 44 (1993)].

Translated by G. Skrebtsov

Physics of the Solid State, Vol. 45, No. 3, 2003, pp. 486–493. Translated from Fizika Tverdogo Tela, Vol. 45, No. 3, 2003, pp. 460–467.

MAGNETISM AND FERROELECTRICITY

Conductivity in a Disordered Medium and Carrier Localization in Weakly Doped Lanthanum Manganites

N. I. Solin and S. V. Naumov

Institute of Metal Physics, Ural Division, Russian Academy of Sciences, ul. S. Kovalevskoĭ 18, Yekaterinburg, 620219 Russia
e-mail: suhorukov@imp.uran.ru

Received January 9, 2002; in final form, May 14, 2002

Abstract—The dc and 9.2-GHz electrical resistivities and magnetoresistance observed in $La_{1-x}A_xMnO_3$ crystals (A = Sr, Ce, $x \le 0.1$) in the temperature interval 77–300 K are accounted for by the contributions due to carriers, both nonlocalized and localized in the valence-band tail and near the Fermi level. The localized-state tail extends to a depth of 0.15–0.25 eV inside the band gap, and the hopping activation energy varies from 0.06 to 0.15 eV, depending on the sample composition. Within the temperature region where magnetic ordering sets in, the variations of the electrical resistivity and magnetoresistance with temperature and magnetic field are caused by variations in the carrier mobility and concentration. *© 2003 MAIK "Nauka/Interperiodica".*

1. INTRODUCTION

The interest in lanthanum manganites stems from the possibility of achieving high (colossal) values of magnetoresistance (CMR) in these compounds at room temperature, which is an effect essential for applications. The nature of the electrical resistivity and magnetoresistance in these materials remains, however, unclear. Two opinions dominate presently on this point. It was shown in [1] that the double exchange model [2] is not capable of accounting for the experimental data on the semiconductor–metal transition in $La_{1-x}Sr_xMnO_3$ (x = 0.2–0.3), and it was assumed in [1, 3] that the electrical properties can be explained by the polaron mechanism, which is based on a strong electron–phonon coupling originating from the Jahn–Teller splitting in the Mn^{3+} ion.

The other viewpoint postulates that the magnetic and electrical properties of the manganites can be explained in terms of double exchange, assuming the carriers to be localized as a result of spin disorder and of randomly distributed nonmagnetic inhomogeneities [4–6]. Calculations [5] show that in the presence of an appropriate nonmagnetic disorder, spin disorder in the paramagnetic region can give rise to carrier localization at the Fermi level and to the Anderson semiconductor–metal transition near T_C at x = 0.2–0.3.

The dc and microwave electrical resistivity and magnetoresistance measurements carried out in this study showed that the dc and microwave electrical resistivity of lanthanum manganite single crystals doped lightly by Sr^{2+} and Ce^{4+} ($La_{1-x}A_xMnO_3$, A = Sr, Ce; $x \le 0.1$), in which case metal–nonmetal transition does not yet occur, can be explained in terms of the model of conduction in a disordered medium with carriers localized at the valence band edge. Magnetic ordering reduces carrier localization, thus changing both the concentration and mobility of the carriers.

2. SAMPLES AND EXPERIMENTAL TECHNIQUES

Single crystals of $LaMnO_3$ (LMO), $La_{0.93}Ce_{0.07}MnO_3$ (LCe7ar), $La_{0.9}Ce_{0.1}MnO_3$ (LCe10),[1] and $La_{0.93}Sr_{0.07}MnO_3$ (LSr7) were grown by the floating-zone technique with radiative heating in an argon environment [7], and $La_{0.93}Ce_{0.07}MnO_3$ (LCe7air) crystals were grown by the same technique but in air. The $La_{0.9}Sr_{0.1}MnO_3$ (LSr10) single crystals belong to the series of samples used in earlier magnetic, electrical, and other physical studies [8–10]. The samples were single-phase and had orthorhombic crystal structure at room temperature.

The dc electrical resistivity was measured following the standard four-probe method using a voltmeter with an input resistance above 10^9 Ω. The microwave electrical conductivity was studied using a resonance technique [11, 12]. The magnetic-transition temperatures were obtained by measuring the magnetic susceptibility at a frequency of 1 kHz.

3. RESULTS

Figure 1 presents temperature dependences of the electrical resistivities ρ_0 and ρ_{mw} and of the magnetoresistances MR_0 and MR_{mw}, defined as $[\rho(H) - \rho(0)]/\rho(0)$, measured with a dc current and at a frequency of 9.2 GHz, respectively, on an $La_{0.9}Sr_{0.1}MnO_3$ single crystal. The peaks in the magnetic susceptibility

[1] Recent studies show the real cerium content in this single crystal to be 6%.

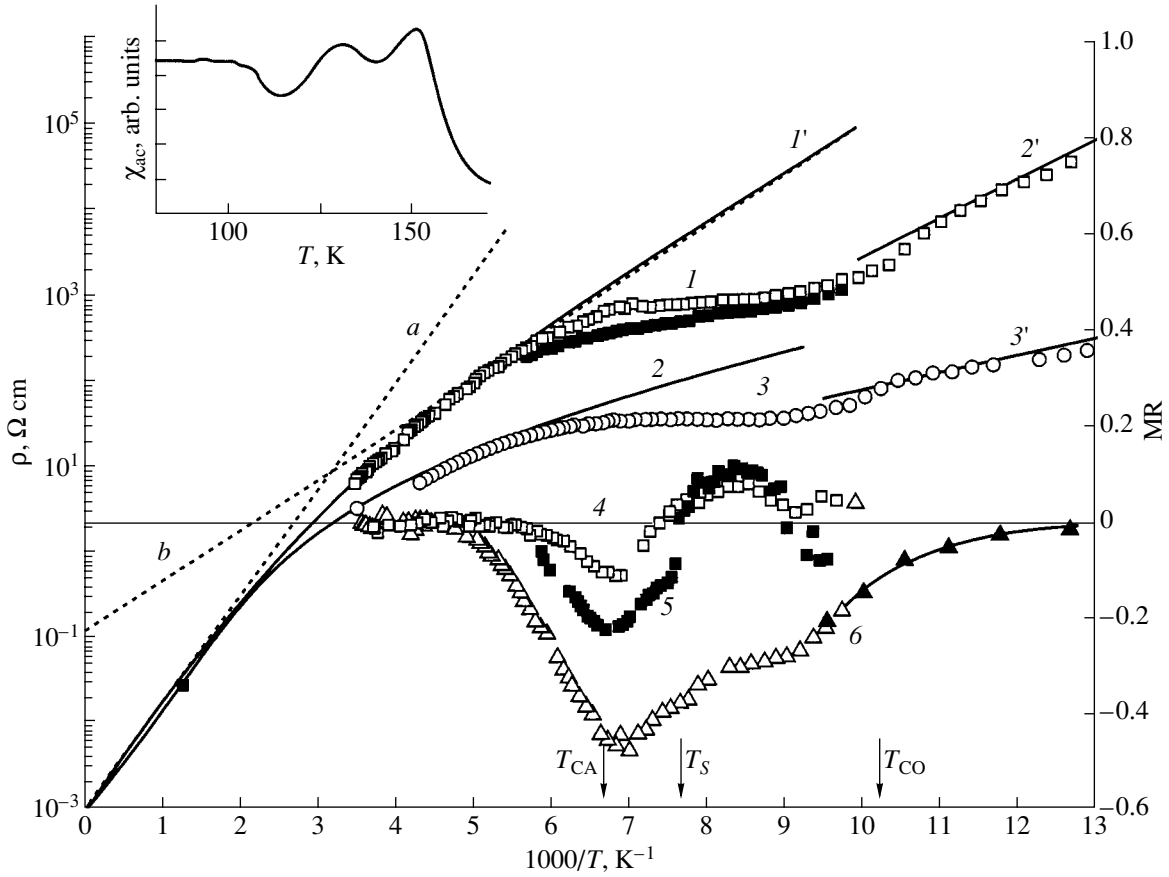

Fig. 1. Temperature dependences of the electrical resistivity (curves *1–3*) and magnetoresistance (curves *4–6*) of $La_{0.9}Sr_{0.1}MnO_3$ obtained in the dc regime (curves *1, 2, 5, 6*) and at 9.2 GHz (curves *3, 4*) in magnetic fields *H* (kOe): (*1, 3*) 0, (*4, 5*) 6.5, and (*6*) 17. Solid curves *1'–3'* are calculated ρ_0 and ρ_{mw}; dashed curves *a* and *b* are contributions from nonlocalized and localized carriers to ρ_0, respectively. The inset shows the temperature dependence of the initial magnetic susceptibility of $La_{0.9}Sr_{0.1}MnO_3$ measured at 1 kHz.

χ_{ac} (inset to Fig. 1) lie at the well-known temperatures of the phase and structural transitions that $La_{0.9}Sr_{0.1}MnO_3$ undergoes within the narrow temperature interval from 150 to 100 K. According to the phase diagrams in [13, 14], a paramagnet-canted-antiferromagnet transition occurs at $T_{CA} \approx 148$ K. According to neutron diffraction data [14], a phase with polaron ordering (charge ordering, CO) of the Mn^{3+} and Mn^{4+} ions sets in below $T_{CO} \approx 100$ K; this process is accompanied by a transition to a ferromagnetic state with a higher magnetization [10, 15]. Around $T \approx 103$ K, the compound undergoes a phase transition from an orthorhombic phase with Jahn–Teller distortions to a pseudocubic phase [9].

We readily see (Fig. 1) that although the dc and ac electrical resistivities differ by more than two orders of magnitude, which indicates their different nature, they follow approximately the same temperature behavior and the value of MR_{mw} is comparatively large, about one half the dc magnetoresistance ($MR_{mw} \approx -0.12$ and $MR_0 \approx -0.2$ in a field of 6.5 kOe). The relations $\rho_0(T)$ and $\rho_{mw}(T)$ (constructed with due account of the data on high-temperature ρ_0 of $La_{0.9}Sr_{0.1}MnO_3$ [13]) exhibit an activated character over some temperature ranges (straight lines in Fig. 1) with features near the phase transition temperatures; the values of ρ_0 and ρ_{mw} grow monotonically with decreasing temperature down to $T \sim 150$ K; then, within the temperature interval $T \cong$ 150–100 K, they only weakly depend on temperature; and, below $T \sim 100$ K, ρ_0 and ρ_{mw} increase again.

Both dc and microwave measurements reveal a peak of negative magnetoresistance near $T_{CA} \approx 148$ K, which is characteristic of manganites. In weak fields, $H <$ 6.5 kOe, MR_0 and MR_{mw} are positive in the region $T \approx$ 130–100 K. The magnitude of the positive MR_0 depends on the magnetic-field orientation with respect to the crystallographic axes. In higher fields, if temporal effects are excluded [16] (the data for *6* in Fig. 1 were obtained in fast magnetic-field sweeps), MR_0 is seen to fall off monotonically with decreasing temperature, so that $MR_0 \approx -0.06$ at 77 K in a magnetic field of 17 kOe. As follows from the shape and intensity of

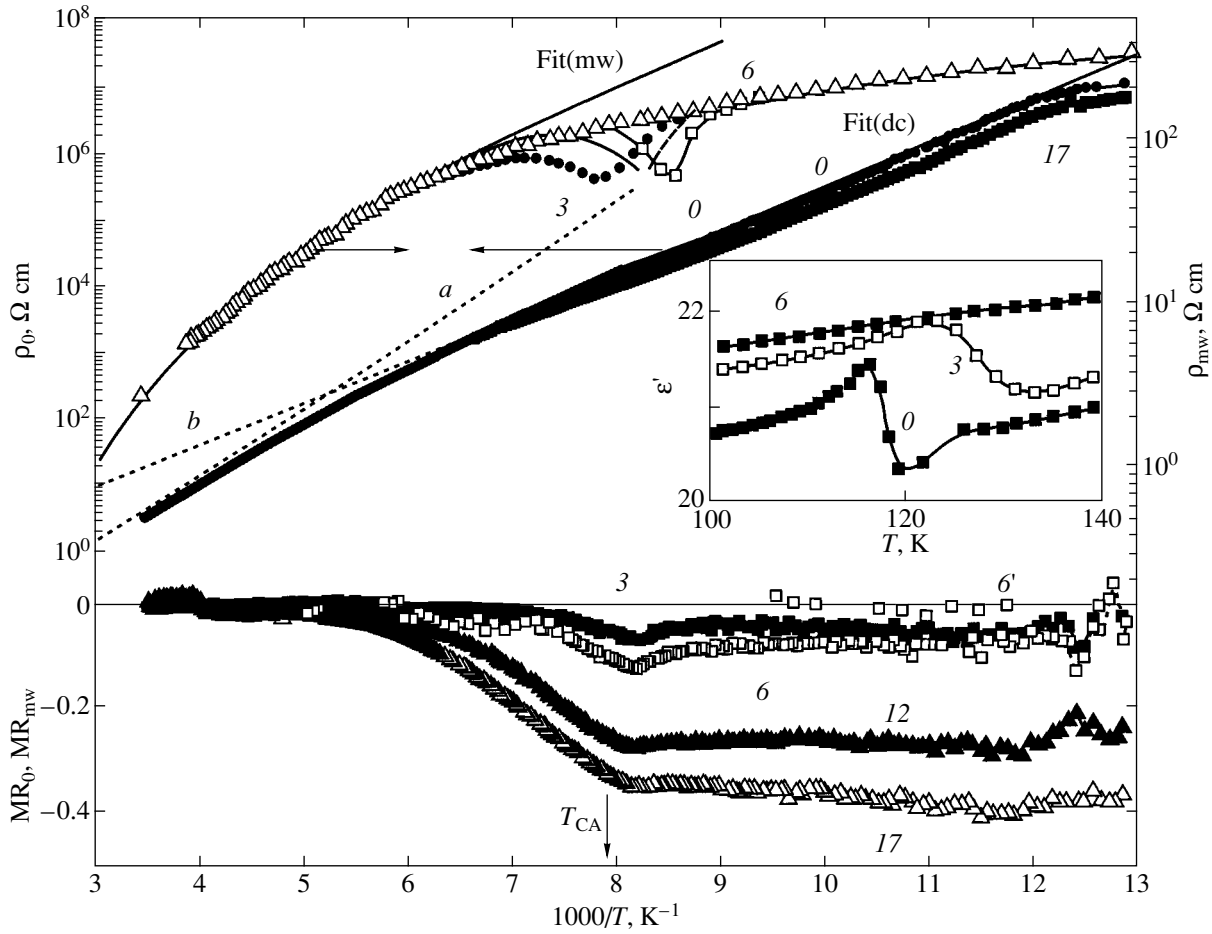

Fig. 2. Temperature dependences of the electrical resistivity and magnetoresistance of a $La_{0.93}Sr_{0.07}MnO_3$ sample obtained in the dc regime and at 9.2 GHz (MR_{mw} is represented by open squares *6*'). Solid curves Fit(dc) and Fit(mw) refer to calculation of ρ_0 and ρ_{mw}; dashed curves *a* and *b* are calculated contributions from nonlocalized and localized carriers to ρ_0, respectively. The inset shows the temperature dependence of the dielectric permittivity ε'. The figures adjoining the curves specify the magnetic field in kOe.

the x-ray diffraction lines of a sample with Sr concentration $x = 0.1$ [9], the pseudocubic and distorted Jahn–Teller phases can obviously coexist in the interval $T \approx$ 125–82 K. Below $T_S \approx 130$ K, phase separation possibly occurs; i.e., charge or orbital ordering sets in part of the crystal. The χ_{ac} anomaly and the positive magnetoresistance near 130 K can be accounted for by an increase in the coercive force or in the anisotropy field induced by such inhomogeneities.

In $La_{0.9}Sr_{0.1}MnO_3$ single crystals, the values of ρ_0, ρ_{mw}, MR_0, and, MR_{mw} and of the microwave magnetic, μ*, and dielectric, ε*, susceptibilities depend on time below $T \approx 97$–100 K. For instance, ρ_0 grows in magnitude at 77 K by several tens of percent with characteristic times $\tau_1 \approx 3 \times 10^3$ s and $\tau_2 \approx 5 \times 10^4$ s.

The temperature dependences of ρ_0 of $La_{0.93}Sr_{0.07}MnO_3$ can be fitted by two exponentials (lines *a* and *b* in Fig. 2). Note the small dip in ρ_0 below T_{CA}. Magnetic-field-dependent peaks in ρ_{mw} and in dielectric permittivity ε' (inset to Fig. 2) were found to exist in a narrow temperature interval $T = 120 \pm 10$ K. The anomalies in ρ_{mw} and ε' practically disappear upon application of a magnetic field of 6 kOe. The values of MR_0 are comparatively large and do not decrease, as is the case in single-crystal manganites, but remain constant instead and even grow with decreasing temperature below $T_{CA} \approx 132$ K. The MR_0 peak near T_{CA} is characteristic of the manganites and is observed only in weak fields. Below T_{CA}, we have $|MR_0| \sim H$, and above T_{CA}, we have $|MR_0| \sim H^2$; this behavior is typical of manganites. Beyond the ρ_{mw} anomaly, above $T \approx 140$ K, the values of MR_{mw} at 6 kOe coincide approximately with those of MR_0 measured with a dc current and below 105 K, with those of $MR_{mw} \approx 0$ (open squares in Fig. 2).

The electrical resistivities ρ_0 of the undoped and cerium-doped lanthanum manganites (Fig. 3) grow rapidly with decreasing temperature and become too high to be measured ($\rho_0 > 10^7$–10^8 Ω cm) already for $T > T_{CA}$. The $\rho_0(1/T)$ relations approach an activated behav-

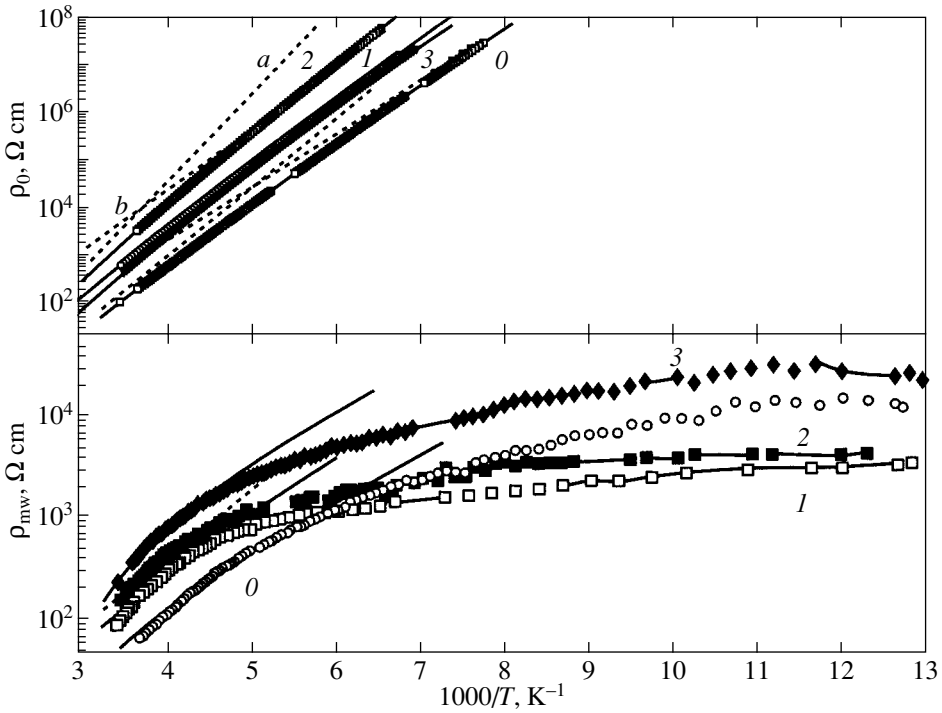

Fig. 3. Temperature dependences of the electrical resistivity measured in the dc regime and at 9.2 GHz for (*0*) $LaMnO_3$, (*1*) $La_{0.93}Ce_{0.07}MnO_3$ (air), (*2*) $La_{0.93}Ce_{0.07}MnO_3$ (argon), and (*3*) $La_{0.9}Ce_{0.1}MnO_3$. Solid curves refer to calculation of ρ_0 and ρ_{mw}; dashed curves *a* and *b* are contributions from nonlocalized and localized carriers to ρ_0, respectively.

ior within a broad range of variation of the electrical resistivity (straight lines *a* and *b* in Fig. 3). In the paramagnetic region, the magnetic field affects ρ_0 only weakly; indeed, at room temperature, the change in ρ_0 is less than 10^{-3} in a field of 17 kOe. In undoped $LaMnO_3$, the best conductor among these samples, a small negative magnetoresistance, $MR_0 \approx -2$ to -3%, was observed in a field of 18 kOe near the magnetic-ordering temperature $T \approx 140$ K.

The magnitude of ρ_{mw} grows exponentially at high temperatures and depends only weakly on temperature in the low-temperature domain (Fig. 3). Measurements of the sign of thermopower suggest that all samples are *p*-type semiconductors at room temperature.

4. DISCUSSION

The temperature behavior of the electrical resistivity of the samples studied (Figs. 1–3) may be due to variation in the activation energy with decreasing temperature in a transition from one conduction mechanism to another, which is characteristic of conductivity in glassy (disordered) semiconductors [17]. As for the low conductivity observed in samples doped with Sr and Ce to up to a level of 10%, it can be assigned to the presence of imperfections in the crystal (spin disorder, random impurity distribution, etc.); as a result, carriers are captured in traps near the Mn^{4+} and Mn^{2+} ions and localized states are formed in the band gap near the valence or conduction band edge. The dc and ac electrical conductivity of such a disordered semiconductor is governed by the following three mechanisms [17].

(1) Transport of nonlocalized carriers. The dc (hole) conductivity can be written as

$$\begin{aligned}\sigma_0 &= \sigma_{\min}\exp[-(E_F - E_V)/kT] \\ &= \sigma_{\min}\exp[-\Delta E_1/kT],\end{aligned} \tag{1}$$

where E_F is the Fermi level; the energy E_V, Mott's mobility edge, separates nonlocalized from localized states; and the minimum metallic conductivity is $\sigma_{\min} \approx 300$–$10^3$ Ω^{-1} cm^{-1}. This mechanism does not provide any contribution in the ac mode of operation below $\approx 10^{15}$ Hz.

(2) Hopping of carriers localized in the valence band tail. For this process, the contributions to the dc and ac conductivities can be presented in the form

$$\begin{aligned}\sigma_0 &= \sigma_2\exp[-(E_F - E_B + W_1)/kT] \\ &= \sigma_2\exp[-\Delta E_2/kT],\end{aligned} \tag{2}$$

$$\begin{aligned}\sigma_\omega &\sim \sigma(\omega)\exp[-(E_F - E_B)/kT] \\ &= \sigma^0_{mw}\exp[-E_{mw}/kT],\end{aligned} \tag{3}$$

Electrical and magnetic parameters of lanthanum manganite single crystals

Crystal	LMO	LMO [18]	LCe7air	LCe7ar	LCe10	LSr7	LSr10
σ_{min}, Ω^{-1} cm^{-1}	800	800	800	900	800	800	1100
$E_F - E_V$, meV	290	327	335	367	326	204	250
σ_2, Ω^{-1} cm^{-1}	12	10	10	10	10	9	9
$E_F - E_B + W_1$, meV	219	216	241	266	239	130	118
$E_F - E_B$, meV	89	95	109	123	93	55	55
σ^0_{mw}, Ω^{-1} cm^{-1}	0.36	0.20	0.5	0.15	0.06	0.8	1.3
W_1, meV	130	121	132	143	146	75	63
$E_B - E_V$, meV	201	228	226	244	233	149	195
T_{CA}, K	142	–	138	138	139	132	148
							127
T_{CO}, K							97

where W_1 is the hopping activation energy, $E_B - E_V$ is the localized-state tail, $\sigma(\omega) \sim \omega^s$, and $s \approx 0.8$–1 for manganites [18].

(3) Hopping of carriers localized near the Fermi level, for which we can write

$$\sigma_0 = \sigma_3 \exp[-W_2/kT], \quad (4)$$

where $\sigma_3 \leq \sigma_2$ and W_2 is the hopping activation energy. In this case, the ac conductivity is proportional to temperature or does not vary with temperature at all.

The solid lines in Figs. 1–3 show the temperature dependences of ρ_0 and ρ_{mw} of our samples calculated from this model. We readily see that the temperature dependence of $\rho_0(T)$ in the paramagnetic temperature region can be satisfactorily described, within a broad range of electrical resistivity variation, by the contributions from nonlocalized and localized carriers (dashed curves *a* and *b*, respectively), which were calculated from Eqs. (1) and (2) with the values of ΔE_1, ΔE_2, σ_{min}, and σ_2 listed in the table. The values of ρ_0 at $T = 800$ K [13] obtained on a sample of a composition similar to $La_{0.9}Sr_{0.1}MnO_3$ (filled squares in Fig. 1) also closely fit the calculated curve.

The measured values of ac electrical conductivity are determined by the dc electrical conductivity and the conductivity due to the alternating character of the current itself. The contribution to the ac electrical conductivity derives from carrier hopping into localized states in the valence band tail and is given by Eq. (3). This contribution and the contribution due to the dc electrical conductivity, which is given by Eqs. (1) and (2), satisfactorily describe the experimental temperature dependence $\rho_{mw}(T)$ for $La_{0.93}Sr_{0.07}MnO_3$ and $La_{0.9}Sr_{0.1}MnO_3$ in the paramagnetic region (solid curves in Figs. 1, 2). The contribution from this mechanism in the undoped and cerium-doped samples prevails apparently only within a narrow interval below room temperature (solid curves in Fig. 3). Because of the large values of $E_{mw} = E_F - E_B$ (see table), the contribution from this mechanism falls off rapidly with decreasing temperature, opening the way for other mechanisms, which are apparently associated with carrier hopping near the Fermi level. The weak dependence of ρ_{mw} on temperature, which is characteristic of this mechanism, is clearly represented in the low-temperature domain in Fig. 3.

Thus, the electrical conductivity of all samples in the paramagnetic region can be described assuming part of the carriers to be localized near the valence band edge. The values of σ_{min} and σ_2 are close to the theoretical figures and to those usually observed in disordered media [17]. As seen from the table, the tail of localized states $E_B - E_V$ extends to a comparatively large depth, 0.15–0.25 eV, into the band gap, depending on composition. The hopping activation energy in undoped and cerium-doped manganite samples differs insignificantly, $W_1 \approx 0.13$–0.15 eV; exhibits a trend to growth with increasing degree of compensation (cerium concentration); and decreases in samples doped with strontium to $W_1 \approx 0.06$ eV. The data on $\rho_0(T)$ and $\rho_{mw}(T)$ quoted for $LaMnO_3$ at 1 GHz [18] satisfactorily fit this model, and we obtained approximately the same parameters for this sample as for the $LaMnO_3$ sample studied by us (see table).

The increase in the resistivity observed under doping with Ce^{4+} may be attributed to the compensation of holes (Mn^{4+} ions), which apparently exist in undoped $LaMnO_3$ due to the presence of lanthanum and oxygen vacancies. Hole compensation is the highest in the LCe7ar single crystal grown in argon. The assumption of hole compensation is corroborated by the increase in the activation energy $E_F - E_V$ and $E_F - E_B$ observed to occur with variation of the cerium concentration.

An analysis of $La_{0.9}Sr_{0.1}MnO_3$ thermopower measurements [19] shows the Seebeck coefficient to follow an activated behavior at high temperatures (up to

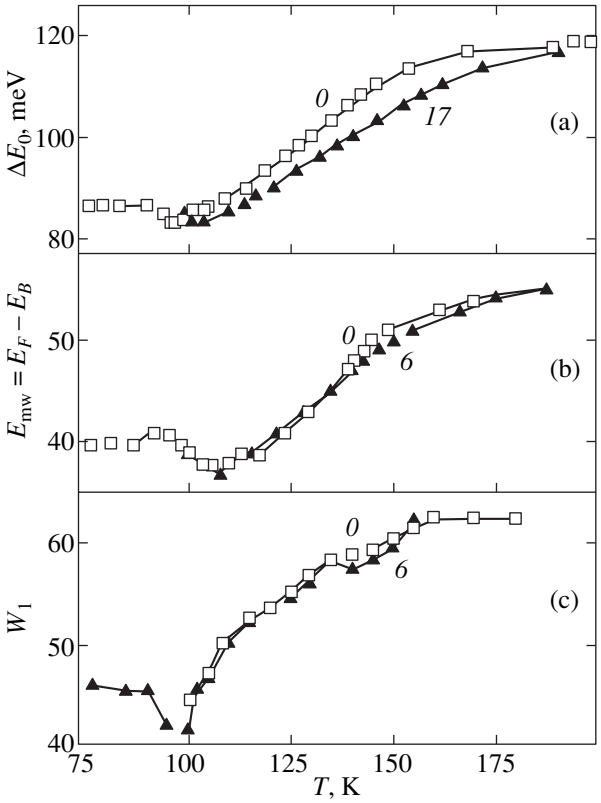

Fig. 4. Temperature dependences (a, b) of the activation energy of electrical resistivity measured (a) in the dc regime and (b) at 9.2 GHz and (c) of the hopping activation energy W_1 of $La_{0.9}Sr_{0.1}MnO_3$. The figures adjoining the curves specify the magnetic field in kOe.

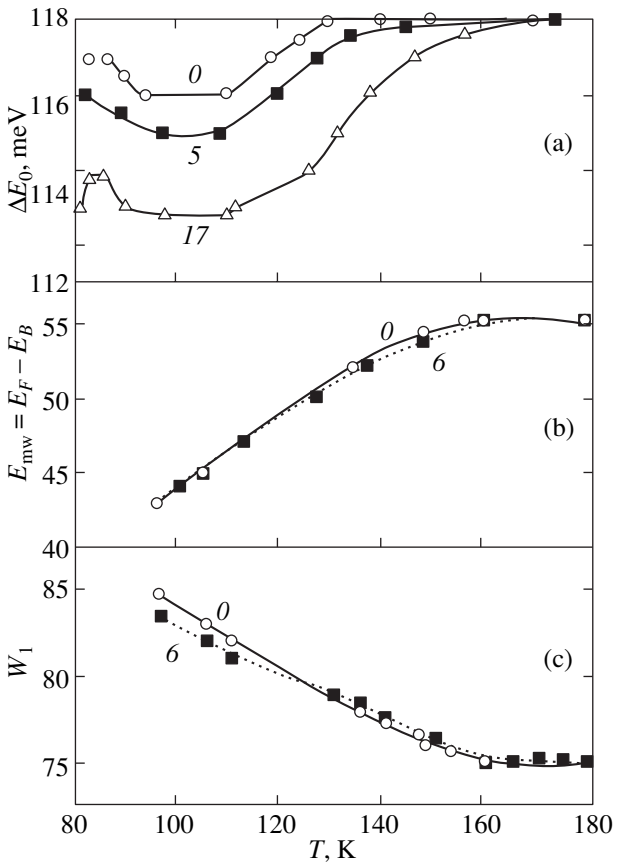

Fig. 5. Same as in Fig. 4, but for $La_{0.93}Sr_{0.07}MnO_3$. The figures adjoining the curves specify the magnetic field in kOe.

~160 K), $S = k/e^*(E_S/kT + A)$ [17], with $E_S = 53 \pm 5$ meV. We believe that the closeness between the results of microwave measurements and dc thermopower studies also argues for the validity of the proposed conduction model.

The narrow temperature interval within which the anomaly in ρ_{mw} of $La_{0.93}Sr_{0.07}MnO_3$ is observed, the strong magnetic field dependence of ρ_{mw}, and the absence of the anomaly in ρ_0 in the dc current (Fig. 2) suggest that the ρ_{mw} anomalies near T_{CA} do not have any bearing on the conductivity in the disordered phase and are apparently due to domains. Such peaks are usually attributed to Debye-type relaxation losses [20] appearing in a medium where an electron can reside in two or several stationary states, separated by a potential barrier E_D, and hop between ions in different valence states, for instance, Mn^{3+} and Mn^{4+}. Maxima in the temperature dependence of $\sigma_\omega(T)$ were observed to exist at low frequencies in $La_{1-x}Sr_xMnO_3$, and the potential barrier for relaxation was estimated as $E_D \approx 86$ and 90 meV for $x = 0$ and 0.05, respectively [17]. Using the data from [17], one comes to the estimate $E_D \approx 50$ meV for $La_{0.93}Sr_{0.07}MnO_3$.

The electrical resistivity of our samples observed on their transfer to the magnetically ordered state can be explained in terms of the same model of conduction in a disordered medium. As seen from Figs. 1 and 2, the contribution from nonlocalized carriers to $\rho_0(T)$ of the $La_{0.9}Sr_{0.1}MnO_3$ and $La_{0.93}Sr_{0.07}MnO_3$ samples (curves *a*) becomes negligible as one approaches the Curie temperature T_C. In this case, the changes in $\rho_{mw}(T)$ and $\rho_0(T)$ induced by magnetic ordering can be described by Eqs. (2) and (3), in which the activation energies ΔE_2 and E_{mw} are changed from their values in the paramagnetic region listed in the table.

Figures 4 and 5 display temperature dependences of ΔE_2, $E_{mw} \equiv E_F - E_B$, and W_1 for the $La_{0.9}Sr_{0.1}MnO_3$ and $La_{0.93}Sr_{0.07}MnO_3$ samples, which were calculated from Eqs. (2) and (3) under this assumption. The calculations for $La_{0.93}Sr_{0.07}MnO_3$ were made outside the temperature region ~105–135 K, with the contribution from relaxation loss neglected.

As seen from Figs. 4 and 5, the changes in resistivity occurring in both samples under magnetic ordering with decreasing temperature originate from the decrease in $E_F - E_B$; i.e., they are due to the Fermi level approaching the edge of the valence band tail, in other

words, due to an increase in carrier concentration. This suggests that magnetic ordering affects carrier localization. If carriers are released from traps, this should give rise to an increase in the number of acceptors involved in conduction and to a lowering of the Fermi level. The value of $E_F - E_B$ varies more strongly in a sample with a higher strontium doping level. The variation of $E_F - E_B$ with temperature in $La_{0.9}Sr_{0.1}MnO_3$ can be fitted by a relation approximately proportional to the magnetization squared, $E_F - E_B \sim M^2$ (the data on magnetization were taken from [10]).

The hopping activation energy W_1 for these samples behaves, however, in a radically different way. As seen from the table and Figs. 4 and 5, the hopping activation energies W_1 for the two samples do not differ markedly. On transition to the magnetically ordered state, the hopping activation energy W_1 decreases in the ferromagnetic $La_{0.9}Sr_{0.1}MnO_3$ and increases in the antiferromagnetic $La_{0.93}Sr_{0.07}MnO_3$, to become nearly twice the value of W_1 in $La_{0.9}Sr_{0.1}MnO_3$. The decrease in W_1 in the ferromagnetic state agrees with the assumption [1] of the electron–phonon coupling playing a role in the nature of CMR in manganites. One may also explain this qualitatively as being due to the energy gain on electron hopping between the Mn^{3+} and Mn^{4+} ions depending on the spin orientation due to competition between the double and indirect exchange in a canted antiferromagnet; indeed, in a canted antiferromagnet, the energy gain decreases compared with that in a ferromagnet with parallel spins [2]; i.e., the activation energy of hopping between Mn^{3+} and Mn^{4+} should increase. The same reasoning applies to the increase in W_1 induced by electron doping with cerium (see table). Compensation of holes (Mn^{4+}) by cerium makes indirect exchange predominant, which may give rise to an increase in W_1.

The slowing down in the growth of the electrical resistivity of $La_{1-x}Sr_xMnO_3$ ($x \approx 0.01$) in the temperature interval 150–100 K and the sharp increase below $T \approx 100$ K (Fig. 1) are sometimes considered as being due to a transition first to the ferromagnetic metallic and afterwards to the ferromagnetic insulating phase under orbital or charge ordering [19, 21, 22]. As seen from Fig. 4, below the temperature of the structural transition, $T_{CO} \approx 100$ K, the activation energies W_1 and $E_F - E_B$ no longer decrease with decreasing temperature and are stabilized at a constant level, as a result of which the weak growth of $\rho_0(T)$ in the interval 150–100 K transfers to an exponential rise below 100 K; this sharp increase is assigned to a transition to the insulating phase. Actually, however, there is no transition to either the metallic or the insulating phase. The features in the behavior of $\rho_0(T)$ near 150–100 K are due to a change in carrier localization in the valence band tails accompanying the magnetic and charge ordering, with the corresponding changes in the activation energies. In the $\log\rho_0(1/T)$ plots, the electrical resistivity is seen to grow at low temperatures even slower than it does at high ones (Fig. 1). According to the double-exchange model, electron transfer between the Mn^{3+} and Mn^{4+} ions in the ferromagnetic phase should proceed easier; this agrees with the sharp, ~10 meV (Fig. 4c), decrease in W_1 in the temperature interval $T = 110$–100 K where the transition to the ferromagnetic phase occurs [10, 15]. However, no further decrease in W_1 is observed, because orbital ordering hinders electron transfer between the Mn^{3+} and Mn^{4+} ions, which now requires the overcoming of an additional potential barrier, thus stabilizing W_1. Orbital ordering accounts for the fact that $La_{0.9}Sr_{0.1}MnO_3$ does not exhibit metallic conductivity at low temperatures in the ferromagnetic phase.

An analysis of the temperature dependences of ρ_0, ρ_{mw}, MR_0, and MR_{mw} made using Eqs. (2) and (3) shows that the electrical resistivity ρ_0 of $La_{0.9}Sr_{0.1}MnO_3$ varies in a magnetic field at $T \approx 150$ K because of an increase in both the mobility and concentration of the carriers (a decrease in W_1 and $E_F - E_B$). The variation of the activation energies W_1 and $E_F - E_B$ with magnetic field ranges from ~0.1 to 0.4 meV/kOe. The origin of the negative magnetoresistance MR_0 of $La_{0.93}Sr_{0.07}MnO_3$ at high temperatures (above $T_{CA} = 132$ K) lies primarily in the decrease in $E_F - E_B$, i.e., in the carrier concentration. Below 110 K, the magnetoresistance of $La_{0.93}Sr_{0.07}MnO_3$ is $MR_{mw}(7\ kOe) \approx 0$. This means that the large value of MR_0 for $La_{0.93}Sr_{0.07}MnO_3$, which persists below T_{CA} (Fig. 2), is due to a decrease in the hopping activation energy W_1, i.e., to an increase in carrier mobility in a magnetic field.

5. CONCLUSION

Thus, we have studied the electrical resistivity and magnetoresistance, both in the dc regime and at a frequency of 9.2 GHz, in single crystals of weakly doped lanthanum manganites $La_{1-x}A_xMnO_3$ (A = Sr, Ce; $x \leq 0.1$) in the temperature interval 77–300 K. The results obtained were discussed in terms of the model of conduction in a disordered medium with carrier localization in the valence band tail and were explained as being due to the contributions from nonlocalized and localized carriers. In the magnetic-ordering region, variations in the electrical resistivity and magnetoresistance with temperature or magnetic field are caused by variation in both the mobility and concentration of the carriers. The results indicate that magnetic ordering entails a change in carrier localization.

ACKNOWLEDGMENTS

The authors are indebted to A.M. Balbashov and Ya.M. Mukovskiĭ for growing the single crystals for the study and to V.S. Gaviko for useful discussions of the x-ray measurements.

This study was supported by the Russian Foundation for Basic Research (project no. 02-02-16429) and the Ministry of Science and Technology (contract no. 40.012.1.1.1153.14/02).

REFERENCES

1. A. J. Millis, P. B. Littlewood, and B. I. Shraiman, Phys. Rev. Lett. **74** (25), 5144 (1995).
2. C. Zener, Phys. Rev. **82**, 403 (1957); P. W. Andersen and H. Hasegawa, Phys. Rev. **100**, 675 (1955); P. G. de Gennes, Phys. Rev. **118**, 141 (1960).
3. H. Röder, J. Zang, and A. R. Bishop, Phys. Rev. Lett. **76** (8), 1356 (1996); A. J. Millis, R. Mueller, and B. I. Shraiman, Phys. Rev. B **54**, 5389 (1996); Phys. Rev. B **54**, 5405 (1996).
4. C. M. Varma, Phys. Rev. B **54** (10), 7328 (1996).
5. L. Sheng, D. Y. Xing, D. N. Sheng, and C. S. Ting, Phys. Rev. Lett. **79**, 1710 (1997).
6. Q. Li, J. Zang, A. R. Bishop, and C. M. Soukoulis, Phys. Rev. B **56**, 4541 (1997).
7. A. M. Balbashov, S. G. Karabashev, Ya. M. Mukovskii, and S. A. Sverkov, J. Cryst. Growth **167**, 365 (1996).
8. V. E. Arkhipov, V. P. Dyakina, Ya. Klyamut, *et al.*, Pis'ma Zh. Éksp. Teor. Fiz. **68**, 39 (1998) [JETP Lett. **68**, 42 (1998)]; V. E. Arkhipov, I. Varkhul'ska, D. Vlosevich, *et al.*, Fiz. Met. Metalloved. **88** (5), 27 (1999).
9. V. E. Arkhipov, V. S. Gaviko, A. V. Korolev, and V. E. Naĭsh, Fiz. Tverd. Tela (St. Petersburg) **41** (6), 1064 (1999) [Phys. Solid State **41**, 969 (1999)].
10. A. V. Korolev, V. Ye. Arkhipov, V. S. Gaviko, *et al.*, J. Magn. Magn. Mater. **213** (1), 63 (2000).
11. L. I. Buravov and I. F. Shchegolev, Prib. Tekh. Éksp., No. 2, 171 (1971).
12. N. I. Solin, S. V. Naumov, and A. A. Samokhvalov, Fiz. Tverd. Tela (St. Petersburg) **42** (5), 899 (2000) [Phys. Solid State **42**, 925 (2000)]; A. B. Davydov, N. I. Solin, and G. L. Shtrapenin, Defektoskopiya, No. 8, 95 (1982); N. I. Solin, A. B. Davydov, and G. L. Shtrapenin, Defektoskopiya, No. 2, 77 (1991).
13. A. A. Mukhin, V. Yu. Ivanov, V. D. Travkin, *et al.*, Pis'ma Zh. Éksp. Teor. Fiz. **68** (4), 331 (1998) [JETP Lett. **68**, 356 (1998)].
14. Y. Yamada, O. Hino, S. Nohdo, and R. Kanao, Phys. Rev. Lett. **77** (5), 904 (1996).
15. K. Ghosh, R. L. Greene, S. E. Lofland, *et al.*, Phys. Rev. B **58** (13), 8206 (1998).
16. N. I. Solin and I. V. Kochev, in *Abstracts of 2nd Joint International Conference on Magnetoelectrics* (Yekaterinburg, 2000), p. 97.
17. N. F. Mott and E. A. Davis, *Electronic Processes in Non-Crystalline Materials* (Clarendon, Oxford, 1979; Mir, Moscow, 1982).
18. A. Seeger, P. Lunkenheimer, J. Hemberger, *et al.*, J. Phys.: Condens. Matter **11**, 3273 (1999).
19. N. N. Loshkareva, Yu. P. Sukhorukov, and É. A. Neĭfel'd, Zh. Éksp. Teor. Fiz. **117** (1), 440 (2000) [JETP **90**, 389 (2000)].
20. H. Frolich, *Theory of Dielectrics: Dielectric Constant and Dielectric Loss*, 2nd ed. (Clarendon, Oxford, 1986; Inostrannaya Literatura, Moscow, 1960).

Translated by G. Skrebtsov

Physics of the Solid State, Vol. 45, No. 3, 2003, pp. 494–498. Translated from Fizika Tverdogo Tela, Vol. 45, No. 3, 2003, pp. 468–471.

MAGNETISM AND FERROELECTRICITY

Hall Effect in $La_{1-x}Sr_xMnO_3$ Crystals

V. V. Mashkautsan*, R. I. Zaĭnullina*, N. G. Bebenin*, V. V. Ustinov*, and Ya. M. Mukovskiĭ**

** Institute of Metal Physics, Ural Division, Russian Academy of Sciences, ul. S. Kovalevskoĭ 18, Yekaterinburg, 620219 Russia*
e-mail: vlad_mashk@imp.uran.ru
*** Moscow Institute of Steel and Alloys, Leninskiĭ pr. 4, Moscow, 117936 Russia*
Received May 27, 2002

Abstract—A study of the temperature dependences of the ordinary and anomalous Hall coefficients and of the Hall mobility of carriers in single crystals of the ferromagnetic manganites $La_{1-x}Sr_xMnO_3$ ($x = 0.15, 0.20, 0.25$) was carried out in the temperature interval from 85 to 400 K. The nature of the carriers and the conduction mechanisms in these compounds are discussed. © *2003 MAIK "Nauka/Interperiodica".*

1. INTRODUCTION

The present broad interest in the lanthanum manganites is due to the colossal magnetoresistance (CMR) they exhibit. Despite intense experimental studies of the properties of manganites, the mechanism underlying the CMR in these compounds is still not clearly understood. One of the methods that makes it possible to establish the nature of the carriers and of the conduction mechanisms is based on studying the Hall effect. However, studies conducted thus far (see, e.g., [1–10]) have not provided unambiguous conclusions concerning the CMR mechanism, which can be attributed partly to inadequate treatment of the experimental data obtained in those studies.

The Hall effect has been studied mostly in thin films; only one publication [6] reports on investigating a series of bulk single crystals $La_{1-x}Sr_xMnO_3$ with various values of x. However, the temperature region in which the maximum magnetoresistance is observed to exist was not covered in that paper and insulating compositions with $x < 0.17$ were not studied (the concentration-driven metal–insulator transition in the $La_{1-x}Sr_xMnO_3$ system occurs at a critical concentration $x_c \approx 0.17$).

The present communication reports on an investigation of the Hall effect in $La_{1-x}Sr_xMnO_3$ single crystals performed in the concentration region x including x_c and within a temperature interval including the Curie temperature T_C; in other words, we studied the compositions and temperatures where the CMR effect reaches the highest level. The data obtained are used to establish the mechanisms responsible for conduction in the above manganites.

2. SAMPLES AND EXPERIMENTAL TECHNIQUE

$La_{1-x}Sr_xMnO_3$ single crystals ($x = 0.15, 0.20, 0.25$) were grown following the floating-zone technique [11]. The electrical resistivity ρ was measured using the standard four-probe method. The Hall resistivity ρ_{Hall} was determined in the temperature region from 85 to 400 K in magnetic fields of up to 14.5 kOe. The Hall voltage was measured following the potentiometric technique. To exclude spurious effects, the Hall voltage measurements were conducted for two directions of the magnetic field and of the current through the sample. The samples subjected to the ρ and ρ_{Hall} measurements were plate-shaped and had the dimensions $10 \times 3.5 \times 1$ mm. Indium contacts were deposited ultrasonically on the samples. The magnetization curves were obtained with a vibrating-sample magnetometer on smaller plates of the same shape in a magnetic field directed perpendicular to the plate plane. The Curie temperature derived using the method of thermodynamic coefficients is 232, 308, and 340 K for $x = 0.15$, 0.20, and 0.25, respectively.

The Hall resistivity ρ_{Hall} in ferromagnets is given by [12]

$$\rho_{Hall} = R_0 B + R_S M, \quad (1)$$

where R_0 and R_S are the ordinary and anomalous Hall coefficients, respectively; B is the magnetic induction; and M is the magnetization. In thin plates, B differs very little from the external magnetic field strength H. In the ferromagnetic phase, in the region of the paramagnetic-magnetization process, we have

$$M = M_S + \chi H, \quad (2)$$

where M_S is the spontaneous magnetization and χ is the susceptibility of the paramagnetic process. Thus,

$$\rho_{Hall} \cong (R_0 + \chi R_S) H + R_S M_S. \quad (3)$$

To find the coefficients R_0 and R_S, one has to perform magnetic measurements. However, for $T \ll T_C$, because of the small values of χ, the coefficient R_0 is much large than χR_S and can be derived in the region of the para-

magnetic process from the slope of the linear part of the $\rho_{Hall}(H)$ curve without carrying out magnetic measurements. This is how coefficient R_0 was determined in most studies. In materials exhibiting CMR, however, of most interest is the region near T_C where the paramagnetic process is essential and the field dependence of the magnetization is no longer linear. In this case, for determination of coefficients R_0 and R_S, Eq. (1) can be conveniently recast in the form

$$\rho_{Hall}/H = R_0 + R_S(M/H). \quad (4)$$

On constructing the ρ_{Hall}/H dependence on M/H, one can derive the coefficient R_S from the slope of the curve and the coefficient R_0 from the intercept on the ordinate axis [13–17].

In the paramagnetic phase, where $M = \chi H$, Eq. (1) assumes the form $\rho_{Hall} = R_{eff}H$, where $R_{eff} = R_0 + \chi R_S$ is the effective Hall coefficient. In this temperature region, the ordinary and anomalous Hall coefficients can no longer be separated using the above method. However, if the coefficients R_0 and R_S depend only weakly (compared with χ) on temperature, they can be found by plotting R_{eff} as a function of χ. This approach was used in studies on certain ferromagnetic alloys [18, 19].

3. RESULTS OF MEASUREMENTS

Figure 1 plots temperature dependences of the electrical resistivity $\rho(T)$. These curves are similar to the graphs presented in [20]. The $La_{0.85}Sr_{0.15}MnO_3$ single crystal differs from $La_{0.80}Sr_{0.20}MnO_3$ and $La_{0.75}Sr_{0.25}MnO_3$ in that its resistivity is higher by an order of magnitude and follows a semiconductor behavior at low temperatures, whereas $La_{0.80}Sr_{0.20}MnO_3$ and $La_{0.75}Sr_{0.25}MnO_3$ exhibit a metallic-type behavior with $d\rho/dT > 0$ for $T < T_C$.

The $\rho_{Hall}(H)$ relations behave similarly for all the single crystals studied. Figure 2 illustrates the field dependences of the Hall resistivity ρ_{Hall} measured in the $La_{0.85}Sr_{0.15}MnO_3$ single crystal. Within the temperature interval investigated, we have $\rho_{Hall} < 0$. In the ferromagnetic region, ρ_{Hall} is observed to vary linearly with H for $H \geq 7$ kOe.

Figures 3 and 4 display temperature dependences of the coefficients R_0 and R_S derived from the $\rho_{Hall}(H)$ and $M(H)$ relations for the single crystals studied. Measurements of the Hall voltage on the $La_{0.85}Sr_{0.15}MnO_3$ single crystal were complicated by the high electrical resistivity, which resulted in a noticeable scatter (compared with the other samples) in the values of R_0 and R_S. For the same reason, we could not, unfortunately, measure the Hall voltage in $La_{0.85}Sr_{0.15}MnO_3$ in the paramagnetic region. For $T < T_C$, the $R_0(T)$ dependences obtained for $La_{0.85}Sr_{0.15}MnO_3$ and the other two single crystals differ substantially from one another. In

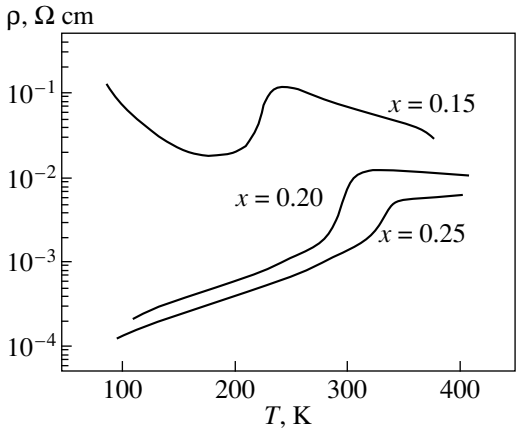

Fig. 1. Temperature dependence of the electrical resistivity ρ in $La_{1-x}Sr_xMnO_3$ single crystals.

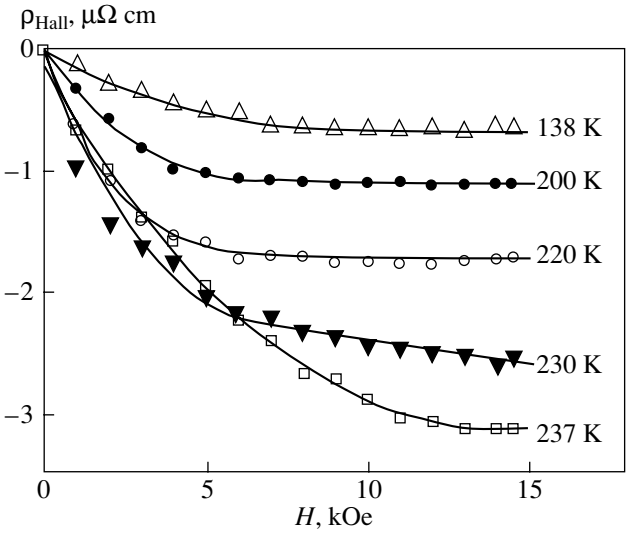

Fig. 2. Field dependences of the Hall resistivity ρ_{Hall} in the $La_{0.85}Sr_{0.15}MnO_3$ single crystal.

$La_{0.80}Sr_{0.20}MnO_3$ and $La_{0.75}Sr_{0.25}MnO_3$, the coefficient R_0 is positive and depends only weakly on temperature, while in the $La_{0.85}Sr_{0.15}MnO_3$ single crystal at $T <$ 150 K, the ordinary Hall coefficient is negative, despite doping being of the hole type, and is strongly temperature-dependent. As one approaches the Curie point, R_0 increases rapidly in all samples and reaches a maximum near T_C.

The anomalous Hall coefficient (Fig. 4) is negative in the single crystals studied. For $T \ll T_C$, the coefficient R_S is weakly temperature dependent. As one approaches T_C, the $R_S(T)$ dependence becomes strong. In the vicinity of the Curie point, the coefficient R_S in $La_{0.85}Sr_{0.15}MnO_3$ and $La_{0.75}Sr_{0.25}MnO_3$ reaches a mini-

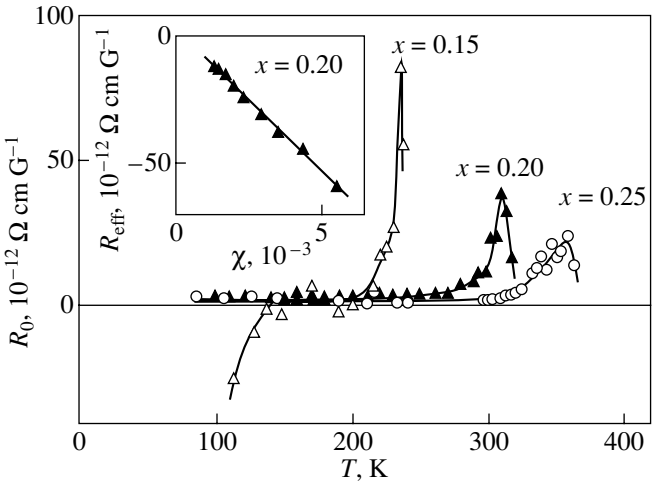

Fig. 3. Temperature dependence of the ordinary Hall coefficient R_0 in $La_{1-x}Sr_xMnO_3$ single crystals. Inset shows the dependence of the effective Hall coefficient R_{eff} in $La_{0.80}Sr_{0.20}MnO_3$ on the susceptibility χ of the paraelectric process.

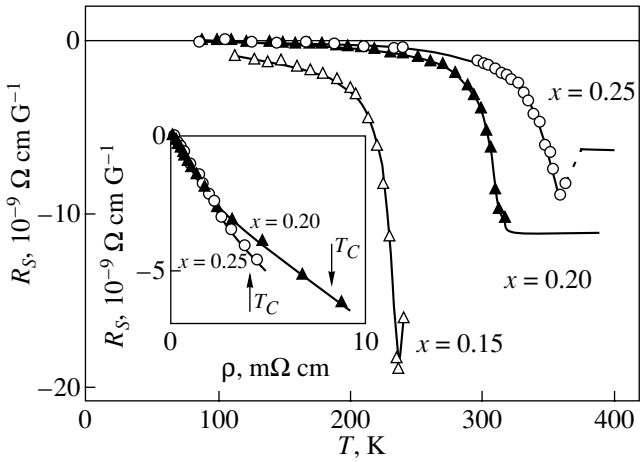

Fig. 4. Temperature dependence of the anomalous Hall coefficient R_S in $La_{1-x}Sr_xMnO_3$ single crystals. Horizontal segments approximate the coefficient R_S estimated from the R_{eff} vs. χ dependence. Inset shows the dependence of the coefficient R_S on resistivity ρ of $La_{0.80}Sr_{0.20}MnO_3$ and $La_{0.75}Sr_{0.25}MnO_3$.

mum. $La_{0.80}Sr_{0.20}MnO_3$ does not exhibit an extremum in the $R_S(T)$ dependence.

We plotted R_{eff} as a function of χ to find R_0 and R_S in the paramagnetic region. As seen from the inset to Fig. 3, the coefficient R_{eff} for the $La_{0.80}Sr_{0.20}MnO_3$ single crystal depends linearly on χ in the interval $320 < T < 390$ K. The $La_{0.75}Sr_{0.25}MnO_3$ single crystal behaves similarly in the temperature interval $375 < T < 400$ K. Thus, we succeeded in estimating the coefficients R_0 and R_S in the $La_{0.80}Sr_{0.20}MnO_3$ and $La_{0.75}Sr_{0.25}MnO_3$ single crystals in the paramagnetic temperature range. The results obtained for R_S are shown by horizontal line segments in Fig. 4. Unfortunately, the ordinary Hall coefficient is determined with too large an error in this method; therefore, we do not present these results here.

4. DISCUSSION OF RESULTS

Lanthanum manganites exhibit strong magnetic and nonmagnetic disorder [21]. The transport properties of materials of this type are determined by the relative position of the mobility edge E_C and the Fermi level E_F [22]. If the Fermi level E_F lies in the region of delocalized states, the crystal is a metal. In these conditions, the Hall mobility μ_{Hall} should decrease with increasing temperature. The coefficient R_0 should be constant and positive in the case of hole doping. As transfer occurs from the ferromagnetic to paramagnetic state, the mobility edge shifts, because of increasing magnetic disorder, from the top of the band to its center and can cross the Fermi level at a certain temperature. If E_F lies in the region of localized states, then the crystal is an insulator and conduction can occur in two ways: (i) through thermally activated hopping of carriers with energies near E_F, in which case the coefficient R_0 should be negative irrespective of the carrier sign [22], and (ii) through carrier excitation to the mobility edge, in which case, in manganites, the coefficient R_0 should be positive in the temperature region dominated by carrier activation to the mobility edge because the Aharonov–Bohm loop includes four manganese ions [17]. The Hall mobility μ_{Hall} should be of the order of 0.1 cm^2/(V s) in this case [22].

Let us turn now to our experimental results. Figure 5 displays the temperature dependence of Hall mobility $\mu_{Hall} = R_0/\rho$. The $\mu_{Hall}(T)$ relations obtained for the $La_{0.80}Sr_{0.20}MnO_3$ and $La_{0.75}Sr_{0.25}MnO_3$ single crystals

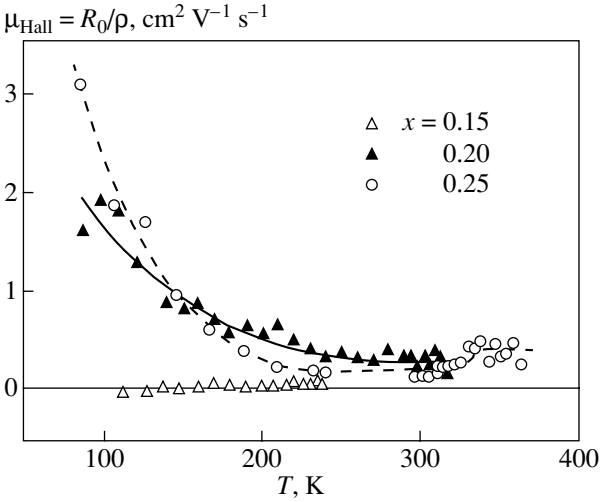

Fig. 5. Temperature dependence of the Hall mobility μ_{Hall} in $La_{1-x}Sr_xMnO_3$ single crystals.

behave similarly; namely, for $T < 200$ K, with increasing temperature, μ_{Hall} decreases from a few units to ≈ 0.2–0.3 cm^2/(V s), to become practically temperature-independent thereafter. In $La_{0.85}Sr_{0.15}MnO_3$, at low temperatures, we have $\mu_{Hall} < 0$; with increasing temperature, the Hall mobility becomes positive and reaches a value slightly smaller than 0.1 cm^2/(V s) near T_C.

The decrease in the Hall mobility with increasing temperature (Fig. 5) and the positive and weakly temperature-dependent coefficient R_0 (Fig. 3) suggest that the majority carriers in the $La_{0.80}Sr_{0.20}MnO_3$ and $La_{0.75}Sr_{0.25}MnO_3$ single crystals for $T < 200$ K are holes in the metallic state and that the resistivity grows because of the decrease in the mobility of the carriers. Calculation of the hole concentration using the expression $R_0 = (ecn_h)^{-1}$ shows that n_h noticeably exceeds the value expected from the doping level. This may indicate the existence of a substantial electron contribution to R_0 [7, 8, 15, 23]. This conjecture is also corroborated indirectly by band structure calculations [24].

The negative sign of the coefficient R_0 in $La_{0.85}Sr_{0.15}MnO_3$ and the fast decrease in the resistivity at $T < 150$ K indicate that, for low temperatures, conduction occurs in this single crystal primarily through hopping between localized states. In the vicinity of T_C, however, the main mechanism responsible for conduction in $La_{0.85}Sr_{0.15}MnO_3$ is hole activation to the mobility edge, because μ_{Hall} is positive and close to 0.1–0.3 cm^2/(V s) in order of magnitude.

For $T > 200$ K, in $La_{0.80}Sr_{0.20}MnO_3$ and $La_{0.75}Sr_{0.25}MnO_3$, $\mu_{Hall} \approx 0.2$ cm^2/(V s) (Fig. 5) and the coefficient R_0 is positive (Fig. 3). Hence, for these temperatures, the variation of both the resistivity and the coefficient R_0 in single crystals with $x = 0.20$ and 0.25, as in $La_{0.85}Sr_{0.15}MnO_3$, is due to the variation of carrier concentration in delocalized states.

The inset to Fig. 4 shows the dependences of R_S on resistivity ρ constructed for $La_{0.80}Sr_{0.20}MnO_3$ and $La_{0.75}Sr_{0.25}MnO_3$. Each curve consists of two linear segments, the boundary between them corresponding to the onset of a fast rise in resistance, R_0 and $|R_S|$. The points to the left of the break relate primarily to the metallic state; therefore, the proportionality of R_S to the resistivity apparently indicates that the contribution of "skew" scattering to R_S is dominant.

In the vicinity of T_C, a linear dependence of R_S on ρ is observed both in crystals with $x = 0.20$ and 0.25 and in $La_{0.85}Sr_{0.15}MnO_3$. The temperature dependence of R_S in this region is most likely dominated by the variation in the concentration of mobile carriers. A similar behavior of R_S was observed by us earlier in single-crystal $La_{0.80}Ba_{0.20}MnO_3$ [17] and polycrystalline $La_{0.60}(Eu,Gd)_{0.07}Sr_{0.33}MnO_3$ [23].

5. CONCLUSIONS

Thus, an analysis of Hall effect data suggests that conduction in $La_{0.85}Sr_{0.15}MnO_3$ at low temperatures occurs primarily through carrier hopping between localized states and near T_C, through hole activation to the mobility edge.

For $T < 200$ K, the majority carriers in $La_{0.80}Sr_{0.20}MnO_3$ and $La_{0.75}Sr_{0.25}MnO_3$ are holes in the metallic state and the rise in the resistivity is due to their decreased mobility. For $T > 200$ K, the temperature dependence of the electrical resistivity should be assigned, as in $La_{0.85}Sr_{0.15}MnO_3$, to the variation of carrier concentration in delocalized states.

In the vicinity of T_C, the temperature behavior of the ordinary and anomalous Hall coefficients is determined, in all the single crystals studied, by the variation of the mobile carrier concentration.

ACKNOWLEDGMENTS

This study was supported by the Russian Foundation for Basic Research (project nos. 00-02-17544, 00-15-96745) and by the RAS-sponsored Young Scientists Contest (project no. 70).

REFERENCES

1. J. Nunez-Requeiro, D. Gupta, and A. Kadin, J. Appl. Phys. **79** (8), 5179 (1996).
2. P. Wagner, D. Mazilu, L. Trappeniers, *et al.*, Phys. Rev. B **55** (22), R14721 (1997).
3. P. Wagner, I. Gordon, A. Vantomme, *et al.*, Europhys. Lett. **41** (1), 49 (1998).
4. G. Jakob, F. Martin, W. Westerburg, and H. Adrian, Phys. Rev. B **57** (17), 10252 (1998).
5. P. Matl, N. P. Ong, Y. F. Yan, *et al.*, Phys. Rev. B **57** (17), 10248 (1998).
6. A. Asamitsu and Y. Tokura, Phys. Rev. B **58** (1), 47 (1998).
7. S. H. Chun, M. B. Salamon, and P. D. Han, Phys. Rev. B **59** (17), 11155 (1999).
8. S. H. Chun, M. B. Salamon, and P. D. Han, J. Appl. Phys. **85** (8), 5573 (1999).
9. M. Jaime, H. Hardner, M. B. Salamon, *et al.*, Phys. Rev. Lett. **78** (5), 951 (1997).
10. S. H. Chun, M. B. Salamon, Y. Tomioka, and Y. Tokura, Phys. Rev. B **61** (14), R9225 (2000).
11. D. Shulyatev, S. Karabashev, A. Arsenov, and Ya. Mukovskii, J. Cryst. Growth **198/199**, 511 (1999).
12. S. V. Vonsovskiĭ, *Magnetism* (Nauka, Moscow, 1971; Wiley, New York, 1974), Vols. 1 and 2.
13. N. G. Bebenin, R. I. Zaĭnullina, V. V. Mashkautsan, *et al.*, Zh. Éksp. Teor. Fiz. **113** (3), 981 (1998) [JETP **86**, 534 (1998)].
14. R. I. Zaĭnullina, N. G. Bebenin, V. V. Mashkautsan, *et al.*, Fiz. Tverd. Tela (St. Petersburg) **40** (11), 2085 (1998) [Phys. Solid State **40**, 1889 (1998)].

15. N. G. Bebenin, R. I. Zainullina, V. V. Mashkautsan, *et al.*, Phys. Status Solidi A **175**, 659 (1999).
16. R. I. Zaĭnullina, N. G. Bebenin, V. V. Mashkautsan, *et al.*, Fiz. Tverd. Tela (St. Petersburg) **42** (2), 284 (2000) [Phys. Solid State **42**, 292 (2000)].
17. N. G. Bebenin, R. I. Zaĭnullina, V. V. Mashkautsan, *et al.*, Zh. Éksp. Teor. Fiz. **117** (6), 1181 (2000) [JETP **90**, 1027 (2000)].
18. I. K. Kikoin, Zh. Éksp. Teor. Fiz. **10** (11), 1242 (1940).
19. N. P. Grazhdankina, L. A. Matyushenko, and Yu. S. Bersenev, Fiz. Tverd. Tela (Leningrad) **10** (3), 670 (1968) [Sov. Phys. Solid State **10**, 527 (1968)].
20. A. Urushibara, Y. Moritomo, T. Arima, *et al.*, Phys. Rev. B **51** (20), 14103 (1995).
21. N. G. Bebenin and V. V. Ustinov, J. Phys.: Condens. Matter **10**, 6301 (1998).
22. N. F. Mott and E. A. Davis, *Electronic Processes in Non-Crystalline Materials* (Clarendon, Oxford, 1979; Mir, Moscow, 1982).
23. N. G. Bebenin, R. I. Zaĭnullina, V. V. Mashkautsan, *et al.*, Fiz. Tverd. Tela (St. Petersburg) **43** (3), 482 (2001) [Phys. Solid State **43**, 501 (2001)].
24. D. A. Papaconstantopoulos and W. E. Pickett, Phys. Rev. B **57** (20), 12751 (1998).

Translated by G. Skrebtsov

Physics of the Solid State, Vol. 45, No. 3, 2003, pp. 499–502. Translated from Fizika Tverdogo Tela, Vol. 45, No. 3, 2003, pp. 472–475.

MAGNETISM AND FERROELECTRICITY

Magnetic Properties of the Quasi-Two-Dimensional Crystal $(CH_3NH_3)_2CuBr_4$

N. V. Fedoseeva*†, N. V. Volkov*, and G. S. Patrin**

** Kirensky Institute of Physics, Siberian Division, Russian Academy of Sciences, Akademgorodok, Krasnoyarsk, 660036 Russia*

*** Krasnoyarsk State University, pr. Svobodnyĭ 79, Krasnoyarsk, 660041 Russia*

e-mail: pat@iph.krasnoyarsk.su

Received May 29, 2002

Abstract—The magnetic properties of $(CH_3NH_3)_2CuBr_4$ quasi-two-dimensional crystals were studied experimentally. The magnetic-field and temperature dependences of magnetization were measured for various magnetic field orientations relative to the crystallographic axes. Possible reasons for features in the behavior of the magnetization are discussed. © *2003 MAIK "Nauka/Interperiodica".*

1. INTRODUCTION

Crystals of the family $(C_nH_{2n+1}NH_3)_2BX_4$ (where $n = 1, 2, \ldots$; B is a transition metal; and X stands for a halogen) exhibit a rich variety of physical properties [1]. Ions of the transition metal B in the crystal structure are located in the octahedra formed by ions of halogen X and lie in the planes bridged by the $(C_nH_{2n+1}NH_3)_2$ groups. These crystals have a layered structure and exhibit quasi-two-dimensional magnetic properties. By properly varying the ion-B and halogen-X species or the length of the bridge between the planes (by varying n), one can purposefully control the type of magnetic order, the anisotropic properties, and magnetic-ordering temperature of the crystal. We shall restrict our consideration to the $n = 1$ case (the methyl ammonium group $(CH_3NH_3) \equiv$ MA). The crystals whose magnetic properties have been best studied are MA_2BCl_4, where B is either Mn or Cu. The MA_2MnCl_4 crystals are easy-axis antiferromagnets with $T_N = 45$ K. Their magnetic properties are described satisfactorily in terms of the isotropic quasi-two-dimensional Heisenberg interaction [2]. Replacement of Mn by Cu results in the MA_2CuCl_4 crystals being easy-plane ferromagnets with $T_c = 9$ K.

Substituting bromine for chlorine substantially changes the exchange interaction in crystals of this family, with the type of magnetic order and the ordering temperature changing accordingly. This communication reports on a study of the magnetic properties and the interactions responsible for the experimentally observed features in the MA_2CuBr_4 crystals.

† Deceased.

2. EXPERIMENTAL TECHNIQUE

MA_2CuBr_4 crystals were grown from a solution. The composition was verified using x-ray diffraction. The crystals have orthorhombic symmetry and space group *Pabc*. The unit-cell parameters at room temperature are $a = 7.814$ Å, $b = 7.639$ Å, and $c = 19.167$ Å. The unit cell contains four formula units and, hence, four magnetic ions. Quasi-static magnetic measurements were carried out with a self-compensating superconducting-coil magnetometer [3]. The measurements were performed within the temperature range $T = 4.2$–300 K, with the temperature maintained to within ±0.1 K.

3. EXPERIMENTAL RESULTS

MA_2CuBr_4 is a poorly studied member of the $MA_2Cu(Cl,Br)_4$ family; relevant information on this member in the literature is very scarce. Data on the magnetic susceptibility $\chi(H)$ measured in fields $H \leq 8$ kOe and on the specific heat C_v studied in the interval $T = 4$–20 K were first published in [4]. It was found that this crystal is antiferromagnetic with $T_N \approx 15.8$ K and that the antiferromagnetism vector is aligned with the **c** axis. The $\chi(H)$ relation measured in the **H** ∥ **c** geometry exhibits an anomaly at $H = 5.2$ kOe, which is assigned to a spin-flop transition.

A Br NMR study is described in [5]. The main result achieved in [5] reduces to a refinement of the data on the magnetic structure below T_N. The NMR data are interpreted and are found to agree satisfactorily with quasi-static data [4] when considered in terms of the four-sublattice antiferromagnet model, provided one assumes the sublattice magnetic moments to lie in the (**c**, **b**) plane and to be canted from the **c** axis at an angle $\beta = \pi m \pm 27°$ ($m = 0.1$).

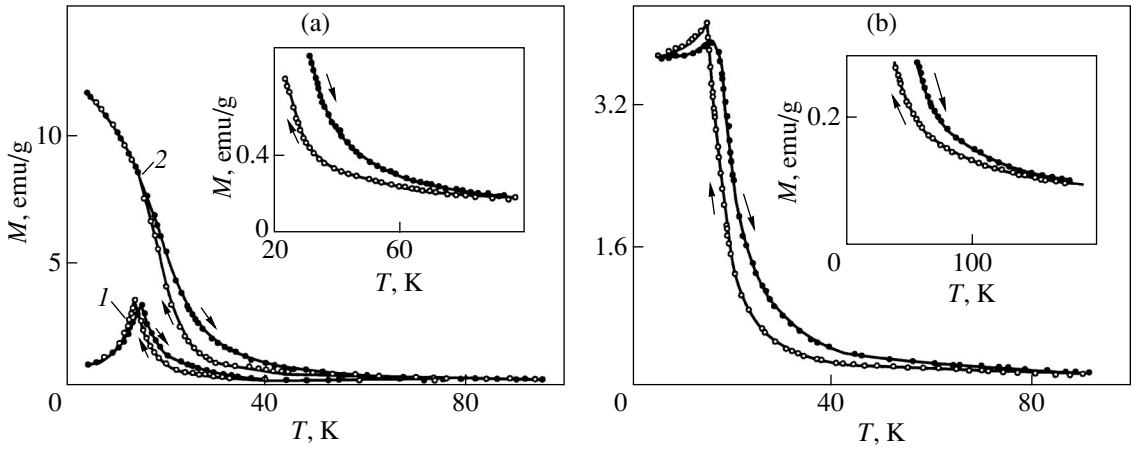

Fig. 1. Temperature dependences of magnetization of the $(CH_3NH_3)_2CuBr_4$ crystal. (a) **H** ∥ **c**, magnetic field is equal to: (*1*) H_1 = 2.16 kOe and (*2*) H_2 = 11 kOe; (b) **H** ⊥ **c**, magnetic field is H_1 = 3.76 kOe. The insets show high-temperature parts of these relations measured in the field H_1. Arrows specify the direction of temperature variation.

We performed a comprehensive investigation of the magnetization of MA_2CuBr_4 crystals in magnetic fields $H \leq 60$ kOe. The main experimental results obtained can be summarized as follows.

3.1. Magnetically Ordered State

Figure 1 presents temperature dependences of the magnetization $M(T, H)$ measured in the geometries **H** ∥ **c** (Fig. 1a) and **H** ⊥ **c** (Fig. 1b). In the first case, the measurements were performed both below and above the saturation field, while in the second, the experiment was performed below the saturation field. One readily sees a nonzero magnetic moment to exist at low temperatures in fields considerably lower than the spin-flop field. The curves obtained in a field $H \cong 11$ kOe are typical of a ferromagnet (curve *2* in Fig. 1a). The temperature behavior of $M(T)$ exhibits a hysteresis for both magnetic-field directions. In the **H** ∥ **c** case, hysteresis starts near $T \cong 100$ K (inset to Fig. 1a), while in the **H** ⊥ **c** geometry, it becomes evident in the region of $T \cong 150$ K (inset to Fig. 1b). The temperatures of the maxima in magnetization, which are identified with the temperatures T_N of phase transitions to the antiferromagnetic state, are also different for the heating and cooling runs. For instance, for **H** ∥ **c** and H = 3.76 kOe, the maximum in $M(T)$ obtained in a cooling run lies approximately 1.8 K lower than that measured in a heating run. As the field H increases, the temperature corresponding to the maximum in $M(T)$ decreases for both magnetic field directions, irrespective of the direction of temperature variation. Note also a strong dependence of the magnetization tails on magnetic field.

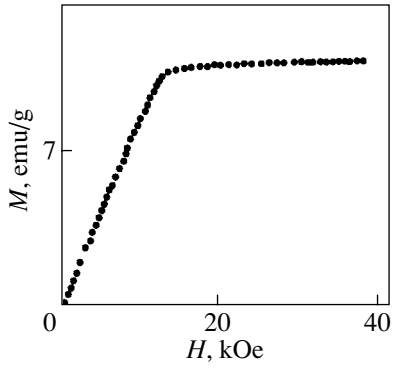

Fig. 2. Field dependence of magnetization measured in the **H** ⊥ **c** geometry. T = 4.2 K.

Figure 2 shows a field dependence of magnetization obtained in the **H** ⊥ **c** geometry at T = 4.2 K. Its pattern is typical of a Heisenberg uniaxial antiferromagnet placed in a magnetic field perpendicular to the principal axis and does not change with temperature for $T < T_N$ [6]. Only the saturation magnetization depends on temperature. The field dependence of magnetization in the **H** ∥ **c** geometry has a more complicated pattern (Fig. 3). Curve *1*, measured at T = 4.2 K, illustrates the main relevant features. The magnetization passes through an inflection point at $H_{c1} \cong 5$ kOe associated with a spin-flop transition, then the slope of the magnetization curve changes in the field H_c, the sublattices collapse at H_{c2}, and saturation sets in. In contrast to a uniaxial two-sublattice antiferromagnet, one clearly observes the fields H_{c1} and H_c to be separated. Note that the break at the field H_c practically disappears at $T \geq 10$ K. As seen from Fig. 3, the values of all critical fields plotted vs. temperature fall on straight lines to within experimental error.

3.2. Paramagnetic Region

Figure 4 gives an idea of the behavior of magnetization in the paramagnetic region. It appears unusual that

the $M(H)$ curve deviates widely from a linear course in such weak fields and that this deviation is seen to persist up to high temperatures despite the fact that $T_N \approx 15$ K. In addition to the temperature hysteresis, one clearly sees the existence of a field hysteresis up to $T \cong 30$ K. As follows from the high-temperature asymptotic behavior of the experimental data treated in terms of standard molecular-field theory under the assumption of Heisenberg interaction, the magnetization obeys the Curie–Weiss law at temperatures $T \geq 200$ K, with $\Theta_c^{\parallel} = -80$ K and $\Theta_c^{\perp} = -190$ K. In this approach, the relation between Θ_c and the exchange parameters is given by $\Theta_c^{\alpha} = 2\mu^{\alpha}\sum_m Z_m J_m/[3k_B(g^{\alpha}\mu_B)^2]$ [7], where α stands for "$\parallel$" or "$\perp$" (the rest is a matter of traditional notation). Therefore, the first explanation that comes to mind is that the magnetic moment per copper ion and/or the exchange constants are anisotropic; this conclusion does not agree with the Heisenberg interaction between the copper ions (electron configuration d^9, $S = 1/2$).

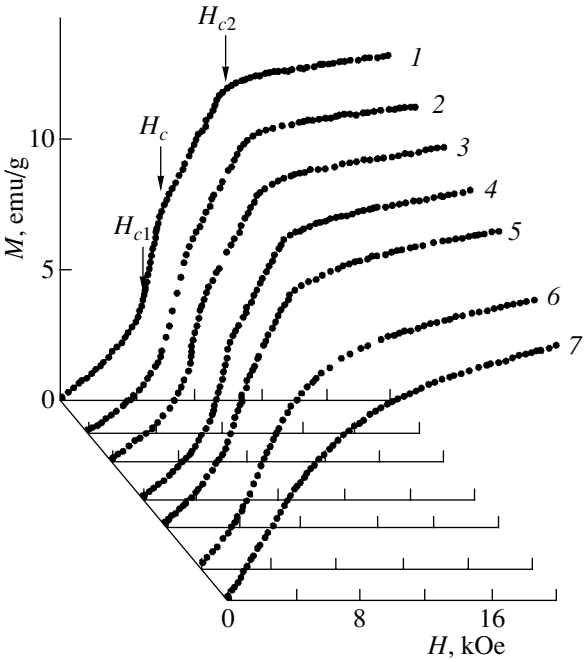

Fig. 3. Field dependences of magnetization measured in the **H** || **c** geometry. T (K): (*1*) 4.2, (*2*) 6, (*3*) 8, (*4*) 10.5, (*5*) 12.5, (*6*) 15, and (*7*) 17.

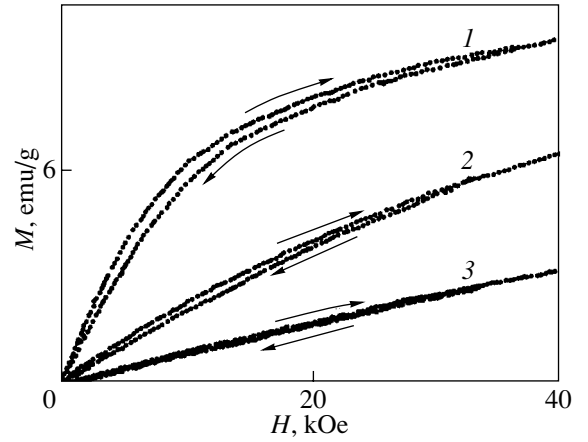

Fig. 4. Field dependences of magnetization in the paramagnetic region measured in the **H** || **c** geometry. T (K): (*1*) 18, (*2*) 25, and (*3*) 39.

4. DISCUSSION

The most interesting results of our study that require interpretation are the high paramagnetic temperatures $|\Theta_c|$ observed at a low transition temperature to long-range order and the reasons for the formation of a crossed magnetic structure in the magnetically ordered region. Clearly, these observations should find explanation within a common approach. We assume, as a working hypothesis, that the Jahn–Teller character of copper ion interaction and the quasi-two-dimensional structure of the crystal play a major role here.

At low temperatures, an MA_2CuBr_4 crystal resides in the monoclinic phase with a very small distortion angle, so that one may assume, as a zero approximation, that the crystal is orthorhombic. The layers containing the magnetic copper ions in the octahedral environment of the halogens have perovskite structure in these crystals, with the layers being bound by weak van der Waals forces [8]. In these conditions, the copper ions in a layer are coupled through indirect exchange interaction, which should be considered with due account of its Jahn–Teller character [9]. Each layer exhibits ferromagnetic orbital ordering (with the local quantization axis canted away from the principal axis at an angle β) and antiferromagnetic spin ordering. It is the magnitude of the spin exchange interaction that determines the value of T_N. Although no long-range order can appear in the two-dimensional case [10], the situation becomes different in the presence of any long-range interaction. It may be conjectured that ions located in different layers are coupled by an interaction which results in antiferromagnetic orbital ordering mediated by the phonon field, so that the quantization axes in the adjoining layers are canted at angles $\pm\beta$. It is known [9] that this interaction can be strongly anisotropic and, as a consequence, can give rise to the effective exchange parameter becoming dependent on both the temperature and magnetic field. Thus, under certain conditions, a crossed antiferromagnetic spin configuration may form.

A more detailed theoretical description of magnetic ordering in MA_2CuX_4 crystals will be given in a later publication.

ACKNOWLEDGMENTS

The authors are indebted to A.P. Perepelitsa for providing the single crystals and to A.D. Balaev for the high-temperature measurements of the magnetic susceptibility.

This study was supported by the federal program "Universities of Russia: Basic research."

REFERENCES

1. K. S. Aleksandrov, N. V. Fedoseeva, and I. P. Spevakova, *Magnetic Phase Transitions in Halide Crystals* (Nauka, Novosibirsk, 1983).
2. N. V. Fedoseeva, V. K. Korolev, A. F. Bovina, and A. P. Perepelitsa, in *Physical Properties of Magnets* (Inst. Fiz. Sib. Otd. Akad. Nauk SSSR, Krasnoyarsk, 1990), p. 61.
3. A. D. Balaev, Yu. V. Boyarshinov, M. M. Karpenko, and B. P. Khrustalev, Prib. Tekh. Éksp., No. 3, 167 (1985).
4. Y. Kimishima, J. Phys. Soc. Jpn. **49**, 62 (1980).
5. Y. Suzuki, K. Tsuru, Y. Kimishima, and H. Kubo, J. Phys. Soc. Jpn. **50**, 1479 (1981).
6. E. A. Turov, A. V. Kolchanov, V. V. Men'shinin, I. F. Mirzoev, and V. V. Nikolaev, *Symmetry and Physical Properties of Antiferromagnets* (Fizmatlit, Moscow, 2001).
7. J. S. Smart, *Effective Field Theories of Magnetism* (Saunders, London, 1966; Mir, Moscow, 1968).
8. K. S. Aleksandrov and B. V. Beznosikov, *Perovskite-like Crystals* (Nauka, Novosibirsk, 1997).
9. K. I. Kugel' and D. I. Khomskiĭ, Usp. Fiz. Nauk **136**, 621 (1982) [Sov. Phys.–Usp. **25**, 231 (1982)].
10. M. E. Lines, J. Phys. Chem. Solids **31**, 101 (1970).

Translated by G. Skrebtsov

Physics of the Solid State, Vol. 45, No. 3, 2003, pp. 503–507. Translated from Fizika Tverdogo Tela, Vol. 45, No. 3, 2003, pp. 476–479.

MAGNETISM AND FERROELECTRICITY

Effect of the Magnetic Field in the Plane of a Garnet Ferrite Film with Orthorhombic Magnetic Anisotropy on the Dynamics of Domain Walls

V. V. Randoshkin*, V. A. Polezhaev*, N. N. Sysoev*, Yu. N. Sazhin, and V. N. Dudorov****

** Moscow State University, Vorob'evy gory, Moscow, 119899 Russia*

*** Joint Laboratory of Magneto-Optoelectronics, Institute of General Physics, Russian Academy of Sciences, Mordovian State University, Bol'shevistkaya ul. 68, Saransk, 430000 Russia*

Received February 7, 2002; in final form, June 19, 2002

Abstract—The effect of an in-plane magnetic field on the dependence of the domain-wall velocity on the acting magnetic field is investigated for bismuth-containing garnet ferrite single-crystal films of the composition $(Bi,Y,Pr)_3(Fe,Ga)_5O_{12}$ with the (210) orientation. The in-plane magnetic field is applied along the ⟨120⟩ and ⟨001⟩ crystallographic axes. The domain-wall velocity is measured in directions perpendicular and parallel to the in-plane magnetic field. © *2003 MAIK "Nauka/Interperiodica".*

1. INTRODUCTION

In bismuth-containing garnet ferrite single-crystal films of the composition $(Bi,Y,Pr)_3(Fe,Ga)_5O_{12}$ with the (210) orientation and orthorhombic magnetic anisotropy, the domain-wall velocity V exceeds 1 km/s [1–6]. It is found that the dependences of V on the acting magnetic field H in films of close chemical compositions differ substantially [2–4]. For bismuth-containing garnet ferrite single-crystal films with unidirectional anisotropy of the domain-wall velocity, the shape of the dynamic domains and the domain-wall velocity V depend strongly on the in-plane magnetic field H_{in}.

For a number of bismuth-containing garnet ferrite single-crystal films of the composition $(Bi,Y,Pr)_3(Fe,Ga)_5O_{12}$ with the (210) orientation, the dependence of the domain-wall velocity on the acting magnetic field exhibits, at first glance, classical behavior: after the initial linear portion, the $V(H)$ curve shows a small peak followed by a saturation portion in which the differential mobility of domain walls is considerably less than their initial mobility [1–5]. However, high-speed photographic (HSP) observations of dynamic domains in magnetic fields at approximately the midpoint of the linear portion in the $V(H)$ curve have revealed that dynamic domain walls undergo irregular distortions which are not reproducible from pulse to pulse [5, 6]. This implies that the linear portion of the $V(H)$ curve corresponds to nonstationary motion of domain walls, which is contradictory to the theory proposed in [7]. More detailed investigations [8] have demonstrated that, for bismuth-containing garnet ferrite single-crystal films with orthorhombic magnetic anisotropy, the crossover to the second linear portion with an increased differential mobility is due to the appearance of spatial distortions of domain walls. It was inferred that the second linear portion can be associated with the radiation of spin waves initiating local rotations of the magnetization vector in the vicinity of the moving domain wall [9].

The purpose of the present work was to investigate the effect of an in-plane magnetic field on the dynamics of domain walls in bismuth-containing garnet ferrite single-crystal films of the composition $(Bi,Y,Pr)_3(Fe,Ga)_5O_{12}$ with the (210) orientation, which are characterized by the classical curve $V(H)$.

2. EXPERIMENTAL TECHNIQUE

The experiments were performed on a universal setup [10] providing high-speed photographic observations with the use of the magnetization reversal technique [11]. The magnitude of orthorhombic magnetic anisotropy was judged from the maximum (H_{max}) and minimum (H_{min}) in-plane magnetic fields at which the domain structure disappeared [9].

In order to investigate the dynamics of domain walls, the initial bismuth-containing garnet ferrite single-crystal film was magnetized to saturation with the magnetic bias field H_b = 43 Oe applied along the normal to the film surface. The pulsed magnetic field H_p was applied in the opposite direction with the use of a pair of pancake coils. The film to be studied was sandwiched between the pancake coils. We recorded the image of the reversed domain that nucleated at a point defect. It should be noted that we failed to obtain reversed domains for some combinations of magnetic fields.

1063-7834/03/4503-0503$24.00 © 2003 MAIK "Nauka/Interperiodica"

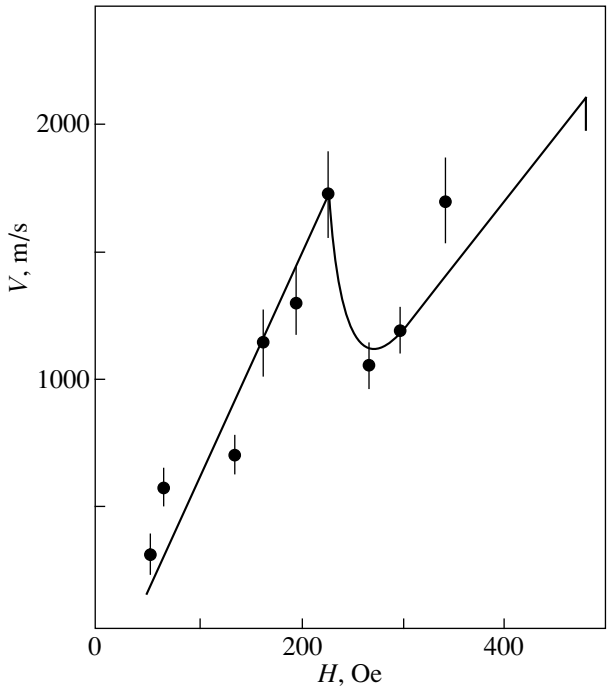

Fig. 1. Dependence of the domain-wall velocity V on the acting magnetic field H in the absence of an in-plane magnetic field.

The data reported in this paper refer to the sample with the thickness $h = 7.3$ μm, the equilibrium width of strip domains $\omega = 16.3$ μm, the collapse field of bubble domains $H_0 = 20.0$ Oe, the minimum magnetic field $H_{min} = 2000$ Oe, and the maximum magnetic field $H_{max} = 4800$ Oe.

The acting magnetic field was determined using a method described in [11],

$$H = H_p - H_b,$$

i.e., without regard for the tilt of the easy magnetization axis. As a result, the first portion of the $V(H)$ curve, in some cases, intersects the abscissa axis at negative H values. The in-plane magnetic field was applied along the ⟨120⟩ and ⟨001⟩ directions in the film plane. Note that the former direction corresponds to the minimum in-plane magnetic field at which the domain structure disappears, whereas the latter direction is associated with a maximum magnetic field. We measured the velocity of domain walls moving in directions perpendicular and parallel to the in-plane magnetic field.

3. RESULTS AND DISCUSSION

The results of measurements are presented in Figs. 1–6 and in the table. The measurements were carried out at three fixed values of the in-plane magnetic field H_{in}. The geometry of the experiment (the mutual orientation of the ⟨120⟩ crystallographic direction, the in-plane magnetic field vector, and the domain-wall velocity vector) is shown at the top of Figs. 2–6. The domain-wall velocity V for each field H was determined by averaging the results of five measurements. The spread of the results obtained in the measurements is shown by vertical segments. For clarity, these segments are connected by solid lines. Note that the spread in the experimental data is caused by distortions of dynamic domains [5], which are not reproducible from pulse to pulse, rather than by a low accuracy of measurements, which can reach 3% [11]. For a sufficiently extended initial linear portion in the $V(H)$ curve, we determined

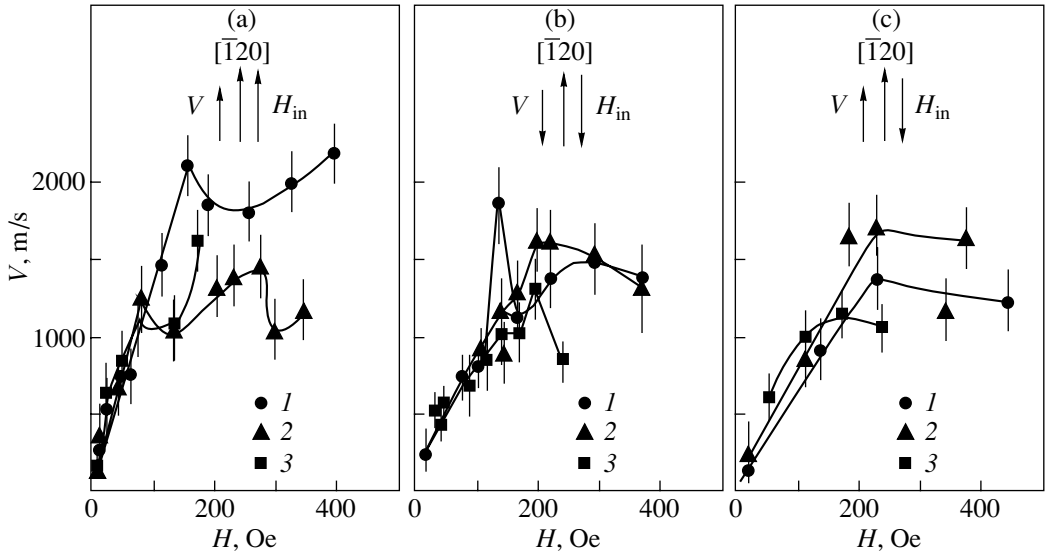

Fig. 2. Dependences of the velocity V of domain walls moving along the in-plane magnetic field H_{in} applied parallel to the ⟨120⟩ crystallographic axis on the acting magnetic field H. H_{in}, Oe: (*1*) 134, (*2*) 268, and (*3*) 402. The geometry of the experiment is shown at the top of all the figures.

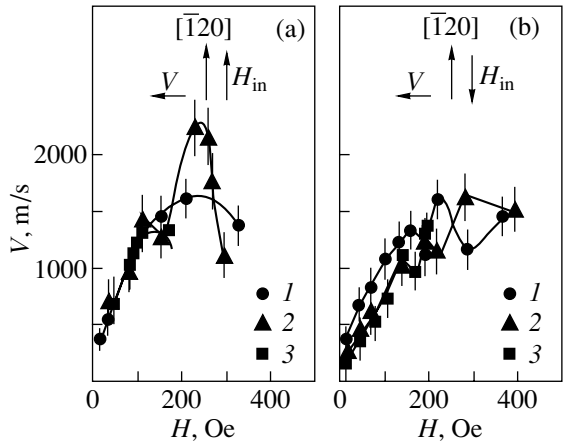

Fig. 3. Dependences of the velocity V of domain walls moving in the direction perpendicular to the in-plane magnetic field H_{in} applied along the ⟨120⟩ crystallographic axis on the acting magnetic field H. H_{in}, Oe: (*1*) 134, (*2*) 268, and (*3*) 402.

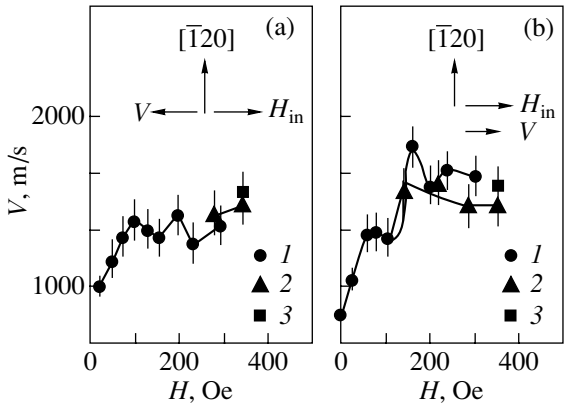

Fig. 4. Dependences of the velocity V of domain walls moving along the in-plane magnetic field H_{in} applied normally to the ⟨120⟩ crystallographic axis (along the ⟨001⟩ direction) on the acting magnetic field H. H_{in}, Oe: (*1*) 134, (*2*) 268, and (*3*) 402.

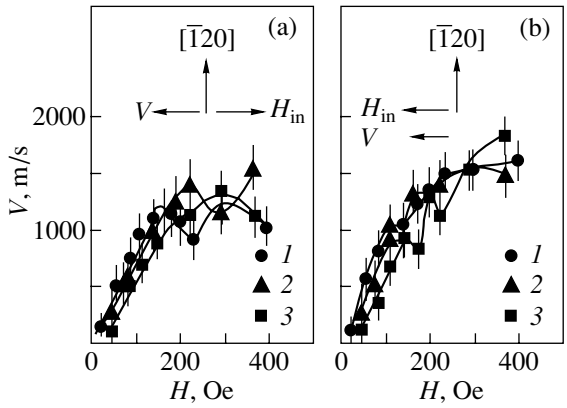

Fig. 5. Dependences of the velocity V of domain walls moving along the in-plane magnetic field H_{in} applied normally to the ⟨120⟩ crystallographic axis (opposite to the ⟨001⟩ direction) on the acting magnetic field H. H_{in}, Oe: (*1*) 134, (*2*) 268, and (*3*) 402.

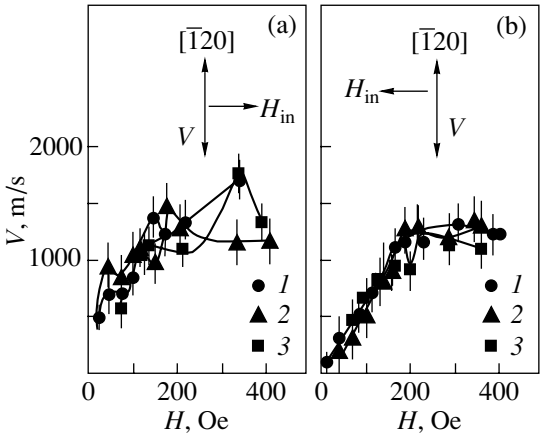

Fig. 6. Dependences of the velocity V of domain walls moving in the direction perpendicular to the in-plane magnetic field H_{in} applied normally to the ⟨120⟩ crystallographic axis (along the ⟨001⟩ direction) on the acting magnetic field H. H_{in}, Oe: (*1*) 134, (*2*) 268, and (*3*) 402.

its slope (the domain-wall mobility μ) and the domain-wall velocity V_p corresponding to the terminal point of this portion. The table presents these parameters and the maximum velocity V_{max} of domain walls, which was measured in the experiment.

Figure 1 shows the dependence $V(H)$ in the absence of an in-plane magnetic field. The slope of the initial portion in the $V(H)$ curve is 8.6 m/(s Oe), and the terminal point of this portion corresponds to the domain-wall velocity V_p = 1730 m/s. The maximum domain-wall velocity V_{max} measured in this experiment is equal to 2170 m/s.

The dependences $V(H)$ for a domain wall moving along the in-plane magnetic field applied parallel to the ⟨120⟩ crystallographic axis are displayed in Fig. 2a. A comparison of Figs. 1 and 2a shows that, in the case when the in-plane magnetic field H_{in} = 134 Oe is applied along the direction corresponding to the minimum magnetic field H_{min} at which the domain structure disappears, the slope of the initial portion of the $V(H)$ curve increases to 12.1 m/(s Oe), the domain-wall velocity V_p increases to 2120 m/s, and the maximum domain-wall velocity V_{max} remains almost constant (see table). A further increase in the in-plane magnetic field H_{in} leads to a decrease in both the domain-wall velocity

Dynamic parameters of bismuth-containing garnet ferrite single-crystal films

No.	Figure no.	H_{in} = 134 Oe			H_{in} = 268 Oe			H_{in} = 402 Oe		
		μ, m/(s Oe)	V_p, m/s	V_{max}, m/s	μ, m/(s Oe)	V_p, m/s	V_{max}, m/s	μ, m/(s Oe)	V_p, m/s	V_{max}, m/s
1	2*a*	12.1	2120	2200	13.5	1250	1440	8.7	1080	1620
2	2*b*	7.4	…	1870	7.6	…	1600	5.2	…	1310
3	2*c*	6.4	1400	1400	7.0	1710	1710	…	…	1140
4	3*a*	7.1	1100	2050	5.8	1440	2820	8.5	1330	1330
5	3*b*	10.9	830	1620	6.5	1010	1600	6.5	700	1330
6	4*a*	14.3	980	1700	…	…	1340			1370
7	4*b*	4.5	1150	1570	…	…	1270	…	…	1350
8	5*a*	8.6	1010	1270	8.0	1170	1550	7.1	1130	1360
9	5*b*	12.5	1080	1650	11.1	930	1510	9.0	970	1850
10	6*a*	…	…	1700	…	…	1450	…	…	1760
11	6*b*	6.6	1150	1350	6.6	1260	1310	6.1	860	1310

V_p and the maximum domain wall velocity V_{max}, and the range of acting magnetic fields in which the domain wall exists becomes narrower. Note that, at H_{in} = 268 Oe, the domain-wall mobility is maximum in all the experiments (see table). Moreover, it is seen from Fig. 2a that the dependence $V(H)$ can exhibit two local minima (curve *2*) instead of a single minimum as in Figs. 1 and 2a (curve *1*).

Figures 2b and 2c depict the dependences $V(H)$ for domain walls moving in opposite directions along the in-plane magnetic field applied parallel to the ⟨120⟩ crystallographic axis but in the opposite direction to that shown in Fig. 2a. The narrow peak in curve *1* (Fig. 2b) is most likely associated with the unidirectional anisotropy of the domain-wall velocity. A comparison of Figs. 1, 2b, and 2c demonstrates that, in the in-plane magnetic field H_{in} = 402 Oe, the range of acting magnetic fields H in which the reversed domains nucleate decreases by a factor of approximately two.

The dependences $V(H)$ for domain walls moving in the direction perpendicular to the in-plane magnetic field H_{in} applied along the ⟨120⟩ crystallographic axis are shown in Fig. 3. It can be seen that, for both directions of the in-plane magnetic field, the dependences $V(H)$ exhibit two local minima (curve *2* in Fig. 3a, curve *1* in Fig. 3b). For the geometry of the experiment presented in Fig. 3a, the domain-wall velocity is maximum; i.e., V_{max} = 2820 m/s (see table). At H_{in} = 402 Oe (curves *3* in Figs. 3a, 3b), the range of acting magnetic fields H in which the reversed domains nucleate becomes significantly narrower than that observed in weaker in-plane fields H_{in} (curves *1*, *2* in Figs. 3a, 3b).

Figure 4 represents the dependences $V(H)$ for domain walls moving in opposite directions along the in-plane magnetic field H_{in} applied normally to the ⟨120⟩ crystallographic axis (along the ⟨001⟩ direction). For this geometry of the experiment, the in-plane magnetic field in which the domain structure disappears reaches a maximum. It can be seen that, for both directions of the domain-wall motion, the dependence $V(H)$ exhibits two local minima (curves *1* in Figs. 4a, 4b). In a sufficiently strong in-plane magnetic field, no nucleation of reversed domains occurs in an H range adjacent to the ordinate axis (curves *2*, *3* in Figs. 4a, 4b). The stronger the in-plane magnetic field H_{in}, the wider this range.

It is worth noting that the in-plane magnetic field, when applied in the opposite direction to that shown in Fig. 4, does not substantially affect the nucleation of reversed domains (Fig. 5). Note also that the range of pulsed magnetic fields H_p in which the reversed domains nucleate almost coincides with that observed in the absence of an in-plane magnetic field (H_{in} = 0, Fig. 1). As can be seen from Fig. 5b (curve *1*), the dependence $V(H)$ is characterized by two local minima.

Figure 6 shows the dependences $V(H)$ measured in the in-plane magnetic field H_{in} applied normally to the ⟨120⟩ crystallographic axis (along the ⟨001⟩ direction). In this case, the domain walls move along the ⟨120⟩ axis. It can be seen that, for this geometry of the experiment, the $V(H)$ curves also contain local minima (for example, curve *1* in Fig. 6a), even though they are less pronounced.

4. CONCLUSIONS

Thus, it was demonstrated that bismuth-containing garnet ferrite single-crystal films of the composition $(Bi,Y,Pr)_3(Fe,Ga)_5O_{12}$ with the (210) orientation are characterized by the following features.

(i) The in-plane magnetic field applied along the ⟨001⟩ crystallographic axis prevents nucleation of

reversed domains upon pulsed magnetization reversal of the film.

(ii) The domain-wall velocity reaches a maximum when the in-plane magnetic field is applied along the ⟨120⟩ crystallographic axis and the domain wall moves along the ⟨001⟩ crystallographic axis.

(iii) The domain-wall mobility reaches a maximum when the in-plane magnetic field is applied along the ⟨001⟩ crystallographic axis and the domain wall moves along the ⟨120⟩ crystallographic axis.

(iv) For certain directions and magnitudes of the in-plane magnetic field, the dependence of the domain-wall velocity on the acting magnetic field exhibits two local minima.

REFERENCES

1. V. V. Randoshkin, V. I. Chani, M. V. Logunov, *et al.*, Pis'ma Zh. Tekh. Fiz. **15** (14), 42 (1989) [Sov. Tech. Phys. Lett. **15**, 553 (1989)].
2. V. V. Randoshkin, in *Thin Films and Beam-Solid Interaction*, Ed. by L. Huang (Elsevier, Amsterdam, 1991), Vol. 4, p. 267.
3. V. V. Randoshkin, Tr. Inst. Obshch. Fiz., Ross. Akad. Nauk **35**, 49 (1992).
4. V. V. Randoshkin, M. V. Logunov, and Yu. N. Sazhin, Fiz. Tverd. Tela (Leningrad) **32** (5), 1456 (1990) [Sov. Phys. Solid State **32**, 849 (1990)].
5. V. V. Randoshkin, M. V. Logunov, and Yu. N. Sazhin, Zh. Tekh. Fiz. **66** (2), 201 (1996) [Tech. Phys. **41**, 225 (1996)].
6. V. V. Randoshkin, M. V. Logunov, and Yu. N. Sazhin, in *Abstracts of XIV All-Russian School–Seminar on New Magnetic Materials in Microelectronics* (Moscow, 1994), Part 2, p. 32.
7. A. P. Malozemoff and J. C. Slonczewski, *Magnetic Domain Walls in Bubble Materials* (Academic, New York, 1979; Mir, Moscow, 1982).
8. V. V. Randoshkin and Yu. N. Sazhin, Fiz. Tverd. Tela (in press).
9. V. V. Randoshkin and Yu. N. Sazhin, Zh. Tekh. Fiz. **66** (8), 83 (1996) [Tech. Phys. **41**, 790 (1996)].
10. V. V. Randoshkin, M. V. Logunov, and V. B. Sigachev, Prib. Tekh. Éksp., No. 5, 247 (1985).
11. V. V. Randoshkin, Prib. Tekh. Éksp., No. 2, 155 (1995).

Translated by N. Korovin

Physics of the Solid State, Vol. 45, No. 3, 2003, pp. 508–512. Translated from Fizika Tverdogo Tela, Vol. 45, No. 3, 2003, pp. 480–484.

MAGNETISM AND FERROELECTRICITY

High-Temperature Properties of the Manganites: Manifestation of a Paramagnetic-Phase Inhomogeneity?

N. A. Babushkina*, E. A. Chistotina*, K. I. Kugel', A. L. Rakhmanov**, O. Yu. Gorbenko***, and A. R. Kaul'*****

** Russia Research Center Kurchatov Institute, pl. Kurchatova 1, Moscow, 123182 Russia*
e-mail: babushkina@imp.kiae.ru
*** Institute of Theoretical and Applied Electrodynamics, Russian Academy of Sciences, Moscow, 125412 Russia*
**** Moscow State University, Vorob'evy gory, Moscow, 119992 Russia*
Received June 20, 2002

Abstract—An analysis was made of the magnetic susceptibility, electrical resistivity, and magnetoresistance of $(La_{1-y}Pr_y)_{0.7}Ca_{0.3}MnO_3$ samples differing in Pr content and enriched in the oxygen isotope ^{18}O. At high temperatures, all samples were paramagnetic insulators, while below 60 K, part of them transferred to a ferromagnetic metallic state. All the samples exhibit practically identical behavior of the susceptibility, resistivity, and magnetoresistance in the high-temperature region, despite a noticeable difference between their properties at low temperatures; more specifically, the magnetoresistance grows quadratically with magnetic field within a broad range of temperatures and magnetic fields and scales with increasing temperature close to $1/T^5$. A combined analysis of the magnetic susceptibility and magnetoresistance indicates the possible existence of an inhomogeneous state with considerable ferromagnetic correlations in the paramagnetic region. © *2003 MAIK "Nauka/Interperiodica".*

1. INTRODUCTION

A diversity of supported ordering types (charge, orbital, magnetic) is characteristic of manganites. The interrelation between the various order parameters gives rise to a rich variety of effects, with colossal magnetoresistance being the most remarkable of them [1]. The trend to phase separation and the formation of inhomogeneous states also plays an important part in the physics of the manganites. Phase separation is most essential near the phase transition lines. There are indications, however, that the state of the system is inhomogeneous even in the paramagnetic region and exhibits substantial ferromagnetic (FM) correlations [2–4].

This communication reports on an analysis of the magnetoresistance and magnetic susceptibility of the manganites $(La_{1-y}Pr_y)_{0.7}Ca_{0.3}MnO_3$ $(0.5 \le y \le 1)$. In this region of Pr concentrations, substitution of ^{18}O for ^{16}O brings about substantial changes to the properties of the system under study [5, 6], which was used to broaden the diversity of the samples without changing their chemical composition. The study was carried out at high temperatures ($80 < T < 300$ K) and magnetic fields ($H < 4$ T), in which our samples did not exhibit long-range FM order and their conductivity $\sigma(T)$ followed nonmetallic behavior. However, even in the nonmetallic phase, the magnetoresistance of manganites MR = $(\sigma(H) - \sigma(0))/\sigma(0)$ is fairly large (it can reach as high as 100%) and increases quadratically with the field, MR = $a(T)H^2$, over a broad range of parameter variation. The coefficient $a(T)$ exhibits a strong temperature dependence in all the samples studied and scales as $1/T^5$. The experimental data obtained were analyzed in terms of the available model concepts on electron transport in the manganites. It was shown that the observed effects can be accounted for by assuming the existence of an inhomogeneous state with substantial FM correlations in the paramagnetic region. The inclusion of spin-dependent electron tunneling between correlated regions permits one to explain the strong temperature dependence of magnetoresistance in a straightforward way.

2. SAMPLES

Samples of the system $(La_{1-y}Pr_y)_{0.7}Ca_{0.3}MnO_3$ differing in $0 \le y \le 1$ and enriched to different levels in the ^{18}O isotope were described in detail in our previous publications [5, 6]. The samples were 7-mm-long bars, 1×1 mm in cross section. Five samples with different low-temperature behavior of the electrical resistivity $\rho(T)$ were chosen for the study:

(1) $(La_{0.25}Pr_{0.75})_{0.7}Ca_{0.3}MnO_3$ with ^{16}O, exhibiting a metal–insulator transition at $T_{MI} = 87$ K;

(2) $(La_{0.25}Pr_{0.75})_{0.7}Ca_{0.3}MnO_3$ with 30% ^{18}O and $T_{MI} = 58$ K;

(3) $(La_{0.25}Pr_{0.75})_{0.7}Ca_{0.3}MnO_3$ with the ^{16}O isotope fully replaced by ^{18}O;

(4) $Pr_{0.7}Ca_{0.3}MnO_3$ with ^{16}O;

(5) $Pr_{0.7}Ca_{0.3}MnO_3$ with ^{18}O.

Samples 3–5 remain insulators down to the lowest temperatures covered.

1063-7834/03/4503-0508$24.00 © 2003 MAIK "Nauka/Interperiodica"

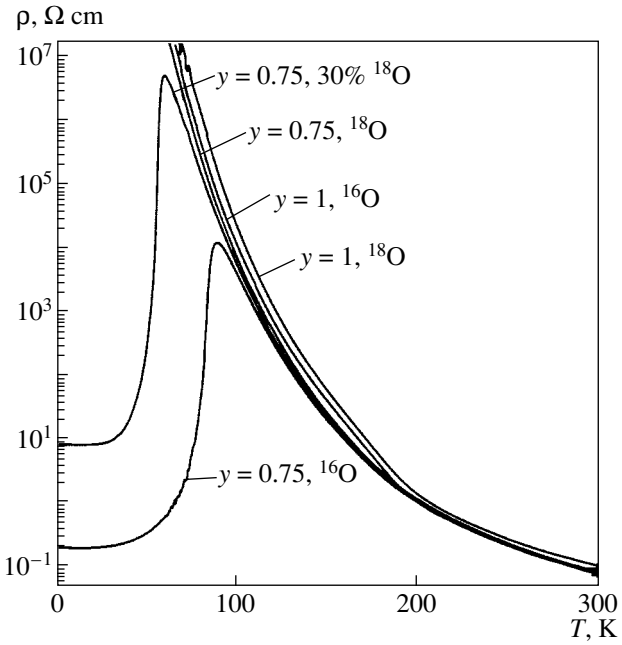

Fig. 1. Temperature dependence of the electrical resistivity $\rho(T)$ in zero magnetic field obtained on the five samples studied.

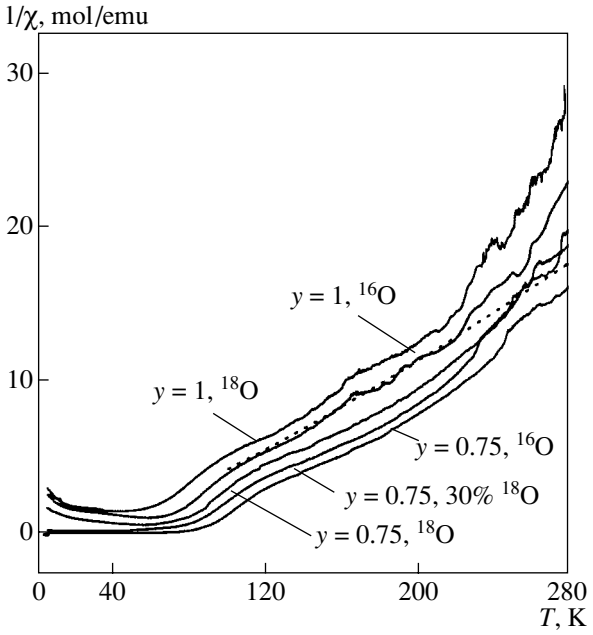

Fig. 2. Temperature dependence of the inverse magnetic susceptibility $1/\chi(T)$. Solid lines are experimental data, and dashed line is the theoretical curve calculated for the FM phase concentration 5%, $S = 2$, $g = 2$, $N_{\text{eff}} = 130$, and density of the material 6.2 g/cm^3.

3. EXPERIMENTAL RESULTS

Figure 1 presents the temperature dependence $\rho(T)$ obtained in zero magnetic field for the above five samples. The electrical resistivity measurements were conducted in the dc mode using a standard four-probe method at temperatures T ranging from 4.2 to 300 K. The data presented are in agreement with those published earlier [5]. Note that the $\rho(T)$ dependences measured for all the samples in the high-temperature region are very similar and can be fitted by a thermal activation law:

$$\rho(T) = \rho_0 T^{\gamma} \exp\left(\frac{E_g}{k_B T}\right). \quad (1)$$

Within experimental accuracy, the activation energy E_g is practically independent of the choice of γ. Equation (1) is in agreement with the data obtained by other researchers on similar samples [7, 8]. Note also that this relation follows from a theoretical description of transport properties in nonmetallic phase-separated manganites [9].

Earlier measurements of the low-frequency magnetic susceptibility χ were conducted on similar samples in [5, 10]. An analysis of those results [10] permitted the conclusion that an inhomogeneous state exists in the paramagnetic region. Figure 2 plots $1/\chi(T)$ graphs for the samples studied. The $1/\chi(T)$ curves obtained in the high-temperature region are qualitatively similar, despite the differences in the structure of the low-temperature state revealed by neutron scattering measurements [6]. Indeed, for $y = 0.75$, the sample with ^{18}O has a uniform antiferromagnetic (AFM) state, while the sample with ^{16}O is separated into macroscopic FM and AFM regions [6]. The $\chi(T)$ curve can be fitted by the Curie–Weiss law, $\chi = C/(T - \Theta)$, with a positive Θ increasing with temperature. The positive value of Θ and a large magnetic susceptibility as compared to typical values for antiferromagnets suggest the existence of noticeable FM correlations, which apparently provide a major contribution to χ.

The magnetoresistance measurements of the samples were conducted in the temperature range 80–273 K and magnetic fields of up to 4 T. The current and the magnetic field were directed along the length of the sample. In all the samples studied, the conductivity increased with increasing magnetic field H. The relative variation in the conductivity was found to obey the universal quadratic law $\text{MR} = a(T)H^2$ practically throughout the magnetic-field and temperature ranges covered. Near the insulator–metal transition, noticeable deviations from the quadratic law appear at low temperatures. The inset to Fig. 3 illustrates the MR(H) dependence measured for the $Pr_{0.7}Ca_{0.3}MnO_3$ sample with ^{16}O in the temperature range $T = 80$–273 K. Plotted in Fig. 3 is the temperature dependence of the coefficient a. We readily see that the quantity $a(T)$ falls off rapidly (following a law close to $1/T^5$).

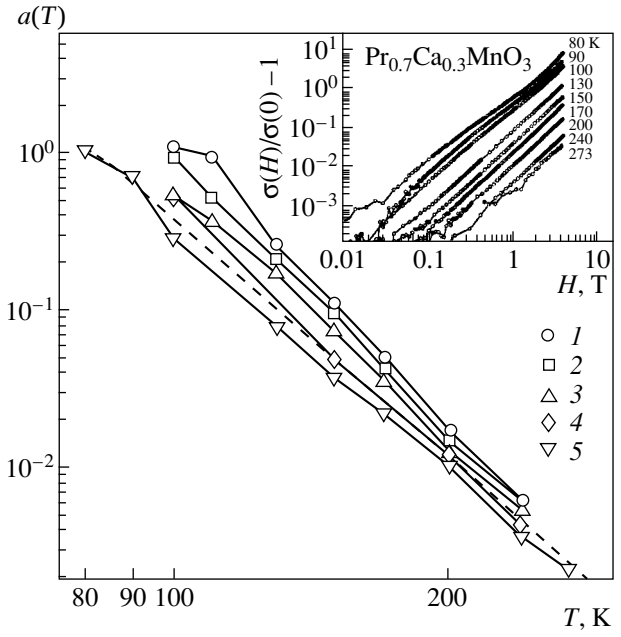

Fig. 3. Temperature dependence of the coefficient a in the expression MR = $a(T)H^2$ for various samples. Symbols are experimental data for (*1*) ^{16}O, y = 0.75; (*2*) 30% ^{18}O, y = 0.75; (*3*) ^{18}O, y = 0.75; (*4*) ^{16}O, y = 1; and (*5*) ^{18}O, y = 1; dashed line is calculation based on Eq. (8) made for S = 2, g = 2, Z = 6, N_{eff} = 130, J/k_B = 15 K, H_a = 0.5 T, and cosβ = 1. Inset shows field dependence of the magnetoresistance of the $Pr_{0.7}Ca_{0.3}MnO_3$ sample with ^{16}O obtained at various temperatures.

4. DISCUSSION OF THE RESULTS

Thus, the temperature dependences of the electrical resistivity, magnetic susceptibility, and magnetoresistance in the high-temperature region behave in a very similar way, both qualitatively and quantitatively, for all the samples studied (Figs. 1–3). This provides a convincing argument for the transport properties being determined by a common mechanism in the nonmetallic phase of these materials. As already pointed out, present-day theoretical concepts of manganite properties [1–4] and data available on the magnetic susceptibility suggest a possible presence of strong FM correlations in our samples in the paramagnetic region. Another possible indication of the existence of correlated regions is the relatively large and strongly temperature-dependent magnetoresistance. Indeed, because the measured electrical resistivity follows activation law (1), it appears natural to conjecture that the magnetoresistance of the manganites in the nonmetallic region is related to the variation of the band gap in the carrier mobility $E_g(H)$ with increasing magnetic field [1]. Therefore, we can write

$$\text{MR} = \exp[-(E_g(H) - E_g)/k_B T] - 1. \qquad (2)$$

In accordance with the current concepts of the band structure of magnetically ordered materials (within, e.g., the *s–d* model), the magnetoresistance can be expressed as a quadratic function of the magnetic moment M, which has been confirmed experimentally (see, e.g., [1]). This also agrees with our results obtained in the low-field region, where $M = \chi H$. In pure dimensionality considerations, in the case of MR $\ll$ 1, Eq. (2) can be recast as

$$\text{MR} = -\frac{\chi^2 H^2 \Delta E_g}{M_s^2 k_B T}, \quad \Delta E_g = \frac{E_g(M^2) - E_g}{(M/M_s)^2}, \qquad (3)$$

where M_s is the saturation magnetization. Substituting the experimental data on MR and χ into Eq. (3) and setting $4\pi M_s$ = 1 T in order to make an estimate for $Pr_{0.7}Ca_{0.3}Mn^{16}O_3$ at T = 150 K, we obtain $\Delta E_g \sim 0.1$ eV, which is considerably larger than the energy of any magnetic ordering per magnetic ion. Note that this estimate of ΔE_g is typical of manganites of similar composition in the temperature region covered [1]. Even this rough estimate indicates that the mechanism controlling the magnetoresistance should be determined by regions sufficiently large in size. This reflects a physical situation of a general nature. If a system is in a state with uncorrelated magnetic atoms, then the energy of interaction of atoms with the magnetic field $\mu_B S_g H$ (where μ_B is the Bohr magneton, g is the Landé factor, and S is the atomic spin) at temperatures of 100 K or higher is too small (compared with $k_B T$) to noticeably affect the state of the system and its transport properties. Note also that in addition to the comparatively large magnetoresistance, its strong temperature dependence [which does not follow in an obvious way from Eq. (3)] must be explained.

Now, let us consider the magnetoresistance in the high-temperature domain in terms of the fairly simple model of electron transport in a system with strong FM correlations. The conventional approach to the conductivity of manganites (for instance, the double-exchange model) [1] assumes the FM correlated regions to possess a higher conductivity. Therefore, if these regions do not overlap, the main contribution to the resistivity is due to the tunneling of charge carrier between them. The corresponding probability depends, in particular, on the mutual orientation of the electron spin and the atomic spins in the regions involved in the tunneling. Straightforward estimation shows that in fields of the order of 1 T, the electron spin orientation remains practically unchanged after tunneling to a distance of a few lattice constants. An electron leaving one FM correlated region enters another with the same spin orientation. Therefore, the transition probability depends on the mutual orientation of the magnetic moments of the correlated regions. The orientation of the magnetic moments of FM correlated regions along the applied magnetic field enhances the transition probability and, thus, reduces the resistivity with increasing magnetic field; this exactly is observed experimentally.

Let us express the conductivity of the system as $\sigma(H) = \sigma_0 \langle \Sigma(H) \rangle$, where $\Sigma(H)$ is the spin contribution to

the electron tunneling probability and angle brackets denote volume averaging. In this notation, MR = $\langle\Sigma(H)\rangle/\langle\Sigma(0)\rangle - 1$. The quantity σ_0 for the particular case of the above model was calculated in [9].

We consider N identical, nonoverlapping regions (droplets) with a preferential orientation of the atomic moments within each of them. We denote the effective magnetic moment of such a droplet by $M_{\text{eff}} = \mu_B g N_{\text{eff}} S$, where N_{eff} is the effective number of magnetic atoms in a droplet ($SN_{\text{eff}} \gg 1$). Neglecting the magnetic interaction between the droplets, the free energy of a droplet in a magnetic field can be presented in the form [11]

$$U(H) = U(0) - M_{\text{eff}}(H\cos\theta + H_a\cos^2\psi), \qquad (4)$$

where θ is the angle between the applied field H and the direction of M_{eff}, H_a is the anisotropy field, and ψ is the angle between the anisotropy axis and the direction of the droplet's magnetic moment (for the sake of simplicity, the anisotropy is assumed to be uniaxial). Note that the conventional magnetic anisotropy associated with the crystal field in manganites is small [12]. In these conditions, H_a is determined primarily by the shape factor [13]. For instance, for an ellipsoid, we have $H_a = \pi m_{\text{eff}}(1 - 3\tilde{N})$, where m_{eff} is the magnetic moment of a droplet per unit volume and $\tilde{N}$ is the corresponding demagnetization factor. H_a turns out to be of the order of 1 T already at a comparatively small deviation from sphericity and for typical values of the parameters.

Let **H** be parallel to the z axis, with the anisotropy axis lying in the (x, z) plane at an angle β to the vector **H**. Then, $\cos\psi = \sin\theta\sin\beta\cos\varphi + \cos\theta\cos\beta$, where φ is the angle between the x axis and the projection of vector $\mathbf{M}_{\text{eff}}$ onto the (x, y) plane. In the classical limit, each orientation of $\mathbf{M}_{\text{eff}}$ is characterized by a probability

$$P(H, \theta, \varphi) = A(H)\exp[M_{\text{eff}}(H\cos\theta + H_a\cos^2\psi(\theta, \varphi))/k_BT], \qquad (5)$$

where $A(H)$ is a normalization factor. The stationary states of an electron are those with the preserved spin projection $s = \pm 1/2$ onto the effective field direction in an FM correlated region. Let an electron interact with Z magnetic atoms in a droplet ($Z < N_{\text{eff}}$). The energy of this interaction is $E_s = -JSZs$, where J is the exchange integral. Assuming JSZ to be of the order of the Curie temperature, one readily sees that E_s greatly exceeds the energy of electron spin interaction with the magnetic field if $H \ll 100$ T. In this case, the effective field coincides in direction with $\mathbf{M}_{\text{eff}}$ and the probability of an electron having a spin projection s can be written as

$$P_s = \frac{\exp(-E_s/k_BT)}{2\cosh(E_s/k_BT)}. \qquad (6)$$

An electron transferred to another droplet is acted upon by an effective field directed at an angle ν to the original field, where $\cos\nu = \cos\theta_1\cos\theta_2 + \sin\theta_1\sin\theta_2\cos(\varphi_1 - \varphi_2)$ and indices 1 and 2 label the droplets. Therefore, the work expended in transporting an electron from the first to the second droplet is $\Delta E_s = E_s(1 - \cos\nu)$. Accordingly, the probability of transfer from one droplet to another is proportional to $\exp(-\Delta E_s/k_BT)$. Finally, taking into account all the probability factors and averaging over the droplets, we come to the expression

$$\langle\Sigma(H)\rangle = \int_0^{2\pi} d\varphi_1 \int_0^{2\pi} d\varphi_2 \int_0^{\pi} \sin\theta_1 d\theta_1 \times \int_0^{\pi} \sin\theta_2 d\theta_2 P(\theta_1, \varphi_1)P(\theta_2, \varphi_2) \times \sum_{s = \pm 1/2} P_s(\theta_1)\exp(-\Delta E_s/k_BT). \qquad (7)$$

In the high-temperature region, Eqs. (5)–(7) yield

$$\text{MR} = \frac{2}{225}(\cos^2\beta - 1/3)\frac{\mu_B^3 S^5 N_{\text{eff}}^3 Z^2}{(k_BT)^5} g^3 J^2 H_a H^2. \qquad (8)$$

Here, Z is the number of nearest neighbors of the magnetic atom. This expression is formally valid if k_BT greatly exceeds the characteristic energies, namely, E_s, the Zeeman energy $\mu_B g S N_{\text{eff}} H$, and the magnetic anisotropy energy $\mu_B g S N_{\text{eff}} H_a$. Numerical calculations show that Eq. (8) remains valid for k_BT of the order of and even slightly less than these energies.

The magnetoresistance given by Eq. (8) depends explicitly on the angle β between the anisotropy axis and the applied magnetic field. However, if the anisotropy is determined primarily by the shape effect, it appears only natural to assume that the long axes of the droplets are oriented preferentially along the applied magnetic field. Note that the current is directed along the magnetic field. Hence, droplets oriented along with the magnetic field provide a larger relative contribution to the conductivity, thus efficiently suppressing the effect of possible droplet misorientation. Therefore, in our subsequent estimation, we shall assume $\cos\beta \approx 1$.

Thus, the above simple model correctly reproduces the experimental dependence of the magnetoresistance on magnetic field and temperature, MR ~ H^2/T^5. For a numerical estimate, we set $S = 2$, $g = 2$, and $Z = 6$; in view of the above estimates, one can also set $H_a = 0.5$ T and $J/k_B = 15$ K. Then, Eq. (8) yields good quantitative agreement with experiment for $N_{\text{eff}} \sim 10^2$. The corresponding dependence for $N_{\text{eff}} = 130$ is shown in Fig. 3 as a dashed line. Equation (5) permits one to calculate the magnetic susceptibility $\chi(T)$ in a straightforward way. Using the above parameters and 5–10% for the concentration of FM correlated regions, we obtain a

correct order-of-magnitude estimate for the same value of $N_{\text{eff}} \sim 10^2$. The calculated $\chi(T)$ relation is shown as a dashed curve in Fig. 2. As seen from Figs. 2 and 3, the proposed model offers a reasonable approximation to the experimental data. The characteristic size of an FM correlated region turns out to be of the order of five lattice constants, which is close to the structure of the small-scale ferron-type phase separation [3, 4] and is in accord with the small-angle neutron-scattering data reported in [14].

5. CONCLUSION

Thus, our experimental data and their analysis made in terms of a simple model suggest the possible existence of an inhomogeneous state with strong FM correlations even in the paramagnetic region. Note, however, that the above qualitative picture does not reveal the mechanisms underlying the formation of the inhomogeneous state and needs further refinement.

ACKNOWLEDGMENTS

The authors are indebted to A.N. Taldenkov for providing data on the magnetoresistance of the samples and for valuable criticisms in discussing the results obtained in this study.

This study was supported by the Russian Foundation for Basic Research (project nos. 01-02-16240, 02-02-16708, 00-15-96570), CRDF (project no. RP2-2355-MO-02), INTAS (project no. 01-2008), and NWO (project no. 047-008-017).

REFERENCES

1. M. B. Salamon and M. Jaime, Rev. Mod. Phys. **73** (3), 583 (2001).
2. E. Dagotto, T. Hotta, and A. Moreo, Phys. Rep. **344**, 1 (2001).
3. E. L. Nagaev, Phys. Rep. **346**, 387 (2001).
4. M. Yu. Kagan and K. I. Kugel', Usp. Fiz. Nauk **171**, 577 (2001) [Phys.–Usp. **44**, 553 (2001)].
5. N. A. Babushkina, A. N. Taldenkov, L. M. Belova, *et al.*, Phys. Rev. B **62** (10), R6081 (2000).
6. A. M. Balagurov, V. Yu. Pomjakushin, D. V. Sheptyakov, *et al.*, Phys. Rev. B **64**, 024420 (2001).
7. G. Jakob, W. Westerburg, F. Martin, and H. Adrian, Phys. Rev. B **58** (22), 14966 (1998).
8. M. Ziese and C. Srinitiwarawong, Phys. Rev. B **58** (17), 11519 (1998).
9. A. L. Rakhmanov, K. I. Kugel, Ya. M. Blanter, and M. Yu. Kagan, Phys. Rev. B **63**, 174424 (2001).
10. N. A. Babushkina, L. M. Belova, A. N. Taldenkov, *et al.*, J. Phys.: Condens. Matter **11**, 5865 (1999).
11. L. D. Landau and E. M. Lifshitz, *Course of Theoretical Physics*, Vol. 8: *Electrodynamics of Continuous Media*, 3rd ed. (Nauka, Moscow, 1982; Pergamon, New York, 1984).
12. A. M. Oles and L. F. Feiner, Phys. Rev. B **65**, 052414 (2002).
13. A. G. Gurevich and G. A. Melkov, *Magnetic Oscillations and Waves* (Nauka, Moscow, 1994; CRC Press, Boca Raton, FL, 1996).
14. J. M. De Teresa, M. R. Ibarra, P. Algarabel, *et al.*, Phys. Rev. B **65**, 100403 (2002).

Translated by G. Skrebtsov

Physics of the Solid State, Vol. 45, No. 3, 2003, pp. 513–518. Translated from Fizika Tverdogo Tela, Vol. 45, No. 3, 2003, pp. 485–489.

MAGNETISM AND FERROELECTRICITY

Dynamics of Domain Walls in Bismuth–Ytterbium-Containing Garnet Ferrite Films in the Vicinity of the Angular Momentum Compensation Point

V. V. Randoshkin*, V. A. Polezhaev*, N. N. Sysoev*, and Yu. N. Sazhin**

** Moscow State University, Vorob'evy gory, Moscow, 119899 Russia*

*** Joint Laboratory of Magneto-Optoelectronics, Institute of General Physics, Russian Academy of Sciences, Mordovian State University, Bol'shevistkaya ul. 68, Saransk, 430000 Russia*

Received February 18, 2002; in final form, June 22, 2002

Abstract—The dependence of the domain-wall velocity V on the acting magnetic field H is investigated for $(Bi,Yb)_3(Fe,Ga)_5O_{12}$ garnet ferrite single-crystal films in the vicinity of the angular momentum compensation point at different temperatures. The films are grown by liquid-phase epitaxy from a supercooled solution melt on $Cd_3Ga_5O_{12}$ substrates with the (111) orientation. It is demonstrated that, in these films, the precessional mechanism is not responsible for the motion of domain walls but there arises an internal effective magnetic field that weakens the acting magnetic field. © *2003 MAIK "Nauka/Interperiodica".*

1. INTRODUCTION

Bismuth-containing garnet ferrite single-crystal films with angular momentum compensation are widely used for the purpose of increasing the speed of response of magneto-optic bubble-domain devices whose operation is based on the domain-wall motion [1]. At present, bismuth-containing garnet ferrite single-crystal films with angular momentum compensation have been synthesized for all rapidly relaxing rare-earth elements that, in combination with bismuth, induce uniaxial magnetic anisotropy. Among these rare-earth elements are europium [2–5], praseodymium [6], dysprosium [7], holmium [8], erbium [9], thulium [10–13], and ytterbium [14]. As a rule, garnet ferrite single-crystal films are grown through liquid-phase epitaxy from a supercooled solution melt on isomorphic substrates.

Earlier investigations of the dependence of the domain-wall velocity V on the acting magnetic field H for europium-, thulium-, and erbium-containing garnet ferrite films in the vicinity of the angular momentum compensation point at different temperatures have demonstrated that, in all cases, the initial portion of the $V(H)$ curve is linear and its extension passes approximately through the origin of the coordinates [15]. The further behavior of the dependence $V(H)$ is determined by the dimensionless attenuation parameter α. At $\alpha > 1$, the first linear portion is adjacent to the second linear portion with a smaller slope. At $\alpha < 1$, the first and second linear portions are separated by a nonlinear portion. In strong magnetic fields, the dependence $V(H)$, in some cases, exhibits an additional (linear or nonlinear) portion in which the differential mobility is higher than that in the preceding portion and can even exceed the initial mobility of domain walls [12, 16]. It has been inferred that the additional portion is attributed to the domain-wall motion occurring through the mechanism associated with the radiation of spin waves [16, 17].

The aim of the present work was to elucidate how the temperature affects the dependence $V(H)$ for bismuth–ytterbium-containing garnet ferrite single-crystal films of the composition $(Bi,Yb)_3(Fe,Ga)_5O_{12}$ with angular momentum compensation.

2. SAMPLE PREPARATION AND EXPERIMENTAL TECHNIQUE

Bismuth–ytterbium-containing garnet ferrite single-crystal films of the composition $(Bi,Yb)_3(Fe,Ga)_5O_{12}$ were grown from a $PbO–B_2O_3–Bi_2O_3$-based solution

Parameters of bismuth–ytterbium-containing garnet ferrite single-crystal films at room temperature

Sample no.	**I**-4	**II**-1	**III**-4	**III**-5
R_1	19.19	19.44	20.32	20.32
R_2	3.637	3.631	3.425	3.425
R_3	19.96	20.56	20.95	20.95
R_4	0.1197	0.1161	0.1199	0.1199
h, μm	7.1	11.4	7.5	13.2
W, μm	21.5	10.0	6.0	8.6
H_0, Oe	9.8	51	83	95
H_K, Oe	4500	730	750	810
T_N, °C	58	129	110	122
μ, cm/(s Oe)	…	78	165	153

1063-7834/03/4503-0513$24.00 © 2003 MAIK "Nauka/Interperiodica"

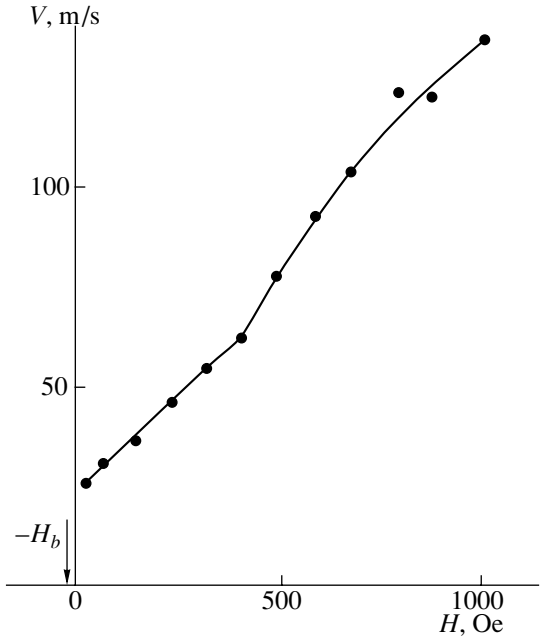

Fig. 1. Dependence of the domain-wall velocity V on the acting magnetic field H for sample **I**-4. The arrow indicates the magnetic bias field.

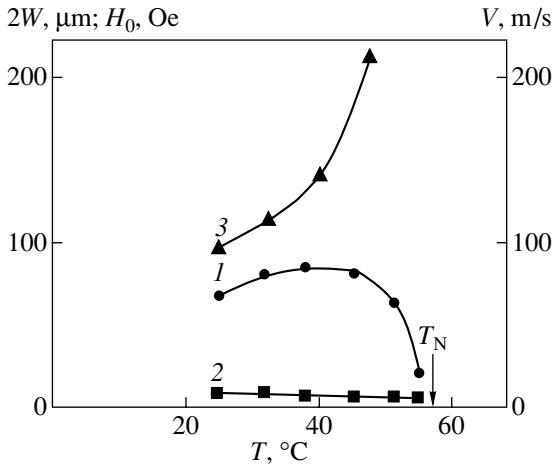

Fig. 2. Temperature dependences of (*1*) the period of equilibrium strip domains $2W$, (*2*) the collapse field of bubble domains H_0, and (*3*) the domain-wall velocity V at H_p = 517 Oe and H_b = 13 Oe for sample **I**-4. The arrow indicates the Néel temperature T_N.

melt on $Cd_3Ga_5O_{12}$ substrates with the (111) orientation. The composition of the batch used in growing the epitaxial films is characterized by the following molar ratios of components:

$$R_1 = Fe_2O_3/Yb_2O_3,$$

$$R_2 = Fe_2O_3/Ga_2O_3,$$

$$R_3 = (PbO + Bi_2O_3)/B_2O_3,$$

$$R_4 = (Yb_2O_3 + Fe_2O_3 + Ga_2O_3)/(Yb_2O_3 + Fe_2O_3 + Ga_2O_3 + PbO + Bi_2O_3 + B_2O_3).$$

The table presents the ratios R_1–R_4 for solution melts **I**–**III** and the parameters of the samples whose properties are discussed in this paper. The designations used in the table are as follows: h is the film thickness, W is the equilibrium width of strip domains, H_0 is the collapse field of bubble domains, H_K is the field of uniaxial magnetic anisotropy, T_N is the Néel temperature, and μ is the initial mobility of domain walls. The Arabic numeral in the sample labeling represents the order number of a particular film in the series of bismuth–ytterbium-containing garnet ferrite single-crystal films sequentially grown under the same conditions from the relevant solution melt, which is denoted by the Roman numeral. The difference between the magnetic and dynamic parameters for samples **III**-4 and **III**-5 indicates that the solution melt undergoes degradation [18].

As can be seen from the table, the parameters R_1 (R_2, R_3, or R_4) differ by no more than ±3%. The error in determining the quantitative composition of the grown films also does not exceed ±3%. When changing over from solution melt **I** to solution melt **III**, the ytterbium concentration decreases (the ratio R_1 increases), whereas the gallium concentration increases (the ratio R_2 decreases). As a consequence, the saturation magnetization $4\pi M_s$ of samples in series **II** should be larger than that of samples in series **I** [1]. The increase in the saturation magnetization $4\pi M_s$ correlates with the increase in the collapse field of bubble domains H_0 (see table).

The experiments were performed on a universal setup [19] providing high-speed photographic observations with the use of the magnetization reversal technique [20]. The initial bismuth–ytterbium-containing garnet ferrite single-crystal film was magnetized to saturation with the magnetic bias field H_b applied along the normal to the film surface. The pulsed magnetic field H_p was applied in the opposite direction with the use of a pair of pancake coils. The film to be studied was placed in the midplane between the pancake coils. We recorded the image of the reversed domain that nucleated at a point defect. At a sufficiently large distance from the nucleation center, the acting magnetic field can be represented in the form [20]

$$H = H_p - H_b. \quad (1)$$

3. RESULTS AND DISCUSSION

The dependence $V(H)$ for sample **I**-4 is shown in Fig. 1, in which the arrow indicates the magnetic bias field. It can be seen that, in this case, the first portion of the $V(H)$ curve is linear with a slope of 9.1 cm/(s Oe) and its extension intersects the ordinate axis. This value is more than one order of magnitude smaller than the initial domain-wall mobility, which is characteristic of the films under investigation [14]. Therefore, we can make the inference that the first experimentally observed portion of the dependence shown in Fig. 1 is

not the initial portion of the $V(H)$ curve. The experimental technique used in this work and described in detail in [19] failed when used to perform measurements in weak magnetic fields; hence, we cannot observe the initial portion of the dependence $V(H)$. Under the assumption that the first experimental point in the $V(H)$ curve (Fig. 1) is the terminal point of the initial linear portion, we obtain $\mu = 79$ cm/(s Oe).

The second experimentally observed portion of the $V(H)$ curve (Fig. 1) is nonlinear; in this case, the differential mobility μ_0 exceeds the initial mobility. This portion of the $V(H)$ curve can be associated with the domain-wall motion occurring through the mechanism of spin wave radiation [16]. The fact that the initial point of this portion lies in the range $H < H_K$ can be explained by the presence of a transition surface layer with a decreased magnetic anisotropy in the studied sample.

Figure 2 depicts the temperature dependences $2W(T)$, $H_0(T)$, and $V(T)$ at the magnetic field $H = 504$ Oe for sample **I**-4. The observed increase in the domain-wall velocity upon heating is caused by the increase in the effective gyromagnetic ratio. However, this sample does not exhibit angular momentum compensation in the temperature range from 0 K to the Néel temperature T_N.

The curve $V(H)$ for sample **II**-1 is plotted in Fig. 3. As can be seen from Fig. 3, the $V(H)$ curve consists of two linear portions separated by a nonlinear portion. Note that the slope of the second linear portion [71 cm/(s Oe)] differs only slightly from the slope of the first linear portion [78 cm/(s Oe)]. Let us now assume that the dependence $V(H)$ can be adequately described in terms of the one-dimensional theory of domain-wall motion. According to this theory, the first and second linear portions of the $V(H)$ curve (Fig. 3) are associated with the stationary and precessional motion of domain walls. Within this approximation, we use the following relationship for the dimensionless attenuation parameter [11]:

$$\alpha = (\mu/\mu_0 - 1)^{-1/2}. \qquad (2)$$

As a result, we obtain $\alpha = 3.2$. However, as was shown earlier in [15], the $V(H)$ curve at this value of the dimensionless attenuation parameter contains no nonlinear portion [15]. Therefore, the second linear portion adjacent to the nonlinear portion of the $V(H)$ curve should be attributed to the domain-wall motion occurring through the mechanism of spin wave radiation [12, 16]. This hypothesis is supported by the fact that, in a narrow range of acting magnetic fields H at the boundary between the nonlinear and second linear portions of the $V(H)$ curve, the circular reversed domains undergo spatial distortions similar to those observed in thulium-containing garnet ferrite single-crystal films in the vicinity of the angular momentum compensation point [12].

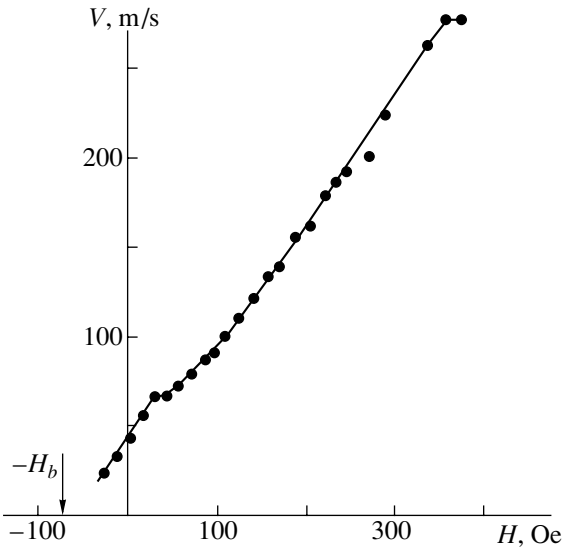

Fig. 3. Dependence of the domain-wall velocity V on the acting magnetic field H for sample **II**-1. The arrow indicates the magnetic bias field.

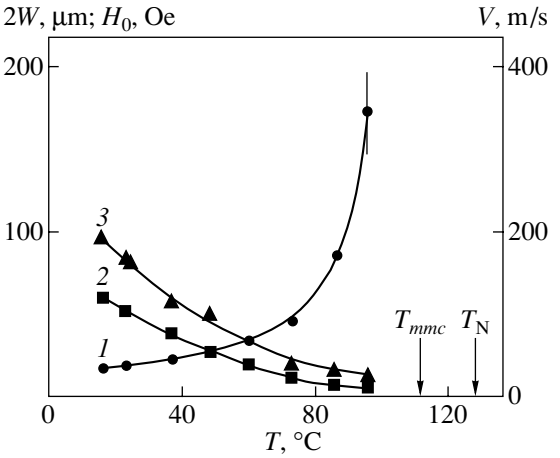

Fig. 4. Temperature dependences of (*1*) the period of equilibrium strip domains $2W$, (*2*) the collapse field of bubble domains H_0, and (*3*) the domain-wall velocity V at $H_p = 168$ Oe and $H_b = 72$ Oe for sample **II**-1. Arrows indicate the temperature of magnetic moment compensation T_{mmc} and the Néel temperature T_N.

The dependence $V(H)$ shown in Fig. 3 exhibits unusual behavior: the initial points of the first linear portion lie in the range of negative H values. This behavior can be explained by the fact that the internal effective magnetic field is directed along the bias field. It is assumed that the internal effective magnetic field can be induced, for example, by a high-coercivity transition surface layer whose state remains unchanged under the action of the pulsed magnetic field. The formation of this layer is indirectly confirmed by the fact that, upon heating, the film, as a whole, approaches the magnetic moment compensation point T_{mmc} (Fig. 4).

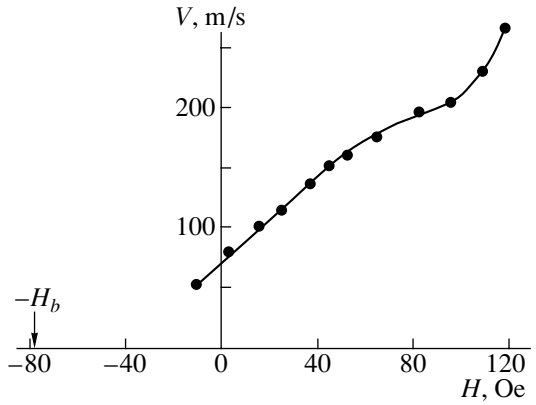

Fig. 5. Dependence of the domain-wall velocity V on the acting magnetic field H for sample **III**-4. The arrow indicates the magnetic bias field.

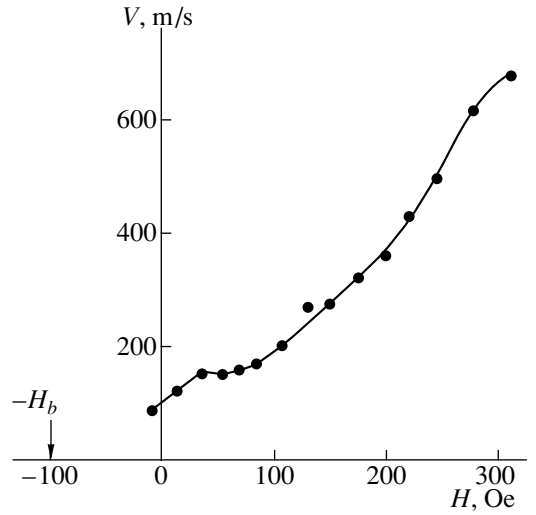

Fig. 6. Dependence of the domain-wall velocity V on the acting magnetic field H for sample **III**-5. The arrow indicates the magnetic bias field.

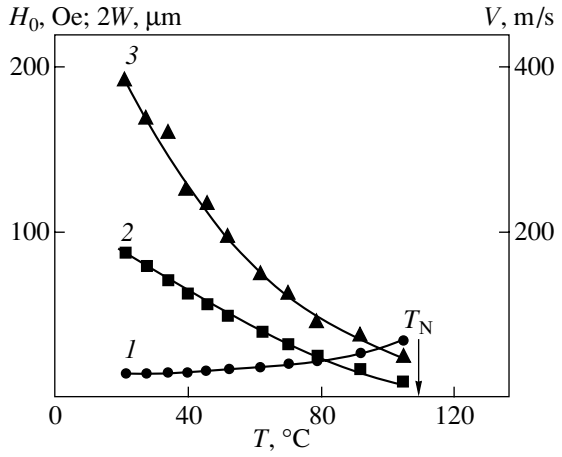

Fig. 7. Temperature dependences of (*1*) the period of equilibrium strip domains $2W$, (*2*) the collapse field of bubble domains H_0, and (*3*) the domain-wall velocity V at H_p = 152 Oe and H_b = 93 Oe for sample **III**-4. The arrow indicates the Néel temperature T_N.

It should be noted that, upon heating, sample **II**-1, unlike sample **I**-4, is characterized by a monotonic increase in the period of equilibrium strip domains (curve *1* in Fig. 4) and a monotonic decrease in the domain-wall velocity at a constant field H (curve *3* in Fig. 4). This suggests that the angular momentum compensation point lies in the temperature range below room temperature.

Figures 5 and 6 represent the dependences $V(H)$ for samples **III**-4 and **III**-5, respectively. It can be seen that, for these samples, the $V(H)$ curve consists of an initial linear portion, a nonlinear portion, and a portion with an increased differential mobility. A similar behavior of the dependences $V(H)$ was observed earlier in [14]. As in the case of sample **II**-1, the initial points of the first linear portion lie in the range of negative H values and the extension of this portion intersects the abscissa axis between the points $H = -H_b$ and 0. Therefore, the internal effective magnetic field in bismuth–ytterbium-containing garnet ferrite single-crystal films is weaker than the bias field.

The temperature dependences $2W(T)$, $H_0(T)$, and $V(T)$ at a constant field H for samples **III**-4 and **III**-5 are shown in Figs. 7 and 8, respectively. Upon heating, samples **III**-4 and **III**-5, like sample **II**-1, are characterized by an increase in the period of equilibrium strip domains (curves *1* in Figs. 7, 8) and a decrease in the domain-wall velocity at a constant field H (curves *3* in Figs. 7, 8). For all the studied samples, the collapse field of bubble domains decreases with an increase in the temperature (curves *2* in Figs. 2, 4, 7, 8). The temperature dependence of the critical velocity V_{cr}, which corresponds to the terminal point of the first linear portion in the $V(H)$ curve for sample **III**-5, is also depicted in Fig. 8 (curve *4*). It can be seen that the temperature dependence of the critical velocity for this sample exhibits a maximum at the angular momentum compensation point, as is the case with thulium-containing films [12].

Figure 9 shows the dependences $V(H)$ measured at different temperatures but in the same bias field. As is clearly seen from this figure, an increase in the temperature leads to a shift of the $V(H)$ curves toward the right. This indicates that the internal effective magnetic field, like the saturation magnetization, decreases upon heating of bismuth–ytterbium-containing garnet ferrite single-crystal films.

As can be seen from Fig. 9, the largest initial linear portion of the $V(H)$ curve is observed at T = 30.5°C. This temperature is close to the angular momentum compensation point. As could be expected [12], the domain-wall mobility decreases away from the angular momentum compensation point.

It is worth noting that the second linear portion, whose slope is considerably smaller than the slope of the first linear portion, is absent in all the $V(H)$ curves (Figs. 1, 3, 5, 6, 9). Recall that the presence of the second linear portion in the $V(H)$ curve is characteristic of

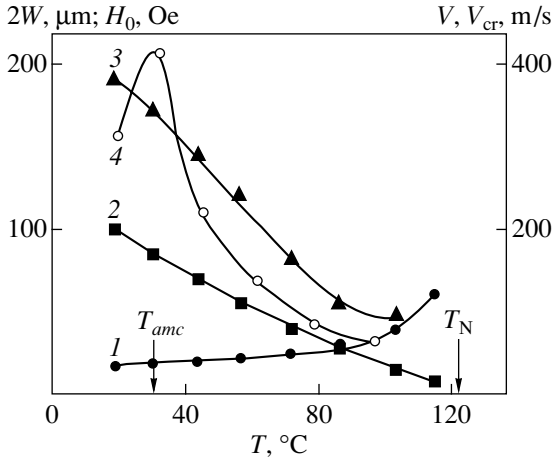

Fig. 8. Temperature dependences of (*1*) the period of equilibrium strip domains $2W$, (*2*) the collapse field of bubble domains H_0, (*3*) the domain-wall velocity V at H_p = 297 Oe and H_b = 99 Oe, and (*4*) the critical velocity V_{cr} at the terminal point of the initial linear portion in the $V(H)$ curve for sample **III**-5. Arrows indicate the temperature of angular momentum compensation T_{amc} and the Néel temperature T_N.

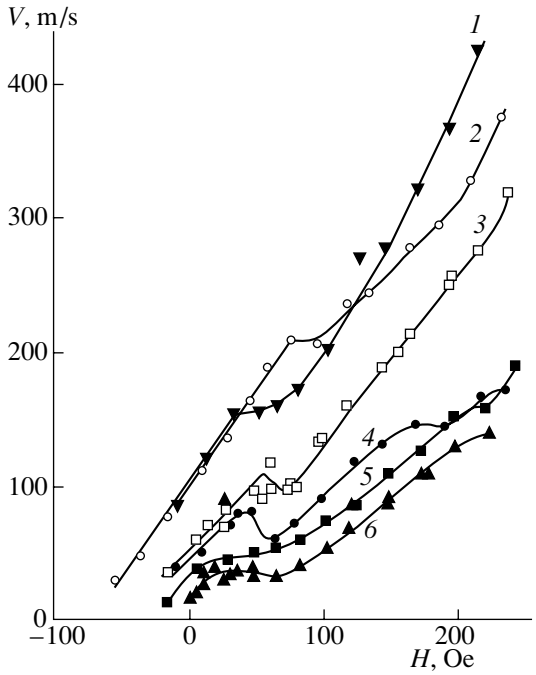

Fig. 9. Dependences of the domain-wall velocity V on the acting magnetic field H for sample **III**-5 at the magnetic bias field H_b = 100 Oe and different temperatures. T, °C: (*1*) 18, (*2*) 30.5, (*3*) 44, (*4*) 60.5, (*5*) 78.5, and (*6*) 96.5.

europium- [3], erbium- [9], and thulium-containing [12] garnet ferrite single-crystal films with bismuth in the vicinity of the angular momentum compensation point. Therefore, the precessional mechanism is not responsible for the motion of domain walls in ytterbium-containing films. Apparently, this circumstance can be associated with the internal effective magnetic field.

4. CONCLUSIONS

Thus, bismuth–ytterbium-containing garnet ferrite single-crystal films of the composition $(Bi,Yb)_3(Fe,Ga)_5O_{12}$ were examined in the vicinity of the angular momentum compensation point upon pulsed magnetization reversal. The results obtained in this study can be summarized as follows. (i) The dependence of the domain-wall velocity on the acting magnetic field has no portion that can be attributed to the precessional mechanism of domain-wall motion. (ii) There arises an internal effective magnetic field that weakens the acting magnetic field. (iii) The internal effective magnetic field does not exceed the magnetic bias field. (iv) The initial domain-wall mobility and the critical velocity corresponding to a disturbance of the stationary domain-wall motion reach a maximum at the angular momentum compensation point.

REFERENCES

1. V. V. Randoshkin and A. Ya. Chervonenkis, *Applied Magneto-Optics* (Énergoatomizdat, Moscow, 1990).
2. V. I. Zorya, I. Yu. Zueva, V. V. Randoshkin, *et al.*, Zh. Tekh. Fiz. **54** (7), 1381 (1984) [Sov. Phys. Tech. Phys. **29**, 802 (1984)].
3. V. V. Randoshkin and V. B. Sigachev, Zh. Tekh. Fiz. **58** (12), 2350 (1988) [Sov. Phys. Tech. Phys. **33**, 1432 (1988)].
4. V. V. Randoshkin, M. V. Logunov, Yu. N. Sazhin, *et al.*, Pis'ma Zh. Tekh. Fiz. **18** (4), 71 (1992) [Sov. Tech. Phys. Lett. **18**, 122 (1992)].
5. V. V. Randoshkin, V. V. Efremov, and E. É. Shusherova, Pis'ma Zh. Tekh. Fiz. **19** (2), 43 (1993) [Tech. Phys. Lett. **19**, 54 (1993)].
6. V. V. Randoshkin, V. V. Efremov, M. V. Logunov, and Yu. N. Sazhin, Pis'ma Zh. Tekh. Fiz. **19** (2), 28 (1993) [Tech. Phys. Lett. **19**, 48 (1993)].
7. A. A. Aĭrapetov, M. V. Logunov, V. V. Randoshkin, *et al.*, Pis'ma Zh. Tekh. Fiz. **18** (4), 79 (1992) [Sov. Tech. Phys. Lett. **18**, 125 (1992)].
8. A. A. Aĭrapetov, M. V. Logunov, V. V. Randoshkin, *et al.*, Fiz. Tverd. Tela (St. Petersburg) **34** (5), 1640 (1992) [Sov. Phys. Solid State **34**, 871 (1992)].
9. V. V. Randoshkin and V. B. Sigachev, Fiz. Tverd. Tela (Leningrad) **29** (9), 2658 (1987) [Sov. Phys. Solid State **29**, 1531 (1987)].
10. N. V. Zabolotnaya, V. V. Osiko, V. V. Randoshkin, *et al.*, Pis'ma Zh. Tekh. Fiz. **10** (13), 788 (1984) [Sov. Tech. Phys. Lett. **10**, 331 (1984)].
11. V. V. Randoshkin and V. B. Sigachev, Pis'ma Zh. Éksp. Teor. Fiz. **42** (1), 34 (1985) [JETP Lett. **42**, 41 (1985)].
12. V. V. Randoshkin and V. B. Sigachev, Fiz. Tverd. Tela (Leningrad) **32** (1), 246 (1990) [Sov. Phys. Solid State **32**, 138 (1990)].

13. N. A. Loginov, M. V. Logunov, and V. V. Randoshkin, Fiz. Tverd. Tela (Leningrad) **31** (10), 58 (1989) [Sov. Phys. Solid State **31**, 1684 (1989)].
14. A. A. Aĭrapetov, M. V. Logunov, and V. V. Randoshkin, Pis'ma Zh. Tekh. Fiz. **18** (2), 74 (1992) [Sov. Tech. Phys. Lett. **18**, 53 (1992)].
15. V. V. Randoshkin, Fiz. Tverd. Tela (St. Petersburg) **37** (3), 652 (1995) [Phys. Solid State **37**, 355 (1995)].
16. V. V. Randoshkin, Fiz. Tverd. Tela (St. Petersburg) **39** (8), 1421 (1997) [Phys. Solid State **39**, 1260 (1997)].
17. V. V. Randoshkin and V. B. Sigachev, Fiz. Tverd. Tela (Leningrad) **28** (5), 1522 (1986) [Sov. Phys. Solid State **28**, 859 (1986)].
18. V. V. Randoshkin, N. V. Vasil'eva, K. V. Stashun, and M. V. Stashun, Neorg. Mater. **35** (1), 1 (1999).
19. V. V. Randoshkin, M. V. Logunov, and V. B. Sigachev, Prib. Tekh. Éksp., No. 5, 247 (1985).
20. V. V. Randoshkin, Prib. Tekh. Éksp., No. 2, 155 (1995).

Translated by Borovik-Romanova

Physics of the Solid State, Vol. 45, No. 3, 2003, pp. 519–528. Translated from Fizika Tverdogo Tela, Vol. 45, No. 3, 2003, pp. 490–499.

MAGNETISM AND FERROELECTRICITY

Detection and Study of Magnetic Micro- and Nanostructures Using Dark-Field Optical Microscopy

V. I. Belotelov, A. S. Logginov, and A. V. Nikolaev

Moscow State University, Vorob'evy gory, Moscow, 119899 Russia

e-mail: bvi@osc.phys.msu.ru

Received April 8, 2002; in final form, July 1, 2002.

Abstract—The features of magnetic-microstructure imaging were studied using various configurations of dark-field magnetooptical microscopy. The potentials and limitations of the dark-field method were experimentally and theoretically analyzed as applied to magnetism studies. The experimental data showed the possibility of magnetooptical detection of localized magnetic structures of size smaller than or of the order of 0.1 μm. To calculate the angular spectrum of light scattered at magnetic inhomogeneities within a theoretical model, the method of electrodynamic tensor Green functions was employed. Within the theoretical model, a procedure was proposed and analyzed which allows real-time visualization of magnetization reversal of solitary single-domain nanoparticles or their regular arrays in order to study their dynamic and static characteristics. © *2003 MAIK "Nauka/Interperiodica".*

1. INTRODUCTION

Detailed study of the magnetization distributions on submicrometer spatial scales and the development of the corresponding high-resolution techniques is presently one of the most important problems in applied and fundamental micromagnetism. In the past decade, significant progress has been made in the development of methods for studying micro- and nanostructures with the advent and onrush of magnetic force microscopy, which is a version of scanning probe microscopy [1]. Currently, magnetic force microscopy is characterized by the best spatial resolution in studying magnetic microstructures (tens of nanometers [2]). However, its application offers a number of problems: complicated interpretation and identification of images, the uncontrollable influence of the microprobe on the magnetization distribution in samples and vice versa, the problem of positioning the force microscope tip above a surface point under study, and the low scanning velocity, which makes real-time observation of fast processes impossible [3].

However, dark-field optical microscopy techniques feature significant unrealized potential for detecting and studying such magnetic formations as domain boundaries and substructures (Bloch lines, Bloch points) characterized by an intricate magnetization distribution and a characteristic size of tenths and hundredths of a micrometer.

Dark-field optical microscopy is widely used in the studies of phase objects in physics, mineralogy, biology, etc. [4]. In the simplest version of this method, a sample is illuminated through a condenser with a diaphragmed center, so that the light flux incident onto the sample represents a hollow cone (Fig. 1). If the objective aperture is smaller than the condenser aperture, only light scattered at the sample phase structure hits the objective, forming a structure image.

In terms of spatial resolution, the dark-field method is virtually equivalent to conventional optical microscopy [4]. At the same time, the detection sensitivity of the method under consideration is much higher than that of conventional transmission microscopy, since the image is not subject to background illumination. This makes it possible to apply the dark field to observe and detect phase inhomogeneities smaller than or of the order of fractions of a micrometer (ultramicroscopy). Submicrometer magnetic structures may also be related to such phase inhomogeneities, because one can use the magnetooptical (Faraday, Kerr, Cotton–Mouton) effects. Currently, such magnetic structures attract significant inter-

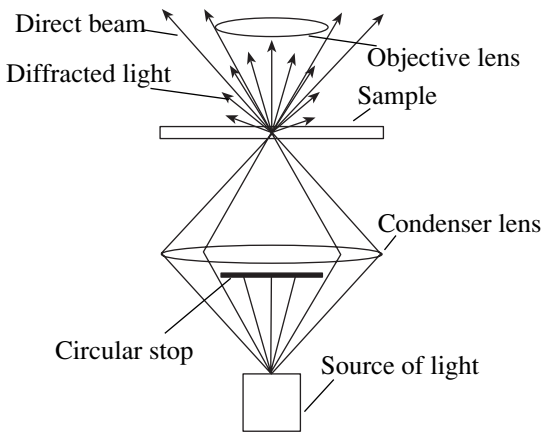

Fig. 1. Scheme of phase-object observation using the dark-field method.

1063-7834/03/4503-0519$24.00 © 2003 MAIK "Nauka/Interperiodica"

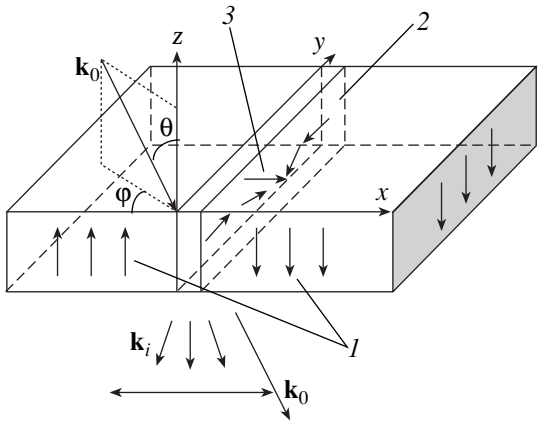

Fig. 2. Magnetization distribution in (*1*) domains, the (*2*) domain wall, and (*3*) Bloch line in a ferrite-garnet film. The optical scheme of observation: φ is the azimuth angle of the light incidence plane, θ is the light incidence angle, $\mathbf{k}_0$ is the incident light wave vector, and $\mathbf{k}_i$ is the scattered light wave vector.

est in the context of searches for new methods for data recording, storing, and reading.

The dark-field method was first applied to study magnetic media in [5], where the domain structure was visualized in ferrite-garnet (FG) films. A significant contribution to the development of magnetooptical dark-field microscopy was made by Thiaville and coworkers [6, 7], who optically detected vertical Bloch lines (VBLs) in FG films and described the visualization mechanism.

The VBLs represent stable magnetic vortices and separate domain wall (DW) regions of opposite polarity [8]. The VBL sizes in many typical FG films do not exceed tenths of a micrometer. In [6, 7], experiments were carried out using the anisotropic dark-field microscopy (ADM) method, which is a modification of the conventional dark-field method wherein a narrow beam is cut out from the dark-field illumination cone. In [6, 7], the light incidence plane was normal to the domain wall planes, which corresponded to the azimuth angle φ = 0° (Fig. 2).

In the ADM images obtained in [6, 7] there is no illumination from domains, while DWs are seen as contrast lines. Some portions of these lines exhibit lighter or darker regions, which are VBLs of different magnetic topology (Fig. 3, φ = 0°). Further studies showed that the possibility of observing Bloch lines in this dark-field configuration is related to the microscopic DW tilt in the VBL localization regions [9] rather than to light scattering immediately on the magnetization distribution in the Bloch line.

Over several years, the authors of this paper developed a dark-field method to observe submicrometer magnetic structures. Observations according to the Thiaville technique were successfully carried out and characteristic VBL images were obtained in [10, 11]. Furthermore, another dark-field configuration making it possible to observe Bloch lines was used. In this configuration, the light incidence plane is parallel to the domain walls, which corresponds to the azimuth angle φ = 90° (Fig. 2) [11]. There is no illumination either from domains or DWs in the images obtained in this configuration, while the VBLs are visualized as bright symmetric objects (Fig. 3, φ = 90°) regardless of magnetic topology. The theoretical study reported in [12] allowed us to conclude that the VBL visualization mechanism in the case under study differs from that suggested in [9] and is associated with light scattering on the VBL magnetic structure.

Thus, the results obtained in [6, 9–12] showed that the dark-field method can be used to detect magnetic structures of size ~0.1 μm. Varying the specific observation geometry [e.g., the angle θ of light incidence and the angle φ formed by the light incidence plane and the DW plane (Fig. 2)], it becomes possible to obtain various images of magnetic microstructures. In this case, the possibility of imaging through various mechanisms is not improbable. At the same time, many aspects related to the features of the dark-field microscopy methods as applied to magnetic studies, their potentials, and limitations remain obscure.

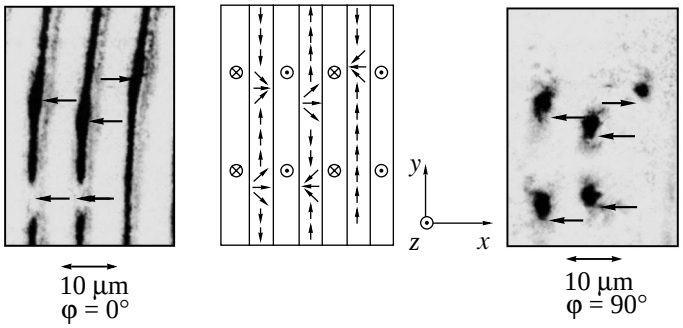

Fig. 3. Typical images of domain walls and Bloch lines obtained in observation configurations corresponding to the azimuth angles of light incidence φ = 0° and 90° (contrast is inverted). The central pattern schematically shows the magnetic structure of the sample region under study. The Bloch lines are indicated by arrows.

In this paper, we further develop the approach suggested in [12] to describe the magnetic structures imaged by the dark-field method. The approach is based on electrodynamic tensor Green functions. The potentials of various configurations of the ADM method are studied on the basis of the theory we developed and the corresponding experiments.

2. MAGNETOOPTICAL DIFFRACTION OF LIGHT AND MAGNETIC STRUCTURE IMAGING IN DARK-FIELD MICROSCOPY

Light diffraction from magnetic inhomogeneities in magnetic films was considered in [6, 13–15]. Most of those studies were devoted to determining the diffraction pattern resulting from the interaction between light and magnetic media. Little attention was given to the properties of the magnetic structure images produced by the optical system.

This study is dedicated specifically to the features of magnetic-structure images formed in various configurations of dark-field microscopy. According to [12], we consider the problem using the method of electrodynamic tensor Green functions.

The tensor Green functions $D_{\mu\nu}(\mathbf{r}, \mathbf{r}')$ are defined by the equations

$$\left(\frac{\partial^2}{\partial x_\lambda \partial x_\mu} - \delta_{\lambda\mu}\frac{\partial^2}{\partial x_\mu^2} - \varepsilon(\mathbf{r})\frac{\omega_0^2}{c^2}\delta_{\lambda\mu}\right)D_{\mu\nu}(\mathbf{r}, \mathbf{r}') = -\delta_{\lambda\nu}\delta(\mathbf{r}-\mathbf{r}'),$$

which are solved with ordinary Maxwell boundary conditions. Therefore, the expressions for the fields derived using the Green functions *a priori* meet these boundary conditions. The method of Green functions makes it possible to derive analytical formulas for the Fourier transform of the electric field of a diffracted wave.

Let us consider a film of a cubic ferrimagnet of thickness l placed on a transparent nonmagnetic substrate (Fig. 4). The middle plane of the film is taken to be the xy plane of the frame of reference. The unit vector directed along the film magnetization is $\mathbf{m} = \dfrac{\mathbf{M}}{M} = \mathbf{i}\cdot m_x + \mathbf{j}\cdot m_y + \mathbf{k}\cdot m_z$, where $\mathbf{M}$ is the magnetization vector of the film. Assuming that only the first-order (in magnetization) magnetooptical (MO) effects take place, the dielectric tensor of the film is given by (see [16])

$$\varepsilon = \varepsilon(\mathbf{r})I + igm(\mathbf{r}), \qquad (1)$$

where $\varepsilon(\mathbf{r})$ is the dielectric constant of the medium in the absence of magnetization ($\mathbf{M} = 0$), I is the unit tensor, g is the magnitude of the gyration vector $\hat{\mathbf{g}} = g\hat{\mathbf{m}}$, and

$$m(\mathbf{r}) = \begin{pmatrix} 0 & -m_z(\mathbf{r}) & m_y(\mathbf{r}) \\ m_z(\mathbf{r}) & 0 & -m_x(\mathbf{r}) \\ -m_y(\mathbf{r}) & m_x(\mathbf{r}) & 0 \end{pmatrix}.$$

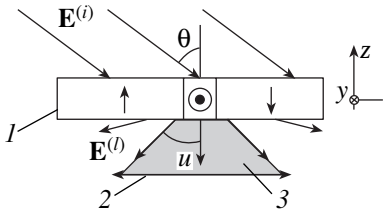

Fig. 4. Dark-field patterning: (*1*) magnetic film (a magnetic structure consisting of two domains separated by a domain wall), (*2*) objective, and (*3*) cone of light passing through the objective.

Let the film magnetization be uniform along the z axis; this is typically assumed when describing magnetization distributions in magnetic films [8]. Therefore, to avoid unreasonably extensive computations, we consider an effective infinitely thin layer instead of a magnetic film of thickness l. In this case, the phase shift (dependent on the film thickness and the gyration vector) between oppositely polarized circular waves at the film output is taken into account, within the model under consideration, by introducing an effective parameter G in the right-hand side of the Maxwell equation [see Eq. (2)].

Let a linearly polarized plane monochromatic wave with $\mathbf{E}^{(i)}(\mathbf{r}, t) = \mathbf{E}^{(i)}\exp[i(\mathbf{k}_0\mathbf{r} - \omega_0 t)]$ be incident on the plate at an angle θ (Fig. 4). Then, with allowance for Eq. (1), the Maxwell equation is written as

$$\mathrm{curlcurl}\mathbf{E}(\mathbf{r}) - k_0^2\varepsilon(\mathbf{r})\mathbf{E}(\mathbf{r}) = k_0^2((\varepsilon-1)\mathbf{E} + G[\mathbf{m}\times\mathbf{E}])\delta(z), \qquad (2)$$

where $\varepsilon(\mathbf{r}) = 1$ outside the substrate (plate) and $\varepsilon(\mathbf{r}) = \varepsilon$ inside the substrate.

Equation (2) with the small parameter G can be solved by the method of successive approximations. In this case, we restrict ourselves to the first approximation: $\mathbf{E} = \mathbf{E}^{(0)} + \mathbf{E}^{(1)}$, where $\mathbf{E}^{(0)}$ is the electric field neglecting the magnetic properties of the medium and $\mathbf{E}^{(1)}$ is the electric field of the light wave diffracted from the magnetization distribution.

Expressions for the field $\mathbf{E}^{(0)}$ are well known and are conventionally written as Fresnel formulas. The Fourier transform of the field $\mathbf{E}^{(1)}$ can be obtained using the Fourier transforms of the Green functions

$$d_{\mu\nu}(\mathbf{k}_\parallel, z, z') = \int d(\mathbf{r}_\parallel - \mathbf{r}_\parallel')\exp(-i\mathbf{k}_\parallel(\mathbf{r}_\parallel - \mathbf{r}_\parallel'))D_{\mu\nu}(\mathbf{r}, \mathbf{r}'), \qquad (3)$$

where $\mathbf{r}_\parallel$ and $\mathbf{r}_\parallel'$ are the radius-vector components lying in the xy plane and $\mathbf{k}_\parallel$ is the wave-vector component parallel to the xy plane (Fig. 2). The Fourier transforms of the Green functions are determined by solving ordinary differential equations. This procedure is outlined in [17].

Thus, taking into account Eq. (3), we write

$$\hat{E}_\mu^{(1)}(\mathbf{k}_\parallel, z) = -k_0^2 G d_{\mu\nu}(\mathbf{k}_\parallel, z, 0-)\hat{m}_{\nu k}(\mathbf{k}_\parallel - \mathbf{k}_\parallel^0)\hat{E}_k^{(0)}(\mathbf{k}_\parallel^0, 0-), \quad z < 0, \tag{4}$$

where $\mathbf{k}_\parallel = (k_x, k_y, 0)$ is the projection of the wave vector onto the film plane; $d_{\mu\nu}(\mathbf{k}_\parallel, z, z')$ are the Fourier transforms of the Green functions; $d_{\mu\nu}(\mathbf{k}_\parallel, z, 0-) = \lim_{z' \to 0-} d_{\mu\nu}(\mathbf{k}_\parallel, z, z')$ and $\hat{m}_{\nu k}(\mathbf{k}_\parallel)$ are the Fourier transforms of the elements of the tensor m; and $\hat{E}_k^{(0)}(\mathbf{k}_\parallel^0, 0-) = \lim_{z' \to 0-} \hat{E}_k^{(0)}(\mathbf{k}_\parallel^0, z')$.

Relation (4) describes the angular spatial spectrum of the field of the wave diffracted from the magnetic structure. The scattered wave field can be written as a superposition of electromagnetic plane waves with various wave vectors $\mathbf{k}_\parallel$ and complex amplitudes defined by Eqs. (4).

Based on Eqs. (4), one can theoretically investigate studies of images obtained in direct light or by using various modifications of the dark-field technique.

The microscopic image is formed by those spatial Fourier components of the wave field that arrive at the microscope objective. A set of harmonics passed through the system is controlled by the objective numerical aperture NA = $n\sin u$, where n is the refractive index of the medium surrounding the objective and u is the aperture angle of the objective (Fig. 4). Thus, the features of the image formed in the optical system are controlled by the inverse Fourier transform that takes into account only the field harmonics passed through the system:

$$E_\mu^{(1)} = \frac{1}{4\pi^2} \int\limits_{\{\mathbf{k}_\parallel\}} d\mathbf{k}_\parallel \hat{E}_\mu^{(1)} e^{i\mathbf{k}_\parallel}, \tag{5}$$

where $\{\mathbf{k}_\parallel\}$ is the set of wave-vector components $\mathbf{k}_\parallel$ of harmonics passed through the optical system.

3. BASIC PROPERTIES OF MAGNETOOPTICAL DIFFRACTION. IMAGING CONDITIONS

On the basis of the analytical expressions in Section 2, without recourse to a numerical experiment, some conclusions can be drawn as to the conditions of magnetic-structure imaging in dark-field microscopy.

Since we restrict ourselves to the approximation linear with respect to magnetization and consider only the gyrotropy (Faraday) effect, the pattern obtained depends on the interaction of light with only those magnetization components that have a nonzero projection onto the incident light wave vector $\mathbf{k}_0$. Furthermore, light diffraction takes place only if these magnetization components vary along the vector $\mathbf{k}_0$. Thus, if some magnetization components in the structure under study vary only along a single direction, we can study either the distribution of these components or (eliminating information on them from the image) other components of the vector **M** by varying the relative positions of the illumination beam and the magnetic structure.

The magnetooptical diffraction is characterized by the following important property. Within the Faraday effect approximation, light subjected to interaction with a magnetic structure is polarized in the plane normal to the polarization plane of incident light, whereas the light diffracted from nonmagnetic inhomogeneities of the sample remains nonpolarized. Therefore, when observing magnetic structures in the dark-field configurations, the polarizer and analyzer should be crossed in order to eliminate the component of light scattered on nonmagnetic inhomogeneities.

4. POTENTIALS OF VARIOUS DARK-FIELD MICROSCOPY SCHEMES

Based on the approach described above, we analyze possible applications of the dark-field method in magnetic studies.

Let the samples under consideration have the crystallographic orientation ⟨111⟩ and a periodic structure of stripe domains with Bloch-type domain walls [8]. The vector **M** in a DW uniformly rotates when one goes from one domain to the next; i.e., the magnetization rotation angle is proportional to the corresponding coordinate. Thus, in the frame of reference with the z and x axes perpendicular to the film and DW planes, respectively (Fig. 2), the magnetization vector components inside a Bloch wall centered at $x = 0$ are written as

$$m_x = 0, \quad m_y = \cos\left(\frac{\pi x}{\Delta}\right), \quad m_z = \sin\left(\frac{\pi x}{\Delta}\right)$$

where Δ is the DW width parameter [8].

First of all, we expand on some basic properties of dark-field images.

4.1. General Properties of Dark-Field Images

Based on general considerations of magnetooptical diffraction and by analogy with "conventional" dark-field microscopy, one might expect magnetic inhomogeneities representing an **M** change over distances of the order of the used light wavelength λ to be adequately displayed in the magnetooptical dark field. Indeed, a numerical experiment showed that the intensity of images in the dark-field method and their consistency with the real distribution of the vector **M** depend on the size of the light-diffraction region. For example, if this region is much larger than the wavelength λ of light used for observation, the image brightness is extremely low and the image itself does not always adequately reflect the real magnetization distribution in the sample. If the inhomogeneity size is smaller than λ,

such a structure can be visualized; however, its visible size will correspond to the resolution limit of the optical system.

The following two basic cases of magnetooptical diffraction can be distinguished.

(i) Light scattering from a magnetic inhomogeneity acting as a transitional domains between regions with different (due to the Faraday effect) phase characteristics which does not interact immediately with incident light because of the corresponding mutual orientation of the wave vector and the magnetization in an inhomogeneity (e.g., a DW separating two uniformly magnetized domains or a VBL separating DW regions of opposite polarity, see Figs. 3, 5a).

(ii) Light scattering on an inhomogeneity surrounded by regions with identical phase characteristics, e.g., on a solitary submicrometer domain (Fig. 5).

When the inhomogeneity size r (Fig. 5) is smaller than λ, the situation is as follows. In the first case, the image features are independent of the transition region width, since diffraction takes place from the refractive-index jump and the total change in **M** (hence, in the refractive index) is nonzero on the scale of the wavelength λ. In the second case, the image brightness is abruptly lowered as the inhomogeneous-region size decreases. This effect is due to the fact that the resulting change in **M** tends to zero over distances comparable to λ (Fig. 5).

4.2. Spatial Resolution and Detection Sensitivity of the Dark-Field Method

We now discuss important characteristics of optical observation, such as the spatial resolution and detection sensitivity.

As mentioned in Section 1, the resolution of dark-field optical microscopy is almost equivalent to the resolution of transmission microscopy [4]. A numerical simulation of images of infinitely thin DWs shows that the dark-field method allows their observation as separate objects if the distances between them are not shorter than 0.6 μm (at $\lambda = 0.5$ μm, NA = 0.4). This estimate corresponds to the resolution limit according to the Rayleigh criterion at given NA and λ and conforms to the general consideration of the dark-field method resolution in [4].

In contrast to the spatial resolution, the detection sensitivity of magnetooptical dark-filed microscopy is much higher than that of conventional bright-field microscopy. Indeed, in the latter case, a micromagnetic structure is generally observed against the background of illumination from domains; therefore, the signal-to-background ratio is of importance in observing the structure.

In the case of observation in scattered light, there is no background illumination from magnetically uniform regions in any magnetic configuration. Hence, in observing submicrometer **M** inhomogeneities, the signal-to-noise ratio, which is much larger than the signal-to-background ratio in the case of bright-field microscopy, is of importance.

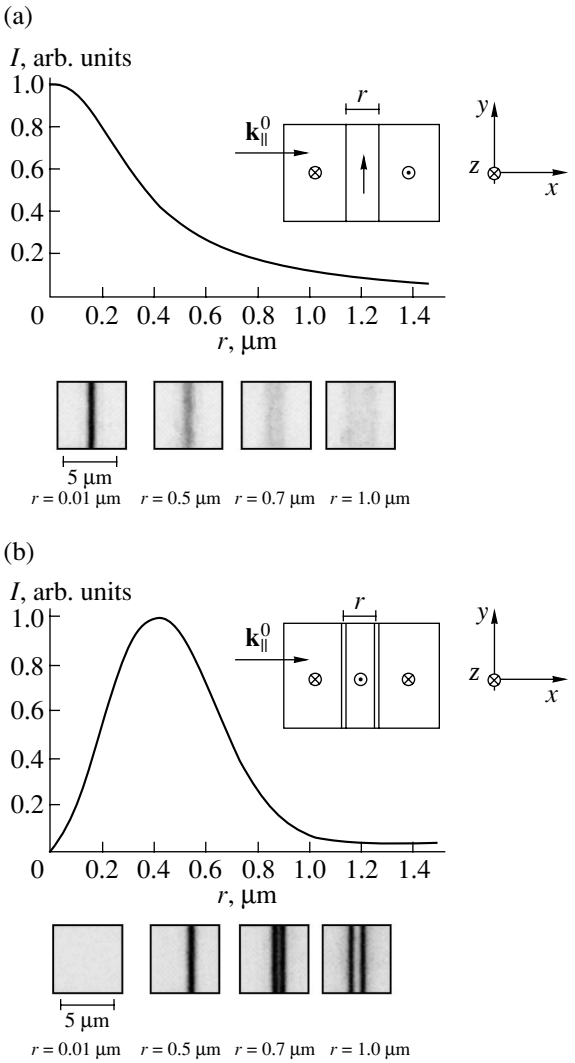

Fig. 5. Dependences of the image intensity for (a) a DW separating two uniformly magnetized domains and (b) a solitary domain on their size r. In case (b), the DWs are assumed to be infinitely thin. The corresponding calculated images are shown under both dependences. In the simulation, the incident light wavelength and the numerical aperture of the optical system were taken to be $\lambda = 0.5$ μm and NA = 0.4, respectively. The insets show the corresponding magnetic configurations and the illumination directions.

To demonstrate the high detection sensitivity of ADM, we calculated (for $\lambda = 0.5$ μm, NA = 0.4) the images of two domains, 2 and 0.1 μm in size (Fig. 6). The former domain is reliably detected in both cases of conventional transmission microscopy (the polarizer and analyzer are crossed, which corresponds to the "DW contrast" observation) and ADM. For the latter domain, a different situation arises: the 0.1-μm domain is beyond the optical resolution and cannot be detected using the conventional method. In the anisotropic dark

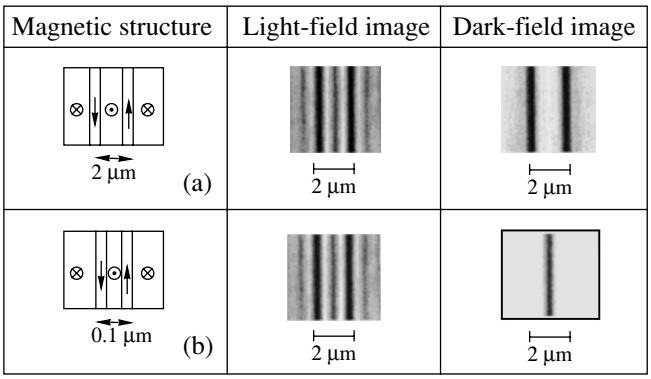

Fig. 6. Calculated images of two domains (a) 2 and (b) 0.1 μm in size. (The contrast is inverted, λ = 0.5 μm, NA = 0.4.)

field, the domain image is not quite adequate: the domain walls are not resolved. Nevertheless, the domain is confidently detected.

5. OBSERVATION OF THE COLLAPSE OF BUBBLE DOMAINS

In order to compare the detection sensitivities of ADM and conventional transmission microscopy and to estimate the ADM potentials for visualization of magnetic submicrometer particles, we experimentally observed the collapse of bubble domains (BDs). The experimental high-speed-photography (HSP) and dark-field setup is described in detail in [18].

The experiment was carried out using a uniaxial magnetic film of $(BiTm)_3(FeGa)_5O_{12}$ ferrite-garnet characterized by the following parameters: ⟨111⟩ crystallographic orientation, domain spacing of 8.5 μm, specific Faraday rotation of 17300 deg/cm, saturation magnetization of $4\pi M_s$ = 173 G, uniaxial anisotropy constant K_u = 4500 erg/cm^3, quality factor Q = 3.8, film thickness of 7.5 μm, and magnetic field of the BD collapse H_{col} = 125 Oe.

A dc bias magnetic field H = 110 Oe was applied normally to the film surface, because of which the stripe domains that were magnetized oppositely to the field narrowed to 3 μm. Rectangular magnetic field pulses 500 ns in duration with amplitude H = 25 Oe were applied along the dc bias field. The pulses partitioned the stripe domains magnetized oppositely to the bias field into separate BDs, which then collapsed. This process was observed using the HSP [19] and ADM methods, as well as the conventional bright-field method with crossed and nearly crossed polarizers (the DW contrast and domain contrast, respectively).

In the HSP method, the sample was illuminated by nanosecond optical pulses applied with a tuned delay with respect to the magnetic field pulses perturbing the domain structure.

By varying the time shift t between the leading edge of a magnetic field pulse and the illumination pulse, one can obtain magnetooptical images of instantaneous dynamic configurations of magnetization and observe the evolution of the magnetization structure response to an external magnetic field.

The experimental technique did not allow us to observe the formation and collapse of the same BD simultaneously in both the dark-field and transmission configurations. It was also technically difficult to make continuous or sequential observations of the size variation of a fixed domain. Nevertheless, by comparing images of various stages of the BD formation and collapse in various observation configurations, we revealed the basic recurrent stages of the process (Fig. 7).

The characteristic time of the initiation of stripe-domain partitioning into BDs is ~150 ns. In this case, nonuniform compression of domains is observed, which is probably caused by the difference in dynamic characteristics between various domain regions (due to

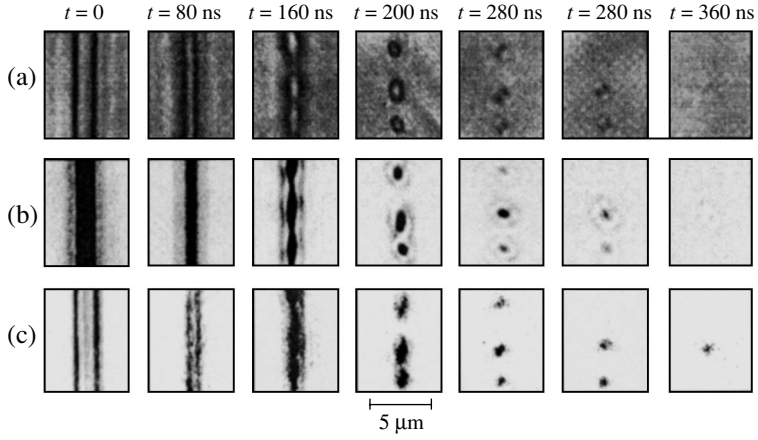

Fig.7. Observation of the dynamic transformation of the stripe domain structure in an external periodic bias magnetic field in three different observation configurations: transmission microscopy with (a) domain-wall and (b) domain contrasts and (c) anisotropic dark-field microscopy at φ = 90° (the contrast is inverted).

the presence of Bloch lines in the DW). At $t \sim 200$ ns, domains are generally already partitioned into separate fragments, which are, in fact, BDs. In all three cases, the observed image sizes of formed BDs decrease in time down to 0.8 μm, which is, in fact, the resolution limit of this optical system (NA = 0.4, λ= 0.5 μm). The image contrast also decreases. Probably, this is caused by a decrease in the real sizes of domains to hundreds and tens of nanometers; however, it is also not improbable that a change in their magnetic structure also somewhat contributes to the process. There are several models describing bubble domain collapse: with the formation of an end-face DW and with a nonuniform (across the thickness) decrease in the BD diameter [8]. However, it is not clear which process took place in the experiments we carried out. One can see from Fig. 7 that BDs are almost undetectable in both bright-field cases at $t \sim 350$ ns, because their images fade against background illumination. However, BDs can be visualized using ADM on the same time scale. Since the background is dark (we note that the contrast is inverted in Fig. 7), the pattern contrast becomes worse to a lesser extent, while the brightness decreases by hundreds of times. At later moments of time, it fails to visualize BDs in all three observation configurations.

These experimental results confirm our statement that the detection sensitivity of ADM is high when detecting magnetic submicrometer structures. The high contrast of dark-field images is limited only by the noise level of the receiving system. Thus, the technique of magnetooptical dark-field microscopy has great potential for the detection of solitary magnetic submicrometer structures. Let us next consider the possible application of the dark-field method to the study of static and dynamic characteristics of single-domain magnetic nanoparticles.

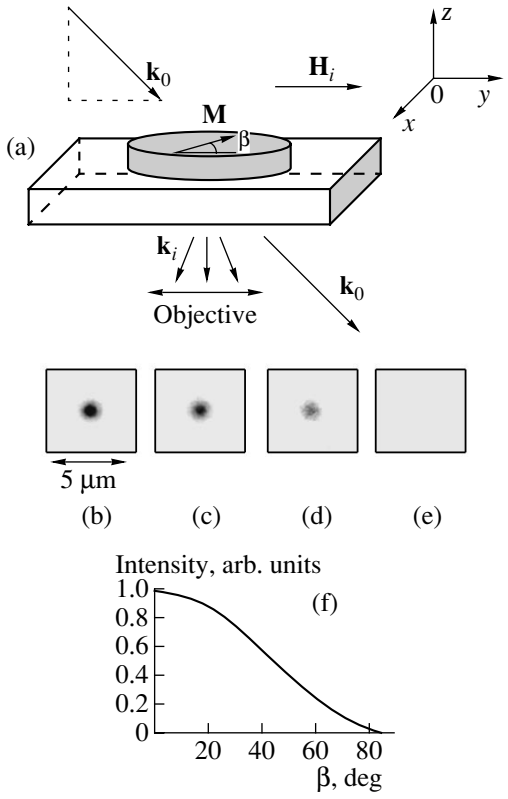

Fig. 8. Simulation of magnetization reversal images of a single-domain nanoparticle 50 nm in diameter in ADM at various angles β between the nanoparticle magnetization vector and the light incidence plane (incident light is polarized in the incidence plane; NA = 0.4, λ = 0.5 μm). (a) The light incidence geometry and (b–e) the patterns at (b) β = 0°, (c) 30°, (d) 60°, and (e) 90°. (f) The dependence of the relative intensity of the nanoparticle image on the angle β (the contrast is inverted).

6. POTENTIALS OF DARK-FIELD MICROSCOPY OF THE STUDY OF MAGNETIC NANOPARTICLES

Quantum magnetic disks, which are new media for data recording and reading [20, 21], are currently developed on the basis of nanoparticles. Data may be recorded on such disks in the ordinary way, namely, by applying local magnetic fields. Therefore, magnetization reversal of nanoparticles attracts particular interest [22]. Calculations show this process to be rather intricate. This is because a single-domain structure can become polydomain [23] or vortical [22, 24] during magnetization reversal if the particle sizes exceed several tens of nanometers.

Furthermore, if the distances between particles are of the order of their dimensions, the interaction between the magnetic moments of neighboring particles has a significant effect on magnetization reversal [25]. Small particle sizes complicate corresponding experiments. For example, experiments on magnetization reversal of nanoparticles by using scanning magnetic-force microscopy (such as those reported in [26]) do not allow one to study all the features of the process and, in principle, give no information on its dynamic characteristics.

The high sensitivity of the ADM method suggests its possible application for magnetic nanoparticles.

Let us consider a solitary single-domain particle 50 nm in diameter whose magnetization vector is aligned with an external magnetic field initially directed along the substrate and light-incidence planes (Fig. 8).

When the field direction is reversed in the substrate plane, reversal of the particle magnetization occurs. We assume that the nanoparticle magnetization **M** gradually turns through 180° and again becomes aligned with the field. Let the angle between the particle magnetization and the incident light plane be β.

The calculated nanoparticle images in the case of ADM observations at various magnetization reversal stages are shown in Figs. 8b–8f. One can see that the intensity of the pattern heavily depends on the orientation of the vector **M**. The brightness is maximum when

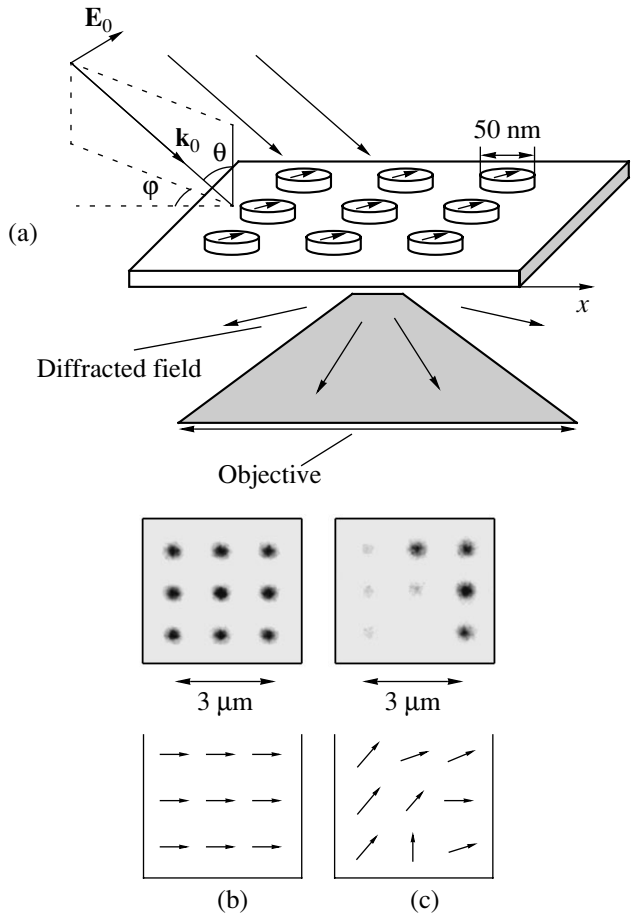

Fig. 9. (a) Scheme of ADM observation of a nanoparticle array and (b, c) the dark-field array images obtained at a distance between particles of 0.6 μm and various magnetization orientations of particles (the contrast is inverted, NA = 0.4, λ = 0.5 μm).

the particle is magnetized in the incidence plane (β = 0°) and decreases in the course of magnetization reversal (with increasing β) following the law $I = I_0\cos^2\beta$.

Thus, the ADM technique is sensitive to the orientation of the nanoparticle magnetization vector and, being simple, may be useful and handy for studying the magnetization reversal. Combination of the ADM technique with a high-speed photography setup presents a means for studying this process *in situ* with at least a nanosecond temporal resolution [18], i.e., during exposure to magnetic field pulses. We note that, according to theoretical and experimental estimations, the time of nanoparticle magnetization reversal is 10^{-12}–10^{-9} s [27, 28].

Let us pass from a solitary nanoparticle to an array of uniformly distributed nanoparticles (Fig. 9). When the distance between nanoparticles exceeds 0.6 μm (λ = 0.5 μm, NA = 0.8), particles are visualized separately and, as in the case of a solitary particle, their magnetization state can be immediately observed (Fig. 9b). In this case, one can study the simultaneous magnetization reversal of the whole set of nanoparticles, the mutual influence of particles during magnetization reversal of only a fraction of the array, the nonuniformity in the magnetization direction of separate particles can be detected (Fig. 9c), etc.

If the distances between separate are particles shorter than the light wavelength λ, the particle images merge and the array is represented as a uniformly illuminated field. Although separate observation of particles is impossible, some conclusions can be drawn as to the static and dynamic properties of the system by studying the image brightness in various illumination geometries and by measuring the time dependence of the ADM pattern intensity during magnetization reversal.

If all nanoparticles have uniform properties, the image of the remagnetized array of particles in ADM will be similar to that described above and shown in Fig. 8, which illustrates the magnetization reversal of a solitary nanoparticle. However, in practical cases, separate particles of the array can exhibit nonuniform properties, which manifests itself, e.g., in different rates of **M** turning of separate particles. When considering this situation, we will suppose that a pulsed external magnetic field applied in the direction opposite to the initial uniform magnetization of the array of particles causes the vector **M** of nanoparticles to turn gradually through 180° and to become aligned with the field. We accept that the array contains a certain number of "fast" particles which are remagnetized quicker than others by a factor of 1.4. Their relative concentration is *N*.

The calculated time dependences of the ADM image intensity during magnetization reversal of arrays with concentrations $N = 0$, 0.25, and 0.4 of fast particles are shown in Fig. 10. One can see that the dependence changes its shape with the number of fast particles: at $N = 0$, the dependence is symmetrical; as *N* increases, the minimum shifts to shorter times and the dependence shape becomes more asymmetrical.

The ADM technique can also yield data on the magnetization state of an array of particles in the static case. Indeed, by varying the azimuth angle φ of light incidence (Fig. 9), one can construct the dependence of the array image intensity on the angle φ. The shape of the curves will depend on the scatter in the nanoparticle magnetization directions. To check this conclusion, we numerically simulated the ADM image in the case where there are *N* percent of nanoparticles whose vector **M** is directed at an angle of 45° to the magnetization direction of other particles. One can see from Fig. 11 that the minima and maxima shift in position with the number *N*, while the peak intensity decreases.

As follows from the above discussion, notwithstanding the fact that separate ADM observation of nanoparticles is impossible at distances between particles shorter than λ, the change in the dark-field image intensity during the array magnetization reversal allows one to determine the average rate of remagnetization

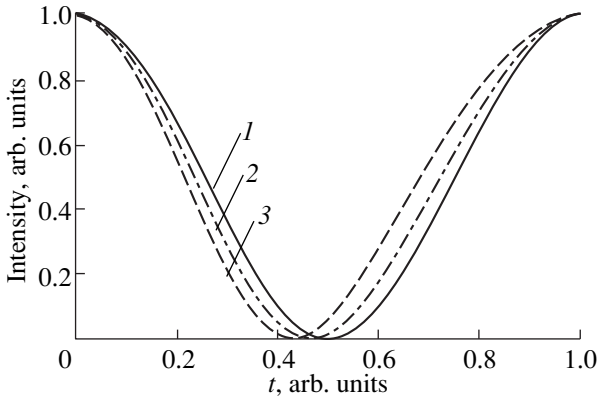

Fig. 10. Calculated time dependences of the image intensity for an array of nanoparticles (50 nm in diameter, arranged at distances of 50 nm from each other) during the magnetization reversal caused by an instantaneous change in the external magnetic field direction by 180°. Curves *1–3* correspond to the relative concentrations $N = 0$, 0.25, and 0.4 of ("fast") particles characterized by the rate of magnetization vector turn exceeding that for the majority of particles by a factor of 1.4. $T = 1$ is the time in which the magnetization of the majority of particles becomes aligned with the external field.

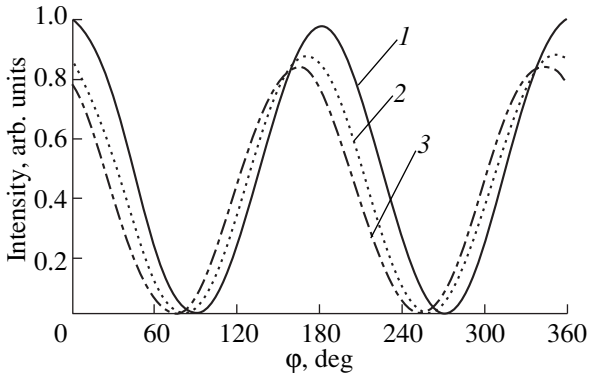

Fig. 11. Calculated dependences of the image intensity for an array of single-domain nanoparticles on the azimuth angle φ of light incidence. Curves *1–3* correspond to the relative concentrations $N = 0$, 0.25, and 0.4 of particles whose magnetization is directed at an angle of 45° to the magnetization direction of other particles.

and to detect the presence of particles exhibiting dynamic properties differing from those of the majority of particles. Furthermore, the dependence of the image intensity on the azimuth angle φ of light incidence allows one to estimate the scatter in the particle magnetization directions in the static case.

7. CONCLUSIONS

Thus, we have considered a theoretical model of magnetic-microstructure imaging using the method of dark-field optical microscopy. To calculate the angular spectrum of scattered light, the method of electrodynamic tensor Green functions was used.

The experimental and theoretical results obtained show that the technique of anisotropic dark-field observation allows one to visualize magnetic submicrometer structures and (in combination with the HSP method) to study their dynamics.

An experimental technique was suggested for studying the magnetization reversal of a solitary single-domain nanoparticle or an array of nanoparticles.

ACKNOWLEDGMENTS

This study was supported by the Russian Foundation for Basic Research, program "Support for Leading Scientific Schools" (V. V. Migulin School, projects no. 00-15-96782, 01-02-16595), the federal program "Russian Universities—Basic Research," and INTAS (grant no. 99-01839).

REFERENCES

1. Y. Martin and H. K. Wickramasinghe, Appl. Phys. Lett. **50** (20), 1455 (1987).
2. S. Hosaka, A. Kikukawa, and Y. Honda, Appl. Phys. Lett. **65** (26), 3407 (1994).
3. I. V. Yaminskiĭ and A. M. Tishin, Usp. Khim. **68** (3), 187 (1999).
4. R. W. Ditchburn, *Light*, 2nd ed. (Blackie, London, 1963; Nauka, Moscow, 1965).
5. B. Kuhlow and M. Lambeck, Physica B & C (Amsterdam) **80**, 374 (1975).
6. A. Thiaville, F. Boileau, J. Miltat, and L. Arnaud, J. Appl. Phys. **63** (8), 3153 (1988).
7. A. Thiaville and J. Miltat, IEEE Trans. Magn. **26** (5), 1530 (1990).
8. A. P. Malozemoff and J. C. Slonczewski, *Magnetic Domain Walls in Bubble Materials* (Academic, New York, 1979; Mir, Moscow, 1982).
9. A. Thiaville, J. Ben Youssef, Y. Nakatani, and J. Miltat, J. Appl. Phys. **69** (8), 6090 (1991).
10. A. S. Logginov, A. V. Nikolaev, and V. V. Dobrovitski, IEEE Trans. Magn. **29** (11), 2590 (1993).
11. A. S. Logginov, A. V. Nikolaev, and V. N. Onishchuk, in *Proceedings of Conference on Physics of Condensed States* (Sterlitamak. Gos. Pedagog. Inst., Sterlitamak, 1997), Vol. 2, p. 50.
12. V. I. Belotelov, A. S. Logginov, and A. V. Nikolaev, Radiotekh. Élektron. (Moscow) **46** (7), 870 (2001).
13. B. D. Laĭkhtman and V. Yu. Petrov, Fiz. Tverd. Tela (Leningrad) **20** (10), 3630 (1978) [Sov. Phys. Solid State **20**, 2098 (1978)].
14. V. K. Peterson, Fiz. Tverd. Tela (Leningrad) **23** (3), 910 (1981) [Sov. Phys. Solid State **23**, 526 (1981)].
15. I. F. Gismyatov and D. I. Sementsov, Fiz. Tverd. Tela (St. Petersburg) **42** (6), 1043 (2000) [Phys. Solid State **42**, 1075 (2000)].
16. A. K. Zvezdin and V. A. Kotov, *Magnetooptics of Thin Films* (Nauka, Moscow, 1988).

17. A. A. Maradudin and D. L. Mills, Phys. Rev. B **11** (6), 1392 (1975).
18. A. S. Logginov, A. V. Nikolaev, E. P. Nikolaeva, and V. N. Onishchuk, Zh. Éksp. Teor. Fiz. **117** (3), 571 (2000) [JETP **90**, 499 (2000)].
19. L. P. Ivanov, A. S. Logginov, and G. A. Nepokoĭchitskiĭ, Zh. Éksp. Teor. Fiz. **84** (3), 1006 (1983) [Sov. Phys. JETP **57**, 583 (1983)].
20. K. O'Grady and H. Laidler, J. Magn. Magn. Mater. **200**, 616 (1999).
21. R. L. White, J. Magn. Magn. Mater. **209**, 1 (2000).
22. R. Pulwey, M. Rahm, J. Biberger, *et al.*, IEEE Trans. Magn. **37** (4), 2076 (2001).
23. W. Wernsdorfer, K. Hasselbach, A. Sulpice, *et al.*, Phys. Rev. B **53** (6), 3341 (1996).
24. V. Novosad, K. Yu. Guslienko, H. Shima, *et al.*, IEEE Trans. Magn. **37** (4), 1416 (2001).
25. M. F. Hansen and S. Morup, J. Magn. Magn. Mater. 184, 262 (1998).
26. G. D. Skidmore, A. Kunz, E. Dahlberg, and C. E. Campbell, UMSI Res. Rep. **99** (191), 1 (1999).
27. D. P. E. Dickson, N. M. K. Reid, and C. A. Hunt, J. Magn. Magn. Mater. **125**, 345 (1994).
28. W. Wernsdorfer, E. Bonet Orozco, K. Hasselbach, *et al.*, Phys. Rev. Lett. **78** (9), 1791 (1997).

Translated by A. Kazantsev

Physics of the Solid State, Vol. 45, No. 3, 2003, pp. 529–533. Translated from Fizika Tverdogo Tela, Vol. 45, No. 3, 2003, pp. 500–504.

MAGNETISM AND FERROELECTRICITY

Large Positive Magnetoresistance Effect in Metal–Insulator Nanocomposites in Weak Magnetic Fields

A. E. Varfolomeev* and M. V. Sedova**

** Russian Research Center Kurchatov Institute, pl. Kurchatova 1, Moscow, 123182 Russia*
e-mail: varfol@imp.kiae.ru
*** Institute of Problems in Applied Electrodynamics, Russian Academy of Sciences, ul. Izhorskaya 13/19, Moscow, 127412 Russia*

Received July 3, 2002

Abstract—Studies of the magnetoresistance of granular Fe/SiO_2 films within the compositional range corresponding to insulators revealed a large positive magnetoresistance. The positive magnetoresistance reaches 10% in magnetic fields ~100 Oe at room temperature and exhibits slow response times (~2 min) to stepped magnetic-field variation. The nature of the effect is apparently associated with the influence of ferromagnetic cluster aggregates of iron nanoparticles on the magnetoresistance. *© 2003 MAIK "Nauka/Interperiodica".*

1. The interest in the magnetoresistance of granular films (nanocomposites), i.e., of ultradisperse grains of magnetic metals (Fe, Co, Ni) embedded in insulating matrices (SiO_2, Al_2O_3), was stimulated by the observation of giant negative magnetoresistance (NMR) in these materials. NMR in such systems reaches a value of a few percent at room temperature and ~10% at the liquid-nitrogen temperature in magnetic fields $H \sim 10$ kOe [1, 2]. The NMR effect originates from spin-dependent tunneling between nanoparticles whose magnetic moments are aligned with the magnetic field and is, therefore, observed in sufficiently strong magnetic fields. This communication reports on an experimental observation of a positive magnetoresistance (PMR) of ~10% in granular Fe/SiO_2 films in weak magnetic fields, ~100 Oe.

Samples selected for study were prepared by ion beam cosputtering of an Fe + SiO_2 composite target. The desired metal-to-insulator ratio in the samples was achieved by properly varying the target composition. The volume content of iron in the samples varied from 64 to 34%. The films were about 500 nm thick and 2 mm wide. Planar contacts were deposited on top of the films to make electrical measurements possible. The distance between the contacts was 7 mm. The sample resistance varied from 4×10^3 to $3 \times 10^8\ \Omega$, depending on the iron content. Electron microscope studies showed the iron grains in the films to be less than 50 Å in size. Mössbauer spectra obtained in the temperature range 77–300 K revealed only a singlet, with no sextet associated with magnetic-field-induced splitting present (to within ~10%), which implies that the grains are superparamagnetic (SPM) in this temperature range. The technique used to prepare the samples and their characterization were described in considerable detail in [3]. The magnetoresistance, defined as $[R(H) - R(H = 0)]/R(H = 0)$, was measured at room temperature in magnetic fields of up to $H = 14$ kOe oriented differently with respect to the sample plane and the current flow direction. The variation of sample resistance with time under a stepped increase or decrease in the magnetic field was registered with an H307 recorder and a computer. The resistance was measured with an E6-13A teraohmmeter.

Earlier studies [3] revealed that Fe/SiO_2 nanocomposites with an Fe volume fraction $x > 0.6$ behave similar to bulk Fe at room temperature, while for $x < 0.5$, the conduction of these nanocomposites has an activated hopping character. Figure 1 displays field dependences of the magnetoresistance of samples with different iron contents; these dependences were measured after the first sample exposure to the magnetic field. Samples with an iron content $x = 0.3$–0.5 placed in fields below $H \sim 10$ kOe revealed NMR below the percolation threshold; i.e., the resistance $R(H)$ decreased with increasing magnetic field. The maximum NMR for these samples was ~1% in fields $H \approx 10$ kOe at room temperature. In higher fields, $H > 10$ kOe, some samples exhibit isotropic PMR, with $R(H)$ beginning to grow; this effect has not been described earlier in the literature (Fig. 1). This observation of PMR does not contradict the existence of NMR in the same fields; in other words, the NMR and PMR effects coexist, while having different onset times of equilibrium resistance under stepped magnetic-field variation. After a sudden stepped increase in the magnetic field, one initially observes a negative change in resistance, which is replaced by its slow positive growth; i.e., there is no delay in the NMR response, whereas the steady-state

1063-7834/03/4503-0529$24.00

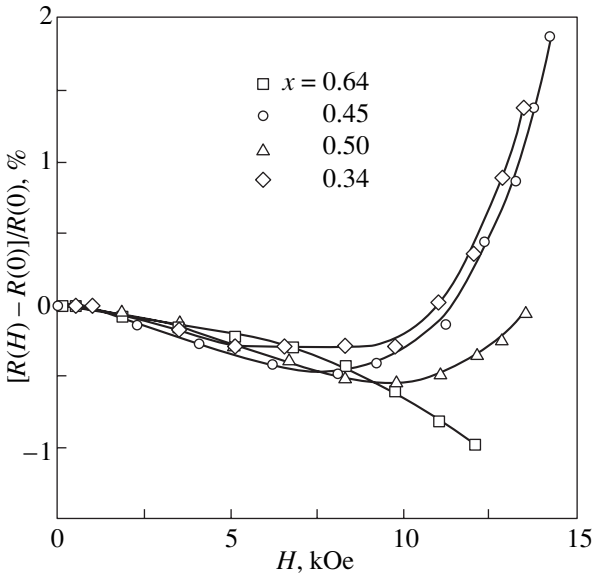

Fig. 1. Field dependences of the magnetoresistance of samples with different volume contents of iron, x, measured at T = 300 K.

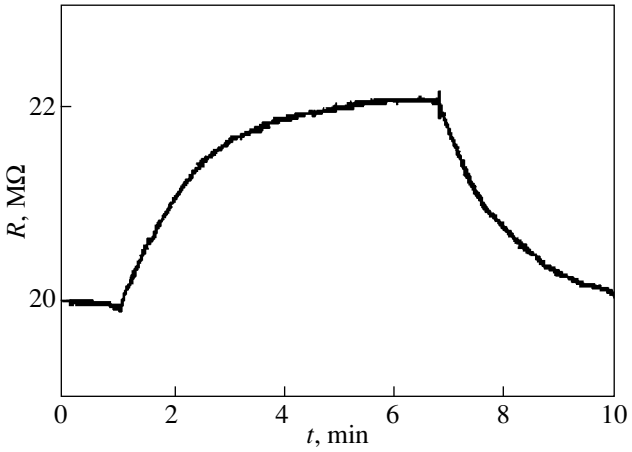

Fig. 2. Variation of the magnetoresistance with time after the application (t = 1 min) and removal (t = 7 min) of a magnetic field H = 100 Oe.

value of PMR in fields $H > 10$ kOe is reached after a fairly long time (of the order of a few minutes).

We also observed that if a sample revealed PMR in fields $H > 10$ kOe, it showed a large PMR afterwards in weak magnetic fields down to $H \sim 100$ Oe. Figure 2 illustrates the PMR effect as a dependence of the resistance on the time registered on the recorder under a stepped magnetic-field variation from 0 to 100 Oe and back for a sample with an iron content $x = 0.45$ treated preliminarily by exposure to a magnetic field H = 13 kOe. The resistance of the sample, initially of $\approx 2 \times 10^7\ \Omega$ at room temperature, changed by as much as $\approx 2 \times 10^6\ \Omega$, i.e., by ≈10%, in a magnetic field of 100 Oe. The characteristic PMR response time to a stepped change in the field was about 2 min in weak fields. Figure 3 shows the field dependence of magnetoresistance measured within the range 0–14 kOe on a sample exhibiting the PMR effect in weak ($H < 100$ Oe) and strong ($H > 10$ kOe) fields. In fields $H < 100$ Oe, the PMR effect is strong. In fields 100 Oe $< H <$ 10 kOe, PMR saturates. In these fields, the variation of the magnetoresistance is accounted for by the well-known NMR effect, which originates from spin-dependent tunneling between SPM particles. For $H > 10$ kOe, both NMR and PMR are observed.

The PMR effect seen in weak fields has a number of distinctive features. PMR saturates already at $H \approx 100$ Oe, i.e., in substantially weaker fields than those required for NMR to set in. Immediately after application of a strong magnetic field $H > 10$ kOe, PMR did not necessarily reach its maximum value in weak fields; however, if the sample was thereafter repeatedly subjected to a weak field $H \sim 100$ Oe, the magnitude of PMR in a weak field increased to its maximum value, which attained ~10% for some samples (Figs. 2, 3). The PMR effect is isotropic (i.e., it does not depend on the mutual orientation of the magnetic field and the current) and is characterized by a long response time (2–3 min) to a stepped magnetic-field change (Fig. 2). After exposure to a strong field, PMR in weak fields is observed to persist in samples for several (~3) days, to finally disappear. For the PMR effect in weak fields to recover after this disappearance, the sample had to be subjected again to a strong magnetic field $H > 10$ kOe.

A more comprehensive investigation of the PMR dependence on magnetic field under a successive stepped increase and decrease in the field, which was performed in the range –100 to +100 Oe, and under a change in the field orientation revealed the existence of several reproducible steps and of a hysteresis (Fig. 4). In some cases, after a stepped variation of the magnetic field, the resistance also changed in steps rather than gradually. Such jumps in conductivity were better pronounced in Fig. 4 in the fields in which strong changes in magnetoresistance occurred. Figure 5 displays the time evolution of the resistance and of its derivative, obtained after a stepped decrease in the magnetic field from –100 to –90 Oe in the course of measuring the field dependence of magnetoresistance shown in Fig. 4.

We studied the dependence of the magnitude of PMR on the volume content of iron in the samples at a fixed field H = 100 Oe. The largest change in magnetoresistance was observed for a volume content of iron $x \approx 0.45$ (Fig. 6).

2. In our opinion, interpretation of the PMR effect in a weak magnetic field should be based on the assumption that in a given system, there is a domain structure with fairly large magnetic moments capable of orienting in a weak magnetic field. Indeed, a magnetic field $H \approx 100$ Oe is not strong enough to produce a notice-

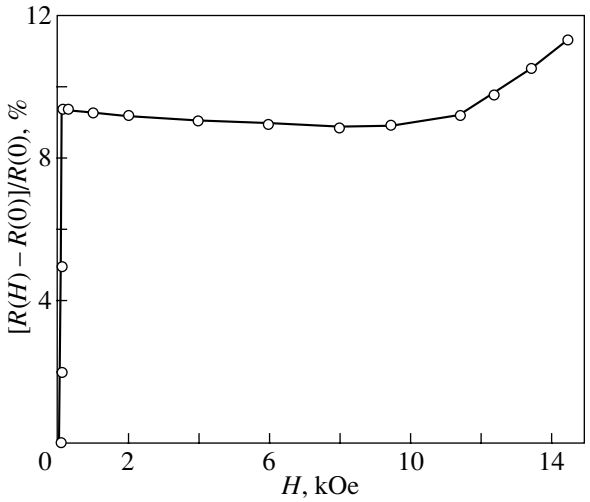

Fig. 3. Field dependence of the magnetoresistance of a sample ($x = 0.45$) after preliminary exposure to a field $H >$ 10 kOe.

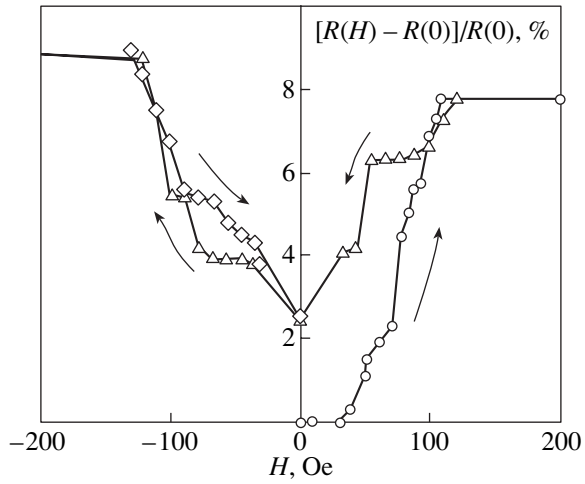

Fig. 4. Field dependence of PMR for a sample with $x = 0.5$ in weak magnetic fields, obtained after preliminary exposure of the sample to a field $H > 10$ kOe. Arrows specify the direction of variation in the magnetic field.

able orientation of the magnetic moments of SPM iron grains. It is conceivable that this effect is associated with domains in ferromagnetic (FM) regions where there are iron grain clusters in the nanocomposite. In principle, nanoparticles in such a cluster might not even be in contact with one another. If the magnetic moments of these nanoparticles interact strongly enough and align in an ordered manner, such a magnetic cluster may form an FM region consisting of one or several domains in the nanocomposite. Each of the domains or cluster domains is actually a group of nanoparticles which possesses a large net magnetic moment capable of orienting as a whole in weak magnetic fields. To orient the magnetic moments of SPM iron nanoparticles ~50 Å in size, the applied field should be ~10 kOe; therefore, in order for the cluster domain magnetic moment to align with a magnetic field ~100 Oe, the number of nanoparticles in such a cluster has to be ~100. The FM and SPM components were observed to coexist in Fe/SiO_2 and Ni/SiO_2 nanocomposites at a high enough concentration of SPM particles in the range $x = 0.3$–0.5, i.e., above a certain threshold value for cluster formation but below the threshold for percolation (see, e.g., [4, 5]). In these conditions, the magnetic properties of the nanocomposites changed sharply for $x > 0.3$ due to cluster formation. At the same time, iron nanoparticles of a fairly small size, which are not bound in clusters and do not interact with one another, remain superparamagnetic at room temperature.

PMR first appears in fields $H > 10$ kOe (Fig. 1); to observe this effect in weak fields $H < 100$ Oe, one has to expose the samples preliminarily to fields $H > 10$ kOe. It may be conjectured that when the magnetic moments of nanoparticles are fully aligned with a strong magnetic field, FM order arises in the cluster aggregates. Domain structure formation in the FM regions apparently comes to completion after the samples have been repeatedly exposed to a weak field $H \approx 100$ Oe that alternates in direction, which obviously produces some misorientation of the domain magnetic moments. In this case, the PMR increases in weak fields to a certain constant value (up to ~10%). The experimental observation of the disappearance of the PMR effect in the absence of a magnetic field after a period of a few (~3) days at room temperature may be explained by the gradual disordering of the magnetic moments of nanoparticles in a domain at room temperature; this process occurs more slowly than that with SPM grains, with the domain finally dissolving. The interaction between the nanoparticles making up a domain imposes an additional potential barrier for the temperature-induced rotation of a particle's moment, with the result that a domain can break down in a few days. The domain decay time determines the lifetime of the PMR effect in weak fields, after which the samples must be exposed again to a strong field for the domains to be restored.

Note that dipole interaction may be responsible for the ordered arrangement of the nanoparticle magnetic moments in a cluster domain. The energy of magnetic dipole interaction between Fe nanoparticles $d \sim 50$ Å in diameter and containing $N \sim 4 \times 10^3$ atoms is $\mu^2/d^3 \sim 5 \times 10^{-14}$ erg (assuming a moment of $\approx 2.2\mu_B$ per iron atom, where μ_B is the Bohr magneton), which corresponds to a temperature of about 360 K. Indeed, in our case, the PMR effect disappears in a weak field after ~3 days of storage at room temperature; therefore, it may be conjectured that the FM region disordering temperature for our samples (an analog of the Curie temperature for FM clusters in the given system), at which the domains break down into SPM particles, is close to room tem-

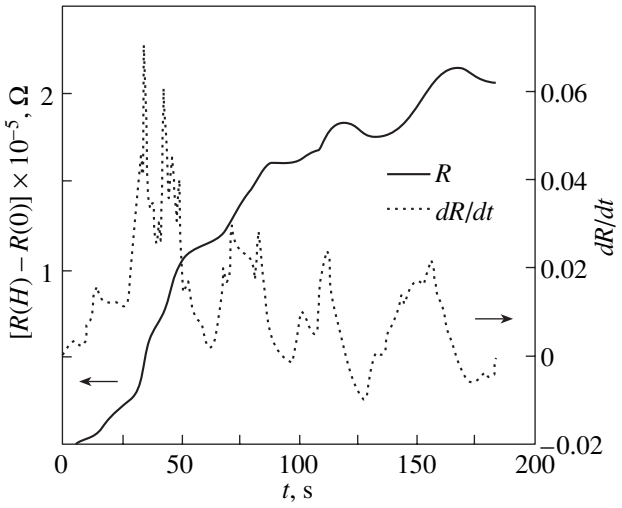

Fig. 5. Variation of resistance $R(H = -100\ \text{Oe}) - R(H = -90\ \text{Oe})$ with time after a stepped decrease in the magnetic field from –100 to –90 Oe (see Fig. 3), and its first derivative (dashed line).

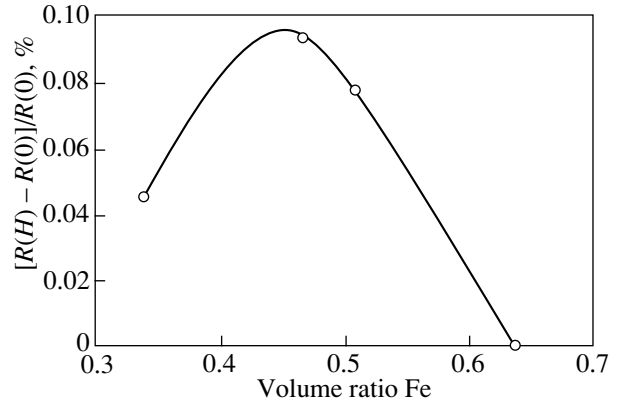

Fig. 6. PMR vs. volume iron fraction dependence measured in a field $H = 100$ Oe.

perature. Weiss' molecular-field theory for ferromagnets makes it possible to estimate the analog of the molecular field for a cluster domain [6]:

$$H_W = 4kT_c/\mu \approx 10^4\ \text{Oe},$$

where $T_c \sim 300$ K is the temperature at which the ordered arrangement of nanoparticle moments in a cluster domain breaks down in our case (an analog of the Curie temperature) and $\mu \sim 10^3\mu_B$ is a nanoparticle's magnetic moment. This estimate agrees with our assumption that, in fields $H > 10$ kOe, domains start to form from nanoparticle clusters.

This interpretation of the PMR effect offers an explanation for the observed field dependence and time evolution of magnetoresistance in weak magnetic fields (Figs. 4, 5). The jumps in conductivity observed in this case can be connected, by analogy with the Barkhausen jumps in magnetization, with the magnetic-moment rearrangement of domains, which behave like domains in ferromagnets. The magnetization of single ferromagnetic clusters is capable of efficiently influencing the magnetoresistance of the sample as a whole because of the limited number of hopping conduction paths in the given system, which is below the percolation threshold. Note also that the fraction of particles in the FM regions of the nanocomposites studied is fairly small compared with that in the SPM regions; it apparently less than 10%, because no lines associated with magnetic splitting were found, to within 10%, in the Mössbauer spectra of the samples.

Thus, in our opinion, the PMR effect observed in fields $H < 100$ Oe is initiated by magnetic-moment orientation of the FM cluster domains. In fields 100 Oe < $H < 10$ kOe, the domain moments are fully aligned and PMR reaches saturation. In these fields, as already mentioned, the variation of magnetoresistance originates from the NMR effect, which is accounted for by spin-dependent tunneling between the SPM particles. SPM particles are located in intercluster regions of the samples studied and constitute the larger part of all particles. In fields $H > 10$ kOe, both NMR and PMR are observed. The manifestation of the PMR in such fields may be assigned to both the growth of already existing domains and the nucleation of new ones.

We are not aware of any previous observation of isotropic PMR in granular films with magnetic nanoparticles. In our opinion, theoretical interpretation of the sign of the PMR effect remains an open problem. Note, for instance, that, as pointed out in an analysis of the NMR effect in nanocomposites performed in [7], the explanation of NMR proposed in [8] based on the additional magnetic energy that must be gained or lost by an electron in spin-dependent tunneling between particles with oppositely directed magnetic moments should actually result in PMR. Further studies are obviously required to find an adequate interpretation of the PMR effect in metal–insulator nanocomposites.

Thus, large room-temperature PMR (up to 10%) has been observed for the first time in granular films of an insulating matrix with embedded iron particles in weak magnetic fields (~100 Oe). In order to explain the nature and characteristic features of the PMR, in our opinion, the part played by ferromagnetic cluster aggregates of nanoparticles surrounded by SPM iron grains needs to be taken into account.

ACKNOWLEDGMENTS

The authors are indebted to V.M. Cherepanov for the Mössbauer measurements and to A.N. Lagar'kov for his encouragement.

REFERENCES

1. J. L. Gittleman, Y. Goldstein, and S. Bozovski, Phys. Rev. B **5**, 3609 (1972).
2. A. Milner, A. Gerber, B. Groisman, *et al.*, Phys. Rev. Lett. **76**, 475 (1996).
3. B. A. Aronzon, A. E. Varfolomeev, D. Yu. Kovalev, *et al.*, Fiz. Tverd. Tela (St. Petersburg) **41** (6), 944 (1999) [Phys. Solid State **41**, 857 (1999)].
4. G. N. Kakazei, A. F. Kravets, N. A. Lesnik, *et al.*, J. Appl. Phys. **85** (8), 5654 (1999).
5. J. G. Lin, C. Y. Huang, H. Sang, *et al.*, IEEE Trans. Magn. **34**, 375 (1998).
6. S. V. Tyablikov, *Methods in the Quantum Theory of Magnetism*, 2nd ed. (Nauka, Moscow, 1975; Plenum, New York, 1967).
7. J. Inoue and S. Maekawa, Phys. Rev. B **53** (18), R11927 (1996).
8. J. S. Helman and B. Abeles, Phys. Rev. Lett. **37** (21), 1429 (1976).

Translated by G. Skrebtsov

Physics of the Solid State, Vol. 45, No. 3, 2003, pp. 534–541. Translated from Fizika Tverdogo Tela, Vol. 45, No. 3, 2003, pp. 505–512.

MAGNETISM AND FERROELECTRICITY

The Nature of Low-Frequency Raman Scattering in Congruent Melting Crystals of Lithium Niobate

N. V. Surovtsev*, V. K. Malinovskiĭ*, A. M. Pugachev*, and A. P. Shebanin**

** Institute of Automatics and Electrometry, Siberian Division, Russian Academy of Sciences, Universitetskiĭ pr. 1, Novosibirsk, 630090 Russia*

e-mail: malinovsky@iae.nsk.su

*** Joint Institute of Geology and Geophysics, Siberian Division, Russian Academy of Sciences, pr. Nauki 3, Novosibirsk, 630090 Russia*

Received June 4, 2002

Abstract—Raman spectra of congruent melting crystals of lithium niobate are studied. It is shown that a band near ~100 cm^{-1} corresponds to first-order Raman scattering and is due to nonstoichiometry of the crystal. The adequacy of various models for description of this band is discussed. © *2003 MAIK "Nauka/Interperiodica".*

1. INTRODUCTION

The lithium niobate ($LiNbO_3$) crystal is one of the most popular objects of investigation in solid-state physics. This ferroelectric crystal is extensively used in acoustics, acoustooptics, nonlinear optics, and in memory devices.

High-quality congruent melting crystals of lithium niobate can be grown with large sizes [1]. In congruent crystals, [Li]/[Nb] ≈ 0.94, which differs significantly from the stoichiometric composition [2] ([Li] and [Nb] are the Li and Nb atomic concentrations, respectively). The concentration of intrinsic defects in a lithium niobate crystal is high (approximately 6% of the crystal unit cells), which allows one to investigate physical effects caused by disorder. A study of the role of disorder in such a model crystal may provide a new understanding of the nature of ferroelectric relaxors and amorphous materials.

Raman scattering (RS) in lithium niobate involves optical phonons of A_1 and E symmetry [3, 4]. The Raman spectra of congruent $LiNbO_3$ crystals contain a relatively broad low-frequency band near 100 cm^{-1}. (In some papers, this band is described as a set of peaks.) This band is missing from the Raman spectra of pure stoichiometric crystals [5, 6]. Opinions differ as to the nature of the band at 100 cm^{-1}. In earlier papers [7, 8], this band was attributed to RS by E phonons; its appearance in the geometries where only RS by A_1 phonons is allowed was assumed to be a result of the breakdown of the selection rules caused by internal mechanical stresses in the crystal (the authors of [9] also held this viewpoint). In [10], the band at ~100 cm^{-1} in the spectrum of a congruent $LiNbO_3$ crystal was interpreted as difference combinations of three low-frequency branches of A_1- and E-symmetry optical vibrations and it was reported that the intensity of this band decreased dramatically at liquid-nitrogen temperatures. Most other researchers also interpret the band at 100 cm^{-1} in the Raman spectrum of $LiNbO_3$ as second-order scattering [5, 6, 11–13], but there is no general consensus as to its details; in [12, 13], for instance, the band is assumed to be due to A_1 phonons, whereas in [5], this band is associated with both A_1 and E phonons. In [14, 15], a model was proposed in which the band at ~100 cm^{-1} is attributed to a superstructure formed by clusterlike defects and corresponds to first-order RS by optical phonons of the superlattice.

Thus, although many papers have been devoted to the problem, there is no general agreement among authors even as to the main experimental characteristics of the band at ~100 cm^{-1} in the Raman spectra of congruent lithium niobate crystals. In this paper, we determine the basic properties of this band, such as its symmetry and the order of the Raman scattering. The results are compared with the earlier published results and the reasons for the discordance between the experimental data are discussed. In Section 3, we discuss various models proposed for describing the low-frequency band in the Raman spectra of congruent $LiNbO_3$ crystals and the consistency between these models and the experimental data.

2. EXPERIMENTAL RESULTS

RS experiments were performed on lithium niobate crystals in the form of a parallelepiped with its edges were parallel to the crystallographic axes. The Raman spectra were recorded at room temperature for nominally pure congruent crystals and for $LiNbO_3$ crystals of a close-to-stoichiometric composition.

The Raman spectra were taken with a double-grating U1000 spectrometer using the 458 and 514 nm lines of an argon laser and the 647 nm line of a krypton laser. The Raman spectra of lithium niobate samples were

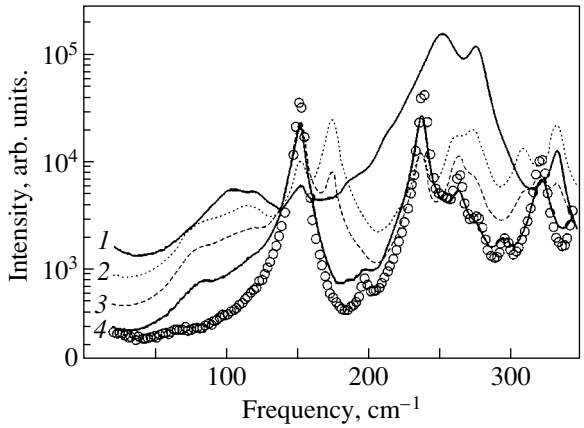

Fig. 1. Raman spectra of a congruent $LiNbO_3$ crystal taken at $T = 300$ K in different polarization geometries: (*1*) *x*(*zz*)*y*, (*2*) *z*(*xx*)*y*, (*3*) *z*(*xz*)*y*, and (*4*) *x*(*zx*)*y*. Circles represent a Raman spectrum of a stoichiometric $LiNbO_3$ crystal measured in the *x*(*zx*)*y* geometry.

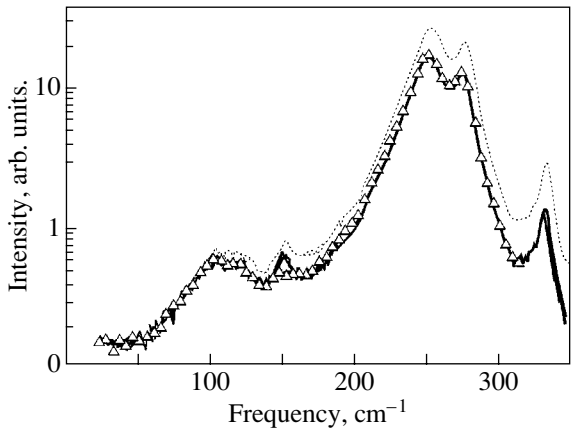

Fig. 2. Raman spectra of a congruent $LiNbO_3$ crystal measured at $T = 300$ K in the *x*(*zz*)*y* geometry at different excitation lines: (dotted line) $\lambda = 458$, (solid lines) 514, 647, and (triangles) 1064 nm.

also measured with a modified DFS-24 spectrometer [16] using the 1064 nm line of a cw neodymium laser. The measurements covered the range 10–400 cm^{-1}; the spectral widths of slits were 2 cm^{-1}.

Figure 1 shows the Raman spectra of a congruent crystal ($\lambda = 514$ nm) measured at room temperature in different polarization geometries. For the weak lines to be seen in this figure, a logarithmic scale is used for the RS intensity. It can be seen that, in all polarization geometries, a Raman band is seen at ~100 cm^{-1}, with its intensity being approximately an order of magnitude lower than those of the main lines. It is easy to verify that, in the A_1(TO)-phonon geometry, the band at ~100 cm^{-1} cannot be assigned to *E*-symmetry excitations manifesting themselves due to crystal imperfections, as assumed in [7–9]. Indeed, in that case, all vibrational *E* modes would have been observed; that is, the band at ~100 cm^{-1} would have been accompanied by an order of magnitude stronger line near 150 cm^{-1}, which is inconsistent with the experimental spectrum (Fig. 1). Furthermore, it is seen from Fig. 1 that the shape and position of the band at ~100 cm^{-1} are different in the A_1(TO)-phonon geometry and in the other RS geometries.

In [12], it was reported that the band at ~100 cm^{-1} was not observed in the geometry where RS by *E* phonons is allowed. This result is inconsistent with our observations. The disagreement is accounted for by the fact that, in [12], *E* phonons were observed in the *x*(*zx*)*y* geometry, where the 153 cm^{-1} line is much stronger than the band at ~100 cm^{-1} and the latter becomes invisible against the background of the 153 cm^{-1} line if a linear intensity scale is used. In Fig. 1, the intensity scale is logarithmic; the band at ~100 cm^{-1} is also clearly seen in this RS geometry. The existence of this band in the Raman spectrum of a congruent crystal in the *x*(*zx*)*y* geometry becomes more evident when this spectrum is compared with the Raman spectrum of a stoichiometric crystal (circles in Fig. 1). Thus, an analysis of the spectra presented in Fig. 1 allows one to conclude that the band at ~100 cm^{-1} appears in the Raman spectra of congruent $LiNbO_3$ crystals in all polarization geometries where A_1 or *E* phonons are allowed.

When a Raman spectrum is analyzed in a fairly large range, one should take into account that fluorescence can contribute to the measured spectra. In order to reveal the possible contribution from fluorescence and resonance RS, we measured the Raman spectra of lithium niobate using various excitation lines (Fig. 2). It can be seen from Fig. 2 that the spectra are virtually identical, which allows one to conclude that there is no contribution from fluorescence for excitation lines $\lambda > 500$ nm and no resonance RS. A small contribution from fluorescence in the case of the excitation lines $\lambda = 458$ nm is revealed by comparing them with the other Raman spectra. The small peak at approximately 150 cm^{-1} is missing from the spectrum for $\lambda = 1064$ nm, because the photorefractive effect does not arise at this wavelength [17] and, therefore, the experimental polarization conditions can be met more exactly.

The spectra of a congruent $LiNbO_3$ crystal recorded in the *x*(*zz*)*y* geometry at $T = 300$ and 77 K are shown in Fig. 3. In order to exclude the trivial temperature dependence (for the Stokes part of the spectrum, we have $I \propto (n + 1)$, where $n = 1/[\exp(h\nu/kT) - 1]$ is the Bose–Einstein distribution function), Fig. 3 presents the normalized RS intensity $I/(n + 1)\nu$. A small increase in the intensity of the *E*-symmetry lines at the lower temperature is due to the fact that the polarization conditions are met less exactly. However, the contribution from these lines to the integrated intensity is small and will be ignored in the analysis performed below.

The main lines of the Raman spectrum narrow with decreasing temperature, because the phonon lifetime increases [18]. The Raman spectra presented in Fig. 3 are normalized to the integrated intensity of the 252 and

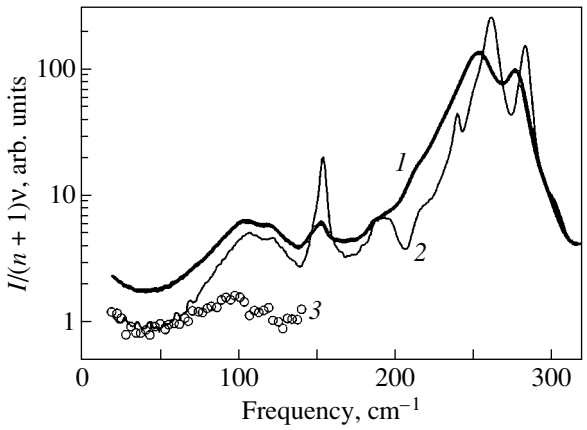

Fig. 3. Raman spectra $I/(n + 1)\nu$ (normalized to the Bose–Einstein factor) of a congruent $LiNbO_3$ crystal taken at (*1*) $T = 300$ and (*2*) 77 K, and (*3*) the difference between these spectra.

274 cm^{-1} lines (integration is performed over the range 170–315 cm^{-1}), which allows one to take into account the line narrowing as the temperature is decreased. It can be seen from Fig. 3 that the intensity of the band at ~100 cm^{-1} remains unchanged. The small increase in the intensity of the spectrum near 100 cm^{-1} with an increase in temperature is due to the contribution from multiphonon RS and does not exceed 20% of the intensity at 300 K. The difference between the two spectra in the range 40–140 cm^{-1} shown in Fig. 3 is approximately constant or a weakly increasing monotonic function (a small nonmonotonic contribution is due to the band position shifting with temperature).

It can easily be shown that the temperature-independent ~100 cm^{-1} band intensity normalized to the Bose–Einstein factor is inconsistent with this band being due to second-order RS. For example, if we assume, as in [10], that some contribution to the 100 cm^{-1} band comes from the difference combination of the excitations at 252 and 152 cm^{-1}, then the corresponding RS intensity will be proportional to the product $[n(\nu = 252\ \text{cm}^{-1}, T) + 1]n(\nu = 152\ \text{cm}^{-1}, T)$. In this case, the 100-cm^{-1}-band intensity normalized to the Bose–Einstein factor should change by a factor of 8.5 as the temperature is varied from 80 to 300 K. This change is inconsistent with the experimental data (Fig. 3). Therefore, the temperature dependence of the Raman spectra presented in Fig. 3 strongly suggests that the band at ~100 cm^{-1} is due to first-order RS.

This result contradicts the conclusion, made in [5, 10], that the temperature dependence of the intensity of the band at ~100 cm^{-1} is consistent with the assignment of this band to second-order RS. This contradiction to [10] is due to the fact that the authors of [10] compared the Raman spectra normalized to the maximum intensity of the 153 cm^{-1} line and did not take into account the change in the width of this line with decreasing temperature. If one normalizes the intensities of the spectra from [10] to the integrated intensity of the 153 cm^{-1} line, then the result will become consistent with the conclusion that the band at ~100 cm^{-1} is due to first-order RS. In [5], the band at ~100 cm^{-1} was attributed to second-order RS on the basis of the experimental data taken from [9], according to which the RS at $T >$ 600 K is strongly dependent on temperature. Indeed, in the region of 100 cm^{-1}, there is a contribution from multiphonon RS; this contribution is small at room temperature (~20% of the intensity of the band at ~100 cm^{-1}, Fig. 3) but becomes dominant at high temperatures because of its strong temperature dependence. However, for the band at ~100 cm^{-1}, the multiphonon Raman spectrum is only an additional background, which depends on frequency only weakly and whose intensity decreases sharply as the temperature is decreased. Therefore, on the basis of the sharp temperature dependence of the RS intensity in the region of ~100 cm^{-1} at high temperatures, it would be incorrect to conclude that the band at ~100 cm^{-1} is due to second-order RS.

Thus, to sum up, it follows from the experimental data on RS in lithium niobate that the band at ~100 cm^{-1} arises in the Raman spectra of congruent $LiNbO_3$ crystals and is missing from the spectra of stoichiometric samples. This band can be assigned to first-order RS and is observed in all polarization geometries of RS experiments.

3. MODELS

Now, we discuss various interpretations of the band at ~100 cm^{-1} in the Raman spectra of congruent lithium niobate crystals.

3.1. Fundamental Vibrational Mode of the Crystal [7–9]

This model does not give an explanation of why the band at 100 cm^{-1} is missing from the Raman spectra of stoichiometric crystals. Furthermore, this band could not be assigned to phonons of a certain symmetry, since the band arises in all polarization geometries of RS experiments.

3.2. Second-Order Raman Scattering [5, 6, 11–13]

The models in which the band at ~100 cm^{-1} is assumed to be due to second-order RS are inconsistent with the experimental data on the temperature dependence of the RS intensity.

Thus, for a model of the band at ~100 cm^{-1} to be adequate, the following two properties of the band have to be taking into account: this band (i) belongs to the first-order Raman spectrum and (ii) is missing from the Raman spectra of stoichiometric crystals.

The band at ~100 cm^{-1} in the spectra of congruent crystals can be interpreted in two fundamentally differ-

ent ways. First, this band can be assigned to additional vibrational modes associated with stoichiometric defects. The other interpretation involves the breakdown of the wave-vector selection rules in congruent crystals. In this case, defects due to nonstoichiometry do not affect the crystal vibration spectrum itself, but, in the Raman spectra, there appear vibrational modes that do not correspond to the Γ point of the Brillouin zone. General analysis of the situation for lithium niobate crystals is complicated by the fact that acoustic modes contribute to the region of 100 cm^{-1} of the Raman spectrum [20]; therefore, the band in question can be assigned not only to optical but also to acoustic phonons. In what follows, we will discuss different suppositions as to the nature of the band and the type of excitations corresponding to it.

3.3. Fundamental Vibrational Mode of a Defect Superlattice

This model was proposed in [14, 15], and its predictions correlate well with the experimental data, which suggest that the band under study belongs to the first-order Raman spectrum and corresponds to a vibrational mode associated with defects. If one assumes that the symmetry properties of vibrations of the defect structure are similar to those of the perfect crystal, then the dependence of the band shape on the RS geometry (Fig. 1) can be adequately described in terms of the model in question under the assumption that the vibrational modes of the defect structure can be separated into E- and A_1-symmetry modes.

However, some problems remain unsolved with the model proposed in [14, 15]. First, structural analysis of lithium niobate crystals has not revealed any superlattice in them. Further, numerical calculations have not been performed to confirm the presence of a band at ~100 cm^{-1} in the Raman spectrum of a crystal with stoichiometric defects. As shown below, there are also problems with the description of the band profile within the model in question.

The large width of the band (~30 cm^{-1}, Fig. 3) does not vary with decreasing temperature, which suggests that the band broadening is inhomogeneous. This broadening cannot be explained by a mechanical-stress distribution in the crystal. Figure 4 shows the band profile recorded in the $x(zz)y$ geometry and its approximation by two Gaussians (inhomogeneous broadening of Raman bands due to a mechanical-stress distribution is usually characterized by a Gaussian profile); the Gaussians are fitted to the two well-pronounced peaks of the band. It can be seen from Fig. 4 that the fitted curve is inadequate for description of the low-frequency slope of the band.

Thus, there are difficulties in describing the profile of the band at ~100 cm^{-1} in terms of the model involving optical phonons of a defect superlattice. In this case, in our opinion, the assumption of defect ordering is unnecessary (at least, when the band at ~100 cm^{-1} is dealt with); it would appear more reasonable to include optical-type vibrations of an imperfect unit cell.

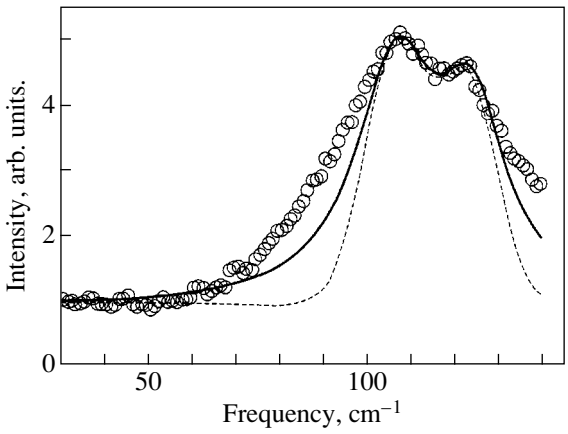

Fig. 4. Raman spectrum of a congruent $LiNbO_3$ crystal measured at $T = 80$ K in the $x(zz)y$ geometry and its approximations by a sum of two Gaussians (dashed curve) and a sum of two Lorentzians (solid curve).

3.4. Optical Vibrational Mode of an Imperfect Crystal Unit Cell

In this model, the band at ~100 cm^{-1} corresponds to first-order RS by optical vibrations localized in the vicinity of a crystal unit cell with a stoichiometric defect. Localization is taken here to mean that the eigenvector of an optical vibrational mode is conserved in the vicinity of the imperfect unit cell. In the frequency region under study, there are also (high-frequency) vibrations of the acoustic modes of the crystal. Therefore, as the distance from the defect increases, an optical vibrational mode of the imperfect unit cell transforms into acoustic modes of the crystal. In solid-state physics, such a vibrational mode is termed a resonance mode [21]. If such modes possess E and A_1 symmetry, then the model at hand can explain the dependence of the band position on the RS geometry (Fig. 1). The shape of a spectral line corresponding to resonance vibrations is described by a Lorentzian curve [21]. It can be seen from Fig. 4 that the experimental profile of the band at ~100 cm^{-1} cannot be closely approximated by a combination of two Lorentzians. Therefore, the model at hand is inadequate for description of the shape of the band. To develop this model further, one should numerically calculate the frequencies of vibrational modes of the crystal unit cell with a stoichiometric defect.

3.5. Acoustic Mode of an Imperfect Crystal Unit Cell

The band that appears in the Raman spectrum of a nonstoichiometric crystal can be assumed to be associated with an acoustic vibrational mode localized in the

vicinity of a crystal unit cell with a stoichiometric defect (e.g., an Li vacancy). By taking into account the size of the crystal unit cell and the velocity of sound in $LiNbO_3$ crystals, the frequency of the localized acoustic mode is found to be on the order of the frequency 100 cm^{-1} of the band in question (Fig. 1).

Let us consider the imperfect crystal unit cell and let us assume that its elastic moduli are different from those of its environment. Then, the frequency of a phonon localized on this unit cell can be found to be [22]

$$\nu_d = S\frac{u}{D}. \quad (1)$$

Here, S is a constant of order unity, which depends on the shape of the inhomogeneity and on the type of vibration ($S = 0.7$–0.85 for various types of vibration of a free sphere and $S = 0.5$ for a cube or a linear inhomogeneity); u is the velocity of sound; and D is the inhomogeneity dimension. The value of ν_d as calculated from Eq. (1) depends on the size of the defect and on the type of acoustic wave, because the velocities of longitudinal and transverse acoustic waves are different (4 and 7 km/s, respectively [23]). For example, for $S = 0.5$ and $D = 5.1$ Å (which is equal to the lattice parameter a [23]), we find $\nu_d = 130$ cm^{-1} for transverse vibrations. Thus, the order-of-magnitude estimate of the frequency of the acoustic mode localized on the imperfect unit cell is close to the frequency 100 cm^{-1} of the band under study (Fig. 1).

According to the model in question, there is an excess density of states in the low-frequency range of the vibrational-mode spectrum of a congruent crystal. Furthermore, due to defects, acoustic phonons are scattered more strongly than in stoichiometric crystals. These effects should be manifested in the specific heat and thermal conductivity at low temperatures. A comparison of the experimental values of these quantities for congruent and stoichiometric crystals was performed in [24], and it was found that the specific heats of these crystals are identical and the thermal conductivity of congruent crystals have no additional contribution from phonon scattering by defects. The difference in thermal conductivity between congruent and stoichiometric $LiNbO_3$ crystals at $T > 20$ K observed in [24] was due to the probabilities of umklapp processes [25] in phonon–phonon scattering being different. Thus, the model at hand lacks support from the experimental data on the specific heat and thermal conductivity at low temperatures.

Another problem arises in interpreting the position of the band at ~100 cm^{-1} in terms of the model involving localized acoustic modes. As seen from Fig. 1, in the $x(zz)y$ geometry of RS, the band position is shifted to higher frequencies (the first maximum is at ≈103 cm^{-1}) in comparison with that in the other geometries (where the first maximum is at ≈82 cm^{-1}). In terms of the model in question, the weak dependence of the band position on the polarization geometry might be conjectured to be due to the band under study being associated with different fundamental vibrational modes depending on the RS geometry. Vibrational modes that are predominantly longitudinal will be observed in polarized Raman spectra and produce weakly depolarized RS, whereas torsion vibrations usually cause strong depolarization. However, it can be seen from Fig. 1 that the position of the band under study is the same in polarized and depolarized Raman spectra.

The problem could be solved by taking into account the deviation of the dispersion curves of the acoustic modes from a linear law at frequencies as low as 50–120 cm^{-1} (as is the case with low-lying acoustic branches in $LiNbO_3$ crystals; see calculations in [26]). The dispersion curves for phonons with large wave vectors flatten out [26], because the vibration frequency depends on the relative positions of the atoms in a crystal unit cell. In this case, however, since the vibrational modes of imperfect unit cells in question are highly localized, these modes cannot be divided into acoustic and optical ones and the model under discussion becomes similar to that considered in Subsection 3.4.

Thus, there are problems to be solved with the model involving acoustic modes of the imperfect crystal unit cell. The validity of this model could be tested by measuring the specific heats of stoichiometric and congruent lithium niobate crystals in the range 10–100 K and by making a comparison between them to an accuracy of better than 1%.

3.6. Models Assuming Breakdown of Wave-Vector Selection Rules

Such models have been proposed for both acoustic and optical phonon branches in crystals with some disorder. In [27], for example, acoustic phonons in the presence of polarizability fluctuations (so-called electrical disorder) were considered in order to describe low-frequency RS in crystals with orientational disorder. Acoustic vibrations were assumed to be well-defined plane waves, which contribute to low-frequency RS through spatial fluctuations in the polarizability. In the model proposed in [27], the correlator of the plane polarizability wave induced by an acoustic phonon decays rapidly in space due to electrical disorder; therefore, the wave-vector selection rules will be broken and the density of acoustic vibrational states will be manifested in the low-frequency Raman spectrum. A similar model was proposed in [28] for describing the low-frequency Raman spectra of glasses. In that model, mechanical disorder (fluctuations in phase of atomic displacements produced by a traveling acoustic wave) was also taken into account, in addition to electrical disorder.

There are also models which allow for the effect of the breakdown of the wave-vector selection rules for optical phonons in imperfect crystals and microcrystal-

lites, for example, the spatial-correlation model proposed in [29], where the uncertainty in the wave vector of a phonon in a microcrystallite is taken into account. In this case, an additional contribution to the low-frequency Raman spectrum can be due to optical phonons having larger wave vectors if the phonon frequency decreases noticeably with increasing wave vector (as is the case in microcrystalline films [30]). However, such a breakdown of the selection rules occurs in the long low-frequency tail of a Raman band, which is also allowed in a perfect crystal. This feature is inconsistent with the fact that, in the Raman spectrum of a congruent lithium niobate crystal, the band at ~100 cm^{-1} is separated from allowed lines; therefore, the spatial-correlation model [29] is inapplicable to the case considered in this paper. Another, more general reason why breakdown of the wave-vector selection rules for optical phonons cannot account for the band at ~100 cm^{-1} in the Raman spectrum of a congruent $LiNbO_3$ crystal is the fact that there are no optical phonons in the spectral range below 115 cm^{-1} [26].

An alternative model is one in which the density of vibrational states is manifested in the Raman spectrum due to wave-vector selection rule breakdown (WSRB) for acoustic phonons. We note that the models proposed in [27, 28] cannot be directly applied to the case considered in this paper, because the Martin–Brenig model [28] is developed in the continuum approximation (i.e., the dispersion law is linear) and the model proposed in [27] also does not allow one to correctly take into account the atomic structure of the material when considering real crystals.

The model in which the density of acoustic vibrational states is manifested in the Raman spectrum of a congruent crystal can explain the dependence of the position of the band under study on the RS geometry (Fig. 1). Such a dependence is due to the difference in the dispersion law between A_1 and E acoustic phonons [26] (the selection rule with respect to the eigenvector of an acoustic mode is assumed to hold in RS).

This model can also explain the independence of the position of the second maximum from the RS geometry (Fig. 1). This independence can be due to the fact that the dispersion curves of longitudinal phonons and A_1(TO) phonons become flattened at approximately the same frequency (according to calculations made in [26]).

Since the above discussion is based, to a large extent, on the calculations performed in [26], the question arises as to whether those calculations are sufficiently correct. The point is that the dispersion curves constructed in [20] on the basis of neutron scattering data do not flatten noticeably up to frequencies of ~120 cm^{-1}. Whether this discrepancy is due to a mistake in the calculations performed in [26] or to a lack of experimental data in the corresponding frequency range in [20] is not clear. According to the dispersion curves presented in [20], the Debye approximation is valid up to frequencies of 100–120 cm^{-1}, while the density of vibrational states calculated in [26] exhibits a non-Debye behavior at frequencies as low as 60 cm^{-1}.

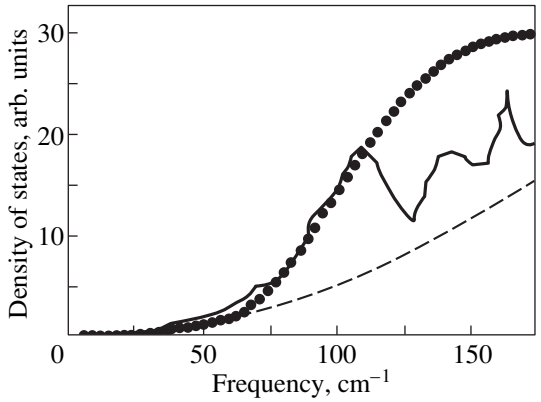

Fig. 5. Densities of vibrational states taken from [26] (solid curve) and calculated from the experimental data on low-temperature specific heat (circles). Dashed curve is the Debye approximation.

In order to verify the calculations in [26], we calculated the density of vibrational states from the experimental data on the low-temperature specific heat of lithium niobate crystals [24, 33] using the technique described in [31, 32]. Figure 5 compares the calculated density of states with that taken from [26]. The dashed curve in Fig. 5 corresponds to the Debye approximation, in which the specific heat $C_P(T)$ varies as the third power of temperature at $T < 10$ K. It is seen that the curve calculated from the data on the specific heat and the curve taken from [26] agree closely with each other (the discordance between them in the range above 110 cm^{-1} is accounted for by the fact that, in this range, the technique [31, 32] used to calculate the former curve is insensitive to narrow peaks in the density of vibrational states) and deviate from the Debye approximation curve in the range above ~60 cm^{-1}. Thus, the comparison shows that there are no serious mistakes in the calculations of acoustic branches in [26].

The acoustic-phonon WSRB model of the band at ~100 cm^{-1} in the Raman spectrum of a congruent lithium niobate crystal was discussed qualitatively. A more rigorous treatment would allow one to find the position and shape of the band at ~100 cm^{-1} using the acoustic-phonon dispersion curves. For example, a qualitative analysis reveals that one might expect a maximum due to E(TO) phonons to exist in the range 45 to 65 cm^{-1} (since the dispersion curves exhibit extrema in this range [26]), which is far below the position of the lowest frequency maximum of the band, ~82 cm^{-1}. Whether a more rigorous model will be able to explain this discordance is not clear.

Since the development of a rigorous model may prove to be an intricate problem, it is of interest to carry out investigations in a frequency range where the continuum approximation is valid, for instance, in the

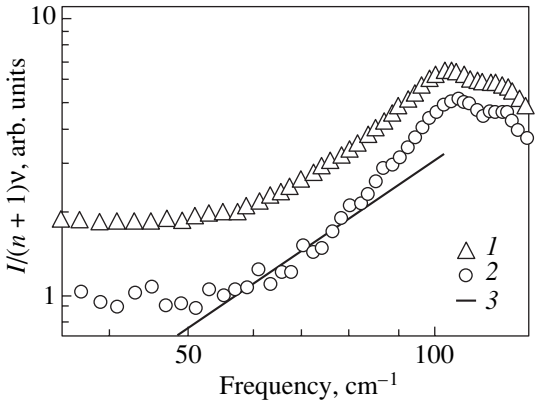

Fig. 6. Raman spectra $I/(n + 1)\nu$ (normalized to the Bose–Einstein factor) of a congruent $LiNbO_3$ crystal measured in the $x(zz)y$ geometry at (*1*) $T = 300$ and (*2*) 77 K; straight line *3* corresponds to a quadratic frequency dependence.

region of the low-frequency wing of the band, where the dispersion law of acoustic phonons is linear. Acoustic-phonon WSRB models in the continuum approximation with a Debye density of states predict a power-law frequency dependence of the RS intensity normalized to the Bose–Einstein factor:

$$I_n(\nu) = I(\nu)/[(n+1)\nu] \propto \nu^{\beta}, \qquad (2)$$

where $I(\nu)$ is the Stokes component of the Raman spectrum. The quantity $I_n(\nu)$ in Eq. (2) is proportional to the coupling constant involved in the Shuker–Gamon equation [34] for the RS intensity corresponding to a vibrational excitation of frequency ν. The exponent is $\beta = 2$ if the electrical-disorder mechanism [28] or phonon decay due to Rayleigh scattering by defects [35, 36] is dominant and $\beta = 0$ if the mean free path of phonons is in inverse proportion to the frequency squared [36, 37]. We compared Eq. (2) with the experimental data under the assumption that this equation is valid for acoustic A_1 phonons in the frequency range below 80 cm^{-1}, since, according to the calculations made in [26], the dispersion law of these phonons is linear for frequencies $\nu <$ 70–80 cm^{-1}. Figure 6 shows the Raman spectra in the $x(zz)y$ geometry and a straight line corresponding to a quadratic frequency dependence. It is seen that, although the experimental spectrum in the range 60 to 80 cm^{-1} is consistent with the quadratic frequency dependence, this frequency range is too short for the quadratic dependence to be well established. Below 60 cm^{-1}, the experimental normalized intensity in the wing of the Raman band is frequency-independent. A comparison of the Raman spectra at two different temperatures (Fig. 3) shows that this frequency-independent intensity can be due to multiphonon RS contribution rather than to first-order RS. An experimental study of the Raman spectra at temperatures below 80 K may provide additional pertinent information. However, our experimental setup enabled us to perform such a study.

Thus, the acoustic-phonon WSRB models are of considerable promise for explaining the band at ~100 cm^{-1} in the Raman spectra of congruent $LiNbO_3$ crystals. However, these models should be modified so as to take into account the positions of atoms in the crystal unit cell, and low-temperature RS studies (at $T < 80$ K) should be carried out.

4. CONCLUSION

We have experimentally investigated the low-frequency Raman spectra of lithium niobate crystals associated with stoichiometric defects. The band near the frequency 100 cm^{-1} in the Raman spectrum of a nonstoichiometric (congruent) crystal was shown to correspond to first-order Raman scattering. Different methods and models proposed for describing this band were discussed.

The analysis of the various models of the band at ~100 cm^{-1} revealed that none of these models can be preferred decidedly. The models in which additional localized vibrational modes arise or the density of acoustic vibrational states is manifested in the Raman spectra as a result of breakdown of the wave-vector selection rules show the most considerable promise. Further theoretical and experimental studies should be made with the aim, in particular, of constructing a model that can describe the shape of the Raman band. Measurement and comparison of the low-temperature specific heats of congruent and stoichiometric lithium niobate crystals, as well as measurements of low-temperature Raman spectra, may provide some insight into the problem.

ACKNOWLEDGMENTS

The authors are grateful to A.E. Batalov for measuring Raman spectra at the excitation line 1.064 μm and to S.M. Kostritskiĭ for the loan of the stoichiometric lithium niobate crystal.

This study was supported by the Russian Foundation for Basic Research (project no. 02-02-16112) and the Russian Academy-of-Sciences (Siberian Division) Foundation for Interdisciplinary Research.

REFERENCES

1. Yu. S. Kuz'minov, *Lithium Niobate and Tantalate as Materials for Nonlinear Optics* (Nauka, Moscow, 1975).
2. S. C. Abrahams and P. Marsh, Acta Crystallogr. B **42**, 61 (1986).
3. R. F. Schaufele and M. J. Weber, Phys. Rev. **152** (2), 705 (1966).
4. A. S. Barker, Jr. and R. Loudon, Phys. Rev. **158** (2), 433 (1967).
5. A. Ridah, P. Bourson, M. D. Fontana, and G. Malovichko, J. Phys.: Condens. Matter **9** (44), 9687 (1997).
6. A. de Bernabé, C. Prieto, and A. de Andrés, J. Appl. Phys. **79** (1), 143 (1996).

7. I. P. Kaminow and W. D. Johnston, Jr., Phys. Rev. **160** (3), 519 (1967).
8. W. D. Johnston, Jr. and I. P. Kaminow, Phys. Rev. **168** (3), 1045 (1968).
9. Y. Okamoto, Ping-chu Wang, and J. F. Scott, Phys. Rev. B **32** (10), 6787 (1985).
10. R. Claus, G. Borstel, E. Wiesendanger, and L. Steffan, Z. Naturforsch. A **27**, 1187 (1972).
11. V. S. Gorelik, S. V. Ivanova, I. P. Kucheruk, *et al.*, Fiz. Tverd. Tela (Leningrad) **18** (8), 2297 (1976) [Sov. Phys. Solid State **18**, 1340 (1976)].
12. V. S. Gorelik, Tr. Fiz. Inst. im. P.N. Lebedeva, Akad. Nauk SSSR **132**, 15 (1982).
13. N. V. Sidorov and Yu. N. Serebryakov, in *Proceedings of II International Conference on Real Structure and Properties of Noncentrosymmetric Crystals* (Aleksandrov, 1995), p. 338.
14. N. V. Sidorov, M. N. Palatnikov, Yu. A. Serebryakov, *et al.*, Neorg. Mater. **33** (4), 496 (1997).
15. N. V. Sidorov, M. N. Palatnikov, and V. T. Kalinnikov, Opt. Spektrosk. **82** (1), 38 (1997) [Opt. Spectrosc. **82**, 32 (1997)].
16. A. E. Batalov, Thesis (Novosibirsk State Univ., Novosibirsk, 2001).
17. M. E. Lines and A. M. Glass, *Principles and Applications of Ferroelectrics and Related Materials* (Oxford Univ. Press, Oxford, 1977; Mir, Moscow, 1981).
18. P. G. Klemens, Phys. Rev. **148** (2), 845 (1966).
19. A. Ridah, M. D. Fontana, and P. Bourson, Phys. Rev. B **56** (10), 5967 (1997).
20. M. R. Chowdhury, G. E. Peckham, and D. H. Saunderson, J. Phys. C: Solid State Phys. **11** (8), 1671 (1978).
21. A. Maradudin, Solid State Phys. **18**, 273 (1966).
22. E. Duval, A. Boukenter, and B. Champagon, Phys. Rev. Lett. **56** (12), 2052 (1986).
23. *Acoustical Crystals*, Ed. by M. P. Shaskol'skaya (Nauka, Moscow, 1982).
24. E. Pérez-Enciso and S. Vieira, Phys. Rev. B **57** (21), 13359 (1998).
25. J. M. Ziman, *Electrons and Phonons* (Clarendon, Oxford, 1960; Inostrannaya Literatura, Moscow, 1962).
26. K. Parlinsky, Z. Q. Li, and Y. Kawazoe, Phys. Rev. B **61** (1), 272 (2000).
27. E. Whalley and J. E. Bertie, J. Chem. Phys. **46** (4), 1264 (1967).
28. A. J. Martin and W. Brenig, Phys. Status Solidi B **64**, 163 (1964).
29. P. Parayanthal and F. H. Pollak, Phys. Rev. Lett. **52** (20), 1822 (1984).
30. W. J. Zhang and S. Matsumoto, Phys. Rev. B **63** (7), 073201 (2001).
31. N. V. Surovtsev, Avtometriya, No. 4, 51 (2001).
32. N. V. Surovtsev, Phys. Rev. E **64** (11), 061102 (2001).
33. R. Villar, E. Gmelin, and H. Grimm, Ferroelectrics **69**, 165 (1986).
34. R. Shuker and R. W. Gamon, Phys. Rev. Lett. **25** (4), 222 (1970).
35. J. Jäckle, in *Amorphous Solids: Low-Temperature Properties*, Ed. by W. A. Phillips (Springer, Berlin, 1981).
36. E. Duval, L. Saviot, N. Surovtsev, *et al.*, Philos. Mag. B **79** (11/12), 2051 (1999).
37. L. Saviot, E. Duval, N. V. Surovtsev, *et al.*, Phys. Rev. B **60** (1), 18 (1999).

Translated by Yu. Epifanov

Physics of the Solid State, Vol. 45, No. 3, 2003, pp. 542–546. Translated from Fizika Tverdogo Tela, Vol. 45, No. 3, 2003, pp. 513–517.

MAGNETISM AND FERROELECTRICITY

Influence of Weak Pulsed Magnetic Fields on Triglycine Sulfate Crystals

M. N. Levin*, V. V. Postnikov, M. Yu. Palagin***, and A. M. Kostsov***

** Voronezh State University, Universitetskaya pl. 1, Voronezh, 394693 Russia*

e-mail: levin@lev.vsu.ru

*** Voronezh State Forestry Engineering Academy, Voronezh, 394613 Russia*

**** Voronezh State Technical University, Moskovskiĭ pr. 14, Voronezh, 394026 Russia*

Received April 9, 2002; in final form, June 17, 2002

Abstract—The influence of weak (≤0.02 T) pulsed magnetic fields on the ferroelectric and dielectric characteristics of nominally pure triglycine sulfate crystals was detected for the first time. A short-term (seconds) pulsed magnetic impact caused long-term (hundreds of hours) changes in the coercive field and the temperature dependences of the dielectric constant, the dissipation factor, and the relaxation time of the dielectric constant near the ferroelectric phase transition. It was assumed that the effects detected were caused by unpinning of domain walls and dislocations from stoppers, followed by the formation of new defect and domain structures.

1. INTRODUCTION

To date, a rather large amount of experimental data has been accumulated indicating the unique capability of rather weak (<1 T) pulsed magnetic fields (PMFs) to significantly affect the structure and properties of various nonmagnetic solid-state materials. Examples of PMF-induced effects are the impurity phase decay in alkali halide crystals (AHCs) [1], plasticity changes (magnetoplastic effect) in AHCs and nonmagnetic metals [2–4], and structural changes in silicon crystals [5], III–V [6, 7] and II–VI [8] semiconductor compounds, oxide glasses [9], molecular crystals [10], and crystallizing polymers [11, 12].

As is known, ferroelectrics can also be sensitive to magnetic fields [13]. Strong magnetic fields (>10 T) can change the fundamental parameters of ferroelectrics, such as the Curie temperature and soft-mode frequency [14, 15]. Weaker fields (<1 T) can effect the domain structure dynamics by interacting with magnetic moments of moving domain walls (magnetodomain effect) [16–18]. In particular, the magnetic influence on starting chaos fields in triglycine sulfate (TGS) crystals is explained by the magnetodomain effect [19]. Magnetic fields change the interaction between mobile charged defects and domain walls, which manifests itself, e.g., as a change in the dielectric loss [20]. Recently, the magnetoplastic effect was directly observed in ferroelectric crystals [21].

All these facts testify that it is expedient to search for new PMF-induced effects in ferroelectrics; it is quite probable that these effects will be detected.

This work is the first where the influence of weak (≤0.02 T) PMFs on the ferroelectric, dielectric, and structural characteristics of nominally pure TGS crystals was studied. The TGS $(CH_2NH_2COOH)_3 \cdot H_2SO_4$ crystal was taken as a model object, since its domain structure is distinguished by high sensitivity to external influences and its ferroelectric and dielectric properties has been studied sufficiently [22, 23].

2. EXPERIMENTAL

First of all, in this study, in contrast to many previous works, we controlled changes in the magnetoelectric characteristics after the magnetic exposure rather than during it.

The ferroelectric characteristics of the TGS crystal, such as the coercive field E_c and the Curie point T_c (temperature of the ferroelectric phase transition), were measured. The dielectric properties were studied by measuring the temperature dependences of the active component of the dielectric constant, $\varepsilon'(T)$, and the dissipation factor $\tan\delta(T)$ near the ferroelectric phase transition. The changes in the TGS crystal structure caused by defects were indirectly controlled by measuring the temperature dependence of the isothermal relaxation time of the dielectric constant of the crystal whose thermodynamic equilibrium was disturbed by a PMF. This method, based on an analysis of the dynamics of the domain wall–point-defect system, was earlier efficiently applied to a study of imperfect TGS crystal structure with the thermodynamic equilibrium disturbed by an electric field [24, 25].

A nominally pure TGS single crystal was grown by temperature-controlled cooling of a supersaturated aqueous solution. Samples were cut out from the single crystal as rectangular (7 × 7 mm) plates 0.5 mm thick with the polar *Y* axis perpendicular to the plate plane.

After polishing and washing in dehydrated ethyl alcohol, silver electrodes were applied to the large faces through thermal evaporation in vacuum. Before the studies, the samples were annealed in air at $T = 350$ K for 3 h.

The samples were exposed to a series of $N = 1500$ symmetric triangular magnetic-field pulses $\tau = 40$ μs long with amplitude $B = 0.02$ T and a repetition rate of 20 ms. The PMF was produced by a capacitor periodically discharged through a low-inductance solenoid and was monitored by the discharge current in the solenoid circuit and by the induction voltage at a test inductance coil. Samples in the ferroelectric and paraelectric phases were exposed to the PMF at $T = 293$ and 328 K, respectively. The ferroelectric Y axis was oriented parallel or perpendicular to the direction of the magnetic field.

The spontaneous polarization and the frequency dependence of the coercive field E_c were measured using the conventional Sawyer–Tower technique [22].

The dielectric constant and the dissipation factor were measured before and after the PMF exposure using a Tesla BM484 bridge (with a sinusoidal test signal of frequency $\omega = 10^4$ Hz and amplitude 0.5 V) in a special thermostat with the temperature controlled by a VRT-2 system. The temperature was measured with a platinum resistance thermometer within a margin of error $\leq 2.5 \times 10^{-3}$ K. The temperature variation rate, adjusted in the course of heating, was 1.2 K/h near T_c.

The experiment was carried out as follows. After measuring the initial values of $\varepsilon'(T)$ and $\tan\delta(T)$, a sample was removed from the thermostat and placed into the solenoid. After the PMF exposure in the solenoid, the sample was again connected to the measuring circuit in the thermostat, wherein the temperature was maintained 1.5 K lower than the initial value of T_c.

A series of samples cut out from the same crystal was used to study the isothermal relaxation of the dielectric constant after the PMF exposure in the temperature range 318–322.5 K adjacent to the Curie point on the polar-phase side. The exposures and measurements at a certain temperature for each sample were carried out *in situ* in a special (molybdenum-glass) measuring cell with a bifilarly wound heater. The cell with the sample, measuring electrodes, and platinum thermometer was placed inside the solenoid inducing the PMF. We note that the platinum thermometer did not degrade under the PMF exposure, as distinct from the initially used germanium thermometer. The whole system was thoroughly heat-insulated. The cell temperature was controlled by the VRT-2 system. The time dependences of the dielectric constant relaxation were measured at the temperature of the exposure, starting from the moment of PMF switching off.

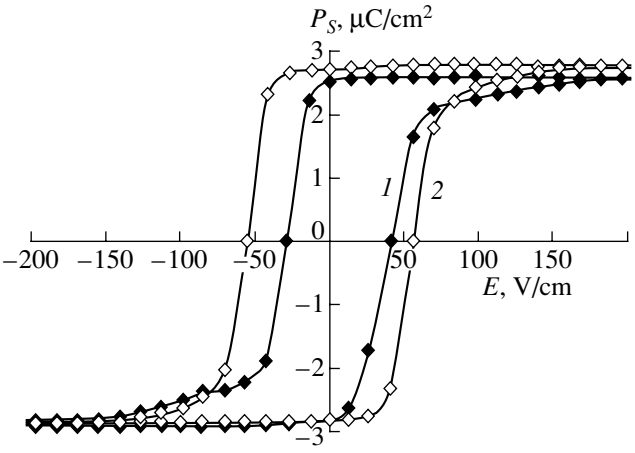

Fig. 1. Influence of the exposure of a TGS sample in the ferroelectric phase at $T = 293$ K to a pulsed magnetic field on the shape of the ferroelectric hysteresis loop (*1*) for the initial sample and (*2*) after a 30-s PMF exposure; the measurements were carried out at $T = 310$ K.

3. EXPERIMENTAL RESULTS

The exposure to a PMF caused a long-term change in the ferroelectric parameters of TGS crystals, more specifically, to an increase in the coercive field E_c and a shift of the Curie point T_c.

The typical loops of the ferroelectric hysteresis in the case of the ferroelectric phase before and after the PMF exposure are shown in Fig. 1. We note that the initial loop is shifted along the electric-field axis. The PMF exposure widened the ferroelectric loop and made it symmetric. The initial asymmetric shape of the hysteresis loop was completely restored in ten days after the PMF exposure if the sample was kept at room temperature in air.

The direction of the Curie point shift depended on the phase state of the sample exposed to the PMF. From the temperature dependences of the dielectric constant $\varepsilon'(T)$ (Fig. 2), one can see that the ferroelectric transition temperature decreased by ~0.1 K when the sample was exposed in the polar phase. The Curie point shift, as determined from the $\varepsilon'(T)$ dependences, correlates well with the same shift of the main maximum in the temperature dependence of $\tan\delta(T)$ shown in Fig. 3. The Curie point T_c returned to its initial value upon repeated measurements with the same samples.

The $\varepsilon'(T)$ and $\tan\delta(T)$ dependences of the samples exposed to a PMF in the paraelectric phase are shown in Figs. 4 and 5, respectively. In this case, the maxima of $\varepsilon'(T)$ and $\tan\delta(T)$ are shifted by $\Delta T_c \sim 0.1$ K to higher temperatures. The Curie point T_c returned to its initial value upon repeated measurements with the same samples.

The PMF exposure also caused a significant change in the $\varepsilon'(T)$ and $\tan\delta(T)$ shape in the region of the ferroelectric transition point.

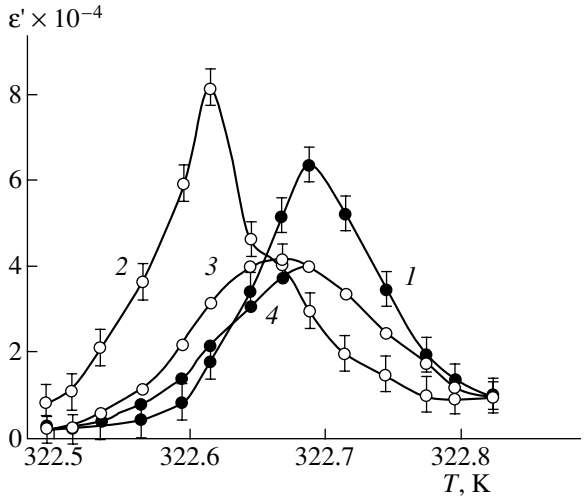

Fig. 2. Temperature dependences of the dielectric constant ε'(*T*) of a TGS sample in the ferroelectric phase at *T* = 293 K exposed to a PMF for 30 s: (*1*) the initial dependence and (*2–4*) 1, 24, and 48 h after the PMF exposure, respectively.

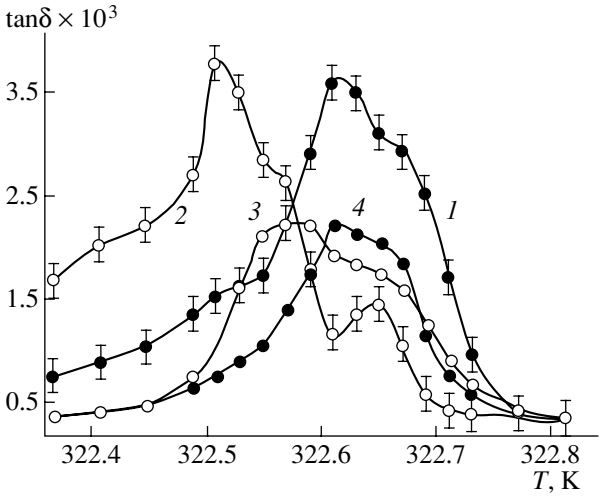

Fig. 3. Temperature dependences of the dissipation factor tanδ(*T*) of a TGS sample in the ferroelectric phase at *T* = 293 K exposed to a PMF: (*1*) the initial dependence and (*2–4*) 1, 24, and 48 h after the PMF exposure, respectively.

The Curie point T_c of the crystal exposed to the PMF in the ferroelectric phase decreased, while the dielectric constant maximum increased (Fig. 2). The restoration of the initial value of T_c was accompanied by a decrease in this maximum to a value that was lower than the initial value. The PMF exposure of the crystal in the paraelectric phase caused an immediate decrease in the dielectric constant maximum (Fig. 4).

A characteristic feature of the PMF-induced changes in the temperature dependences of tanδ(*T*) is splitting of the initial peak of tanδ(*T*) into two peaks, which took place after PMF exposure of the TGS crystal in both the ferroelectric (Fig. 3) and paraelectric phases (Fig. 5). Repeated measurements exhibited the tendency to restoration of the shape of the tanδ(*T*) dependence with a single maximum.

Figure 6 displays the temperature dependence of the isothermal-relaxation time $\tau_\varepsilon(T)$ of the dielectric constant of the TGS crystal; this dependence was constructed using a set of curves of isothermal relaxation of the dielectric constant for a series of samples each of which was exposed to a PMF and relaxed at the temperature indicated in Fig. 6.

The effects described above were observed when exposing the TGS crystals to a pulsed magnetic field directed along the polar *Y* axis. No effects were observed in the case of the *Y* axis being perpendicular to the pulsed magnetic field.

4. DISCUSSION

Our studies showed that weak PMFs cause significant changes in the coercive field, dielectric constant, and dissipation factor of the TGS crystals.

Since these effects were first detected in this study and the complete phenomenological pattern was not established, no more than a hypothetical interpretation of the results is possible at this stage.

The coercive-field increase due to the PMF exposure can be a manifestation of the crystal becoming more imperfect, because of which repolarization of the ferroelectric crystal is hampered by an additional interaction between defects and domain walls.

The domain wall pinning by defects decreases the contribution from domain lateral motion to the dielectric constant ε'(*T*), which explains its decrease after PMF exposure of samples in the paraelectric phase. Since samples exposed in the paraelectric phase were transferred to the ferroelectric phase before ε'(*T*) mea-

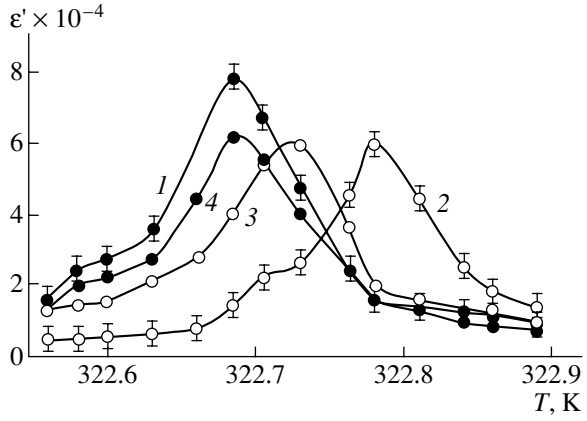

Fig. 4. Temperature dependences of the dielectric constant ε'(*T*) of a TGS sample in the paraelectric phase at *T* = 328 K exposed to a PMF for 30 s: (*1*) the initial dependence and (*2–4*) 1, 24, and 48 h after the PMF exposure, respectively.

surements, a domain structure was formed in those crystals whose defect structure was changed by the PMF exposure.

In the case of PMF exposure in the ferroelectric phase, an increase in the dielectric constant of the TGS crystal was observed immediately after the PMF exposure.

This effect can be caused by unpinning of domain walls from initial point defects (pinning centers), much as the well-known magnetoplastic effect is caused by unpinning of dislocations from paramagnetic stoppers. The assumed unpinning of domain walls from stoppers under the action of a PMF increased their mobility and, hence, the contribution from domain lateral displacements to the crystal dielectric constant, with the domain walls not having time to be pinned at newly generated defects. At longer times after the PMF exposure, diffusive collection of defects at domain walls and additional pinning of the domain structure at PMF-induced defects took place, which caused a decrease in the dielectric constant during repeated measurements.

The vanishing of the shift of the ferroelectric hysteresis loop along the electric-field axis observed after the PMF exposure indicates that the internal electric field (that existed in the initial crystal) disappeared. The internal field could be induced by polar defects ordered and pinned at domain walls. The disappearance of the internal field after a PMF exposure can be caused by unpinning of defects from domain walls and disordering of their electric moments.

As is known, the internal field has an effect on the ferroelectric transition temperature. A classical example is the Curie point increasing when the TGS crystal is doped with alanine [22].

The internal-field decrease due to disordering of defects after their unpinning from domain walls explains the decrease in the phase transition temperature T_c due to the PMF exposure in the ferroelectric phase; the reverse process (ordering of defects during their pinning at domain walls) explains the T_c increasing when the crystal is exposed in the paraelectric phase.

The shape of the $\tau_\varepsilon(T)$ dependence shown in Fig. 6 is similar to the previously studied temperature dependence of the relaxation time $\tau_2(T)$ of a domain-wall–point defects system whose equilibrium was disturbed by an electric field [24, 25]. This similarity confirms the assumption that the equilibrium state of the TGS crystal exposed to a PMF in the ferroelectric phase is disturbed due to unpinning of domain walls from stoppers. According to [24, 25], the decrease in the system relaxation time in the lower temperature branch of the $\tau_\varepsilon(T)$ dependence is explained by a thermal increase in the diffusivity of point defects unpinned from domain walls and the increase in the system relaxation time in the higher-temperature branch of the $\tau_\varepsilon(T)$ dependence is caused by weakening of the interaction between domain walls and stoppers as the crystal approaches the ferroelectric phase transition point.

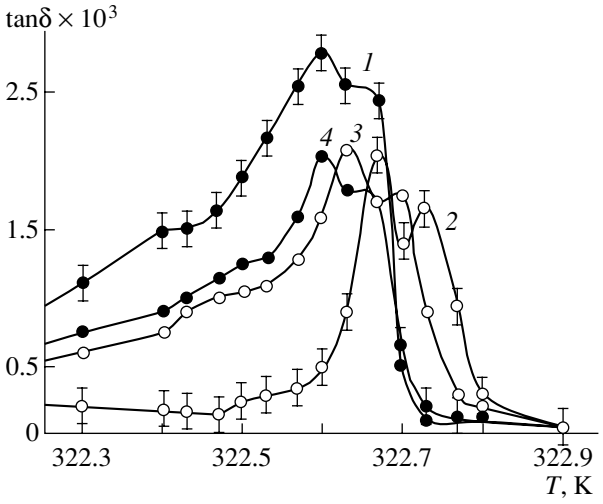

Fig. 5. Temperature dependences of dissipation factor $\tan\delta(T)$ of a TGS sample in the paraelectric phase at T = 328 K exposed to a PMF: (*1*) the initial dependence and (*2*–*4*) 1, 24, and 48 h after the PMF exposure, respectively.

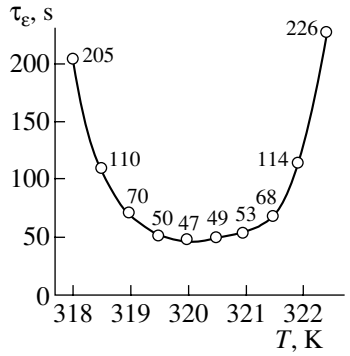

Fig. 6. Dependence of the relaxation time of the dielectric constant on the temperature at which TGS samples were exposed to a PMF; the exposure time was 30 s for all samples.

It might be assumed that, in contrast to the exposure to electric fields, the PMF not only unpins domain walls from stoppers but also produces new defects differing from the initial ones. It is not improbable that initial defects and/or products of their decay, unpinned by the PMF from both domain walls and dislocations existing in the crystal, participate in the generation of new defects.

Thus, the PMF-induced changes in the ferroelectric and dielectric parameters of TGS crystals can be caused by unpinning of initial defects from domain walls and dislocations, as well as by a decay of the initial complexes of point defects, followed by mobile point defects forming metastable defect complexes and by the formation of a new domain structure.

The effects described above are paradoxical because an energy effect of magnetic fields of as low as $B \sim 0.02$ T is negligible and cannot cause the observed phenomena ($\mu_B B < 10^{-4} kT$ at $B \leq 0.02$ T, where μ_B is the Bohr magneton). It is also hardly probable that PMF-induced electric fields are responsible for the effects observed, since these fields are directed normally to the polar (twofold) axis of the ferroelectric crystal and do not exceed 10 V/cm (see the estimation in [5]).

It is agreed that, in diamagnetic crystals, weak magnetic fields lift the forbiddenness of the electron transitions with spin flip that change the chemical-bond strength in defect complexes [26, 27]. For example, the singlet–triplet transitions in short-lived radical pairs, generated by paramagnetic point defects with broken bonds in the dislocation cores, explain dislocation unpinning from stoppers in the case of magnetoplastic effects.

As is well known, nominally pure TGS crystals contain paramagnetic impurities, including Fe^{3+} centers [22]. It is not improbable that these centers stabilize some complexes that can decay under the action of a PMF. However, the microscopic structure of defects that act as stoppers of domain walls in TGS crystals has not yet been established [28], which complicates the analysis of the mechanisms of the effects detected.

However, it should be emphasized that there is a difference between the PMF-induced effects detected in TGS and the magnetoplastic effects observed in AHCs and metals. The effects in TGS were observed in fields ≤0.02 T, which are lower than the typical threshold ~0.1 T for magnetoplastic effects characterized by the known Δg mechanism [27]. Such weak magnetic fields are characteristic of the hyperfine interaction between electron and nuclear spins [29]. This suggests that hydrogen bond protons participate in the electron transitions responsible for the PMF-induced effects in TGS. This assumption could be confirmed through detection of changes in the imperfect structure of TGS and/or other crystals with hydrogen bonds caused by the resonant effect (distinguishing between the hyperfine interaction and the Δg mechanism [29]) of a weak dc magnetic field.

REFERENCES

1. G. I. Distler, V. M. Kanevskiĭ, V. V. Moskvin, *et al.*, Dokl. Akad. Nauk SSSR **268** (3), 591 (1983) [Sov. Phys. Dokl. **28**, 43 (1983)].
2. V. I. Al'shits, R. Voska, E. V. Darinskaya, and E. A. Petrzhik, Fiz. Tverd. Tela (St. Petersburg) **35** (1), 70 (1993) [Phys. Solid State **35**, 37 (1993)].
3. Yu. I. Golovin, R. B. Morgunov, D. V. Lopatin, and A. A. Baskakov, Kristallografiya **43** (6), 1115 (1998) [Crystallogr. Rep. **43**, 1056 (1998)].
4. O. A. Datsko, Fiz. Tverd. Tela (St. Petersburg) **44** (2), 289 (2002) [Phys. Solid State **44**, 300 (2002)].
5. M. N. Levin and B. A. Zon, Zh. Éksp. Teor. Fiz. **111** (4), 1373 (1997) [JETP **84**, 760 (1997)].
6. V. N. Davydov, E. A. Loskutova, and E. N. Naĭden, Fiz. Tekh. Poluprovodn. (Leningrad) **23** (9), 1596 (1989) [Sov. Phys. Semicond. **23**, 989 (1989)].
7. V. I. Alekseenko, Zh. Tekh. Fiz. **70** (6), 63 (2000) [Tech. Phys. **45**, 732 (2000)].
8. V. P. Vlasov, F. A. Zaitov, V. M. Kanevskiĭ, *et al.*, Fiz. Tverd. Tela (St. Petersburg) **34** (10), 3264 (1992) [Sov. Phys. Solid State **34**, 1747 (1992)].
9. V. I. Alekseenko, Zh. Tekh. Fiz. **68** (10), 50 (1998) [Tech. Phys. **43**, 1181 (1998)].
10. Yu. A. Osip'yan, Yu. I. Golovin, D. V. Lopatin, *et al.*, Pis'ma Zh. Éksp. Teor. Fiz. **69** (2), 110 (1999) [JETP Lett. **69**, 123 (1999)].
11. M. N. Levin and N. N. Matveev, Zh. Fiz. Khim. **75** (10), 1886 (2001).
12. Yu. I. Golovin and R. B. Morgunov, Fiz. Tverd. Tela (St. Petersburg) **43** (5), 827 (2001) [Phys. Solid State **43**, 859 (2001)].
13. H. Schmid, Ferroelectrics **161** (1–4), 1 (1994).
14. R. Comes, S. M. Shapiro, B. C. Frases, and G. Shirane, Phys. Rev. B **24**, 1559 (1981).
15. V. P. Zenchenko, B. G. Vekhter, and I. B. Bersuker, Zh. Éksp. Teor. Fiz. **82** (5), 1628 (1982) [Sov. Phys. JETP **55**, 943 (1982)].
16. S. A. Flerova, O. E. Bochkov, and I. L. Tsinman, Fiz. Tverd. Tela (Leningrad) **24** (8), 2505 (1982) [Sov. Phys. Solid State **24**, 1424 (1982)].
17. S. A. Flerova and I. L. Tsinman, Kristallografiya **32** (4), 1047 (1987) [Sov. Phys. Crystallogr. **32**, 615 (1987)].
18. O. L. Orlov, S. A. Popov, S. A. Flerova, and I. L. Tsinman, Pis'ma Zh. Tekh. Fiz. **14** (2), 118 (1988) [Sov. Tech. Phys. Lett. **14**, 52 (1988)].
19. S. A. Gridnev, K. S. Drozhdin, and V. V. Shmykov, Fiz. Tverd. Tela (St. Petersburg) **42** (2), 318 (2000) [Phys. Solid State **42**, 326 (2000)].
20. S. A. Gridnev, K. S. Drozhdin, and V. V. Shmykov, Kristallografiya **42** (6), 1135 (1997) [Crystallogr. Rep. **42**, 1058 (1997)].
21. B. I. Smirnov, N. N. Peschanskaya, and V. I. Nikolaev, Fiz. Tverd. Tela (St. Petersburg) **43** (12), 2154 (2001) [Phys. Solid State **43**, 2250 (2001)].
22. M. E. Lines and A. M. Glass, *Principles and Applications of Ferroelectrics and Related Materials* (Oxford Univ. Press, Oxford, 1977; Mir, Moscow, 1981).
23. M. V. Tsedrik, *Physical Properties of Crystals of the Triglycine Sulfate Family* (Nauka i Tekhnika, Minsk, 1986).
24. B. N. Prasolov and I. A. Safonova, Izv. Ross. Akad. Nauk, Ser. Fiz. **59** (9), 69 (1995).
25. B. N. Prasolov, N. V. Postnikova, and I. A. Safonova, Izv. Ross. Akad. Nauk, Ser. Fiz. **61** (5), 1002 (1997).
26. Yu. Golivin and R. B. Morgunov, Chem. Rev. **23**, 23 (1998).
27. M. Molotskii, Mater. Sci. Eng. A **287**, 248 (2000).
28. A. V. Shil'nikov, A. P. Pozdnyakov, V. N. Nesterov, *et al.*, Fiz. Tverd. Tela (St. Petersburg) **43** (8), 1516 (2001) [Phys. Solid State **43**, 1576 (2001)].
29. A. L. Buchachenko, R. Z. Sagdeev, and K. M. Salikhov, *Magnetic and Spin Effects in Chemical Reactions* (Nauka, Novosibirsk, 1978).

Translated by A. Kazantsev

Physics of the Solid State, Vol. 45, No. 3, 2003, pp. 547–552. Translated from Fizika Tverdogo Tela, Vol. 45, No. 3, 2003, pp. 518–522.

MAGNETISM AND FERROELECTRICITY

Effect of Organic Dyes on the Dielectric Properties of KH_2PO_4 Crystals

S. V. Grabovskiĭ, I. V. Shnaĭdshteĭn, and B. A. Strukov

Moscow State University, Vorob'evy gory, Moscow, 119899 Russia

Received June 26, 2002

Abstract—The effect of organic dyes on the dielectric properties of KH_2PO_4 (KDP) crystals is studied over a wide range of temperatures. The dielectric properties of KDP crystals doped with molecules of the Chicago Sky Blue and Amaranth organic dyes are investigated for the first time. The dye molecules can be incorporated into the crystal lattice of KDP and selectively paint the pyramidal growth sectors of the crystal. The influence of dye organic impurities on the domain contribution to the permittivity is analyzed with due regard for the sectoral crystal structure. It is demonstrated that, upon doping of KDP crystals with organic dyes, the blocking effect of background impurities on domain walls is substantially weakened in the prismatic growth sector of the crystal in the polar phase. This leads to a noticeable change in the dielectric properties, specifically to an increase in the domain contribution to the permittivity of the crystal. *© 2003 MAIK "Nauka/Interperiodica".*

1. INTRODUCTION

The dielectric properties of KH_2PO_4 (KDP) crystals, unlike other ferroelectrics, exhibit unusual behavior in the ferroelectric phase. In particular, KDP crystals below the Curie point T_C possess an anomalously high permittivity over a rather wide range of temperatures [1]. It is known that similar anomalies in the dielectric properties of KDP crystals are caused by the domain structure [2]. The dynamic properties of the domain structure of ferroelectric materials (including KDP crystals) are substantially affected by defects of different types. Upon introduction of impurities into a ferroelectric material, it is possible to trace changes in the dielectric properties associated with the domain structure and to obtain valuable information on the dynamics of domain walls. In this work, we investigated the dielectric properties of KDP crystals doped with organic dyes.

Numerous experimental investigations into the influence of radiation-induced defects and impurities on the dielectric properties of KDP crystals have revealed that the presence of defects in the structure leads to a change in the temperature dependence of the permittivity at temperatures below the Curie point T_C. The formation of structural defects upon irradiation [3] and introduction of chromium ions [4] and potassium hydroxide [5] affects the level of the plateau in the temperature dependence of the permittivity over the entire range below the Curie temperature T_C. As the defect concentration increases, the plateau in the dependence gradually disappears. This implies that the contribution of the domain mechanism to the permittivity decreases as the result of a decrease in the mobility of domain walls due to their pinning by structural defects.

For nominally pure KDP crystals, the degree of structure imperfection is determined by the content of inorganic impurities that are necessarily present in initial salt solutions. First and foremost, these are Sn^{4+}, Cr^{3+}, Fe^{3+}, and Al^{3+} polyvalent metal ions, which inevitably occur in the form of background impurities at a content of 10^{-4}–10^{-3} wt % in crystallization solutions [6]. Among all cation impurities that naturally exist in single crystals, Fe^{3+} and Al^{3+} ions are contained in maximum amounts. It is these ions that are responsible for the formation of a defect structure of KDP crystals in the course of their growth [7]. In our recent work [15], we showed that the distribution of structural defects over the growth sectors in KDP crystals grown by the rapid technique [9] differ from that in the crystals grown by the traditional method.

A more intricate situation arises with organic dyes [10]. The majority of organic dyes are not involved in an inorganic lattice [11]. However, recently, Subramony *et al.* [12] studied the rapid growth of KDP crystals from aqueous solutions containing organic dyes and found that a number of dyes (for example, the Chicago Sky Blue and Amaranth organic dyes [12]) are adsorbed by the KDP crystal in the course of crystallization. Moreover, these authors revealed an interesting effect associated with the selective staining of growth sectors in the crystal: the organic dyes are incorporated only into the pyramidal growth sector, whereas the prismatic sector remains colorless (Fig. 1).

The selective adsorption of dyeing dopants by different crystal faces can be explained in terms of the positive charge at a face of the pyramid and the neutral charge at the prismatic growth sector [13, 14]. Since the organic dye molecules each involve four negatively charged functional groups SO_3^-, they tend to be adsorbed by a

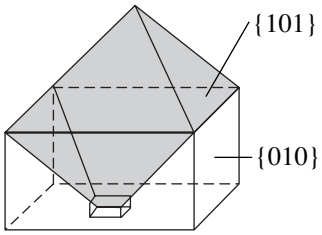

Fig. 1. Schematic representation of the incorporation of the Chicago Sky Blue and Amaranth organic dyes into the growth sectors of a KDP crystal.

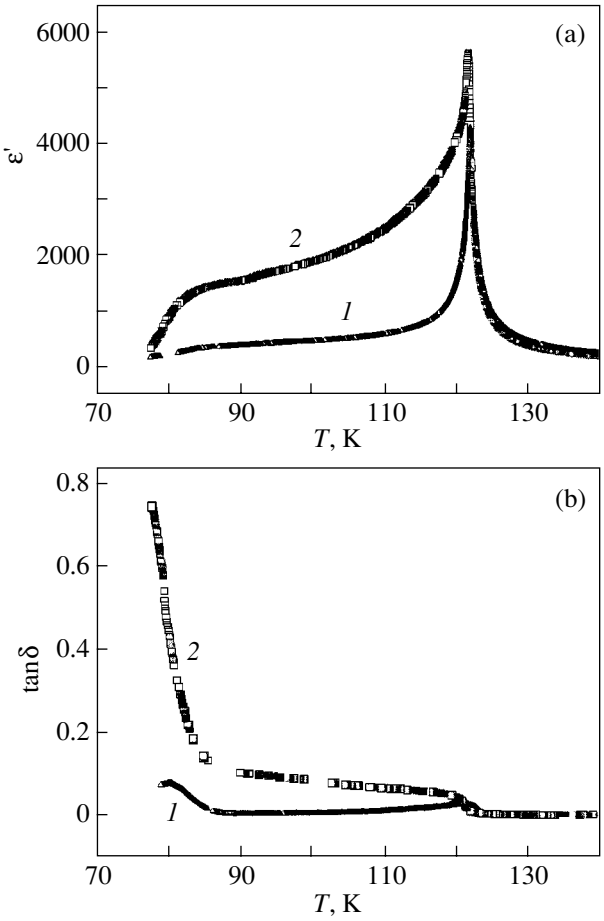

Fig. 2. Temperature dependences of (a) the permittivity and (b) the dielectric loss tangent for (*1*) pyramidal and (*2*) prismatic growth sectors in KDP crystals doped with the Chicago Sky Blue dye.

positively charged face of the pyramid. Furthermore, it is believed that, although the structural units of an inorganic crystal are not isomorphic to the organic dye molecules, the interatomic distances in the crystal and the dye molecules can insignificantly differ along preferred planes. As a consequence of the stereochemical affinity, the crystal face aligned parallel to the preferred plane can be slightly distorted and, thus, appears to be locally isomorphic to the dye molecule [10].

The aim of the present work was to investigate how the Chicago Sky Blue and Amaranth organic dyes affect the dielectric properties of KDP crystals and to elucidate the mechanism of selective incorporation of these dyes into the growth sectors of the KDP crystals. For this purpose, we carried out dielectric measurements and analyzed the results obtained.

2. EXPERIMENTAL TECHNIQUE AND RESULTS

The experiments were performed using KDP crystals doped with the Chicago Sky Blue and Amaranth organic dyes. The molecular structures of these dyes were described in [12]. The crystals were grown by the rapid growth technique on a point seed from an aqueous solution containing ~10^{-4} g of the dye per gram of the KDP salt. The incorporation of dyes into the crystal structure occurred only at temperatures below 40°C, i.e., when the crystal already reached a sufficiently large size. The growth rate of the crystals was equal to 6–10 mm/day. The final sizes of KDP crystals doped with the Chicago Sky Blue and Amaranth organic dyes were $5 \times 5.5 \times 6$ and $8 \times 8.5 \times 6.5$ cm, respectively.

In the course of crystal growth, the dye molecules were incorporated only into the pyramidal growth sector, whereas the prismatic sector remained colorless. According to the spectroscopic data, the dyed sectors of the crystal contained 1.4–2 dye molecules per 10^5 KDP molecules.

The samples used in our investigations were prepared from the dyed (pyramidal) and colorless (prismatic) regions of the crystal. The mean area of the samples whose preferred plane was perpendicular to the **c** polar axis was 5×8 mm, and the sample thickness was 1 mm. The sample faces perpendicular to the **c** axis were coated with a thin layer of silver paste.

The experimental results obtained for KDP crystals doped with organic dye molecules were compared with those for undoped crystals (grown by the traditional and rapid methods) with due regard for their sectoral structure.

The temperature dependences of the permittivity were measured during cooling from room temperature to the liquid-nitrogen temperature. The experimental conditions were similar to those described in our previous work [15].

Figures 2 and 3 depict the temperature dependences of the permittivity and the dielectric loss tangent for KDP crystals doped with the Chicago Sky Blue and Amaranth organic dyes, respectively. These curves were obtained for the pyramidal (dyed) and prismatic (colorless) growth sectors.

It is found that the temperature dependences of the permittivity coincide in the paraelectric phase from room temperature to the Curie point. Taking into account the absolute error in the temperature measurements ($\Delta T \approx \pm 0.1$ K), the Curie temperature T_C of dyed

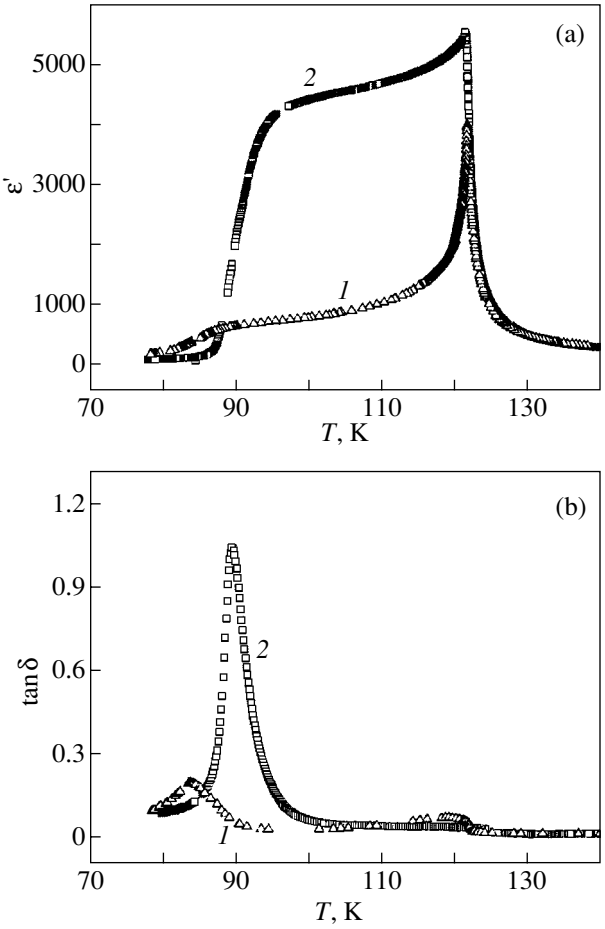

Fig. 3. Temperature dependences of (a) the permittivity and (b) the dielectric loss tangent for (*1*) pyramidal and (*2*) prismatic growth sectors in KDP crystals doped with the Amaranth dye.

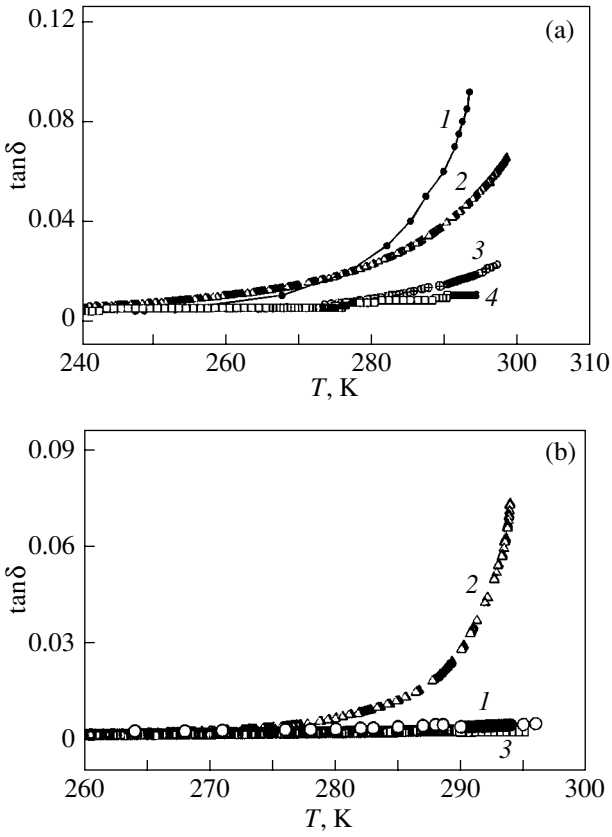

Fig. 4. Temperature dependences of the dielectric loss tangent for (a) pyramidal and (b) prismatic growth sectors in pure and doped KDP crystals in the vicinity of room temperature: (*1*) pure KDP crystal grown by the rapid method, (*2*) KDP crystal doped with the Chicago Sky Blue dye, (*3*) KDP crystal doped with the Amaranth dye, and (*4*) pure KDP crystal grown by the traditional method.

crystals is no different from that of the pure crystal and is equal to 121.8 K.

As can be seen from Figs. 2 and 3, the temperature dependences of the permittivity measured for dyed pyramidal sectors exhibit neither a clear maximum nor an anomalous plateau. For the prismatic growth sectors, the temperature dependences of the dielectric properties show a different behavior. In this case, the permittivity ε_C at the Curie point reaches larger values and anomalous permittivities are observed over a wide range below the Curie temperature. Moreover, there is a temperature range characterized by a rapid decrease in the permittivity ε and a maximum of the dielectric loss tangent $\tan\delta$. This range corresponds to freezing of the domain structure.

For prismatic growth sectors in the KDP crystal doped with the Amaranth organic dye (Fig. 3), the permittivity in the temperature range of the plateau is substantially higher than that for all the other crystals under investigation, the temperature dependence of $\tan\delta$ exhibits a clearly defined maximum corresponding to the temperature T_F of freezing of the domain structure, and this temperature is approximately 10 K higher than that for the other crystals.

Figure 4 shows the portions of the temperature dependences of the dielectric loss tangent in the vicinity of room temperature for the pyramidal and prismatic growth sectors. From analyzing these portions, we can judge the electrical conductivity of the crystals and the structure imperfection.

3. DISCUSSION

Earlier [8], we compared the experimental data on the dielectric properties of the pyramidal growth sectors in pure and dyed KDP crystals and drew the tentative inference that the decrease in the domain contribution to the permittivity is caused by organic dopants, which, even at very low concentrations, suppress the motion of domain walls. In [8], the pure (undoped) crystals were grown by the traditional method. However, our further investigations demonstrated that the

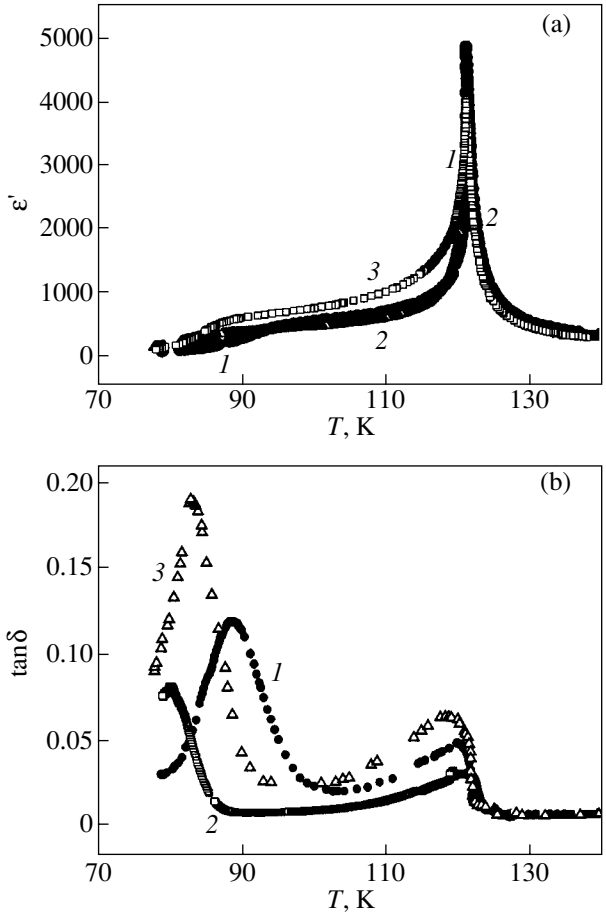

Fig. 5. Temperature dependences of (a) the permittivity and (b) the dielectric loss tangent for pyramidal sectors in pure and doped KDP crystals at low temperatures: (*1*) pure KDP crystal, (*2*) KDP crystal doped with the Chicago Sky Blue dye, and (*3*) KDP crystal doped with the Amaranth dye.

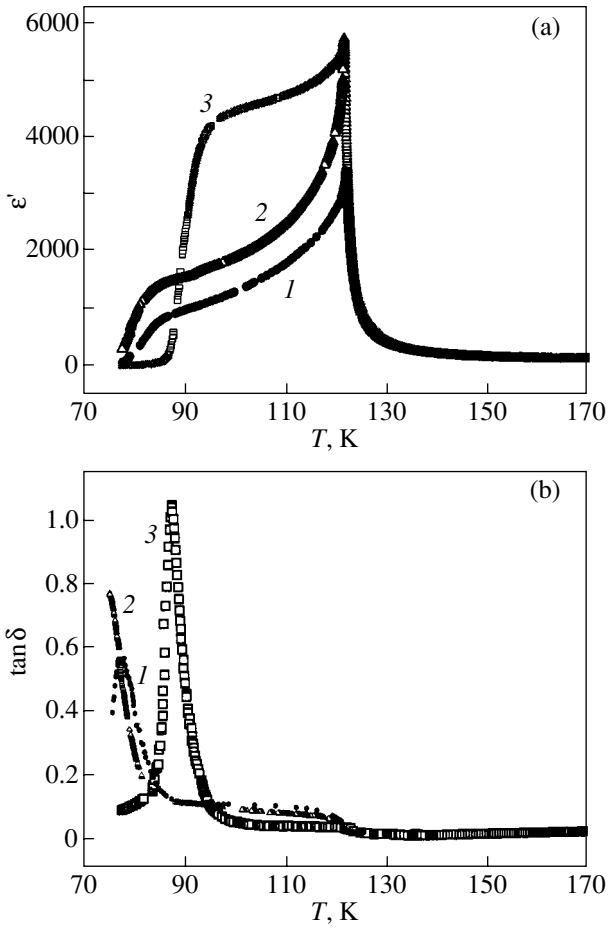

Fig. 6. Temperature dependences of (a) the permittivity and (b) the dielectric loss tangent for prismatic sectors in pure and doped KDP crystals at low temperatures: (*1*) pure KDP crystal, (*2*) KDP crystal doped with the Chicago Sky Blue dye, and (*3*) KDP crystal doped with the Amaranth dye.

dielectric properties of pyramidal sectors in the pure crystal grown by the rapid method substantially differ from those in the pure crystal grown by the traditional method [15]. It had become evident that a comparison of the dielectric properties should be performed using a pure crystal also grown by the rapid method. Furthermore, it is necessary to compare the data obtained for growth sectors of the same type, because the properties of different-type sectors also differ significantly. The results of the dielectric measurements of pure and dyed KDP crystals grown by the rapid method are compared in Figs. 5 and 6. As follows from the comparison of the data obtained for pyramidal growth sectors in pure and dyed crystals (Fig. 5a), the dye molecules virtually do not affect the domain contribution to the permittivity. This means that the organic dyes are not responsible for the decrease in the permittivity of the crystals in the temperature range of the plateau. The observed decrease in the permittivity can be associated with the initial structure imperfection of the pyramidal sectors in the crystal grown by the rapid method.

In the case of pyramidal growth sectors, the organic dye molecules incorporated into the lattice of KDP crystals affect their properties in the following way: the maximum in the permittivity slightly decreases (Fig. 5a), and the freezing temperature T_F shifts to the low-temperature range (Fig. 5b). The latter observation is in good agreement with the available data on the influence of inorganic impurities (CR^{3+} and KOH) on the freezing temperature [4, 16].

For prismatic growth sectors, the plateaulike portions in the temperature dependences of the permittivity of KDP crystals doped with organic dyes appear to be considerably larger than those of pure crystals (Fig. 6a). This can be explained in terms of the mechanism of incorporation of organic impurities into the growth sectors of the crystal under investigation and the results obtained by Barsukova *et al.* [17], who studied the growth of KDP crystals in the presence of organic impurities. In [17], it was found that the presence of organic additives (such as glycerol, ethylene glycol, and sodium ethylenediaminetetraacetate) in the initial

solution used for growing KDP crystals leads to an increase in the growth rate of the prismatic sector and a noticeable decrease in the concentration of background impurities in it. These findings were explained by the formation of stable complexes between organic additives and background impurities, which, in turn, partially suppresses their effect on the prismatic sector and, at the same time, does not affect the pyramidal sector. It was noted that the complex formation plays an important role at low concentrations of organic additives, which is actually observed for our crystals.

A comparison of the permittivities ε_C for prismatic growth sectors in pure and dyed crystals allows us to draw the following inference about the role played by organic dye impurities. The organic dye molecules contained in the initial solution impede the incorporation of background impurity ions into the prismatic sectors of the growing crystal and, thus, weaken their effect. As a result, the prismatic sector of the dyed crystal is affected by background impurities to a smaller extent; i.e., the concentration of background impurities in this sector decreases. In turn, this leads to changes in the dielectric properties of the prismatic sector (Fig. 6a). In particular, an appreciable increase in the permittivity is observed in the temperature range of the plateau. This can be explained by the increase in the contribution of the domain-wall motion to the permittivity of a purer crystal due to depinning of domain walls at background impurities.

Analysis of the experimental results obtained also demonstrates that the two organic dyes have different effects on the dielectric properties of the crystals. It can be seen from Fig. 6a that, for prismatic growth sectors, the domain contribution to the permittivity upon introduction of the Amaranth organic dye increases to a considerably larger extent than upon introduction of the Chicago Sky Blue dye. This means that the content of background impurities in the prismatic growth sector of the KDP crystal doped with the Amaranth dye is less than that of the KDP crystal containing the Chicago Sky Blue dye. Therefore, the Amaranth dye more strongly impedes the incorporation of background impurities into the crystal. This is especially true in regard to the background impurities responsible for the interaction with domain walls.

The above explanation is confirmed by visual observations of the grown crystals. The prismatic growth sector in the KDP crystal doped with the Amaranth dye is more developed than that in the KDP crystal with the Chicago Sky Blue dye. This implies that the growth rate of the prismatic sector in the KDP crystal containing the Amaranth dye is substantially higher; i.e., the blocking effect of background impurities on domain walls in the prismatic sector of the KDP crystal containing the Amaranth dye is weaker than that in the KDP crystal doped with the Chicago Sky Blue dye.

In the prismatic sector of the KDP crystal containing the Amaranth dye, the content of background impurities becomes so low that the domain contribution to the permittivity increases to values corresponding to classical KDP crystals. Consequently, the temperature hysteresis of the permittivity ε_C in the vicinity of the Curie temperature T_C coincides with that observed for the classical crystal. In other words, the addition of the Amaranth dye to the solution used for growing the crystal leads to improvement of the quality of the prismatic sector in the crystal. As a result, the properties of this crystal become similar to the properties of the pure KDP crystal grown by the traditional method.

The data presented in Fig. 4 also agree in part with the above inferences. As room temperature is approached, the increase in the dielectric loss tangent $\tan\delta$ is due primarily to an increase in the electrical conductivity, which is governed by proton hopping diffusion in the crystals. It is known that an increase in the concentration of impurities in the KDP crystals results in an increase in the proton conductivity [5, 18]. However, in our case, we cannot expect there to be a direct correlation between the effect of structural defects on the domain contribution to the permittivity and their effect on the electrical conductivity. Actually, the electrical conductivity should be analyzed with due regard for the effects of background polyvalent impurities and dye molecules. It can be seen from Fig. 6 that the aforementioned correlation is observed for the Amaranth organic dye. As regards the KDP crystals doped with the Chicago Sky Blue organic dye, the appreciable increase in the dielectric loss tangent $\tan\delta$ for the prismatic sector (Fig. 4b) suggests that the background impurities can reach considerably higher concentrations than those in the crystals doped with the Amaranth dye.

4. CONCLUSIONS

Thus, it was revealed that, despite the low content (approximately 10^{-4} mol %), the organic dyes have a noticeable effect on the dielectric properties of the KDP crystals. In particular, it was shown that the organic dye molecules incorporated into the crystal lattice of KDP have no direct effect on the dielectric properties of the pyramidal growth sector but indirectly affect the dielectric properties of the prismatic sector due to efficient interaction with the background impurities responsible for the defect structure of this sector in the KDP crystal.

The results obtained in the dielectric measurements demonstrated that, upon doping of KDP crystals with organic dyes, the dye molecules are incorporated into the pyramidal growth sector of the crystal and leave the prismatic sector colorless. These molecules virtually do not affect the degree of structural imperfection of the pyramidal sector and are responsible for the decrease in the concentration of background impurities in the prismatic sector. As a consequence, the permittivity of the prismatic sector of the crystal in the polar phase increases significantly and the temperature dependence of the permittivity exhibits a plateau typical of high-quality KDP crystals.

ACKNOWLEDGMENTS

We would like to thank N.P. Zaĭtseva and L. Carman for supplying the KDP crystal samples doped with the Chicago Sky Blue and Amaranth dyes and also B. Kahr and L.N. Rashkovich for their interest in our investigation.

This work was supported by the Russian Foundation for Basic Research, project nos. 02-02-16261 and 02-02-06818.

REFERENCES

1. P. Bornarel, A. Fouskova, P. Guyon, and J. Lajzerowicz, in *Proceedings of the International Meeting on Ferroelectricity, Prague, 1966*, Vol. 2, p. 81.
2. A. S. Sidorkin, *Domain Structure in Ferroelectrics and Related Materials* (Fizmatlit, Moscow, 2000).
3. L. N. Kamysheva, N. A. Burdanina, and O. K. Zhukov, Izv. Akad. Nauk SSSR, Ser. Fiz. **34**, 2612 (1970).
4. L. N. Kamysheva, N. A. Burdanina, O. K. Zhukov, *et al.*, Kristallografiya **14**, 940 (1969) [Sov. Phys. Crystallogr. **14**, 816 (1969)].
5. E. Nakamura, Ferroelectrics **135**, 237 (1992).
6. N. Zaitseva and L. Carman, Prog. Cryst. Growth Charact. Mater. **43**, 1 (2001).
7. L. N. Rashkovich, *KDP-Family Single Crystals* (Hilger, London, 1991).
8. I. V. Shnaĭdshteĭn, B. A. Strukov, S. V. Grabovskiĭ, *et al.*, Fiz. Tverd. Tela (St. Petersburg) **43**, 2184 (2001) [Phys. Solid State **43**, 2276 (2001)].
9. L. N. Rashkovich, Vestn. Akad. Nauk SSSR **9**, 15 (1984).
10. B. Kahr and W. Gurney, Chem. Rev. **101**, 893 (2001).
11. H. Blathner, B. Matthias, and W. Merz, Helv. Phys. Acta **19**, 415 (1946).
12. J. A. Subramony, S. H. Jang, and B. Kahr, Ferroelectrics **191**, 293 (1997).
13. S. A. de Vries, P. Goedtkind, S. L. Bennet, *et al.*, J. Cryst. Growth **205**, 202 (1999).
14. S. L. Gliko, P. Zaitseva, and L. N. Rashkovich, Mater. Res. Soc. Symp. Proc. **620**, M9.9.1 (2000).
15. S. V. Grabovskiĭ, I. V. Shnaĭdshteĭn, and B. A. Strukov, Kristallografiya **48**, 131 (2003) [Crystallogr. Rep. **48** (2003)].
16. K. Kuramoto, H. Motegi, and E. Nakamura, Jpn. J. Appl. Phys., Suppl. **24** (24-2), 562 (1985).
17. M. L. Barsukova, V. A. Kuznetsov, T. M. Okhrimenko, *et al.*, Kristallografiya **37**, 1003 (1992) [Sov. Phys. Crystallogr. **37**, 533 (1992)].
18. E. D. Yakushkin, E. P. Efremova, and A. I. Baranov, Kristallografiya **46**, 904 (2001) [Crystallogr. Rep. **46**, 830 (2001)].

Translated by O. Borovik-Romanova

Physics of the Solid State, Vol. 45, No. 3, 2003, pp. 553–558. Translated from Fizika Tverdogo Tela, Vol. 45, No. 3, 2003, pp. 00–00.

LATTICE DYNAMICS AND PHASE TRANSITIONS

The Formation of Surface Electroacoustic Shear Wave in a Piezoelectric Crystal

S. V. Tarasenko and T. N. Tarasenko

Donetsk Physicotechnical Institute, National Academy of Sciences of Ukraine, Donetsk, 83114 Ukraine

Received May 20, 2002

Abstract—It is illustrated by specific example that, near a dipole-active intrinsic ferroelastic phase transition characterized by a single-component order parameter, a surface electroacoustic shear wave can arise, if spatial dispersion is included, even in the case of the surface of a piezoelectric crystal being rigidly fixed. © *2003 MAIK "Nauka/Interperiodica".*

1. INTRODUCTION

As is well known, a electroacoustic shear wave is the result of hybridization between a transverse phonon of the SH type and an electric-dipole (ED)-active excitation of the medium [1] and, therefore, can be used as a very sensitive acoustooptic tool in studying ED-active phase transitions (i.e., transitions for which the order parameter is a linear combination of components of the electric polarization vector **P** [1, 2]). In studying the critical dynamics of such transitions, the acoustooptic spectroscopic methods become far more efficient if the ED-active phase transition is of the soft-mode type and the acoustic shear wave in question involves the ED-active soft mode [3]. In the case of opaque media, the spectroscopic study of surface electroacoustic excitations is of importance; these excitations are the result of hybridization between a phonon and an ED-active excitation in the presence of a quasi-two-dimensional defect, such as the surface of the crystal. Analysis of the spectrum of surface acoustic waves can be helpful not only in the case of phase transitions of the surface-reconstruction type but also in the case of ED-active phase transitions in the bulk. In the latter case, it is necessary that the surface acoustic waves be hybridized with the ED-active soft mode, because the dynamic characteristics of such waves might be expected to change significantly in the vicinity of the phase transition point. An example of the transitions mentioned above is a single-component, ED-active phase transition of the soft-mode type, which occurs from a paraelectric phase ($T > T_C$, where T_C is the Curie temperature) to a ferroelectric phase ($T < T_C$) in a uniaxial (along the z axis) piezoelectric crystal with symmetry D_{2d} (such as KDP) [4].

It was shown in [5] that with the electroacoustic-coupling tensor $\hat{g}$ of such a crystal ($g_{14} = g_{25} \neq 0$, $g_{36} \neq 0$), in the case with a mechanically free surface ($\sigma_{ik} = 0$) with $\mathbf{n} \parallel [100]$ (**n** is a normal to the surface of the crystal), the surface acoustic shear wave cannot arise, irrespective of whether the crystal surface is electrically open (**Dn** = 0, where **D** is the electric induction vector) or electrically closed ($\psi = 0$, $\mathbf{E} \equiv -\nabla\psi$). For the rigidly fixed surface of a piezoelectric crystal (**u** = 0, where **u** is the atomic displacement vector), as shown in [6], surface ED-active waves of the SH type also cannot arise in both cases of **Dn** = 0 and $\psi = 0$ regardless of the structure of the electroacoustic-coupling tensor.

In [7, 8], it was pointed out that the surface electroacoustic SH wave can propagate along the rigidly fixed surface of a piezoelectric crystal if the crystal possesses not only piezoelectric but also piezomagnetic properties.

However, one should take into account that, near the phase transition point, the dynamic properties of a crystal are characterized not only by a sharp decrease in the activation energy for the ED-active soft mode but also by a simultaneous sharp increase in the correlation length of homogeneous fluctuations. Hence, spatial dispersion increases in importance in this case and the critical dynamics of the crystal is affected by defects, including the surface of the sample. Therefore, a consistent theoretical analysis of the spectrum of acoustic waves hybridized with the soft mode in the vicinity of the ED-active phase transition of the soft-mode type should be performed with allowance for both the finite size of the actual crystal and spatial dispersion.

For a single-component, intrinsic ferroelastic phase transition (for which the order parameter is a linear combination of components of the elastic strain tensor u_{ik} [1, 2]), it was shown in [9] that if spatial dispersion and electroacoustic coupling $g_{ikl}P_iu_{kl}$ ($\hat{g}$ is the electroacoustic coupling tensor) are both taken into account, then the surface electroacoustic SH wave with $\mathbf{k} \perp z$, $\mathbf{n} \parallel x$ can propagate near the mechanically free surface of the crystal even in the case where the bulk and surface properties of the medium in question are identical, i.e., where the additional boundary conditions for the z component of the electric polarization vector

1063-7834/03/4503-0553$24.00 © 2003 MAIK "Nauka/Interperiodica"

P at the surface of the ferroelectric crystal ($x = 0$) have the form

$$\partial P_z/\partial x = 0, \quad x = 0. \tag{1}$$

The electroacoustic SH wave will be localized near the surface of the crystal under study ($x = 0$) if the following conditions are satisfied [9] ($\boldsymbol{\rho}_z$ is a small deviation of P_z from its equilibrium value):

$$\boldsymbol{\rho}_z(x \longrightarrow -\infty) \longrightarrow 0, \quad |u(x \longrightarrow -\infty)| \longrightarrow 0. \tag{2}$$

If the surface of the crystal is rigidly fixed and condition (1) is met, then, as shown in [9], this type of surface SH wave cannot exist in the paraelectric phase at any temperature T above the phase transition point T_C regardless of the value of the wave number $k_\perp$. In this case, with boundary conditions (1) and (2), a uniform bulk wave with polarization $P_z \neq 0$ and $\mathbf{k}_z \parallel z$ can propagate along the surface of the ferroelectric crystal at hand in the paraelectric phase ($T > T_C$).

However, all calculations in [9] were performed without regard for electric-dipole interaction in spite of the fact that, as is well known [10], the single-component, intrinsic ferroelastic soft-mode phase transition is ED-active.

In this paper, we find the necessary conditions under which the surface electroacoustic shear wave can propagate in a semi-infinite crystal undergoing an ED-active, intrinsic ferroelastic phase transition in the case where the crystal surface is rigidly fixed and spatial dispersion, as well as electric dipole and electroacoustic interactions, is taken into account. The paper is organized as follows. Section 2 is a description of the model of the phase transition under study and the formulation of the boundary-value problem. In Section 3, we find the types of surface electroacoustic shear waves that consist of three partial waves and can propagate, in the geometry chosen, along the surface of a crystal undergoing a single-component, ED-active ferroelastic phase transition. The spectrum of surface electroacoustic SH waves propagating along the rigidly fixed surface of the crystal is investigated in the case where all three mechanisms responsible for the formation of these waves through hybridization with the soft mode (electric-dipole and electroacoustic interactions and spatial dispersion) are taken into account. In Section 4, the relation is analyzed between the conditions of existence of these surface waves and the local geometry of the wave-vector surface of the corresponding normal electroacoustic modes in an unbounded crystal.

2. BASIC RELATIONS

In order to compare our calculations with the results obtained in [9], we take a piezoelectric crystal belonging to group D_{2d} as an example and assume its properties to be isotropic for the sake of simplicity. For a single-component phase transition ($P_z \neq 0$), the corresponding thermodynamic-potential density can be written as

$$W = 0.5\kappa(\nabla P_z)^2 + 0.5aP_z^2 + g_{14}P_x u_{yz} + g_{25}P_y u_{xz} + g_{36}P_z u_{xy} - \mathbf{PE} + 0.5Ku_{ii}^2 + \mu\left(u_{ik} - \frac{1}{3}\delta_{ik}u_{ll}\right)^2. \tag{3}$$

Here, $\nabla = (\partial/\partial x, \partial/\partial y, \partial/\partial z)$, **P** is the polarization vector, κ is a parameter characterizing the gradient term in the thermodynamic potential, $a = a_1(T - T_C)$ [9–11], K is the bulk modulus, μ is the shear modulus, **E** is the electric field, and δ_{ik} is the unit tensor.

As in [9, 11], for the sake of simplicity, Eq. (3) is derived under the assumption that $|P_z| \gg |P_\perp|$; that is, the longitudinal susceptibility is assumed to be much larger than the transverse one in the vicinity of the phase transition point (single-component ferroelectric phase transition). In this case, in the Coulomb approximation, the electroacoustic dynamics of the piezoelectric crystal under study is described by a closed set of equations consisting of the equation of motion for the z component of the polarization vector **P**, electrostatics equations, and elasticity-theory equations:

$$f\frac{\partial^2 P_z}{\partial t^2} = \frac{\delta W}{\delta P_z}, \quad \varepsilon_{xx}\frac{\partial^2 \psi}{\partial x^2} + \varepsilon_{zz}\frac{\partial^2 \psi}{\partial z^2} = 4\pi\frac{\partial P_z}{\partial z}, \quad \rho\frac{\partial^2 u_i}{\partial t^2} = \frac{\partial^2 W}{\partial u_{ik}\partial x_k}. \tag{4}$$

where f is a coefficient which can be treated as an effective mass [11], ρ is the density of the crystal, ψ is the electrostatic potential, and ε_{ik} is the high-frequency permittivity tensor. Since we will study the spectrum of natural electroacoustic surface vibrations of a semi-infinite crystal ($x < 0$), the set of dynamic equations should be supplemented with the corresponding boundary conditions. As in [7], we assume that the bulk and surface properties of the crystal are identical as far as the order parameter is concerned. Therefore, the boundary condition for the z component of the electric polarization **P** at the surface ($x = 0$) of the ferroelectric crystal has the form of Eq. (1). For the rigidly fixed surface, we have

$$u = 0. \tag{5}$$

The dielectric medium at $x > 0$ has permittivity ε_0 and is assumed to be nonpiezoelectric. In this case, the electrodynamic boundary condition can be taken in the form

$$\frac{\partial \psi}{\partial x} + \beta k_\perp \psi = 0, \quad x = 0, \tag{6}$$

where $\beta = \varepsilon_0 k_\perp/\varepsilon_{xx}$ and $k_\perp$ is the wave number. Thus, for a crystal described by Eq. (3), the surface is electrically open (in the nomenclature introduced in [7]) if $\beta \longrightarrow 0$ and electrically closed if $\beta \longrightarrow \infty$. The electroacoustic wave under study will be localized near the crystal sur-

face $x = 0$ if the following conditions are met simultaneously:

$$\rho_z(x \longrightarrow -\infty) \longrightarrow 0, \quad |u(x \longrightarrow -\infty)| \longrightarrow 0, \quad \psi(x \longrightarrow -\infty) \longrightarrow 0. \tag{7}$$

A calculation shows that, for the unbounded piezoelectric crystal described by Eq. (3), the dispersion relation of normal electroacoustic SH waves resulting from hybridization with the soft optical mode has the following form at $T > T_C$ ($\mathbf{k} \in xz$; $\mathbf{u} \parallel y$):

$$\omega^2 = \omega_0^2 + c^2k^2 + \omega_d^2\frac{\varepsilon k_z^2}{\varepsilon k_z^2 + k_x^2} + \omega_{pe}^2\frac{k_z^2 - \omega^2/s_t^2}{k^2 - \omega^2/s_t^2}. \tag{8}$$

where $\mathbf{k}^2 = k_x^2 + k_z^2$, $\omega_0^2 = a/f$; $\omega_d^2 = 4\pi/f$; $\omega_{pe}^2 = g_{36}^2/(\mu f)$, $c^2 = \kappa/f$; $\varepsilon = \varepsilon_{zz}/\varepsilon_{xx}$, $s_t^2 = \mu/\rho$. Therefore, in the semi-infinite ($x < 0$) ferroelectric crystal described by Eqs. (3) and (4), the spatially dependent displacement u_y can be represented as a combination of three partial waves:

$$u_y = \sum_{j=1}^{3} A_j \exp(q_j x)\exp(i\omega t - ik_\perp z), \tag{9}$$

where $k_\perp = k_z$, A_j are arbitrary constants ($j = 1, 2, 3$) and q_j are the roots of the bicubic equation

$$q^6 - P_1q^4 + P_2q^2 - P_3 = 0,$$

$$P_1 = (2 + \varepsilon)k_\perp^2 + \frac{1}{c^2}\left[\omega_0^2 - \omega^2\left(1 + \frac{c^2}{s_t^2}\right)\right],$$

$$P_2 = \frac{\omega_0^2 + (1 + \varepsilon)c^2k_\perp^2 + \omega_{pe}^2 - \omega^2}{c^2}\left[k_\perp^2 - \frac{\omega^2}{s_t^2}\right] + \frac{\omega_0^2 + c^2k_\perp^2 + \omega_d^2 - \omega^2}{c^2}\varepsilon k_\perp^2, \tag{10}$$

$$P_3 = \frac{\omega_0^2 + c^2k_\perp^2 + \omega_d^2 + \omega_{pe}^2 - \omega^2}{c^2}\left[k_\perp^2 - \frac{\omega^2}{s_t^2}\right]\varepsilon k_\perp^2.$$

On the basis of Eqs. (9) and (10), considering the frequency ω and the wave-vector component $k_\perp$ parallel to the crystal surface as given parameters, we can determine possible types of propagating electroacoustic SH waves with $\mathbf{k} \in xy$ and $\mathbf{u} \parallel y$, depending on the character of their spatial localization near the crystal surface at $x = 0$. A calculation shows that, in the case of $\mathbf{n} \parallel x$, the piezoelectric crystal under study can support propagating surface electroacoustic SH waves ($q_{1,2,3}^2 > 0$) if the frequency ω and the wave number $k_\perp$ satisfy one of the following sets of inequalities:

$$\omega^2 < s_t^2k_\perp^2, \quad 0 \le k_\perp^2 \le k_*^2,$$

$$\omega^2 < \omega_-^2(k_\perp), \quad k_*^2 \le k_\perp^2 \le k_0^2,$$

$$\omega_+^2(k_\perp) \le \omega^2 \le \omega_0^2 + \omega_{pe}^2 + \omega_d^2 + c^2k_\perp^2, \quad k_\perp > k_+,$$

$$k_*^2 = (\omega_0^2 + \omega_d^2)/(s_t^2 - c^2), \tag{11}$$

$$k_\pm^2 = 0.5A \pm (0.25A^2 - B)^{1/2},$$

$$A = \left[\frac{\omega_0^2 + \omega_d^2 + \omega_{pe}^2}{s_t^2} + \frac{\omega_d^2}{\varepsilon c^2}\left(1 - \frac{c^2}{s_t^2}\right) + \frac{\omega_{pe}^2}{c^2}\right]\frac{s_t^2}{s_t^2 - c^2},$$

$$B = \left[\frac{\omega_0^2 + \omega_d^2 + \omega_{pe}^2}{s_t^2 - c^2}\right]\frac{\omega_d^2}{\varepsilon c^2}.$$

Here, $\omega_\pm^2(k_\perp)$ are the real, positive roots of the equation $D(\omega, k_\perp) = 0$, where $D(\omega, k_\perp)$ is the discriminant of bicubic equation (10) and k_0 is the root of the equation $\omega_-^2(k_0) = 0$. In the elastostatic limit ($\omega^2 \ll s_t^2k_\perp^2$) and for $\varepsilon = 1$, the quantities $\omega_\pm(k_\perp)$ and k_+^2 in Eqs. (11) are given by

$$\omega_\pm^2(k_\perp) = \omega_0^2 \pm 2\sqrt{\omega_d^2 + \omega_{pe}^2}ck_\perp, \quad k_+ \equiv \sqrt{\omega_d^2 + \omega_{pe}^2}/c. \tag{12}$$

The crystal described by Eq. (3) will support a generalized surface electroacoustic wave consisting of three partial waves ($q_1^2 > 0$, $\mathrm{Re}\,q_{2,3}^2 \neq 0$; $\mathrm{Im}\,q_{2,3}^2 \neq 0$) with $\mathbf{k} \in xz$ if the following necessary condition is met:

$$\omega_-^2(k_\perp) \le \omega^2 \le \omega_+^2(k_\perp), \quad k_\perp > k_*. \tag{13}$$

Thus, it follows from Eqs. (9) and (10) that the crystal under study will support an ED-active shear wave forming through hybridization with the ferroelectric soft mode and localized near the surface $x = 0$ if both the frequency ω and wave number $k_\perp$ ($\mathbf{k} \parallel z$) satisfy Eqs. (11) or (13). However, this condition is necessary but not sufficient for surface waves (9) and (10) to exist, because the dispersion relation for the surface electroacoustic wave under study is also a condition of existence for nontrivial solutions to the equations that follow from the set of boundary conditions (1) and (5)–(7) for the partial-wave amplitudes A_j involved in Eq. (9).

3. THE FORMATION OF A SURFACE ELECTROACOUSTIC SH WAVE ON THE RIGIDLY FIXED SURFACE OF A PIEZOELECTRIC CRYSTAL

The dispersion relation of surface ED-active shear waves propagating along the surface of the piezoelectric crystal described by Eq. (3) is a nontrivial solution to the boundary-value problem (1) and (5)–(7) for the unknown amplitudes $A_{1,2,3}$ in the case where the spatial dependence of the y component of the atomic displacement vector $\mathbf{u}$ ($\mathbf{k} \in xz$) is described by Eqs. (9) and (10). In this case, for an arbitrary value of β, the dispersion relation determines (in an implicit form) the spectrum of surface electroacoustic SH waves as

$$\begin{gathered}\det A_{ik} = 0, \quad 1 \le i, \quad k \le 3,\\ A_{i1} = q_i(q_i^2 - \varepsilon k_\perp^2)(q_i^2 - k_\perp^2 + \omega^2/s_t^2),\\ A_{i2} = (q_i + \beta k_\perp)(q_i^2 - k_\perp^2 + \omega^2/s_t^2),\\ A_{i3} = q_i(q_i^2 - \varepsilon k_\perp^2).\end{gathered} \tag{14}$$

It follows from Eqs. (14) that, at $\beta = 0$, we have a uniform bulk polarization wave with $P_z \neq 0$ and with the dispersion law

$$\omega^2 = \omega_0^2 + \omega_d^2 + \omega_{pe}^2 + c^2 k_\perp^2. \tag{15}$$

For arbitrary values of ε and β, dispersion equation (14) has a root $\omega = s_t k_*$ and $k_\perp = k_*$. An analysis of Eqs. (10) and (14) shows that this root is an end point of the spectrum of the surface electroacoustic SH wave (14); at this point, two of the three partial waves involved in the surface wave described by Eq. (10) transform into a uniform bulk wave. In general, the set of equations (10) and (14) can be solved only using numerical methods.

For $q_3 \ll q_{1,2}$, the spectrum of the surface electroacoustic shear wave in the short-wavelength limit ($\omega \ll s_t k_\perp$) can be found in an explicit form for any value of β:

$$\Omega_s^2(k_\perp) \approx \omega_0^2 + \omega_d^2 + \omega_{pe}^2 + c^2 k_\perp^2 - \frac{\beta^2 \omega_d^4}{4c^2 k_\perp^2}. \tag{16}$$

By comparing this solution with Eqs. (11) and (12), it is easy to verify that Eq. (16) corresponds to a surface electroacoustic SH wave consisting of three partial waves with $q_{1,2,3}^2 > 0$. In the case of $\beta = 0$, Eq. (16) reduces to Eq. (15) for the spectrum of uniform bulk polarization waves. It follows from Eq. (16) that the surface wave under study can propagate along the rigidly fixed surface of a piezoelectric crystal characterized by boundary conditions (1) and (5)–(7) only if $\beta\omega_d \neq 0$.

In essence, the surface electroacoustic SH wave under study can be thought of as a surface Coulomb phonon polariton of the TM type forming through hybridization between the soft ferroelectric mode and an acoustic SH phonon in the vicinity of an ED-active ferroelastic phase transition. In order to clarify the question of whether the condition $\beta \neq 0$ is always necessary for the existence of a surface electroacoustic wave consisting of three partial waves or if this condition is associated with the elastic boundary condition, we calculate the spectrum of this surface wave with $\mathbf{k} \in xz$ ($\mathbf{u} \parallel y$) in the same short-wavelength limit as that in which Eq. (16) was derived, but for more general boundary conditions at the surface of the crystal ($x = 0$):

$$\begin{gathered}\partial P_z/\partial x = 0, \quad \alpha\sigma_{xy} + k_\perp u_y = 0, \quad x = 0,\\ \partial\psi/\partial x + \beta k_\perp \psi = 0, \quad x = 0.\end{gathered} \tag{17}$$

The localization conditions for the electroacoustic SH wave under study are taken in the form of Eqs. (7) as before.

In this case, with allowance for Eqs. (9) and (10), the dispersion relation can be represented in the form

$$\begin{gathered}\det A_{ik} = 0, \quad 1 \le i, \quad k \le 3,\\ A_{i1} = q_i(q_i^2 - \varepsilon k_\perp^2)(q_i^2 - k_\perp^2 + \omega^2/s_t^2),\\ A_{i2} = (q_i + \beta k_\perp)(q_i^2 - k_\perp^2 + \omega^2/s_t^2),\\ A_{i3} = (q_i k_\perp + \alpha(k_\perp^2 - \omega^2/s_t^2))(q_i^2 - \varepsilon k_\perp^2).\end{gathered} \tag{18}$$

We solve Eq. (18) in the particular case of $\alpha \ll 1$ and $\beta \ll 1$, where the terms proportional to $\alpha\beta$ ($\alpha\beta \ll \alpha$, $\beta \ll 1$) can be neglected. The calculated spectrum of the surface electroacoustic SH wave consisting of three partial waves can be represented in this case in the form

$$\Omega_s^2(k_\perp) \approx \omega_0^2 + \omega_d^2 + \omega_{pe}^2 + c^2 k_\perp^2 - \frac{\alpha^2 \omega_{pe}^4 + \beta^2 \omega_d^4}{4c^2 k_\perp^2}. \tag{19}$$

By comparing Eq. (18) with Eqs. (9)–(12), it is easy to verify that if $\alpha \neq 0$, then the dispersion relation in the case under consideration corresponds to the surface electroacoustic SH wave consisting of three partial waves with $q_{1,2,3}^2 > 0$ and forming through hybridization with the soft mode not only for $\beta \neq 0$ but also for $\beta = 0$.

A calculation shows that if boundary conditions (17) at the surface of a piezoelectric crystal described by Eq. (3) are such that $1/\alpha = 0$ and $1/\beta = 0$ (a mechanically free interface between a piezoelectric crystal and an ideal metal), then, in the elastostatic limit ($\omega \ll s_t k_\perp$), the spectrum of the electroacoustic SH wave with three partial waves with $\mathbf{k} \in xz$ can be found in an explicit form from Eqs. (10) and (18) in a wider range of wave numbers and frequencies. In particular, for $\varepsilon \ll 1$, the dispersion relation has the form

$$\begin{gathered}\Omega_s^2(k_\perp) \approx 0.5N_1 + \sqrt{0.25N_1^2 - N_2},\\ N_1 = 2\omega_0^2 + c^2 k_\perp^2,\\ N_2 = \omega_0^2(\omega_0^2 + c^2 k_\perp^2) - c^2 k_\perp^2(\omega_d^2 + \omega_{pe}^2).\end{gathered} \tag{20}$$

In terms of the classification of the possible types (for the given geometry of the boundary-value problem) of surface electroacoustic SH waves consisting of three partial waves based on Eqs. (9) and (11)–(13), the spectrum described by Eq. (20) for $k_\perp < k_c$ corresponds to the generalized surface electroacoustic SH wave with three partial waves ($q_1^2 > 0$, $\mathrm{Re}\,q_{2,3}^2 \neq 0$; $\mathrm{Im}\,q_{2,3}^2 \neq 0$), while, in the case of $k_\perp > k_c$, the surface electroacoustic SH wave with three partial waves $q_{1,2,3}^2 > 0$ arises near the interface between a piezoelectric crystal described by Eq. (3) and an ideal metal (e.g., superconductor). In the same approximation as that in which Eq. (20) was derived, the wave number k_c is found from Eq. (12) to be

$$k_c = \frac{3\sqrt{\omega_d^2 + \omega_{pe}^2}}{2c}. \qquad (21)$$

4. RELATION BETWEEN THE LOCALIZATION CONDITION AND THE SHAPE OF A CONSTANT-FREQUENCY SURFACE

As shown in [12], the formation of a generalized surface electroacoustic shear wave near the mechanically free surface of a piezoelectric (piezomagnetic) crystal of the symmetry in question is closely related to the local geometry of a cross section of the constant-frequency surface of the proper SH wave of the corresponding type in an unbounded crystal.

An analysis shows that, in the case of an electroacoustic SH wave consisting of three partial waves, the condition for localization of this wave near the surface of the crystal is related to the local geometry of the refraction (slowness) surface (calculated in the electrostatic approximation) of the corresponding proper electroacoustic shear wave in an unbounded crystal.

If the normal **n** to the surface of the piezoelectric crystal under study and the propagation direction $\mathbf{k}_\perp/|\mathbf{k}_\perp|$ of the electroacoustic SH wave lie in the *xz* plane, then it follows from Eq. (8) that, in the case where acoustic retardation is neglected ($\omega/s_t \longrightarrow 0$, elastostatic approximation), the intersection of the constant-frequency surface ($\omega = \mathrm{const}$) of the proper electroacoustic SH wave in an unbounded crystal described by Eq. (3) and the $k_x k_z$ plane in the **k** space is described by the equation

$$c^2k^2 = \omega^2 - \omega_{pe}^2\cos^2\vartheta - \omega_d^2\varepsilon/(\varepsilon + \tan^2\vartheta), \qquad (22)$$

where $\tan\vartheta = k_x/k_z$. Using Eq. (20), it can be shown that if the inequalities

$$\omega_0^2 < \omega^2 < \omega_0^2 + 2\omega_{pe}^2 + \omega_d^2(1+\varepsilon)/\varepsilon \qquad (23)$$

are satisfied, the curve described by Eq. (22) has portions with a negative Gaussian curvature, its maximum being reached at $\vartheta = 0$. By comparing this result with the spectra of surface electroacoustic SH waves given by Eqs. (16) and (19), one can conclude that the presence of a portion with negative Gaussian curvature on the curve described by Eq. (22) is a necessary condition for conversion of this type of proper waves in the unbounded crystal into the corresponding surface wave. In addition, the normal **n** to the surface of the piezoelectric crystal must be perpendicular to the direction along which the magnitude of the negative Gaussian curvature is maximum; otherwise, the surface wave will be a leaky wave. In the latter case, the partial waves responsible for nondissipative relaxation of the leaky wave are those normal modes for which the corresponding hollows in the refraction surface in the **k** space contain the hollow corresponding to the leaky wave in question. As shown above, only if spatial dispersion is taken into account can the electroacoustic and electric-dipole interactions together bring about the formation of a surface electric-dipole SH wave consisting of three partial waves near the interface between a piezoelectric and a nonpolar dielectric crystal. In this case, the minimum phase velocity of the soft (ferroelectric) mode in an unbounded crystal must be less than the minimum phase velocity of the acoustic shear mode.

5. CONCLUSIONS

The results of our study are as follows.

(1) For a single-component, ED-active intrinsic ferroelectric bulk phase transition, taken as an example, the conditions were determined under which, depending on the external parameters (frequency ω, wave number $k_\perp$), spatial dispersion and the electroacoustic and electric-dipole interactions together can bring about the formation of a surface electroacoustic SH wave hybridized with the soft mode and consisting of three partial waves even in the case of the surface of the crystal being rigidly fixed.

(2) In the elastostatic limit, a solution to the corresponding boundary-value problem was found and it was shown that the character of the electroacoustic shear wave localized near the surface of a piezoelectric crystal depends on the value of the wave number. If $k_\perp < k_c$, the dispersion curve found corresponds to a generalized surface shear wave consisting of three partial waves ($q_1^2 > 0$, $\mathrm{Re}\,q_{2,3}^2 \neq 0$; $\mathrm{Im}\,q_{2,3}^2 \neq 0$). At $k_c \neq 0$, this dispersion curve passes smoothly into that for the surface electroacoustic SH wave with $q_{1,2,3}^2 > 0$.

(3) The effect of the electrodynamic and elastic boundary conditions on the formation of surface waves of this type was studied, and it was shown that this type of local excitation can be thought of as a Coulomb phonon polariton of the TM type forming through hybridization between the shear acoustic mode and the soft ferroelectric mode.

(4) The formation of the surface wave studied was shown to be dictated by the local geometry of the con-

stant-frequency surface for the corresponding normal vibrational mode in an unbounded crystal. The surface wave can arise if (a) in an unbounded crystal the minimum phase velocity of the soft mode is less than the minimum phase velocity of the shear acoustic mode and (b) the direction of the normal **n** to the surface of the polarized crystal and the wave propagation direction along the interface ($\mathbf{k}_\perp/|\mathbf{k}_\perp|$) coincide with mutually perpendicular directions along which critical fluctuations increase anomalously near the ferroelastic phase transition of the soft-mode type in the absence of dipole–dipole interaction. The normal **n** must also be parallel to the direction along which anomalously large fluctuations near the ED-active intrinsic ferroelastic phase transition under study are not suppressed in the unbounded crystal when both the linear striction and dipole–dipole interaction are included [2, 11].

ACKNOWLEDGMENTS

The authors are grateful to I.E. Dragunov and V.M. Yurchenko for their encouragement and helpful discussions.

REFERENCES

1. A. D. Bruce and R. A. Cowley, *Structural Phase Transitions* (Taylor and Francis, Philadelphia, Pa., 1981; Mir, Moscow, 1984).
2. A. Z. Patashinskiĭ and V. L. Pokrovskiĭ, *Fluctuation Theory of Phase Transitions*, 2nd ed. (Nauka, Moscow, 1982; Pergamon, Oxford, 1979).
3. *Light Scattering near Phase Transitions*, Ed. by H. Z. Cummins and A. P. Levanyuk (North-Holland, Amsterdam, 1983; Nauka, Moscow, 1990).
4. R. Blinc and B. Zeks, *Soft Modes in Ferroelectrics and Antiferroelectrics* (North-Holland, Amsterdam, 1974; Mir, Moscow, 1975).
5. C. C. Tseng, J. Appl. Phys. **41** (6), 2270 (1970).
6. J. Lothe and D. M. Barnett, J. Appl. Phys. **47** (5), 1799 (1976).
7. V. I. Alshits, A. N. Darinskii, and J. Lothe, Wave Motion **16**, 265 (1992).
8. V. I. Alshits, A. N. Darinskii, J. Lothe, and V. I. Lubimov, Wave Motion **19**, 113 (1994).
9. S. V. Tarasenko, Kristallografiya **45** (2), 313 (2000) [Crystallogr. Rep. **45**, 282 (2000)].
10. A. P. Levanyuk and B. A. Strukov, *Physical Principles of Ferroelectric Phenomena in Crystals* (Nauka, Moscow, 1983).
11. V. V. Tarasenko and E. V. Chenskiĭ, Zh. Éksp. Teor. Fiz. **83** (3), 1089 (1982) [Sov. Phys. JETP **56**, 618 (1982)].
12. Yu. A. Kosevich and E. S. Syrkin, Fiz. Tverd. Tela (Leningrad) **28** (1), 248 (1986) [Sov. Phys. Solid State **28**, 134 (1986)].

Translated by Yu. Epifanov

Physics of the Solid State, Vol. 45, No. 3, 2003, pp. 559–565. Translated from Fizika Tverdogo Tela, Vol. 45, No. 3, 2003, pp. 529–534.

LOW-DIMENSIONAL SYSTEMS AND SURFACE PHYSICS

On the Differential Conductivity of Semiconductor Superlattices

Yu. A. Romanov

Institute of the Physics of Microstructures, Russian Academy of Sciences, Nizhni Novgorod, 603950 Russia
e-mail: romanov@ipm.sci-nnov.ru

Received April 5, 2002

Abstract—The nature of negative differential conductivity (NDC) of a semiconductor superlattice was studied. It is shown that the presence of regions with a negative effective mass in a Brillouin miniband is not necessary for NDC to set in. NDC exists even in superlattices with parabolic and superquadratic miniband dispersion relations, where the electron effective mass is positive everywhere and, in this case, is fully determined by Bragg reflections of the electron. When the electron Bragg reflections are suppressed by optical phonons, NDC can disappear completely. NDC is retained only if there is a sizable region with a negative effective mass in the miniband. © *2003 MAIK "Nauka/Interperiodica".*

1. INTRODUCTION

The semiconductor superlattice (SL) is a single-crystal structure with a chemical composition that varies periodically in space at distances (1–10 nm) which exceed the periods of the crystal lattices of the materials it is made of. An additional periodic (superlattice) potential forms in such a structure, which gives rise to a breakup of the quasi-momentum Brillouin zones and of the allowed electron energy bands of a uniform starting material into a set of relatively narrow (10^5–10^7 cm^{-1}) Brillouin minibands and narrow (10^{-3}–10^{-1} eV) allowed and forbidden energy minibands [1–3]. Because of the smallness of these minibands, electron Bloch oscillations (BOs) occur [4] and Wannier–Stark levels [5] arise in an SL even in relatively weak static electric fields (10^2–10^4 V/cm). These oscillations and levels originate from electron Bragg reflections in the superlattice potential, which has a comparatively large spatial period. The BOs are characterized by a frequency $\Omega_c = eE_cd/\hbar$ and a quasi-classical amplitude of spatial oscillations $Z_c = \Delta/2eE_c$, where E_c is the electric field directed along the SL axis with a period d and energy miniband width Δ. Significantly, Ω_c does not depend on the miniband dispersion relation and is determined only by the period of the SL and the magnitude of the electric field in it. The miniband dispersion relation manifests itself in the anharmonicity of the spatial (but not momentum) oscillations of the electron. For the conventionally assumed sine dispersion law of a one-dimensional SL miniband, oscillations are harmonic. The existence of BOs in an SL has been convincingly confirmed in a number of experiments [6–11].

Another important feature of the SL is the presence of regions with negative effective mass in a Brillouin miniband [2]. These regions may be of considerable size. For instance, for a sine dispersion law, the effective mass is negative in one half of a Brillouin miniband. Minibands of two- and three-dimensional SLs contain regions with a negative longitudinal and/or transverse effective mass [12].

Both the negative effective mass [2, 13] and BOs [1, 14] of the electron may give rise to the onset of negative differential conductivity (NDC) in a solid. In natural crystals, BOs do not occur and NDC does not arise because of the large size of the Brillouin zones. In an SL, both factors operate. The actual part they play in the onset of NDC is, however, still unclear. The statement [2] that NDC in an SL is due primarily to the existence of regions with a negative effective mass in an electronic miniband is erroneous. Unfortunately, this wrong point of view is widely accepted (see, e.g., [15, 16] and references therein).

This study deals with the origin of NDC in semiconductor SLs. Section 2 discusses the *I–V* characteristics of SLs with an arbitrary miniband dispersion relation and how the static NDC is connected with the electron BOs and with the presence of regions with negative effective mass in a miniband. In Section 3, the same aspects are studied for SLs in which Bragg reflection of the electron is replaced, partially or completely, by an instantaneous drop of the electron to the bottom of the miniband after it has reached the top of the miniband, for instance, through emission of an optical phonon (two- or one-sided streaming).

2. *I–V* CURVE OF A SUPERLATTICE WITH AN ARBITRARY MINIBAND DISPERSION RELATION

To reveal the part played by the BOs and negative electron effective mass in the onset of NDC, we compare *I–V* curves of the following four SL types.

(1) An SL with a sine miniband dispersion law, used conventionally in calculations,

$$\varepsilon_3(k_3) = \frac{\Delta}{2}[1 - \cos(k_3 d)], \quad (1)$$

where $\varepsilon_3(k_3)$ and k_3 are the electron energy and quasi-wave vector along the SL axis, respectively. In this case, the region of negative effective mass takes up exactly one half of the Brillouin miniband.

(2) An SL whose miniband does not at all contain a region of negative effective mass. The most revealing (and, naturally, idealized) case here is an SL with a "parabolic" dispersion law:

$$\varepsilon_3(k_3) = \hbar^2 k_3^2/2m_3, \quad -\pi/d < k_3 < \pi/d. \quad (2)$$

In this case, we have only Bragg reflection points $k_3 = \pm\pi/d$.

(3) SLs with various relative dimensions of the region of negative electron effective mass in the Brillouin miniband. This case is well illustrated by the dispersion relation

$$\varepsilon_3(k_3) = \frac{\hbar^2}{2m_3}\begin{cases}(\pi/k_i d)k_3^2, & 0 \le |k_3| \le k_i \\ (\pi/d)^2 - \dfrac{(\pi/d - |k_3|)^2}{1 - k_i d/\pi}, & k_i < |k_3| \le \pi/d,\end{cases} \quad (3)$$

which is made up of a direct and an inverted parabola joined at points $\pm k_i$ (continuous function and its first derivative). The width of the miniband in this dispersion relation (used in [2])

$$\Delta = \frac{1}{2m_3}\left(\frac{\hbar\pi}{d}\right), \quad (4)$$

does not depend on the position of the inflection point k_i and is a given quantity. The electron effective mass is positive in the lower region of the miniband ($0 < |k_3| < k_i$) and negative in its upper part ($k_i < |k_3| < \pi/d$). For $k_i = \pi/d$, Eq. (3) transforms into the above parabolic dispersion relation with positive effective mass m_3, and for $k_i = 0$, into a parabolic relation with negative effective mass $-m_3$. The quantity $\beta \equiv k_i d/\pi$ is the relative volume of electronic states with negative effective mass in the Brillouin miniband.

(4) An SL in which the electron BOs are partially or completely suppressed, e.g., because of the electron emitting an optical phonon at the top of the miniband.

Let us find first the *I–V* curve of an SL with an arbitrary dispersion law of the one-dimensional miniband, taking into account the transient process following instantaneous switching of a static electric field. For the sake of simplicity, we start with the Boltzmann equation with the collision integral taken in the τ approximation:

$$\frac{\partial f(\mathbf{k}, t)}{\partial t} + \frac{e\mathbf{E}(t)}{\hbar}\frac{\partial f(\mathbf{k}, t)}{\partial \mathbf{k}} = -\frac{f(\mathbf{k}, t) - f_0(\varepsilon, T)}{\tau}, \quad (5)$$

where $\varepsilon \equiv \varepsilon(\mathbf{k})$ is the energy of an electron, $\mathbf{k}$ is its three-dimensional quasi-wave vector; $f(\mathbf{k}, t)$ and $f_0(\varepsilon, T)$ are the field-perturbed and equilibrium (at the lattice temperature T) electron distribution functions, respectively; and τ is the electron distribution relaxation time, with the field $\mathbf{E}(t)$ directed along the SL axis. Using the periodicity of the $\mathbf{k}$ space, we expand the functions of interest to us here in Fourier series:

$$\varepsilon(\mathbf{k}) = \sum_{\nu=-\infty}^{\infty} \varepsilon(\nu, k_\perp)\exp(i\nu k_3 d), \quad (6)$$

$$f_0(\varepsilon, T) = \sum_{\nu=-\infty}^{\infty} F_\nu(k_\perp)\exp(i\nu k_3 d), \quad (7)$$

$$f(\mathbf{k}, t) = \sum_{\nu=-\infty}^{\infty} F_\nu(k_\perp)\exp(i\nu k_3 d)\Phi_\nu(t), \quad (8)$$

where

$$F_\nu(k_\perp) = \frac{d}{2\pi}\int_{-\pi/d}^{\pi/d} f_0(k)\exp(-i\nu k_3 d)dk_3, \quad (9)$$

$$F_\nu = F_{-\nu}^*,$$

and $k_\perp$ is the electron quasi-wave vector component orthogonal to the SL axis. Substituting Eq. (8) into Eq. (5), we obtain a rate equation for the multicomponent function $\Phi_\nu(t)$

$$\tau\frac{d\Phi_{nu}(t)}{dt} = [1 + i\nu\tau\Omega(t)]\Phi_\nu(t) = 1, \quad \Omega(t) = \frac{edE(t)}{\hbar} \quad (10)$$

subject to the boundary conditions

$$\Phi_\nu(0) = 1. \quad (11)$$

The functions introduced here can be used to find the mean quantities (energy, velocities, current, etc.); for example,

$$\varepsilon(t) = \sum_{\nu=-\infty}^{\infty} \bar{\varepsilon}(-\nu)\Phi_\nu(t), \quad (12)$$

$$j(t) = \frac{1}{2}\sum_{\nu=1}^{\infty} j_{0\nu}\Phi_\nu(t) + \text{c.c.}, \quad (13)$$

where

$$\bar{\varepsilon}(\nu) = 2\int \varepsilon(\nu, k_\perp) F_\nu(k_\perp) \frac{d^2 k_\perp}{(2\pi)^2}, \tag{14}$$

$$j_{0\nu} = -2ine\bar{V}_3(-\nu) = -2ned\hbar^{-1}\nu\bar{\varepsilon}(-\nu)$$

$$= -\frac{4ed}{\hbar}\nu\int F_\nu(k_\perp)\varepsilon(k)\exp(i\nu k_3 d)\frac{d^3 k}{(2\pi)^3}, \tag{15}$$

$$j_{0\nu}^* = -j_{0,-\nu}.$$

Substituting now dispersion relations (1) and (2) into Eq. (15) yields

$$j_{0\nu} = \delta_{\nu 1} j_0,$$

$$j_0 = \frac{end}{\hbar}\left(\frac{\Delta}{2} - \langle\varepsilon_3\rangle_0\right) \tag{16}$$

$$= (end\Delta/2\hbar) I_\nu\left(\frac{\Delta}{2T}\right) I_0^{-1}\left(\frac{\Delta}{2T}\right)$$

for the sine dispersion law and

$$j_{0\nu} = (-1)^{\nu+1}\frac{2\hbar ne}{md}\nu^{-1}\exp\left(-\frac{\pi^2 T}{4\Delta}\nu^2\right), \tag{17}$$

$$\Delta = \frac{\hbar^2\pi^2}{2md^2}$$

for the parabolic dispersion relation. Here, $\langle\varepsilon_3\rangle_0$ is the average equilibrium longitudinal energy of the electron and $I_\nu(x)$ are modified Bessel functions. The second equality in Eq. (16) is written for Maxwellian statistics at an arbitrary T, and Eq. (17) is written for Maxwellian statistics at $T < \Delta$. In the τ approximation, considered by us here, electron motion perpendicular to the SL axis does not affect the SL longitudinal conductivity (except the $j_{0\nu}$ coefficients); therefore, we shall drop the argument $k_\perp$ in the expressions for the electron energy and distribution function in what follows.

In the case of a static electric field switched on instantaneously at time $t = 0$, a solution to Eq. (10), subject to boundary condition (11), can be written as

$$\Phi_\nu(t) = \frac{1}{1 + i\nu\Omega_c\tau}\{1 + i\nu\Omega_c\tau\exp[-(i\nu\Omega_c + \tau^{-1})t]\}. \tag{18}$$

Substituting Eq. (18) into Eqs. (12) and (13) and taking into account that $\bar{\varepsilon}(\nu)$ and $j_{0\nu}$ are real, we obtain the following expressions for the current and average electron energy (with inclusion of the transient process):

$$j(t) = \sum_{\nu=1}^{\infty} j_{0\nu}\frac{\nu\Omega_c\tau}{1 + (\nu\Omega_c\tau)^2}\{1 - \exp(-t/\tau) \times [\cos(\nu\Omega_c\tau) - \nu\Omega_c\tau\sin(\nu\Omega_c\tau)]\}, \tag{19}$$

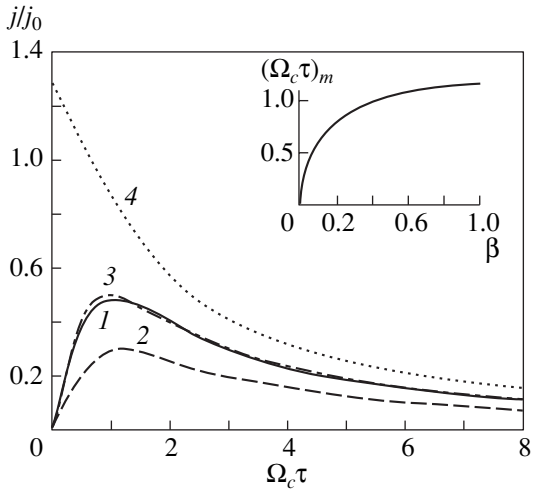

Fig. 1. *I–V* curves of an SL with (*1*) a sine miniband and parabolic minibands with (*2*) $k_i = \pi/d$, (*3*) $\pi/2d$, and (*4*) 0. Inset shows the position of the current maximum plotted vs. relative extent of the region of negative effective mass in a miniband, $\beta = k_i\pi/d$.

$$\varepsilon(t) = 2\sum_{\nu=1}^{\infty}\frac{\bar{\varepsilon}(\nu)}{1 + (\nu\Omega_c\tau)^2}\{1 + \nu\Omega_c\tau\exp(-t/\tau) \times [\nu\Omega_c\tau\cos(\nu\Omega_c\tau) + \sin(\nu\Omega_c\tau)]\} + \bar{\varepsilon}(0). \tag{20}$$

Equations (19) and (20) are valid for a one-dimensional SL model with an arbitrary miniband dispersion relation. Substituting the partial current amplitudes (16) and (17) for $T \longrightarrow 0$ into Eq. (19) and performing summation over ν, we find steady-state *I–V* curve for an SL with a sine and a parabolic miniband dispersion law, respectively,

$$j_c = j_0\frac{\Omega_c\tau}{1 + (\Omega_c\tau)^2}, \tag{21}$$

$$j_c = \tilde{j}_0\left[\Omega_c\tau - \frac{\pi}{\sinh(\pi/\Omega_c\tau)}\right], \tag{22}$$

where $j_0 = ne\Delta d/\hbar$, $\tilde{j}_0 = (2/\pi)^2 j_0$, n is the electron concentration, and the miniband width Δ was chosen, for the sake of convenience, to be the same for both dispersion laws. The *I–V* curves described by Eqs. (21) and (22) are plotted in Fig. 1. We readily see a clearly pronounced NDC, with the position and amplitude of the current maximum being similar in both cases: $(\Omega_c\tau)_m = 1$ and 1.174 and $(j_c/j_0)_m = 0.5$ and 0.3, respectively. As is evident from Eq. (17), the contribution from the first harmonic ($\nu = 1$) to the current becomes dominant with increasing lattice temperature; therefore, the abovementioned quantitative difference between the *I–V* characteristics wanes. Thus, the existence of regions with negative effective mass in a miniband is not a necessary condition for the onset of static NDC in an SL. The presence of such regions can only reduce the criti-

cal fields at which NDC arises. The negative effective mass can become a dominant factor for the formation of NDC only if the effective mass is negative in a sizable part of the Brillouin miniband.

To illustrate the last statement, let us find the *I–V* curve of an SL with the miniband dispersion relation given by Eq. (3). For simplicity, we neglect thermal spread in the equilibrium electron distribution function and set $f_0(k_3) = 2\pi n\delta(k_3)$. In this case, the steady-state solution to Eq. (5) can be written as

$$f_c(k_3) = \frac{2\pi nd}{\Omega_c\tau}\exp\left(-\frac{k_3 d}{\Omega_c\tau}\right) \times \begin{cases} \left[1-\exp\left(-\frac{2\pi}{\Omega_c\tau}\right)\right]^{-1}, & 0 < k_3 < \pi/d \\ \left[\exp\left(\frac{2\pi}{\Omega_c\tau}\right)-1\right]^{-1}, & -\pi/d < k_3 < 0. \end{cases} \quad (23)$$

The distribution function (23), which was found in the τ approximation (and this is its shortcoming), does not depend on the miniband dispersion law, thus making it easier to reveal the part played by the latter in the onset of NDC (and this is the merit of this approximation). Substituting Eqs. (3) and (23) into the expression for the current

$$j = \frac{e}{\hbar}\int_{-\pi/d}^{\pi/d}\frac{\partial\varepsilon(k_3)}{\partial k_3}f(k_3)\frac{dk_3}{2\pi} \quad (24)$$

we find the *I–V* curve for an SL with various relative dimensions of the region of negative effective mass in its miniband:

$$j = \tilde{j}_0(\pi/k_i d)\Omega_c\tau\left\{1-\frac{\sinh[(\pi-k_i d)/\Omega_c\tau]}{(1-k_i d/\pi)\sinh(\pi/\Omega_c\tau)}\right\}. \quad (25)$$

For $k_i = \pi/d$, Eq. (25) transforms to Eq. (22), and for $k_i = 0$, we have

$$j = \tilde{j}_0[\pi\coth(\pi/\Omega_c\tau) - \Omega_c\tau]. \quad (26)$$

Relation (25) is plotted in Fig. 1 for $k_i = 0$, $\pi/2d$, and π/d. In the first case, the SL differential conductivity is naturally negative even in infinitely low fields because of the effective mass being negative throughout the miniband. The *I–V* curve calculated for $k_i = \pi/2d$ (the region of negative effective mass occupies one half of the miniband) practically coincides with that of an SL with a sine miniband dispersion law.

Anharmonicity in the dispersion relation induces BO harmonics [see Eqs. (19), (20)] with comparatively large amplitudes in the transient current and average electron energy. Hence, investigation of transient processes (triggered by a fast field switching on or off) permits one to reconstruct the SL miniband dispersion law. Direct observations of electron Bloch oscillations in an SL [6–11] support the possibility of such a reconstruction.

3. *I–V* CURVE OF A SUPERLATTICE WITH NO BLOCH OSCILLATIONS PRESENT

Let us find now the *I–V* curve of an SL in which the Bragg reflection of an electron is replaced, partially or completely, by its return to the bottom of the miniband immediately after it has reached the miniband top (for instance, through emission of an optical phonon). For the sake of simplicity, we shall assume that the miniband width Δ is equal to or slightly larger than the optical phonon energy ($\hbar\omega_0$) and that the time (and duration) of the optical phonon emission by an electron is shorter than the other relaxation times, i.e., $\tau_0 \ll \tau$. If there is no electron scattering in the passive energy region ($\varepsilon < \hbar\omega_0$) and the BOs are completely suppressed by optical phonons, then electrons perform periodic motion with a frequency $2\Omega_c$ in the quasi-momentum space, while in the coordinate space, electron perform periodic motion with the same frequency $2\Omega_c$ and translational motion with a velocity

$$\langle V\rangle = (d/\pi\hbar)\int_0^{\pi/d}\frac{\partial\varepsilon(k_3)}{\partial k_3}dk_3.$$

In these conditions, the electron distribution function in quasi-momentum in strong fields becomes sharp-peaked, with the problem actually reducing (and not only in terms of the model) to a nearly one-dimensional case. This distribution is usually referred to in the literature as streaming. It is essential that the penetration depth of an electron into the active region (with energies $\varepsilon > \hbar\omega_0$), i.e., the "phonon roof rigidity," is determined by the miniband top rather than by the time τ_0. Therefore, streaming in an SL may be substantially narrower than that in bulk materials. Furthermore, if τ_0 is not short enough, there is a probability $1-\alpha$ of an electron in a strong field being reflected from the miniband boundary without emitting an optical phonon. In this case, the electron oscillations will be characterized by two frequencies, Ω_c and $2\Omega_c$, and the electron distribution function, while being also sharp-peaked, will not vanish for both positive and negative values of k_3. Let us find this distribution function (for a one-dimensional model).

To simplify the subsequent analysis, we shall assume the probability of optical-phonon emission α to be a constant independent of the electric field. [The expressions to be derived here (but not the graphs) will also remain valid in the case where α is field-dependent.] The electron behavior in the passive region will be described by kinetic equation (5) with $f_0(k_3) = 2\pi n\delta(k_3)$ and the boundary condition

$$f(-\pi/d) = (1-\alpha)f(\pi/d). \quad (27)$$

In this approximation, a solution to Eq. (5) for the electron distribution function in a static field E_c can be written as

$$f_c(k_3) = \frac{2\pi nd}{\Omega_c\tau} \times \frac{\exp(-k_3 d/\Omega_c\tau)}{(1-\exp(-\pi/\Omega_c\tau))[1+(1-\alpha)\exp(-\pi/\Omega_c\tau)]} \times \begin{cases} 1, & 0 < k_3 < \pi/d \\ (1-\alpha)\exp(-2\pi/\Omega_c\tau), & -\pi/d < k_3 < 0. \end{cases} \quad (28)$$

Substituting Eqs. (28), (1), and (3) into Eq. (24), we obtain the *I–V* curve of the SL with inclusion of the optical-phonon emission probability at the miniband boundary:

$$j_c = j_0 \frac{\Omega_c\tau}{1+(\Omega_c\tau)^2} \times \frac{1-(1-\alpha)\exp(-\pi/\Omega_c\tau)}{1+(1-\alpha)\exp(-\pi/\Omega_c\tau)} \coth\left(\frac{\pi}{2\Omega_c\tau}\right) \quad (29)$$

for a sine dispersion law, and

$$j_c = \tilde{j}_0(\pi/k_i d)\Omega_c\tau\left\{1 - \frac{2\cosh[(\pi - k_i d)/\Omega_c\tau] - \alpha[1-\exp(-(\pi-k_i d)/\Omega_c\tau)]}{(1-k_i d/\pi)[2\sinh(\pi/\Omega_c\tau) - \alpha(1-\exp(-\pi/\Omega_c\tau))]}\right\} \quad (30)$$

for dispersion law (3). In particular, for parabolic dispersion law (2), Eq. (30) yields

$$j_c = \tilde{j}_0\left[\Omega_c\tau\frac{(2-\alpha)\pi}{2\sinh(\pi/\Omega_c\tau) - \alpha[1-\exp(-\pi/\Omega_c\tau)]}\right]. \quad (31)$$

Equations (29)–(31) generalize Eqs. (21), (22), (25), and (26) to the case of an arbitrary probability of optical-phonon emission at the miniband boundary and coincide with the latter equations for $\alpha = 0$. The *I–V* curves (29) and (30) are plotted in Fig. 2 for $k_i = 0$, $0.1\pi/d$, and π/d with $\alpha = 1$. The *I–V* curve described by Eq. (30) with $k_i = \pi/2d$ practically coincides with that of Eq. (29) and, therefore, is not shown in Fig. 2. As follows from an analysis of Eq. (30) and the graphs plotted, NDC can arise in an SL in the absence of Bragg reflections only if $k_i d < \pi/2$. NDC becomes significant for substantially smaller values of k_i. Figure 3 presents *I–V* curves for SLs with (*1*) sine and (*2*) parabolic dispersion laws, which are plotted for different values of the optical-phonon emission probability at the miniband boundary.

Thus, the negative effective mass can be a dominant factor in the onset of NDC in an SL only if the effective mass is negative in a sizable part of the Brillouin miniband. Otherwise (i.e., as a rule), the Bragg reflection of electrons is the major cause of the NDC in SLs. At the same time, the presence of regions of negative effective mass in a miniband may directly account for the recent experimental observation of the self-induced Shapiro effect in an SL [15], as well as for other phenomena caused by inversion in hot electron distributions.

The existence of static NDC in SLs gives rise to nucleation of moving strong and weak field domains (the Gunn effect), which has already been used to develop a microwave generator (up to 150 GHz) [17]. On the other hand, the development of a terahertz-range Bloch generator [2] requires suppression of the low-frequency (static) NDC (see, e.g., [18]), which accounts for the onset of a competing comparatively low-frequency domain instability. The reason for this lies in that, for BOs to exist, the obvious condition $\Omega_c\tau > 1$ has to be met; this is the condition (for an SL with a sine miniband dispersion law) for the onset of static NDC. As we have just seen, static NDC can be suppressed by optical phonons throughout the field range covered. This is possible with the dispersion laws considered by us, provided that the probability of optical phonon emission at the miniband boundary is $\alpha = 1$ (Fig. 3). In this case, however, the BOs disappear, thus putting an end to the discussion of a Bloch generator. However, if BOs are essentially anharmonic, then one may hope to achieve generation at frequencies $\omega \approx \nu\Omega_c > \tau^{-1}$ ($\nu = 2, 3, \ldots$) in fields with $\Omega_c\tau < 1$, i.e., within the part of the *I–V* curve that has a positive differential but negative dynamic conductivity. (This possibility was studied for an SL with two tunneling-coupled minibands [19].) Thus, we can point out the following factors favoring realization of a Bloch generator: (i) shift of the static NDC region toward higher static fields ($\Omega_c\tau > 1$), (ii) BO anharmonicity, and (iii) suppression of static NDC for $\alpha < 1$. The first two factors do exist, to some extent, in an SL with a parabolic miniband. The third factor can be realized in an SL with a superquadratic dispersion law, for instance, of the form

$$\varepsilon(k_3) = \frac{\hbar^2}{2}\begin{cases} k_3^2/m_1, & 0 < |k_3| < \pi/2d \\ k_3^2/m_2 - (\pi/d)(1/m_2 - 1/m_1)(|k_3| - \pi/4), & \\ \pi/2d < |k_3| < \pi/d, & \end{cases} \quad (32)$$

which consists of two parabolas ($m_{1,2} > 0$) joining at the points $k_3 = \pm\pi/2d$, i.e., at the miniband center. In the region $0 < |k_3| < \pi/2d$, the electron has a positive effective mass equal to m_1, and in the region $\pi/2d < |k_3| < \pi/d$, a positive mass m_2. The case of $m_1 \gg m_2$ is of the most interest from the standpoint of application. A dispersion relation qualitatively similar to Eq. (32) oper-

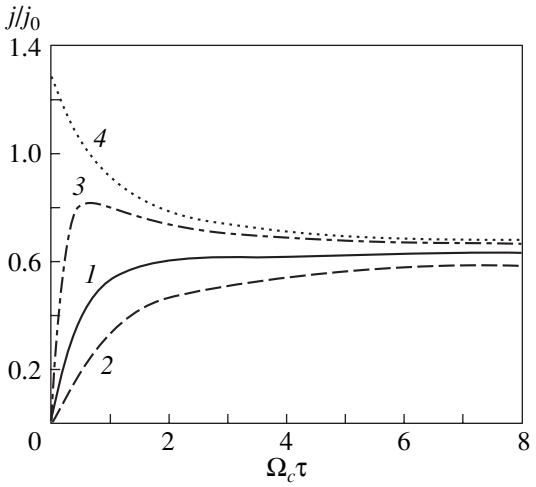

Fig. 2. *I–V* curves of an SL with (*1*) a sine miniband and parabolic minibands with (*2*) $k_l = \pi/d$, (*3*) $0.1\pi/d$, and (*4*) 0 calculated for the one-sided streaming case ($\alpha = 1$).

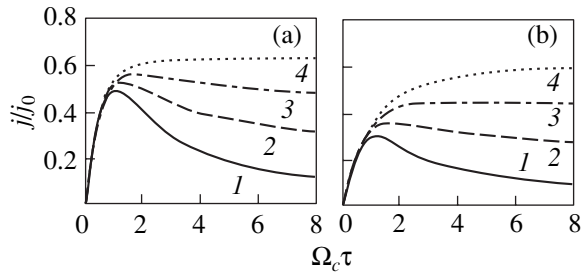

Fig. 3. *I–V* curves of an SL calculated for different probabilities of optical phonon emission at the miniband boundary. (a) Sine miniband, (b) parabolic miniband with $k_l = \pi/d$ and (*1*) $\alpha = 0$, (*2*) 0.5, (*3*) 0.8, and (*4*) 1.

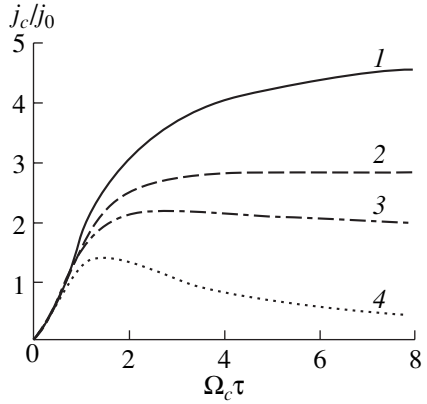

Fig. 4. *I–V* curves of an SL with superquadratic dispersion calculated for $\eta = 10$ and (*1*) $\alpha = 0$, (*2*) 0.5, (*3*) 0.7, and (*4*) 1.

ates in hole quantum layers [20] and, hence, can be realized in planar SLs based on such layers. Figure 4 presents *I–V* curves for an SL with dispersion law (32) and $\eta \equiv m_1/m_2 = 10$, which were calculated using Eqs. (21) and (28). Here, $j_0 = ne\hbar/m_1 d$. These relations suggest a possibility of suppression of the static SL NDC while retaining the BOs and, particularly, their harmonics. The high-frequency negative conductivity of SLs characterized by various dispersion relations of their minibands will be discussed in a separate publication.

4. CONCLUSIONS

Thus, we have shown that static NDC originates in an SL primarily from electron Bragg reflections and electron BOs. The presence of regions of negative effective mass in a miniband is not a prerequisite for this effect. NDC exists even in SLs with parabolic and superquadratic dispersion in the minibands that do not contain such regions. Static NDC can be absent in SLs in which BOs are strongly suppressed by optical phonons (the one-sided streaming mode). In SLs with other than sine minibands, NDC regions may be either absent or shifted toward strong fields with the BOs retained, thus giving one grounds to hope for the development of a Bloch generator operating under conditions of suppressed domain instability. Because purposeful tailoring of the electron energy spectrum in heterostructures is presently a solvable problem, a theoretical search for systems with optimal dispersion laws, which would provide suitable conditions for the existence of coherent BOs in the ranges where *I–V* curves exhibit a positive differential conductivity, is in no case an abstract idea.

The results of the present study were obtained using the Boltzmann equation in the τ approximation and, thus, require a more comprehensive inclusion of electron scattering mechanisms. It is, however, the simplicity itself of the approximations employed that permitted us to reveal certain qualitative features in the electron transport in an SL (and, possibly, in other systems as well); these features will undergo only quantitative modifications when subjected to a more rigorous consideration.

ACKNOWLEDGMENTS

This study was supported by the Russian Foundation for Basic Research (project no. 01-02-1644) and the Ministry of Industry and Science of the Russian Federation.

REFERENCES

1. L. V. Keldysh, Fiz. Tverd. Tela (Leningrad) **4** (8), 2265 (1962) [Sov. Phys. Solid State **4**, 1658 (1962)].
2. L. Esaki and R. Tsu, IBM J. Res. Dev. **14** (1), 61 (1970); P. Lebwohl and R. Tsu, J. Appl. Phys. **42** (6), 2664 (1970).
3. M. I. Ovsyannikov, Yu. A. Romanov, V. N. Shabanov, and R. G. Loginova, Fiz. Tekh. Poluprovodn. (Leningrad) **4** (12), 2225 (1970) [Sov. Phys. Semicond. **4**, 1919

(1970)]; Yu. A. Romanov, Fiz. Tekh. Poluprovodn. (Leningrad) **5** (7), 1434 (1971) [Sov. Phys. Semicond. **5**, 1256 (1971)].

4. F. Bloch, Z. Phys. **52**, 555 (1928); C. Zener, Proc. R. Soc. London, Ser. A **145**, 523 (1934).
5. G. H. Wannier, Phys. Rev. **117**, 432 (1960); Rev. Mod. Phys. **34**, 645 (1962).
6. J. Feldmann, K. Leo, J. Shah, *et al.*, Phys. Rev. B **46**, 7252 (1992).
7. K. Leo, P. H. Bolivar, F. Bruggemann, *et al.*, Solid State Commun. **84**, 943 (1992).
8. C. Waschke, H. G. Roskos, R. Schwedler, *et al.*, Phys. Rev. Lett. **70**, 3319 (1993).
9. V. G. Lyssenko, G. Valusis, F. Löser, *et al.*, Phys. Rev. Lett. **79**, 301 (1997).
10. M. Sudzius, M. Sudzius, V. G. Lyssenko, *et al.*, Phys. Rev. B **57**, R12693 (1998).
11. F. Löser, Yu. A. Kosevich, K. Köhler, and K. Leo, Phys. Rev. B **61**, R13373 (2000).
12. Yu. A. Romanov and E. V. Demidov, Fiz. Tekh. Poluprovodn. (Leningrad) **31** (3), 308 (1997) [Semiconductors **31**, 252 (1997)].
13. H. Kroemer, Phys. Rev. **109**, 1856 (1958).
14. V. A. Yakovlev, Fiz. Tverd. Tela (Leningrad) **3** (7), 1983 (1961) [Sov. Phys. Solid State **3**, 1442 (1962)].
15. A. A. Ignatov, K. F. Renk, and E. P. Dodin, Phys. Rev. Lett. **70**, 1996 (1993).
16. E. H. Cannon, K. N. Alekseev, and F. V. Kusmartsev, Phys. Rev. Lett. **85**, 1302 (2000).
17. E. Schomburg, R. Scheuerer, S. Brandl, *et al.*, Electron. Lett. **35** (17), 12 (1999).
18. H. Kroemer, cond-mat/0007482; cond-mat/0009311.
19. L. K. Orlov and Yu. A. Romanov, Fiz. Tekh. Poluprovodn. (Leningrad) **19** (10), 1877 (1985) [Sov. Phys. Semicond. **19**, 1157 (1985)]; Izv. Vyssh. Uchebn. Zaved., Radiofiz. **32** (3), 282 (1989).
20. Y. C. Chang and R. B. James, Phys. Rev. B **39**, 12672 (1989).

Translated by G. Skrebtsov

Physics of the Solid State, Vol. 45, No. 3, 2003, pp. 566–572. Translated from Fizika Tverdogo Tela, Vol. 45, No. 3, 2003, pp. 535–541.

LOW-DIMENSIONAL SYSTEMS AND SURFACE PHYSICS

Thermal Conductivity of HgSe Loaded in the Pore Lattice of a Synthetic Opal Single Crystal

V. N. Bogomolov*, N. F. Kartenko*, D. A. Kurdyukov*, L. S. Parfen'eva*, V. V. Popov*, L. M. Sorokin*, I. A. Smirnov*, H. Misiorek, A. Jezowski**, and J. Hutchison*****

** Ioffe Physicotechnical Institute, Russian Academy of Sciences, Politekhnicheskaya ul. 26, St. Petersburg, 194021 Russia*
e-mail: igor.smirnov@pop.ioffe.rssi.ru
*** Institute of Low-Temperature and Structural Research, Polish Academy of Sciences, Wrocław, 50-950 Poland*
**** Department of Materials, University of Oxford, Oxford, OXI 3PH UK*

Received June 18, 2002

Abstract—Samples of the opal + HgSe nanocomposite with 100% filling of the first-order opal pores by mercury selenide were prepared. The effective thermal conductivity κ_{eff} and electrical resistivity ρ_{eff} were measured in the temperature range T = 5–200 K, and the thermopower coefficient α was measured in the interval 80–300 K. The coefficient α of HgSe in opal was shown to remain the same as that in bulk mercury selenide samples with similar carrier concentrations. The mechanism of carrier scattering in the HgSe loaded in opal also did not change. The total thermal conductivity κ_{tot}^0 and electrical resistivity ρ^0 were isolated from κ_{eff} and ρ_{eff}, and the electronic (κ_e^0) and lattice (κ_{ph}^0) components of thermal conductivity of HgSe in opal were determined. The magnitude of κ_{ph}^0 was found to be considerably smaller than κ_{ph} of bulk HgSe with the same carrier concentration throughout the temperature interval studied (5–200 K). For $T > 20$ K, this behavior of $\kappa_{ph}^0(T)$ is accounted for by the presence of specific impurities and defects forming in HgSe, and for $T < 20$ K, by the onset of boundary scattering of phonons in the bottlenecks of the horn-shaped channels connecting first-order octahedral and tetrahedral opal pores loaded by mercury selenide. *© 2003 MAIK "Nauka/Interperiodica".*

1. INTRODUCTION

This investigation is a continuation of the study into the thermal conductivity of single-crystal synthetic opals and related nanocomposites, started by the present authors in 1995 [1–7], and deals with the opal + HgSe nanocomposite.

The crystal structure of opals is described in considerable detail in [1–9]. To facilitate understanding of the experimental data reported in this communication, the main features of the specific structure of opals should be recalled.

The crystal structure of opal is made up essentially of closely packed spheres of amorphous SiO_2 typically ~2000–2500 Å in diameter (first-order spheres). These spheres contain a set of densely packed spheres of smaller diameter, ~300–400 Å (second-order spheres), which, in turn, are formed from densely packed particles of the of the order of 100 Å in size (third-order spheres).

An array of densely packed spheres has pores of octahedral and tetrahedral types, interconnected by horn-shaped channels. Depending on the actual sphere order, the pores can also be divided into pores of first, second, and third order. The diameters of the first-order octahedral and tetrahedral pores and channels are 800, 400, and 300 Å, respectively.[1]

The total theoretical opal porosity is 59% (The first-, second-, and third-order pores occupy 26, 19, and 14% of the volume, respectively). The real total porosity of the single-crystal opals grown by us was, however, ~46–50% because of partial sintering of the second- and third-order spheres of amorphous SiO_2 [10]. The volume of the first-order pores remained ~26%.

The first-order amorphous SiO_2 spheres and pores form closely packed face-centered cubic lattices with the parameter a ~ 3000–4000 Å.

The thermal conductivity of synthetic opal single crystals depends substantially on the method of their preparation and the degree of structural perfection [6].

First-order opal pores can be loaded, using various methods (chemical, melt injection under pressure, or impregnation of the sample by a filler material), by metals, semiconductors, or insulators and form in this way regular three-dimensional composites with a cubic lattice of the filler with the parameter a ~ 3000–4000 Å [8]. Depending on the actual technique employed to load the opal pores by fillers and on the quality of the opal single crystals into which they are incorporated, one can obtain at least two types of nanocomposites [7], i.e., in which (i) the opal pores are filled to 100% or (ii)

[1] Octahedral and tetrahedral pores can be conveniently visualized as spheres interconnected by cylindrical channels [8].

the pores are not completely filled, so that the opal crystal consists of "islands" of regular filling separated by a filler-free opal matrix.

Thus, to correctly interpret the experimental data obtained on a nanocomposite, one needs to know the actual pattern of opal-pore loading by the filler.

The goal of this study was to measure the effective thermal conductivity $\kappa_{eff}(T)$ of the opal + HgSe nanocomposite and, most importantly, to investigate the specific features in the behavior of the total thermal conductivity $\kappa^0_{tot}(T)$ and of the lattice thermal conductivity $\kappa^0_{ph}(T)$ of HgSe embedded in the opal pores.

2. PREPARATION OF THE SAMPLES, THEIR CHARACTERIZATION, AND EXPERIMENTAL TECHNIQUES

The opal pores in the opal + HgSe nanocomposite were filled by HgSe sublimation under a large temperature gradient. The HgSe used for this purpose was synthesized from the elements via a gas-phase reaction performed in a two-zone furnace. The mercury used was ChDA grade, and the selenium was OSCh 16-5. To obtain HgSe of stoichiometric composition, an opal + HgSe sample was annealed under isothermal conditions in mercury vapor at $T \sim 280$°C in a sealed evacuated quartz ampule. This method was used successfully to fill the opal first-order pores by mercury selenide close to 100%. The degree of opal-pore loading could be judged from measurements of the sample density. The density of an opal + HgSe sample with first-order pores filled to 100% by mercury selenide should be 3.14 g/cm^3. The density of the opal + HgSe nanocomposite prepared by us was 3.0 g/cm^3.

The opal + HgSe nanocomposite sample studied measured $1.5 \times 0.72 \times 7$ mm.

The phase analysis of the nanocomposite thus obtained and the determination of the HgSe unit-cell parameter in the opal were performed using diffraction patterns made in CuK_α radiation (with an Ni filter) on a DRON-2 diffractometer (Fig. 1).

As follows from the diffraction pattern in Fig. 1a, the starting opal is an amorphous material. Moreover, the diffraction pattern in Fig. 1b attests to the formation of single-phase crystalline HgSe in the opal. The unit-cell parameter of bulk HgSe (sphalerite) is 6.087 Å [11], while that of HgSe loaded into the opal is 6.09(1) Å.

The opal + HgSe nanocomposite was also studied with a JEOL 4000 EXII electron microscope. The nanocomposite sample intended for these studies was first ground with a fine-grained emery cloth (1200 grains/mm^2) down to a thickness of ~50–60 μm and then ion-beam thinned (Ar^+) to make it transparent to electrons.

An electron micrograph of the opal clearly reveals an ordered array of monodisperse silicate spheres. The

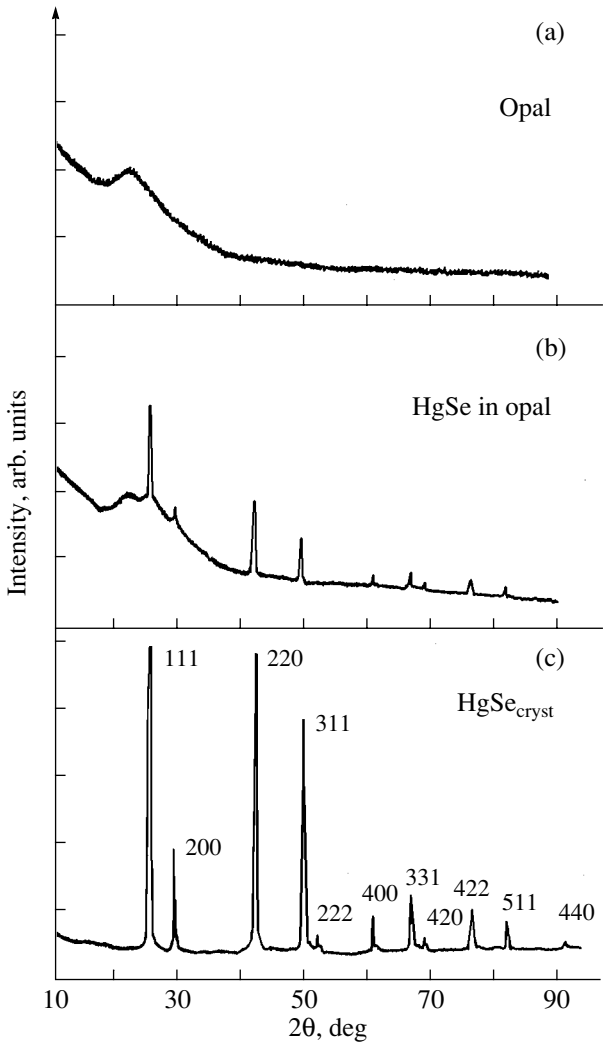

Fig. 1. Diffractometric intensity curves of (a) opal, (b) HgSe loaded in the opal, and (c) bulk HgSe.

opal pores (both octahedral and tetrahedral) were found to be filled completely, such that the cluster took up the whole pore volume. Thus, a cluster structure formed. The clusters in the image have a dark contrast, which shows them to consist of a material that strongly absorbs electrons. Microdiffraction patterns of sufficiently thin parts of the clusters made it possible to identify them with the cubic lattice of mercury selenide. Inspection of large areas of the sample (10×10 μm) permitted the conclusion that the pore filling was close to 100% of the total volume.

It should be pointed out that, in some pores, mercury selenide crystallized in the form of a single-crystal cluster. Figure 2 presents an image of such a cluster obtained in the high-resolution mode. The microdiffraction pattern (inset to Fig. 2) consists of points, which is characteristic of a single crystal. An analysis of this diffraction pattern shows that the material crys-

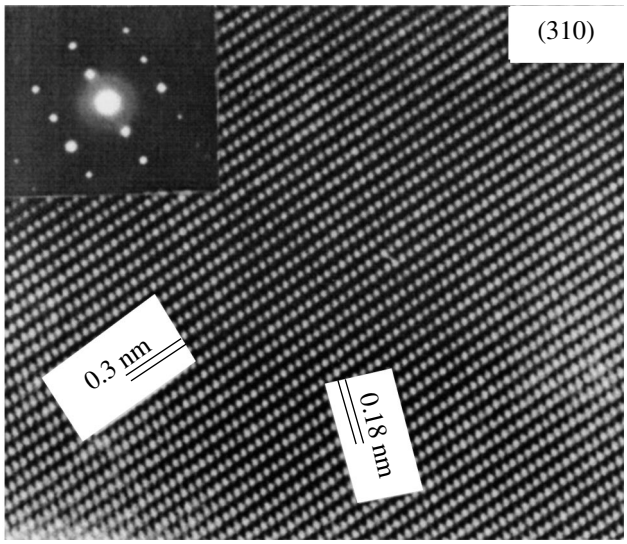

Fig. 2. Electron-microscopical image of a single-crystal HgSe cluster in the opal, Inset shows a point diffraction pattern for the cluster.

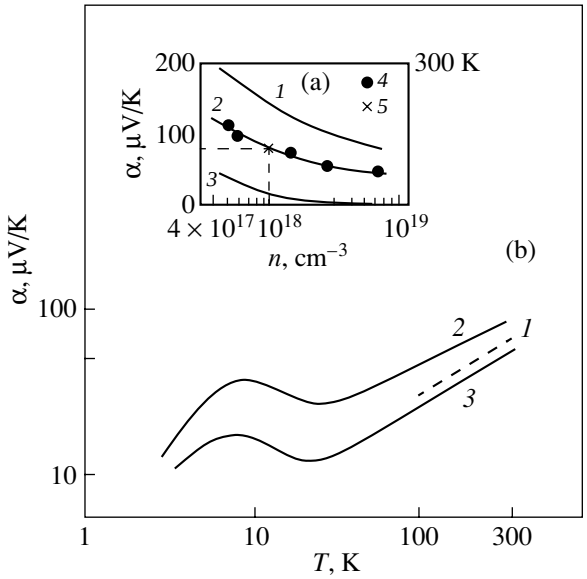

Fig. 3. (a) Curves *1–3* are calculated concentration dependences of thermopower for various carrier scattering mechanisms: (*1*) $r = 1.5$, (*2*) 0.5, and (*3*) –0.5; (*4*) experimental values of thermopower for bulk HgSe samples at 300 K taken from [14]; and (*5*) thermopower at 300 K for the opal + HgSe nanocomposite. (b) Temperature dependences of thermopower (*1*) of the opal + HgSe nanocomposite (for HgSe in the opal, $n \sim 1 \times 10^{18}$ cm^{-3}), and of bulk HgSe crystals [14] with various electron concentrations *n*: (*2*) 3.7×10^{17} and (*3*) 1×10^{18} cm^{-3}.

tallizing in the opal pores is indeed mercury selenide with a cubic lattice and the unit-cell parameter ~6.09 Å.

The effective thermal conductivity and electrical resistivity ρ_{eff} of the opal + HgSe nanocomposite were measured in the interval 5–200 K in a vacuum of 10^{-5} mm Hg on a setup similar to that employed in [12], and the thermopower coefficient α was studied in the interval 100–300 K on the setup used in [13].

3. EXPERIMENTAL RESULTS

The data obtained on $\alpha(T)$ are shown graphically in Figs. 3b (curve *1*) and 3a (point *5*). It was found that the opal matrix does not affect the magnitude of α of HgSe loaded in the opal pores, as had already been pointed out by us when measuring α of the opal + PbSe nanocomposite [3]. The thermopower turned out to be the same as in bulk HgSe crystals [14] with similar carrier concentrations. The carrier scattering mechanism corresponding to $r = 0.5$ retained its character in HgSe embedded in the opal.[2] In theory, $r = 0.5$ relates to two carrier scattering mechanisms [14, 15], namely, those with involvement of optical (for $T > \Theta$, where Θ is the Debye temperature) and piezoelectric acoustic lattice vibrations (Fig. 3a).

The data on α permitted us to estimate the carrier concentration in the HgSe loaded in the opal. It was found to be $\sim 1 \times 10^{18}$ cm^{-3}.

Figures 4a, 4b (curve *2*), and 5 (curve *1*) present experimental data for $\rho_{eff}(T)$ and $\kappa_{eff}(T)$ obtained for the opal + HgSe nanocomposite. For comparison, Fig. 4b (curve *1*) also displays the values of ρ for bulk HgSe with $n \sim 1 \times 10^{18}$ cm^{-3} taken from [16], and Fig. 5 (curve *2*) shows data for κ_{ph} of a single crystal of synthetic opal whose pores were also loaded by HgSe.[3]

4. DISCUSSION

As already mentioned, the goal of this study was to investigate the specific features in the behavior of the lattice thermal conductivity of HgSe embedded in opal pores.[4] To do this, one has, first, to isolate the total thermal conductivity κ_{tot}^0 of HgSe embedded in the opal pores from the experimental data on κ_{eff} of the opal + HgSe nanocomposite.

There is a wealth of relations expressing the thermal conductivity of composite materials [5, 20–24]. We chose the relations presented in [24], which were quoted as providing satisfactory agreement with exper-

[2] The parameter *r* is the exponent in the energy dependence of the carrier relaxation time $\tau \sim \tau_0 \varepsilon^r$. The values $r = -0.5$ and 1.5 relate to carrier scattering from acoustic lattice vibrations and impurity ions, respectively (Fig. 3a).

[3] As shown by us in [6], the value of κ_{ph} of single crystals of synthetic opals depends substantially on both the method of crystal preparation and the degree of their perfection. Therefore, when analyzing results on the thermal conductivity of a nanocomposite, it is necessary to know the thermal conductivity of the specific opal whose pores were loaded by the filler in the given experiment.

[4] Our conference reports [17–19] quoted preliminary data on κ_{eff} of the opal + HgSe nanocomposite. No analysis of the experimental results was, however, offered.

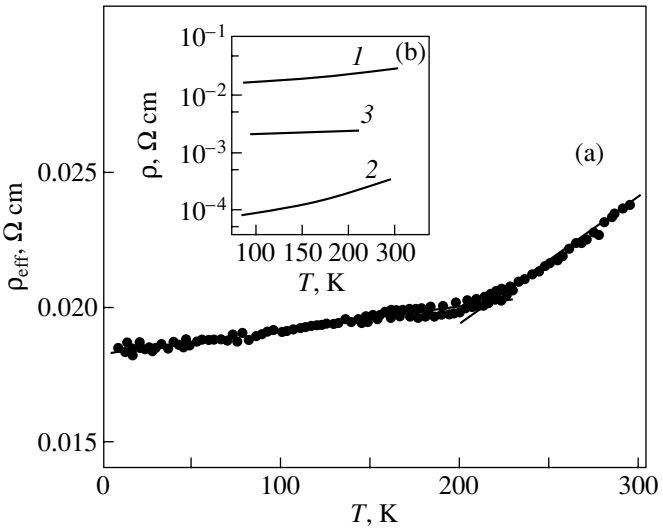

Fig. 4. (a) Temperature dependence of effective electrical resistivity ρ_{eff} of the opal + HgSe nanocomposite. (b) Temperature dependences (*1*) of the electrical resistivity of bulk HgSe ($n = 1 \times 10^{18}$ cm^{-3}) [16], (*2*) of ρ_{eff} of the opal + HgSe nanocomposite, and (*3*) of ρ^0 of HgSe embedded in opal first-order pores.

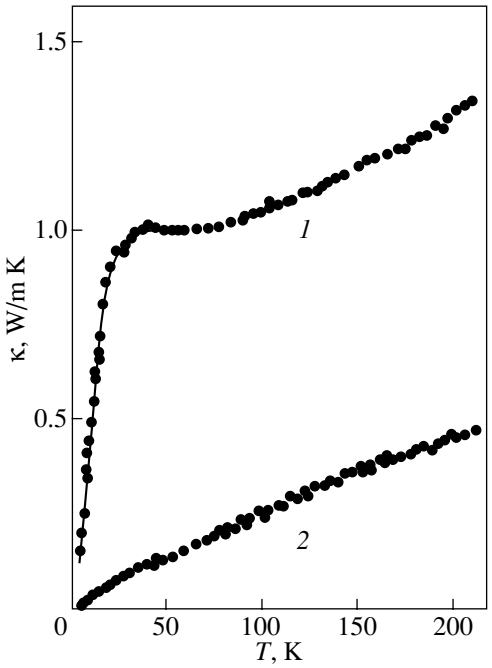

Fig. 5. Temperature dependences (*1*) of κ_{eff} of the opal + HgSe nanocomposite and (*2*) of κ_{ph} of a synthetic opal single crystal with the first-order pores filled by HgSe.

imental values for a sufficiently large number of composites. According to [24],

$$\kappa_{comp}/\kappa_{mat} = (1-P)\sqrt{1-P} + \sqrt[4]{P}\nu, \quad (1)$$

where κ_{comp} and κ_{mat} are the thermal conductivities of the composite and of the matrix, respectively; P is the material porosity;

$$\nu = \kappa_{por}/\kappa_{mat}; \quad (2)$$

and κ_{por} is the thermal conductivity of the filler loaded in the matrix pores.

The matrix in the opal + HgSe nanocomposite consists of amorphous SiO_2 opal spheres. As already mentioned, their porosity P' (second- and third-order porosity) for our single-crystal opal samples is ~20%. The matrix thermal conductivity was calculated as [24]

$$\kappa_{mat} = \kappa_{am.SiO_2}[(1-P')\sqrt{1-P'}]. \quad (3)$$

The values of $\kappa_{por} = \kappa^0_{tot}$ for HgSe in the opal pores calculated from Eqs. (1)–(3) are displayed graphically in Fig. 6 (curve *1*).

HgSe is a semiconductor. The total thermal conductivity of bulk mercury selenide samples is the sum of the lattice and electronic components [13, 16, 25–29]. The same relation holds for the HgSe embedded in the opal pores:

$$\kappa^0_{tot} = \kappa^0_{ph} + \kappa^0_e, \quad (4)$$

where κ^0_{ph} and κ^0_e are the lattice and electronic components, respectively, of the thermal conductivity of HgSe in opal pores and κ^0_e is derived from the Wiedemann–Franz law

$$\kappa^0_e = LT/\rho^0, \quad (5)$$

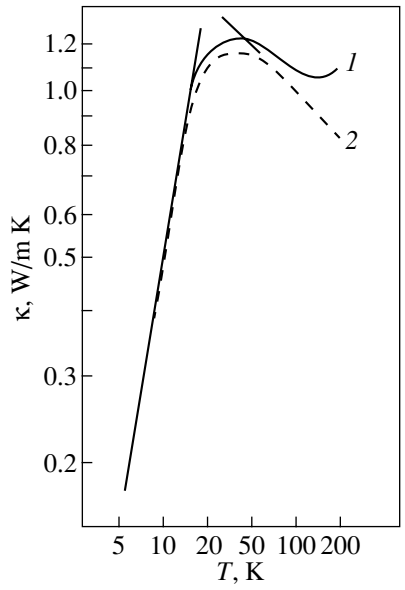

Fig. 6. Temperature dependence (*1*) of the total thermal conductivity and (*2*) of its lattice component for HgSe embedded in opal first-order pores.

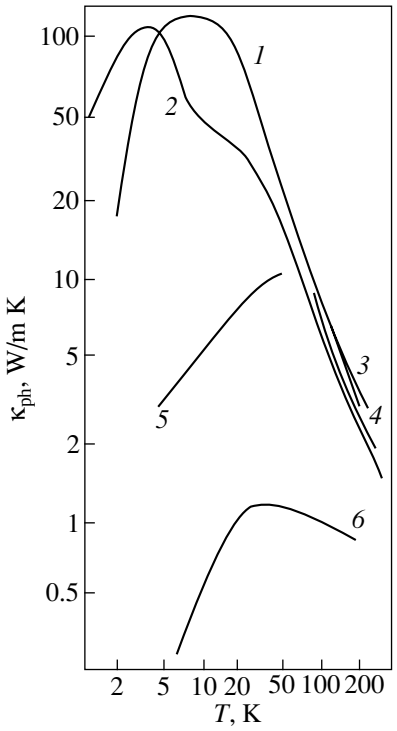

Fig. 7. Temperature dependences (*1*–*5*) of κ_{ph} of bulk HgSe samples with different carrier concentrations, and (*6*) of HgSe embedded in opal first-order pores, $n \sim 1 \times 10^{18}$ cm^{-3}. n (cm^{-3}): (*1*) ~0.5×10^{18} [13], (*2*) ~3×10^{18} [25, 26], (*3*) ~3×10^{19} [27], (*4*) ~1×10^{18} [16], and (*5*) ~4×10^{20} (Fe impurity) [29].

where L is the Lorenz number and ρ^0 is the electrical resistivity of HgSe in the opal pores. To estimate κ_e^0, we have to separate ρ^0 out of the experimental values of ρ_{eff} (Fig. 4a). To do this, we used calculated graphs that allow one to isolate the electrical resistivity of the filler loaded in porous objects [21]. The results of this calculation are displayed in Fig. 4b (curve *3*).

The resistivity ρ^0 of HgSe embedded in opal pores varies in the interval 10–200 K from 1.85×10^{-3} to 1.97×10^{-3} Ω cm. In bulk HgSe (with $n \sim 1 \times 10^{18}$ cm^{-3}), $\rho_{77\,K} \sim 1 \times 10^{-4}$ Ω cm [26], which is a factor of approximately 18 smaller than ρ^0 of HgSe embedded in first-order opal pores.

The calculation of ρ^0 in the opal made by us using the graphs from [21] is supported by data from [8] and unpublished results of the present authors on measurements of the Hall constant, ρ_{eff}, and of its variation in a magnetic field for the opal + HgSe nanocomposite. Interesting and unexpected results were obtained. The value of ρ_{eff} at 77 K for the nanocomposite under study was found to be, as in our case, ~1.9×10^{-2} Ω cm. An analysis of the experimental data on the above three effects made with due account of the real parameters of the first-order opal pore array [8] yielded very unusual results.

It was found that the 77-K carrier concentrations in HgSe embedded in the octahedral pores and channels of the opal are different. In the former case, the concentration is ~1.75×10^{18} cm^{-3}, and in the latter, ~8×10^{18} cm^{-3} (the corresponding values of ρ^0 are also different). It appears as though the mercury selenide "drops" in the pores were interconnected through higher conductivity "wires" of HgSe in the channels. The average value of ρ^0 of the HgSe embedded in the opal is ~1.96×10^{-3} Ω cm. The calculated carrier mobilities $\mu_{77\,K}$ (R/ρ^0) for HgSe loaded in the opal pores and channels were found to be similar and equal to ~690 cm^2/V s (for bulk HgSe with $n \sim 1 \times 10^{18}$ cm^{-3}μ, the mobility is 36800 cm^2/V s [13]).

Now, using the obtained values of ρ^0 one can calculate κ_e^0 from Eq. (5). Equation (5) also contains, however, the Lorenz number L. According to [13, 16, 25–28], at moderate temperatures (80–400 K), the value of L in bulk HgSe becomes smaller (because of the inelastic carrier scattering) than the Sommerfeld value L_0 ($L_0 = 2.45 \times 10^{-8}$ W Ω/K^2) characteristic of degenerate semiconductors (as well as of semimetals and metals). In bulk samples with a carrier concentration ~1×10^{18} cm^{-3} κ_e contributes noticeably for $T > 80$ K to the total thermal conductivity (~9–17% for T = 90–200 K [13]) but the contribution drops sharply with decreasing temperature (~1% for $T \lesssim 10$ K [26]).

For the sake of simplicity (and because of the lack of information on the behavior of $L(T)$ for HgSe in opal), we shall assume in our calculations that $L = L_0$ within the temperature interval covered. It was found that even for these values of the Lorenz number κ_e^0 is much smaller than κ_{ph}^0 and cannot noticeably affect the general conclusions as to the character of $\kappa_{ph}^0(T)$ for the HgSe embedded in the opal pores.

The $\kappa_{ph}^0(T)$ relation is shown graphically in Fig. 6 (curve *2*). It should be pointed out that, within the temperature region $T > 50$ K, $\kappa_{ph}^0 \sim T^{-0.3}$, which is characteristic of heavily defected materials.

Let us turn now to an analysis of the data obtained for κ_{ph}^0. Figure 7 presents, together with the data for κ_{ph}^0, the values of κ_{ph} for bulk HgSe samples taken from [13, 16, 25–27, 29]. Two features in the behavior of $\kappa_{ph}^0(T)$ should be pointed out.

(1) Throughout the temperature region covered, the value of κ_{ph}^0 is by far smaller than κ_{ph} of bulk samples.

(2) For $T < 20$ K, κ_{ph}^0 decreases strongly. For instance, the ratio $\kappa_{ph}/\kappa_{ph}^0$ (where κ_{ph} corresponds to the values for bulk HgSe samples [26], curve *2* in Fig. 7) is equal to 3, 37, 92, and 500 at 200, 20, 10, and 5 K, respectively.

The decrease in κ_{ph}^0 compared with κ_{ph} of bulk samples for $T > 20$ K can be accounted for by the fact that, in HgSe embedded in the opal pores, there are specific defects, such as vacancies and breaks in the filler array, surface defects, dislocations, and defects associated with stresses in the filler material. The presence of defects that strongly scatter phonons in the filler material is also indicated, as already mentioned, by the temperature dependence of the experimentally measured κ_{ph}^0 at $T > 50$ K ($\kappa_{ph}^0 \sim T^{-0.3}$).

The strong decrease in κ_{ph}^0 for $T < 20$ K can be due to the onset of boundary phonon scattering in the bottlenecks of the horn-shaped channels connecting the octahedral and tetrahedral first-order opal pores filled by mercury selenide. Let us consider this point in more detail.

Note an interesting feature associated with heat transport in opal-based nanocomposites in which first-order pores are loaded to 100% by the filler. The heat flux in a nanocomposite occurs over two parallel channels: (i) the amorphous SiO_2 spheres making up the opal and (ii) the filler material chains [8], such as a filled tetrahedral (octahedral) pore to a filled horn-shaped channel to a filled tetrahedral (octahedral) pore to a filled horn-shaped channel and so on.

In this case, knowledge of the matrix-to-filler thermal-conductivity ratio is essential. One may conceive of the following possibilities: (1) κ of the matrix is less than κ of the filler; in this case, the heat flux will propagate predominantly over the filler-material chains; and (2) κ of the matrix is larger than κ of the filler; here, the heat will propagate primarily over the matrix.

The opal + HgSe nanocomposite should be assigned to the first of the above versions.

Let us consider the behavior of $\kappa_{ph}^0(T)$ of HgSe embedded in the opal pores for $T < 20$ K (curve *6* in Fig. 7) based on the proposed scheme of heat transport in this nanocomposite and the standard relation for the thermal conductivity of solids

$$\kappa_{ph} = (1/3)C_V l \bar{v}, \qquad (6)$$

where l is the phonon mean free path, C_V is the specific heat at constant volume, $\bar{v} = (2v_\perp + v_\parallel)/3$ is the average sonic speed, and $v_\perp$ and $v_\parallel$ are the transverse and longitudinal sound velocities, respectively.

The heat flux in the opal + HgSe nanocomposite, as already mentioned, propagates predominantly over HgSe chains. At certain temperatures, the phonon mean free path may become comparable to the dimensions of the bottlenecks in the horn-shaped channels connecting the octahedral (and tetrahedral) opal pores filled by mercury selenide.

As the temperature is further lowered, l becomes constant under these conditions and, because $\bar{v}$ is only weakly temperature-dependent, κ_{ph}^0 will start to decrease with temperature as $C_V(T)$ in accordance with Eq. (6) [$\kappa_{ph}^0(T) \sim C_V(T)$].

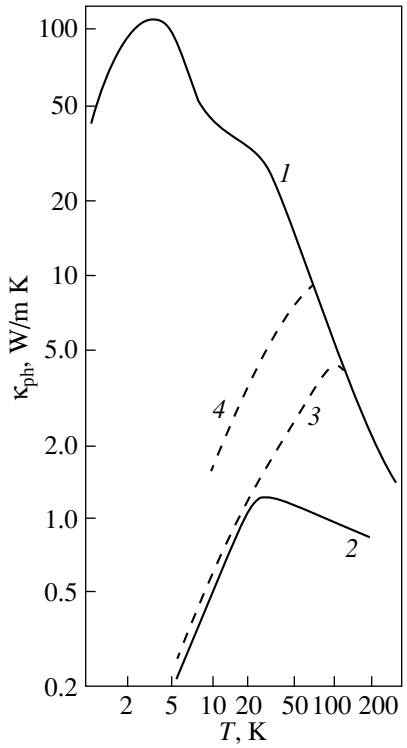

Fig. 8. Temperature dependence of κ_{ph} of (*1*) a bulk HgSe sample ($n = 3 \times 10^{18}$ cm^{-3} [25, 26]) and (*2*) HgSe loaded in the opal first-order pores ($n = 1 \times 10^{18}$ cm^{-3}). Dashed curves represent κ_{ph} calculated from Eq. (6) for values of l equal to (*3*) 100 and (*4*) 300 Å.

To check this conjecture, we calculated the mean free path of phonons in a bulk HgSe crystal for the temperature interval 10–300 K using Eq. (6). In the calculations, we used the data on κ_{ph} of HgSe (with $n \sim 3 \times 10^{18}$ cm^{-3}) [25, 26], C_V [30–32], $\bar{v}$ [11, 25, 33], and the density of the crystal [25, 26, 33, 34].

The $l(T)$ relation permitted us to determine the temperatures at which l becomes comparable to the size of the bottleneck (for two possible versions of $l = 100$ and 300 Å) and to calculate, from Eq. (6), the values of $\kappa_{ph}(T)$ corresponding to these conditions (curves *3*, *4* in Fig. 8). It was found that, for $T < 20$ K, $\kappa_{ph}^0(T)$ practically coincides with κ_{ph} calculated from Eq. (6) assuming $l = \text{const} = 100$ Å.

Therefore, one can assume that, at low temperatures ($T < 20$ K), the thermal conductivity of the filler loaded in the opal pores is governed by boundary phonon scattering in the bottlenecks of the horn-shaped channels connecting the filled first-order octahedral (and tetrahedral) pores of the opal. The regular arrangement of these bottlenecks in the opal filler array plays an important role in this process.

5. CONCLUSIONS

Thus, the results reported in [6] and the data obtained in the present experiment permit a general conclusion as to the behavior of the thermal conductivity of opals and related nanocomposites.

The thermal conductivity of opals over a broad temperature range is determined primarily by the quality of contacts between the amorphous SiO_2 spheres, and the thermal conductivity of the filler at low temperatures (assuming the opal pores to be filled to 100%, the case where κ of the matrix is less than κ of the filler) is determined by boundary phonon scattering in the bottlenecks of the horn-shaped channels connecting the filled opal octahedral (and tetrahedral) pores.

ACKNOWLEDGMENTS

This study was supported by the Russian Foundation for Basic Research (project nos. 00-02-16883, 02-02-17657) within bilateral agreements between the Russian and Polish Academies of Sciences.

REFERENCES

1. V. N. Bogomolov, L. S. Parfen'eva, A. V. Prokof'ev, *et al.*, Fiz. Tverd. Tela (St. Petersburg) **37** (11), 3411 (1995) [Phys. Solid State **37**, 1874 (1995)].
2. V. N. Bogomolov, D. A. Kurdyukov, L. S. Parfen'eva, *et al.*, Fiz. Tverd. Tela (St. Petersburg) **39** (2), 392 (1997) [Phys. Solid State **39**, 341 (1997)].
3. L. I. Arutyunyan, V. N. Bogomolov, N. F. Kartenko, *et al.*, Fiz. Tverd. Tela (St. Petersburg) **39** (3), 586 (1997) [Phys. Solid State **39**, 510 (1997)].
4. L. I. Arutyunyan, V. N. Bogomolov, N. F. Kartenko, *et al.*, Fiz. Tverd. Tela (St. Petersburg) **40** (2), 379 (1998) [Phys. Solid State **40**, 348 (1998)].
5. V. N. Bogomolov, N. F. Kartenko, D. A. Kurdyukov, *et al.*, Fiz. Tverd. Tela (St. Petersburg) **41** (2), 348 (1999) [Phys. Solid State **41**, 313 (1999)].
6. V. N. Bogomolov, L. S. Parfen'eva, I. A. Smirnov, *et al.*, Fiz. Tverd. Tela (St. Petersburg) **44** (1), 170 (2002) [Phys. Solid State **44**, 176 (2002)].
7. V. N. Bogomolov, L. S. Parfen'eva, L. M. Sorokin, *et al.*, Fiz. Tverd. Tela (St. Petersburg) **44** (6), 1017 (2002) [Phys. Solid State **44**, 1061 (2002)].
8. V. N. Bogomolov and T. M. Pavlova, Fiz. Tekh. Poluprovodn. (St. Petersburg) **29** (5–6), 826 (1995) [Semiconductors **29**, 428 (1995)].
9. V. G. Balakirev, V. N. Bogomolov, V. V. Zhuravlev, *et al.*, Kristallografiya **38** (3), 111 (1993) [Crystallogr. Rep. **38**, 348 (1993)].
10. V. V. Ratnikov, Fiz. Tverd. Tela (St. Petersburg) **39** (5), 956 (1997) [Phys. Solid State **39**, 856 (1997)].
11. T. Dietl and W. Szymanska, J. Phys. Chem. Solids **39**, 1041 (1978).
12. A. Jezowski, J. Mucha, and G. Pompe, J. Phys. D: Appl. Phys. **20**, 1500 (1987).
13. S. A. Aliev, L. L. Korenblit, and S. S. Shalyt, Fiz. Tverd. Tela (Leningrad) **8** (3), 705 (1966) [Sov. Phys. Solid State **8**, 565 (1966)].
14. S. A. Aliev, L. L. Korenblit, and S. S. Shalyt, Fiz. Tverd. Tela (Leningrad) **7** (6), 1673 (1965) [Sov. Phys. Solid State **7**, 1357 (1965)].
15. S. S. Shalyt and S. A. Aliev, Fiz. Tverd. Tela (Leningrad) **6** (7), 1979 (1964) [Sov. Phys. Solid State **6**, 1563 (1965)].
16. I. A. Smirnov and S. A. Aliev, Fiz. Tverd. Tela (Leningrad) **10** (9), 2643 (1968) [Sov. Phys. Solid State **10**, 2080 (1968)].
17. V. N. Bogomolov, L. S. Parfeneva, A. V. Prokofiev, *et al.*, in *Abstracts of 14th International Conference on Thermoelectrics* (Russ. Acad. Sci., St. Petersburg, 1995), p. 83.
18. V. N. Bogomolov, D. A. Kurdyukov, L. S. Parfeneva, *et al.*, in *Abstracts of International Symposium on Nanostructures: Physics and Technology-96* (Russ. Acad. Sci., St. Petersburg, 1996), p. 298.
19. V. N. Bogomolov, L. S. Parfeneva, A. V. Prokofiev, *et al.*, in *Abstracts of 3rd Bilateral Symposium on Physics of Novel Materials* (Cologne, Germany, 1997), p. 18.
20. G. N. Dul'nev, Inzh.–Fiz. Zh. **9** (3), 399 (1965).
21. G. N. Dul'nev and Yu. P. Zarichnyak, *Thermal Conductivity of Mixtures and Composition Materials* (Énergiya, Leningrad, 1974).
22. R. E. Meredith and C. W. Tobias, J. Appl. Phys. **31**, 1270 (1960).
23. K. W. Garrett and H. M. Rosenberg, J. Phys. D: Appl. Phys. **7**, 1247 (1974).
24. E. Ya. Litovskiĭ, Izv. Akad. Nauk SSSR, Neorg. Mater. **16** (3), 559 (1980).
25. D. A. Nelson, J. G. Broerman, E. C. Poxia, and C. R. Whitsett, Phys. Rev. Lett. **22** (17), 884 (1969).
26. C. R. Whitsett, D. A. Nelson, J. G. Broerman, and E. C. Paxhia, Phys. Rev. B **7** (10), 4625 (1973).
27. S. A. Aliev and D. G. Arasly, Fiz. Tekh. Poluprovodn. (Leningrad) **7** (10), 2000 (1973) [Sov. Phys. Semicond. **7**, 1334 (1973)].
28. S. M. Wasim, B. Fernández, and R. Aldana, Phys. Status Solidi A **76**, 743 (1983).
29. I. G. Kuleev, A. T. Lonchakov, and I. Yu. Arapova, Fiz. Tekh. Poluprovodn. (St. Petersburg) **34** (4), 402 (2000) [Semiconductors **34**, 389 (2000)].
30. P. V. Gul'tyaev and A. V. Petrov, Fiz. Tverd. Tela (Leningrad) **1** (3), 368 (1959) [Sov. Phys. Solid State **1**, 330 (1959)].
31. V. I. Bogdanov, Yu. Kh. Vekilov, A. E. Kadyshevich, and A. D. Levin, Fiz. Tverd. Tela (Leningrad) **12** (10), 3001 (1970) [Sov. Phys. Solid State **12**, 2422 (1970)].
32. N. N. Sirota, N. P. Gavaleshko, V. V. Novikova, *et al.*, Fiz. Tverd. Tela (Leningrad) **30** (4), 1237 (1988) [Sov. Phys. Solid State **30**, 719 (1988)].
33. A. Lehoczky, D. A. Nelson, and C. R. Witsett, Phys Rev. **188** (3), 1069 (1969).
34. O. M. Krasil'nikov, Yu. Kh. Vekilov, V. M. Bezborodova, and A. V. Yushin, Fiz. Tekh. Poluprovodn. (Leningrad) **4** (11), 2122 (1970) [Sov. Phys. Semicond. **11**, 1821 (1970)].

Translated by G. Skrebtsov

Physics of the Solid State, Vol. 45, No. 3, 2003, pp. 573–578. Translated from Fizika Tverdogo Tela, Vol. 45, No. 3, 2003, pp. 542–547.

LOW-DIMENSIONAL SYSTEMS AND SURFACE PHYSICS

Simulation of Interstitial Atoms in Two-Dimensional Nanocrystals

V. A. Lagunov† and A. B. Sinani

Ioffe Physicotechnical Institute, Russian Academy of Sciences, Politekhnicheskaya ul. 26, St. Petersburg, 194021 Russia
e-mail: alfred@mdlab.ioffe.rssi.ru

Received April 19, 2002; in final form, August 15, 2002

Abstract—The molecular-dynamics method is used to study the emergence of interstitial atoms at a free face of a 2D nanocrystal. Two new types of coordination of the interstitial defect are discovered: a symmetric trifolium coordination and a linear coordination of compressed atoms. It is shown that, in the case of linear coordination, a dislocation dipole is formed in the 2D crystal lattice; the dipole is characterized by a high mobility facilitating the arrival of an interstitial atom at a free face of the crystal. The cases of transition of an interstitial atom from one type of coordination to another, depending on the crystal temperature, are studied in a computer experiment. © *2003 MAIK "Nauka/Interperiodica".*

Point defects (vacancies and interstitial atoms) noticeably affect the mechanical behavior of a crystal [1–2]. However, theoretical investigations have been confined so far to the development of plausible models of defects, which form the basis of calculation of the energy of formation and motion of these defects in the crystal lattice. Publications on the simulation of such defects and variation of their configuration in time at various temperatures are scarce in number.

Here, we model interstitial atoms in crystals in which Lennard-Jones forces of pair interaction operate between particles. The computer program from [3] makes it possible to calculate, with a high degree of accuracy, the potential energy of the crystal and, hence, the energy of formation of interstitial atoms, which is a small fraction of the total energy of the crystal. This program also makes it possible to trace the time variation of defects. The method of deep cooling of samples in the quasi-isothermal regime (QIR) [4], such that the kinetic energy of atoms is removed from the crystal every time it attains its maximum value, makes it possible to carry out computer experiments at close-to-zero temperatures.

Computer simulation of a solitary interstitial atom in a two-dimensional crystal is worked out as follows. First, the atom being implanted is placed at an interstitial position of the crystal lattice, and then its relaxed state, i.e., the state in which the motion of atoms in the crystal ceases with a preset accuracy and their positions are stabilized, is determined in the QIR. In view of a large value of the Lennard-Jones force acting between the interstitial atom and lattice atoms at the first stage of implantation and a nonzero probability of emergence of the atom from the crystal lattice, calculations were carried out, in accordance with [5], with an order of magnitude smaller integration step Δt. This step was taken equal to $0.002T$, where T is the period of natural lattice vibrations in the 2D crystal.

The time variation of the minimal atomic spacing between the interstitial atom and atoms of the matrix at the initial phase of formation of the interstitial-type defect is shown in Fig. 1. In the relaxed state of the defect, this distance is close to 0.9 of the equilibrium atomic spacing a. Figure 1 shows rapid relaxation of the defect over a time interval on the order of a fraction of T; it is seen that the QIR method used here effectively suppresses wave processes in the crystal.

The relaxed configuration of the defect obtained in this way is shown in Fig. 2a. For the sake of visualization, we show only the surroundings of the interstitial

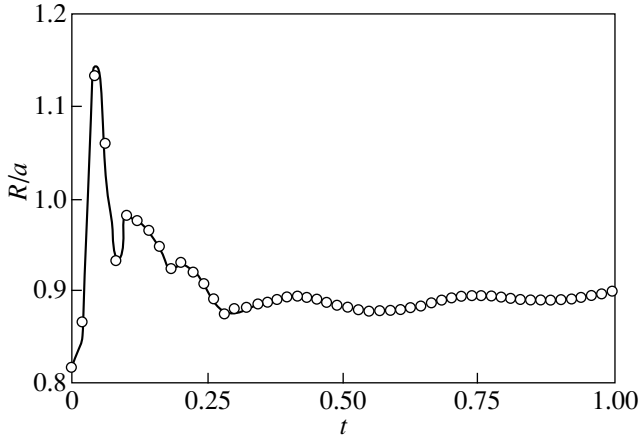

Fig. 1. Time variation of atomic spacing between the interstitial atom and matrix atoms during the creation of the interstitial defect.

† Deceased.

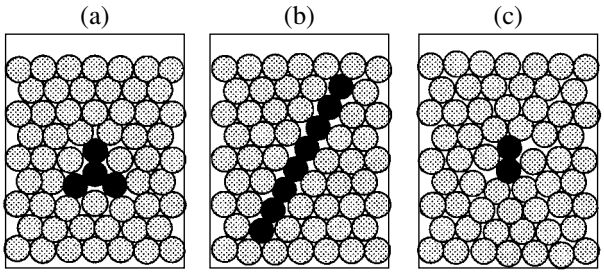

Fig. 2. Types of coordination of the interstitial defect: (a) trifolium coordination, (b) linear coordination, and (c) dumbbell coordination.

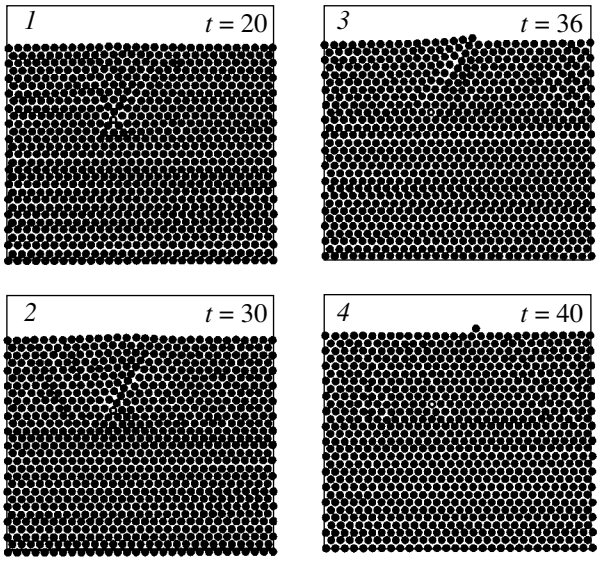

Fig. 3. Cinema frames depicting the motion of the interstitial defect at a low temperature.

atom in a small neighborhood in the crystal at instant $t = 4$ (time t is measured in periods of natural lattice vibrations). It can be seen that the interstitial atom and three atoms of close-packed lattice the form a starlike complex with third-order symmetry, viz., a trifolium (shown by dark circles in the figure). The central atom of the complex is three-coordinated, its three nearest neighbor atoms are five-coordinated, and its three nearest neighbor atoms of the perfect crystal are seven-coordinated.

The defect with such a configuration has a low mobility in the low-temperature range; this was confirmed in computer experiments performed for an interstitial atom in the central region of the crystal. However, in the case of a noticeably asymmetric position of the interstitial atom relative to the free edges of the sample, the defect was transformed into another (linear) configuration under the action of an uncompensated strong elastic impulse, which was reflected from the surface and arrived at the neighborhood of the interstitial atom.

The linear type of coordination of the interstitial atom emerging spontaneously in computer experiments is shown in Fig. 2b. The configuration of the defect at the beginning of its motion is depicted. In this case, a cooperative structure is formed in which an extended group of close-packed atoms appears in one of three intersecting rows of atoms in the 2D crystal. In terms of dislocations, such a defect can be treated as a dislocation dipole consisting of two dislocations of opposite sign moving in the same direction. The slip lines of these dislocations are displaced relative to each other by an atomic spacing. This defect is distinguished by a very high mobility. Even at a low temperature, the defect starts moving towards the nearest edge of the crystal, which ultimately results in quick "transportation" of the interstitial atom to the free boundary of the crystal.

The frames in Fig. 3 demonstrate the motion of the interstitial defect to the free edge of the sample at a low temperature; the entire kinetic energy of atoms was removed from the crystal, according to the QIR method, at the instants when this energy attained its maximum value. The values of time (in lattice vibration periods) elapsed from the beginning of the experiments are indicated; the interstitial atom is shown by a light circle. Figure 4 shows the atomic-spacing distribution in three neighboring rows of atoms. Light and dark symbols on the curves depict atoms in the compression and expansion regions, respectively.

It can be seen from Fig. 4 that the compression region includes eight to nine atoms within its half-width, while the expansion region is much narrower and constitutes approximately two or three atomic spacings. In the case of a stationary defect, the strain distribution in the compression zone has a triangular shape. It can be seen that dislocations diverge during their motion. It is worth noting that the expansion regions of two dislocations propagate at different velocities, which follows from the time variation of the distance between the peaks in the atomic-spacing distributions over the rows of atoms in the expansion regions. The velocity of propagation of the compression zone is close to half the sum of the velocities of the expansion regions.

In computer experiments, the potential energy of the entire crystal was recorded with a high degree of accuracy. Figure 5 shows the time variation of potential energy, except in the short time interval corresponding to implantation of the interstitial atom. The figure shows the decrease in the potential energy of the crystal over a time interval from $t = 20$ to 40, which is synchronized with the emergence of the interstitial atom from the crystal observed in Figs. 3 and 4. According to the data presented in Fig. 5, the energy of formation of an

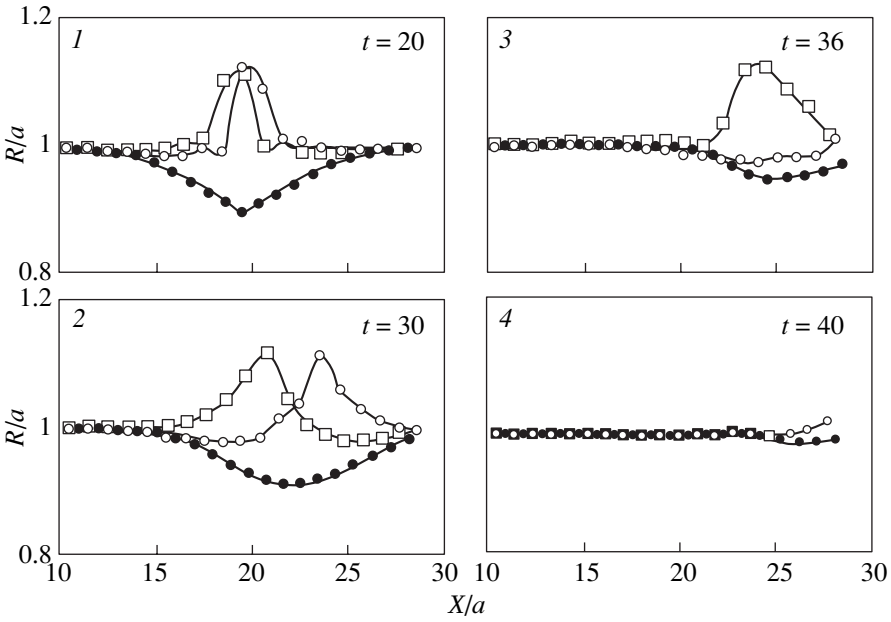

Fig. 4. Curves describing the distribution of atomic spacing in three adjacent rows of atoms at a low temperature.

interstitial atom in the 2D crystal amounts to 11.9 of the dissociation energy D.

It would be interesting to study the effect of temperature on the kinetics of motion of the interstitial atom. For such experiments, we prepared the configuration of an interstitial atom, relaxed over time $t = 4$ and obtained for the defect position remaining stationary under deep cooling of the crystal. Then, a preset kinetic energy was supplied to the entire crystal and was randomly distributed among the atoms. Computer experiments were carried out in isolation from the external medium, and the deep cooling regime (QIR) was put in operation at the final stage.

After the kinetic energy was supplied to the sample, its average value, due to anharmonicity of pair interaction, amounted to approximately 0.47 of the initial kinetic energy and not to 0.5, as in the case of a harmonic crystal. The cinema frames in Fig. 6 show the motion of the interstitial defect to the free edge of the sample for the average initial kinetic energy K_0 of atoms amounting to 0.1 of the dissociation energy D. The figure shows only part of the crystal; the interstitial atom is marked by a cross.

When the crystal is heated, the interstitial defect can experience, in addition to directed motion towards the nearest edge of the sample, a random diffusive jump. Such events took place between frames *1* and *3*, but then a transition to the linear type of coordination of the defect was observed followed by rapid athermal emergence of the defect at the lateral surface of the crystal.

A search for the most compressed atom in the crystal was carried out using a specially developed procedure for detecting the location of the interstitial atom at a considerable distance from the free surface of the crystal in the case where the defect was located between two dislocations. Figure 7 shows the time variation of the coordinate Y of the most compressed atom with a step $\Delta t = 0.1T$ for three different initial temperatures of the crystal.

In order to find the reason for the strong spread in the curves (especially in the case of elevated experimental temperatures), Fig. 7 also shows fragments of curves obtained with a high time resolution for short time intervals, which clearly illustrate typical features of motion of the interstitial atom at three temperatures. These fragments show that, in the case of zero initial temperature (curve *1*), the interstitial atom performs approximately one jump during the lattice vibration

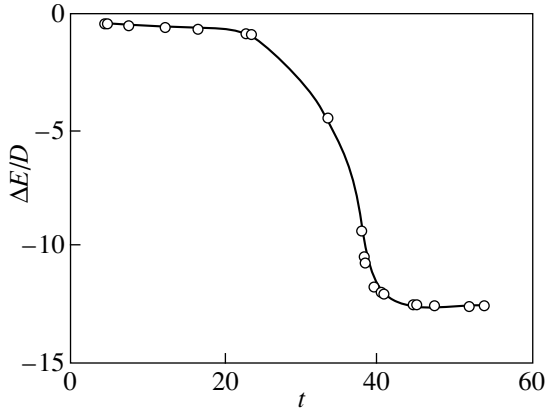

Fig. 5. Variation of the potential energy of the nanocrystal associated with motion of the interstitial atom.

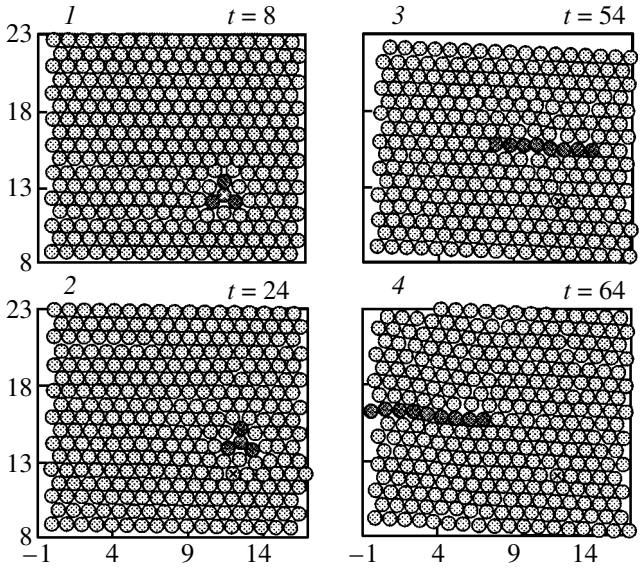

Fig. 6. Cinema frames depicting the motion of the interstitial defect for $K_0 = 0.1D$.

period and remains at rest for 0.6–0.8 of a period. However, at elevated temperatures (curves *2*, *3*) the position of the most compressed atom in a group of 4–6 atoms is displaced in two opposite directions, which is the main reason for the observed spread.

The results presented in Fig. 7 show that, as the crystal temperature increases, the emergence of the interstitial atom at the free surface of the crystal is decelerated. At the last stage, the average velocity of the defect, in accordance with Fig. 7, amounts to $(0.5–0.8)a$ per lattice vibration period. A higher velocity (of the order of $1.0a/T$) was observed at the last stage of the emergence of the interstitial atom for zero initial temperature in the crystal lattice undistorted by thermal motion.

The procedure worked out here also enables us to reconstruct the trajectory of the interstitial atom in the crystal lattice by replacing the $x(t)$ and $y(t)$ dependences in parametric form by an explicit $y(x)$ dependence. Figure 8 shows such a trajectory in the case where the average initial kinetic energy of crystal atoms is equal to $0.2D$. For the sake of convenience, time marks are used in the form of light crosses against the shaded background with a step of five lattice vibration periods; these marks provide information on the location of the defect. The figure shows that, in the case of thermal motion of atoms, the interstitial atom moves over the lattice as a Brownian particle, which randomly changes the direction and velocity of its motion. For $t \cong 16$ and 40, the motion of the defect becomes directional to a certain extent, which can be attributed to the transformation of the interstitial atom into a dislocation dipole observed at low temperatures (Fig. 3).

The motion of the interstitial defect and its transformation upon a change in the direction of motion in the case of linear coordination of the defect is shown in Fig. 9 (frames *1–3*, *4–6*). The frames were obtained at selected instants as a result of a special tracing proce-

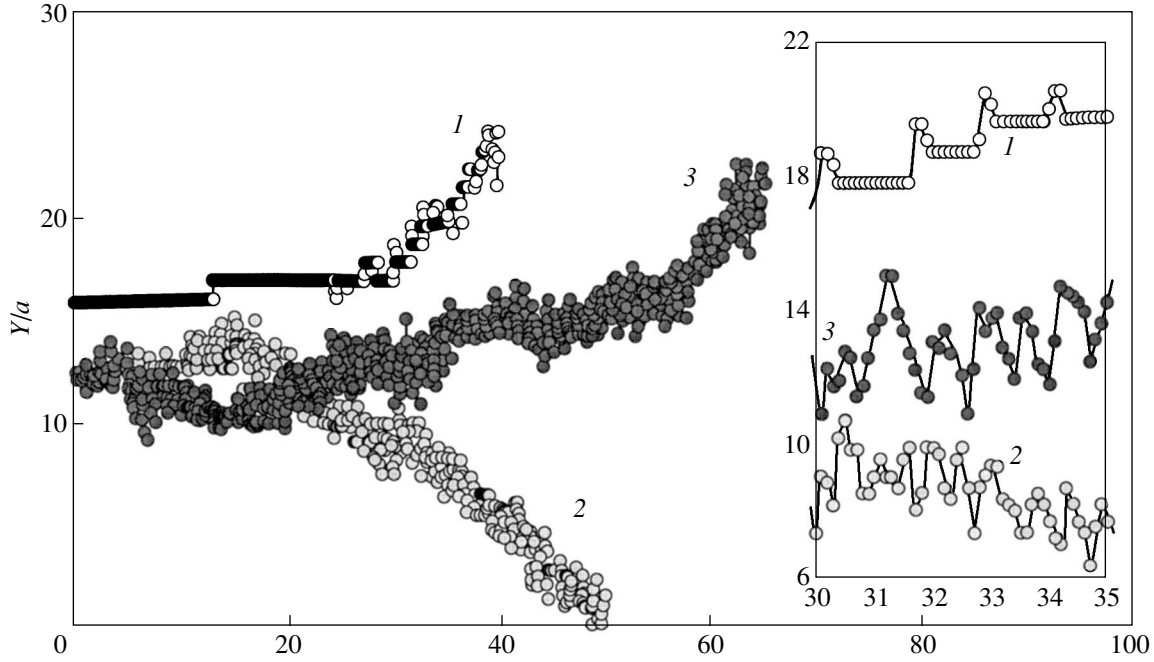

Fig. 7. Curves describing the time variation of coordinate Y of the most compressed atom at various temperatures: (*1*) $K_0 = 0$, the curve is recorded using the QIR method; (*2*) $K_0 = 0.1D$; and (*3*) $K_0 = 0.2D$.

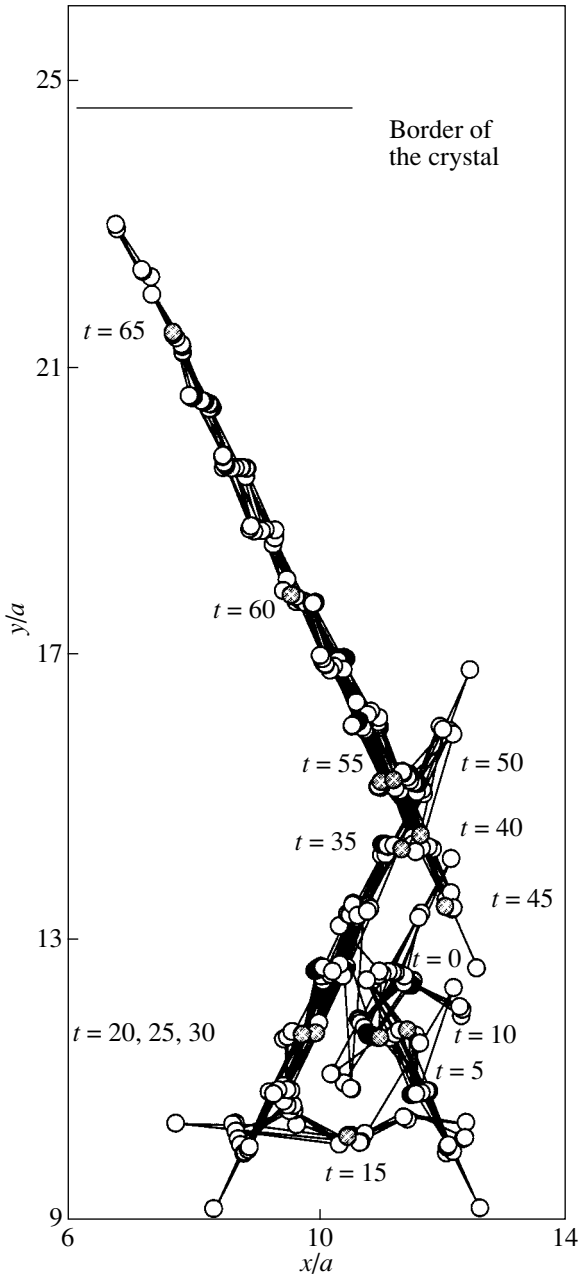

Fig. 8. Trajectory of motion of the interstitial defect for $K_0 = 0.2D$.

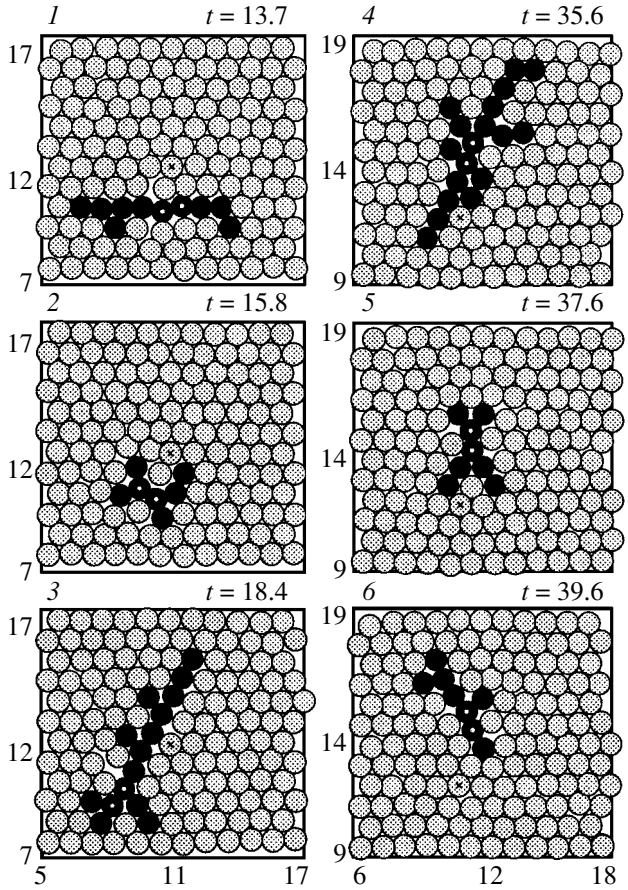

Fig. 9. Cinema frames depicting the motion of the interstitial defect for $K_0 = 0.2D$.

dure revealing a simply connected group of atoms with a preset degree of compression. Light dots indicate the pair of atoms that is the most compressed, dark circles correspond to atoms whose neighbors experience compression to an atomic spacing exceeding half the maximum distance between atoms, and crosses mark the initial position of the implanted atom.

Analysis of the results proved that, in the regions of rectilinear motion of the defect (Fig. 8), the interstitial atom is in the linear coordination in a strongly compressed linear row of atoms together with an accompanying dislocation dipole. The frames in Fig. 9 indicate, first, that the distortion field caused by the interstitial atom has a large range, which is mainly confined to one row of atoms in the case of linear motion of the defect; second, a rapid (over one or two lattice vibration period) transformation of the linear coordination (dislocation dipole) into a point defect and its reverse conversion upon a change in the direction of motion; and, third, that the lifetime of another point configuration of the interstitial atom described in the literature [1], viz., the dumbbell configuration, is short (Fig. 2c). It can be seen from Figs. 2c and 9 (frame *5*) that such a configuration is a sort of superposition of two strongly compressed trifoliums with a common ray. The configuration is extremely unstable and exists for less than a lattice vibration period at the moment of transition of the interstitial atom from one row of atoms to another.

Thus, the interstitial atom in the 2D lattice has a low mobility and resembles a Brownian particle only at high temperatures. However, its configuration can easily be transformed into a dislocation dipole, which may ensure directional motion of the defect to the crystal boundary even at low temperatures. As the temperature

increases, the probability of direct and inverse transitions between the point-defect and dislocation-dipole states, leading to a change in the slip direction of the linear defect, becomes appreciable. It is important to emphasize that, although the thermal motion increases the mobility of the defect, the time of its emergence at the free surface of the crystal increases due to the Brownian component of its trajectory.

REFERENCES

1. A. C. Damask and G. J. Dienes, *Point Defects in Metals* (Gordon and Breach, New York, 1963; Mir, Moscow, 1966).
2. Takamura Jin Ichi, in *Physical Metallurgy*, Ed. by R. Cahn (North-Holland, Amsterdam, 1965; Mir, Moscow, 1968), Vol. 3, p. 87.
3. V. A. Lagunov, Fiz. Tverd. Tela (Leningrad) **28** (11), 3466 (1986) [Sov. Phys. Solid State **28**, 1950 (1986)].
4. V. A. Lagunov and A. B. Sinani, Fiz. Tverd. Tela (St. Petersburg) **43** (4), 644 (2001) [Phys. Solid State **43**, 670 (2001)].
5. V. A. Lagunov and A. B. Sinani, Fiz. Tverd. Tela (St. Petersburg) **38** (6), 1791 (1996) [Phys. Solid State **38**, 987 (1996)].

Translated by N. Wadhwa

Physics of the Solid State, Vol. 45, No. 3, 2003, pp. 579–585. Translated from Fizika Tverdogo Tela, Vol. 45, No. 3, 2003, pp. 548–554.

LOW-DIMENSIONAL SYSTEMS AND SURFACE PHYSICS

Formation and Properties of a Binary Adsorbed Layer in a Two-Component Adsorption System (Sm + Yb)–Si(111)

M. V. Kuz'min, N. V. Mikhaĭlov, and M. A. Mittsev

Ioffe Physicotechnical Institute, Russian Academy of Sciences, ul. Politekhnicheskaya 26, St. Petersburg, 194021 Russia

e-mail: M.Kuzmin@pop.ioffe.rssi.ru

Received March 13, 2002; in final form, April 26, 2002

Abstract—Low-energy electron diffraction, thermodesorption spectroscopy, and contact potential difference techniques were used in a first study on the coadsorption of Sm and Yb atoms on the Si(111) surface. At comparatively low coverages, in both one-component adsorption systems of the rare-earth metal–Si(111) type and the two-component system (Sm + Yb)–Si(111), the same sequence of diffraction patterns of the $(n \times 1)$ type, where $n = 3$, 5, and 7, was observed. This indicates that Sm and Yb atoms occupy the same adsorption centers in a mixed film. At higher coverages, at which the $(\sqrt{3} \times \sqrt{3})R30°$ reconstruction forms in the case of the Sm–Si(111) system and the surface undergoes the 2×1 reconstruction in the Yb–Si(111) system, the structure of the mixed film is governed by the ytterbium coverage θ(Yb). At low ytterbium coverages, θ(Yb) < 0.15, superposition of the $(\sqrt{3} \times \sqrt{3})R30°$ and (2×1) diffraction patterns is observed. For θ(Yb) > 0.15, however, the former pattern disappears, whereas the latter persists. A comparison of this evolution of a binary adsorbed layer with the properties of the Sm–Si(111) and Yb–Si(111) systems indicates its anomalous character. *© 2003 MAIK "Nauka/Interperiodica".*

1. INTRODUCTION

In the literature a wealth of data on the metal–Si(111) adsorption systems has been accumulated (see, e.g., [1, 2]). It has been shown, in particular, that the atomic structure of a two-dimensional (2D) adsorbed metal film forming on the silicon surface is determined primarily by the electronic structure of the adsorbate atoms and that adsorption of metals having a similar electronic structure produces, as a rule, similar reconstructions. For instance, metals of Group III (e.g., B [3], Al [4], Ga [5, 6], In [7]) form a hexagonal structure with a $(\sqrt{3} \times \sqrt{3})R30°$ unit cell on Si(111), whereas Group-II metals (for example, Mg [8], Ca [9–11], Ba [12]), as well as divalent rare-earth metals (REMs) Yb [13, 14] and Eu [15], exhibit a trend to forming $n \times 1$ reconstructions consisting of atomic chains.

However, despite the considerable interest expressed in the phenomenon of metal adsorption on the (111) surface of silicon, as well as in the physical and chemical properties of the 2D surface layers forming in the process, there are comparatively few studies dealing with ($M1$ + $M2$)–Si(111) adsorption systems in which two different metals, $M1$ and $M2$, are codeposited on Si. Before the present study, information on coadsorption of REM atoms on the surface of a semiconductor was totally lacking. Incidentally, the two-component adsorbed films forming in such systems may be of considerable interest, both from a scientific standpoint and as having application potential. This interest stems from the possibility of preparing ultrathin surface layers with unusual properties that cannot be realized in the simpler, one-component metal–silicon adsorption systems. Indeed, in ultrathin binary adsorbed layers, lateral interaction couples not only like atoms (as in the case of one-component adlayers) but also atoms of different chemical natures, which may give rise, in principle, to the formation of novel surface alloys and reconstructions.

The present study deals with one ($M1$ + $M2$)–Si(111) adsorption system, namely, a thin-film (Yb + Sm)–Si(111) structure obtained by codeposition of two REMs, ytterbium and samarium, on the silicon surface. When deposited at low, submonolayer coverages, each of these REMs forms 3×2, 5×1, and 7×1 2D reconstructions on Si(111); by contrast, at high coverages, the corresponding structures are substantially different [13, 16–19]. The energies required to remove atoms of Yb [16] and Sm [18] from one-component adsorbed layers deposited on Si(111) into vacuum also differ markedly. It thus appeared reasonable to expect that this difference would make it possible to expel atoms of one adsorbate in a two-component Sm + Yb film adsorbed onto the Si(111) surface by using atoms of another adsorbate, with the subsequent formation of novel binary adsorption structures.[1] Guided by these intuitive notions, we focused our attention on investigating the formation and properties of a binary adsorbed layer in the (Yb + Sm)–Si(111) film system.

[1] The formation of new reconstructions in the transition layer at the REM–Si(111) interface is a topical problem in the preparation of high-quality REM silicide epitaxial films.

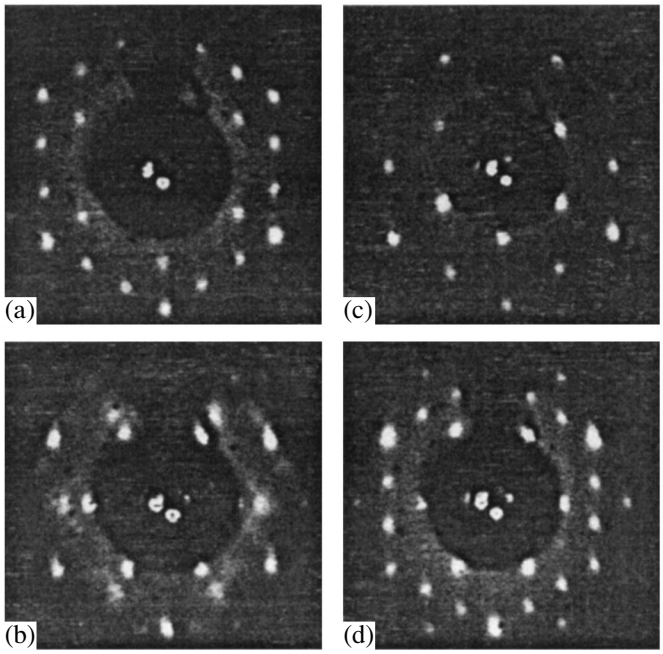

Fig. 1. Diffraction patterns for the (Sm + Yb)–Si(111) system: (a) 3×1, (b) $\sqrt{3}$, (c) 2×1, and (d) $(\sqrt{3} \times \sqrt{3})R30° + (3 \times 1)$.

2. EXPERIMENTAL TECHNIQUE

The experiments were performed *in situ* in an ultrahigh-vacuum (UHV) setup providing a base pressure of 6×10^{-11} Torr, which was described in considerable detail in our earlier publications [15, 16]. The Si samples were phosphorus-doped *n*-type substrates with an electrical resistivity of 7.5 Ω cm, and were cut in thin $40 \times 2 \times 0.3$-mm ribbons from polished plates with a predominantly (111) oriented surface. The cleanness and atomic structure of the surfaces of these samples and of the adsorbate films deposited on them were checked using Auger electron spectroscopy and low-energy electron diffraction (LEED). The substrates were heated by a direct flow of dc or ac electric current through the substrates. The sample temperature in the region $T \leq 1000$ K was measured with an IRCON (infrared) pyrometer and at $T \geq 1000$ K, with a PYRO optical pyrometer.

Yb and Sm were deposited on the surfaces to be studied from tantalum ampules. During the experiments, the pressure in the UHV chamber was maintained in the interval 4×10^{-10}–2×10^{-9} Torr, depending on the evaporator temperature. One monolayer of each of the adsorbates, $\theta(\text{Sm}) = \theta(\text{Yb}) = 1$, was nominally identified with the adsorbed atom concentration 7.84×10^{14} cm^{-2} equal to the Si atom concentration on a nonreconstructed Si(111) 1×1 surface. The rate of metal deposition on the substrate was about 0.01 monolayer per second. The crystal surface was cleaned completely of adsorbates by high-temperature annealing to 1500 K. The rate of desorption of Yb or Sm atoms from the surface was measured with a mass spectrometer. After complete removal of REM atoms from the substrate and cooling to room temperature, the diffractometer screen quickly displayed the (7×7) diffraction pattern characteristic of an atomically clean, ordered (111) surface of this semiconductor. The quality of this electron diffraction pattern did not deteriorate following multiple depositions of adsorbed layers on the substrate and their subsequent evaporation into vacuum.

The experimental data presented in Section 3 of this communication were obtained using LEED, contact-potential difference (CPD), and thermodesorption spectroscopy (TDS). The TDS was employed to obtain spectra of two types, $\nu(\text{Sm}) = f(T)$ and $\nu(\text{Yb}) = f(T)$, where $\nu(\text{Sm})$ is the desorption rate of Sm atoms from the surface, $\nu(\text{Yb})$ is the same for the Yb atoms, and T is the sample temperature. The $\nu(\text{Sm}) = f(T)$ spectra were obtained for (Sm + Yb)–Si(111) film structures with the same samarium coverages, $\theta(\text{Sm})$, but different ytterbium coverages, $\theta(\text{Yb})$, before the increase in sample temperature and the start of TD measurements. The $\nu(\text{Yb}) = f(T)$ spectra were measured in the same manner, but in this case, $\theta(\text{Sm})$ was varied at a fixed $\theta(\text{Yb})$.

3. RESULTS AND DISCUSSION

3.1. LEED

We obtained diffraction patterns from an Si surface coated by a binary Yb + Sm adsorbed film for a number of $\theta(\text{Sm})$ and $\theta(\text{Yb})$ values. Below, we consider three series of such patterns measured for the three values of $\theta(\text{Yb})$: 0.07, 0.22, and 0.44. During the REM deposition, the substrate temperature was maintained, unless otherwise specified, at 800 K. The temperature was maintained high in order for ordered two-dimensional structures of REM atoms to form in adsorption on the silicon surface. The LEED patterns were studied both at room and higher temperatures, up to T = 900 K, at which ytterbium, the more easily vaporizable adsorbate, starts to desorb from the surface of the system. The LEED pattern symmetry did not change within the above temperature interval.

3.1.1. $\theta(\text{Yb}) = 0.07$. Deposition of this amount of ytterbium atoms on Si(111) 7×7 produced a (3×1) diffraction pattern with an enhanced background. The (7×7) reflections became very weak. Deposition of Sm improved the observed diffraction pattern. The (3×1) reflections grew stronger, the background decreased, and the (7×7) reflections disappeared completely already at $\theta(\text{Sm}) = 0.03$. This diffraction pattern is shown in Fig. 1a. It practically did not change up to coverages $\theta(\text{Sm}) = 0.12$.

Attempts at deciphering the (3×1) diffraction pattern, which was also observed earlier in the Yb–Si(111) and Sm–Si(111) system were made in [13, 14]. According to those studies, this pattern can be identified in

direct space with a 2D chain structure with a 3×2 unit cell. Therefore, these results give one grounds to conclude that, at low coverages, the ytterbium and samarium atoms in the (Sm + Yb)–Si(111) system cooperate in forming the 3×2 reconstruction. Note that the diffraction pattern corresponding to this reconstruction was the best, as already mentioned, within the coverage interval $0.10 \le \theta(\mathrm{Yb}) + \theta(\mathrm{Sm}) \le 0.19$. The upper boundary of this interval is close to the theoretical value of θ at which the 3×2 structure is formed completely (1/6 monolayer, $\theta = 0.17$). One may thus conclude that Sm and Yb atoms occupy the same adsorption centers in the cell of the 3×2 structure.

Increasing the samarium coverage in the interval $\theta(\mathrm{Sm}) = 0.12$–$0.15$ was accompanied by an increase in the background. After the coverage reached $\theta(\mathrm{Sm}) = 0.18$, fractional-order reflections in the (3×1) diffraction pattern acquired the shape of an ellipse extended toward the nearest integer reflections. Finally, at $\theta(\mathrm{Sm}) = 0.22$ (total coverage $\theta(\mathrm{Yb}) + \theta(\mathrm{Sm}) = 0.29$), the (3×1) pattern was replaced by a (5×1) structure, which persisted up to $\theta(\mathrm{Sm}) = 0.25$.

As the coverage was increased still more, to the interval $0.28 \le \theta(\mathrm{Sm}) \le 0.48$, the patterns observed could not be identified reliably because of their poor quality. Finally, at $\theta(\mathrm{Sm}) = 0.48$, the characteristic pattern shown in Fig. 1b appeared. This pattern represents a combination of $(\sqrt{3} \times \sqrt{3})R30°$ reflections with additional broad spots. The latter are located close to the superstructural reflections of the $(\sqrt{3} \times \sqrt{3})R30°$ pattern. This pattern persists as $\theta(\mathrm{Sm})$ is increased. Note that the same diffraction pattern was observed with the one-component Sm–Si(111) adsorption system [14, 18–20]. For the sake of brevity, the diffraction pattern of Fig. 1b will be denoted by $(\sqrt{3})$ and the corresponding structure, by $\sqrt{3}$ or $\sqrt{3}$–Sm.

Thus, at low ytterbium concentrations in the two-component (Sm + Yb)–Si(111) adsorption system, the sequence of the LEED patterns and of the corresponding 2D structures in direct space, which change with increasing silicon coverage by samarium atoms, is, on the whole, similar to the sequence observed in the case of the simpler, one-component Sm–Si(111) adsystem.

3.1.2. $\theta(\mathrm{Yb}) = 0.22$ and 0.44. At $\theta(\mathrm{Yb}) = 0.22$ and $\theta(\mathrm{Sm}) = 0$, (3×1) patterns could be discriminated against an enhanced background. Deposition of a 0.05 Sm monolayer on this surface transferred this pattern to (5×1). At $\theta(\mathrm{Sm}) = 0.10$, the background in the micrograph increased, and for $\theta(\mathrm{Sm}) = 0.15$–$0.20$, the image could no longer be identified. Finally, at $\theta(\mathrm{Sm}) = 0.25$ (total coverage, $\theta(\mathrm{Yb}) + \theta(\mathrm{Sm}) = 0.47$), the (2×1) structure shown in Fig. 1c appeared on the diffractometer screen. This pattern did not exhibit any changes with further deposition of samarium.

In the $\theta(\mathrm{Yb}) = 0.44$ case, the (2×1) pattern was seen before the Sm deposition. The brightness of the fractional reflections observed in this pattern was relatively weak. For the samarium coverage close to $\theta(\mathrm{Sm}) = 0.05$, the (2×1) superstructural reflections became more distinct and bright and the diffuse background waned. A further increase in Sm coverage did not produce any noticeable changes in the (2×1) diffraction pattern.

In summary, we should stress the important difference between ytterbium-poor two-component adsystems (the case of $\theta(\mathrm{Yb}) = 0.07$), on the one hand, and systems enriched with this metal (the cases $\theta(\mathrm{Yb}) = 0.22$, 0.44), on the other. This difference consists, first, in that, at high total coverages $\theta(\mathrm{Yb}) + \theta(\mathrm{Sm})$, the structure forming in the former case is $\sqrt{3}$ and in the latter, 2×1, which comes as a surprise. Indeed, according to earlier studies [16, 18], the chemisorption bonding of Sm atoms with the substrate is stronger than that of the Yb atoms. One could thus expect that the geometry of two-dimensional structures in the (Yb + Sm)–Si(111) system would be determined primarily by Sm atoms and, hence, that the reconstructions produced by adsorption of these atoms together with Yb atoms on the Si(111) surface would follow the same sequence as that in the Sm–Si(111) system. As seen from the above data, however, this expectation fails for the $\sqrt{3}$ reconstruction. For $\theta(\mathrm{Yb}) = 0.22$ and 0.44, the 2×1 structure forms instead in the two-component adsystem. This should be apparently attributed to the $\sqrt{3}$–Sm structure being fairly unstable and to its formation being energetically unfavorable for a sufficient amount of Yb atoms. Note that, in the Sm–Si(111) system, this structure is also not very stable and, as shown in our earlier study [18], transforms irreversibly to the 7×1 structure when the substrate is heated to 1100 K; this transition is not accompanied by any change in the surface concentration of Sm atoms.

We used LEED in this study to determine the coverage $\theta(\mathrm{Yb})$ at which the $\sqrt{3} \longrightarrow 2 \times 1$ transition occurs in the (Yb + Sm)–Si(111) system. This was done by depositing various amounts of Yb atoms on the $\sqrt{3}$–Sm structure at a silicon crystal temperature of 800 K. It was established that the $\sqrt{3} \longrightarrow 2 \times 1$ transition takes place within the coverage interval $\theta(\mathrm{Yb}) = 0.10$–$0.15$, in which both patterns are seen to coexist on the diffractometer screen. For $\theta(\mathrm{Yb}) > 0.15$, the $(\sqrt{3})$ diffraction pattern disappears completely, leaving the (2×1) structure. The latter remains unchanged with increasing $\theta(\mathrm{Sm})$ coverage. Thus, a relatively small addition of Yb atoms (0.10–0.15 monolayers) to the surface concentration of Sm atoms is enough to destroy the $\sqrt{3}$–Sm structure. Comparing this figure with a similar value $\theta = 0.43$, at which 2×1 reconstruction also starts in the Yb–Si(111) system, we come to the conclusion that the 2×1–(Sm + Yb) structure is formed with the participation not only of Yb atoms but also of Sm atoms. The lat-

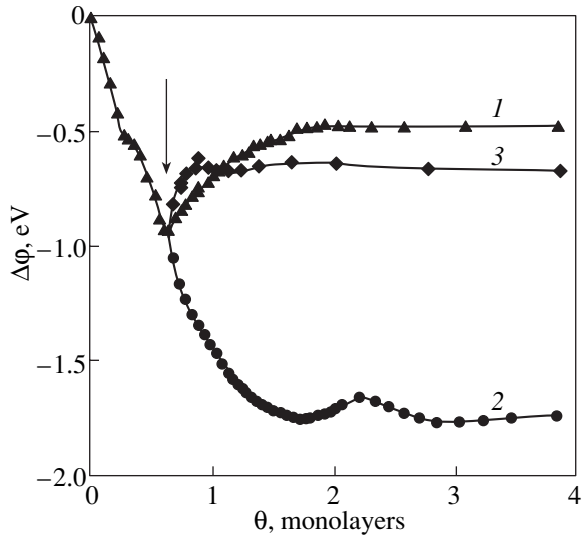

Fig. 2. Work function plotted vs. coverage for the systems (*1*) Sm–Si(111) and (*2*, *3*) (Sm + Yb)–Si(111). During Yb deposition on the $\sqrt{3}$–Sm structure, the substrate temperature was maintained equal to (*2*) 300 and (*3*) 800 K.

ter gives us grounds to suggest that this structure is a new, previously unobserved surface phase,.

The experimental data obtained in this study permit a conclusion that the $\sqrt{3} \longrightarrow 2 \times 1$ transition is a thermally activated process with a fairly high activation energy. This conclusion follows, for instance, from the observation that if Yb atoms are deposited on the $\sqrt{3}$–Sm structure not at 800 K, as was done in the above experiments, but at T = 300 K, the $\sqrt{3} \longrightarrow 2 \times 1$ transition does not occur. In this case, for $\theta(\mathrm{Yb}) \geq 0.1$, one observes on the diffractometer screen a superposition of the $(\sqrt{3} \times \sqrt{3})R30°$ and (3×1) diffraction patterns, with part of the reflections lacking in the latter (Fig. 1d). This implies that the mobility of Yb atoms on the surface is high enough to produce an ordered adsorbed layer even at room temperature. In spite of this, however, the $\sqrt{3} \longrightarrow 2 \times 1$ transition does not take place.

3.2. CPD

According to Subsection 3.1, the (Yb + Sm)–Si(111) system undergoes a $\sqrt{3} \longrightarrow 2 \times 1$ structural rearrangement in the coverage region $\theta(\mathrm{Yb}) = 0.1$–$0.15$. These reconstructions differ considerably from each other in geometric structure. Therefore, one could expect their electronic properties to also differ considerably. In testing this conjecture, we used the CPD method, which is very sensitive to the electronic state of the surface. We present below experimental data obtained by this method. However, prior to turning to analyzing there data, a more detailed consideration of the atomic structure of the $\sqrt{3}$ reconstruction in the Sm–Si(111) system would be expedient. According to current notions [14], this structure is formed by two layers of samarium atoms. The lower layer consists of trivalent atoms and has a hexagonal structure. This layer accounts for the $(\sqrt{3} \times \sqrt{3})R30°$ reflections in the observed $(\sqrt{3})$ diffraction pattern. The top layer, which is visualized in direct space using scanning tunneling microscopy, is formed by divalent Sm atoms and is poorly ordered. This layer produces broadened spots in the diffraction pattern [14]. Obviously enough, the reconstruction in question differs considerably in atomic structure from the 2×1 chain structure [13, 14].

Figure 2 plots the work function $\Delta\varphi = \varphi - \varphi_0$ (φ_0 and φ are, respectively, the work functions of a clean Si(111)–7×7 face and of the same face after deposition on it of either Sm or Sm + Yb) versus coverage. Curve *1* was obtained for a Sm–Si(111) system heated to 900 K. The minimum of this curve, lying at $\theta(\mathrm{Sm}) = 0.62$ (identified by an arrow), corresponds to the two-layer $\sqrt{3}$–Sm reconstruction just discussed and is equal to $\Delta\varphi = -0.93$ eV. This clearly pronounced feature indicates that the work function of the Si(111) coated by the above structure is substantially lower than the analogous figures for $n \times 1$ chain structures forming at lower coverages. The reasons for this difference, as discussed earlier in [19, 20], are the existence of an oriented electric dipole moment formed by Sm^{2+} and Sm^{3+} ions in the double surface layer of the $\sqrt{3}$–Sm reconstruction (Fig. 3a).

If one deposits Yb at room temperature on the $\sqrt{3}$–Sm reconstruction, the value of φ will decrease even further. Curve *2* in Fig. 2 illustrates the dependence of the work function on coverage $\theta(\mathrm{Yb})$ for this case. The value of $\theta(\mathrm{Sm})$ at which Yb was deposited on the $\sqrt{3}$ reconstruction was 0.62. Plotted on the horizontal axis for this dependence are the values of the total coverage, $\theta(\mathrm{Yb}) + \theta(\mathrm{Sm})$. The decrease in the work function occurring as a result of Yb deposition is due, in our opinion, to the incorporation of electropositive atoms of this REM into the top layer of the $\sqrt{3}$–Sm reconstruction (Sm^{2+} atoms) and to the formation of the corresponding extra dipole moment between the atoms of the first and second layers in the adsorbed film (Fig. 3b). This interpretation fits the LEED data well. According to these data (Subsection 3.1), the broad spots in the diffraction pattern obtained for the $\sqrt{3}$–Sm reconstruction (Fig. 1b) become replaced already at low Yb coverages by (3×1) reflections from the top layer of the adsorbate (Fig. 1d); at the same time, the reflections due to the true $(\sqrt{3} \times \sqrt{3})R30°$ structure (the bottom layer) remain unchanged.

The situation changes radically in the case where ytterbium is deposited on the $\sqrt{3}$–Sm reconstruction at a high temperature or where the substrate, together with the Yb layer deposited on its surface at room temperature, is heated at higher temperatures. Curve *3* in Fig. 2 illustrates the concentration dependence of the work function obtained with Yb deposited on a sample heated to 800 K. Deposition of ytterbium atoms is seen to bring about a fast rise in the work function. At $\theta(Yb) = 0.3$, $\Delta\varphi$ becomes equal to –0.63 eV and its growth stops. The limiting value $\Delta\varphi = -0.63$ eV coincides with analogous values obtained for the 2×1 structure in the Yb–Si(111) system and the ytterbium silicide and exceeds the values of $\Delta\varphi$ for the samarium silicide by 0.17 eV in absolute magnitude. This indicates that not only the structure but also the electronic properties of the two-component (Sm + Yb)–Si(111) system formed by depositing even a comparatively small amount of Yb on the $\sqrt{3}$–Sm structure coincide with those of the Yb–Si(111) system. We believe that clues to explaining these observations should be looked for in the following. One may conceive of the formation of more than one two-dimensional reconstruction in each of the one-component systems Sm–Si(111) and Yb–Si(111) at any submonolayer coverage. The reconstruction to be realized in an experiment, however, is that which is energetically preferable. Adding a second component, even in a small amount, may qualitatively change the situation, making reconstruction with another structure energetically more favorable. The $\sqrt{3} \longrightarrow 2 \times 1$ phase transition occurring when ytterbium is added to the Sm–Si(111) system is apparently of this nature. Based on this approach, it appears reasonable to conjecture that the transition from the $\sqrt{3}$ structure to the 2×1 rather than to any other structure should be attributed to 2×1 being the energetically preferable structure in the Yb–Si(111) one-component system.

3.3. TDS

As follows from the results presented in Subsection 3.1, Sm and Yb atoms can occupy the same adsorption centers in the 3×2, 5×1, and 7×1 chain structures. These data, however, do not provide an answer to the question of how the adlayer will form in cases where the total number of Sm and Yb atoms exceeds the number of adsorption centers in any of the structures. We employed the TDS method to obtain the relevant information. The TDS experiments established, first of all, that the TD spectra $\nu(Sm) = f(T)$ and $\nu(Yb) = f(T)$ obtained for the (Yb + Sm)–Si(111) system do not depend on its prehistory. It was found, first, that the shape of these spectra does not depend on the sequence in which the adsorbates were deposited on the sample and, second, that neither is of this spectra affected by the substrate temperature at which the deposition was carried out (300–800 K).

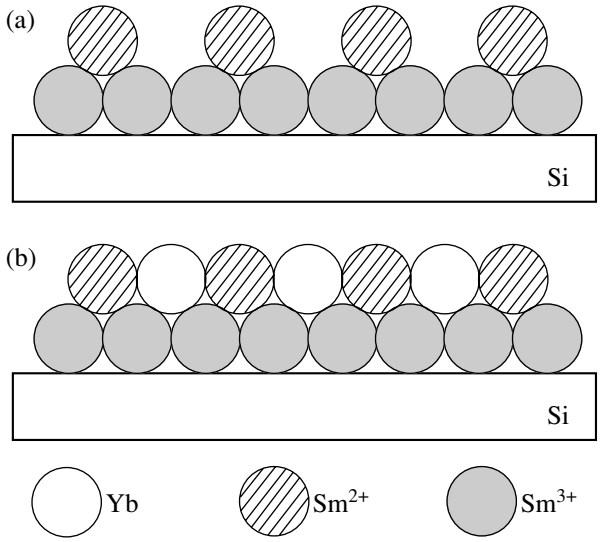

Fig. 3. Arrangement of adsorbed atoms in the structures (a) $\sqrt{3}$ –Sm and (b) (Sm + Yb)–Si(111) (obtained at room temperature).

A characteristic feature of the $\nu(Sm) = f(T)$ spectra (not presented in this communication) is that they do not depend on the $\theta(Yb)$ coverage and are fully identical in shape, for all values of this coverage, to the TD spectra obtained for the Sm–Si(111) system studied by us earlier [18]. The reason for this is that, at the temperatures at which samarium starts to desorb [18], the surface is already practically free of ytterbium [16, 21].

The situation with the $\nu(Yb) = f(T)$ spectra is radically different. Their shape and structure depended considerably on the actual amount of Sm deposited on the surface. This is particularly well illustrated in Fig. 4, which shows two series of such spectra measured at fixed coverages $\theta(Yb) = 0.22$ and 0.44. For $\theta(Sm) = 0$, the TD spectra (spectra *1*) contain either two "adsorption" peaks, A_1 and A_2, or four such peaks, A_1, A_2, A_3, and A_4, depending on the concentration of adsorbed Yb atoms. These spectra are identical to those obtained by us earlier [16, 21]. As the $\theta(Sm)$ coverage increases, the spectra start to transform. In the $\theta(Yb) = 0.22$ case (Fig. 4a), within the coverage interval $\theta(Sm) = 0$–0.15 (spectra *1–4*), peak A_1 disappears gradually, peak A_2 grows, and a new peak, A_3, appears at $\theta(Sm) = 0.10$. Subsequently, peaks A_2 and A_3 merge and their position on the temperature scale varies nonmonotonically with $\theta(Sm)$.

The TD spectra of the other series, with $\theta(Yb) = 0.44$ (Fig. 4b), evolve in a similar manner. In the coverage interval $\theta(Sm) = 0$–0.15 (spectra *1–4*), peaks A_1 and A_2 decrease in amplitude, with the first of them leading, while peaks A_3 and A_4 grow. At $\theta(Sm) = 0.15$, peak A_1 disappears and, at $\theta(Sm) = 0.2$, it is followed by peak A_2; then, at $\theta(Sm) \geq 0.4$, peaks A_3 and A_4 merge and the spectra become similar in shape to those obtained in the

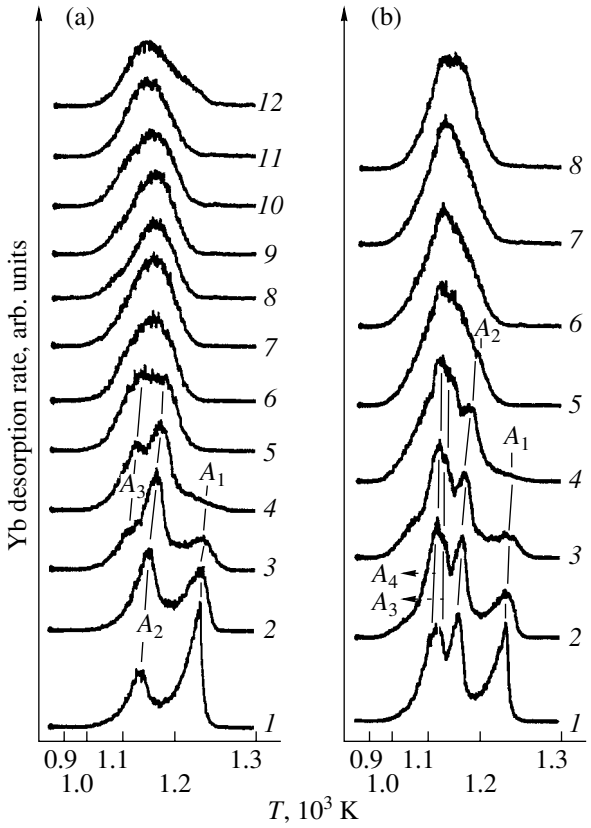

Fig. 4. TD spectra ν(Yb) = $f(T)$. (a) θ(Yb) = 0.22 and θ(Sm) is equal to (*1*) 0, (*2*) 0.05, (*3*) 0.1, (*4*) 0.15, (*5*) 0.2, (*6*) 0.25, (*7*) 0.3, (*8*) 0.4, (*9*) 0.5, (*10*) 0.8, (*11*) 1.5, and (*12*) 6. (b) θ(Yb) = 0.44 and θ(Sm) is equal to (*1*) 0, (*2*) 0.05, (*3*) 0.1, (*4*) 0.15, (*5*) 0.22, (*6*) 0.4, (*7*) 0.8, and (*8*) 2.

preceding series for θ(Sm) ≥ 0.25 (spectra *6*–*12* in Fig. 4a).

An analysis of the above TD spectra measured for θ(Sm) ≤ 0.15 and their comparison with the LEED data permit the conclusion that Sm atoms substitute practically completely for the Yb atoms in the 3×2 structure in this coverage interval. This result finds a natural explanation if one draws on the data reported in [16, 18]. According to those data, the energy E_0 required to remove an Sm atom from the 3×2 structure into vacuum exceeds that for an Yb atom by about 0.5 eV. This implies that the 3×2 reconstruction formed by Yb atoms is energetically less favorable than the same structure formed by Sm atoms.

The evolution of the ν(Yb) = $f(T)$ spectra for θ(Sm) > 0.15 (Fig. 4) can be interpreted along the same lines. The redistribution of the peaks in these spectra (the decrease of peaks A_2 and the growth of peaks A_3 and A_4 in amplitude) gives one grounds to assume that substitution of samarium atoms for ytterbium also occurs at higher coverages θ(Sm).[2] This conclusion likewise appears reasonable, because, in order to draw it, one has only to compare the temperature regions within which Sm and Yb atoms desorb (see above).

[2] A case in point is the coverages at which the $\sqrt{3}$–Sm structure does not yet form.

4. CONCLUSIONS

Thus, the results of our present study suggest that, within the low-coverage region, in which Sm and Yb atoms form $n \times 1$ and $n \times 2$ chain structures, the former atoms substitute for the latter. At higher coverages, where only adsorption of Yb atoms on the silicon surface is accompanied by the formation of a 2×1 chain reconstruction, while adsorption of Sm atoms leads to the formation of a more complicated structure $\sqrt{3}$, coadsorbing ytterbium gives rise to the $\sqrt{3} \longrightarrow 2 \times 1$ phase transition.

ACKNOWLEDGMENTS

This study was supported by the State research Program of the Ministry of Science and Technology of the Russian Federation "Surface Atomic Structures," grant no. 2.5.99.

REFERENCES

1. W. Mönch, in *Springer-Verlag Series in Surface Science* (Springer, Berlin, 1993), Vol. 22.
2. S. Hasegawa, X. Tong, S. Takeda, *et al.*, Prog. Surf. Sci. **60**, 89 (1999).
3. Ph. Avouris, In.-W. Lyo, F. Bozso, and E. Kaxiras, J. Vac. Sci. Technol. A **8**, 3405 (1990).
4. H. Huang, S. Y. Tong, W. S. Yang, *et al.*, Phys. Rev. B **42**, 7483 (1990).
5. J. Nogami, S. I. Park, and C. F. Quate, Surf. Sci. **203**, L631 (1988).
6. J. Zegenhagen, J. R. Patel, P. Freeland, *et al.*, Phys. Rev. B **39**, 1298 (1989).
7. D. M. Cornelison, C. S. Chang, and I. S. T. Tsong, J. Vac. Sci. Technol. A **8**, 3443 (1990).
8. O. Kubo, A. A. Saranin, A. V. Zotov, *et al.*, Surf. Sci. **415**, L971 (1998).
9. A. A. Saranin, V. G. Lifshits, K. V. Ignatovich, *et al.*, Surf. Sci. **448**, 87 (2000).
10. A. A. Baski, S. C. Erwin, M. S. Turner, *et al.*, Surf. Sci. **476**, 22 (2001).
11. T. Sekiguchi, F. Shimokoshi, Tadaaki Nagao, and S. Hasegawa, Surf. Sci. **493**, 148 (2001).
12. H. H. Weitering, Surf. Sci. **355**, L271 (1996).
13. C. Wigren, J. N. Andersen, R. Nyholm, *et al.*, Phys. Rev. B **47**, 9663 (1993).
14. C. Wigren, J. N. Andersen, R. Nyholm, *et al.*, Phys. Rev. B **48**, 11014 (1993).

15. T. V. Krachino, M. V. Kuz'min, M. V. Loginov, and M. A. Mittsev, Appl. Surf. Sci. **182**, 115 (2001).

16. T. V. Krachino, M. V. Kuz'min, M. V. Loginov, and M. A. Mittsev, Fiz. Tverd. Tela (St. Petersburg) **39** (2), 256 (1997) [Phys. Solid State **39**, 224 (1997)].

17. T. V. Krachino, M. V. Kuz'min, M. V. Loginov, and M. A. Mittsev, Fiz. Tverd. Tela (St. Petersburg) **39** (9), 1672 (1997) [Phys. Solid State **39**, 1493 (1997)].

18. T. V. Krachino, M. V. Kuz'min, M. V. Loginov, and M. A. Mittsev, Fiz. Tverd. Tela (St. Petersburg) **40** (2), 371 (1998) [Phys. Solid State **40**, 341 (1998)].

19. T. V. Krachino, M. V. Kuz'min, M. V. Loginov, and M. A. Mittsev, Fiz. Tverd. Tela (Leningrad) **40** (10), 1937 (1998) [Phys. Solid State **40**, 1758 (1998)].

20. T. V. Krachino, M. V. Kuz'min, M. V. Loginov, and M. A. Mittsev, Phys. Low-Dimens. Semicond. Struct., No. 9/10, 95 (1999).

21. M. V. Kuz'min, M. V. Loginov, and M. A. Mittsev, Pis'ma Zh. Tekh. Fiz. **21** (19), 73 (1995) [Tech. Phys. Lett. **21**, 803 (1995)].

Translated by G. Skrebtsov

Physics of the Solid State, Vol. 45, No. 3, 2003, pp. 586–589. Translated from Fizika Tverdogo Tela, Vol. 45, No. 3, 2003, pp. 555–558.

LOW-DIMENSIONAL SYSTEMS AND SURFACE PHYSICS

Vibrational States of the Cu(100) Surfaces with Nickel Adlayers

G. G. Rusina[1], I. Yu. Sklyadneva[1, 2], and E. V. Chulkov[2, 3]

[1] *Institute of Strength Physics and Materials Science, Siberian Division, Russian Academy of Sciences, Akademicheskiĭ pr. 2/1, Tomsk, 634021 Russia*

[2] *Donostia International Physics Center (DIPC), San Sebastian/Donostia, 20018 Spain*

[3] *Universidad del País Vasco/Euskal Herriko Unibertsitatea, San Sebastian/Donostia, 20080 Spain*

e-mail: rusina@sms.tsc.ru

Received April 29, 2002

Abstract—The vibrational spectra of the Cu(100) surface covered with one or two Ni monolayers are calculated using the embedded-atom method. The surface relaxation, the dispersion of surface phonons, and the polarization of vibrational modes of the adsorbate and the substrate are discussed in detail. The theoretical results are in good agreement with experimental data and can be used for their interpretation. The changes observed in the interatomic interactions upon application of nickel adsorbates to the copper substrate are considered. © *2003 MAIK "Nauka/Interperiodica".*

1. INTRODUCTION

The dynamic properties of metal surfaces covered with adsorbates have attracted the particular attention of many researchers, because an adsorbed layer modifies the spectrum of surface phonons and encourages the generation of new localized or resonant modes. Moreover, investigation of the vibrational spectra can provide a better insight into the mechanisms of interaction between substrates and adlayers [1, 2].

Phonon modes of clean Cu and Ni surfaces and surfaces of these metals covered with adsorbates, for the most part, have been experimentally studied using high-resolution electron energy loss spectroscopy [3] and inelastic helium-atom scattering [1]. In particular, Stuhlmann and Ibach [3] examined the dispersion of the Rayleigh mode and surface resonance along the $\overline{\Gamma M}$[(100)] direction for a Cu(100) surface covered with one (1 ML) or two (2 ML) Ni monolayers. As a rule, the experimental results have been theoretically interpreted in the framework of the models of force constants fitted to the experimental behavior of the Rayleigh mode [3].

In the present work, the vibrational spectra of n ML Ni/Cu(100) (n = 1, 2) relaxed surfaces were calculated using the embedded-atom method. Within this approach, the total energy contains a contribution determined by the electron density and characterizing the multiparticle interactions [4, 5]. The embedded-atom method has been successfully employed to analyze the surface properties of pure metals, alloys, and materials covered with adsorbates [5–8].

2. COMPUTATIONAL TECHNIQUE

In the framework of the embedded-atom method [4, 5], the potential energy has the form

$$E = \sum_i F_i(\rho_i) + 1/2\sum_{ij}\varphi(r_{ij}). \quad (1)$$

In this relationship, the first term describes the multiparticle effects and the second term represents the pair atomic potential. Here, F_i is the energy of the embedded atom, which is determined by the electron density ρ_i at the ith site, and r_{ij} is the distance between the ith and jth atoms. The electron density ρ_i is defined as a superposition of atomic electron densities:

$$\rho_i = \sum_{i \neq j}\rho_j^a(r_{ij}), \quad (2)$$

where the densities ρ_j^a are found from the solution of the problem for a free atom in the local-density functional approximation [9]. We took into account the interatomic interactions up to and including the fourth coordination shell. The parameters of the method were determined by fitting to the experimental data on the sublimation energies, equilibrium volumes, energies of vacancy formation, bulk moduli, and elastic moduli for copper and nickel, as well as on the energy of formation of a nickel–copper alloy [5].

3. RESULTS AND DISCUSSION

The equilibrium location of the surface layers (the relaxed geometry) was determined using the molecular dynamics technique at zero temperature. According to

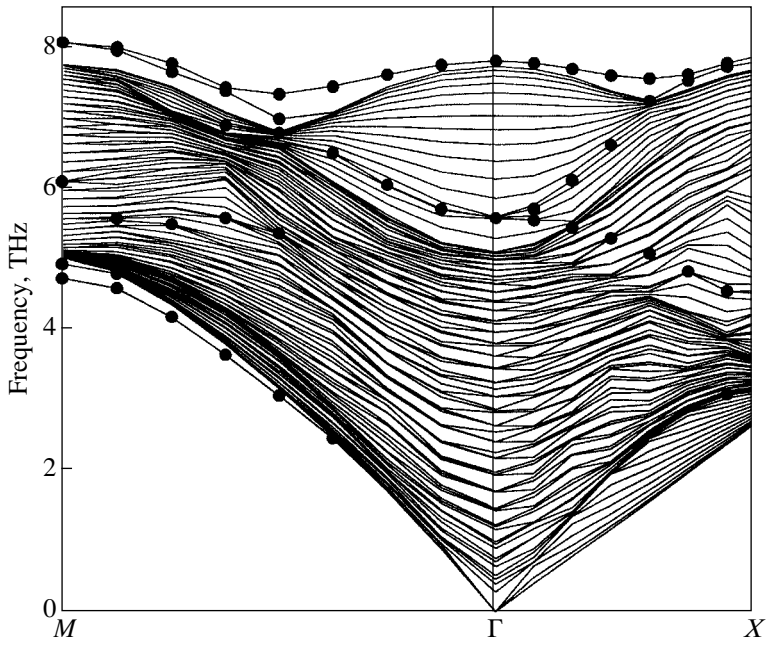

Fig. 1. Calculated phonon dispersion curves for a 2 ML Ni/Cu(100) relaxed 30-layer film. Closed circles indicate the surface states.

the molecular dynamics calculations for the 1 ML Ni/Cu(100) surface, the distance $d_{\mathrm{Ni–Cu_1}}$ between the surface layers is 9.6% shorter than the interlayer distance in bulk copper. For the 2 ML Ni/Cu(100) surface, the first interlayer distance $d_{\mathrm{Ni_{(s)}–Ni_{(i)}}}$ (the subscripts *s* and *i* refer to the surface and interface, respectively) is 3.7% shorter than the interlayer distance in bulk nickel. The distance $d_{\mathrm{Cu_1–Ni_{(i)}}}$ between the substrate and the nickel interfacial adlayer also decreases by 2% and actually corresponds to the interlayer distance in nickel. Note that, in both cases, the surface layer of the substrate relaxes toward the adlayers. As a result, the first interlayer distance $d_{\mathrm{Cu_1–Cu_2}}$ increases by 0.4–1.2%. This behavior is not characteristic of clean surfaces of face-centered cubic metals with (100) and (111) close packings, in which the change in the interlayer distance near the surface, as a rule, does not exceed a few percent. In particular, the relaxation of the upper atomic layer for Cu(100) and Ni(100) is approximately equal to 1.4–2.0%, which agrees well with the calculations performed in [10, 11]. Therefore, the results obtained indicate that, on the one hand, the application of nickel adlayers to the substrate brings about an increase in the surface relaxation. On the other hand, an increase in the thickness of the nickel coating and the distance from the nickel surface layer to the copper substrate leads to a decrease in the relaxation of the surface layer.

The vibrational spectra were calculated in the framework of the thin film model. For this purpose, we used a Cu(100) 30-layer film covered with one or two $p(1\times1)$ monolayers of nickel on both sides. The dispersion curves were calculated for the 1 ML Ni/Cu(100) and 2 ML Ni/Cu(100) relaxed surfaces along all the directions of the two-dimensional Brillouin zone. The spectrum of surface states for 1 ML Ni/Cu(100) was described in detail in our earlier work [8]. The main feature revealed in this system resides in the fact that there occurs a strong hybridization of the vertically polarized mode of the nickel adlayer with the Rayleigh mode of the substrate as the magnitude of the wave vector **k** decreases. The frequency of the vibrational state of the Cu(100) surface decreases considerably more rapidly than that of the Ni(100) surface [3, 8]. The smaller the magnitude of the wave vector **k**, the deeper the penetration of the Rayleigh mode into the substrate and the weaker the effect of the adsorbate. As a consequence, this mode for small magnitudes of **k** behaves like a Rayleigh mode of the Cu(100) surface. Another feature is the appearance of high-frequency surface states above the bulk phonon spectrum.

Figure 1 shows the dispersion curves for the 2 ML Ni/Cu(100) surface along the $\overline{\Gamma M}$ and $\overline{\Gamma X}$ directions of the two-dimensional Brillouin zone. In this paper, we will restrict our consideration to the special case of the aforementioned two directions, because the experimental data for these directions are available in the literature [3]. As can be seen from Fig. 1, there exist two surface states below the projection of the bulk modes along the $\overline{\Gamma M}$ direction. The lower surface state with a frequency of 4.72 THz at the *M* point represents the Rayleigh mode of the substrate and can be associated with vibrations of the substrate atoms in the direction perpendicular to the surface. The upper surface state man-

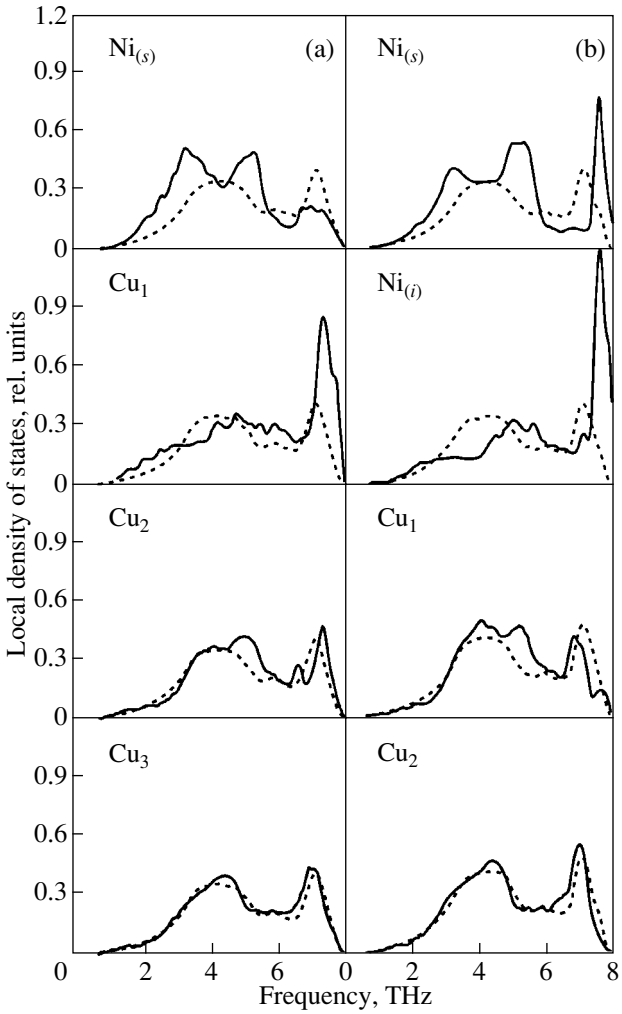

Fig. 2. Local densities of states for the (a) 1 ML Ni/Cu(100) and (b) 2 ML Ni/Cu(100) surfaces (solid lines) and for the central layer of the copper film (dashed lines).

ifests itself only in the vicinity of the *M* point (at a frequency of 4.93 THz), is completely localized at the Ni surface layer, and exhibits a polarization identical to that of the former state. Therefore, the application of the second Ni adlayer to the Cu(100) surface brings about the generation of the Rayleigh mode of the adlayer. The analogous state is absent in the case of one Ni monolayer. According to the experimental data obtained by Stuhlmann and Ibach [3], the frequency of the lower surface state for the 2 ML Ni/Cu(100) system is equal to 4.95 THz at the *M* point, which is in good agreement with our results. It should be noted that, above the bulk phonon spectrum, there exists a doubly degenerate surface state (along each direction of the two-dimensional Brillouin zone) which is 100% localized in the adlayers. In the $\overline{\Gamma M}$ and $\overline{\Gamma X}$ directions, this mode is split into two modes attributed to longitudinal and vertical vibrations of atoms (the lower and upper modes, respectively). In this situation, the vibrational modes are predominantly (~80%) localized at the Ni interfacial layer. A similar state is observed in the $\overline{\Gamma X}$ direction but is associated with transverse vibrations of atoms in the plane of the interfacial layer.

It should be emphasized that only the lower mode in the $\overline{\Gamma M}$ direction is completely localized at the substrate. All the other surface states either are associated with atomic vibrations of the nickel adlayers or correspond to mixed modes, i.e., when both the substrate and adsorbate atoms participate in vibrations. This suggests a strong hybridization of the vibrational states of the substrate and the adlayers. Another feature is the appearance of high-frequency surface modes at the Γ point. These states are characteristic of vicinal (stepped) metal surfaces [12] and are not observed for the (100) and (111) surfaces of face-centered cubic metals.

The local densities of states for the 1 ML Ni/Cu(100) and 2 ML Ni/Cu(100) surfaces are depicted by solid lines in Fig. 2. In addition, the dashed lines in this figure represent the local densities of states for the central layer of the copper film (the densities of states are normalized to unity). It can be seen from Fig. 2 that the local density of states for the surface layer exhibits three peaks. The main contribution to the first peak is made by the low-frequency modes located below the bulk states. The second peak is determined by the states at the Brillouin zone boundary in the band gaps. All these states are characterized by mixed vibrations. The third (high-frequency) peak is associated with longitudinal and transverse vibrations of the adlayer atoms. As is clearly seen from Fig. 2b, the surface states are predominantly (~70%) localized at the Ni interfacial layer. Furthermore, the phonon modes are softened as compared to the bulk states. However, this softening is substantially less pronounced than that for the Cu(100) and Ni(100) clean surfaces [10, 11]. Analysis of the local densities of states shows that even the second layer of the substrate is virtually identical to the central layer of the film.

A change in the interatomic interactions upon application of adsorbates to the substrate noticeably affects the vibrational spectra. In this respect, we calculated the force constants for the 1 ML Ni/Cu(100) and 2 ML Ni/Cu(100) surfaces. The results of our calculations indicate that the interatomic interactions in the plane of the Ni interfacial layer are significantly weaker (by ~50%) than those in bulk nickel. Such a weakening is not typical of the Cu(100) and Ni(100) clean surfaces and could be caused by the substrate. The change observed in the interatomic interaction has defied explanation in terms of surface relaxation alone. In this case, consideration must also be given to the change in the electronic structure of the nickel film. The theoretical calculations performed by Wang Ding-Sheng *et al.* [13] demonstrated that, in these systems, the electron orbitals of copper and nickel atoms undergo a strong

hybridization and charge transfer occurs from the substrate to the Ni interfacial layer. The force constants of interaction between the first two layers in the 1 ML Ni/Cu(100) and 2 ML Ni/Cu(100) systems are 20–30% larger than those in bulk metals. This situation is characteristic of the (100) surface of face-centered cubic metals and has been observed for the Cu(100) and Ni(100) clean surfaces [3]. The interatomic interactions in the Cu_1 surface layer of the substrate are somewhat stronger (by ~3.5%) than those in the bulk of the copper film. A comparison shows that our data on the force constants are in good agreement with the results obtained in [3].

4. CONCLUSIONS

Thus, the above calculations of the equilibrium surface geometry allowed us to make the inference that the surface covered with an Ni monolayer undergoes a relaxation. An increase in the thickness of the nickel coating and the distance from the nickel surface layer to the copper substrate leads a decrease in the relaxation of the surface layer. The vibrational states were calculated for the 1 ML Ni/Cu(100) and 2 ML Ni/Cu(100) surfaces. It was demonstrated that, in the former system, strong hybridization of the vertically polarized vibrational mode of the nickel adlayer with the Rayleigh mode of the substrate is observed at small magnitudes of the wave vector **k**. The Rayleigh mode of the adsorbate is absent and appears only after the application of the second Ni adlayer to the substrate. For the 2 ML Ni/Cu(100) system, virtually all the surface states are localized at the nickel adlayers. The specific feature of this system is the generation of high-frequency surface modes at the Γ point. Similar modes are characteristic of only vicinal surfaces of face-centered cubic metals. Analysis of the force constants for the 1 ML Ni/Cu(100) and 2 ML Ni/Cu(100) surfaces revealed that the interatomic interactions in the nickel interfacial layer are substantially weaker than those in bulk nickel. Moreover, it was found that the force constants of interaction between the first two layers in these systems exceed the constants for bulk metals.

ACKNOWLEDGMENTS

This work was supported by the Ministry of Industry, Science, and Technology of the Russian Federation, project no. 40-012.1.1.1153.

REFERENCES

1. R. Berndt, J. P. Toennies, and Ch. Woll, J. Electron Spectrosc. Relat. Phenom. **44**, 183 (1987).
2. W. Daum, J. Electron Spectrosc. Relat. Phenom. **44**, 271 (1987).
3. C. Stuhlmann and H. Ibach, Surf. Sci. **219**, 117 (1989).
4. M. S. Daw and M. I. Baskes, Phys. Rev. B **29**, 6443 (1984).
5. S. M. Foiles, M. I. Baskes, and M. S. Daw, Phys. Rev. B **33**, 7983 (1986).
6. T. S. Rahman and J. E. Black, Phys. Rev. B **48**, 5530 (1993).
7. J. E. Black, Z. J. Tian, and T. S. Rahman, Surf. Sci. **291**, 215 (1993).
8. I. Yu. Sklyadneva, G. G. Rusina, and E. V. Chulkov, Surf. Sci. **433–435**, 517 (1999).
9. W. Kohn and L. J. Sham, Phys. Rev. A **140**, 1133 (1965).
10. M. Rocca, S. Lehwald, H. Ibach, and T. S. Rahman, Surf. Sci. **171**, 632 (1986).
11. M. Wutting, R. Franchy, and H. Ibach, J. Phys. B **65**, 71 (1986).
12. I. Yu. Sklyadneva, G. G. Rusina, and E. V. Chulkov, Surf. Sci. **416**, 17 (1998).
13. Wang Ding-Sheng, A. J. Freeman, and H. Krakauer, Phys. Rev. B **26** (3), 1340 (1982).

Translated by O. Borovik-Romanova

Physics of the Solid State, Vol. 45, No. 3, 2003, pp. 590–597. Translated from Fizika Tverdogo Tela, Vol. 45, No. 3, 2003, pp. 559–566.

LOW-DIMENSIONAL SYSTEMS AND SURFACE PHYSICS

Interactions of Surface States of Copper with Transition Metals and Cesium

D. V. Chudinov[1], S. E. Kul'kova[1, 2], and I. Yu. Smolin[2]

[1] *Tomsk State University, Tomsk, 634050 Russia*

[2] *Institute of Strength Physics and Materials Science, Siberian Division, Russian Academy of Sciences, Akademicheskiĭ pr. 2/1, Tomsk, 634021 Russia*

e-mail: kulkova@ms.tsc.ru

Received April 16, 2002

Abstract—The pseudopotential augmented-plane-wave method was used to study the surface structure of thin copper films with monolayers of Co, Ni, and Cs. Local densities of electron states, distributions of charge densities in the layers, and electron energy spectra are analyzed. The effect of adsorbates on the electronic properties of the Cu(001) surface and work function are discussed. Satisfactory agreement with available experimental data has been obtained. © *2003 MAIK "Nauka/Interperiodica".*

1. INTRODUCTION

The electron structure and two-dimensional magnetism of thin films of transition metals and their interfaces have remained an object of intense theoretical research for the last two decades. The interest in these properties primarily stems from their possible technological applications. It is known that if a surface layer is formed by magnetic metals, then, with a decrease in the dimensionality of the system, the magnetic moment at the surface is enhanced as compared to the bulk [1–5]. Numerous works (see, e.g., [6–10] and references therein) have been devoted to investigation of the magnetic properties of transition-metal layers on nonmagnetic substrates, making it possible to control the film-growth conditions [6–12]. It was shown that the surface layers of Fe, Co, and Ni were ferromagnetic and their magnetic moments were comparable with those of bulk materials, whereas Cr and Mn form antiferromagnetic layers. Processes that occur at the surface (especially, upon interaction with various adsorbates) have a rather complex nature. Usually, the surface is reconstructed, and the mechanisms of reconstruction remain unclear even in well-studied systems, such as copper or gold. For example, on the surface of copper, the ordered surface alloys MnCu/Cu(001) or NiCu/Cu(001) can form [7, 11–13]; similar processes are observed on substrates of transition metals (NiMn/Ni(001), MnCo/Co(001), etc. [14–16]). *Ab initio* electron-structure calculations permit not only obtaining sufficiently correct information on the structural, magnetic, and electronic properties of such systems, but also making conclusions on the most probable configuration of a reconstructed surface. Changes in the work function φ in multilayer systems consisting of layers of transition metals or of transition-metal layers on an inert substrate are usually no more than a few electron volts; more substantial changes occur if the substrate is coated with layers of alkali metals, which are adsorbed layer-by-layer and possess a high mobility on the surface.

The investigation of the electronic properties of such systems continues to attract attention from researchers [17–24]. To establish the factors that cause a significant decrease in the work function, we first should study the distribution of adsorbate electrons and their interaction with surface states of the substrate. It is known that at low concentrations of cesium (up to approximately 0.3 monolayer (ML)), the work function first decreases sharply, then reaches a minimum, increases insignificantly, and goes onto a fixed level [24]. In addition, no more than 1 ML of Cs can be deposited on the surface of metals or semiconductors at room temperature, since the heat of adsorption is very small and the atoms of the second layer have only a small lifetime at the surface. In this connection, it is precisely the investigation of surface processes at low coverages that is of the greatest interest. Such calculations, as a rule, are conducted in terms of the "jellium" model for the adsorbates [22, 23]. In another approach, the adsorbate, like the substrate, is simulated by atomic layers [20, 21, 24, 25]. In this case, it is more difficult to simulate the ranges of low adsorbate concentrations, since huge supercells have to be calculated, which requires large computing resources. On the other hand, it is precisely this approach that can separate the interactions responsible for the formation of the adsorbate–substrate bonds and the preference for various positions of the adsorbate atoms on the substrate [24, 25]. In this work, we study the interaction of surface states of copper with adlayers of cobalt, nickel, and cesium.

1063-7834/03/4503-0590$24.00

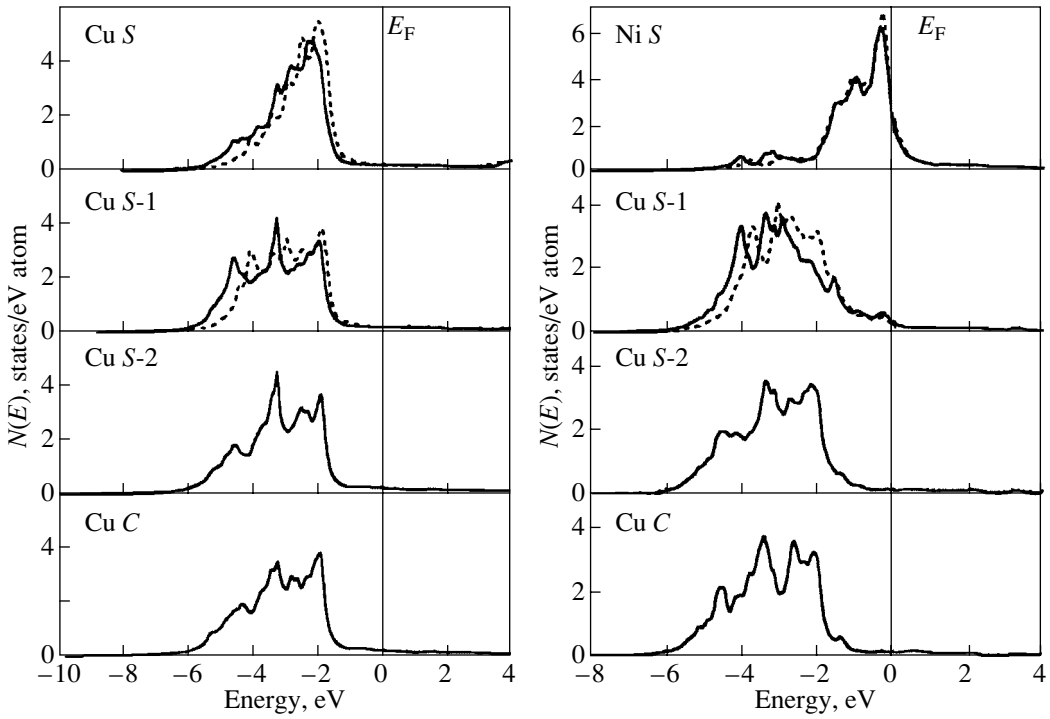

Fig. 1. Local densities of states for relaxed seven-layer Cu(001) films and a monolayer of Ni on Cu(001). *C* and *S* denote a central and a surface atom, respectively; *S*-1 and *S*-2 show the position of a layer relative to the surface. The dashed lines show the densities of states for unrelaxed films.

2. COMPUTATION TECHNIQUE

The electron structure of copper thin films with monolayers of Ni, Co, and Cs was calculated using the spin-polarized full-potential linearized augmented-plane-wave (FP LAPW) method [26] in the local-spin-density approximation (LSDA) for the exchange-correlation potential. The (001) surface was simulated by five-layer to nine-layer films that were periodically repeated in the direction perpendicular to the surface and separated by vacuum spaces. The thickness of vacuum spaces was selected so as to exclude the interaction of atoms at the film surfaces. As calculations show, the thickness of a vacuum layer should be no less than two lattice parameters of the bulk material in the case of Co and Ni layers on the surface and three or four lattice parameters for Cs. The expansions of the crystal potential and charge density inside muffin-tin spheres into series were restricted to $l_{max} = 10$. The nonspherical contributions to the charge density and the potential inside the spheres were taken into account to $l_{max} = 4$. In the interstices (spaces between spheres), plane waves with vectors of up to $K_{max} = 4$ au^{-1} were used. The potential in the interstices was represented in the form of a Fourier expansion; summation over reciprocal-lattice vectors was restricted to $G_{max} = 12$. The self-consistency procedure was conducted over 15 and 21*k* points and stopped when the change in the total energy became less than 10^{-4} Ry. The theoretically calculated parameter of the fcc lattice of copper equal to 3.55 Å is in good agreement with the data of [6], but is somewhat smaller than the experimental value (3.61 Å). Two inner layers were assumed to be separated by a fixed interlayer spacing d_0 equal to that in the bulk material. The spacings between other layers were optimized in terms of Newton's dynamics. The work function of the surface was determined as the difference between the values of the potential in the middle of the vacuum region and the Fermi energy.

3. RESULTS AND DISCUSSION

The results of calculations of the local density of electron states (LDOS) for a relaxed seven-layer copper film and Ni/Cu(001) are displayed in Fig. 1. Similar to [6], we obtained that even a five-layer film satisfactorily reproduces the surface structure and electron characteristics of copper. The small negative relaxation ($\Delta d_{ij}/d_0 = -3.3\%$, where Δd_{ij} is the spacing between the *i*th and *j*th layers) for the first interlayer spacing (i.e., for the distance between the surface and subsurface layers) satisfactorily agrees with the value –3.1% obtained in [6] but exceeds the experimental value –2.4% [27]. The work function is equal to 4.75 eV (4.83 eV in [6]), which satisfactorily agrees with experiment ($\varphi = 4.59$–4.77 eV [28–30]). In the case of the five-layer copper film with 1 ML of Ni, an additional peak appears near the Fermi level E_F, which is caused by contributions from nickel, whereas, in the presence of a Co layer, E_F falls precisely onto the

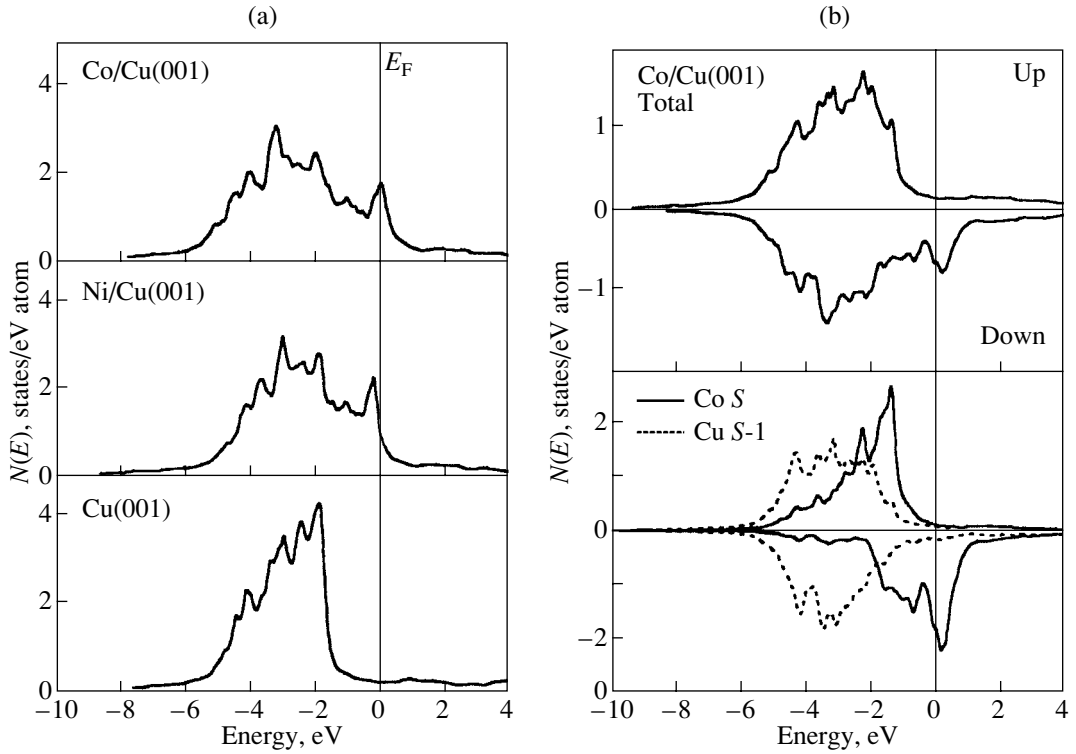

Fig. 2. Total densities of states depending on (a) the adsorbate and (b) the magnetic state of the film. The figures also show the spin densities of states for the surface and subsurface atoms in the Co/Cu(001) system.

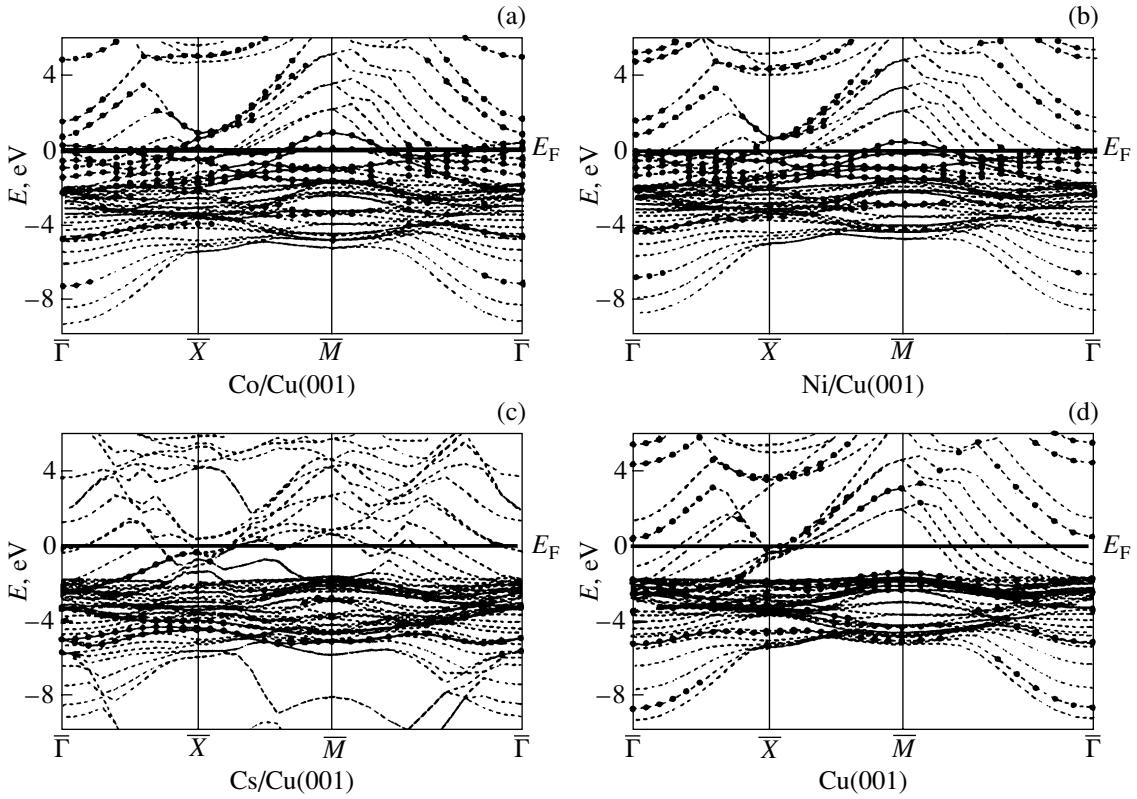

Fig. 3. Dispersion curves $E(k)$ for monolayers of (a) Co, (b) Ni, and (c) Cs on Cu(001) and (d) for Cu(001). The surface states (i.e., states with the degree of localization exceeding 80% in the surface and subsurface layers and in vacuum) are shown by solid circles.

peak of the density of states (DOS) (Fig. 2a), which may serve as evidence of structural instability in such a system. For 1 ML of Ni on Cu(001), we obtained a sufficiently large negative relaxation: $\Delta d_{12}/d_0 = -12.5\%$, which satisfactorily agrees with the value –9.6% found in calculations for a 30-layer system and with the value –10% obtained in [31]. Note that the relaxation is very sensitive to the lattice parameter in the plane of the film. As was shown by our calculations, in the case of paramagnetic monolayers of nickel and cobalt on a copper substrate, the work function changes insignificantly and reaches 5.13 and 5.30 eV in Ni/Cu and Co/Cu, respectively. The last result is also in agreement with the value 5.31 eV given in [6]. Spin-polarized calculations for Co/Cu(001) show the preferable formation of a ferromagnetic Co layer on the surface with a magnetic moment equal to 1.77 μ_B (1.71 μ_B calculated in [6] and 1.77 ± 0.1 μ_B experimentally determined in [32]). In this case, the surface magnetic moment only insignificantly exceeds that for bulk hcp cobalt (1.56 μ_B). Adsorption of cobalt leads to a small polarization of the substrate, which decays very quickly with depth in the film. The value of the magnetic moment for copper at the interface is positive and equals 0.019 μ_B (0.024 μ_B given in [6]). The magnetic moment oscillates, but the oscillations are pronounced to a much smaller extent than, e.g., those found in [33, 34] in titanium alloys with cobalt or iron. The LDOSs for the magnetic layer Co/Cu(001) are given in Fig. 2b. The splitting of states with different spins leads to a shift of the sharp maximum in the $N(E)$ curve toward lower energies (to –1.4 eV) in the case of spins directed along the magnetization (these states are completely filled), whereas the states with opposite spins are partly unoccupied and shifted to above the Fermi energy, so that the center of gravity of the *d* band is located at 0.3 eV. The states of the subsurface layer virtually do not change as compared to those obtained in the paramagnetic case. The gain in the total energy for the magnetic state is only 0.67 eV. The work function decreases by 0.13 eV and agrees well with the value 5.16 eV obtained in [6]. The magnetic moment of nickel is known to be 0.3–0.6 μ_B [11]. In this case, the electron structure and the work function differ only insignificantly from the results obtained in the paramagnetic calculation.

Figure 3 displays dispersion curves for the three above systems calculated for the symmetry directions of the two-dimensional Brillouin zone (BZ). The results indicate the appearance of surface states caused by cobalt and nickel, whereas the concentration of surface states of copper becomes smaller; moreover, their energy decreases. The classification of surface states is frequently performed using the Shockley–Tamm scheme, but this classification is too simplified and does not describe all states, since it is based on simple, one-dimensional models. For each surface state, we determined the degree of localization and the orbital composition—the characteristics that are useful for analyzing

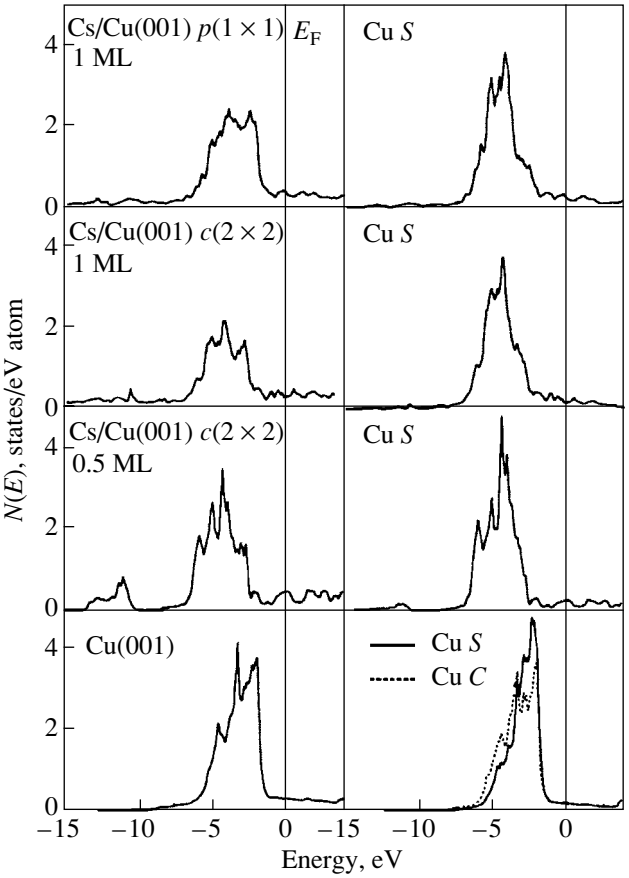

Fig. 4. Evolution of the total and local densities of states upon cesium adsorption. In the lower right-hand panel, the local density of states for the central copper layer is shown.

interactions of these states of the substrate with adsorbates. The tables of these characteristics require a large amount of space and, therefore, are not given here. Note that, in general, all surface states have symmetry of the *d* type and only few of them contain an admixture of *s* and *p* orbitals. In addition, strong *d*–*d* hybridization of the states occurs when monolayers of transition metals are formed at the copper substrate.

In the case where CuNi/Cu(001), CuMn/Cu(001), or NiMn/Ni(001) surface alloys were formed, which were found to be preferable over monolayers of metals on copper or nickel substrates [7, 11, 14, 15]; the work function also changed only by fractions of an electron volt. When studying titanium alloys with Fe, Co, and Ni [34], we showed that the values of the work function were close to those of the corresponding surfaces of pure metals; i.e., the work function depends to a greater degree on the characteristics of the surface layer than on the composition of other layers. A similar picture was obtained in terms of the jellium model [23] for the adsorption of alkali metals, e.g., cesium, on substrates of transition and noble metals.

In this work, we tried to describe the behavior of Cs in the same manner as in the case of Ni and Co (see

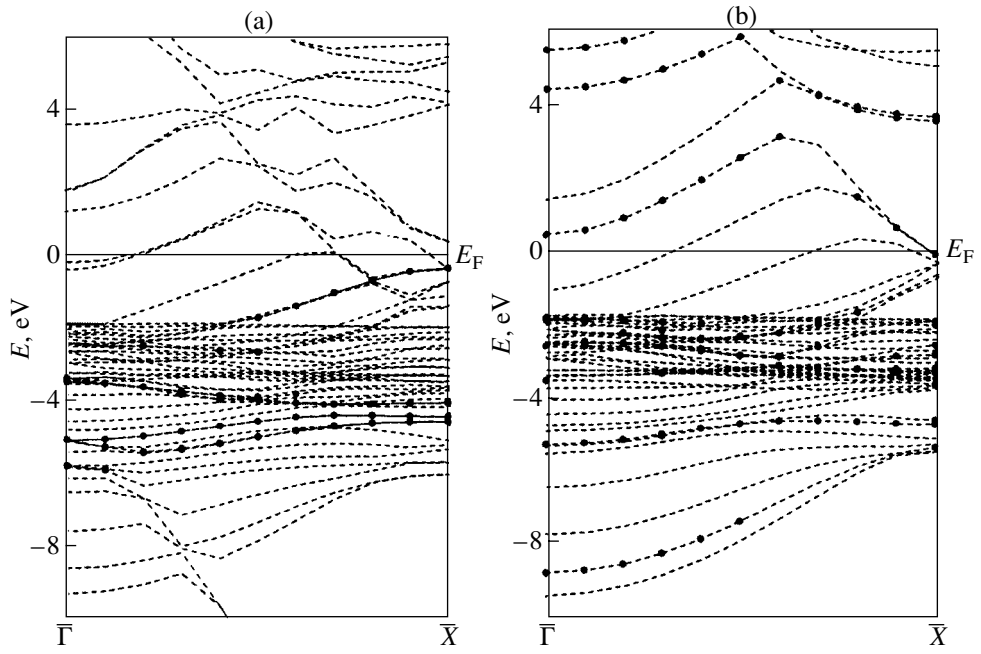

Fig. 5. Dispersion curves $E(k)$ along the Δ direction in the BZ for (a) Cs/Cu(001) and (b) Cu(001).

above), namely, as an additional atomic layer. Several calculations were performed for both the $p(1 \times 1)$ and $c(2 \times 2)$ structures in order to reduce the concentration of the adsorbate. The use of the $c(2 \times 2)$ and $p(1 \times 1)$ structures for analyzing adsorption does not lead to substantial changes in electron characteristics but significantly reduces the required computational capability in the latter case. The evolution of the total and local densities of states for this case is displayed in Fig. 4. Although the DOS of Cs is sufficiently uniformly distributed over the entire energy range, the greatest contribution comes from cesium only near the bottom of the *d* band of copper and near the Fermi level. In fact, the states from –8 eV to approximately –25 eV (they are not given in full in Fig. 4) are caused by the contributions from Cs. Changes in the LDOS of the surface copper atom are pronounced more strongly than in the jellium model [23], in particular, the center of gravity is shifted from the Fermi level, but on the whole the results are in good agreement with those obtained in [23]. An analysis of partial densities of states of cesium and of the surface and subsurface copper atoms shows that the interaction of the adsorbate with the substrate has a local character and depends on the geometry of the adsorbate [24, 25], i.e., on its position with respect to the substrate atoms. It is evident that the changes will be most significant for the surface states of copper located near the Fermi energy. We recall that the *d* band of copper is occupied almost completely. To the surface states, we refer only those states whose wave functions are localized in the surface and subsurface layers and in vacuum spaces for which the probability of localization of the wave function is greater than 80%. The existence of a sharp peak shifted toward the top of the *d* band as compared to the DOS of the bulk material may be related to strongly localized Tamm states lying in the interval from –2.0 to –3.0 eV. The photoemission spectra exhibit a substantial weakening of the sharp maximum near the upper boundary of the *d* band upon chemisorption of various adsorbates on the Cu(001) surface [35]; note that this weakening is independent of the photon energy and the adsorbate nature and that this effect is explained by the properties of only the substrate itself. The surface states are shifted upon chemisorption because of the formation of bonds with hemisorbed particles. For example, at the $\bar{\Gamma}$ point of the BZ near the Fermi level, there is a state with an almost parabolic band (Fig. 5b). In [23], this state is considered to be surface-related; in our calculation, this state will be surface if we use a weaker criterion (a less than 75% probability of localization). Figure 6a displays a contour map of distribution of the charge density for this state. As the authors of [23] assert, it is precisely this state (with a dz^2 symmetry) that is predominant upon the interaction with cesium. In our scheme, this state is not a pure dz^2 state but does contain admixtures of *s* and *pz* orbitals. Upon chemisorption, cesium electrons gradually begin interacting with surface states located near the Fermi energy, which leads to their occupation and shift from E_F, as well as to the appearance of other cesium-related states with a parabolic dispersion law below the Fermi energy. At the same time, we should note surface states lying near point $\bar{X}$, which are not shown in [23]. These states are located much closer to the Fermi level than the above state at the $\bar{\Gamma}$ point of the

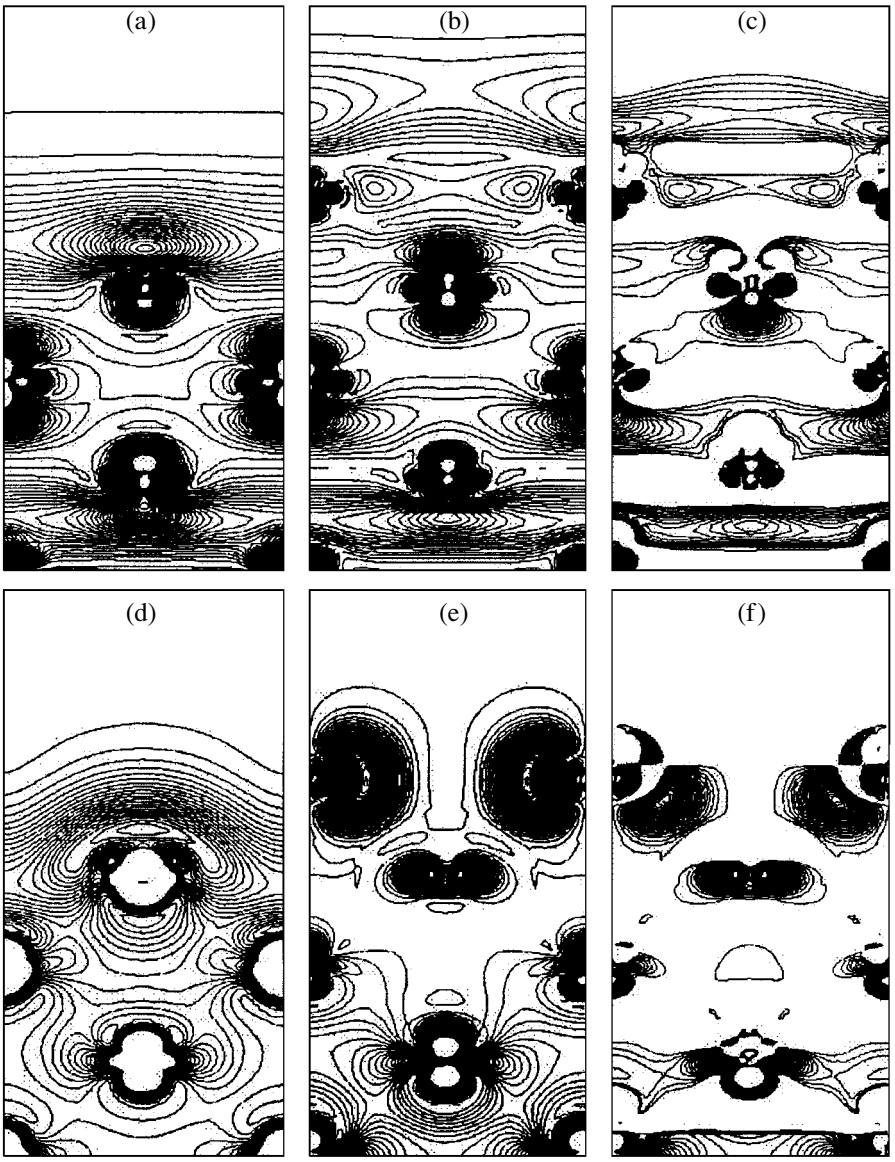

Fig. 6. Contour maps of the distribution of charge densities for surface states located near the Fermi level at the points (a, b) $\bar{\Gamma}$ and (d, e) $\bar{X}$ in Cu(001) and Cs/Cu(001), respectively. (c, f) The differences in the concentrations of the valence electrons at the same point of the BZ for the above two systems, respectively.

BZ. The charge density of the state at the point $\bar{X}$ is shown in Fig. 6d. This state has a more complex orbital composition (dx^2 and $px + py$) and is shifted upon the interaction with cesium away from the Fermi level. In the same energy range, a series of cesium-related surface states appears near –17 eV (Fig. 5a). The states lying near the $\bar{X}$ point of the BZ may be responsible for a small peak in the DOS curve in the immediate vicinity of E_F (Fig. 4). In addition, in copper with a single cesium monolayer, surface states lying above the Fermi level are completely absent.

Some of the above features can be due to the different approaches used in our work and in [23]. It is evident that in our model the interactions are local and depend on the position of the adsorbate at the substrate. In the jellium model, substantial changes are only related to a redistribution of charge in the region of the jellium–vacuum contact, whereas we also take into account changes that are observed below the bottom of the *d* band, in the range from –10 to –26 eV, where states caused by cesium appear. In part, these states are shown in Fig. 4, which also displays the total DOS of copper with a coating of 0.5 ML of Cs. The bonding of cesium and copper is determined by strongly hybridized *s–s* and *s–d* states. We should also note the appearance of localized *p*-type Cs states near the Fermi energy. Figures 6c and 6f show positive values of the differences in the charge densities of valence electrons

of pure copper and copper coated with cesium at the $\bar{\Gamma}$ and $\bar{X}$ points. As is seen from the figure, the cesium–copper interaction is pronounced more strongly for the $\bar{X}$ rather than for the $\bar{\Gamma}$ point, in contrast to [23]. An analysis of the results obtained shows that the potential barrier decreases upon cesium adsorption and the electrons of the adsorbate sufficiently uniformly fill the substrate. With increasing cesium concentration, the fraction of the transferred charge decreases and part of the charge remains on the cesium-adlayer side (see Figs. 6c, 6f).

The estimation of the work function φ for 1-ML Cs/Cu(001) yields a very sharp decrease in φ as compared to its value for pure copper. At the same time, the value obtained (φ = 2.83 eV) is somewhat overestimated; the experimentally obtained value is 2.07 eV, while the jellium model gives φ = 1.7 eV [23]. The calculations for the $c(2 \times 2)$ structure yield even greater values, 3.39 and 3.16 eV for 0.5 and 1 ML of cesium, respectively, but satisfactorily reproduce the result for pure copper (4.76 eV). A further decrease in Cs concentration to 0.25 ML for Cs/Cu(001) did not lead to a substantial change in φ. The estimations performed for Cs adsorbed on a nine-layer Au(001) film indicate a decrease in the work function from 5.48 to 2.19 eV. The work function for Au(001) is in good agreement with both experiment (5.1–5.5 eV) and with the value 5.39 eV found in [36]. The authors of [23] obtained a value of 6.4 eV for Au(001), which exceeds the experimental value by 1 eV. This is explained in [23] by the unsatisfactory description of the substrate as a three-layer film. However, as was shown in our investigations for the three-layer film Cu(001) $c(2 \times 2)$ and in [6], the work function only slightly changes beginning precisely from this thickness. At the same time, we believe that this film thickness cannot be used to correctly describe the dependence of the work function on the cesium concentration. In addition, the equilibrium position of the adsorbate should be correctly determined. In our calculation, the location of Cs was considered to be fixed on a relaxed substrate. Unfortunately, such a calculation requires large computational resources. Note that the work function estimated in our work for Cs/Au(001) (2.19 eV) is in satisfactory agreement with the result of [23] (1.9 eV) and with experimental values (1.81–2.0 eV [23, 37]). In this case, the lighter cesium atoms appear not to cause any strong changes in the interlayer spacings.

4. CONCLUSIONS

Thus, the results obtained permit us to conclude that the film model satisfactorily describes the interaction between an adsorbate and a metal and can be applied even for such adsorbates as cesium. The calculations show a significant decrease in the work function due to the chemisorption of cesium (in contrast to cobalt and nickel) on a copper substrate, although the value of φ itself is overestimated as compared to the experimental value. Knowledge of the distributions of local electron densities and charge densities is very useful for analyzing the magnitude of reactivity of a surface. We distinguished magnitude of states responsible for the adsorbate–metal interaction. If the adsorbate is a transition metal, then strong *d–d* hybridization of the states of the adsorbate and the copper substrate (or the transition-metal substrate) is observed. At the same time, the interaction of the copper surface with cesium is determined by *s–s* and *s–d* hybridization. The reactivity of the surface is primarily determined by local interactions, although in the case of cesium its states almost uniformly cover the substrate; therefore, the dependence on the location of the adsorbate is less significant in this case than, e.g., in the case of hydrogen–metal interactions. Unfortunately, it is very difficult to investigate the sufficiently low concentrations of adsorbates within the film model. It is commonly assumed at present that it is the ionic component of bonding, predominant in the case of low concentrations of cesium, that is responsible for the sharp decrease in the work function. This problem requires additional investigation; however, it is evident that, beginning from 0.25 ML of Cs on Cu(001) or Au(001) surfaces, the work function is almost completely determined by the characteristics of cesium, as in the case of multilayer structures of transition metals or in alloys, in which the work function mainly depends on the characteristics of the surface layer rather than on the composition of the substrate.

ACKNOWLEDGMENTS

This work was supported in part by the Russian Foundation for Basic Research, project no. 02-02-16336a.

REFERENCES

1. J. Jepsen, J. Madsen, and O. K. Andersen, Phys. Rev. B **26** (6), 2790 (1982).
2. S. Ohnishi, A. J. Freeman, and M. Weinert, Phys. Rev. B **28** (12), 6741 (1983).
3. C. L. Fu and A. J. Freeman, Phys. Rev. B **33** (3), 1755 (1986).
4. C. L. Fu and A. J. Freeman, J. Magn. Magn. Mater. **69** (1), L1 (1987).
5. Chun Li, A. J. Freeman, and C. L. Fu, J. Magn. Magn. Mater. **75** (1), 53 (1988).
6. R. Pencheva and M. Scheffler, Phys. Rev. B **61** (3), 2211 (2000).
7. M. Eder, J. Hafner, and E. G. Moroni, Phys. Rev. B **61** (17), 11492 (2000).
8. P. Scheffer, C. Krembel, M. C. Hanf, and G. Gewinner, Surf. Sci. **400** (1), 95 (1998).
9. S. Blugel and P. Dederichs, Europhys. Lett. **9** (6), 597 (1989).
10. S. Blugel, Appl. Phys. A: Mater. Sci. Process. **63** (7), 595 (1996).
11. D. Spisak and J. Hafner, J. Phys.: Condens. Matter **12** (7), L139 (2000).

12. M. Wuttig, Y. Gauthier, and S. Blugel, Phys. Rev. Lett. **70** (23), 3619 (1993).
13. D. Spisak and J. Hafner, Phys. Rev. B **61** (6), 4160 (2000).
14. O. Rader, W. Gudat, C. Carbone, *et al.*, Phys. Rev. B **55** (8), 5404 (1997).
15. D. Spisak and J. Hafner, J. Phys.: Condens. Matter **11** (33), 6359 (1999).
16. S. Meza-Aguilar, O. Elmouhssine, H. Dreysse, and C. Demangeat, Comput. Mater. Sci. **17** (6), 464 (2000).
17. H. P. Bonzel, Surf. Sci. **43** (1), 8 (1988).
18. P. Soukiassian, R. Riwan, J. Lecante, *et al.*, Phys. Rev. B **31** (8), 4911 (1985).
19. N. D. Lang and W. Kohn, Phys. Rev. B **3** (4), 1215 (1971).
20. E. Wimmer, A. J. Freeman, J. R. Hiskes, and A. M. Karo, Phys. Rev. B **28** (6), 3074 (1983).
21. S. R. Chubb, E. Wimmer, A. J. Freeman, *et al.*, Phys. Rev. B **36** (8), 4112 (1987).
22. Ning Wang, K. Chen, and Ding-Sheng Wang, Phys. Rev. Lett. **56** (25), 2759 (1986).
23. Ru-Gian Wu and Ding Sheng Wang, Phys. Rev. B **41** (1), 18 (1990).
24. A. Eichler, J. Hafner, and G. Kresse, J. Phys.: Condens. Matter **8** (40), 7659 (1996).
25. Kim Jai Sam, G. Lee, Y. M. Koo, *et al.*, Int. J. Hydrogen Energy **27** (4), 403 (2002).
26. P. Blaha, K. Schwarz, and J. Luitz, *WIEN97* (Vienna Univ. of Technology, 1997); P. Blaha, K. Schwarz, P. Sorantin, and S. B. Trickey, Comput. Phys. Commun. **59** (5), 399 (1990) (improved and updated Unix version of the origin copyrighted WIEN-code).
27. Q. T. Jiang, P. Fenter, and T. Gustafsson, Phys. Rev. B **44** (11), 5773 (1991).
28. P. O. Gartland, S. Berge, and B. J. Slagsvold, Phys. Rev. Lett. **28** (12), 738 (1972).
29. G. A. Hass and R. E. Thomas, J. Appl. Phys. **48** (1), 86 (1977).
30. G. G. Tibbets, J. M. Burkstrand, and J. C. Tracy, Phys. Rev. B **15** (8), 3652 (1977).
31. S. H. Kim, K. S. Lee, H. G. Min, *et al.*, Phys. Rev. B **55** (12), 7904 (1997).
32. P. Srivastova, F. Wilhelm, A. Ney, *et al.*, Phys. Rev. B **58** (9), 5701 (1998).
33. S. V. Mankovsky, A. A. Ostroukhov, V. M. Floka, and V. T. Tcherepin, Vacuum **48** (3), 245 (1997).
34. S. E. Kulkova, D. V. Valujsky, Kim Jai Sam, *et al.*, Phys. Rev. B **65** (8), 85410 (2002).
35. *Theory of Chemisorption*, Ed. by J. R. Smith (Springer, Berlin, 1980; Mir, Moscow, 1983).
36. R. Eibler, H. Erschbaumer, C. Temnitschka, *et al.*, Surf. Sci. **280** (5), 398 (1993).
37. *Tables of Physical Data: Reference Book*, Ed. by I. K. Kikoin (Atomizdat, Moscow, 1976), p. 444.

Translated by S. Gorin

Physics of the Solid State, Vol. 45, No. 3, 2003, pp. 598–602. Translated from Fizika Tverdogo Tela, Vol. 45, No. 3, 2003, pp. 567–571.

POLYMERS AND LIQUID CRYSTALS

Specific Features of the Approximation of the Dielectric Spectra of Alkylcyanobiphenyl Liquid Crystals

B. A. Belyaev, N. A Drokin, V. F. Shabanov, and V. N. Shepov

Kirensky Institute of Physics, Siberian Division, Russian Academy of Sciences, Akademgorodok, Krasnoyarsk, 660036 Russia

e-mail: belyaev@iph.krasn.ru

Received June 5, 2002

Abstract—The frequency dependences of the longitudinal and transverse permittivities of oriented nematic liquid crystals belonging to the alkylcyanobiphenyl group *n*CB (*n* = 5–8) are measured in the relaxation region in the meter and decimeter wavelength ranges. It is established that the dispersion of the longitudinal permittivity is well approximated by the sum of two Debye processes with different relaxation times. The frequency dependence of the transverse permittivity is represented by the dispersion relation with a continuous distribution of relaxation times in a specified time range. It is demonstrated that, in the high-frequency range (f > 200 MHz), in which the dielectric spectra exhibit a number of weakly pronounced dispersion features, the total dispersion of the permittivity is adequately described by the sum of relaxation and resonance processes. © *2003 MAIK "Nauka/Interperiodica".*

1. INTRODUCTION

As a rule, the observed dependence of the permittivity of liquid crystals on the frequency f has been analyzed in terms of the orientational (dipole) mechanisms of dielectric polarization of rigid anisotropic molecules [1–3]. Within this approach, the dispersion of the longitudinal (parallel) $\varepsilon_\parallel(f)$ and transverse (perpendicular) $\varepsilon_\perp(f)$ permittivities of an oriented liquid crystal is associated with rotations of molecules about the long and short molecular axes. It is well known that, for liquid crystals with a large positive anisotropy (for example, liquid crystals belonging to the alkylcyanobiphenyl group *n*CB), the low-frequency (f = 0.1–10 MHz) part of the dispersion of the longitudinal permittivity $\varepsilon_\parallel(f)$ is well approximated by a simple Debye equation with one relaxation time [4–6]. The frequency dependences of the transverse permittivity $\varepsilon_\perp(f)$ are characterized by noticeable deviations from the Debye behavior in the low-frequency and microwave ranges. A more correct approximation of the dependence $\varepsilon_\perp(f)$ can be obtained using the Cole–Davidson or Havriliak–Negami relations [7, 8]. However, the assessment of the accuracy of the above approximations is complicated by the lack of experimental information. Traditionally, the permittivity in the microwave frequency range has been measured at several fixed frequencies with the use of measuring cells of different designs. The errors in these dielectric measurements differ significantly. In the majority of works dealing with the permittivity, the dielectric dispersion was determined only up to frequencies f ~ 10–15 MHz.

In our recent work [9], we carefully measured the dielectric spectra of liquid crystals of the *n*CB group in the decimeter wavelength range. It was found that, for all the liquid crystals studied, an increase in the frequency is accompanied by the appearance of several low-intensity narrow-band dispersion regions of the resonance nature, which are clearly distinguished against the background of the slowly descending orientational part of the dispersion of the real permittivities $\varepsilon'_\perp(f)$ and $\varepsilon'_\parallel(f)$. It should be noted that similar dispersion regions were revealed earlier for a 5CB crystal [10]. The resonances were observed in the frequency range 200 MHz < f < 1000 MHz. As was shown in our previous work [11], the real part of the dielectric spectra $\varepsilon'(f)$ can be approximated by the sum of two processes described in terms of the Debye equation for dipole relaxation and the appropriate equations for dielectric resonances. However, such a simple approximation leads not only to disagreement between theory and experiment in certain spectral ranges but also to a considerable difference between the longitudinal ($\tau_\parallel$) and transverse ($\tau_\perp$) relaxation times calculated in our earlier work [11] and determined by other authors [4–8].

In this work, we measured the dielectric spectra of liquid crystals of the alkylcyanobiphenyl group *n*CB (*n* = 5–8) over a wide range of frequencies (from 1 to 1000 MHz) and analyzed the possible numerical approximations of these spectra in a more correct form.

2. EXPERIMENTAL TECHNIQUE

Since the dispersion dependences $\varepsilon(f)$ of alkylcyanobiphenyl liquid crystals in the frequency range 1–10 MHz were well known, the low-frequency data on the dielectric spectra were taken from [4–6]. These data were complemented by the results of check measurements performed by the resonance method at several frequencies with the use of a Tesla BM560 stan-

dard *Q*-meter and a measuring cell in the form of a parallel-plate capacitor.

As is known, dielectric measurements of materials with the use of resonance methods in the decimeter wavelength range 100–1000 MHz involve considerable difficulties. In our measurements of liquid crystals, this problem was solved using specially devised sensors based on microstrip resonators. The sensor design and the technique used in resonance measurements [11] made it possible to determine the dielectric characteristics of liquid crystals in the aforementioned frequency range with absolute errors no larger than $\delta\varepsilon' \sim 0.05$ and $\delta\varepsilon'' \sim 0.01$.

The longitudinal and transverse permittivities of liquid-crystal samples were measured in the nematic phase in the orienting magnetic field $H = 2.5$ kOe. During measurements of the high-frequency dielectric spectra, the temperature T in a thermostat was maintained accurate to within ±0.1 K. For each sample, the temperature of high-frequency dielectric measurements was chosen equal to the temperature for which the most comprehensive data on the dielectric dispersion in the low-frequency range were available in the literature. As a rule, these temperatures fall in the range $(T_{ni} - 5\ \text{K}) < T < (T_{ni} - 3\ \text{K})$, where T_{ni} is the temperature of transition from the nematic state to the isotropic state.

3. RESULTS AND DISCUSSION

Figure 1 shows the frequency dependences of the real permittivities $\varepsilon'_\perp(f)$ and $\varepsilon'_\parallel(f)$ of the 5CB liquid crystal in the frequency range 1–1000 MHz at the temperature $T = 35$°C. The data on the permittivity in the low-frequency spectral range 1–10 MHz were taken from [4, 5]. The frequency dependences of the permittivities $\varepsilon'_\parallel(f)$ and $\varepsilon'_\perp(f)$ in the Debye approximation with relaxation times $\tau_\parallel = 28$ ns and $\tau_\perp = 3$ ns are depicted by solid and dashed lines, respectively. The approximated dependences correspond to the best agreement between the Debye theory and the experiment in the frequency range 1–10 MHz; however, they cannot be considered a satisfactory approximation over the entire range of measurements. Actually, the experimental points substantially deviate from the curve $\varepsilon'_\parallel(f)$ in the range 15 MHz $< f <$ 500 MHz and from the curve $\varepsilon'_\perp(f)$ at $f > 80$ MHz.

The frequency dependence of the longitudinal permittivity $\varepsilon''_\parallel(f)$ can be more accurately approximated using the sum of two Debye relaxation processes [12]; that is,

$$\varepsilon'_\parallel(f) - n_e^2 = \frac{(\varepsilon'_{\parallel 0} - n_e^2)g_1}{1 + (2\pi f)^2\tau_{\parallel 1}^2} + \frac{(\varepsilon'_{\parallel 0} - n_e^2)g_2}{1 + (2\pi f)^2\tau_{\parallel 2}^2}, \quad (1)$$

where n_e is the extraordinary refractive index, $\varepsilon'_{\parallel 0}$ is the static permittivity, g_1 and g_2 are the weighting factors of two processes ($g_1 + g_2 = 1$), and $\tau_{\parallel 1}$ and $\tau_{\parallel 2}$ are the relaxation times corresponding to these processes. This approximation is based on the results obtained by Buka *et al.* [13], who demonstrated that the frequency dependence of the imaginary part of the permittivity $\varepsilon''_\parallel(f)$ for 7CB and 7OCB liquid crystals can exhibit two absorption maxima.

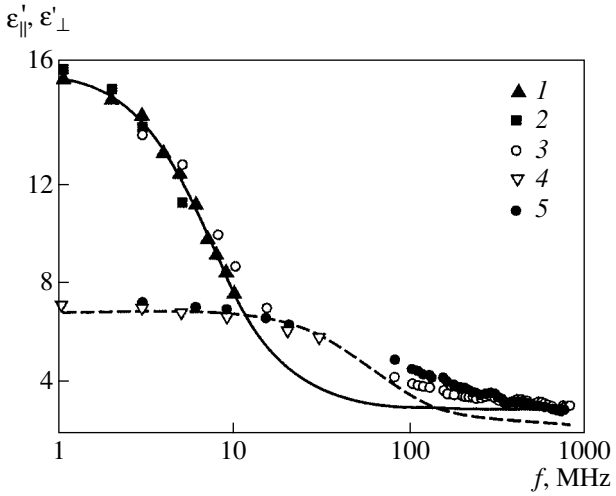

Fig. 1. Frequency dependences of the longitudinal and transverse permittivities of the 5CB liquid crystal and their approximation according to the Debye formulas with (*1, 2, 4*) data taken from [4, 5, 7] and (*3, 5*) data obtained in this work.

The dispersion curve obtained by approximating the experimental data on $\varepsilon'_\parallel(f)$ for the 5CB liquid crystal with the use of formula (1) is represented by the solid line in Fig. 2. This curve was constructed for the following parameters of the liquid crystal: $\varepsilon'_{\parallel 0} = 16.4$, $\tau_{\parallel 1} = 24 \times 10^{-9}$ s, $\tau_{\parallel 2} = 7.0 \times 10^{-10}$ s, $n_e = 1.72$, $g_1 = 0.92$, and $g_2 = 0.08$. As can be seen from Fig. 2, the frequency dependence of the longitudinal permittivity, which is calculated within the proposed approximation based on the sum of two relaxation processes, almost completely coincides with the experimental curve over the entire frequency range covered. Dashed line *1* in Fig. 2 corresponds to the frequency dependence calculated at weighting factors $g_1 = 1$ and $g_2 = 0$ and fits the experimental data well only in the low-frequency dispersion region. Dashed line *2* represents the dispersion dependence obtained at $g_1 = 0.92$ and $g_2 = 0.08$, which, by contrast, agrees reasonably with the experimental data only in the high-frequency dispersion region. Dot-dashed line *3* shows the refractive index n_e^2. As in the case of 5CB liquid crystals, close agreement between the calculated and experimental frequency dependences of the longitudinal permittivity $\varepsilon'_\perp(f)$ is observed for all the alkylcyanobiphenyl liquid crystals under investigation. The parameters of the Debye approximation for these compounds are listed in Table 1.

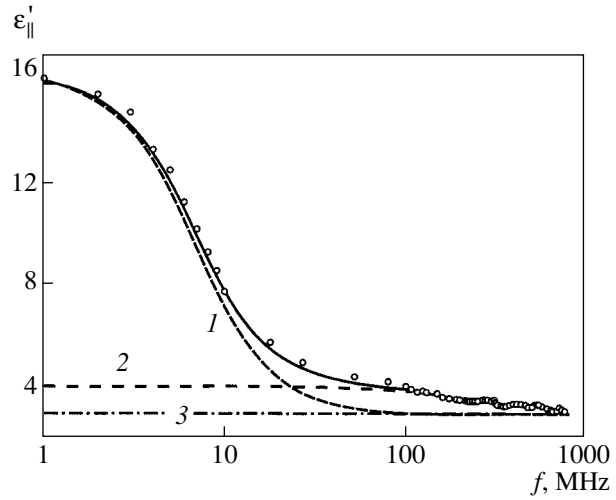

Fig. 2. Frequency dependence of the longitudinal permittivity of the 5CB liquid crystal (points), the approximation by the sum of two Debye processes with different relaxation times (solid line), and the approximations according to the Debye formulas with (*1*) the longest relaxation time and (*2*) the shortest relaxation time. Line *3* indicates the n_e^2 level.

According to the universally accepted concepts regarding the possible mechanisms of dielectric polarization in liquid crystals, the occurrence of two relaxation processes can be explained, in particular, by the misalignment of the dipole moment μ and the long axis of the liquid-crystal molecule. In this case, the longitudinal permittivity contains a contribution from the transverse permittivity and vice versa. This contribution is governed by the transverse component of the dipole moment of molecules. In turn, the transverse component is determined by the deviation of the dipole moment from the long axis of the molecule. As a consequence, the computational formulas for the static permittivities $\varepsilon'_{\parallel 0}$ and $\varepsilon'_{\perp 0}$ include not only the magnitude of the dipole moment of the molecule μ but also the angle β between the dipole moment and the long axis of the molecule [1–3]. The angle β can be estimated from the following condition: the tangent β is equal to the ratio g_2/g_1. The angles β thus calculated are also given in Table 1. Note that, for the liquid crystals studied, these angles do not exceed 5°.

It is of interest that, according to the results obtained in [14, 15], the β angles for 6CB and 7CB liquid crystals are equal to zero. In our opinion, the disagreement with the β angles presented in Table 1 stems from the fact that, in [14, 15], the permittivities were measured in the frequency range up to 10 MHz and the experimental data on $\varepsilon'_\perp(f)$ were approximated by the Debye dependence with one relaxation time. As is known, this approximation adequately describes experimental data in a narrow frequency range.

Analysis showed that the approximation of the transverse permittivity $\varepsilon'_\parallel(f)$ by the sum of two Debye processes with different relaxation times offers poor agreement with the experimental data. The best agreement between the calculated and experimental results for all the samples can be achieved using the equation with a continuous distribution of relaxation times [12]:

$$\varepsilon'_\perp(f) - n_0^2 = (\varepsilon'_{\perp 0} - n_0^2)\int_0^\infty \frac{G(\tau)}{1 + (2\pi f\tau)^2}d\tau, \qquad (2)$$

where n_0 is the ordinary refractive index and $G(\tau)$ is the distribution function of relaxation times. This approximation can be justified by the fact that the observed considerable deviation of the calculated spectrum $\varepsilon'_\perp(f)$ from the experimental points in the high-frequency range (Fig. 1) is most likely due to small-scale motions of mobile molecular fragments, for example, alkyl groups. Intramolecular motions can substantially affect the permittivity starting from the orientational dispersion region up to frequencies in the infrared region. Since intramolecular motions exhibit a wide variety of types, the dielectric relaxation times can be conveniently represented in the form of a continuous distribution in a specified time range. On this basis, the permittivity $\varepsilon'_\perp(f)$ can be approximated by the following asymmetric distribution function of relaxation times [12]:

$$G(\tau) = \frac{1}{A}\left(\frac{1}{\tau^{1-p}}\right) \quad \text{at} \quad \tau_{\perp 2} \le \tau \le \tau_{\perp 1},$$
$$G(\tau) = 0 \quad \text{at} \quad \tau_{\perp 2} > \tau > \tau_{\perp 1}, \qquad (3)$$

where p is a nonvanishing number (less than unity) and A is the weighting factor, which is defined by the expression

$$A = \frac{\tau_{\perp 1}^p - \tau_{\perp 2}^p}{p}. \qquad (4)$$

As a result, the frequency dependences thus numerically approximated for all the *n*CB liquid crystals under investigation agree well with the measured spectra

Table 1. Parameters of the Debye approximation for the longitudinal permittivity of *n*CB liquid crystals

n	$\varepsilon'_{\parallel 0}$	g_1	g_2	$\tau_{\parallel 1} \times 10^9$, s	$\tau_{\parallel 2} \times 10^{10}$, s	β, deg	n_e
5	16.4	0.92	0.08	24	7.0	5.0	1.72
6	16.1	0.95	0.05	38	7.6	3.0	1.68
7	15.2	0.94	0.06	25	8.0	3.7	1.74
8	13.8	0.94	0.06	30	3.9	3.7	1.65

$\varepsilon'_\perp(f)$ over the entire frequency range covered. The sufficiently high accuracy of the proposed approximation is illustrated in Fig. 3. In this figure, the solid line represents the results of calculations and points refer to experimental data on the real part of the transverse permittivity for the 7CB liquid crystal. Table 2 lists the static permittivities $\varepsilon'_{\perp 0}$, the refractive indices n_0, and the boundary relaxation times $\tau_{\perp 1}$ and $\tau_{\perp 2}$ determined for all the studied liquid crystals. This table also presents the relaxation times obtained by approximating the dielectric spectra with the use of the Debye equation with one relaxation time $\tau_\perp$ (as is shown for the 5CB sample in Fig. 1). These relaxation times characterize the rotation of molecules about the long axes and are close in magnitude to the relaxation times determined in [7, 8]. As can be seen, the relaxation times $\tau_\perp$ fall in the range between $\tau_{\perp 1}$ and $\tau_{\perp 2}$. It follows from Table 2 that, as the number of alkyl groups in the liquid-crystal molecule increases, the relaxation time $\tau_{\perp 1}$ decreases by approximately one order of magnitude, whereas the relaxation time $\tau_{\perp 2}$ decreases by more than two orders of magnitude. This indicates that the mobility of alkyl groups increases with increasing n and that their motion makes a considerable contribution to the high-frequency transverse permittivity.

It seems likely that the alkyl tails are also responsible for the resonance dispersion regions observed for all liquid crystals of the alkylcyanobiphenyl group at frequencies $f > 200$ MHz [9, 10]. Although these resonances are characterized by low intensities, they are clearly distinguished in the high-frequency range of the dielectric spectra $\varepsilon'_\parallel(f)$ and $\varepsilon'_\perp(f)$ (Figs. 1–3). The high-frequency portions of the dispersion curves of the longitudinal (open circles) and transverse (closed circles) permittivities for the 7CB liquid crystal are depicted on an enlarged scale in Fig. 4. The dashed line represents the result of the numerical approximation performed for the spectrum $\varepsilon'_\parallel(f)$ according to the above technique, and the dot-dashed line indicates the n_e^2 level to which the permittivity $\varepsilon'_\parallel$ tends when $f \longrightarrow \infty$. The origin of these resonances remains unclear. Most likely, they are associated with the excitation of collective vibrations of the molecular core and one or several nearest methylene fragments of the alkyl tail whose frequencies fall in the decimeter wavelength range.

As can be seen from Fig. 4, the experimental points in the region of the dielectric resonances substantially deviate from the Debye relaxation spectrum for both the longitudinal $\varepsilon'_\parallel(f)$ and transverse $\varepsilon'_\perp(f)$ permittivities. Therefore, in order to approximate more correctly the dielectric spectra of liquids crystals of the alkylcyanobiphenyl group in the microwave range, it is necessary to use equations that describe both relaxation and resonance processes. The frequency dependence of the

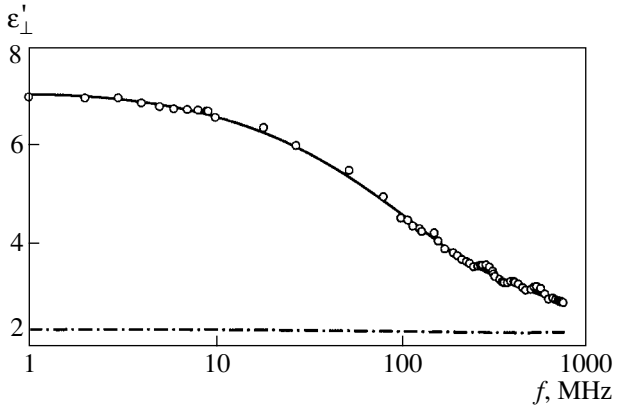

Fig. 3. Frequency dependence of the transverse permittivity of the 7CB liquid crystal (points) and the approximation in terms of according to the Debye relaxation processes with a continuous distribution of relaxation times (solid line). The dot-dashed line indicates the n_0^2 level.

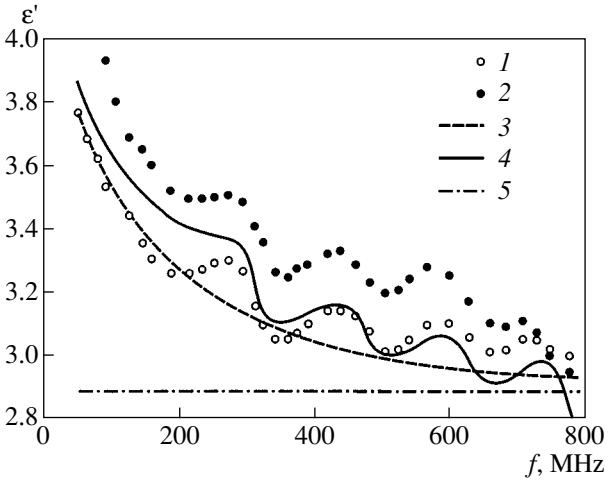

Fig. 4. Frequency dependences of the (*1*) longitudinal and (*2*) transverse permittivities of the 7CB liquid crystal and the approximations of the longitudinal permittivity $\varepsilon_\parallel(f)$ according to (*3*) the Debye formulas and (*4*) the sum of the Debye and resonance processes. Line *5* indicates the n_e^2 level.

real part of the permittivity $\varepsilon'(\omega)$ in the portion involving m resonances can be written in the form [16]

$$\varepsilon'(\omega) - \varepsilon_\infty = \sum_{i=1}^{m} \Delta\varepsilon'_i \left[\frac{\omega_{0i}^2(\omega_{0i}^2 - \omega^2)}{(\omega_{0i}^2 - \omega^2)^2 + r_i^2\omega^2} \right], \qquad (5)$$

Table 2. Parameters of the approximation for the transverse permittivity of *n*CB liquid crystals

n	$\varepsilon'_{\perp 0}$	$\tau_{\perp 1} \times 10^8$, s	$\tau_{\perp 2} \times 10^{12}$, s	$\tau_\perp \times 10^9$, s	n_0
5	6.8	9	60	2.3	1.55
6	6.5	2	98	4.2	1.54
7	6.2	1.2	3	3.4	1.52
8	6.2	1.2	0.15	3.8	1.53

where $\omega_{0i} = 2\pi f_{0i}$ is the frequency of the ith resonance, $\Delta\varepsilon_i'$ is the amplitude of the ith resonance, and r_i is the relaxation frequency of the ith resonance. In Fig. 4, only the first four most intense resonances are clearly seen in the frequency dependences of the permittivities $\varepsilon_\parallel'$ and $\varepsilon_\perp'$ in the range up to 800 MHz. For this reason, the experimental dependence $\varepsilon_\parallel'(f)$ was approximated using the sum of Debye relaxation processes (1) and resonance processes (5) at $m = 4$. The approximating dependence is shown by the solid line in Fig. 4. In the course of the approximation, we determined all the resonance parameters: the natural frequencies $f_{01} = 310$ MHz, $f_{02} = 475$ MHz, $f_{03} = 630$ MHz, and $f_{04} = 780$ MHz; the resonance amplitudes $\Delta\varepsilon_1' = 1.77$, $\Delta\varepsilon_2' = 1.33$, $\Delta\varepsilon_3' = 1.51$, and $\Delta\varepsilon_4' = 1.97$; and the relaxation frequencies $r_1 = 400$ MHz, $r_2 = 550$ MHz, $r_3 = 700$ MHz, and $r_4 = 600$ MHz. It should be noted that the approximation of the transverse permittivity by the sum of Debye relaxation and resonance processes [expressions (2) and (5), respectively] also offers better agreement between the calculated and experimental data.

4. CONCLUSIONS

Thus, the main results obtained in the present work can be summarized as follows: the specific features in the dielectric spectra of liquid crystals of the alkylcyanobiphenyl group were revealed, and the methods of approximating these spectra were proposed and justified. It was demonstrated that the frequency dependence of the longitudinal permittivity $\varepsilon_\perp'(f)$ is well approximated by the sum of two Debye processes with different relaxation times. The transverse permittivity is characterized by a continuous distribution of relaxation times in a specified time range. This distribution is well represented by an asymmetric function. It was shown that the dielectric spectra in the high-frequency range can be adequately described by the sum of the relaxation and resonance processes. The basic parameters of the approximations of the dielectric spectra were determined for all the liquid crystals studied in the *n*CB series.

ACKNOWLEDGMENTS

This work was supported by the Russian Foundation for Basic Research, project no. 00-03-32206.

REFERENCES

1. L. M. Blinov, *Electro-Optical and Magneto-Optical Properties of Liquid Crystals* (Nauka, Moscow, 1978; Wiley, New York, 1983).
2. D. A. Dunmur, M. R. Manterfield, W. H. Miller, and J. K. Dunleavy, Mol. Cryst. Liq. Cryst. **45**, 127 (1978).
3. G. Meier and A. Saupe, Mol. Cryst. **1**, 515 (1966).
4. P. G. Gummins, D. A. Dunmur, and D. A. Laidler, Mol. Cryst. Liq. Cryst. **30**, 109 (1975).
5. B. R. Ratna and R. Shashidar, Mol. Cryst. Liq. Cryst. **42**, 185 (1977).
6. D. Lippens, J. P. Parneix, and A. Chapoton, J. Phys. (Paris) **38**, 1465 (1977).
7. J. M. Wacrenier, C. Druon, and D. Lippens, Mol. Phys. **43** (1), 97 (1981).
8. C. Druon and J. M. Wacrenier, J. Phys. (Paris) **38**, 47 (1977).
9. B. A. Belyaev, N. A. Drokin, V. F. Shabanov, and V. N. Shepov, Fiz. Tverd. Tela (St. Petersburg) **42** (5), 956 (2000) [Phys. Solid State **42**, 987 (2000)].
10. B. A. Belyaev, N. A. Drokin, V. F. Shabanov, and V. N. Shepov, Pis'ma Zh. Éksp. Teor. Fiz. **66** (4), 251 (1997) [JETP Lett. **66**, 271 (1997)].
11. B. A. Belyaev, N. A. Drokin, V. F. Shabanov, and V. N. Shepov, Zh. Tekh. Fiz. **72** (4), 99 (2002) [Tech. Phys. **47**, 470 (2002)].
12. A. A. Potapov and M. S. Mitsek, *Dielectric Polarization* (Irkutsk Gos. Univ., Irkutsk, 1986).
13. A. Buka, P. G. Oven, and A. H. Price, Mol. Cryst. Liq. Cryst. **51**, 273 (1979).
14. E. I. Ryumtsev, S. G. Polushin, A. P. Kovshik, *et al.*, Dokl. Akad. Nauk SSSR **244** (6), 1344 (1979) [Sov. Phys. Dokl. **24**, 118 (1979)].
15. V. N. Tsvetkov, E. I. Ryumtsev, S. G. Polushin, and A. P. Kovshik, Dokl. Akad. Nauk SSSR **254** (3), 619 (1980) [Sov. Phys. Dokl. **25**, 753 (1980)].
16. S. Urban, B. Gestblom, and A. Würflinger, Mol. Cryst. Liq. Cryst. **331**, 113 (1999).

Translated by Borovik-Romanova

Physics of the Solid State, Vol. 45, No. 3, 2003, pp. 603–604.

Instructions for Contributors to the *Fizika Tverdogo Tela* (St. Petersburg) Journal

Manuscripts submitted to the Journal must satisfy the rules given below. Papers in violation of these rules will be rejected.

The manuscript must be accompanied by a covering letter from the institution where the work was performed. The manuscript must be signed by the author (authors) with names (first in initials and surname in full), home addresses, affiliations, and corresponding telephone numbers indicated. The authors should indicate who the corresponding author is. The authors may suggest possible referees for their paper. No proofreading is envisaged. Articles that are rejected are not returned to the authors.

The Journal publishes original papers and invited reviews and overviews concerning various directions in solid-state physics. The main sections of the Journal are as follows.

—Metals and Superconductors.

—Semiconductors and Insulators.

—Defects, Dislocations, and Physics of Strength.

—Magnetism and Ferroelectricity.

—Lattice Dynamics and Phase Transitions.

—Low-Dimensional Systems and Surface Physics.

—Polymers and Liquid Crystals.

—Fullerenes and Atomic Clusters.

Two copies of the manuscript are required. The manuscript should be typed on one side and double-spaced throughout (approximately 30 lines per page, 60 characters per line using 12 or 14 font). The left-hand margin should be no less than 4 cm. Hand-written insets are not acceptable. All pages should be numbered.

On separate sheets, the following data should be given:

—the title of the article,

—authors' complete names (initial before the surname),

—the full name (without any abbreviations) of the institution where the work was performed and its address (postal index, city, country),

—the author's (authors') e-mail address.

The text of the article should be preceded by an abstract (no more than 0.5 type-written page), which should not duplicate the introduction or the conclusion. At the end of the abstract, the institution or fund that supported the research should be indicated (with indication of the grant or project number).

The article should be written in clear, precise language; intermediate calculations should be omitted; and unwieldy or lengthy formulas should be avoided. Authors should avoid repeating in the main text the data presented in tables, graphs, and figure captions and should avoid representing the same numerical results in the form of both tables and graphs. If the sections of the article have no titles, they may be numbered. The abbreviations used in the articles should be explained in the main body of the text.

Measurement units and designations (in the main text, tables, and figures) must be given in Latin.

Illustrations (photographs, charts, and diagrams, all to be referred to as "figures") must be given in duplicate. A minimum number of figures, with a limited number of details, should be used. Figure captions should be given in English.

Figures produced on computer should be of high quality.

Line drawings should be made with Indian ink on white paper or on tracing paper.

Continuous-tone artwork should be presented in the form of glossy photographs. One of the copies should be without letter or number designations (only the image). On the opposite side of the photograph, the upward direction should be indicated with a soft pencil line. Photographs should be attached to the text and not be inserted into it. Paper clips should not be used.

On the opposite side of figures, the authors' names, the article title, and the figure numbers should be indicated.

Figure captions should be presented on a separate sheet. No graphical elements (circles, crosses, or other symbols) should be included in the captions.

Tables should be typed each on separate sheets and be titled. Measurement units must be indicated.

Formulas should be written in large, legible handwriting. Formulas should be numbered continuously throughout the article rather than separately for each section.

In the first copy of the manuscript, *the formulas and designations* should be marked out as follows:

—Greek characters are underlined with a red line,

—script characters are circled with a green pencil,

1063-7834/03/4503-0603$24.00 © 2003 MAIK "Nauka/Interperiodica"

—Gothic characters are circled with a yellow pencil,

—vectors are underlined with a blue line rather than designated with an arrow over the character,

—subscripts and superscripts are marked with a plain pencil using arcs with their ends downward and upward, respectively,

—clearly differentiate between uppercase and lowercase letters that have similar outlines, such as (C, c; K, k; P, p; O, o); letters I (i) and J (j); capital letter i (I) and Arabic number 1 (unity); Arabic 1 and Roman I; vertical bar |, 1 and the prime sign in indices; and Latin *l* (el) and *e*,

—capital letters are underlined with two lines from below ($\underline{\underline{C}}$), while lowercase letters are marked by two bars from above ($\bar{\bar{c}}$).

In the main text, the solidus [/] should be preferably used to designate the operation of division. For exponential functions, the sign "exp" should be used.

Special attention should be paid to the reference format:

—for books, the reference should include the initials and the surnames of all of the authors, the title of the book, the publishing house, year, volume, issue, and the total number of pages (e.g., 54 pp.). If the reference to a particular page is given, then the page number should be indicated after the year, rather than the total number of pages (i.e., p. 54 rather than 54 pp.);

—for periodicals, the reference should contain the initials and the surnames of all authors, the name of the journal, the volume number, the issue number, the first page of the paper, and the year of publication.

For example,

(1) B. P. Aduev, É. D. Aluker, V. V. Gavrilov, R. G. Deich, and S. A. Chernov, Fiz. Tverd. Tela (St. Petersburg) **38**, *12*, 3521 (1996).

(2) V. J. Emery, Phys. Rev. B **14**, *3*, 2989 (1976).

(3) L. D. Landau and E. M. Lifshitz, Kvantovaya mekhanika (Quantum Mechanics), Nauka, M. (1989).

References to Russian publications should be given in Russian.

All references should be given at the end of the manuscript in the order they appear in the main text.

This journal is translated into English and distributed abroad in a joint-cooperation program between the publishers of the *Fizika Tverdogo Tela* journal and the American Institute of Physics.

In sending a manuscript to the editorial office, the authors transfer the copyright to the Russian text and to the translation and publication of the article in English by the American Institute of Physics to the founders and editorial board of the Journal; the authors retain all other rights of possession to the manuscript.

Authors who want to publish their article in the *Fizika Tverdogo Tela* journal must send a letter of the following form to the editorial office.

We, the undersigned authors, ……. …….. …. …
transfer the right of publication to the paper
titled ……
in Russian and English to the institutors and editorial board of the journal *Fizika Tverdogo Tela*.

We confirm that this publication does not violate the copyright of other persons or institutions.

……..
……..Signatures

Date

An electron version of this journal is available at

http://www.ioffe.rssi.ru/journals

Translated by S. Gorin